Informatics Control Measurement
in Economy and Environment Protection

INDEX COPERNICUS INTERNATIONAL

1/2017

Informatyka Automatyka Pomiary

www.e-IAPGOS.pl

w gospodarce i ochronie środowiska

ISSN 2083-0157

Kwartalnik Naukowo-Technicznу

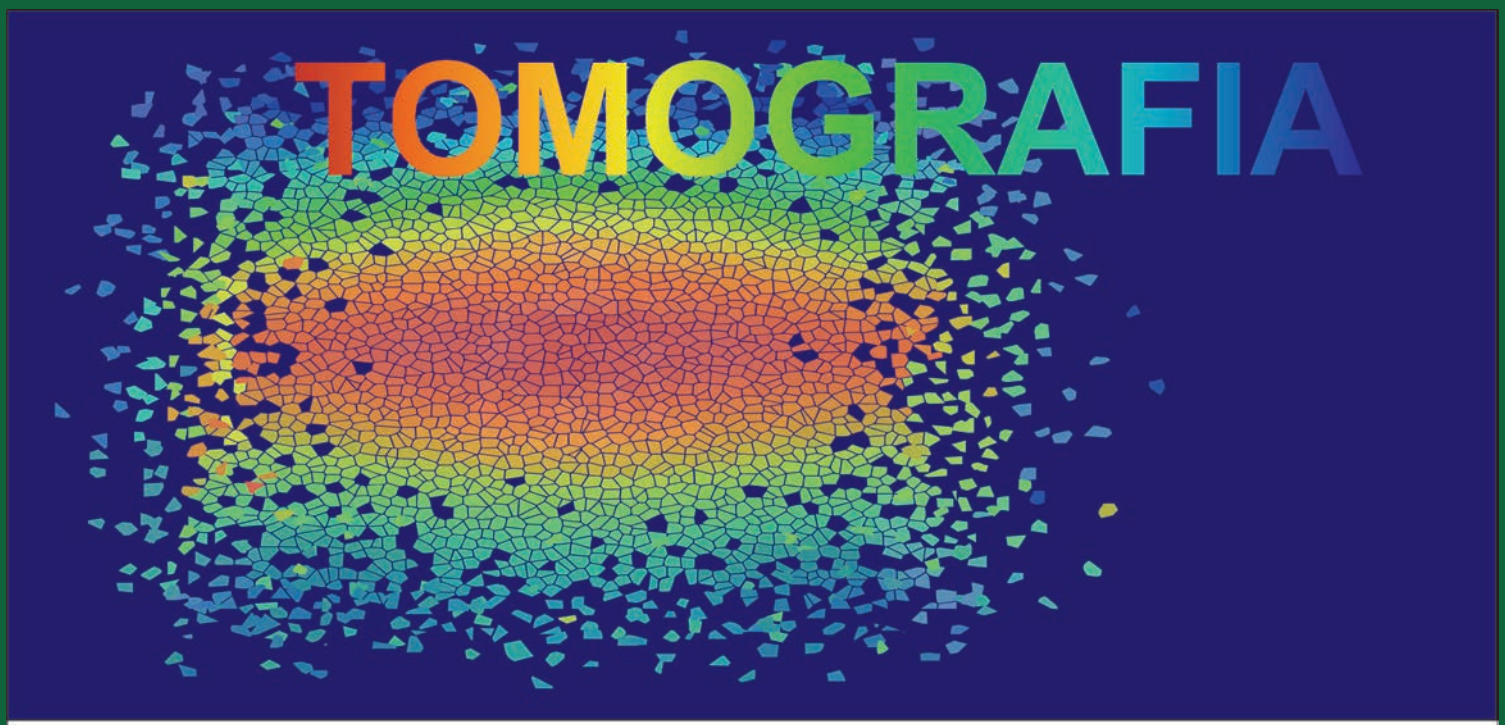

netrix SA
RESEARCH & DEVELOPMENT CENTRE

Instytut Elektrotechniki
Electrotechnical Institute

POLITECHNIKA OPOLSKA

POLITECHNIKA LUBELSKA

POLITECHNIKA WARSZAWSKA
WARSAW UNIVERSITY OF TECHNOLOGY

Politechnika Łódzka

1/2017

styczeń – marzec

Wydanie pod redakcją naukową
prof. dr hab. inż. Waldemara Wójcika

INFORMATYKA AUTOMATYKA POMIARY

W GOSPODARCE i OCHRONIE ŚRODOWISKA

Informatics Control Measurement in Economy and Environment Protection

p-ISSN 2083-0157, e-ISSN 2391-6761, www.e-iapgos.pl

INTERNATIONAL PROGRAMME COMMITTEE – RADA PROGRAMOWO-NAUKOWA

Chairman
Przewodniczący

Waldemar WÓJCIK
Lublin University of Technology,
Lublin, Poland

Members
Członkowie

Kazimierz ADAMIAK
University of Western Ontario,
Ontario, Canada

Darya ALONTSEVA
D.Serikbaev East Kazakhstan
State Technical University,
Ust-Kamenogorsk, Kazakhstan

Shin-ichi AOQUI
Sojo University,
Kumamoto, Japan

Javier BALLESTER
Universidad de Zaragoza,
Saragossa, Spain

Yurii BOBALO
Lviv Polytechnic National
University, Lviv, Ukraine

Oleksy BORYSENKO
Department of Elektronics
and Computer Technics,
Sumy, Ukraine

Hartmut BRAUER
Technische Universität Ilmenau,
Ilmenau, Germany

Kathleen CURRAN
School of Medicine
& Medical Science,
Dublin, Ireland

Milan DADO
University of Žilina,
Žilina, Slovakia

Jarmila DEDKOVA
Brno University of Technology,
Brno, Czech Republic

Andrzej DEMENKO
Poznan University of Technology,
Poznań, Poland

Pavel FIALA
Brno University of Technology,
Brno, Czech Republic

Vladimir FIRAGO
Belarusian State University,
Minsk, Belarus

Ryszard GOLEMAN
Lublin University of Technology,
Lublin, Poland

Jan GÓRSKI
AGH University of Science
and Technology,
Cracow, Poland

Stanisław GRATKOWSKI
West Pomeranian University
of Technology Szczecin,
Szczecin, Poland

Antoni GRZANKA
Warsaw University of Technology,
Warsaw, Poland

Jeni HEINO
Helsinki University of Technology,
Helsinki, Finland

Oleksandra HOTRA
Lublin University of Technology,
Lublin, Poland

Zenon HOTRA
Lviv Polytechnic National
University, Lviv, Ukraine

Mukhtar JUNISBEKOV
M.Kh. Dulaty Taraz
State University,
Taraz, Kazakhstan

Piotr KACEJKO
Lublin University of Technology,
Lublin, Poland

Krzysztof KLUSZCZYŃSKI
Silesian University of Technology,
Gliwice, Poland

Yurii KRAK
Taras Shevchenko National
University of Kyiv,
Kiev, Ukraine

Yurii KRYVONOS
V.M. Glushkov Institute
of Cybernetic of NAS of Ukraine,
Kiev, Ukraine

Piotr KSIĄŻEK
Medical University of Lublin,
Lublin, Poland

Piotr LESIAK
Kazimierz Pułaski
University of Technology
and Humanities in Radom,
Radom, Poland

Georgii LYSYCHENKO
Institute of Environmental
Geochemistry of the National
Academy of Sciences of Ukraine,
Kiev, Ukraine

Volodymyr LYTVYNENKO
Kherson National
Technical University,
Kherson, Ukraine

Artur MEDVIED
Riga Technical University,
Riga, Latvia

Paweł MERGO
Maria Curie-Skłodowska
University, Lublin, Poland

Andrzej NAFALSKI
University of South Australia,
Adelaide, Australia

Il Han PARK
Sungkyunkwan University,
Suwon, Korea

Lucjan PAWŁOWSKI
Lublin University of Technology,
Lublin, Poland

Sergey PAVLOV
Vinnytsia National
Technical University,
Vinnytsia, Ukraine

Liudvikas PRANEVICIUS
Vytautas Magnus University,
Kaunas, Lithuania

Denis PREMEL
CEA Saclay,
Gif-sur-Yvette, France

Jason RILEY
The Eunice Kennedy Shriver
National Institute of Child Health
and Human Development,
Bethesda, USA

Ryszard ROSKOSZ
Gdańsk University of Technology,
Gdańsk, Poland

Tomasz RYMARCZYK
Netrix Group,
Lublin, Poland

Dominik SANKOWSKI
Lodz University of Technology,
Lodz, Poland

Jan SIKORA
Lublin University of Technology,
Lublin, Poland

Stanislav SLOSARCIK
Technical University of Kosice,
Kosice, Slovakia

Jan SROKA
Warsaw University of Technology,
Warsaw, Poland

Bohdan STADNYK
Lviv Polytechnic
National University,
Lviv, Ukraine

Henryka Danuta STRYCZEWSKA
Lublin University of Technology,
Lublin, Poland

Batyrbek SULEMENOV
Kazakh National Research
Technical University
after K.I.Satpayev,
Almaty, Kazakhstan

Mirosław ŚWIERCZ
Bialystok University
of Technology,
Białystok, Poland

Stanisław TARASIEWICZ
Université Laval,
Quebec, Canada

Murielle TORREGROSSA
University of Strasbourg,
Strasbourg, France

Sławomir TUMAŃSKI
Warsaw University of Technology,
Warsaw, Poland

Andrzej WAC-WŁODARCZYK
Lublin University of Technology,
Lublin, Poland

Zygmunt WARSZA
Industrial Research Institute
for Automation and Measurements,
Warsaw, Poland

Sotoshi YAMADA
Kanazawa University,
Kanazawa, Japan

Xiaoyi YANG
Beihang University,
Beijing, China

Mykola YERMOSHENKO
International Academy
of Information Sciences,
Kiev, Ukraine

Athanasios ZACHAROPOULOS
University College London,
London, United Kingdom

Ivan ZHARSKI
Belarusian National
Technical University,
Minsk, Belarus

Cao ZHIHONG
Institute of Soil Science Chinese
Academy of Sciences,
Nanjing, China

Paweł ZHUKOWSKI
Lublin University of Technology,
Lublin, Poland

EDITORIAL BOARD – KOMITET REDAKCYJNY

Editor-in-Chief
Redaktor naczelny

Jan SIKORA
Lublin University of Technology, Lublin, Poland
sik59@wp.pl

Topical Editors
Redaktorzy działowi

Computer Science
Informatyka
Dominik SANKOWSKI
Lodz University of Technology, Lodz, Poland
dsan@kis.p.lodz.pl

Electronics
Elektornika
Pavel FIALA
Brno University of Technology, Brno, Czech Republic
fialap@feec.vutbr.cz

Automatic
Automatyka
Waldemar WÓJCIK
Lublin University of Technology, Lublin, Poland
a.smolarz@pollub.pl

Mechtronics
Mechatronika
Krzysztof KLUSZCZYŃSKI
Silesian University of Technology, Gliwice, Poland
krzysztof.kluszczynski@polsl.pl

EDITOR STAFF – ZESPÓŁ REDAKCYJNY

Deputy Editors
Zastępcy redaktora

Dominik SANKOWSKI
Lodz University of Technology, Lodz, Poland
dsan@kis.p.lodz.pl

Pavel FIALA
Brno University of Technology, Brno, Czech Republic
fialap@feec.vutbr.cz

Andrzej SMOLARZ
Lublin University of Technology, Lublin, Poland
a.smolarz@pollub.pl

Assistant Editor
Sekretarz redakcji

Paweł KOMADA
Lublin University of Technology, Lublin, Poland
p.komada@pollub.pl

Technical Editor
Redaktor techniczny

Tomasz ŁAWICKI
Lublin University of Technology, Lublin, Poland
t.lawicki@pollub.pl

EDITORIAL OFFICE – REDAKCJA

Redakcja czasopisma
Informatyka, Automatyka, Pomiary w Gospodarce i Ochronie Środowiska
Instytut Elektroniki i Technik Informacyjnych
Politechnika Lubelska
ul. Nadbystrzycka 38A
20-618 Lublin
tel. +48 81 53 84 309
fax: +48 81 53 84 312
www.e-iapgos.pl

PUBLISHER – WYDAWCA

Politechnika Lubelska
ul. Nadbystrzycka 38D
20-618 Lublin
tel. +48 81 53 84 100
www.pollub.pl

OTHER INFORMATION – INNE INFORMACJE

Czasopismo jest indeksowane w bazach:

BazTech:	baztech.icm.edu.pl
IC Journals Master List:	www.journals.indexcopernicus.com

Czasopismo znajduje się w wykazie czasopism naukowych opublikowanym w Komunikacie Ministra Nauki i Szkolnictwa Wyższego z dnia 9 grudnia 2016 r. – część B, pozycja 685 – z liczbą punktów przyznawanych za publikację równą 7.

Zasady publikowania artykułów, przygotowania tekstów, zasady etyczne, procedura recenzowania, wykazy recenzentów oraz pełne teksty artykułów dostępne są na stronie internetowej czasopisma:
www.e-iapgos.pl

W celu zwiększenia oddziaływania czasopisma w środowisku naukowym redakcja zaleca:

- w artykułach publikowanych w IAPGOS cytować artykuły z renomowanych czasopism międzynarodowych (szczególnie indeksowanych w bazach Web of Science oraz Scopus) używając oficjalnych skrótów nazw czasopism,
- w artykułach publikowanych w innych czasopismach (zwłaszcza indeksowanych w bazach Web of Science oraz Scopus) cytować prace publikowane w IAPGOS – zwłaszcza posługując się numerami DOI, np.:
  Kluszczyński K. *Modelowanie – umiejętność czy sztuka?* Informatyka, Automatyka, Pomiary w Gospodarce i Ochronie Środowiska – IAPGOS, 1/2016, 4–15, DOI: 10.5604/20830157.1193833.

CONTENTS – SPIS TREŚCI

1. **Laurent Babout, Krzysztof Grudzień, Marcin Janaszewski, Łukasz Jopek**
Study of degradation and granular flow processes using X-ray imaging
Analiza procesów degradacji i przepływu granulatu z wykorzystaniem obrazowania metodą promieni X 5

2. **Robert Banasiak, Radosław Wajman, Tomasz Jaworski, Paweł Fiderek, Paweł Kapusta, Dominik Sankowski**
Two-phase flow regime three-dimensonal visualization using electrical capacitance tomography – algorithms and software
Trójwymiarowa wizualizacja struktur przepływów dwufazowych przy użyciu elektrycznej tomografii pojemnościowej – algorytmy i oprogramowanie 11

3. **Paweł Fiderek, Tomasz Jaworski, Robert Banasiak, Jacek Nowakowski, Jacek Kucharski, Radosław Wajman**
Intelligent system for the two-phase flows diagnosis and control on the basis of raw 3D ECT data
Inteligentny system diagnostyki i sterowania przepływami dwufazowymi na podstawie pomiarów 3D ECT 17

4. **Krzysztof Grudzień, Dominik Sankowski**
Methods for monitoring gravitational flow in silos using tomography image processing
Metody monitorowania przepływu grawitacyjnego w silosach z zastosowaniem przetwarzania obrazów tomograficznych 24

5. **Volodymyr Mosorov, Krzysztof Grudzień, Dominik Sankowski**
Flow velocity measurement methods using electrical capacitance tomography
Metody pomiaru prędkości przepływu z zastosowaniem tomografii pojemnościowej 30

6. **Michał Majchrowicz, Paweł Kapusta, Lidia Jackowska-Strumiłło, Dominik Sankowski**
Acceleration of image reconstruction process in the electrical capacitance tomography 3D in heterogeneous, multi-GPU system
Przyspieszanie procesu rekonstrukcji obrazu w elektrycznej tomografii pojemnościowej 3D z wykorzystaniem heterogenicznego systemu multi-GPU 37

7. **Jacek Nowakowski, Piotr Ostalczyk, Dominik Sankowski**
Application of fractional calculus for modelling of two-phase gas/liquid flow system
Zastosowanie rachunku różniczkowego niecałkowitego rzędu do modelowania przepływów dwufazowych gaz/ciecz 42

8. **Jacek Nowakowski, Robert Banasiak, Radosław Wajman, Dominik Sankowski**
Multi phase flow measurements with the application of ECT/ERT DECART multimodality tomograph
Pomiary przepływów wielofazowych z wykorzystaniem tomografu multimodalnego DECART 46

9. **Andrzej Romanowski, Krzysztof Grudzień, Hela Garbaa, Lidia Jackowska-Strumiłło**
Parametric methods for ECT inverse problem solution in solid flow monitoring
Metody parametryczne w rozwiązywaniu problemu odwrotnego dla monitorowania przepływów materiałów sypkich 50

10. **Tomasz Rymarczyk**
Topological algorithms to solve inverse problem in electrical tomography
Algorytmy topologiczne do rozwiązywania zagadnienia odwrotnego w tomografii elektrycznej 55

11. **Tomasz Rymarczyk, Przemysław Adamkiewicz**
Monitoring damage and dampness in flood embankment by electrical impedance tomography
Tomografia impedancyjna do wyznaczania wilgotności w modelu wału 59

12. **Tomasz Rymarczyk**
Level sets and computational intelligence algorithms to medical image analysis in e-medicus system
Zbiory poziomicowe i algorytmy inteligencji obliczeniowej do analizy obrazów medycznych w systemie e-medicus 63

13. **Tomasz Rymarczyk, Przemysław Adamkiewicz**
Nondestructive method to determine moisture area in historical building
Implementacja algorytmów numerycznych do wyznaczania zawilgoconych obszarów w budynkach historycznych 68

14. **Tomasz Rymarczyk, Paweł Tchórzewski**
Hybrid techniques to solve optimization problems in EIT
Techniki hybrydowe do rozwiązywania zagadnień optymalizacyjnych w ETI 72

15. **Tomasz Rymarczyk**
Using electrical impedance tomography in linear arrays of measurement
Zastosowanie elektrycznej tomografii impedancyjnej w układach pomiaru liniowego 76

16. **Tomasz Rymarczyk, Paweł Tchórzewski, Jan Sikora**
Coupling boundary element method with level set method to solve inverse problem
Połączenie metody elementów brzegowych i zbiorów poziomicowych w rozwiązywaniu zagadnienia odwrotnego 80

17. **Tomasz Rymarczyk, Paweł Tchórzewski, Jan Sikora**
Detection of air gaps in copper-mine ceiling by electrical impedance tomography
Wykrywanie szczelin powietrznych w chodniku kopalni miedzi za pomocą elektrycznej tomografii impedancyjnej 84

18. **Tomasz Rymarczyk, Karol Duda, Paweł Rymarczyk, Daniel Olchowy, Jan Sikora**
Measuring data acquisition hardware for electrical impedance tomography
System akwizycji danych w elektrycznej tomografii impedancyjnej 88

19. **Tomasz Rymarczyk, Przemysław Adamkiewicz, Jakub Szumowski, Konrad Niderla, Łukasz Gołąbek, Jan Sikora**
Concept of detection system to localize inside closed area by radio tomographic imaging
Koncepcja systemu detekcji do lokalizacji wewnątrz obszarów zamkniętych z wykorzystaniem tomografii radiowej 92

20. **Tomasz Rymarczyk, Grzegorz Kłosowski, Przemysław Adamkiewicz, Karol Duda, Jakub Szumowski, Paweł Tchórzewski**
Idea of parametric and semantic open platform smart devices sensor
Koncepcja parametryczno-semantycznej otwartej platformy inteligentnych urządzeń sensorowych 96

21. Tomasz Rymarczyk, Przemysław Adamkiewicz, Paweł Tchórzewski
Idea of electrical tomography system for monitoring lung ventilation
Idea systemu tomografii elektrycznej do monitorowaniu wentylacji płuc ... 101

22. Waldemar Smolik, Jacek Kryszyn, Tomasz Olszewski, Roman Szabatin
Methods of small capacitance measurement in electrical capacitance tomography
Metody pomiaru małych pojemności w elektrycznej tomografii pojemnościowej ... 105

23. Jacek Kryszyn, Waldemar Smolik, Tomasz Olszewski, Roman Szabatin
Development of electrical capacitance tomograph design in the nuclear and medical electronics division
Rozwój konstrukcji elektrycznego tomografu pojemnościowego w zakładzie elektroniki jądrowej i medycznej ... 111

24. Waldemar T. Smolik, Jacek Kryszyn
Linear over ranges iterative algorithms for image reconstruction in electrical capacitance tomography
Przedziałami liniowe iteracyjne algorytmy rekonstrukcji obrazów w elektrycznej tomografii pojemnościowej ... 115

25. Grzegorz Domański, Roman Szabatin, Piotr Brzeski, Bogumił Konarzewski
Needle detector of X-ray and gamma radiation
Detektor igłowy promieniowania X i gamma ... 121

26. Przemysław Wróblewski, Waldemar Smolik
Development of magnetic nanoparticles tomography in nuclear and medical electronics division
Rozwój tomografii nanocząsteczek magnetycznych w zakładzie elektroniki jądrowej i medycznej ... 125

27. Grzegorz Domański, Ryszard Szabatin, Jerzy Kalenik, Adam Jaworski, Przemysław Wróblewski, Waldemar Smolik, Robert Kurjata, Bogusław Konarzewski, Michał Dziewiecki, Janusz Marzec, Krzysztof Zaremba, Marcin Ziembicki, Andrzej Rychter, Jacek Kryszyn, Piotr Brzeski, Jan Szmidt
Gain prediction theory of single foil gas electron multiplier detector
Teoria wzmocnienia jednofoliowego detektora z gazowym powielaniem elektronów ... 130

28. Michał Wieteska, Wojciech Obrębski, Ewa Piątkowska-Janko, Błażej Sawionek, Piotr Bogorodzki
Increasing the signal to noise ratio in low-field MR scanner at department of nuclear and medical electronics
Techniki wzmocnienia stosunku sygnał-szum w niskopolowym skanerze MR w zakładzie elektroniki jądrowej i medycznej ... 133

29. Jacek Kryszyn, Waldemar Smolik
Toolbox for 3D modelling and image reconstruction in electrical capacitance tomography
Pakiet do trójwymiarowego modelowania i rekonstrukcji obrazów w elektrycznej tomografii pojemnościowej ... 137

30. Jacek Kryszyn, Waldemar Smolik
2D modelling of a sensor for electrical capacitance tomography in ectsim toolbox
Dwuwymiarowe modelowanie sondy do elektrycznej tomografii pojemnościowej w pakiecie ectsim ... 146

31. Przemysław Wróblewski, Waldemar Smolik
Coil design with litze wire for magnetic particle spectrometry
Konstrukcja cewki z wykorzystaniem lica do spektrometrii cząstek magnetycznych ... 150

32. Maciej Pańczyk, Jan Sikora
Boundary element method modyfications for use in some impedance and optical tomography applications
Modyfikacje metody elementów brzegowych zastosowane w wybranych aspektach tomografii impedancyjnej i optycznej ... 154

33. Mariusz Rząsa, Ewelina Podgórni
Review of methods of measuring based on optical tomography applicable to determining flow parameters of gas-liquid
Przegląd metod pomiarowych opartych na tomografii optycznej w zastosowaniu do wyznaczania parametrów przepływów gaz-ciecz ... 161

DOI: 10.5604/01.3001.0010.4574

STUDY OF DEGRADATION AND GRANULAR FLOW PROCESSES USING X-RAY IMAGING

Laurent Babout[1], Krzysztof Grudzień[1], Marcin Janaszewski[1,*], Łukasz Jopek[1,*]
[1]Institute of Applied Computer Science, Lodz University of Technology, *Formerly at the Institute of Applied Computer Science

Abstract. *This paper reviews the work that has been done in the past 10 years at the Lodz University of technology about the visualization and the quantification of phenomena related to degradation processes (i.e. stress corrosion cracking in stainless steel, fatigue crack in titanium alloys) in engineering materials as well as granular flow in silos using X-ray imaging (i.e. radiography and (micro)tomography). Besides presenting the experimental protocols, the paper also presents the image processing strategies that have been applied to enable the extraction of characteristic parameters from the volumetric images.*

Keywords: X-ray imaging, damage, gravitational flow, image processing.

ANALIZA PROCESÓW DEGRADACJI I PRZEPŁYWU GRANULATU Z WYKORZYSTANIEM OBRAZOWANIA METODĄ PROMIENI X

Streszczenie. *Artykuł przedstawia przegląd prac badawczych przeprowadzonych w ostatnich 10 latach w Politechnice Łódzkiej, dotyczących wizualizacji oraz analizy ilościowej zjawisk mających miejsce w procesie degradacji materiałów (tj. korozji naprężeniowej stali nierdzewnej, pęknięcia stopów tytanu) oraz przepływu materiałów sypkich w silosach z wykorzystaniem obrazowania metodami opartymi na promieniowaniu X (tzn. radiografii oraz (micro)tomografii). Oprócz przedstawienia metodologii pomiaru, zostały również opisane metody przetwarzania obrazów, pozwalające na wyznaczenie charakterystycznych parametrów badanych procesów z obrazów wolumetrycznych.*

Słowa kluczowe: obrazowanie metodą promieni X, przepływ grawitacyjny, przetwarzanie obrazów

Introduction

Other the past 15 years, X-ray tomography has become a mature non-destructive technique to study internal structure of materials in various fields of applied science (e.g. biomedical engineering, geology, civil engineering or materials science engineering). This has been supported by the constant effort of researchers to push forward both the spatial and temporal resolutions of the technology to the highest. One can chronologically cite the works on increased contrast using phase shift [11, 25], nanotomography [30], (ultra)fast X-ray (micro)tomography [9, 13, 23, 28] or diffraction tomography/microscopy [19, 21, 27, 29]. Besides, the possibility of carrying out diverse types of in situ test (mechanical, environmental) has given the scientists the unique chance to closely investigate the changes over time of the bulk of the objects of interest. However, one of the main drawbacks of X-ray tomography, especially during time lapse or continuous studies is the tremendous amount of data generated that need to be interpreted (a typical tomography scan represents around 8 Gb of memory). Therefore, automated processing of the data is needed to facilitate their characterization.

This paper presents the work that has been carried out by the authors in the past 10 years dealing with time lapse study of degradation processes in engineering material as well as flow processes in granular materials. A focus is also done on the image processing steps that have been thought in order to carry out quantitative characterization of the phenomena undergone by the materials of interest. After briefly presenting the technology at synchrotron and laboratory level, the paper presents 3 different studies in Section 0 dealing with intergranular stress corrosion cracking in austenitic stainless steel, short fatigue crack propagation in lamellar titanium alloy and, finally, silo discharging of cohesionless dry sand. Main image processing and analysis methods are also introduced to the readers, highlighting their importance to extract complex features from the 3D images.

1. Experimental set-ups

The general concept of X-ray tomography is an extension of classical X-ray radiography, and is based on the attenuation of the X-ray beam through the specimen. By acquiring a set of radiographs at different rotation steps of the specimen over 180° or 360°, one can reconstruct the volume of the object using well-known filtered back-projection algorithm [20]. To do so, an X-ray tomography set-up will need three basic equipment elements: an X-ray source (synchrotron light source or electron gun, as mentioned later), a rotation stage where the sample is mounted and a detector, usually combining a fluorescent screen, which converts X-rays to visible light and a set of optic lenses that transfers the light to a CCD camera. Usually, the X-ray beam can be parallel or divergent with a cone shape.

1.1. X-ray microtomography at the European Synchrotron Radiation Facility

Synchrotron radiation facilities are common large-scale scientific infrastructures (APS in the USA, SPRING8 in Japan, DIAMOND in the UK, SOLEIL or the ESRF in France) where X-rays are used to study the matter from different perspectives. For instance, using X-rays at different wavelengths, one can investigate the crystallographic composition of the matter (e.g. using diffraction, spectroscopy, SAXS), its electronic structure and magnetic properties (inelastic scattering, absorption spectroscopy) or its internal structure using X-ray micro/nanotomography.

X-ray synchrotron tomography equipment is usually characterized by a high energy, coherent X-ray beam, which can be monochromatic or polychromatic, depending of the application. For instance, a monochromatic beam will enable to avoid artifacts problems such as beam hardening, hence resulting in images of very high quality, but at limited temporal resolution (typically 1 scan / 15 minutes). However, polychromatic beam will be preferable if continuous scanning is needed (e.g. 1 scan / s), for instance to investigate microstructural changes with temperature, since the X-ray flux will be tremendously larger than for monochromatic beam. The fact that the beam is coherent also gives the possibility to go around the problem of low absorption contrast encountered in some cases such as Al/SiC composites, by enabling to create on the detector so-called phase contrast [11]. Note that the two first studies presented in this paper have been carried out at the X-ray microtomography beamline ID19 of the ESRF (Fig. 1).

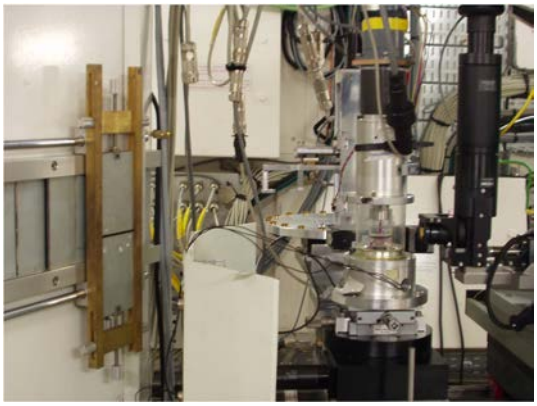

Fig. 1. View of the X-ray microtomography hutch at ID19 (ESRF)

1.2. X-ray tomography laboratory kits

Since the technique has become very popular and the access to synchrotron sources more and more difficult (proposal success rate lower ~10%), numerous companies have developed X-ray tomography laboratory kits dedicated to universities and the industry, mainly for non-destructive inspection for the latter. Classical units, but also more advanced ones (e.g. custom bay for large engineering component investigation or X-ray nanotomography) have been developed to meet customers' need. All are using electron guns as the source to generate X-rays when the electrons, which are collimated using magnets, hit a metal target. Cone X-ray beam are mainly generated in such type of tomography devices. As an example, one can cite the Henry Moseley X-ray Imaging Facility (HMXIF) at the University of Manchester, which owns more the five different X-ray tomography lab kits produced by Zeiss Xradia or Nikon metrologies, in order to investigate objects of different size (up to 30 cm diameter) at different spatial scales (from 100 nm to 100 μm spatial resolution). One of these tomographs is shown in Fig. 2. Note that the third study presented in this paper has been partly performed at this X-ray imaging center.

Fig. 2. View of a Nikon X-ray tomography device owned by the University of Manchester

2. Example of case studies

2.1. Intergranular stress corrosion cracking in stainless steel

The objective of this research study was to investigate how a crack induced by the dual effect of corrosion and external loading (stress corrosion cracking) develop in austenitic stainless steel. The literature predicts that the crack will develop in an intergranular manner for polycrystalline materials such as stainless steel, however nothing was really mentioned about the presence of bridge ligament along the crack path that can be correlated with special low angle grain boundaries.

In that context, Intergranular stress corrosion cracking in a sensitized type 302 stainless steel wire has been observed in situ using high resolution X-ray microtomography. The details of the experimental set-up, which is depicted in Fig. 3, is presented in details in [6]. The spatial resolution was 0.7 μm.

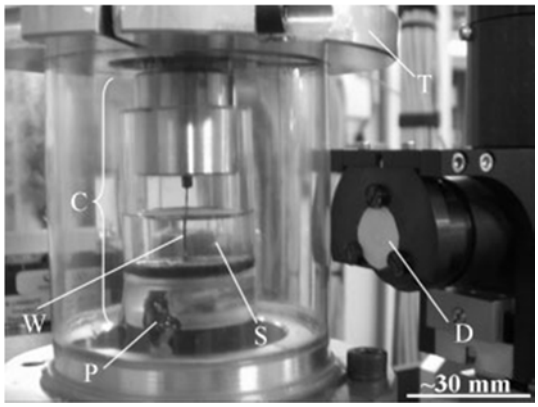

Fig. 3. X-ray microtomography set-up on ID19 for in situ IGSCC experiment presented in [6]. *W: 302SS sample wire, P: platinum counter electrode, S: acid solution, T: tensile machine, D: X-ray detector*

Fig. 4 shows typical images of the crack development during IGSCC. Firstly, one can notice that the cracks have developed from the outside of the sample to the inside (Fig. 4a). Secondly, the crack pattern is intergranular and reveals the presence of grains revealing the polycrystalline nature of the austenitic stainless steel microstructure (Fig. 4a). Thirdly, the crack presents discontinuities along its path, as marked by white circles in Fig. 4a-b, which correspond in 3D to so-called bridge ligaments. The main goal of the study was to detect and extract such feature from the 3D images using dedicated image processing method described below.

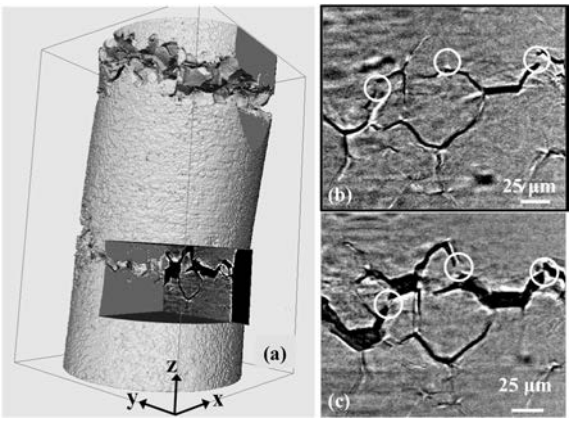

Fig. 4. (a) 3D view and (b-c) sequence of cross-sections showing the development of IGSCC in stainless steel at two different loading time. White circles highlights the presence of bridge ligaments along the crack path. Rearranged from [6]

As it can be seen in Fig. 4a, the crack has developed from the surface of the sample. It is easy to understand that the crack is not a subset of the space since connected to the background. In order to segment it, we have applied the minimal surface for maximal flow algorithm developed by Appleton and Talbot [2] and modified by Kornev et al. [22]. Based on the weighted graph theory, the method simulates the flow of an ideal fluid with isotropic velocity constraints by iteratively updating conditions related to pressure at vertices and inward/outward flow at edges of the graph, the latter being constrained by a function inversely proportional to the gradient of the image. By using a binary source located inside the object to be segmented and a sink which surrounds it, the object volume grows until a energy function, which integrate the normal of the local flow at each point of the object surface is minimized. This is illustrated in Fig. 5, where one can see that the crack is not separated from the background.

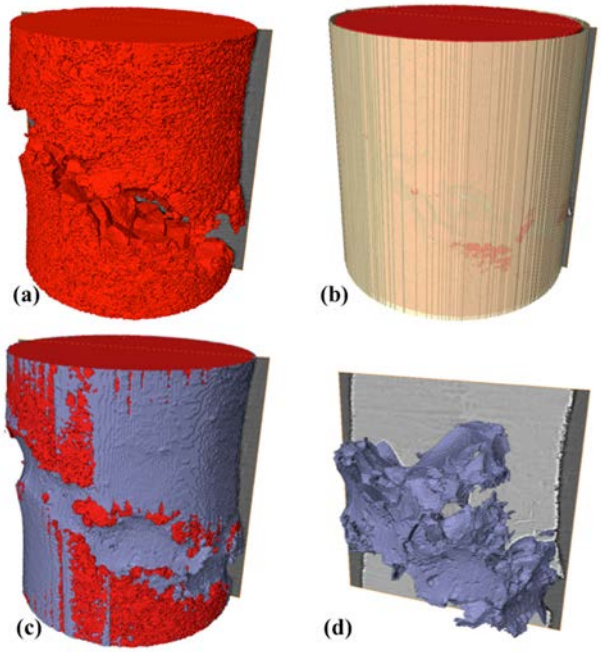

Fig. 5. Application of the minimal surface for maximal flow algorithm to segment open crack. (a) sample serving as source, (b) the sink, (d) the minimal surface and (d) the extracted crack

The reliable extraction of bridge ligaments from X-ray microtomography data requires an image processing strategy. Standard methods, such as histogram-based segmentation, will not isolate the bridges from the material. Indeed, after segmentation of the crack, bridges correspond to holes (or tunnels) in the crack and are part of the surrounding background. Since algorithms to close holes in 3D objects exist, these may be used to extract bridges.

The problem of hole closing is considered in the literature within the general topic of repairing 3D models. Several methods have been developed to correct defects in isosurface and 3D meshes, as mentioned in [17, 18]. One approach, called the Hole Closing Algorithm (HCA), is particularly well suited to detecting holes in a 3D object, such as a bridge ligaments across a crack [1]. The method is based on topological considerations, such as topological number, topology preservation and simple points that are common concepts used in thinning algorithms [12, 26]. The methods has been extended to take into account the thickness of the object surrounding the hole [17] or to close extremities of tunnels [18]. However, the original approach proposed by Aktouf et al. [1] was found to be the most appropriate in the case of bridge ligament segmentation, since by essence holes correspond to portions of grain boundary, which have no thickness, hence represented at most by 3D objects of thickness 1.

Fig. 6 shows an example of the application of the HCA to extract bridge ligaments from a portion of an IGSCC and published in [5]. Investigation of the geometric orientation of the ligaments have shown that many bridges are located on grain boundary facets with the angle between their normal and the loading direction larger than 60°. Note that a study that compared this tomography data with crystallographic orientation of the grains obtained by DCT did not clearly verified the correlation between bridge ligament formation and low Σ boundaries [24], which confirm the complex nature of this degradation process and the challenges that still need to be tackled to understand it.

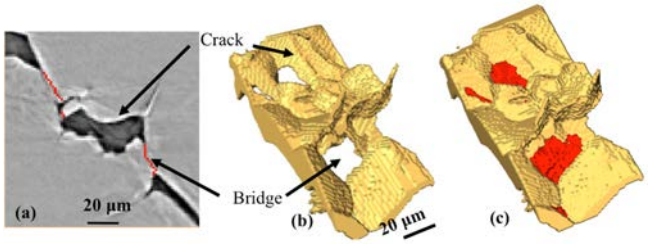

Fig. 6. Hole closing algorithm (HCA) in action. (a) 2d cross section showing crack and bridge. (b) 3D view of the crack showing holes. (c) Holes corresponding to bridges closed using HCA. Rearranged from [5]

2.2. Short fatigue crack in fully lamellar Titanium alloy

The second example of this paper concerns work that has been carried out on short fatigue crack propagation in (α+β) Titanium alloy with fully lamellar microstructure. The main objective was to investigate the interaction of the crack path with the microstructural features of this engineering material, which are the β grain boundaries and the α colonies. Once again, 3D *in situ* investigation was chosen to obtain a non ambiguous set of information, as the crack, initiated at the surface of the sample, propagates in the bulk of the material and strongly interacts with the microstructure.

To do so, an especially designed fatigue machine, depicted in Fig. 7a, was mounted on ID19. Details of the experiments are presented in [10]. The spatial resolution was 0.7 µm as in the previous study (Section 2.1). An exemplar 3D image of the crack branches interacted with the microstructure is shown in Fig. 7b. One can particularly distinguish the deflection of the crack (crack 1) when it has crossed a boundary between 2 α colonies (indicated by dashed curves).

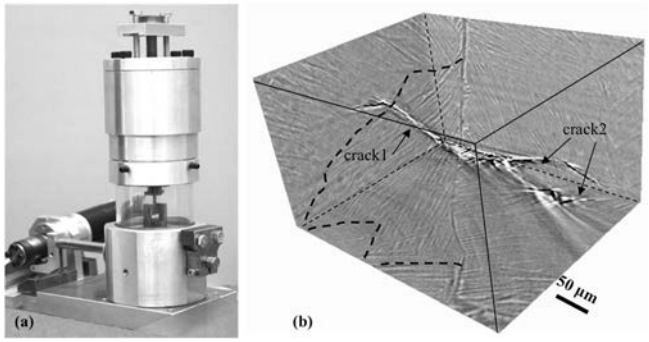

Fig. 7. (a) view of the in situ fatigue machine used for experiment (Courtesy of J.-Y. Buffiere (INSA-Lyon, France)). (b) Visualization of the crack interaction with the Ti lamellar microstructure after 27k fatigue cycles [8]

Because the lamellar microstructure is very complex and can be very tedious to analyze, an image processing strategy has been thought to segment both the crack and the microstructural features mentioned above. Since the lamellar microstructure can be seen as a directional textured image, a directional filter bank with special structuring element presented in Fig. 8 has been thought to capture the local directionality of the lamellae that have nearly planar shapes [3]. The 3D image is convolved with the 13 independent directional filters shown in Fig. 8c and the argument of the maximum response (i.e. the index of the main direction) is selected for each voxel of the image.

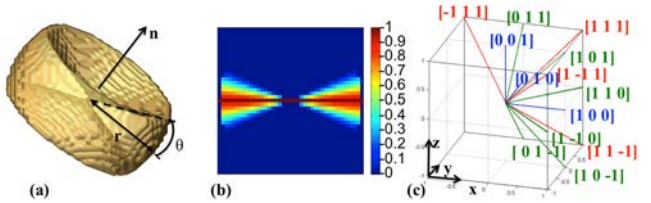

Fig. 8. (a) Isosurface of the CHG filter. (b) 2D filter kernel profile. (c) Bank of principal filter normal directions [3]

The directional filter bank has also shown its utility in the segmentation phase of β-grain boundary (β-gb) [4] and partitioning of the fatigue crack. This is based on the fact that all 3 features correspond to surface objects (their skeleton is a two-dimensional, topological manifold) and present different orientations.

Having segmented the 3 features separately, the last step consists in merging them in the same volume using image registration based on pose estimation (Fig. 9a), since the creation of the crack hinders the segmentation of the Ti microstructure in the tomography scan after fatigue cycling. The quantitative analysis of the interaction between the crack and the TI microstructure can now be performed, as it was described in details in [8]. For example, one can see on Fig. 9b that the crack preferentially propagates in colonies in a trans-lamellar way but perpendicular to the lamellar orientation (blue color), even if a significant portion of the crack also propagates in an inter-lamellar way (red portion). This is the first 3D confirmation of this type of propagation and it is highly probable that translamellar crack with very high angle has crossed lamellae favorably oriented for ⟨a⟩ basal slip while interlamellar crack along lamellae favorably oriented for ⟨a⟩ prismatic slip. A next type of study should combine X-ray microtomography of this kind with high-energy diffraction microscopy, a very recent technique that has shown its potential to get local crystallographic orientation of grains in polycrystalline/polyphase materials such as Ti alloy [29].

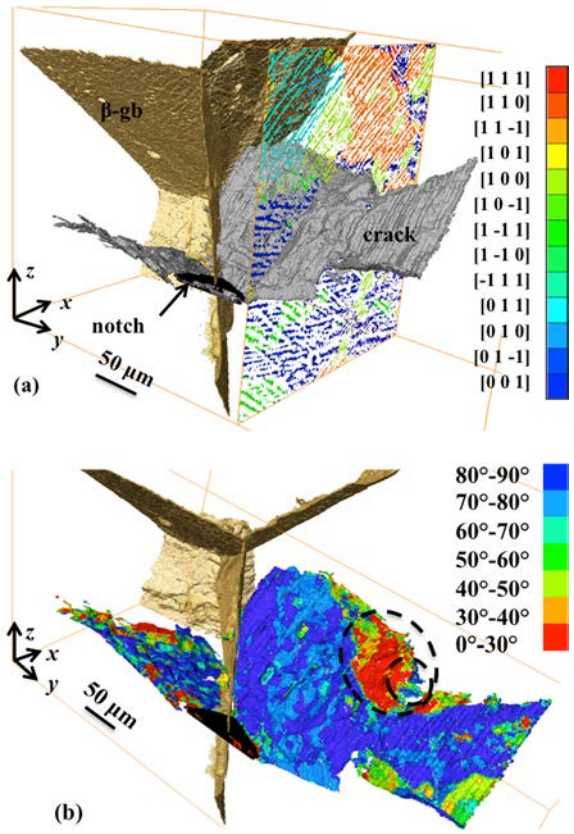

Fig. 9 (a) 3D rendering showing the interaction of the crack with the β grain boundary and the α-lamellae classified w.r.t. their orientation. (b) 3D rendering of the angle between the local crack orientation and lamellar orientation [8]

2.3. Silo discharging of granular materials

The last example presents recent works to investigate dynamic phenomena during silo discharging using X-ray imaging (i.e. X-ray radiography and tomography). This has completed previous Electrical Capacitance Tomography studies performed at the Institute of Applied Computer Science [15, 16]. In all cases were investigated the effect of packing density and silo wall roughness in model rectangular silo.

The first part of the study has concerned silo discharging during mass flow of cohesionless dry sand, looking preferentially to the formation of shear zone at the silo wall during emptying process. This study has been done at the MATEIS laboratory (INSA-Lyon, France) using a GE Phoenix v|tome|x system shown in Fig. 10.

Fig. 10. General view of the X-ray tomography equipment at INSA-Lyon with, in front, the rectangular silo model used for the mass flow study [14]

One of the most important results of the study [14] has shown the pronounced formation of shear zone along silo wall with rough structure depicted in Fig. 11b by red dashed rectangle, as compared with the case of smooth wall. Moreover, the size of shear zone in the case of loose sand packing density seems to be larger than for dense sand. This difference is a direct effect of the increase of sand concentration for loose sand in the whole silo bin section except in the area at the silo wall. In the case of initially dense packing, the concentration in the whole bin section decreases and the difference between the shear zone and the rest of the silo is not as large as for the initially loose sand packing. Another noticeable and obvious dissimilarity between the two packing is the time required to empty the silo. In the case of dense sand, the discharging duration is larger than for loose sand (i.e. typically more about 5 s), as the initial amount of sand for the same height of packing is larger.

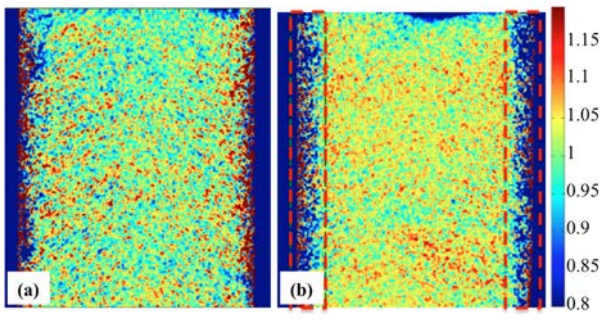

Fig. 11. 2D normalized X-ray radiographs of sand concentration distribution after 1 s of the silo discharging process, (a) loose sand and smooth silo wall, b) loose sand and rough silo wall [14]

A more recent study has focused on the second type of concentric flow, namely funnel flow [7] and was carried out at the HMXIF center at the University of Manchester and experiments were done using a Nikon X-Tek custom 320kV bay. Again, main-

ly X-ray radiography data have been studied to identify the phenomena of funnel creation and geometric characteristics that can be related to the initial packing density of dry sand. Still, time lapse X-ray tomography was also performed to show the evidence that funnel formation, as well as particle tracking during the emptying process could be analyzed.

As far as the initially dense packing is concerned, one can see in Fig. 12 the remarkable contrast between the flow zone and the stagnant ones, greatly facilitating their quantitative study, as explained in [7]. However, the X-ray tomography data have revealed that the width of the funnel flow is not linear along the depth of the silo, but has a rather convex shape, that is to say with a width smaller at the front and back walls of the silo than in the middle. Moreover, studies of different definition of funnel widths, as proposed in Fig. 13, have shown that the most accurate calculation is done when the width is considered at half of the distance from the outlet to the dip (or V-shape) of the upper surface.

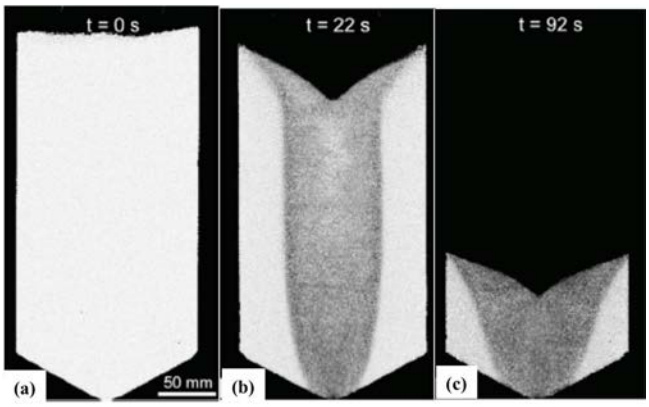

Fig. 12. Sequence of rescaled radiographs highlighting funnel flow for initial dense packing of quartz sand [7]

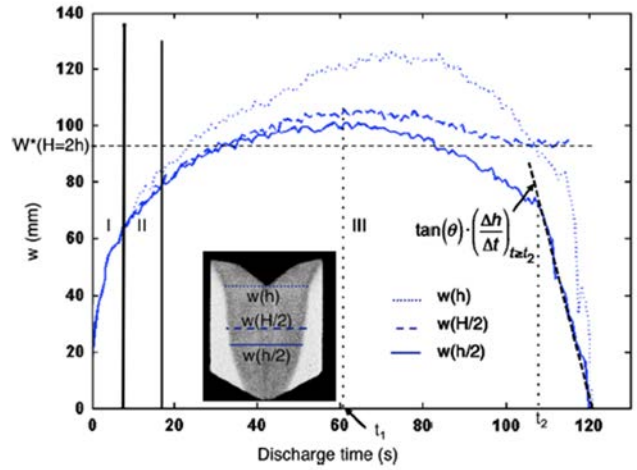

Fig. 13. Evolution of silo width parameters vs. discharge time for the case of dense packing with smooth walls as illustrated in the embedded radiograph. The width W corresponds to the special case when the height at the dip h is 2 times less than the full height H. The trend line, together with the corresponding slope equation of the last part of the width profile w(h/2) when it reaches the hopper wall (i.e. t=t2), is also shown* [7]

As far as the initial loose sand packing is concerned, the flow characteristic is different with so-called semi-mass flow process, that is to say a combination of mass flow at the top of the bin and presence of stagnant zone in the bottom, as pictured in the sequence presented in Fig. 14. One should bear in mind that good visualization of the stagnant zone was only possible by substracting consecutive radiographs (to reveal flow zone w.r.t. stagnant zone) and processing local variance calculation in the image to better reveal the presence of granular concentration fluctuation in the flow zone. Studies of the height of the stagnant zone was therefore made possible and revealed interesting aspects of the semi-mass flow, as shown in Fig. 15. Firstly, the initial height of the stagnant zone H_{SZ} (that is just after the outlet has been opened) is larger for rough wall than for smooth wall conditions, and can be attributed to the increase of particle-wall friction when the wall gets rougher [31]. Secondly, H_{SZ} increases as the discharging time increases (and the height of the bin H_b decreases), until the height of falling material $(H_b(t^*)–H_{SZ}(t^*))$ is about 20% of the initial material height H_b. However, the increase rate is smaller for rough wall and was attributed to the formation of a shear zone with larger wall friction due to the presence of the sand papered wall, which induces movement of the material away from the wall, reducing the possibility of accumulation of sand at the top of the stagnant zone. After t^*, the flow is rather similar to a funnel flow and the decrease of the height H_{SZ} is not dependent on the roughness of the wall. Again, all these valuable quantitative analysis was made possible thanks to appropriate post processing of the radiography images to increase the contrast between stagnant and flow zones.

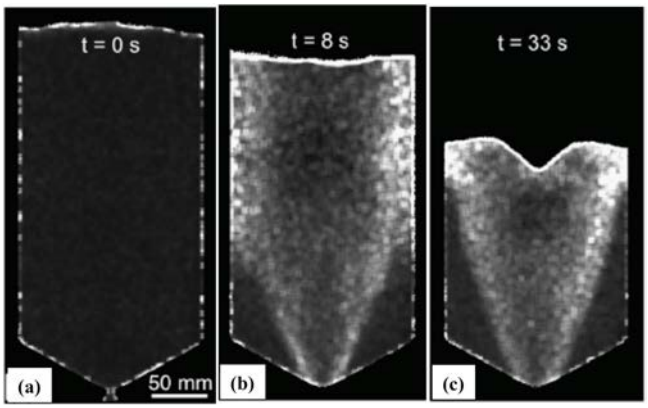

Fig. 14 Sequence of rescaled radiographs highlighting semi-mass flow for initial loose packing of quartz sand [7]

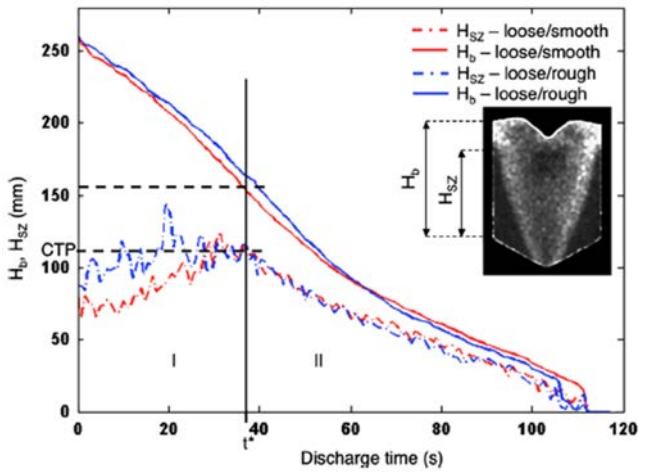

Fig. 15. Change in stagnant zone and funnel dimensions vs. discharge time during complete silo emptying for loose packing within the silo with smooth and rough walls [7]

3. Conclusion

This paper has presented three case studies of physical processes using X-ray (micro)tomography that are, we believe, emblematic of the research interests of the Institute of Applied Computer Science. These will not have been possible without strong collaboration with researchers from INSA-Lyon and the University of Manchester, the two European universities leading the work of materials characterization using X-ray imaging. An important message of the paper is also that, without properly chosen image processing and analysis methods, it is barely impossible to retrieve non-ambiguous quantitative characterization from the material of interest.

Acknowledgments

The authors would like to mention the different grants, which partly financed the work presented in this paper: FP6 Marie Curie DENIDIA project (MTKD-CT-2006-039546) and Polish grants from the Ministry of Science and Higher Education (3687/B/T02/2009/37 and 6522/B/T02/2011/40).

References

[1] Aktouf Z., Bertrand G., Perroton L.: A three-dimensional holes closing algorithm. Pattern Recognition Letters, 23/2002, 523–531.
[2] Appleton B., Talbot H.: Globally minimal surfaces by continuous maximal flows. IEEE Transactions on Pattern Analysis and Machine Intelligence, 28/2006, 106–118.
[3] Babout L., Jopek L., Janaszewski M.: A New Directional Filter Bank for 3D Texture Segmentation: Application to Lamellar Microstructure in Titanium Alloy, in 13th IAPR International Conference on Machine Vision Applications, 2013, 419–422.
[4] Babout L., Jopek L., Janaszewski M.: Extraction of complex microstructural patterns in X-ray microtomography images: application to lamellar titanium alloy, in 7th World Congress on Industrial Process Tomography (WCIPT7), 2013, 703–712.
[5] Babout L., Janaszewski M., Marrow T. J., Withers P. J.: A method for the 3-D quantification of bridging ligaments during crack propagation. Scripta Materialia, 65/2011, 131–134.
[6] Babout L., Marrow T.J., Engelberg D., Withers P.J.: X-ray microtomographic observation of intergranular stress corrosion cracking in sensitised austenitic stainless steel. Materials Science and Technology, 22/2006, 1068–1075.
[7] Babout L., Grudzien K., Maire E., Withers P. J.. Influence of wall roughness and packing density on stagnant zone formation during funnel flow discharge from a silo: An X-ray imaging study. Chemical Engineering Science, 97/2013, 210–224.
[8] Babout L., Jopek Ł., Preuss M.. 3D characterization of trans- and inter-lamellar fatigue crack in (α+β) Ti alloy. Materials Characterization, 98/2014, 130–139.
[9] Bieberle MBarthel., F., Menz H.-J., Mayer H.-G., Hampel U.: Ultrafast three-dimensional x-ray computed tomography. Applied Physics Letters, 98/2011, 034101.
[10] Birosca S., Buffiere J.-Y., Garcia-Pastor F. A., Karadge M., Babout L., Preuss M.: Three-dimensional characterization of fatigue cracks in Ti-6246 using X-ray tomography and electron backscatter diffraction. Acta Materialia, 57/2009, 5834–5847.
[11] Cloetens P., Pateyron-Salome M., Buffiere J. Y., Peix G., Baruchel J., Peyrin F., Schlenker M.: Observation of microstructure and damage in materials by phase sensitive radiography and tomography. Journal of Applied Physics, 81/1997, 5878–5886.
[12] Couprie M., Coeurjolly D., Zrour R.: Discrete bisector function and Euclidean skeleton in 2D and 3D. Image Vision Comput., 25/2007, 1543.
[13] Fischer F., Hoppe D., Schleicher E., Mattausch G., Flaske H., Bartel R., Hampel U.: An ultra fast electron beam x-ray tomography scanner. Measurement Science & Technology, 19/2008.
[14] Grudzien K., Niedostatkiewicz M., Adrien J., Maire E., Babout L.: Analysis of the bulk solid flow during gravitational silo emptying using X-ray and ECT tomography. Powder Technology, 224/2012, 196–208.
[15] Grudzien K., Romanowski A., Chaniecki Z., Niedostatkiewicz M., Sankowski D.: Description of the silo flow and bulk solid pulsation detection using ECT. Flow Measurement and Instrumentation, 21/2010, 198–206.
[16] Grudzien K., Romanowski A., Williams R.A.: Application of a Bayesian approach to the tomographic analysis of hopper fow. Particle and Particle Systems Characterization, 22/2006, 246.
[17] Janaszewski M., Couprie M., Babout L.. Hole filling in 3D volumetric objects. Pattern Recognition, 43/2010, 3548–3559.
[18] Janaszewski M., Postolski M., Babout L.. Robust algorithm for tunnel closing in 3D volumetric objects based on topological characteristics of points. Pattern Recognition Letters, 32/2011, 2231–2238.
[19] Johnson G., King A., Honnicke M.G., Marrow J., Ludwig W.: X-ray diffraction contrast tomography: A novel technique for three-dimensional grain mapping of polycrystals. II. The combined case. Journal of Applied Crystallography, 41/2008, 310–318.
[20] Kak A.C., Slaney M.. Principles of computerized tomographic imaging. New York, 1987.
[21] King A., Johnson G., Engelberg D., Ludwig W., Marrow J.. Observations of intergranular stress corrosion cracking in a grain-mapped polycrystal. Science, 321/2008, 382–385.
[22] Kornev A., Babout L., Janaszewski M., Talbot H.: Outer Surface Reconstruction for 3d Fractured Objects, in Computer Vision and Graphics, Pts 1 and 2, 6374, L. Bolc, R. Tadeusiewicz, L. J. Chmielewski, and K. Wojciechowski, Eds. Berlin: SPRINGER-VERLAG, 2010, 57–64.
[23] Limodin N., Salvo L., Boller E., Suery M., Felberbaum M., Gailliegue S., Madi K.: In situ and real-time 3-D microtomography investigation of dendritic solidification in an Al-10 wt.% Cu alloy. Acta Materialia, 57/2009, 2300–2310.
[24] Ludwig W., King A., Herbig M., Reischig P., Marrow J., Babout L., Lauridsen E.M., Proudhon H., Buffiere J.Y.: Characterization of polycrystalline materials by combined use of synchrotron X-ray imaging and diffraction techniques. JOM, 62/2010, 22–28.
[25] Pfeiffer F., Weitkamp T., Bunk O., David C.: Phase retrieval and differential phase-contrast imaging with low-brilliance X-ray sources. Nature Physics, 2/2006, 258–261.
[26] Saúde A.V., Couprie M., Lotufo R.A.: Discrete 2D and 3D euclidean medial axis in higher resolution. Image and Vision Computing, 27/2009, 354–363.
[27] Spear A.D., Li S.F., Lind J.F., Suter R.M., Ingraffea A.R.: Three-dimensional characterization of microstructurally small fatigue-crack evolution using quantitative fractography combined with post-mortem X-ray tomography and high-energy X-ray diffraction microscopy. Acta Materialia, 76/2014, 413–424.
[28] Suery M., Adrien J., Landron C., Terzi S., Maire E., Salvo L., Blandin J.-J.: Fast in-situ X-ray micro tomography characterisation of microstructural evolution and strain-induced damage in alloys at various temperatures. International Journal of Materials Research, 101/2010, 1080–1088.
[29] Wielewski E., Menasche D.B., Callahan P.G., Suter R.M.: Three-dimensional α colony characterization and prior-β grain reconstruction of a lamellar Ti–6Al–4V specimen using near-field high-energy X-ray diffraction microscopy. Journal of Applied Crystallography, 48/2015, 1165–1171.
[30] Withers P.J.: X-ray nanotomography. Materials Today, 10/2007, 26–34.
[31] Yang Y., Rotter M., Ooi J., Wang Y.: Flow Channel Boundaries in Silos. Chemical Engineering & Technology, 34/2011, 1295–1302.

Prof. Laurent Babout
e-mail: laurent.babout@p.lodz.pl.

Prof. L. Babout obtained his PhD degree in 2002 from INSA-Lyon (France) and DSc degree in 2011 from the Lodz University of Technology (TUL). Currently he holds a position of associate professor at TUL. His scientific interest covers X-ray tomography and 3D image processing, with main focus on materials science applications. Prof. L. Babout is a SIAM member, TMS member and author or co-author of more than 100 scientific papers, books and chapters.

Ph.D. Krzysztof Grudzień
e-mail: kgrudzi@iis.p.lodz.pl

Assistant Professor of Applied Computer Science at Lodz University of Technology. Member of Polish Information Processing Society and ACM Lodz Chapter. He obtained PhD in 2007 in the field of Computer Science, Process Tomography specialty.
His research interests include applications of non-invasive imaging techniques and identification of dynamic industrial processes parameters, development of algorithms for image processing and analysis with particular reference to the analysis of sequences of 2D tomography images gathered from ECT and X-ray tomography systems.

Ph.D. Eng. Marcin Janaszewski
e-mail: marcin.janaszewski.ext@zeiss.com

Contractor in Michael Bailey Associates Group, currently working as Senior Software Developer for Carl Zeiss GmbH, Research and Development Department. He obtained PhD in 2003 in the field of Computer Science. His interests include pattern recognition, image processing, digital topology and geometry, applications of 3D image processing in material science and medicine.

Ph.D. Eng. Łukasz Jopek
e-mail: l.jopek@pixel.com.pl

Software Developer at Pixel Technology (Lodz, Poland). He currently works in a research project, which focuses on segmentation and analysis of medical images. He obtained his PhD in 2014 in the field of Computer Science from the Lodz University of Technology. His interests include pattern recognition, image processing, image texture analysis, applications of 2D/3D image processing in material science and medicine.

otrzymano/received: 20.09.2016 *przyjęto do druku/accepted: 15.02.2017*

DOI: 10.5604/01.3001.0010.4575

TWO-PHASE FLOW REGIME THREE-DIMENSONAL VISUALIZATION USING ELECTRICAL CAPACITANCE TOMOGRAPHY – ALGORITHMS AND SOFTWARE

Robert Banasiak, Radosław Wajman, Tomasz Jaworski, Paweł Fiderek, Paweł Kapusta, Dominik Sankowski
Lodz University of Technology, Institute of Applied Computer Science

Abstract. *This paper presents the software for comprehensive processing and visualization of 2D and 3D electrical tomography data. The system name as TomoKIS Studio has been developed in the frame of DENIDIA international research project and has been improved in the frame of Polish Ministry of Science and Higher Education Project no 4664/B/T02/2010/38. This software is worldwide unique because it simultaneously integrates the process of tomographic data acquisition, numerical FEM modeling and tomographic images reconstruction. The software can be adapted to specific industrial applications, particularly to monitoring and diagnosis of two-phase flows. The software architecture is composed of independent modules. Their combination offers calibration, configuration and full-duplex communication with any tomographic acquisition system with known and open communication protocol. The other major features are: online data acquisition and processing, online and offline 2D/3D images linear and nonlinear reconstruction and visualization as well as raw data and tomograms processing. Another important ability is 2D/3D ECT sensor construction using FEM modeling. The presented software is supported with the multi-core GPU technology and parallel computing using Nvidia CUDA technology.*

Keywords: Electrical capacitance tomography, fluid flow measurement, reconstruction algorithms

TRÓJWYMIAROWA WIZUALIZACJA STRUKTUR PRZEPŁYWÓW DWUFAZOWYCH PRZY UŻYCIU ELEKTRYCZNEJ TOMOGRAFII POJEMNOŚCIOWEJ – ALGORYTMY I OPROGRAMOWANIE

Streszczenie*. W artykule autorzy przedstawiają środowisko komputerowe do kompleksowego przetwarzania i wizualizacji tomograficznych danych pomiarowych. Oprogramowanie TomoKIS Studio powstało w Instytucie Informatyki Stosowanej PŁ w ramach projektu DENIDIA i zostało rozwinięte w ramach projektu MNiSW nr 4664/B/T02/2010/38. Zbudowane oprogramowanie jest unikalne w skali światowej, gdyż integruje w sobie proces pozyskiwania danych pomiarowych, modelowanie numeryczne oraz proces konstruowania obrazów tomograficznych, z możliwością adaptacji dla różnych aplikacji przemysłowych, w szczególności dla potrzeb monitorowania i diagnostyki przepływów dwufazowych gaz-ciecz. Architektura aplikacji oparta jest na zestawie niezależnych modułów, które pozwalają na w pełni dwukierunkową komunikacją, konfigurację oraz kalibrację dowolnego urządzenia tomografii elektrycznej z otwartym protokołem pomiarowym, akwizycję i przetwarzanie danych pomiarowych on-line, liniową oraz nieliniową rekonstrukcję obrazów 2D i 3D w czasie rzeczywistym, a także wizualizację surowych danych pomiarowych i tomogramów. Istotnym elementem systemu jest moduł numerycznego modelowania czujników pojemnościowych wykorzystujący metodę elementów skończonych, oparty na autorskich algorytmach generowania siatek MES komputerowych modeli czujników pojemnościowych. Architektura prezentowanego systemu została zaprojektowana przy użyciu obliczeń równoległych na procesorach graficznych, z wykorzystaniem technologii Nvidia CUDA.*

Słowa kluczowe: elektryczna tomografia pojemnościowa, pomiary przepływów, algorytmy rekonstrukcji

Introduction

In the frame of research carried out in the Institute of Applied Computer Science at Lodz University of Technology there was build a dedicated software named *TomoKISStudio* for the three dimensional tomographic data on-line visualization. There was implemented a set of modules for communication with any of the tomography devices held in the department's research laboratory and the modules for the 3D image reconstruction and visualization. The mentioned modules offer the following functionality:

- full-duplex communication with electrical tomography devices,
- calibration and configuration,
- measurement data acquisition and processing,
- raw and normalized measurement data visualization,
- linear and non-linear iterative 3D image reconstruction including implementation of parallel computing based on Microsoft OpenMP, NVidia CUDA
- on-line 3D image presentation,
- a possibility of easy development by adding a new modules.

The application was implemented using concurrent programming. That means that singular modules are working in their own threads. Additionally, the linear algebra computing engine is based on CUDA - parallel computing technique powered by Nvidia and the Microsoft Visual Studio C++ environment. Thanks to the special directives of work sharing constructs it was possible to share the processes between existing CPUs and GPUs.

As was mentioned before the application can communicate with three electrical tomography devices. There are implemented the modules for communication with capacitance ECT, resistance ERT and dual ECRT tomography. In all of the modules there is a possibility of usage of the rotatable sensor driver [8].

In addition the two of the tomography modules are equipped with the mechanism of automatic measurement channel gains configuration. In order to perform the remote measurement there is build the module with implemented TCP/IP stack for the measurement data transferring through the computer network. Additionally, *TomoKISStudio* application has two plug-ins which significantly enlarge the functionality of the software by the possibility of building the 3D computer model of the capacitance or resistance sensor.

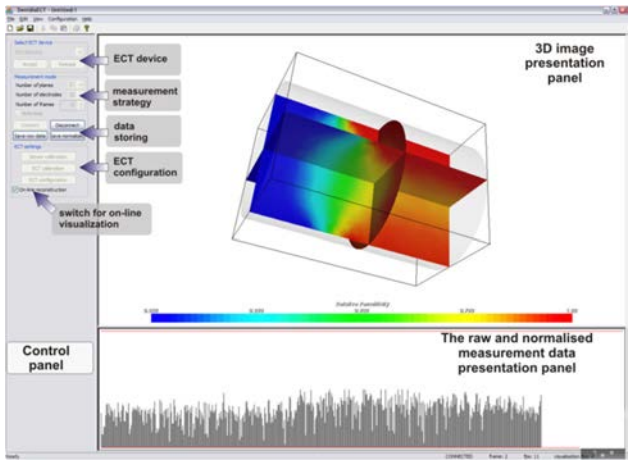

Fig. 1. Graphical user interface of TomoKISStudio application

It is worth mentioning about the module for tomograph simulation. From the previously storied measurement data it is possible to play them with the slower frequency and to reconstruct images with the more demanding algorithm. The figure 2 presents the part of the configuration panel which allows to choose the described devices modules.

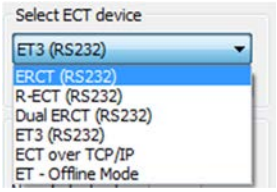

Fig. 2. Choice of the tomography device communication module

The three-dimensional image presentation was performed applying the graphics engine VTK library (*The Visualization ToolKit*). Thanks to this the application presents the images using cut planes or iso-surfaces. Additionally, it is possible to see the raw and normalized measurement data in one graph. This is obviously done in on-line mode.

1. Module for automatic configuration of gains for the measurement channels of the tomograph

In the research department's laboratory for three dimensional capacitance tomography experiments purposes it is used the device named *ET3* which was construct by the research team (dr R. Szabatin) from Institute of Radioelectronics at Warsaw University of Technology [3]. The main feature of this device is the possibility of freely gains configuration for each of the measurement channels. For the 32 electrodes mode there are 496 measurement channels (electrodes pairs) and each of them has 4 configurable elements. There are two amplifiers (4 values of setting for each) and feedback resistor and capacitor (it gives together 12 values of settings). Such diversity of settings caused that the manual tuning of the device is very time-consuming. Simultaneously, there is very important to tune the system as precisely as possible remembering that despite the big and different distances between electrodes and the different sensor geometry the small measurement capacitances should oscillate in the measurement range of the device and additionally should be sensitive enough to the changes of the permittivity distribution between full and empty sensor. Taking the above into consideration the authors of the paper implemented the specialist module which automatically sets the gains for all the measurement channels based on the user conditions and calibrates the measurement unit to the sensor geometry in the same time. In the figure 3 the configuration dialog for *ET3* gains auto-configuration module is presented.

In the figure can also be seen the choice of manual gains settings. In case of the need of manual tune it is only required to click the measurement column on the graph and simply to change the gains settings. The user can quickly diagnose the wrong configuration of the measurement channel and easily correct it.

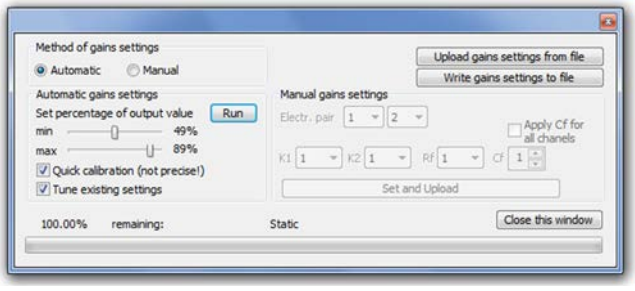

Fig. 3. The dialog window for auto-configuration of the channels gains for the ET3 tomograph

2. TCP/IP data communication module for tomographic data transmission

The measurement noise can be real issue in electrical capacitance system due to very small values of capacitance data. One of solutions for noise minimizing can be reduction of a measurement cables length. There is also another limitation which is a RS232 interface data transmission cable. Given restrictions result in difficulties of performing ECT measurement in two sections in the same time for real industrial applications. As an example of such application two semi-industrial testing facilities built in the author's Institute can be considered. There is 20 meters of distance between them.

To avoid this problem a new measurement data transfer software module has been developed based on TCP/IP networking protocol and client-server communication scheme. A part of this module was embedded in *TomoKISStudio* architecture and it is working as a network client. A server part is dedicated to be as a software component of the PC directly connected to the ECT acquisition hardware – see Figure 4.

The server module includes both: calibration routines and tomography system configuration data. The remaining module features (ex. planes number selection, electrode layout configuration) are included in client part of the TCP/IP module.

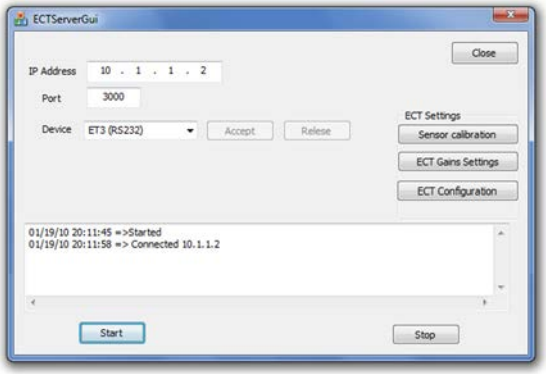

Fig. 4. Example dialog window of TCP/IP communication module – server side

3. Offline tomographics data server module

Apart from real-time online communication between PC and ECT hardware the very important thing is to have a possibility of using offline measurement data previously saved and backed up on storage. Using the offline data we can perform image reconstruction process which is accurate and does not require online and fast view of industrial process. This work can be also done immediately after the research experiment will end. The new offline measurement data serving module has been developed for that purpose. The configuration of this module is simple and requires only setting up of offline measurement data path, selecting their format and choosing a speed of feeding them to a reconstruction module.

Using new offline data feeding module advanced reconstruction techniques can be applied including iterative methods and nonlinear reconstruction algorithms with electric field simulation and sensitivity distribution update. This techniques, on account of their computational complexity, are much time consuming and can need hours to generate single 3-dimensional image but they offer good accuracy and quality for further tomographic data processing. Examples of reconstructed images using different algorithms have been presented in Figure 6. In comparison to the LBP method that is able to achieve 100 frames per second the nonlinear algorithm can require 2h to provide single frame depending on computational power of used PC.

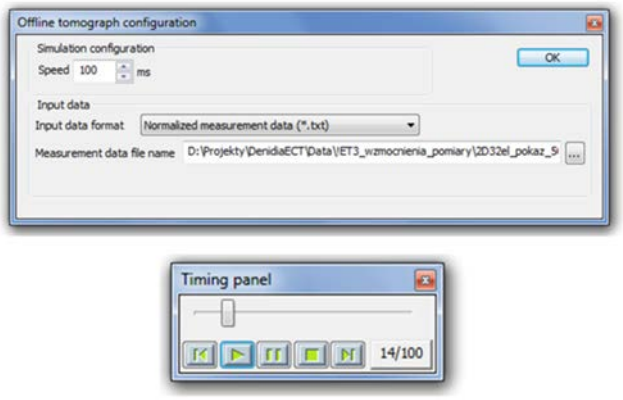

Fig. 5. Example dialog window of the offline data server module

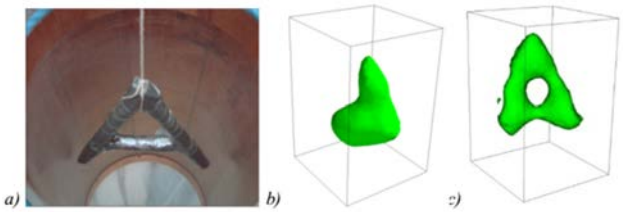

Fig. 6. Example of ECT images reconstructed using two different methods; a) test A-shaped experimental phantom, b) LBP image, c) nonlinear reconstructed image [2]

4. A driver module for rotatable sensor with ECT hardware synchronization and online image reconstruction

The new idea of rotatable ECT sensor [8] in the author's Institute industrial tomography laboratory was also developed. This concept can bring a significant improvement of spatial resolution in reconstructed images by using an increased number of measurement data from the limited number of electrodes. For this purpose an additional driver module for stepping motor control and configuration was designed and implemented. This module is responsible for synchronization of stepping motor rotation with *DenidiaERCT* hardware measurement data transmission. The stepper motor – PC communication is controlled by ActiveX technology that lets to configure main parameters like number of measurement rotation steps, number of rotated electrodes and speed of motor rotation.

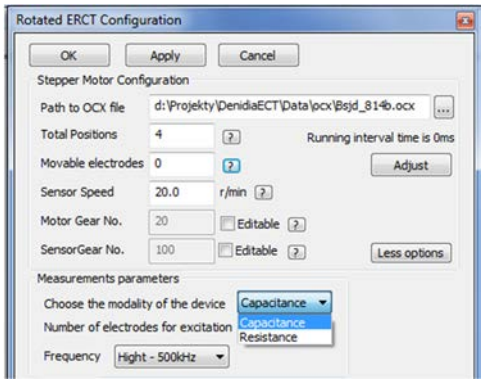

Fig. 7. The rotatable sensor – ECT hardware configuration window

This module also includes a specialized reconstruction submodule that takes into consideration increased amount of measurement data and reconstruct and visualize images in a realtime. There is an important fact that increased number of capacitance data is much more time consuming comparing to a conventional non-rotatable ECT system. The system developed in the Institute of Applied Computer Science is able to provide 2 frames/s using 12-electrode sensor and 4 rotation positions but the number of capacitance data increases from 66 to 264. The current speed of the rotatable ECT system can bring some difficulties for its real especially dynamically unfolded industrial application but the preliminary results are promising for non-invasive monitoring of static or slowly-unfolded processes.

5. Mesh generator for computer model of electrical sensors

The design of an ECT capacitance sensor consists of many different steps. One of the most important is the project of the sensor's computer model, based on a 3D spatial mesh. Before our application has been developed, spatial or plain meshes have been generated with help of external, ready-to-use and mostly universal tools, e.g. NETGEN. However, such tools are intended for general use in many engineering fields and therefore they do not allow implementing all design ideas. For these reasons we developed a *TomoKISStudio* module for automated mesh generation, namely *ERCT Mesh Generator*, which is designed to for both plain (2D) and spatial (3D) meshes ubiquitous in capacitance and impedance tomography.

The presented software has the following features and functionalities:

- ready-to-use and fully configurable mesh-generators for cylindrical sensors. There is no need to write scripts or configuration files, every parameter can be modified via windows dialog boxes,
- implementation of functionality for Complete Model [1] approach.

The Complete Model mesh consists of three layers: the inner layer (marked as M_i in Fig. 8) used as a base for image reconstruction algorithms, the insulation layer (marked as M_t) which is often a material of sensor's tube with electrodes placed on the outer surface (S_2) and the outer layer (M_o) which is insulation between electrodes and shield (S_3) of the sensor,

- The ability to generate meshes for both plain and spatial meshes,
- The ability to set the sparseness value in every point of the sensor as a pair-wise linear function of radius; each value can be freely modified by the designer,
- The ability to setup geometrical parameters of generated mesh, such as thickness of the sensor's tube (insulation layer) or the radius of the image layer (inner layer),
- The ability to setup material parameters in every layer of the sensor, namely electrical permittivity (for capacitance sensors) or resistivity (for impedance sensors),
- Instant generation of mesh data as text files for further use in other software than TomoKISStudio, e.g. Matlab,
- The ability to generate image files for visualization in VTK toolkit, helpful in preparing presentations or papers.

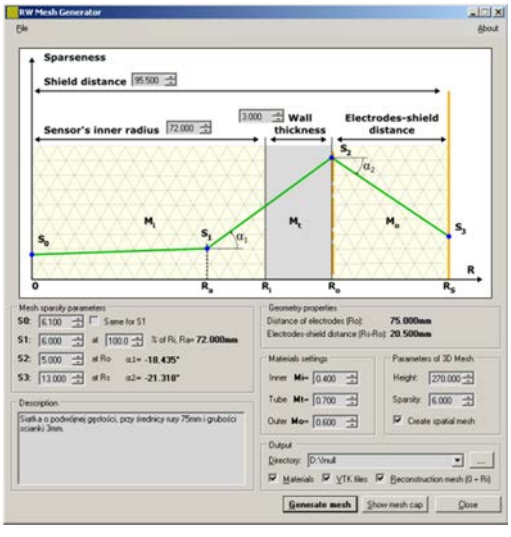

Fig. 8. ERCT mesh generator – presented software for automated generation of sensor meshes

Developed software allows viewing (Fig. 9) in real time the results of entered configuration values as the top cap of the mesh. There are three layers shown, marked with different colors, which correspond to the illustrative draft in the main window (Fig. 8).

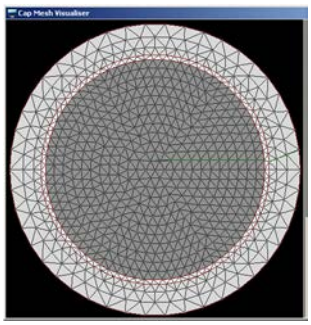

Fig. 9. An example of generated mesh with Complete Model feature turned on

In addition, useful numerical information about the mesh is displayed:

- radius value for each ring in the top cap,
- density (distance between nodes) value for each ring,
- number of nodes on each ring,

and other information important for the duration of electrical field simulations, like number of nodes or finite elements in plain or spatial mesh.

The development of the presented tool is also justified by the instantiation in application for cylindrical sensors in CT, the possibility of rapid expansion and adjustments to new ideas and fields of application. Existing software tools (e.g. Netgen) allow only the amount of flexibility possible in terms of their internal configuration and scripting languages. However, our own software allows fast and easy modifications and interference in any part of its algorithms. In our case, self-developed software allowed to improve research on electrical tomography, including the Complete Model of spatial capacitance and impedance sensors by immediate and automated generation of meshes with different internal configurations.

6. The module for designing spatial distribution of electrodes in electrical tomography sensors

The design and assemblage of a capacitance sensor for 3D ECT is a key task in the overall building process of 3D electrical tomography measurement system. The quality and precision of measurements is therefore strongly affected by two factors: physical (e.g. the materials, precision of electrical components and their assembly) and theoretical (e.g. distribution of electrodes, size of finite elements and density of the model mesh). Our solution partially covers later factor by combining mesh generation (and altering) with designing spatial distributions of electrodes in one monolithic CAD-like environment, namely *Layout Builder* [6] shown in Fig. 10. In following we present main features and functionalities of Layout Builder module:

- utilization and processing of spatial tetrahedral meshes,
- defining the geometric distribution of electrodes on proper surface of the sensor,
- creating distribution of electrodes for cylindrical and rectangular sensors,
- model data files can be generated and stored for later use in electrical field simulation and image reconstruction algorithms,
- an image of spatial distribution of electrodes on the surface can be generated as a bitmap file and used in assembly process of the sensor. Directly, images can be quite helpful in etching of electrodes from copper laminate.

In addition, developed software allows to visualize designed distribution of electrodes (in *3D View* tab) and to export such visualization into data files, compatible with VTK toolkit.

The design process of a typical cylindrical capacitance sensor with help of *Layout Builder* is performed in three steps:

First is to create a distribution of electrodes on the surface of a sensor. To achieve this, proper tools have been developed. They allow to group electrodes in rings (rows of electrodes) and precisely position them on the sensor's surface. Such design can be done coarsely using visual tools or precisely by entering the appropriate numerical values.

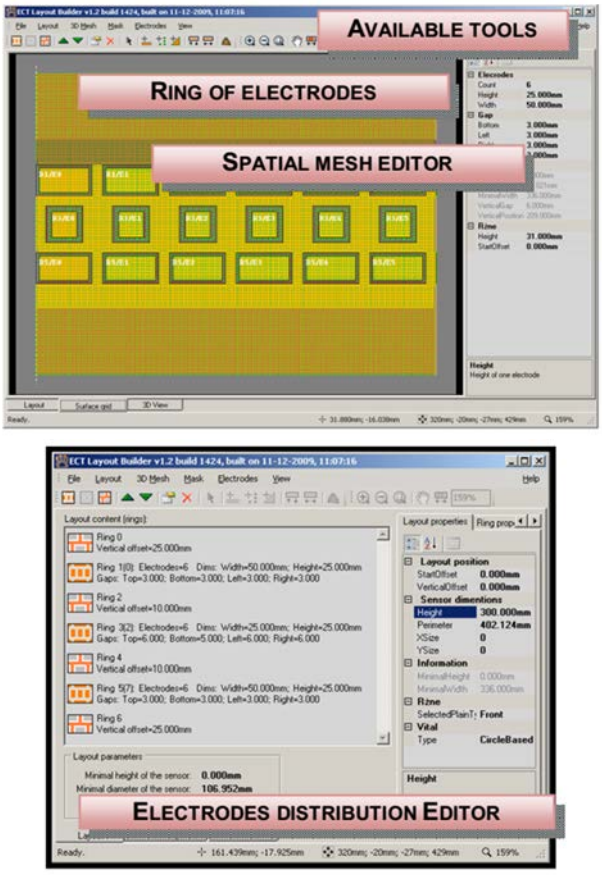

Fig. 10. Graphical User Interface of the Layout Builder software

Second step is to load spatial mesh which will be the sensor geometry base and input data for further reconstruction and visualization algorithms. Loaded mesh should be adjusted to the previously developed distribution of electrodes by moving or adding nodes. This is done in the edit panel of the spatial mesh editor. Similarly for the first step, one can use coarse visual editing tools and adjust mesh with mouse or one can specify exact nodes coordinates values.

Third step is to generate the adjusted mesh required to determine the sensitivity matrix as a vital part of reconstruction algorithms. Reconstructed image uses same mesh in visualization process, hence adjusted mesh is required in imaging process as well.

Preparation of a sensor corresponding to the assumptions of the design is inherently an iterative process. It consists of: creating a numerical model and determining its quality by evaluating the results of simulations, the proper adjustments of the model and re-simulation. Evaluation is based on quality of the modeled electrical field distribution inside the sensor and the reliability of the results of reconstruction. On this basis, adjustments are made to the finite element mesh of the sensor and to the geometric parameters of electrodes - their location, number and size.

So far, such modifications have been performed manually, e.g. by creating source codes for modifying the finite element meshes or manually drawing the distribution of electrodes in graphics software. This was due to a lack of specialized tools for modeling sensors.

The *Layout Builder* software fully automates this process by providing tools that enable simultaneously: designing distribution of electrodes, matching them to the mesh and generating data for subsequent simulations. This result in a significant reduction in time needed to perform a series of numerical models needed to obtain the sensor with the best parameters. It should also add that the developed software holds consistency between the model mesh, the layout and sensor electrodes by eliminating the possibility of human error in various stages of the modelling process.

7. Sensitivity and voltage software analyser

The task of image reconstruction process for the three-dimensional capacitance or resistance tomography is a crucial problem in a tomographic visualization process. The three-dimensional image is built using a set of sophisticated algorithms based on the finite elements grid of 3D ECT or ERT sensor model. The aim of it is to as fast as possible reconstruct the material distribution from the measurement data. Because of the similarity between the 2D and 3D electrical systems the three-dimensional visualization is possible using the deterministic image reconstruction algorithms like methods based on back-projection (one-step or iterative scheme) including non-linear methods [9–11].

The main goal of the method is the linearization of the inverse problem. The linearization assumes that the total change of the measured capacitance for any electrodes pair is equal to the sum of the particle capacitance changes. The mentioned particle change is directly proportional to the change of the electrical field energy in the given image element as a result of the change of the material permittivity value in this element. Such linearization product in the image reconstruction process is the sensitivity matrix.

It is worth to mention that the image reconstruction process commonly performed on "voxels" (i.e. tetrahedrons) in case of 3D ECT is very time consuming. This is due to the large number of image elements which are repeatedly analysed during algorithm life time. The mentioned algorithms involve the matrix computations. The common known "voxel" approach uses matrices which significantly absorb the computer memory. The solution for this inadvertence could be the node-based sensitivity matrix [1]. Moreover, the node-based sensitivity matrix is able to significantly reduce the computation time needed for 3D image reconstruction processing. This reduction is directly proportional to the ratio of the mesh voxels number to the nodes number. The additional advantage is that the final 3D image is already determined directly in the nodes of the mesh and that case there is no need to approximate it in the sense of its further processing before presentation by the graphics engine.

For purposes of this problem the specialist module has been built which supports the two and three dimensional sensitivity analysis of any capacitance or resistance sensor which computer model was generated using the plug-ins described above. This module called *Sensitivity Analyser* (see figure 11) has implemented the following functionality:

- calculation of the potentials distribution for each electrode respecting the assumed permittivity distribution using FEM method,
- calculation the sensitivity matrix for given sensor geometry on the basis of calculated electrical field,
- calculations can be performed for the 2D as well as for the 3D space,
- the Complete Model can be considered,
- three dimensional visualisation of each sensitivity map as well as the electrical field,
- configuration of different visualization effects.

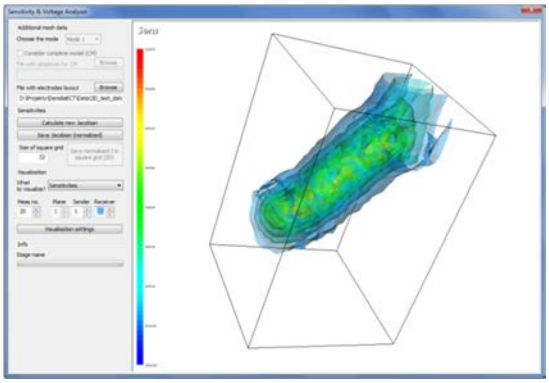

Fig. 11. Graphical user interface of the Sensitivity Analyzer module

8. GPU acceleration

GPGPU (General-Purpose computing on Graphics Processing Units) is a technique of using graphic cards (GPUs), which normally handles graphics rendering, for computations that are usually handled by processor (CPU). Growing interest in GPU computations started with the inability to clock CPU above certain level, because of the limitations of silicon based transistor technology and constant demand for improvements. Because of this interest in multi-core technology and parallel computing started to emerge, even though sequential programs are easier to understand, more natural. There is a limit though of how fast such program can run. Sequential speed up is now based on architecture improvements of the CPU rather than higher clocks, but even this approach has limitations. Parallel programming is not a new idea [4, 5] though till only recently it was reserved for high performance clusters with many processors, the cost of such solution was extremely high. This changed with the introduction of many-core processors to the mainstream market. GPUs fit well in that trend, even take it to another level. Compared to CPU which, today, have maximum of 2 to 12 cores, GPU consist, of dozens, and even hundreds of smaller, simpler cores designed for high-performance calculations. CPUs are built and designed to execute single thread no matter how unpredictable, diverse or complicated it may be as fast as possible. For that they require additional resources such as: complicated mechanisms for predicting branches, cache memory and data prefetch. On the other hand GPUs mostly take care of data computations that are much simpler in their nature and for that reason their execution units, or cores, can be much simpler, which also mean smaller. Thanks to that there can be much more of them on a single chip with numbers reaching dozens or even hundreds. Also, because graphics computations can be easily parallelizable cores in GPU work based on a SIMD (Single Instruction, Multiple Data), or more precisely.

Fig. 12. Dialog window with image reconstruction settings and CUDA acceleration

In the frame of the presented software the authors developed a CUDA code [7] that has been successfully verified using 3D ECT numerical model and 3D image iterative reconstruction approach. A significant speed-up of 3D image reconstruction

process was achieved using cheap market-level graphics processors. Thanks to this module it is possible to perform i.e. Landweber or SIRT image reconstruction with more than 10 iterations and achieve the image rate equal to the 3D 32-electrodes ECT measurement frame rate.

TomoKISStudio just after its start loads CUDA library driver and then tries to find accessibility of any graphics card in the system. In case of successful result of this process in the dialog window with the image reconstruction process settings the CUDA acceleration and the methods supported with the parallel computations are enabled – see fig. 12.

In addition the user is always informed in the status bar of the application about details of the found graphics cards as well as the version of CUDA and VTK libraries – see fig. 13.

Fig. 13. Status bar of TomoKISStudio with information about accessible GPU and CUDA library

9. 3D visualization effects

Because the visualization module for presenting the 3D tomograms, sensitivities and potentials distribution is supported by the VTK library *TomoKISStudio* application performs the image presentation applying different interesting effects. There are:

- the colors values interpolation between the nodes,
- three cross-sectional cut planes freely defined along three axes,
- set of iso-surfaces defined by the threshold value,
- algorithm HAVS (Hardware Assistance Visibility Sorting),
- banded surface maps,
- electric field lines,
- freely configurable levels of transparency for all effects separately,
- legend for the image,
- export of the current image to the file in TIFF format.

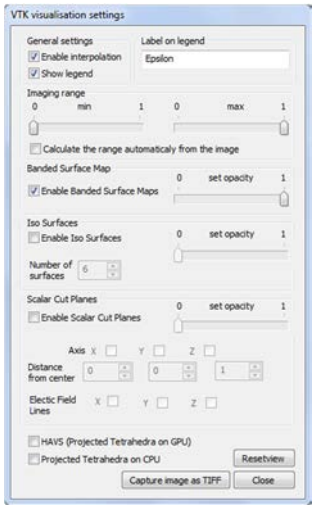

Fig. 14. Dialog window with visualization settings

References

[1] Banasiak R., Wajman R., Sankowski D., Soleimani M.: Three-dimensional nonlinear inversion of electrical capacitance tomography data using a complete sensor model. Progress In Electromagnetics Research (PIER), 100/2010, 219–234.

[2] Banasiak R., Wajman R., Soleimani M.: An efficient nodal Jacobian method for 3D electrical capacitance tomography image reconstruction. 51/2009, 36–39.

[3] Brzeski P., Mirkowski J., Olszewski T., Pląsowski A., Smolik W., Szabatin R.: Multichannel capacitance tomograph for dynamic process imaging. Opto-Electronics Review, 11/2003, 175–180.

[4] Collignon T., Van Gijzen M.: Two implementations of the preconditioned conjugate gradient method on heterogeneous computing grids. International Journal of Applied Mathematics and Computer Science, 20/2010, 109–121.

[5] Janiszowski K.B.: Inversion of square matrices in processors with limited calculation abilities. International Journal of Applied Mathematics and Computer Science2, 13/2003, 199–204.

[6] Jaworski T., Wajman R.: Graphical User Interface for building the spatial definition of the electrodes in 3D Electrical Capacitance Tomography. Zeszyty naukowe Automatyka, AGH, 3/2009.

[7] Kapusta P., Majchrowicz M., Sankowski D., Banasiak R.: Application of GPU Parallel Computing for Acceleration of Finite Element Method Based 3D Reconstruction Algorithms in Electrical Capacitance Tomography. Image Processing & Communications, 17/2012, 339–346.

[8] Liu Z., Babout L., Banasiak R., Sankowski D.: Effectiveness of rotatable sensor to improve image accuracy of ECT system. Flow Measurement and Instrumentation, 21/2010, 219–227.

[9] Soleimani M.: Three-dimensional electrical capacitance tomography imaging. Insight - Non-Destructive Testing and Condition Monitoring, 48/2006, 613–617.

[10] Wajman R., Banasiak R., Mazurkiewicz L., Dyakowski T., Sankowski D.: Spatial imaging with 3D capacitance measurements. Measurement Science and Technology, 17/2006, 2113.

[11] Wang F., Marashdeh Q., Fan L.S., Warsito W.: Electrical capacitance volume tomography: Design and applications. Sensors, 10/2010, 1890–1917.

Ph.D. Eng. Robert Banasiak
e-mail: robert.banasiak@p.lodz.pl

Dr Robert Banasiak is an Assistant Professor at the Institute of Applied Computer Science at Lodz University of Technology in Poland. His work deals with the industrial applications of electrical process tomography, in particular the computational problems of image reconstruction and numerical modelling of capacitance tomography systems.

Ph.D. Eng. Radosław Wajman
e-mail: rwajman@iis.p.lodz.pl

Dr Radosław Wajman is an Assistant Professor at the Institute of Applied Computer Science at Lodz University of Technology in Poland. His research area focuses on the application of three-dimensional capacitance tomography systems for non-invasive monitoring, diagnosis and industrial automatic control system for pneumatic transport of bulk materials and two-phase gas–liquid flows.

Ph.D. Eng. Tomasz Jaworski
e-mail: tjaworski@iis.p.lodz.pl

Dr inż. Tomasz Jaworski is an Assistant Professor at the Institute of Applied Computer Science at Lodz University of Technology in Poland. His work deals with the image processing and fuzzy logic inference.

M.Sc. Eng. Paweł Fiderek
e-mail: p.fiderek@iis.p.lodz.pl

Paweł Fiderek is a Ph.D. student in the Institute of Applied Computer Science in Lodz University of Technology. In his work he deals with the issues in the field of electrical capacitance tomography, artificial intelligence (mainly fuzzy logic), two phase gas-liquid flows recognition, fuzzy control, software engineering, image processing and recognition.

Prof. Dominik Sankowski
e-mail: dsan@iis.p.lodz.pl

Prof. Sankowski is the head of Institute of Applied Computer Science. Hi has formed scientific teams in the following fields: signal processing, image processing and analysis, process tomography, software engineering, artificial intelligence and automatic identification and control of industrial objects in real-time systems. Recent publications have been concerned with issues related to the information society and the computerization of public administration.

otrzymano/received: 20.09.2016 *przyjęto do druku/accepted: 15.02.2017*

DOI: 10.5604/01.3001.0010.4576

INTELLIGENT SYSTEM FOR THE TWO-PHASE FLOWS DIAGNOSIS AND CONTROL ON THE BASIS OF RAW 3D ECT DATA

Paweł Fiderek, Tomasz Jaworski, Robert Banasiak, Jacek Nowakowski, Jacek Kucharski, Radosław Wajman
Lodz University of Technology, Institute of Applied Computer Science

Abstract. *In this paper the new intelligent system for two-phase flows diagnosis and control is presented. The authors developed a fuzzy inference system for two phase flows recognition based on the raw 3D ECT data statistical analysis and fuzzy classification which identify the flow structure in real-time mode. The non-invasive three-dimensional monitoring is possible to conduct even in non-transparent and non-accessible parts of the pipeline. Presented system is also equipped with the two phase gas-liquid flows installation control module based on fuzzy inference which includes the feedback information from the recognition module. The intelligent control module working in a feed-back loop keep the sets of required flow regime. Presented in this paper fuzzy algorithms allow to recognize the two phase processes similar to the human expert and to control the process in the same, very intuitively way. Using of the artificial intelligence in the industrial applications allows to avoid any random errors as well as breakdowns and human mistakes suffer from lack of objectivity. An additional feature of the system is a universal multi-touched monitoring-control panel which is an alternative for commercial solution and gives the opportunity to build user own virtual model of the flow rig to efficiently monitor and control the process.*

Keywords: fuzzy inference, fuzzy logic, fuzzy control, 3D capacitance tomography, raw measurement data analysis, fluid flow measurement and control

INTELIGENTNY SYSTEM DIAGNOSTYKI I STEROWANIA PRZEPŁYWAMI DWUFAZOWYMI NA PODSTAWIE POMIARÓW 3D ECT

Streszczenie. *W artykule zaprezentowany został inteligentny system diagnostyki i sterowania przepływami dwufazowymi gaz-ciecz. Autorzy opracowali rozmyty system wnioskowania oparty o statystyczną analizę i klasyfikację rozmytą surowych danych pomiarowych 3D ECT realizujący w czasie rzeczywistym identyfikację struktury przepływu oraz wyznaczanie objętościowego udziału faz. Nieinwazyjny trójwymiarowy monitoring przepływu możliwy jest w nieprzezroczystych i trudno dostępnych fragmentach rurociągów w czasie rzeczywistym. Prezentowany system wyposażony jest również w moduł sterowania instalacją w oparciu o wnioskowanie rozmyte, któremu na wejście podawane są informacje zwrotne od modułu rozpoznawania. Inteligentny regulator rozmyty pracujący w pętli sprzężenia zwrotnego utrzymuje żądane nastawy parametrów przepływu w oparciu o zadany reżim przepływu. Przedstawione w niniejszym opracowaniu algorytmy rozmyte umożliwiają identyfikację procesów dwu-fazowych w sposób analogiczny do tego, jak to robią specjaliści oraz jednocześnie pozwalają kontrolować proces w ten sam bardzo intuicyjny sposób. Zastosowanie sztucznej inteligencji w aplikacjach przemysłowych pozwala uniknąć przypadkowych ludzkich błędów podatnych na brak obiektywizmu, a także zapobiegać awarii. Cechą dodatkową systemu jest uniwersalny dotykowy panel monitorująco-sterujący stanowiący alternatywę dla drogich komercyjnych rozwiązań umożliwiający budowanie wirtualnego modelu instalacji, aby w szybki i skuteczny sposób móc ją monitorować i nią sterować.*

Słowa kluczowe: wnioskowanie rozmyte, logika rozmyta, rozmyte sterowanie, trójwymiarowa tomografia pojemnościowa, analiza surowych danych pomiarowych, rozpoznawanie i sterowanie przepływu gaz-ciecz

Introduction

In this article the authors presents the new *intelliFlowControl* system for the intelligent two-phase flows diagnosis and control. In figure 1 the flow diagram of the system together with its modules and data flow directions are depicted. The authors developed a fuzzy inference algorithms for the two-phase flows recognition based on the raw 3D ECT data analysis and the fuzzy classification which identifies the flow structures in a real-time mode. The non-invasive three-dimensional monitoring is possible to conduct even in a non-transparent and non-accessible parts of the pipeline. Presented system is also equipped with the two-phase gas-liquid flow installation control module based on the fuzzy inference which includes a feedback information from the recognition module. The intelligent control module works in a feed-back loop and keeps the sets of required flow regime. Presented in this paper fuzzy algorithms allow to recognize the two phase processes similar to the human expert and to control the process in the same, very intuitively way. The usage of the artificial intelligence in the industrial applications allows to avoid any random errors as well as breakdowns and human mistakes which suffer from a lack of objectivity. An additional feature of the system is the universal multi-touched monitoring-control panel which is an alternative for the commercial solutions and gives the opportunity to build user-own virtual model of the flow rig to efficiently monitor and control the process.

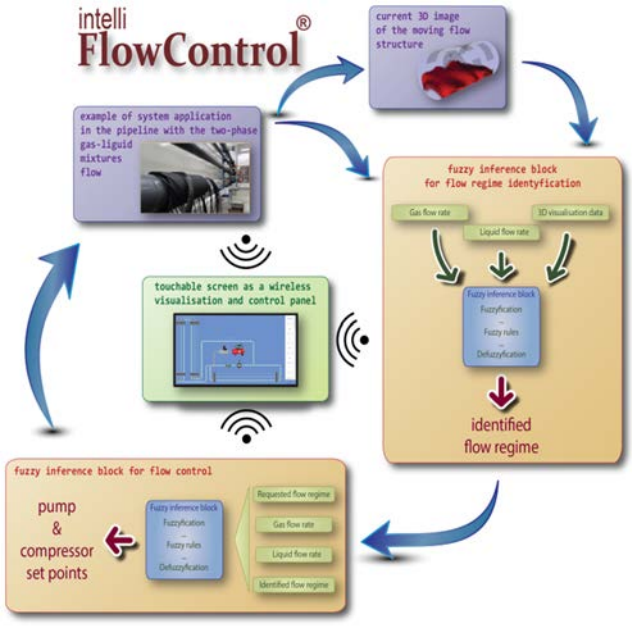

Fig. 1. Flow diagram of intelliFlowControl system

1. The two-phase gas-liquid mixtures flow

The two-phase gas-liquid flows belong to the most rapidly growing trend in fluid mechanics research. In recent years there has been significant, but still insufficient progress in the development of knowledge about these industrial processes.

The two-phase flows arouse growing interest because of their great practical significance. They are closely related to the rapidly developing field of research in bioprocess engineering, biotechnology, environmental engineering, energy, and many other related areas. The two-phase gas-liquid flows are component of many industrial processes [4, 18]. Some possibilities of the industrial applications for the developed system can be found, for example: aeration processes in chemical reactors, flotation processes, water and sewage aeration systems. The main

task of aeration system is a production of proper fraction of aerated liquid and oxygen. Oxygen injection process is important due to the fact that liquid circulation has to be achieved. It helps intensifying a mass transfer process. One of the fundamental problems in this matter is a proper evaluation of the inter-phase surface – this is the crucial parameter from the mass transfer point of view.

The two-phase flow processes also occur in the bubble columns. Their purpose is to implement the various physical and chemical processes. Controlling the size of the interface often determines the intensity of these processes. For example, in the air-lift columns and ejectors [5] the movement of the liquid stream is forced by the gas stream. Such devices are commonly used in the extractive industries (e.g. flotation processes) or to precipitation of some fraction of the liquid in the sedimentation processes, such as degreasing where the size of bubbles is significant.

1.1. Characteristics of the flow types

One of the main challenges in the two-phase flows is a possibility of a priori prediction of features and type of mixture flow on the basis of known apparent velocity values, the properties of individual phases and finally of the flow geometry (like diameter and inclination angle of the pipeline). Many various techniques have been developed to observe and understand mixture flow structures. They vary from the simplest visual observations by different photography techniques through the optoelectronic detectors to the newest methods of using the two- or three-dimensional computed tomography. One of the most commonly tool for the two-phase flow types classification is a flow map which in the form of a diagram represents the flow in term of important and useful parameters providing information about phases rate [5].

The observed structures of the gas-liquid mixture flow in the pipes of the vertical ascending movement are compatible with those presented by Nicklin and Davidson [16]. These structures often classify this type of flow. Five basic flow patterns are known like bubble flow, slug flow, foam flow, ring flow and dispersion flow. When the two-phase mixture is flowing from the top to bottom (counter-flow) the flow structures were defined by Oschinowo and Charles [17]. It is worth to note that these structures relate to a two-phase mixtures of liquids with high viscosity - not exceeding 100 mPa·s. For liquids with a higher viscosity the flow structures have to be defined differently. However, because of the volume constraints of this article the authors decided to indicate only the reference to the relevant publication [24].

Additionally, in case of the horizontal pipelines the distribution of the liquid is influenced by gravity that acts to stratify the liquid to the bottom of the tube and the gas to the top. Flow types for co-current flow of gas and liquid in a horizontal pipeline are categorized in [11] as dispersed, stratified, slug, plug, wavy and annular. It is worth mentioning that additional flow types may be observed which keep features of two (or more) basic flow types listed above. These flow types are called as transitional flows [3] and are dependent on the flow features of which they consist. Therefore, defining the transitional type it is required to add an additional information of its base component types. In figure 3 the reader may observe the crisp borders (blue lines) between the flow types as well as the transitional areas (red lines).

The common methods dedicated for flow identification applied so far can be generalized into three groups:

- the methods based on the analysis of images acquired from a high-speed black and white or color CCD camera (100/200 frames per second) using standard techniques of filtering and edge detection. The classification of the flow structures is based on image segmentation. Also the neural networks with the elements of fuzzy logic [19] used to be applied for the image processing;
- the methods based on the analysis of the measured signals acquired from facilities as flow meters and pressure gauges dedicated for flow monitoring. These signals are analyzed in the field of amplitude or frequency [5,12] and finally the local void fraction and the local volumetric interfacial area can be obtained as the result of fuzzy clustering or neural networks [10];
- the methods based on the tomograms (e.g. capacitance, impedance tomography) analysis. A set of electrodes is placed around the pipe and then the cross-sectional 2D or spatial 3D image is reconstructed [1]. In the literature two main approaches can be found which either perform the 2D image reconstruction with its analysis [13, 27, 28] or direct analysis of the raw measurement data missing the reconstruction process [7, 8].

The proposed novelty described in this article is based on the usage of raw tomographic measurement data (not images) obtained spatially from the Three-Dimensional Electrical Capacitance Tomography (3D ECT) sensor and their direct fuzzy analysis in the way of main structures and flow type recognition. The analysis of the tomographic raw measurement data is actually more effective (also in terms of processing time).

2. Main principles of ECT technique

Electrical Capacitance Tomography (ECT) is the measurement technique which has already been successfully applied for monitoring the two-phase industrial flows in which each of the phases differs with the dielectric permittivity [22, 25]. State-of-the-art concerning the applications of the tomographic techniques for the two-phase gas-liquid flow visualization can be found in many of conference proceedings from World Congresses on Industrial Process Tomography held continuously every 2 years, starting in Buxton, England in 1999. Knowing the relationship between the concentration of ρ and the dielectric permittivity ε it is possible to determine the liquid and gas phase distribution. This in turn allows the identification of the flow structure and measurement of the void fraction. This type of measurement technique seems, in fact, to be the most effective in applications for flows mainly because of its speed and non-destructive feature.

The typical ECT system consists of a capacitance sensor, the measurement unit and finally PC computer. In the scientific works as [27, 28, 26, 31] concerning the ECT applications for two-phase gas-liquid flows monitoring just the two-dimensional images were produced with the flow structures and the phase distribution. The two-dimensional image cannot fully reveal the information about the flow in the measuring area. It is created by averaging the signal across the electrodes ring, creating a cross-sectional image of the pipeline. In this case the spatial phenomena of the electromagnetic field distribution are neglected and additionally in the case of long electrodes this averaging prevents an accurate measurement. It was therefore necessary to develop the three-dimensional capacitance tomography [13, 22, 25]. The information on the entire structure of the flow is obtained by 3D visualization of the material distribution. This type of imaging requires a specific deployment of the measuring electrodes as well as an appropriate measurement procedure.

The principle of ECT technique is based on measuring changes in electric capacitance between the electrodes as a result of changes in the dielectric object located between these electrodes. The dielectric object in this case is a liquid with gas bubbles. The measurement concept is as follow: once the positive potential on one of the electrodes (excited electrode) is set, while others are grounded. The measured values of capacitances are collected and then further electrodes are excited. Having 32 electrodes 3D ECT sensor it is possible to acquire 496 single measurements in one frame with the rate 12 frames/sec.

3. Fuzzy logic

Fuzzy logic is a multi-valued logic and a generalization of the classical two-valued approach. It was proposed by Lotfi Zadeh [29] and is closely related to his theory of fuzzy sets [30]. The fuzzy logic, in opposite to standard two-valued logic, between the state of 0 (false) and the state of 1 (true) extends a number of intermediate values that determine the degree of membership of the element to the investigated collections.

Fuzzy logic is proved to be useful in engineering applications where the classical logic of classifying (only by the criterion of true and false) cannot effectively deal with many ambiguities and contradictions [2]. There is a lot of applications [21] including electronic control systems (machines, vehicles etc.), data mining tasks, or in the construction of expert systems where the fuzzy logic and fuzzy logic based algorithms are in use.

4. The test flow rig

The experimental rig was built in Institute of Applied Computer Science at Lodz University of Technology. Each of the various sections (horizontal and vertical) is equipped with a measuring pipeline at three different internal diameters – respectively 34, 53.6 and 81.4 mm, which allow to test two-phase flow processes at different scales. The length of horizontal measuring section is approximately 7.5m, while the length of vertical one is approximately 4m. All measuring sections contain transparent pipes which allow to visually (e.g. by photo camera) observe a flow structures movement. Pipelines are made of polyvinyl chloride (PVC) and are equipped with valves made of the same material.

The flow facility can be supplied with a fluid by the system which consists of two storage tanks and multi-stage centrifugal pump. In one of the tanks there is a propeller stirrer equipment installed which allows to prepare the research liquid such the aqueous solutions of the various substances. Thanks to the installed electromagnetic flow meters it is possible to precisely designate the volumetric flow rate. The pump CRN's 45 made by Grundfoss company provide the maximum flow stream of the liquid (with a viscosity close to the viscosity of water) pumped into the pipeline at the level of 50m3/h. In addition, the applied screw compressor DMD 100CR allows to obtain the volume stream of air at 1000 l/min with pressure about 7bar. The mentioned conditions overall let to obtain all types of two-phase flows occurring in industrial environments - from the bubble to annular flow.

5. Flow recognition module

The flow recognition mechanism combining three types of processing was developed. The core of the proposed solution, reflecting the main features of the flow map, constitutes the similarity level of the observed flow to the reference one. A supplementary information on the gas and liquid flow streams are introduced for final classification of the given flow, making the whole mechanism more flexible. Since all used data are treated qualitatively the adequate linguistic variables are built using proper fuzzy sets.

5.1. Flow similarity

The set of patterns was built using the expert's opinions (see section 7 – Experimental results). The algorithm for flow similarity level determination was described in details in [6]. The similarity of a given flow to the reference one is determined by the fuzzy clustering of the raw ECT data. FCM (fuzzy c-means) classifier is the most popular classifier based on fuzzy logic. This mechanism allows the classification of a single object to more than one cluster (group) with varying degrees of belongingness – instead of classic two valued logic based classification where an object fully belongs to the cluster or does not belong at all. A characteristic feature of the algorithm is a fact that the shape of each cluster in the feature space is the same and depends on the accepted standards.

Since the similarity can be considered as an inherently imprecise quantity the authors defined and depicted in fig. 2 the linguistic variable *similarity level* that describes the flow similarity using five linguistic terms: *no similarity* (dark blue line), *low similarity* (red line), *medium similarity* (green line), *high similarity* (purple line), *identical* (light blue line).

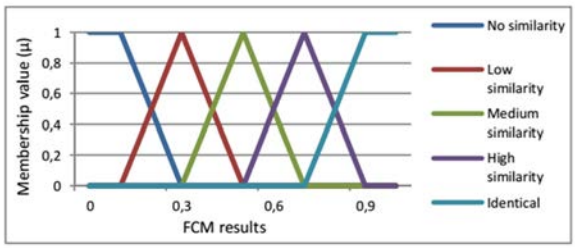

Fig. 2. The flow similarity level of the linguistic variable and the membership functions

In order to decompose the linguistic variable (*membership degree*) into terms the membership functions depicted in fig. 2 need to be used. These functions get the character of a triangular function and are generalized form of characteristic functions of fuzzy sets (terms). Implementing the FCM classifier, which returns the similarity (*membership*) degree of analyzed flow to the referenced flow as a value in range <0;1>, the further fuzzy analysis of the flow is possible using calculated membership functions.

5.2. The gas and the liquid flow streams fuzzyfication

In order to describe the liquid and gas flow streams (precisely enough to distinguish the different flow types) the two linguistic variables were defined. Each variable is split into 4 terms:

- Low gas/liquid flow stream;
- Medium low gas/liquid flow stream;
- Medium high gas/liquid flow stream;
- High gas/liquid flow stream;

The ranges and the shapes of the fuzzy sets representing the linguistic terms were determined during the clusterization of the test flows set and were adjusted due to the human expert opinion.

The base membership functions were determined in basis of the trapezoidal-shape functions in which the sections of the trapezoids sides (legs) were replaced with the exponential functions. Thanks to this the non-crisp nature of the border between any of the two-phase flows types is reflected more accurately and is better customizable to the subjective assessment of the user.

The input values of the gas and liquid flow streams were obtained from the research facility measuring system (i.e. flow meters). Due to the relatively low accuracy of the measuring system and its frequent oscillations, these values cannot be considered as crisp values. To reduce the impact of the mentioned factors for the final recognition results the authors decided to use the input values of the gas and liquid flow streams as fuzzy numbers [29].

5.3. Fuzzy inference

Having defined the linguistic variables characterizing qualitatively the chosen features of the flow, the authors built the fuzzy inference machine based on if...then rules reflecting a human expert judgment procedure. Three types of numerical data (i.e. linguistic variables):

- the observed flow similarity to the previously defined flow patterns (i.e. slug flow, plug flow) determined using ECT data and FCM algorithm,
- gas flow stream measured by the research facility,

- liquid flow stream measured by the research facility,

were used as premises of the inference. The linguistic terms: slug, transitional and plug flow, were used in consequences. The set of designed fuzzy rules is presented in the table 1.

Table 1. Fuzzy rules used for fuzzy inference

If			then
Flow similarity	***Gas stream value***	***Liquid stream value***	***The observed flow is***
SP	low	low/mlow/mhigh/ high	plug
MSP	low	low/mlow/ mhigh / high	plug
HSP/MSP	medium low	low/mlow/ mhigh / high	transitional
HSS/SS	medium high	medium low	transitional
MSS	medium low	mlow/low	transitional
MSS	medium low	mhigh / high	slug
HSS/SS	medium high	not medium low	slug
SS	high	low/mlow/ mhigh / high	slug

where:

- MSS/MSP - flow with medium similarity level to the slug /plug flow,
- HSS/HSP - flow with high similarity level to the slug /plug flow,
- SS/SP - flow identical to the slug / plug flow,
- mlow - medium low,
- mhigh - medium high.

The two examples of the fuzzy rules are shown below:

I

if: the observed flow is *high similar* to the plug flow
and the gas flow stream is *medium low*
and the liquid flow stream is *medium low*
then: the observed flow is transitional flow

II

if: the observed flow is *identical* to the slug flow
and the gas flow stream is *medium high*
and the liquid flow stream is *medium low*
then: the observed flow is transitional flow

6. Fuzzy regulator principles

In the fuzzy regulator dedicated for the two-phase type control a decomposition of the input signal into two classes and two methods of their fuzzyfication is performed. The first class includes two input signals which determines the current state of the process i.e. the quantity of the phases supplied to the process. These signals are given as a linguistic variables which values are described with the membership functions. In this class the linguistic variables are treated as the 5-elements set: (V, T, D, G, M), where:

- V – is the name of the variable e.g. liquid stream,
- T – is the set of terms, verbal labels naming the values of the variable V e.g. small,
- D – is the consideration domain in where the linguistic variable V is defined, which describes the areas of D e.g. $D \in (0;50)\frac{m^3}{h}$,
- G – is the syntactic rule, which grammar has a character which can generate the derivative terms – the T labels e.g. T(liquid stream) = {..., "middle small", "middle", "middle large", ...}
- M – is the semantic rule, which set to the each linguistic value named l the meaning M(l).

Moreover, *M(l)* describes the fuzzy set defined in *D*. The example for *l="Middle"*:

$$M\text{:Middle} \rightarrow SR;\ \mu_{SR}(x);\ \ x \in D, \tag{1}$$

where: *SR* is the fuzzy set defined with the membership function μ_{RS} in the domain *D*.

In this class the fuzzified signals are the measurement values retrieved from the measurement instruments of the flow rig.

There is a disadvantage with the fuzzyfying the input signals using the classic method because in this case the values fluctuation of the input signal during its analysis is not considered and in case of such dynamic process like two-phase gas-liquid flow it is not acceptable. The most common method for the preparation of the measurement data series for the fuzzyfication purpose is their averaging. Unfortunately, the mean value does not consider the dynamic changes of the measured signal what is very important determining the control parameters for the process. The next inconvenience applying the classic fuzzy regulator is the lack of possibility of changing the shape and/or the type of the membership function for the decomposition of the linguistic variables describing the input signal into the terms [14] In case of the described here linguistic variables it is not also considered the classic fuzzyfication module. When the inference (fuzzy) rules do not cover the linguistic variables which are describing the current state of the process, then their conclusions always are of the same character dependent only on the value of the linguistic variable (*given type of the two-phase flow*)

The input signal in the regulator is therefore given in the form of the fuzzy number defined with the following membership function:

$$\mu_{\mathrm{is}}(x) = \begin{cases} 0 \rightarrow x \leq \bar{\mathrm{x}} - \sigma \\ \frac{1}{\sigma}\mathrm{x} - (\frac{\bar{\mathrm{x}}}{\sigma} + 1) \rightarrow x \in (\bar{\mathrm{x}} - \sigma; \bar{\mathrm{x}} > \\ -\frac{1}{\sigma}\mathrm{x} + (\frac{\bar{\mathrm{x}}}{\sigma} + 1) \ \rightarrow x \in (\bar{\mathrm{x}}; \bar{\mathrm{x}} + \sigma) \\ 0 \rightarrow x \geq \bar{\mathrm{x}} + \sigma \end{cases}, \tag{2}$$

where $\mu_{\mathrm{is}}(\mathrm{x})$ is the value of the membership function for $\mathrm{x} \in \mathrm{d}$, where: d – is the measurements range, $\bar{\mathrm{x}}$ – is the mean measurement value for the measurement data retrieved in time t, σ – is the standard abbreviation for the measurement data retrieved in time t.

The function $\mu_{\mathrm{is}}(x)$ gets the character of the triangular function. Next, the given fuzzy number is once more fuzzified using classic principles according to the Zadeh's extension principle [20, 29] (i.e. determining the intersection of two fuzzy sets). This approach, not used so far in similar issues, for the first class input signals fuzzyfication considers in the inference process not only the instantaneous or mean values of this signals but also the trend of their changes in the moment of measuring thus eliminating the inadequacy of the measurement system. An additional advantage is the amplifying the system sensitivity which is limited using the non-standard membership functions.

In the regulator there is the possibility of manipulating the shape of the membership function changing only one regulation parameter within the ten step regulation scale $a \in <1;10>$. The base membership functions were determined in basis of the trapezoidal-shape functions in which the sections of the trapezoids sides (legs) were replaced with the exponential functions. Thanks to this the non-crisp nature of the border between any of the two-phase flows types is reflected more accurately and is better customizable to the subjective assessment of the user. Below there is an example of the equation for defining one of the membership functions:

$$\mu_{t_i'}(x) = \begin{cases} 0 \rightarrow \ x \leq x_1 \\ (a_1 x - b_1)^{funMHG1(a)} \rightarrow x \in (x_1\,; x_2) \\ 1 \rightarrow \ x \in <x_2\,; x_3> \\ (-a_2 x + b_2)^{funMHG2(a)} \rightarrow x \in (x_3\,; x_4)\ m^3/h \\ 0 \rightarrow \ x \geq x_4 \end{cases}, \tag{3}$$

where:

$$funMHG1(a) = a_3 a + b_3$$
$$funMHG2(a) = a_4 a + b_4 \tag{4}$$

In the second class of the input signals of the presented fuzzy regulator there are two linguistic variables which express the status about the flow type currently taking place in the rig as well as the flow type required by the user. The linguistic variables in this class differ significantly from those in the first class. The main difference is their decomposition into terms performed in this class using fuzzy relations. Each of the fuzzy relations is defined in the two-dimensional space which determines the dependencies between both phases supplied to the flow rig. It is done in exactly

the same way as construction of the two-phase flow maps [23]. The membership functions which describe the given relations are based on the modified (crisp) between flows boundaries used in the classic flow maps adapted to the special flow rig and thereby define the two-phase flow type on the flow map as a fuzzy set. The both linguistic variables must have the same values set and the same membership functions which define the fuzzy relations in the values sets of those variables.

The fuzzy rules applied in the presented regulator are as follow:

$$\textbf{if } (z_1=t1_{z1}) \textbf{ and } (z_2=t1_{z2}) \textbf{ and } (z_3=t1_{z3}) \textbf{ and } (z_4=t1_{z4}) \textbf{ then } (z_1=t2_{z1}) \textbf{ and } (z_2=t2_{z2}), \quad (5)$$

where:

- z1, z2 –are the first class signals: the fuzzified value of gas stream and fuzzified values of the liquid stream,
- z3, z4– are the second class signals: current flow type and required flow type,
- t_{ij}– is the *i*-th values (term) of the *j*-th input signal.

Thanks to this it is possible to implement the „controlled" transitions between any of two flow types.

The extension premise of the fuzzy rules to the knowledge describing the flow rig state allows the two-phase flow type manipulation without the risk of the rig overloading e.g. to attain the required flow type within some inference cycles.

The inference process in turn is accomplished through the implementation of the modified fuzzified Mamdani-implication.

The outputs of the inference module are two fuzzy sets which represents expected, after finishing the control process, the flow rig state. These outputs actually are the sum of the signals which are the results of the inference rules conclusions.

The defuzzyfication process of the final fuzzy sets is performed in the presented regulator using the well-known *Center of Sums Defuzzyfication* [15] method.

7. Example results

The presented *intelliFlowControl* system was verified using the experimental rig that was built in Institute of Applied Computer Science at Lodz University of Technology. During the research reported herein, the authors focused on three types of flows observed in the horizontal pipeline of the diameter 60mm. The gas flow rate ranged from 0 to 50 m^3/h while the liquid flow ranged from 3 m^3/h to 9 m^3/h. The data were obtained from the 30 test flows and were validated by the human expert which is experienced in the field of the two phase gas-liquid mixtures. The expert's recognition accuracy was verified with the flow map. Considering the comparison results shown in fig. 3 it can be noticed that the flows classified by the expert as the slug flows or the plug flows are placed correctly in the appropriate areas of the flow map. However, some flows were recognized as a transitional ones and placed in the boundary region between the above two flow types. Moreover, several flows classified by the expert as transitional flows were placed definitely in the slug flow area of the flow map.

The experiments were carried out within the following steps:

- set the initial state,
- set by expert the required flow type,
- verification by the expert of the flow type after stabilization (i.e. after crisp regulation made by the regulator).

As a final result of each experiment the compatibility of the stabilized flow type with that set by the expert was checked. The table 2 includes the results of the experiments which cover all possible transitions between the three mentioned before flow types which were possible to observe in the given measurement range of the flow rig.

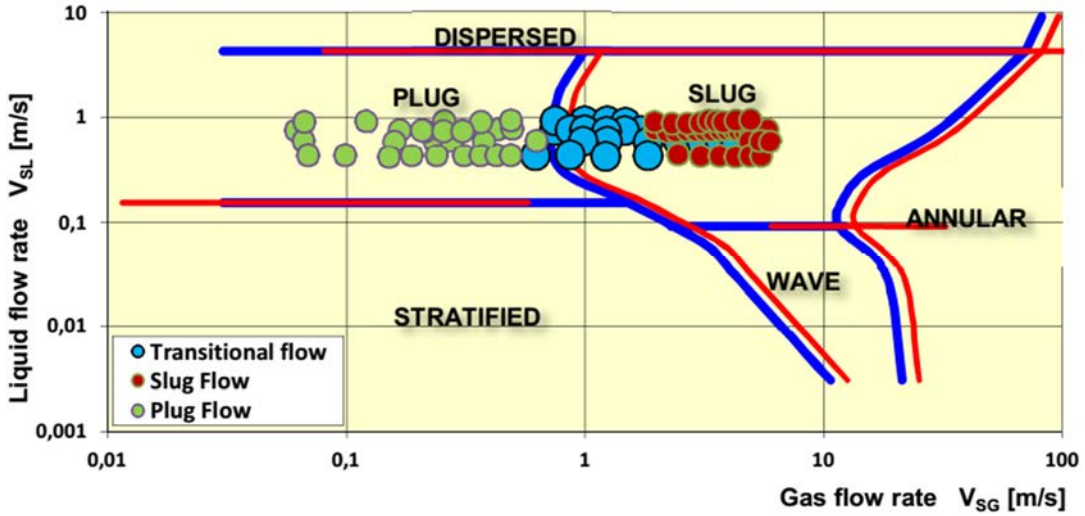

Fig. 3. The flow map with the marked location of the test flows set. The blue lines determines the crisp borders and the red are for transitional areas.

Table 2. Installation control process results

Flow number	1	2	3	4	5	6	7	8	9	10	11	12	13	14	15
Expert recognition	P→T	P→T	P→T	P→T	P→T	P→S	P→S	P→S	P→S	P→S	T→P	T→P	T→P	T→P	T→P
Fuzzy system recognition	P→T	P→T	P→T	P→T	P→T	P→S	P→S	P→S	P→S	P→S	T→P	T→P	T→P	T→P	T→P
Flow number	16	17	18	19	20	21	22	23	24	25	26	27	28	29	30
Expert recognition	T→S	T→S	T→S	T→S	T→S	S→P	S→P	S→P	S→P	S→P	S→T	S→T	S→T	S→T	S→T
Fuzzy system recognition	T→S	T→S	T→S	T→S	T→S	S→P	S→P	S→P	S→P	S→P	S→T	S→T	S→T	S→T	S→T

The description of the symbols used in table 2:

- the notation $T_1 \rightarrow T_2$ – is the transition from the flow type T_1 to the flow type T_2, where:
- P– is the plug flow,
- S– is the slug flow,
- T– is the transitional flow.

The time required for determining the crisp values of the control signals (the loop with the identification and regulator modules) was around 0.25 second and was negligible in comparison to the time needed for flow stabilization which was between 10 and 30 seconds and was highly dependent on the initial and target flow types. The computations were carried on using the PC computer equipped with the i7-3612QM CPU and 8GB under control of Windows 8.1 operating system. The system (identification and regulator modules) was implemented in the Microsoft .NET 4.5 environment using C# programming language. All the input signals were submitted to the system from the exterior measurement units (i.e. 3DECT device, the pump inverter, Brooks flow meters and pressure meters) using the Gigabit Ethernet network and the TCP/IP family protocols.

8. The universal multi-touched monitoring-control panel

An additional module of the system is the software for the multi-touched monitoring-control panel. It is an universal solution which can be easily adapted for any installation rig conditions. Thanks to the development of multi-touch gestures it is possible to control and monitor the process, to change i.e. the pipeline, the supply devices parameters like pump.

The applications provides the components library like bricks used in the installation rig model construction. It consists also of the GUI environment in which the users can develop their own components as the active or passive elements of the model. They can define the element style, functionality as well as the original graphical view assigned to its different state (i.e. opened/closed valve, identified flow regime, received measured value of the pressure).

The integral part of the software is the network module for the diagnostic and control commands multicast transmission. Each model component in the schema includes its ID and takes part in the dynamic data exchange. Thanks to this feature it can in a real-time mode change its appearance or label according to the state of the device that represents.

The new visualization environment designed considering the object-oriented aspects makes a universal good alternative for the expensive commercial solutions dedicated for the industrial processes monitoring and control.

9. Conclusions

The *intelliFlowControl* system with application of fuzzy methods for the purposes of the two phase gas-liquid flows identification and control has been developed. It has been demonstrated that the identification module can be a sufficient alternative to the methods commonly used in this field. A series of experiments have been completed using the test flow rig and the results (human expert contra fuzzy inference) were compared. Fuzzy sets and fuzzy inference supported with the non-invasive 3D ECT diagnosis have proved to be suitable for the identification process applied even for such dynamic phenomena as the two phase flows ensuring the accuracy as good as the human expert work. However, the proper preparation of the inference system mechanism guarantees the high quality of the recognition results.

The control module is characterized not only by the high operating speed but also by the universality of the application. It may support all the two-phase flow rigs where the precise of control is demanded. This precision is reached by the usage of the first class signals and the consideration in the inference process not only the current flow type and the flow type set by the user but also the current state of the flow rig (i.e. the current values of the control signal).Thanks to this approach it is possible to change the two-phase flow type changing only one control parameter about the minimum value which is required to achieve the set flow type and simultaneously without excessive overcharging the flow rig and the supply units.

The system is highly universal of use and easily adaptable to the work conditions by the maintenance stuff of the flow rig. It is because it shares the possibility of individual sets of the parameters as well as the intuitive inference rules. In addition, the innovative approach allows the user of the system to avoid the over-loop state in case when the algorithm would try to reach the unsupported or undesirable flow type.

10. Acknowledgments

This work was sponsored by National Science Centre of Poland as a part of the research project no 2011/01/D/ST6/07209.

Authors would like to thank to Dr Henryk Fidos for his help with the flows understanding and the flow test rig designing and maintenance.

References

[1] Banasiak R, Wajman R, Sankowski D., Soleimani M.: Three-dimensional nonlinear inversion of electrical capacitance tomography data using a complete sensor model Prog. Electromagn. Res., 100/2010, 219–234.
[2] Bellman R.E., Zadeh L.A.: Decision-Making in a Fuzzy Environment Manage. Science, 17B/1970, 141–164.
[3] Brauner N., Maron D.M.: Analysis of stratified/nonstratified transitional boundaries in horizontal gas—liquid flows Chem. Eng. Sci., 46/1991, 1849–1859.
[4] Chhabra R.P., Richardson J.F.: Encyclopedia of Fluid Mechanics ed N P Cheremisinoff (Houston: Gulf), 1986.
[5] Dziubinski M., Fidos H., Sosno M.: The flow pattern map of a two-phase non-Newtonian liquid-gas flow in the vertical pipe. Int. J. Multiph. Flow, 30/2004, 551–563.
[6] Fiderek P., Wajman R., Kucharski J.: Fuzzy clustering based algorithm for determination of the two-phase gas-liquid flows similarity level. Przegląd Elektrotechniczny, 2/2014, 52–55.
[7] Grudzien K., Chaniecki Z., Romanowski A., Niedostatkiewicz M., Sankowski D.: ECT image analysis methods for shear zone measurements during silo discharging process. Chinese J. Chem. Eng., 20/2012, 337–345.
[8] Grudzien K., Romanowski A., Chaniecki Z., Niedostatkiewicz M., Sankowski D.: Description of the silo flow and bulk solid pulsation detection using ECT Flow. Meas. Instrum., 21/2010, 198–206.
[9] Hewitt G.F., Roberts D.N.: Studies of two-phase flow patterns by simultaneous x-ray and flash photography (Berkshire: Atomic Energy Research Establishment, Harwell (England)), 1969.
[10] Ji H.J.H., Huang Z.H.Z., Wang B.W.B., Li H.L.H.: Monitoring system of gas-liquid two-phase flow Proc. 21st IEEE Instrum. Meas. Technol. Conf. (IEEE Cat. No.04CH37510) 3/2004, 2298–2301.
[11] Johnson R.W.: Handbook of Fluid Dynamics ed R W Johnson (CRC Press LLC), 1998.
[12] Li H.L.H., Zhou Z.Z.Z., Hu C.H.C.: Measurement and evaluation of two-phase flow parameters. IEEE Trans. Instrum. Meas. 41/1992, 298–303.
[13] Marashdeh Q., Wang F., Fan L.S., Warsito W.: Velocity measurement of multi-phase flows based on electrical capacitance volume tomography. Proceedings of IEEE Sensors 2007, 1017–1019.
[14] Matía F., Marichal G.N., Jiménez E.: Fuzzy Modeling and Control: Theory and Applications ed F Matía, G N Marichal and E Jiménez (Atlantis Press), 2014.
[15] Mitsuishi T.: Continuity of approximate reasoning using center of sums defuzzification method MIPRO, 2012 Proceedings of the 35th International Convention, 2012, 991–994.
[16] Nicklin D., Wilkes J., Davidson J.: Two-phase flow in vertical tubes. Trans. Inst. Chem. Eng. 40/1962, 61–68.
[17] Oshinowo T., Charles M.E.: Vertical two-phase flow part I. Flow pattern correlations Can. J. Chem. Eng. 52/1974, 25–35.
[18] Pląskowski A., Beck M.S., Thorn R.D.T.: Imaging Industrial Flows – Applications of Electrical Process Tomography (Bristol: IOP Publishing), 1995.
[19] Romanowski A., Grudzien K., Williams R.A.: Analysis and Interpretation of Hopper Flow Behaviour Using Electrical Capacitance Tomography Part. Part. Syst. Charact. 23/2006, 297–305.
[20] Rondeau L., Ruelas R., Levrat L., Lamotte M.: A defuzzification method respecting the fuzzification Fuzzy Sets Syst. 86/1997, 311–320.
[21] Ross T.J.: Fuzzy Logic with Engineering Applications, 3rd edition (UK: Wiley), 2010.
[22] Soleimani M., Wang H., Li Y.Y.W.: A Comparative Study Of 3D Electrical Capacitance Tomography. Int. J. Inf. Syst. Sci. 3/2007, 283–291.
[23] Taitel Y., Dukler A.E.: A model for predicting flow regime transitions in horizontal and near horizontal gas-liquid flow. AIChE J. 22/1976, 47–55.
[24] Taitel Y., Bornea D., Dukler A.E.: Modelling flow pattern transitions for steady upward gas-liquid flow in vertical tubes. AIChE J. 26/1980, 345–354.
[25] Wajman R, Banasiak R, Mazurkiewicz L, Dyakowski T., Sankowski D.: Spatial imaging with 3D capacitance measurements Meas. Sci. Technol. 17/2006, 2113.

[26] Wang F., Marashdeh Q., Fan L.S., Warsito W.: Electrical capacitance volume tomography: Design and applications Sensors 10/2010, 1890–1917.
[27] Xie C.G., Huang S.M., Hoyle B.S., Thorn R., Lenn C., Snowden D., Beck M.S.: Electrical capacitance tomography for flow imaging: system model for development of image reconstruction algorithms and design of primary sensors. Circuits, Devices Syst. IEE Proc. G 139/1992, 89–98.
[28] Xie D., Huang Z., Ji H., Li H.: An Online Flow Pattern Identification System for Gas-Oil Two-Phase Flow Using Electrical Capacitance Tomography. Instrum. Meas. IEEE Trans. 55/2006, 1833–1838.
[29] Zadeh L.A.: Fuzzy sets. Inf. Control 8/1965, 338–353.
[30] Zadeh L.A.: Toward a theory of fuzzy information granulation and its centrality in human reasoning and fuzzy logic. Fuzzy Sets Syst. 90/1997, 111–127.
[31] Zhang H.X.W., L F.: Identification of two-phase flow regimes based on support vector machine and electrical capacitance tomography. Meas. Sci. Technol. 20/2009, 114007.

M.Sc. Eng. Paweł Fiderek
e-mail: p.fiderek@kis.p.lodz.pl

M.Sc. Paweł Fiderek is a Ph.D. student at the Institute of Applied Computer Science at Lodz University of Technology. In his work he deals with issues related to computed tomography, image recognition and artificial intelligence, especially fuzzy logic.

Ph.D. Eng. Tomasz Jaworski
e-mail: tjaworski@kis.p.lodz.pl

Ph.D. Eng. Tomasz Jaworski is an adjunct professor in the Institute of Applied Computer Science at Lodz University of Technology. In his work he deals with issues related to fuzzy logic and image processing.

Ph.D. Eng. Robert Banasiak
e-mail: robert.banasiak@p.lodz.pl

Dr Robert Banasiak is an Assistant Professor at the Institute of Applied Computer Science at Lodz University of Technology in Poland. His work deals with the industrial applications of electrical process tomography, in particular the computational problems of image reconstruction and numerical modelling of capacitance tomography systems.

Ph.D. Eng. Jacek Nowakowski
e-mail: jacnow@kis.p.lodz.pl

Jacek Nowakowski works as an Assistant Professor at the Institute of Applied Computer Science at Lodz University of Technology in Poland. He graduated Mechanical Engineering Faculty and currently his research area focuses on the modelling and control of multiphase flows with the application of fractional calculus. Measurements are based on multimodal tomography developed during his stay in University of Bergen.

Prof. Jacek Kucharski,
e-mail: jkuchars@kis.p.lodz.pl

Professor Jacek Kucharski is a deputy director of the Institute of Applied Computer Science at Lodz University of Technology. In his research he mainly deals with fuzzy logic and thermal problems in electrical engineering.

Ph.D. Eng. Radosław Wajman
e-mail: rwajman@kis.p.lodz.pl

Dr Radoslaw Wajman is an Assistant Professor at the Institute of Applied Computer Science at Lodz University of Technology in Poland. His research area focuses on the application of three-dimensional capacitance tomography systems for non-invasive monitoring, diagnosis and industrial automatic control system for pneumatic transport of bulk materials and two-phase gas–liquid flows.

otrzymano/received: 20.09.2016 *przyjęto do druku/accepted: 15.02.2017*

DOI: 10.5604/01.3001.0010.4577

METHODS FOR MONITORING GRAVITATIONAL FLOW IN SILOS USING TOMOGRAPHY IMAGE PROCESSING

Krzysztof Grudzień, Dominik Sankowski
Lodz University of Technology, Institute of Applied Computer Science

Abstract. *The article presents the methods of monitoring of the process of gravitational silo discharging with aid of tomography techniques. The described methods apply to funnel and mass flow measurement. The core unit of the presented monitoring system is an image-processing module, while the images are obtained with aid of the electrical capacitance tomography. For the funnel type of flow, the outputs of image processing are parameters describing the process flow, location and material concentration in funnel area. In the case of the mass flow regime the presented method provides information about the parameters of shear zones arising by the wall region of the silo that influence the interaction between the bulk and silo construction during silo discharging.*

Keywords*: electrical capacitance tomography, tomography image processing, gravitational flow, granular material*

METODY MONITOROWANIA PRZEPŁYWU GRAWITACYJNEGO W SILOSACH Z ZASTOSOWANIEM PRZETWARZANIA OBRAZÓW TOMOGRAFICZNYCH

Streszczenie*. Artykuł przedstawia metody monitorowania procesu grawitacyjnego opróżniania silosu z materiałów sypkich z zastosowaniem technik tomograficznych. Opisane metody dotyczą pomiaru przepływu kominowego oraz masowego. Głównym elementem systemu monitorowania jest moduł przetwarzania obrazów uzyskanych przy pomocy elektrycznej tomografii pojemnościowej. Wynikiem przetwarzania obrazów są parametry procesu, opisujące lokalizację komina przepływu i koncentracji materiału w jego obszarze dla przepływu kominowego. W przypadku przepływu masowego przedstawiona metoda dostarcza informacji o obszarze strefy ścinania, występującej w obszarze przyściennym silosu, mającą wpływ na wynik interakcji materiału sypkiego i konstrukcji silosu podczas jego rozładunku.*

Słowa kluczowe: elektryczna tomografia pojemnościowa, przetwarzanie obrazów tomograficznych, przepływ grawitacyjny, materiał sypki

Introduction

The range of process tomography applications is very wide. Depending on the objectives of particular application different aspect of applied technique can be considered [7, 20, 24]. In order to choose the best option it is necessary to analyse needs of the speed of measurement acquisition system, image resolution, robustness and cost of the tomography system. Of course these aspects are connected with the process, which have to be measured. The level of dynamic changes of process states and the physic-chemical properties of process components (e.g. conductive or non-conductive materials) should be analysed [19, 21]. Besides these aspects it should be decided what is main function of applied measurement system: investigation works or real-time control. The use of tomography system in laboratory environment allows to be more flexible and easier to apply than in industrial application. However both fields of exploration can be used for other purposes. In order to elaborate better methods for flow monitoring of process, the process has to be investigated and physicochemical phenomena taking place during running process understanding. Such gained knowledge is necessary to prepare effective process control module with implemented algorithm of measurement data processing.

This paper demonstrates application of two different tomography modalities for gravitational flow optimization process from different point of view. The used electrical capacitance tomography systems allow monitoring the state of silo flow in real time. While the X-ray tomography system allows to investigate granular particle distribution in 2D radiography as well as 3D tomography in much higher resolution then in case of ECT, however in much smaller scale. Time resolution in the case of X-ray system is not so important as for the real-time monitoring system.

1. Gravitational flow in silo

Gravitational (gravity) flow is one of types of transport mechanism. Such type of flow is often used in installations of granular material transport system [2, 3, 19, 21]. In industrial installations, depending on purpose of installation, size and shape of silos can be different as well as the material of construction. These elements have significant influence on particle behaviour during flow. Additional factors having impact on the flow consist in the determination of the time variant factors (humidity, temperature conditions, etc.). Usually it is not easy to forecast such dependences during design stage of the container. Some of the characteristic features of the bulk solids flow are dynamic volume changes during processes of receptacle unloading [2, 3, 4, 14, 19]. These changes depend on many factors, such as initial density of the granular material, stress level, mean grain diameter, specimen size and direction of the deformation rate. These parameters can perturb silo flow. On Figure 1 is presented typical material distribution in silo. Depending on the material properties and silo geometry different flow types can occur.

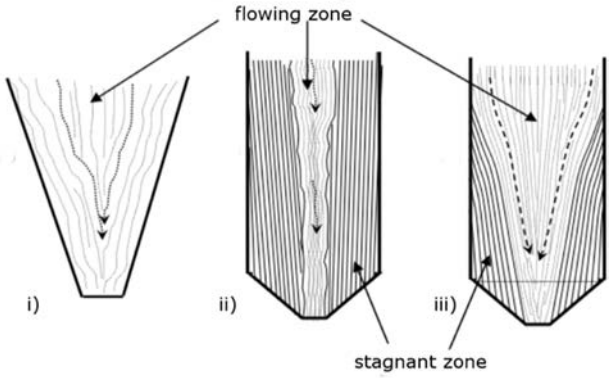

Fig. 1. Principal discharge hopper powder flow, (a) flow regime (mass flow (i), funnel flow (ii), semi-mass flow (iii))

In the case of mass flow material is moving almost at the same velocity in each part of silo [19, 21]. For this type of flow very important phenomena are taking place on boundary the material and silo wall and are manifested in form of dynamic effects. From the diagnosis point of view especially the sand behaviour along the silo wall (at various heights above the outlet) is very important due to these dynamic effects, which can lead to vibrations, serious malfunction or even to construction devastation.

During funnel flow two main regions are observed, e.g. the so-called stagnant zone (located by the walls of container) and funnel flow (usually present in the centre), [19, 21]. Material is flowing only in funnel area, while in the stagnant area is expected to maintain its packing density fraction. The material in the dynamic

region is less densely packed due to the flow forced by discharging process.

The visualisation of material concentration changes and tracking of the process state is very interesting from monitoring and control point of view, when the visualisation and data processing after generate control signal in real-time. Accurate description of the bulk solid concentration (not only during the silo filling, but also during emptying) demands measurement methods of a non-invasive character with possibility of visualization of opaque container. Electrical capacitance tomography (ECT) meets this requirement and allows to monitor and diagnose process of the silo discharging by the observation of the concentration changes of the bulk solid inside the silo cross section in real time [20, 7, 8, 24]. Xray tomography system provides much better quality images, however they are more time consuming to obtain and cost of such system is much higher [10].

2. Electrical Capacitance Tomography

The common approach to tomographic measurement data analysis is their processing in order to obtain reconstructed image of the distribution of required property in the examined cross section area. In the electrical capacitance tomography (ECT) case it will be the dielectric permittivity distribution $\boldsymbol{\varepsilon}$, which is obtained from a vector of independent measurements of capacitances $\boldsymbol{C}$ (Fig. 1). The reconstructed image is typically presented in form of matrix consisted from 32x32 pixels. Each pixel represents relative permittivity value as normalized value, value 1 corresponding to full sensor space for initial particle packing state (particle and air voids mixture) and 0 corresponding to empty sensor (air only). Thus permittivity distribution $\boldsymbol{\varepsilon}$ could be directly related to solid material concentration in sensor space. The procedure of constructing the tomographic image is called image reconstruction, which results in inverse problem solution [11, 25]. The image on Figure 2 shows an example of the reconstructed material concentration distribution inside sensor space based on vector of normalized measurement capacitances $\boldsymbol{C}$ taken from 8-electrodes capacitance sensor ($\boldsymbol{C}$=[$C_{1\text{-}2}$, $C_{1\text{-}3}$, …, $C_{7\text{-}8}$]$_{1x28}$). The main difficulty in image reconstruction for ECT comes from non-linear relationship between the capacitance and permittivity distribution and under-determined nature of the inverse problem [5, 17, 23].

The obtained reconstructed image or image sequence can be further processed and analysed in order to acquire important information about the industrial process. There are applied and widely developed image information analysis and processing methods for image defined in such way [12, 20]. The extraction of industrial process characteristic parameters gives possibility of predicting unwanted incidents and feasibility of the in-depth exploration of dynamic spatial and temporal phenomena occurring during industrial process. Moreover, information derived from tomograms can be used as a signal for monitoring or control of the given process [3, 9].

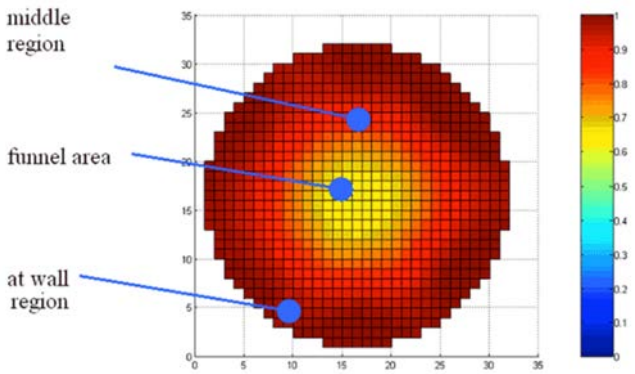

Fig. 2. Tomographic image reconstructed for hopper flow with characteristic funnel flow areas indicated

3. Shear zones analysis during mass flow

The movement of all particles characterizes the mass flow that occurs after opening the silo outlet. One of most important aspects from monitoring point of view are changes in material distribution during silo discharging. The concentration changes in granular materials during silo flow are complex due to appearing localization of the deformation in the form of narrow zones of intense shearing [2, 3, 13, 19, 21]. The shear zones occur along silo walls and also inside of the flowing, initially dense, granular material in the bin section with rough walls and in the hopper part of silo, independently of the wall roughness. The shear zones appearing on the border between silo wall and moving particles, in the case of mass flow, are especially significant from dynamics effect monitoring aspect. These effects are caused by interaction between the silo construction and the flowing granular material. The effects are noticeable as vibrations or pulsations of the silo [13]. On Figure 3 changes of material constriction in time based on sequence of reconstructed images are presented. Reduced concentration, comparing to initial packing density level, records at silo wall and higher in centre of silo is visible. This result was obtained for initially loose packing density and rough silo wall.

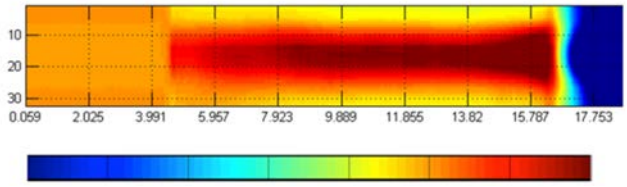

Fig. 3. Visualisation of ECT tomography images in form of topogram [9]

Next figure (Fig. 4) shows changes of material concentration in chosen position of pixels, for two ECT sensor located at different height above silo outlet (1.0m and 1.5m).

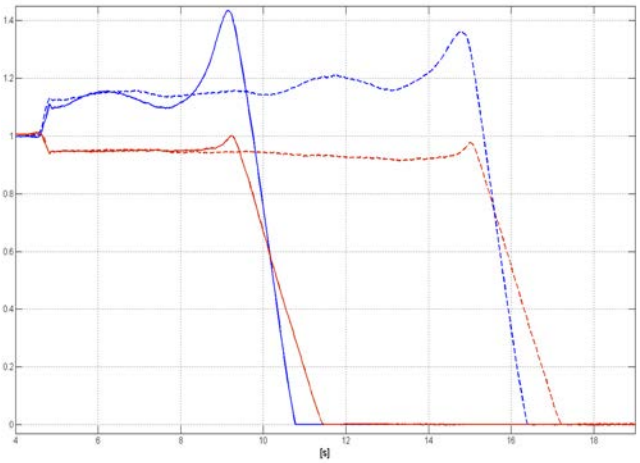

Fig. 4. Material concentration changes for initially loose packing sand and rough silo walls in different area of silo cross-section. Continuous lines represents changes wall-adjacent pixel p(1,15) for reconstruction based-plot. Centre plot (for pixel p(15,15)) – dashed line [9]

The material concentration distribution is validated with use of applied X-ray system. On Figure 5 2D radiography images after processing (normalization) are presented. The shape of silo was rectangular in order to better analyse influence of silo wall on the flow behaviour. At silo wall is visible the shear zone; lower level of material concentration.

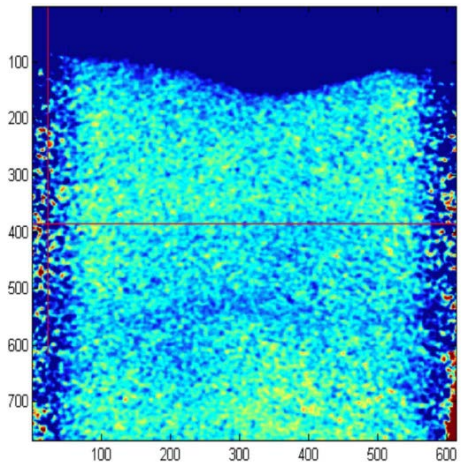

Fig. 5. 2D processed radiography image visualisation of shear zone phenomena [10]

The X-ray visualisation allows investigating silo flow, however utilization of this tomography modality in industrial environment can be unreasonable from real time measurement and cost of system point of view. In order to monitoring shear zones phenomena image processing module based on ECT data was applied, which allows to localize shear zone thickness along silo walls. In case of rough walls, shear zone occurred in wall-adjacent region, and dilatancy reached ~5-8% of initial state (Fig. 6b). The thickness of shear zone, determined with simplified approximation of pixel number (approximation method is described further below), was ~20mm, for silo model 200mm in diameter. Shear zone can be met also, with smaller effect, for smooth wall (Fig. 6a). The previous work showed, the initial packing density rise results in shear zone decrease [2, 4].

In order to determine the shear zone parameters (e.g. material concentration and size), processing method of reconstructed images was applied. Details of this image processing algorithm can be find in [6].The main point of algorithm is image segmentation which allows to determine the indices of all the pixels belonging to shear zone, according to the following formula (eq. 1):

$$\varepsilon(i) = \begin{cases} 2, & \varepsilon(i) \geq (1 - \lambda * \bar{C}) * \bar{\varepsilon} \\ \varepsilon(i), & \varepsilon(i) < (1 - \lambda * \bar{C}) * \bar{\varepsilon} \end{cases}, \text{ i=\{1,…,M\}} \qquad (1)$$

where $\bar{C}$ is a mean of normalized capacitance records, $\bar{\varepsilon}$ is mean of normalized image pixel values, $\varepsilon(i)$ is a consecutive pixel, M is a total number of reconstructed image pixels, and λ is an experimentally chosen value.

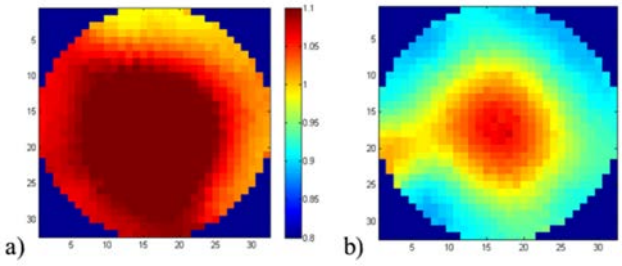

Fig.6. Tomographic visualization (in form of tomogram – full reconstructed cross-section image) of concentration changes – loose sand, at sensor height h=1.0 m, time 7 s of silo discharging a) smooth wall, b) rough wall

After processing (eq. 1) all pixels with value 2 are considered as the non-shear zone area. In the next step of algorithm are determined pixels, which belong to boundary between shear zone area (pixels without modification value ε) and rest of pixels (with value 2). The pixels that belong to shear zone and have at least one neighbourhood pixel from rest of images are marked as boundary pixels. The average distance between boundary pixels and centre of images allows estimating thickness of shear zone. The material concentration in shear zone is calculated as average value for all pixels cover the estimated shear zone. On Figure 7 is presented the characteristic of parameters changes of shear zones.

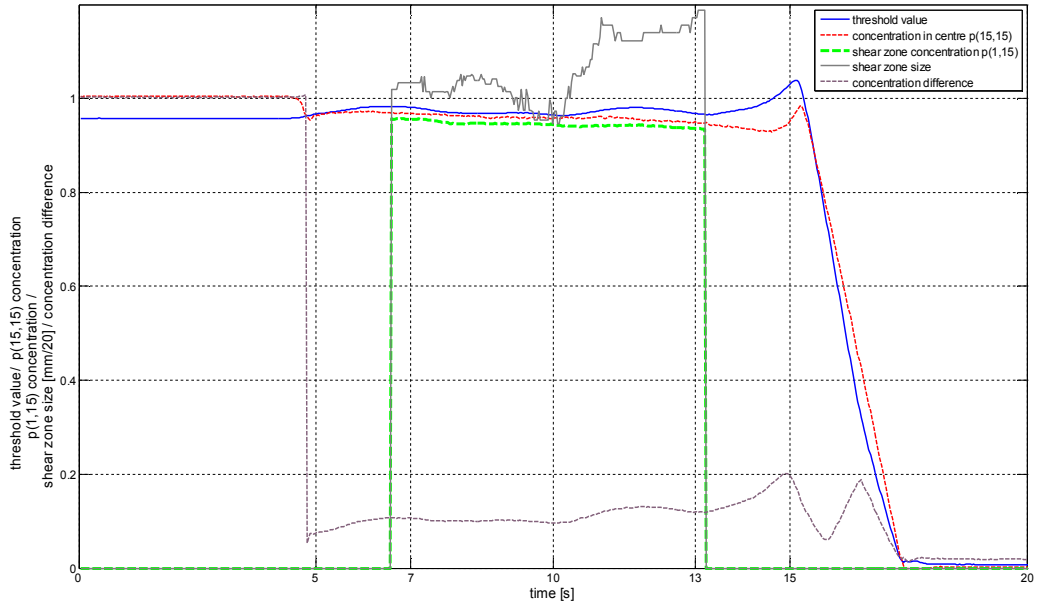

Fig.7. Characteristic plot of shear zone parameters change during silo discharging bulk solid flow [6]

4. Funnel flow, blocked, movement of centre of gravity

The main problems in this type of gravitational flow are blockage, or partially blockage (e.g. arching, ratholing), and slowdown of material flow. During production such situation causes poor product or stopping production and elimination of problems. The proposed method of funnel flow monitoring is based on tracking of area and position of funnel flow in cross-section of silo at height of ECT sensor. Output of algorithm consists in set of funnel parameters: position of centre of gravity funnel area, shape of funnel area and concentration of material in funnel area.

On Figure 8a 3D Xray tomography images of funnel are presented while Figure 8b shows radiography images. X-ray images (radiography and tomography) show material concentration distribution with details over height of silo. In the case of ECT system, the reconstructed image shows concentration

at sensor height above silo outlet and as average value from length of electrodes. The 2D ECT image provides cross-section of silo (Fig. 7).

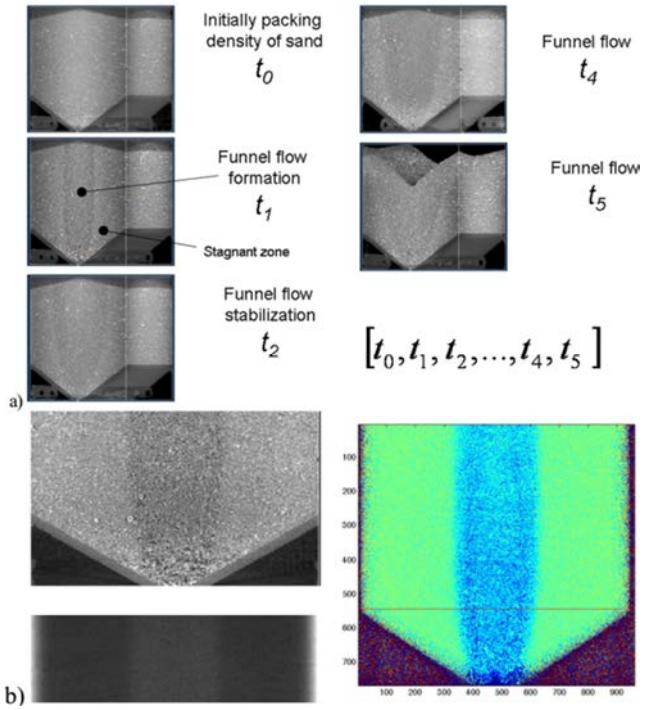

Fig. 8. Xray visualisation of material distribution during funnel flow, a) sequence of 3D reconstructed images, b) zooming of funnel area visualisation with aid of 3D tomography image and 2D radiography image after processing [10]

Stack of ECT reconstructed images gathered during funnel flow is presented on Figure 9. There are visible the concentric areas of cross –section of silo (for the same height) with different level of concentration.

In order to estimate the funnel parameters the spatial segmentation algorithms for tomography image were developed. After the reconstruction and binarization of image (pixels are splited into 2 groups – funnel area and rest of sensor area, based on eq. 1 with other value of λ) pixels belonging to the funnel area are determined. Based on centre of gravity of boundary pixels (boundary between funnel area and stagnant zone) cloud of points around the funnel is constructed. The ellipse axes are determined by applying the least-squares analysis and linear regression methods for these points. Based on centre of ellipse and proportion of ellipse axes (ratio of the major and minor ellipse axes) it is possible to track position of funnel (x_0,y_0), size and shape of funnel area. This information allows to monitor proper discharging process. The main steps of this algorithm are presented on Figure 8.

The presented analysis of tomographic image can be carried out for the sequence of images, which are obtained during silo gravity discharging process, what allow to track state of process. On Figure 11 and 12 results for silo flow without blockage and with partial blockage of silo are presented.

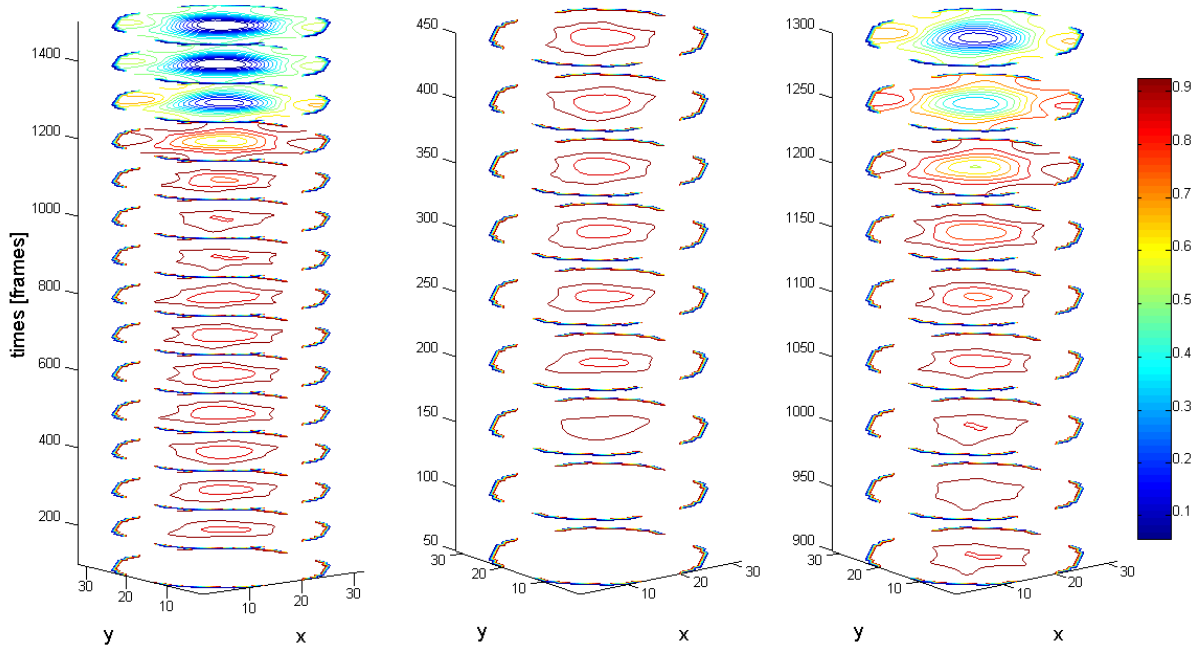

Fig. 9. Stack patterns of combined 2D image sequence reconstructed for fixed sensor location and different funnel size. 1 frame corresponds to 20ms [16]

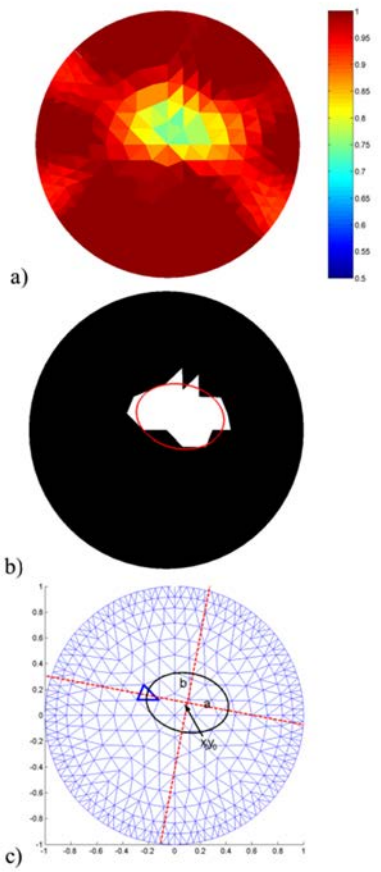

Fig. 10. The main steps in defining the hopper flow parameters. a) reconstruction image, b) image thresholding, c) determined ellipse parameters

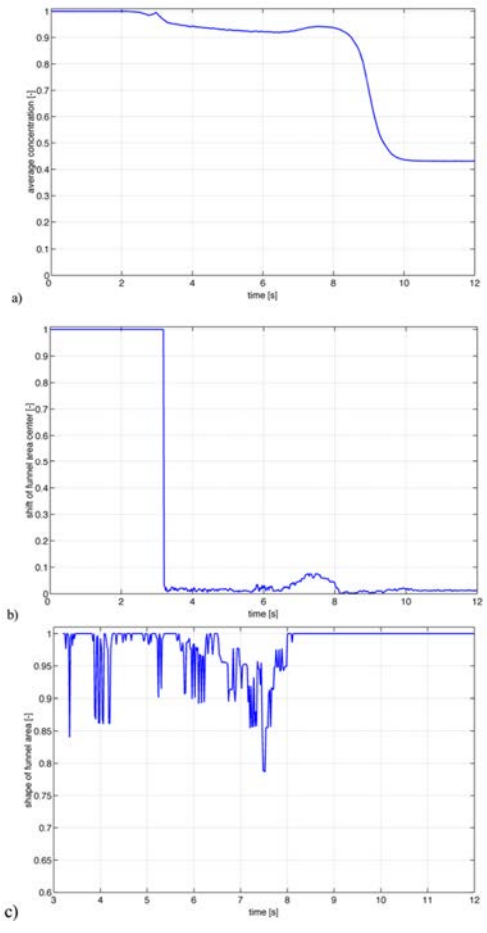

Fig. 11. Funnel parameter for flow without blockage, a) average concentration changes in time, b) position of centre of funnel gravity, c) changes of shape funnel ratio

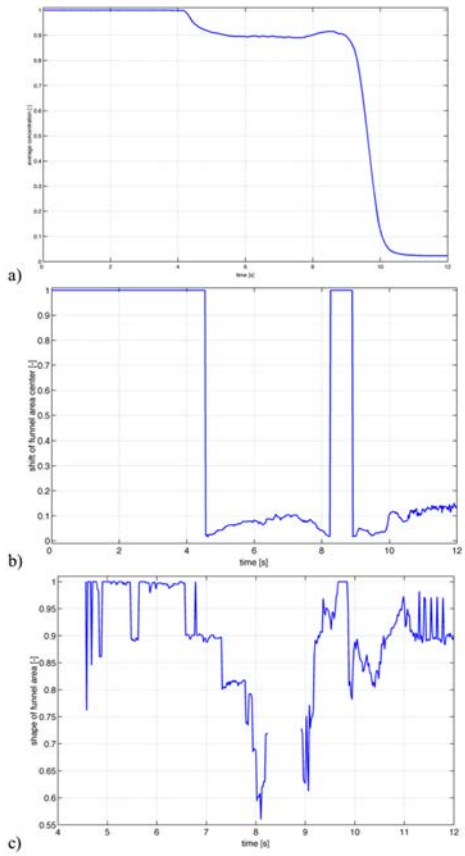

Fig. 12. Funnel parameter for flow with partially blockage, a) average concentration changes in time, b) position of centre of funnel gravity, c) changes of shape funnel ratio

The analysis of presented characteristics show that shape of funnel area is, in case of properly discharging process, different from value 1 (the silo cross-section) up to 0.79 (fig. 11c). For the flow with partial blockage of silo this difference is up to 0.56 (fig. 11c). The main important time range of silo discharging process is until 8 second for blockage silo and until 7 for flow without blockage. This is time between opening the silo outlet and appearing of the upper surface of material at sensor position. The increasing of average concentration changes (8 second for blockage and 7 second for non-blockage flow; fig. 11a, 12a) is caused by measurements attribute of ECT unit, where is observed increasing of capacitance measurements where upper level of material is near the edge of electrodes. For these time windows the difference for both cases is more visible. The blockage of silo flow was prepared in form of bulk particles stuck to silo wall, causing first of all shift of funnel are to non-blocked site of silo. So the different in case of funnel shape, for blocking and non-blocking flow, is not so visible as for value of the shift of funnel centre (fig. 11b, 12b). The shift of centre of funnel area is more visible for blockage flow, where this parameter increased to 0.1 (fig. 12b).

5. Conclusions

The investigations of the silo flow monitoring methods conducted with aid of tomography techniques are fruitful. Their main advantage is the possibility to see inner material distribution without introduction any disturbance into the process. Two main aspects, which can be considered in context of silo flow visualisation are understanding of flow behaviour and monitoring in real-time state of process. Both aspects are presented in paper. ECT systems are suitable to apply in control system, while the X-ray tomography is useful for in-depth analysis of granular flow.

The described methods of mass and funnel flow are based on tomography image processing and analysis. Information, which is analysed, is used gathered from single image, so only spatial information about material distribution is considered. In this case the quality of image has significant impact on results. The

reconstructed algorithm for ECT technique was not discussed in paper. The set of the determined parameters in single time point cannot be as useful as the changes in time of these characteristic parameters of flow. It is necessary to analyse not only values of parameters but also changes of these values over time.

Other aspect, which is necessary to be discussed for tomography visualisation of silo flow, is that stopping the flow by silo operator causes similar measurement and reconstructed image as for non-stopping flow. This feature could be eliminated by temporal analysis of obtained results and have to be solved in the future.

Literature

[1] Banasiak R., Wajman R., Jaworski T., Fiderek P., Fidos H., Nowakowski J., Sankowski D.: Study on two-phase flow regime visualization and identification using 3D electrical capacitance tomography and fuzzy-logic classification. International Journal of Multiphase Flow, 58/2014, 1–14.

[2] Buick J.M., Chavez-Sagarnaga J., Zhing Z., Ooi JY., Pankaj DM., Cambell D.M., Greated C.A.: Investigation of silo-honking: slip-stick excitation and wall vibration. Journal of Engineering Mechanics ASCE, 131(3)/2005, 299–307.

[3] Chaniecki Z., Dyakowski T., Niedostatkiewicz M., Sankowski D.: Application of electrical capacitance tomography for bulk solids flow analysis in silos. Particle and Particle Systems Characterization, 23(3-4)/2006, 306–312.

[4] Dhoriyani M.L., Jonnalagadda K.K., Kandikatla R.K., Rao K.K.: Silo music: sound emission during the flow of granular materials through tubes. Powder Technology, 167/2006, 55–71.

[5] Dyakowski T., Edwards R.B., Xie C.G., Williams RA.: Application of capacitance tomography to gas-solid flows. Chemical Engineering Science, 52/1997, 2099–2110.

[6] Grudzien K., Chaniecki Z., Romanowski A., Niedostatkiewicz M., Sankowski D.: CT Image Analysis Methods for Shear Zone Measurements during Silo Discharging Process. Chinese Journal of Chemical Engineering, 22/2012, 337–345.

[7] Grudzień K., Niedostatkiewicz M., Adrien J., Maire E., Babout L.: Analysis of the bulk solid flow during gravitational silo emptying using X-ray and ECT tomography. Powder Technology, 224/2012, 196–208.

[8] Grudzień K., Romanowski A., Aykroyd RG., Williams RA.: Advanced statistical computing for capacitance tomography as a monitoring and control tool. Intelligent Systems Design and Applications, 2005, 49–54.

[9] Grudzien K., Romanowski A., Chaniecki Z., Niedostatkiewicz M., Sankowski D.: Description of the silo flow and bulk solid pulsation detection using ECT. Flow Measurement and Instrumentation, 21(3)/2009, 198–206.

[10] Grudzień K.: Radiography Image Processing for Analysis of Gravitational Funnel Flow in Silo. Computer Science in Novel Applications, 2012, 137–158.

[11] Lionheart W.R.B.: Review: Developments in EIT reconstruction algorithms: pitfalls, challenges and recent development. Physiol. Meas., 25/2004, 125–142.

[12] Mosorov V.: Flow Pattern Tracing for Mass Flow Rate Measurement in Pneumatic Conveying Using Twin Plane Electrical Capacitance Tomography. Particle & Particle Systems Characterization, 25(3)/2008, 259–265.

[13] Muite B.K., Quinn F.S., Sundaresan S., Rao K.K.: Silo music and silo quake: granular flow-induced vibration. Powder Technology, 145/2004, 190–202.

[14] Niedostatkiewicz M., Tejchman J.: Experimental and theoretical studies on resonance dynamic effects during silo flow, Powder Handling and Processing, 15(1)/2003, 36–42.

[15] Pląskowski A., Beck M.S., Thorn R., Dyakowski T.: Imaging industrial flows, applications of electrical process tomography, Institute of Physics Publishing, Bristol, 1995.

[16] Romanowski A., Grudzień K., Banasiak R., Williams R.A., Sankowski D.: Hopper Flow Measurement Data Visualization: Developments Towards 3D. 5th World Congress on Industrial Process Tomography.

[17] Rymarczyk T., Filipowicz S.F., Sikora J.: Comparing methods of image reconstruction in electrical impedance tomography. Computer Applications In Electrical Engineering, 9/2011, 23–33.

[18] Sankowski D., Sikora J.: Electrical Capacitance Tomography: Theoretical Basis and Applications, edited by Dominik Sankowski and Jan Sikora, Wydawnictwa Książkowe Instytutu Elektrotechniki, 2010.

[19] Schulze D.: Powders and Bulk Solids, Springer, 2008.

[20] Scott D.M., McCann H.: Process Imaging for automatic control, Taylor and Francis Group, 2005.

[21] Seville J.P.K., Tuzun U., Clift R.: Processing of Particulate Solids. Blackie Academic, London, 1997.

[22] Wilde K., Rucka M., Tejchman J.: Silo-quake-measurements, a numerical polar approach and a way for its suppression. Powder Technology, 186(2)/2007, 113–129.

[23] Yang W.Q., Liu S.: Role of tomography in gas/solids flow measurement. Flow Meas. and Instrum., 11/2000, 237–244.

[24] Yang W.Q., Liu S.: Role of tomography in gas/solids flow measurement. Flow Measurement and Instrumentation, 11/2000, 237–244.

[25] Yang W.Q., Peng L.: Image reconstruction algorithms for electrical capacitance tomography. Meas. Sci. Technol. 14/2003, R1–R13.

Ph.D. Eng. Krzysztof Grudzień
e-mail: kgrudzi@iis.p.lodz.pl

Assistant Professor of Applied Computer Science at Lodz University of Technology. Member of Polish Information Processing Society and ACM Lodz Chapter. He obtained PhD in 2007 in the field of Computer Science, Process Tomography specialty.
His research interests include applications of non-invasive imaging techniques and identification of dynamic industrial processes parameters, development of algorithms for image processing and analysis with particular reference to the analysis of sequences of 2D tomography images gathered from the ECT and X-rays tomography systems.

Prof. Dominik Sankowski
e-mail: dsan@iis.p.lodz.pl

Head of the Institute of Applied Computer Science, at the Lodz University of Technology.
He achieved a PhD with distinction (1979), DSc (habilitated doctor - 1989), and granted the title of professor (1998). Since 2001 he has held the position of full Professor. Member of: IEEE Computer Society, Electro-thermal Section of the Polish Academy of Sciences, Group of Experts in the Computer Science specialisation of National Accreditation Committee (PKA). Communication Director of International Society of Process Tomography (ISIPT).
His research interests include Image Processing and Analysis, Pattern Recognition, Artificial Intelligence, Software Engineering, Data Processing, Real-Time Systems, IT Systems in Management, On-line Identification of Industrial Objects, Automation of the Thermal Processes.

otrzymano/received: 20.09.2016 *przyjęto do druku/accepted: 15.02.2017*

DOI: 10.5604/01.3001.0010.4578

FLOW VELOCITY MEASUREMENT METHODS USING ELECTRICAL CAPACITANCE TOMOGRAPHY

Volodymyr Mosorov, Krzysztof Grudzień, Dominik Sankowski
Lodz University of Technology, Institute of Applied Computer Science

Abstract. The current methods of calculating the velocity field based on a twin-plane electrical capacitance system for multiphase flows are presented. The described methods allow to calculate the velocity profile of the multiphase flow in cross-section of industrial installation. The theoretical assumptions of the considered methods are also noticed. The main advantages and disadvantages of the authors' flow velocity measurement methods are discussed.

Keywords: Electrical capacitance tomography, velocity profile, statistical methods

METODY POMIARU PRĘDKOŚCI PRZEPŁYWU Z ZASTOSOWANIEM TOMOGRAFII POJEMNOŚCIOWEJ

Streszczenie. *Artykuł przedstawia przegląd metod wyznaczania prędkości przepływu w oparciu o dwupłaszczowy system pojemnościowej tomografii procesowej. Zaprezentowane metody pozwalają na obliczenie profilu prędkości wielofazowych przepływów w przekroju poprzecznym instalacji przemysłowej. Przeprowadzono także dyskusję nad teoretycznymi założeniami omawianych metod oraz opisano główne zalety i wady autorskich metod pomiaru prędkości przepływów wielofazowych.*

Słowa kluczowe: elektryczna tomografia pojemnościowa, profil prędkości, metody statystyczne

1. Introduction

Modern flowmeters enable us to evaluate how much material has passed through the meter in a certain time (for example kilograms per hour). For single flows, the technology to measure the flow is well understood and flowmeters are widespread. However, many industrial processes use multiphase flows pumped along pipes. The measurement of the multiphase flow of gas, oil, and water is not trivial [2, 19, 20, 23] and significant challenges include:

- the reduction of multiphase flow measurement uncertainties which depends on the measurement conditions;
- making the flow meters less sensitive to changes in the physical properties of the flow components;
- the improvement of stability over time;
- the reduction of the flow regime dependency for the multiphase flow meters.

Electrical Tomography (ET) is a typical completely non-intrusive technique for measuring multiphase flow in pipes [19, 18, 22]. This technique can be used for measuring different kinds of multiphase flows such as gas/solids [11], gas/liquid [17], and liquid/solids [23] flows.

There exist two widely applied types of ET tomography: Electrical Resistance Tomography (ERT) and Electrical Capacitance Tomography (ECT). Currently more papers about flow measurement using ECT [20] and ERT systems [5] have been published.

The flowmeter for measuring the flow rate based on Electrical Capacitance Tomography technique consists of two separate planes of sensors, which measure electrical capacitance between two pairs of electrodes around a pipe.

To calculate the cross sectional distribution of the permittivity of the material (or concentration profiles) inside the pipe from the capacitance measurements an image reconstruction algorithm is used. The images provide instantaneous information on material distribution in the two pipe cross-sections at given locations. With the sensor dimensions we can then calculate the volume flow rate per zone. As result, the integration of the volumetric flow, if the density is known, mass flow can be derived.

Although acquisition and processing were initially seriously limited by computing speed, the commercial ECT systems, which are now available, can produce twin-plane images with real-time image capture and reconstruction at up to 500 complete frames per second. Such systems include major commercial applications such as pneumatic conveying of solids, many flow mixtures within the oil industry, and gas-solid fluidized beds [6, 20].

The basic parameter for flow measurement is a velocity. The article presents the review of the authors' methods, which permit the measurement of a flow velocity more accurately and reliably.

2. Methods for flow velocity calculation in Tomography image Velocimetries – review

The solids motion has a stochastic character and hence typical solid concentration changes within any pixel of two cross-sections can be treated as stochastic stationary process.

Let $x_n(iT)$ and $y_n(iT)$, n=0,...,N-1, where N is the total number of image pixels, define instantaneous distributions of material for the nth pixel of the ith image obtained from the cross-sections X and Y respectively within the frame rate resolution T *(frame per second)*. Nowadays, there exist different methods to calculate the transit time τ of flow propagation from reconstructed images of two planes. Most of them are based on cross-correlation function or spectral density of instantaneous distributions of material for pixels of the reconstructed images [2].

These methods for calculating velocity are based on two main assumptions:

1) The trajectories of motion between these sensors are parallel to the pipe axis (the trajectories are perpendicular to the sensor plane),
2) The changes within any pixel of a pipe cross-section are treated as a stationary or quasi-stationary process and hence the correlation function $R_{xy}(\tau)$ describes the general dependence between any process from the first plane and another from the second plane.

As discussed in the literature [21], the particle transition time τ can be found by cross-correlating corresponding processes $x_n(t)$ and $y_n(t)$. For the reconstructed images obtained within the frame rate T the cross correlation can be calculated as following:

$$R_{x_n y_n}(pT) = \frac{1}{M}\sum_{i=0}^{M-1} x_n(iT)\, y_n((i+p)T), \qquad (1)$$

where p = ..., -1, 0, 1, ... is the shift time in the number of frames; n is the pixel index, M is the number of images for which the cross-correlation is calculated; $x_n(iT)$, $y_n(iT)$ are the numerical values, associated with pixel n from i image obtained from sensors of a plane X and plane Y, respectively, T is time period of a single frame.

In the simplest assumption the shift p_τ at the peak of the correlogram corresponds to a transit time τ of flow structures between two planes, $\tau_x = p_\tau \cdot T$. Knowledge of the transit time τ and distance d between the two sensors enables the solids velocity within nth pixel to be calculated from the following equation (2):

$$v_n = d/\tau = d/p_\tau \cdot T \quad (2)$$

In total, N velocities, which have created a velocity profile, can be calculated $[v_n]$, n=0,…,N-1.

The calculated correlogram has a clearly discernible peak if the flow patterns take a form similar a rectangular impulse (such as flow instabilities referred to as "slugs" and "plugs" in the dense pneumatic conveying transport) over the correlation interval. Consequently, the flow regime (stratified, slug, annular or bubble flow and flow direction) has significant influence for finding a correlogram peak.

The peak may be found by the greatest single value, centre of area or polynomial fitting. The polynomial fitting gives the most consistent results though all the other techniques are available in the software.

Although cross-correlation technique has many advantages, there are, however, many disadvantages. In practice, the following factors have a great influence on finding a peak of cross-correlation function. The correlation is essentially the square of the signal, so within any volume the largest signal changes, and hence the largest flow structures, dominate the result.

The time window must be determined in such a way that correlation function calculated of the flow pattern over the window contains an evident peak.

To skip the limitations of classical approach based on the correlation function for calculation of a flow velocity, several methods were proposed in last decades by the authors.

2.1. The "best-correlated pixels" method [15]

As been noted, the cross-correlation technique for flow velocity measurements is based on the assumption that solids trajectories are parallel and perpendicular to the sensor plane. Therefore, such a method is flow pattern dependent. The method discussed below calculates the flow velocity, that does not require the assumption about the laminar trajectory within a sensor volume. This is important since in many cases trajectories exhibit very complex shapes.

For example, a dense pneumatic conveying is realised by the occurrence of "slugs" and "plugs", which essentially should be analysed as wave propagation phenomena. In this situation, finding a link between actual solids trajectories and the movement of flow instabilities is not straightforward. This constitutes a serious limitation for applying direct cross-correlation techniques. Another limitation factor is that the ECT system can only measure the average solids concentration in a rather large control volume (resulting from both the spatial resolution and the electrode length) compared to the particle size. Consequently, it is not always possible to distinguish between stationary and moving material in the pipe. Transport in the vertical pipe can be in both directions: upward and downward. In vertical conveying there is the added force of gravity acting against the flow of material causing the plugs to compress further, which partially accounts for the concentration being higher than in a horizontal flow. There are also particles 'raining' down from the back of the previous plug, applying stress to the nose of the next plug.

All these factors mean that the flow is usually very dynamic and non-laminar. Classical methods based on correlating corresponding pixels are not suitable for studying such phenomena. There is also the need to improve precision of flow measurements by respecting its dynamic nature in calculations.

The proposed "best correlated pixels" method uses a correlation technique in a new way. Figure 1 shows covariant matrices of a sequence of frames with chosen pixels. These matrices are presented as images where the pixel colour is equal to a value covariant function between the chosen pixel and all other pixels.

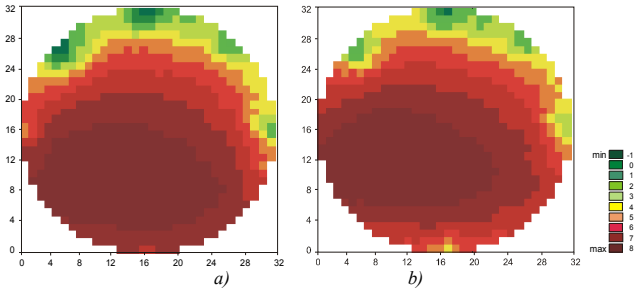

Fig. 1. Covariant matrices of plane X at a moment when particles are moving along the pipe: a) for pixel (15,16); b) for pixel (16,2)

As observed in Fig. 1, the correlation order of pixel neighbourhood is large. In the classical method only corresponding pixels are correlated, but the hypothesis can be advanced by proposing that a signal from one pixel on the first plane is sometimes better correlated with a signal from a non-corresponding pixel on the second plane than with a corresponding pixel. So the idea is to calculate cross-correlation between a pixel from the first plane and some pixels from the second plane. The pixels from the second plane are chosen from the corresponding pixel and its neighbours. The best-correlated pair is taken from the correlation calculations. The idea is shown in Figure 2.

Figure 2 shows cross-section X and the corresponding cross-section Y. The arrows denote the correlation between the pixel $X_{(n,m)}$ and the neighbourhood of the pixel $Y_{(n,m)}$. The best-correlated pair is chosen.

Equation 2 with some modification enables the calculation of the correlation function between a pixel from plane X with several pixels from Y plane as shown in equation 3 below:

$$R_{Xn,mYn-i,m-j}(pT) = \sum_{k=0}^{T-1} X_{n,m}(kT) \cdot Y_{n-i,m-j}(k+p)T, \quad (i,j) \in B \quad (3)$$

where (n,m) are the coordinates of the pixel; $X_{n,m}, Y_{n-i,m-j}$ are the value of the pixel (n,m) on planes X and Y; B is the neighbourhood of pixel (n,m) on plane Y; $B \subset Y$.

The average value of maximum correlation function for best-correlated pixels is about *5%* higher than the maximum correlation function obtained for corresponding pixels. The maximum value of the correlation function is usually about *0.7-0.9* for the normalised correlation function.

The different correlation functions often mean different transit time. In the example shown in Figure 3 the transit time between the corresponding pixels is estimated as *45* ms. The transition time between the best correlated pair is estimated as *65* ms. Thus the solids velocity at pixel $X_{(15,15)}$ is calculated from transit time *45 ms* the result is *2.9* m/s, but if the second transition time is used (*65ms*) the velocity at the same pixel is *2.0* m/s. The difference is quite significant.

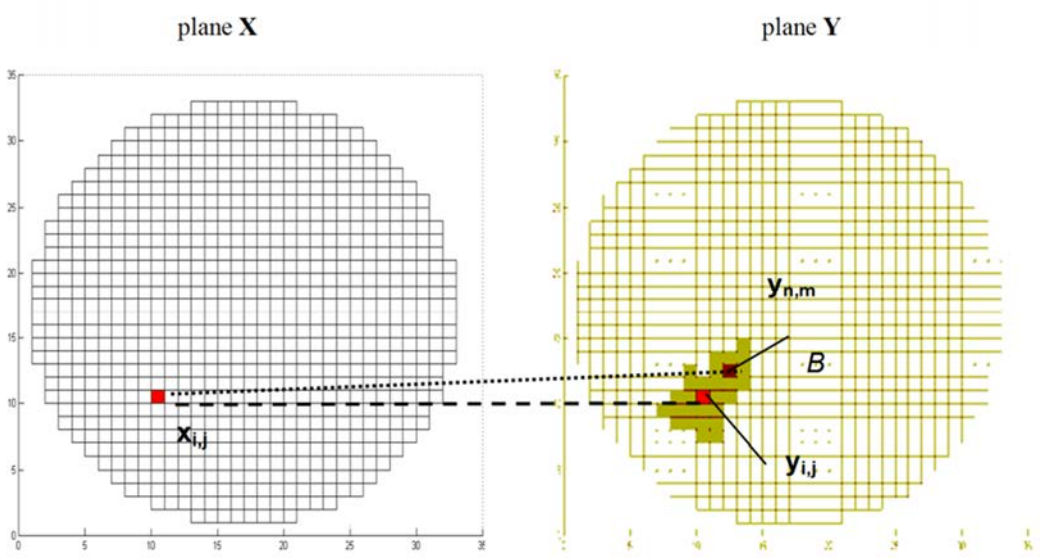

Fig. 2. The principle of the cross correlation between the pixel Xn,m and the neighbourhood of the pixel Yn,m

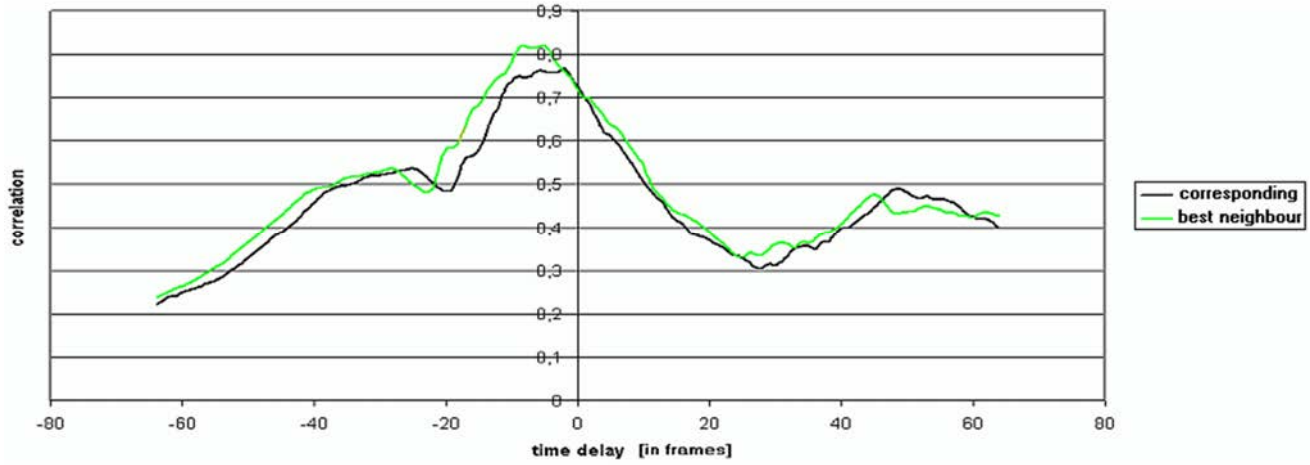

Fig. 3. Example of cross correlation functions for the co-ordinates (n,m)= (15,15) on plane X according to co-ordinates on plane Y: per-to-per- (15, 15); best neighbour - (11, 13). One frame is equal to 0.01 s

If there is a difference between velocity values obtained from corresponding and best correlated pixels there is also a difference between mass flow rate calculated using those two methods of obtaining velocity profile. In one of the experiments mass flow rate equal to 725 kg/h was obtained for the classic method and 736 kg/h for the best-correlated pixels method. The solids flow rate obtained by the weighing method, as reported in [14], was 789 kg/h.

2.2. Flow velocity measurement based on a virtual channel concept [7]

From the viewpoint of using an ECT, the following parameters can be used to characterise a flow:

- a profile velocity,
- an average concentration calculated inside each pixel.

Examples of these characteristics are presented in Fig. 4. As can be seen, these flow parameters are not the same in different cross-section regions. As is shown in the figure, the particles have high and low velocities in different regions of the cross-section (see Fig. 4a). The similar case can be observed for an average concentration profile (see Fig. 4b). The investigation carried out allows the conclusion to be made that flow presents itself as a set of independent variables, which present a certain flow structure changing with time.

Thus, flow structure detection allows one to analyse the behaviour of variables of the separated structures as an alternative to the whole flow analysis. Such variables can be observed as certain spaces between two planes of cross-sections called virtual channels, where the motion of particles has similar properties. Fig. 5 shows an example of such a flow structure as a set of channels. Such analysis allows the behaviour of structures of a flowing medium to be observed and changes in their positions to be defined. In this work, we consider a simplified case of the virtual channel concept where each virtual channel is represented by the connection of identical regions of two planes (see Fig. 5b). These regions are represented by an image called an image of regions, and the flow structure is unequivocally defined by this image (see Fig. 5c).

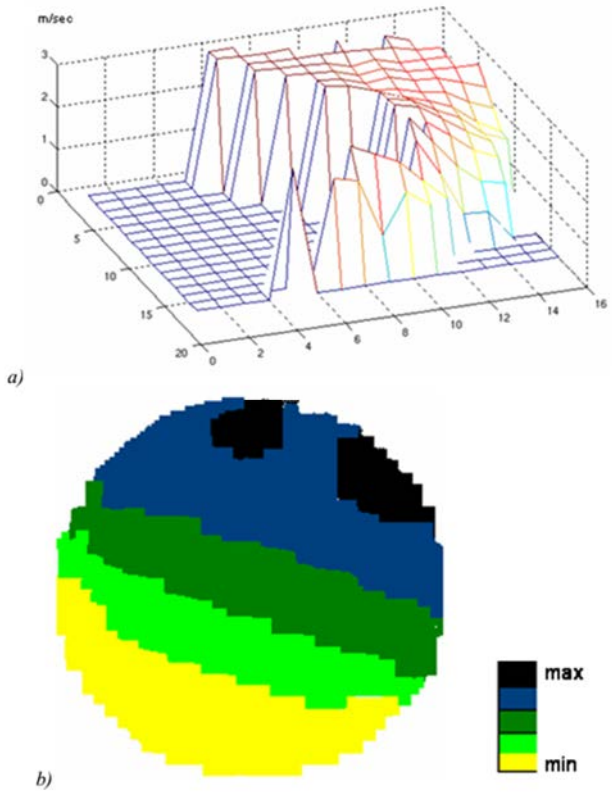

Fig. 4. Profile example in cross-section during a plug (frame numbers 885-930), a) velocity profile; b) average concentration profile

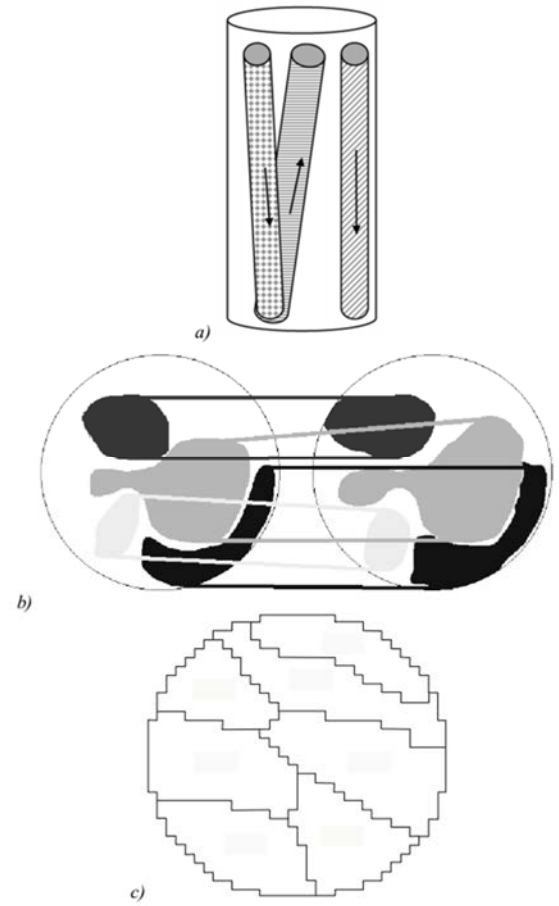

Fig. 5. a) virtual channels concept; b) simplified virtual channels; c: cross-section splitting

The splitting of the cross-section can then be performed periodically, and as a result one obtains sequences of images of regions in which the chosen region corresponds to the virtual channels of the flow.

A stochastic model [15] is used for the detection of virtual channels. In a given model a flow X(t) is defined by an n-dimensional vector $X(t)=[X_i(t)]$ where $i=0,..,N-1$, N – the number of pixel elements. The vector element $X_i(t)$ determines probability change in dielectric permittivity (concentration) inside an i-th pixel, called an elementary process (EP). In notions of this model splitting can be defined as the grouping of the EP processes for both cross-sections into some groups so that their characteristics have similar properties due to chosen homogeneity criterion. In our case a transit time of solids between two planes was selected as criterion.

To calculate the transit time $\{t_i\}$ $i=0,...,N-1$ a classical method was used based on finding the maximum value of a cross-correlation function. As mentioned above there exist probabilistic relationships between the separated velocities $\{v_i\}$ in some regions. For the grouping of EP were proposed to create k possible different groups of obtained set $\{t_i\}$ by "k-means" clustering algorithm. Such grouping is aimed to split EP processes corresponding to the homogeneous elements of a set $\{t_i\}$.

The analysis was performed for tomographic images obtained from a pneumatic conveying flow rig at the Department of Chemical Engineering, UMIST. The details of the system are described by [11]. All the researches were carried out for reconstructed tomographic images of a vertical pipe of a dense pneumatic conveying system. A sequence of a number of plugs appeared, on average, every 3 to 4 seconds. At the end of each sequence some granular material (most likely from the tail of the "train") dropped downwards under the gravity. Firstly, the macroscopic transport in the vertical pipe can take place in both directions: upward and downward. Secondly, in the micro scale, particle transport can be downward (“raining” particles), while, at the same time, plugs in the macroscopic sense travel upwards. The results presented below correspond to the reference gas velocity of 2.2 m s-1 (for an empty pipe).

The proposed k-means clustering algorithm [3] has performed a non-hierarchical divisive group analysis on the input data: a set of EP processes and a set of $\{t_i\}$. The number of group (group elementary processes with similar transit time) is an input to the k-means clustering algorithm. Groups are described by centroids, which are the point whose parameter values - transit time - are the average of a transit time t_i of all elementary processes in the chosen group. It is also known as a representative element. The similarity between EP_i and EP_j processes are measured by using Euclidean distance squared between time t_i and t_j. The main goal of the k-means algorithm is to minimise dissimilarity in elementary processes within each group while maximising this value between elementary processes in a different group. Each EP process is assigned to the centroid (and hence group) with the closest Euclidean distance. New centroids of the k groups are computed after all objects have been assigned. The steps of assigning objects to centroids and computing new centroids are repeated until no objects are moved between the groups.

This method of grouping of elementary processes is conceptually simple:

1) Select k initial cluster centroids, c_1, c_2, c_3, ..., c_k.
2) Assign each instance t_i into the group whose centroid is the nearest to t_i.
3) For each group, recompute its centroid based on elements ti contained in this group.
4) Go to (2) until convergence is achieved.

As already mentioned notion "virtual channel" is represented by group of EP processes. Once the virtual channels have been established a series of parameters like the mean concentration, the velocity, mass flow rate.

The mean concentration $\overline{C_k}$ is calculated as a mean value from the concentration in all pixels, which belong to the region of respective channel:

$$\overline{C_k} = \sum_{i \in I^k} C_i \Big/ N^k \tag{4}$$

where C_i – the material concentration in pixel i, I^k – the set of indexes of pixels which belong to the region k, N^k – the number of pixels in region k.

In a similar way the velocity inside a channel $\overline{V_k}$ can be calculated:

$$\overline{V_k} = \sum_{i \in I^k} V_i \Big/ N^k \tag{5}$$

where V_i – the velocity in pixel i, which belong to the region k of respective channel

The mass flow rate for k channel F_k can be calculated in two ways. Firstly, (let us call this a classical method) the velocity and concentration profiles can be used:

$$F_k^I = \sum_{i \in I^k} 3600 \cdot S \cdot Q \cdot V_i \cdot C_i \, [kg/h] \tag{6}$$

where 3600 – the multiplier derived from the number of seconds in one hour; S – the area of a single pixel; Q – the bulk density of the material.

Another way to calculate the mass flow rate F_k using the concentration $\overline{C_k}$ and the velocity $\overline{V_k}$:

$$F_k^{II} = 3600 \cdot S \cdot Q \cdot N^k \cdot \overline{C_k} \, \overline{V_k} \, [kg/h] \tag{7}$$

The virtual channel concept has verified for different behaviour of the solid particles in a vertical pipe flow:

- determined virtual channels during a plug - (material move upwards along the pipe)
- determined virtual channels at a tail of plug (some material dropped downwards under the gravity).

Fig. 6 presents the example profiles of velocity, concentration, mass flow rate and image of regions for tail of plug. The selected channels parameters are given in table 1.

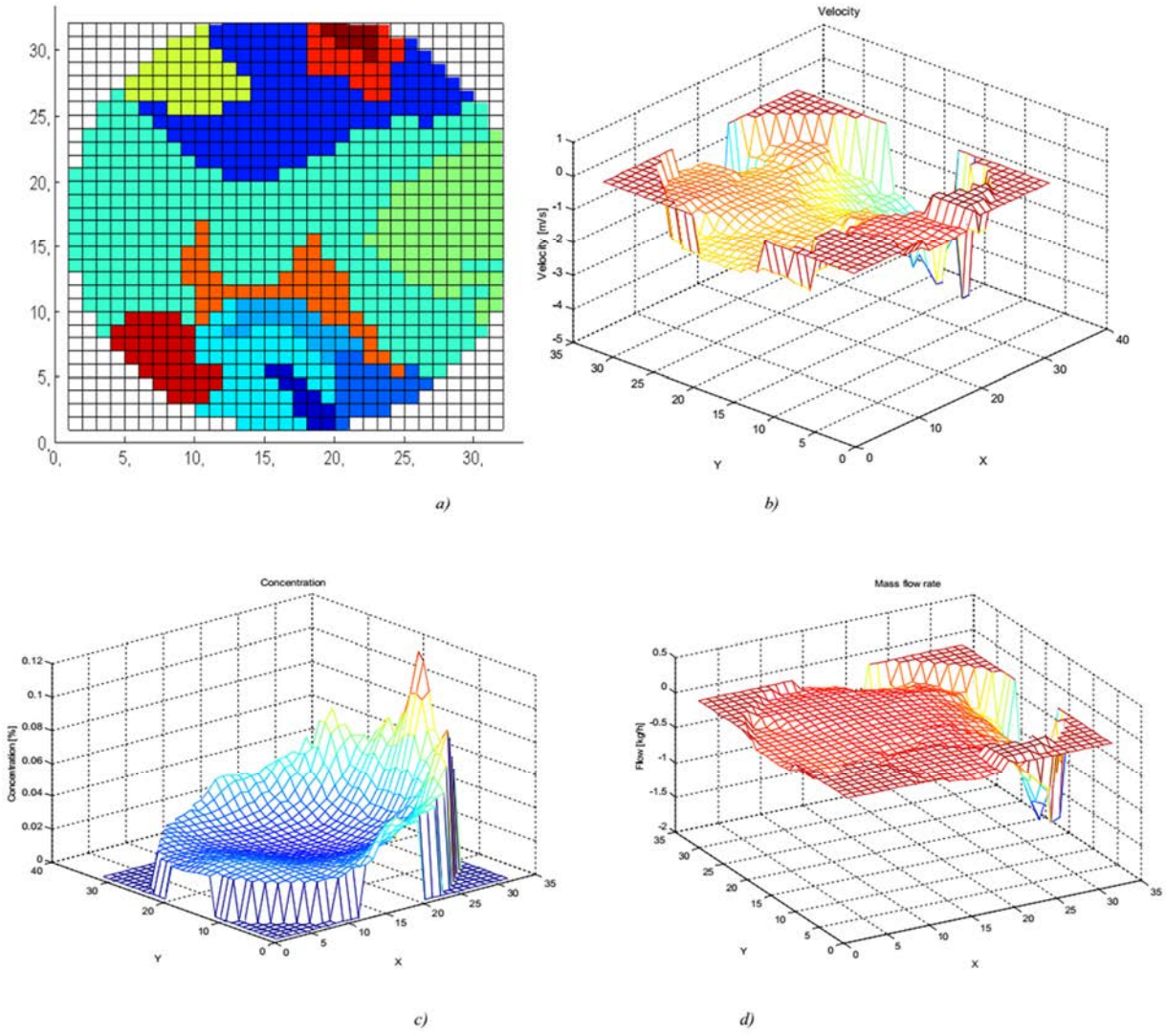

Fig. 6: Example of regions image (a); profiles: velocity (b); concentration (c); mass flow rate(d)

Table 1. Selected channels parameters

group #	mass flow rate [kg/h]		velocity [m/s]	concentration [%]	number of pixels
	F_k^I	F_k^{II}			
1	-16,93	-17,25	-0,81	2,55	136
3	-3,54	-3,53	-0,34	2,97	56
4	-61,73	-59,65	-1,20	2,56	315
5	-60,18	-58,51	-2,19	4,64	94
6	-3,07	-3,08	-0,60	2,18	38
7	-5,26	-5,28	-0,82	2,26	46
8	-0,16	-0,15	-0,02	2,43	35

2.3. Weighted-mean phases method [8]

Although cross-correlation technique has many advantages, there are, however, many disadvantages. In practice, the following factors have a great influence on finding a peak of cross-correlation function. The correlation is essentially the square of the signal, so within any volume the largest signal changes, and hence the largest flow structures, dominate the result.

The time window must be determined in such a way that correlation function calculated of the flow pattern over the window contains an evident peak.

In practice, the typical concentration changes within a pixel for the two planes as the function of a frame number has no evident peak, and thus using one to determine the transit time is not easy. Hence, classical methods calculating a flow velocity based on the correlation of the corresponding pixels are not suitable for certain flow-patterns and finding the peak of a correlogram is ambiguous.

These limitations seriously restrict the application of cross-correlation in flow measurement and the range of operating conditions where reliable answers can be obtained. The weighted-mean phases method (Mosorov 2006) overcomes these limitations permitting the flow velocity to be unambiguously calculated with high robust. It is based on a spectrum analysis of the pixel values of both cross-sections of the tomographic system.

In the case of the weighted-mean phases method, a transit time τ_x is calculated as the weighted-mean value of the time translations τ_k of the same k-harmonics of x_n and y_n signals:

$$\tau_x = \sum_{k=1}^{K}\left[(A_k^x + A_k^y)/\sum_{k=1}^{K}(A_k^x + A_k^y)\right]\cdot\frac{1}{k\cdot\omega_0}(\varphi_k^x - \varphi_k^y) \qquad (8)$$

where A_k^x and A_k^x are the amplitudes and φ_k^x and φ_k^y are the phases of the kth spectral components $S_{xn}(jk\omega_0)$, $S_{yn}(jk\omega_0)$ of the x_n and y_n respectively.

The proposed method can easily be applied to the existing flowmeters based on twin plane tomographic system by upgrading the software. The one has no limitation on the application for other types of modality such as gamma or optical tomography.

The verification of the proposed method that velocity calculated by the proposed method is a little more accurate compared with theoretical velocity (around 5%) than one calculated by the correlation method [2]. The probable reason that the phase method gives better results than the correlation method is that correlation is essentially the square of the signal and hence the largest signal changes dominate the result; therefore the dispersion of these calculated values is small. Otherwise the A weighted-mean phases method is more sensitive even for smaller signal changes. This is probably also the reason that the dispersion of velocity values by the proposed method is higher in comparison with those derived by the correlation method. The results using the pneumatic conveying flow show that the proposed estimator achieves a bit more accuracy. Finally, the proposed estimator is relatively fast in software implementation because two independent FFT transformations are needed instead of correlation function calculation.

3. Conclusion

The described methods enable to obtain the velocity vector (three components vector), not only one component as in classical approach. There are based on the concept of "best correlated pixels", where the pair of pixels has the largest values of the cross-correlation against the other pairs. Contrary to the classical method, this concept does not require the additional assumption concerned with the solids direction within the sensor volume. This is crucial since in many industrially important cases solids trajectories have a complex three-dimensional character.

This method, combined with electrical capacitance tomography, enables determine the particle velocity field, in gas/solids flow. However, it can be combined with other tomographic modalities. The presented results were obtained both for gas/solids flows in vertical and horizontal channels. Future application of this technique for a solids mass flow measurement will help to develop a more accurate solids mass flow meter and allow to analyse, with high accuracy, swirl flow.

References

[1] Arko A., Waterfall R.C., Beck M.S., Dyakowski T., Sutcliffe P., Byars M.: Development of Electrical Capacitance Tomography for Solids Mass Flow Measurement and Control of Pneumatic Conveying Systems. 1st World Congress on Industrial Process Tomography, Buxton, Greater Manchester, April 14–17, 1999, 140–146.

[2] Beck M.S., Pląskowski A.: Cross correlation flowmeters - their design and application. Adam Hilger, Bristol 1987.

[3] Beck M.S.: Correlation in instruments: cross correlation flowmeters. Journal of Physics E: Scientific Instruments, 14/1981, 7–19.

[4] Bolton G.T., Hooper C.W., Mann R., Stitt E.H.: Flow distribution and velocity in a radial flow fixed bed reactor using electrical resistance tomography. 3rd World Congress on Industrial Process Tomography, Banff, Canada 2003, 813–820.

[5] Byars M., Pendleton J.D., Goodeve D.: A New High-Speed Control Interface for an Electrical Capacitance Tomography System. 3rd World Congress on Industrial Process Tomography, Banff, Canada 2003, 631–636.

[6] Corlett A.E.: Determination of Flow Patterns and Void Fraction of Multiphase Flows Using Electrical Capacitance Tomography. 2nd World Congress on Industrial Process Tomography, Hannover, Germany, 29–31 August 2001, 636–643.

[7] Deng X., Dong F., Xu L.J., Liu X.P., Xu L.A.: Measurement of the Gas Phase Velocity in Gas-Liquid Flows Using a Dual-Plane ERT System. 2nd World Congress on Industrial Process Tomography, Hannover, Germany, 29–31 August 2001, 669–676.

[8] Dyakowski T., Mosorov V., Sankowski D., Seaton M., Mazurkiewicz Ł., Grudzień K., Jaworski A.: Virtual Channel Concept for Measuring Solids Mass Flow Rate. 3rd World Congress on Industrial Process Tomography, Banff, Canada, 2003, 535–540.

[9] Etuke E.O., Bonnecaze R.T: Angular Velocity Detection by Means of Electrical Impedance Tomography. Department of Chemical Engineering, The University of Texas at Austin, Austin, USA.

[10] Fehmers G.: Volumetric flow rates from impedance tomography in oil/gas flown. 3rd World Congress on Industrial Process Tomography, Banff, Canada, 2003, 287–292.

[11] Jaworski A.J., Dyakowski T.: Tomographic Measurements of Solids Mass Flow in Dense Pneumatic Conveying. What Do We Need to Know About the Flow Physics? 2nd World Congress on Industrial Process Tomography, Hannover, Germany, 29–31August 2001, 353–361.

[12] Jolliffe I.: Principal Component Analysis. Springer Verlag, New York, 1986.

[13] Loh W.W., Waterfall R.C., Cory J., Lucas G.P.: Using ERT for Multi-Phase Flow Monitoring. 1st World Congress on Industrial Process Tomography, Buxton, Greater Manchester, April 14–17, 1999, 47–53.

[14] Mazurkiewicz Ł.: Solid Velocity Measurements by Cross Correlation Technique – Executive Summary Report. UMIST, The Chemical Engineering Department, September 2001.
[15] Mosorov V., Sankowski D., Mazurkiewicz Ł., Dyakowski T.: The 'best-correlated pixels' method for solid mass flow measurement using electrical capacitance tomography. Measurement Science and Technology, 13(12)/2002, 1810–1814.
[16] Mosorov V.: A method of transit time measurement using twin plane electrical tomography. Measurement Science and Technology, 17(4)/2006, 753–760.
[17] Sankowski D., Sikora J.: Electrical Capacitance Tomography: Theoretical Basis and Applications. IEL, 2010.
[18] Scott D.M., McCann H.: Process Imaging For Automatic Control. Taylor & Francis, 2005.
[19] Spitzer D.W.: Industrial Flow Measurement, The Instrumentation. Systems, and Automation Society, 2005.
[20] Sümer M.P., Helvacı S., Yener H.B., İkizler B., Alparslan A.: Solid-Liquid Two Phase Flow. Elsevier, 2008.
[21] Thorn R., Johansen G.A., Hammer E.A.: Three-Phase Flow Measurement in the Offshore Oil Industry - Is There a Place for Process Tomography? 1st World Congress on Industrial Process Tomography, Buxton, Greater Manchester, April 14-17, 1999, 228–235.
[22] Thorn R., Johansen G.A., Hammer E.A.: Three-Phase Flow Measurement in the Offshore Oil Industry - Is There a Place for Process Tomography? 1st World Congress on Industrial Process Tomography, Buxton, Greater Manchester, April 14-17, 1999, 228–235.
[23] Wang M.: Industrial Tomography Systems and Applications. Woodhead Publishing, 2015.

Ph.D. Eng. Volodymyr Mosorov
e-mail: volodymyr.mosorov@p.lodz.pl

Volodymyr Mosorov received his PhD in 1998 from the State University of Lviv, Ukraine. V. Mosorov was awarded the title of Doctor of Science from AGH University of Science and Technology Krakow Poland in 2009. He is now an associate professor at the Institute of Applied Computer Science of Lodz University of Technology, Poland. His research interests include process tomography systems and its industrial applications. He has been involved in these areas for more than 15 years. Member of the International Society for Industrial Process Tomography. He has published more than 80 technical articles.

Ph.D. Eng. Krzysztof Grudzień
e-mail: kgrudzi@iis.p.lodz.pl

Assistant Professor of Applied Computer Science at Lodz University of Technology. Member of Polish Information Processing Society and ACM Lodz Chapter. He obtained PhD in 2007 in the field of Computer Science, Process Tomography specialty.
His research interests include applications of non-invasive imaging techniques and identification of dynamic industrial processes parameters, development of algorithms for image processing and analysis with particular reference to the analysis of sequences of 2D tomography images gathered from the ECT and X-rays tomography systems.

Prof. Dominik Sankowski
e-mail: dsan@kis.p.lodz.pl

Head of the Institute of Applied Computer Science, at the Lodz University of Technology.
He achieved a PhD with distinction (1979), DSc (habilitated doctor - 1989), and granted the title of professor (1998). Since 2001 he has held the position of full Professor. Member of: IEEE Computer Society, Electro-thermal Section of the Polish Academy of Sciences, Group of Experts in the Computer Science specialisation of National Accreditation Committee (PKA). Communication Director of International Society of Process Tomography (ISIPT).
His research interests include Image Processing and Analysis, Pattern Recognition, Artificial Intelligence, Software Engineering, Data Processing, Real-Time Systems, IT Systems in Management, On-line Identification of Industrial Objects, Automation of the Thermal Processes.

otrzymano/received:20.09.2016 *przyjęto do druku/accepted: 15.02.2017*

DOI: 10.5604/01.3001.0010.4579

ACCELERATION OF IMAGE RECONSTRUCTION PROCESS IN THE ELECTRICAL CAPACITANCE TOMOGRAPHY 3D IN HETEROGENEOUS, MULTI-GPU SYSTEM

Michał Majchrowicz, Paweł Kapusta, Lidia Jackowska-Strumiłło, Dominik Sankowski
Lodz University of Technology, Institute of Applied Computer Science

Abstract. *Electrical capacitance tomography is an innovative method for visualization of industrial processes. One of its main advantages is it's high time resolution that allows to the usage of ECT in systems with high volatility. In recent years there has been significant development of electrical capacitance tomography 3D, which however, has significantly reduced industrial it's applications due to the complicated process of image reconstruction. The authors propose the use of multi-node, multi-GPU system to accelerate the process of image reconstruction in ECT 3D.*

Keywords: Electrical capacitance tomography, reconstruction algorithms, matrix computations, distributed systems.

PRZYSPIESZANIE PROCESU REKONSTRUKCJI OBRAZU W ELEKTRYCZNEJ TOMOGRAFII POJEMNOŚCIOWEJ 3D Z WYKORZYSTANIEM HETEROGENICZNEGO SYSTEMU MULTI-GPU

Streszczenie. *Elektryczna tomografia pojemnościowa jest innowacyjną metodą wizualizacji procesów przemysłowych. Jedną z jej głównych zalet jest duża rozdzielczość czasowa pozwalająca na zastosowanie ECT w instalacjach o dużej zmienności. W ostatnich latach nastąpił znaczący rozwój elektrycznej tomografii pojemnościowej 3D, która jednakże ma znacznie ograniczone zastosowanie przemysłowe ze względu na skomplikowany proces rekonstrukcji obrazu. Autorzy artykułu proponują zastosowanie wielowęzłowego systemu Multi-GPU do przyspieszenia procesu rekonstrukcji obrazu w ECT 3D.*

Słowa kluczowe: elektryczna tomografia pojemnościowa, algorytmy rekonstrukcji, obliczenia macierzowe, systemy rozproszone.

Introduction

Electrical capacitance tomography is an innovative visualization method of industrial processes. One of its main advantages is its high time resolution that allows for the application of ECT in systems with high volatility. In recent years there has been significant development of electrical capacitance tomography 3D, which has significantly reduced industrial use due to the complicated process of image reconstruction. The authors propose the use of a multi-GPU system to accelerate the process of image reconstruction in 3D ECT.

1. Electrical Capacitance Tomography and GPGPU

The electrical capacitance tomography 3D approximation of the spatial distribution of electric permittivity inside the object is calculated using the knowledge capacity measurements with the use of electrodes, which are respectively arranged on the surface of the object. Since 2003 develops a large interest in the use of real, three-dimensional, volumetric ECT, both in static mode, 3D and 4D dynamic. Electrodes on the surface of the sensor provide electrical potential to the area surrounded by the sensor and then measuring its change in the boundary [1].

These measurements are then used in an electrostatic model to determine the dielectric constant of the object [2]. Today, 3D ECT becomes an important tool for visualization in the industry [5].

This imaging technique, however, has one major drawback - in the case of three-dimensional image reconstruction time can be unacceptably long (up to several hours and in some circumstances even days). To break this barrier authors propose a new method for accelerating image reconstruction in ECT using OpenCL technology and Multi-GPU (Graphics Processing Units) systems.

General-Purpose computing on Graphics Processing Units (GPGPU) is a technique of using graphic cards (GPU - Graphics Processing Unit), which normally handles graphics rendering, for computations that are usually handled by processors (CPU - Central Processing Unit). Growing interest in GPU computations started due to constant demand for higher compute capabilities, which was necessary to solve more complex algorithms. Because of this interest multi-core technology and parallel computing started to emerge.

Parallel programming is not a new idea, though till only recently it was reserved for high performance clusters with many processors, the cost of such solution was extremely high [3]. This changed with the introduction of many core processors to the mainstream market. GPUs fit well in that trend, even take it to another level. Compared to CPUs, which today have usually 2 to 16 cores, GPUs consist, of hundreds and even thousands of smaller, simpler cores designed for high-performance calculations. Thanks to that there can be much more of them on a single chip (Fig. 1), which in turn allows running many thousands of threads at once, compared to only few on CPU [3]. All this made development of new algorithms possible, using higher computing power of the GPUs. Many computations that were compute heavy and time consuming can now be made in close to real time, with small investments in hardware compared to the cost of achieving the same results using established methods.

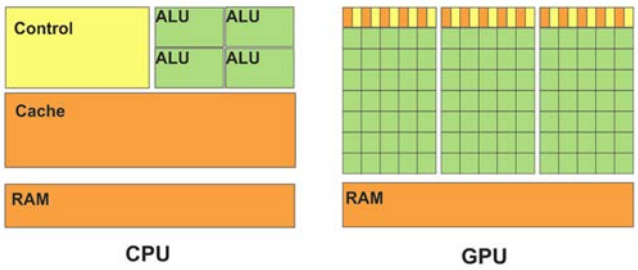

Fig. 1. Comparison CPU and GPU architectures

Moreover, thanks to advancements in computer graphics, multi-GPU systems have been developed – combining multiple graphics processors in a single computer. This allows for further speed-up of computations, provided the algorithms are properly adapted to such configuration, which is not trivial.

2. Developed Solution

The authors propose an innovative approach to 3D image reconstruction in ECT using multi-GPU solutions. Instead of sharing one job (picture frame) between multiple GPUs, each node gets its own frame of video to calculate. Such an approach does not decrease the time needed to calculate a single frame, but by application of the synchronization and load balancing algorithms results can be evenly distributed in time and it is possible to achieve a constant number of frames per second, and thus smooth image. This approach introduces a delay equal to the time required to reconstruction of single image frame by the slowest available GPU, but may be applied effectively in situations when reaction

time is not critical, for example, visualization of already collected data as well as for testing algorithms.

3. Verification

In order to verify the proposed solution authors have implemented a modified version of a Landweber iterative algorithm [6, 7], which can be run on both the CPU and GPU. It is described by the following equation:

$$\boldsymbol{\varepsilon_{k+1}} = \boldsymbol{\varepsilon_k} - \alpha \cdot \mathbf{S}^{\mathbf{T}} \cdot (\mathbf{S} \cdot \boldsymbol{\varepsilon_k} - \mathbf{C_m}) \tag{3}$$

where:

ε_{k+1} – the image obtained in the current iteration,
ε_k – the image obtained in the previous iteration,
α – convergence factor,
S – sensitivity matrix,
C_m – capacity measurements vector.

Execution times of the algorithm using the GPU were then compare with the times for execution on a traditional processor as well as with the algorithm LBP [6], described by the equation:

$$\boldsymbol{\varepsilon} = \mathbf{S} \cdot \mathbf{C} \tag{2}$$

As can be seen from the equation, this algorithm is much less computationally complex, but does not allow for the achievement of such good quality as Landweber's algorithm, and therefore is not the optimal choice for Electrical Capacitance Tomography 3D [7].

CPU tests were conducted on an Intel i7 930 clocked at 2.8 GHz. GPU used for tests were Nvidia Tesla C2070 and server Nvidia Tesla S1070 as well as the GeForce 8600GT, which was not involved in the calculation, and served only for displaying an image. In the case of AMD Radeon HD5970 GPUs were used.

Tests were conducted on two sets of test data (sensitivity matrices). The medium one has about 2.25 million items and will be later in the article called "average mesh". Meshes of this size are often used in the visualization, because they provide satisfactory results within a reasonable time. The second mesh has approximately 11 million data points and occupies over 250 MB after writing to disk and will be later in the article called "large mesh".

For simplicity we assume that the image quality produced by the Landweber's algorithm is proportional to the number of performed iterations. Therefore, tests were conducted at 100, 200 and 400 iterations to test the behavior of the implementation as well as to fully exploit the available hardware computing power.

In the case of GPU always the worst of calculation times were taken into account. The current implementation of OpenCL has a certain instability, so that execution times can vary by 5-10%. Therefore, we decided to pay special attention to the worst times of execution, not the average or the best cases, since worst cases are more important from an environmental perspective for reconstruction in real time.

3.1. CPU Computations

The Authors first carried out calculations using the CPU to achieve exemplary results, which were then compared to those obtained using the GPU. Results have been collected in Table 1.

Table 1. Reconstruction time [ms] for computations using CPU

	Average mesh [ms]	Large mesh [ms]
LBP CPU	32	117
Landweber CPU – 100 iterations	4415	22371
Landweber CPU – 200 iterations	8783	44632
Landweber CPU – 400 iterations	17488	89201

As can be seen reconstruction of a tomographic image frame, using only the conventional processors, can (in so considered cases) take up to 90 seconds, which is not acceptable value in both the visualization and adaptation and optimization of algorithms. It can be also noted that the LBP algorithm is more than an order of magnitude faster than the Landweber's algorithm, but, as we have indicated before, it does not provide as good image quality.

3.2. Single GPU Computations

To measure the acceleration of calculations that can be obtained using a single GPU authors conducted a test using cards AMD Radeon HD5970 GPU and a single component of the computing server Nvidia Tesla S1070.

Table 2. Reconstruction time [ms] for computations using single GPU

	Average mesh [ms]	Large mesh [ms]
Tesla system – 100 iterations	1100	5064
Tesla system – 200 iterations	1697	11050
Tesla system – 400 iterations	4038	22574
System AMD – 100 iterations	1793	9630
AMD system – 200 iterations	3973	17890
AMD system – 400 iterations	9879	35657

As can be seen by analyzing the results listed in Table 2 calculations using GPU Tesla are more than 4 times more efficient than using a conventional processor for 100 iterations, more than five times faster for 200 iterations, and surprisingly only four times faster for 400 iterations. AMD graphics processor was about 2.5 times faster than the CPU for 100 iterations, 2.2 times higher for 200 iterations and 1.8 times higher for 400 iterations.

For a large mesh results do not differ significantly from the previous case. A single GPU Tesla to 4.4-times, 4-times and 3.6 times faster than the CPU for 100, 200 and 400 iterations of the Landweber's algorithm. A single AMD GPU under the same conditions achieved 2.3-fold, 2.5-fold, and again 2.5 times faster with respect to the CPU.

3.3. Multi-GPU system

As shown in Table 2, even application of a single GPU allows for considerable acceleration of tomography computation. But this is not enough, so we conducted a test in configurations of multiple graphics cards (Multi-GPU). In this article we describe cases of configuration consisting of two, four, and all available (five if using Nvidia and eight using AMD) GPUs.

3.4. Landweber's Iterative Algorithm - 2 GPUs

Table 3. Reconstruction time [ms] for a Multi-GPU system – 2 GPUs

	Average mesh [ms]	Large mesh [ms]
Tesla system – 100 iterations	570	2555
Tesla system – 200 iterations	871	5553
Tesla system – 400 iterations	2040	11307
AMD system – 100 iterations	918	4836
AMD system – 200 iterations	2010	8966
AMD system – 400 iterations	4960	17849

For this configuration, the average mesh, compared to the calculation on the processor, Tesla GPUs are 7.7 times, 10 times and 8.6 times faster at 100, 200 and 400 iterations. In the case of AMD it reached 4.8-fold, 4.4-fold and 3.5-fold acceleration of the reconstruction time.

For a large mesh 8.75 times, 8 times and 7.9 times better performance was achieved than in case of single CPU for Nvidia

hardware, and 4.6 times, 5 times, and again 5 times faster calculation time on the AMD GPUs.

3.5. Landweber's Iterative Algorithm - 4 GPU

Table 4. Reconstruction time [ms] for a Multi-GPU system – 4 GPUs

	Average mesh [ms]	Large mesh [ms]
Tesla system – 100 iterations	296	1287
Tesla system – 200 iterations	449	2787
Tesla system – 400 iterations	1033	5664
AMD system – 100 iterations	470	2430
AMD system – 200 iterations	1017	4496
AMD system – 400 iterations	2492	8937

For a configuration with four GPUs and the average mesh gave the following results:

- in the case of Tesla GPU - 14.9 times faster for 100 iterations 20 times faster for 200 iterations and 17 times faster for 400 iterations;
- in the case of the Radeon GPUs - 9.4 times faster for 100 iterations, 8.6 times faster for 200 iterations and 7.2-fold acceleration for 400 iterations.

For a large mesh results are as follows:

- in the case of GPU Tesla - 17.4 - 100 times faster for a 16-fold for 200, and 15.75 times faster for 400 iterations with respect to the CPU;
- The GPU Radeon - 9.20 times faster at 100, 9.9-fold for 200 and 10 - 400 times faster for iteration, compared with the CPU.

3.6. Landweber's Iterative Algorithm - All Available GPUs

In this case the tests were conducted using all available GPUs in the system, which meant 5 for Nvidia and 8 for AMD. The calculation results are shown in Table 5.

Table 5. Reconstruction time [ms] for a Multi-GPU system – all available GPUs

	Average mesh [ms]	Large mesh [ms]
Tesla system – 100 iterations	245	1038
Tesla system – 200 iterations	364	2237
Tesla system – 400 iterations	837	4543
AMD system – 100 iterations	250	1231
AMD system – 200 iterations	524	2263
AMD system – 400 iterations	1266	4487

For average mesh:

- In case of Tesla GPUs calculations were 18.2-fold, 24-fold and 21 times faster than on CPU for respectively 100, 200 and 400 iterations;
- AMD achieved 17.8-fold, 16.8-fold and 13.9-fold acceleration calculation for 100, 200 and 400 iterations.

For a large mesh:

- For Tesla GPU a 21.5 times acceleration time speedup for 100 iterations, 20 times for 200 and 19.65 times for 400 iterations.
- Configuration of AMD was respectively 18.21 - times, 19.7 times and 19.9-times faster for 100, 200 and 400 iterations of the Landweber's algorithm than on CPU.

3.7. GPU Results Comparison

To better visualize the results, and show differences between GPU different manufacturers results were placed on the collective chart for both the case of medium and large nets.

3.8. Average mesh

Using a single GPU solution from Nvidia turned out to be more powerful than the Radeon AMD in each test, 1.6 times, 2.3 times and 2.45 times for the 100, 200 and 400 iterations.

Two Tesla cards were also faster than two AMD cards - 1.5 times for 100 iterations. The difference has widened even for 200 and 400 iterations, where Nvidia cards turned out to be respectively 2.30 times and 2.4 times faster than the Radeon.

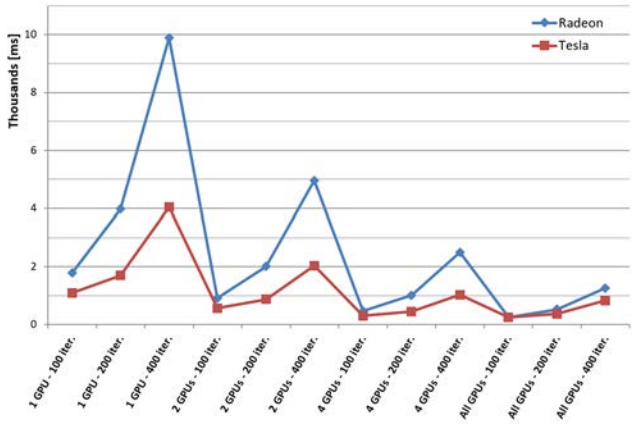

Fig. 2. Comparison of computation times on GPU – average mesh

In the case of four Tesla GPUs were 1.6 times, 2.3 times and 2.4 times (for respectively 100, 200 and 400 iterations) faster than AMD cards. Using all GPU authors found out that 5 Tesla GPUs configuration is only marginally faster than 8 AMD cards - 1.02 times for 100 iterations. In the case of 200 and 400 iterations Nvidia cards again turned out to be 1.4 times and 1.51 times faster. It seems that in the case of the Tesla GPU configurations GeForce 8600 GT which was dedicated only to display an image, played an important role since it looks that with the increase in computational complexity AMD cards most likely were not be able to cope with simultaneous calculation and displaying of a 3D images.

As can be seen in the chart smallest difference in execution time between Nvidia and AMD cards, the average mesh, occurs at 100 iterations, and the largest at 400. Additionally, you it can be also noted that with increasing the number of graphics cards gap is getting smaller. Moreover, adding new cards minimizes the impact on the overall number of iterations computing time.

3.9. Large mesh

For a large mesh single Tesla GPU was 1.90 times faster than AMD Radeon for 100 iterations, 1.61 times faster for 200 iterations and 1.57 times faster for 400 iterations. In the case of multi-GPU configurations for a large mesh difference is even greater. Two Tesla GPUs are 1.82 times faster than the two AMD GPUs for 100 iterations, 1.61 times faster for 200 iterations and 1.57 times faster for 400 iterations. The configuration of four Tesla GPUs was 1.88 times faster than the AMD for 100 iterations, 1.61 times faster for 200 iterations and 1.57 times faster for 400 iterations. In addition, 5 Nvidia Tesla GPU were 1.18 times faster than 8 AMD GPUs for 100 iterations. However, for 200 iteration of AMD configuration it is almost as fast as Tesla and for 400 iterations even little faster.

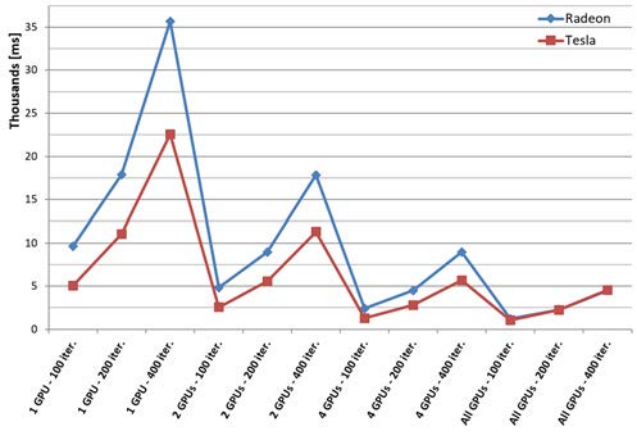

Fig. 3. Comparison of computation times on GPU – large mesh

You will notice that the mesh size has a huge impact on the differences between the Nvidia and AMD GPUs. Even with single GPU, we can see that the difference between the results for 400 iterations is less than in the previous case. In addition, increasing the number of graphics processors further reduces the difference, which completely disappears in the latter case. It is also worth noting that for all the GPU and 400 iteration AMD configuration was slightly faster, which proves that the data size has a huge impact on the performance of the devices.

These results clearly show that for small data sets and a large number of iterations NVIDIA products are a better choice, but when working with meshes of significant sizes AMD GPUs can be just as or even more powerful than Nvidia products.

4. Time-shifted reconstruction

The authors have concentrated their work on improving the speed on-line image reconstruction in 3D Electrical Capacitance Tomography. All the developed algorithm can be however used to test and verify a different approach - where system response time is not as important, as maximum achieved capacity. In this case the authors have prepared a database of 56320 measured capacitance vectors and tried to perform image reconstruction using 100 iterations of Landweber algorithm in shortest time possible. For this the authors have used the approach of vector consolidation [2], that combines input data in bigger packets and allows using faster reconstruction algorithms (Fig. 5). By combining many capacitance vectors into packets of 32 – 128 it converts all the matrix-vector operations into matrix-matrix, which are much more optimal for performing computations on graphic processors.

This approach, however, has one drawback as it introduces a delay to computations as the input data for image reconstruction algorithms is much bigger than usual. However, it also allows for much higher throughput.

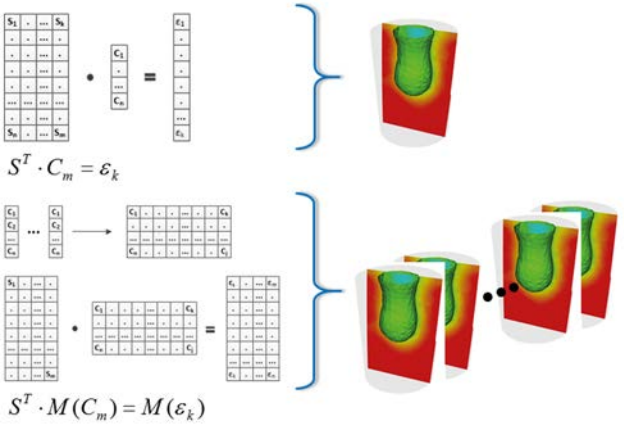

Fig. 4. Vector consolidation approach in 3D ECT image reconstruction

All the results for this test have been gathered in Table 6, as well as presented graphically on Figure 5. It is important to note, that in order to show the results properly, the axis for the CPU results have been scaled compared to GPU.

Table 6. Time-shifted (off-line) reconstruction time [s]

Image vector size	Intel i7 930 CPU [s]	Radeon HD 5970 1GPU [s]	Radeon HD 5970 2 GPUs [s]	Radeon HD 5970 4 GPUs [s]
8488	21270,0	937,2	496,7	257,7
20499	50533,6	1843,6	1004,8	511,6
60896	149841,4	5231,6	2877,4	1464,8
87152	219739,8	6617,6	3672,8	1886,0
157264	403546,2	11831,6	6625,7	3342,4

As can be seen from the data in Table 6 the proposed algorithm, when using a single GPU, is already 20 to 30 times faster than computations on a quad-core CPU. This advantage further increases with adding multiple GPUs to the system. Dual GPU system is up to 60 times faster and quad GPUs are up to 120 times faster than computations on CPU.

This speed advantage using a developed algorithm and Multi-GPU system makes it possible to reconstruct big sets of measurement data in a relatively short time. For example, in case of a resulting image vector, that consists of 157264 elements, performing image reconstruction for the whole test set takes more than four days. Performing the same operation using quad-GPU system this time can be shortened to just one hour. This makes it possible to perform any image analysis on reconstructed images much faster, than was possible before.

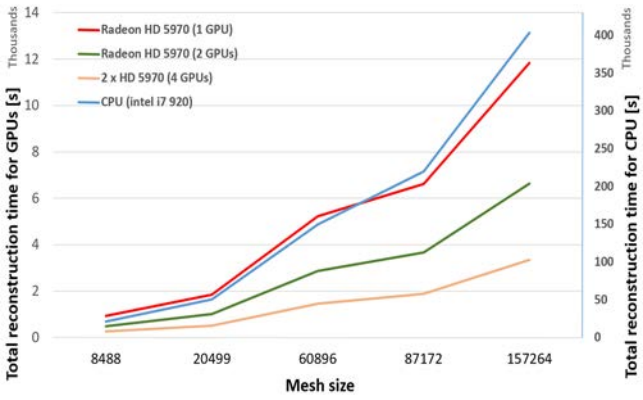

Fig. 5. Total computation time for time-shifted image reconstruction

5. Conclusion

Obtained results confirm the validity of the assumptions made by the authors that by using the proposed approach significant acceleration of the image reconstruction time in Electrical Capacitance Tomography 3D was achieved. In addition, according to the authors, after further work on the visualization algorithms on the GPU and the application of faster graphics processors even better results can be achieved.

The results also show that the great advantage of OpenCL framework, which is the possibility to execute the unmodified code on a variety of devices can also be a limiting factor. The carried tests showed that the developed algorithm prefers Nvidia cards over AMD products, although the latter have a much higher theoretical maximum power (single GPU AMD reaches 2320 GFLOP / s while the Nvidia GPU only 1088 GFLOP / s).

Furthermore, the authors have tested their algorithm not only as a platform for performing on-line reconstruction, but also to radically decrease the time necessary to visualize large sets of measurement data.

Studies have also shown that the use of multiple computers connected together to create a computing network may be a viable option. All the necessary information is stored in GPU RAM, and only measurement data and results (which are relatively small sets of data) have to be transmitted through the network, so its speed should not be a limiting factor.

Bibliography

[1] Banasiak R., Wajman R., Soleimani M.: An efficient nodal Jacobian method for 3d electrical capacitance image reconstruction. Insight Non-Destructive Testing and Condition Monitoring 51(1)/2009, 36–38.

[2] Kapusta P.: Algorytmy równoległego przetwarzania danych pomiarowych i obrazów w wybranych systemach tomografii przemysłowej, PhD Thesis, 2014, 47–50.

[3] Kirk D., Hwu W.: Programming Massively Parallel Processors, Second Edition: A Hands-on Approach. Morgan Kaufmann Publishers, 2012.

[4] Lionheart B.: Reconstruction algorithms for permittivity and conductivity imaging, Proceedings of 2nd World Congress on Industrial Process Tomography, 2001, 4–11.

[5] Soleimani M.: Three-dimensional electrical capacitance tomography imaging. Insight Non-Destructive Testing and Condition Monitoring, 48(10)/2006, 613–617.

[6] Wajman R., Banasiak R., Mazurkiewicz Ł., Dyakowski T., Sankowski D.: Spatial imaging with 3D capacitance measurements. Measurement Science and Technology, 17(8)/2006, 2113–2118.

[7] Yang W.Q., Peng L.: Image reconstruction algorithms for electrical capacitance tomography. Measurement Science and Technology IOP Journal 14/2003, R1–R13.

Prof. Lidia Jackowska-Strumiłło
e-mail: lidia_js@kis.p.lodz.pl

Professor at Lodz University of Technology (TUL), Poland and Vice-Director for didactics in the Institute of Applied Computer Science at TUL. She received the M.Sc., the Ph.D. and the DSc. degrees in electrical engineering from TUL in 1986, 1994 and 2010, respectively. In 1990/91 she has been staying in the Industrial Control Unit at the University of Strathclyde in Scotland where she worked on her Ph.D. project. From 1986 to 1998 she worked in the Institute of Textile Machines and Devices TUL.
Her research interests include computer engineering, modelling of industrial objects and processes, artificial intelligence, computer measurement systems, identification methods, text processing, image processing and analysis.

Prof. Dominik Sankowski
e-mail: dsan@iis.p.lodz.pl

Head of the Institute of Applied Computer Science, at the Lodz University of Technology.
He achieved a PhD with distinction (1979), DSc (habilitated doctor - 1989), and granted the title of professor (1998). Since 2001 he has held the position of full Professor. Member of: IEEE Computer Society, Electro-thermal Section of the Polish Academy of Sciences, Group of Experts in the Computer Science specialisation of National Accreditation Committee (PKA). Communication Director of International Society of Process Tomography (ISIPT).
His research interests include Image Processing and Analysis, Pattern Recognition, Artificial Intelligence, Software Engineering, Data Processing, Real-Time Systems, IT Systems in Management, On-line Identification of Industrial Objects, Automation of the Thermal Processes.

otrzymano/received: 20.09.2016 *przyjęto do druku/accepted: 15.02.2017*

DOI: 10.5604/01.3001.0010.4580

APPLICATION OF FRACTIONAL CALCULUS FOR MODELLING OF TWO-PHASE GAS/LIQUID FLOW SYSTEM

Jacek Nowakowski, Piotr Ostalczyk, Dominik Sankowski
Lodz University of Technology, Institute of Applied Computer Science

Abstract. *In recent years the use of fractional calculus in control system identification is becoming popular and it has found new applications. The paper presents application of fractional calculus for modelling of two-phase gas/liquid flows in a test rig. The installation consists of three horizontal and vertical measuring segments with different diameters, which allow to investigate flows in a wide range of parameters. Flow components supply is measured/controlled by NI PXI system and a set of flow meters/controllers. The paper presents model of the two-phase flow in the above described installation, which leads to precise and accurate flow mathematical model. The main goal of the flow model is to describe steady flow parameters, especially the flow fractions, or type of the flow. The model describes flows more accurately, that classical second order system model.*

Keywords: tomography, electrical capacitance tomography, fractional calculus

ZASTOSOWANIE RACHUNKU RÓŻNICZKOWEGO NIECAŁKOWITEGO RZĘDU DO MODELOWANIA PRZEPŁYWÓW DWUFAZOWYCH GAZ/CIECZ

Streszczenie*. W ostatnich latach wykorzystanie rachunku różniczkowego niecałkowitego rzędu staje się coraz bardziej popularne i znajduje nowe obszary zastosowań. W pracy przedstawiono zastosowanie powyższego rachunku różniczkowego do modelowania przepływów dwufazowych gaz / ciecz. Instalacja badawcza składa się z trzech poziomych i pionowych odcinków pomiarowych o różnych średnicach, które umożliwiają badanie przepływu w szerokim zakresie parametrów. Przepływ komponentów mieszaniny jest mierzony / sterowany przez system NI PXI oraz zestaw przepływomierzy i sterowników. W artykule przedstawiono modelowanie przepływu dwufazowego w wyżej opisanej instalacji, które prowadzi do określenia precyzyjnego modelu matematycznego przepływu. Opracowany model opisuje przepływy dwufazowe dokładniej w porównaniu z klasycznym model opisanym równaniami różniczkowymi drugiego rzędu.*

Słowa kluczowe: tomografia, elektryczna tomografia pojemnościowa, rachunek różniczkowy niecałkowitego rzędu

Introduction

Two-phase gas/liquid flows are important and commonly found in the chemical, food, pharmaceutical and other industries. Examples include installations for hydraulic and pneumatic transport of gas and liquid, apparatus for separating gas from liquid, heat-exchange units, bio-reactors, cooling installations. In nuclear power stations cooling systems, the understanding of two-phase flows as well as monitoring and identification of the flow regime is essential [11]. Another emerging environment of two-phase flows is high computing power electronics, where power dissipation and heat is becoming a bottleneck. Two-phase cooling systems for electronics are exposed for strong flow instabilities, density-wave flow oscillations, which require efficient control systems [12]. Design of hardware configuration and an appropriate mode of operation is a complex task, because the induced fluid motion causes instability of the jet, which may in turn result in pressure and flow rate drop. Therefore, determining properties of the flow, share of the gas phase, parameters of gas bubbles like shape, dimensions, allows making an appropriate tuning control to the process. Application of Electrical Capacitance Tomography (ECT) system acts as a non-invasive method of obtaining information, which allows using it as a tool for imaging of different industrial processes. In the case of gas/liquid flow it is possible to reach higher spatial resolution and shorter time to collect the measurements (more than 100 measurements per second) than conventional measuring methods. An ECT measuring system does not require placing sensors inside the process. This allows to get information from previously inaccessible locations such as a cross-section of a pipeline, interior of a tank or reactor. By using correlation techniques and twin-plane ECT sensors, the velocity and character of the flow can be determined and the flow can be calculated [10].

A semi-industrial test rig for two-phase flows, was built to demonstrate the ECT technique [1]. The process fluid supply system is equipped with Kobold liquid mass flow meters. Installation of these meters allows measurement of different liquid flows, regardless their viscosities and electrical properties, like polypropylene glycol. For measurement of gas flow, two precise mass flow meters/controllers manufactured by Brooks are used. Elements of flow rig control system are shown in Figure 1.

For over 40 years fractional calculus has been a subject of growing interest [5], with successful applications in many scientific and technical fields. Mathematical modelling of real-time physical processes by linear or non-linear, time variant or time invariant fractional-order differential equations can be mentioned. The interest ranges from physics and chemistry to technical like mechanical and electrical to economical and biological processes, analysis and control strategies synthesis. Fractional calculus is becoming popular in many areas, especially in system identification, image processing, automation and control systems [9]. Review of available literature show a lack of publications concerning applications of fractional calculus in process tomography. This article presents preliminary results of research into the use of fractional calculus on two-phase flow modelling.

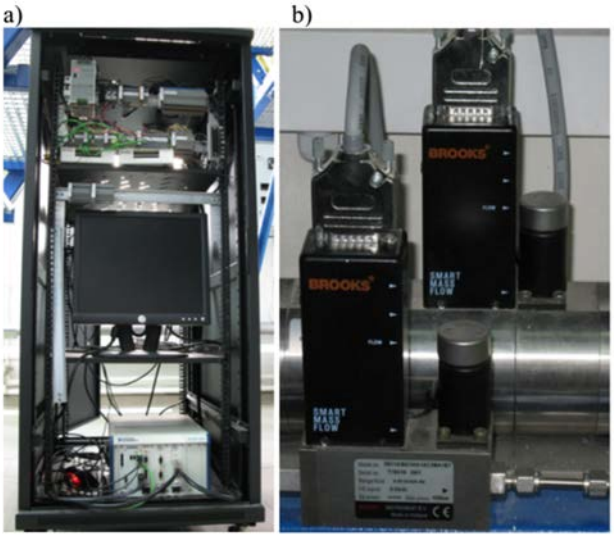

Fig. 1. a) overview of control system, b) Brooks flow meters/controllers

1. Flow Measurement System

Experiment of two-phase flow measurement were performed using the installation as mentioned before [1]. The flow rig is fully controlled by a NI PXI system, which in connection with other data acquisition systems (including ECT) and data processing units allows the measurement of flow parameters like pressures, components supply, ECT measurements with concurrent recordings of the flow image in the transparent segment of the installation located next to an ECT sensor and storing data for off-line post-processing.

Data collected are then processed using a software package "TomoKIS Studio" [3, 4]. The program allows 3D reconstruction of the flow pattern and calculation of the liquid fraction of the flow. Depending on the computer hardware used, it is possible to perform on-line 3D reconstruction with the performance of 10–12 frames per second (FPS) using nVidia Tesla graphics cards and applying CUDA technology implemented in the TomoKIS Studio. Part of the experiments were performed using a computer with nVidia Tesla cards, part using a standard PC and data post processing at approximately 2 FPS. As an example, a TomoKIS Studio screenshot in Figure 2 shows flow pattern reconstruction and liquid fraction computation.

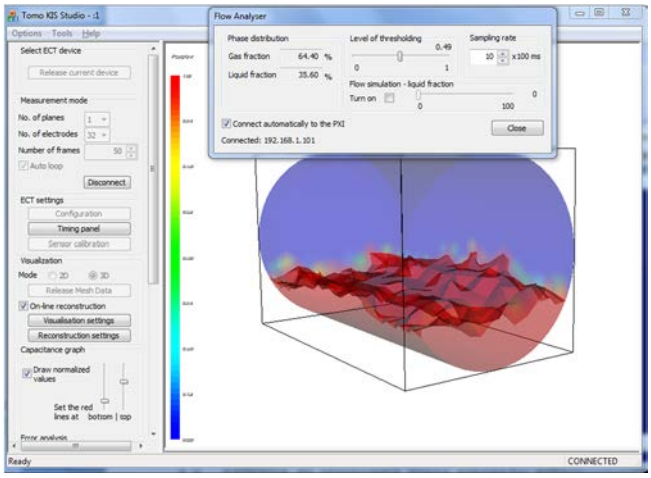

Fig. 2. TomoKIS Studio screenshot of flow image reconstruction

From the reconstructed tomographic images, different flow parameters like bubbles shape and dimensions, share of the various phases in the flow are calculated. The calculated values are used in a control system running LabVIEW by a specially developed dll plug-in and PXI control system. The aim of this research is to identify the flow parameters to build an appropriate model of the flow control system.

Following successful research on fractional calculus in mobile robotics and image processing, authors decided to apply this approach for flow identification and measurements using tomography techniques.

2. Flow Model Based on Fractional Calculus

2.1. Grünwald-Letnikov Form of the Fractional-Order Backward Difference

A definition of the Grünwald – Letnikov fractional-order difference (FOBD) is given below.

Definition: The Grünwald – Letnikov backward difference/sum of a fractional-order $\nu \in \mathbb{R}_+$ is defined as a sum

$$ {}_{0}^{GL}\Delta_k^{(\nu)} f_k = \sum_{i=0}^{k} a_i^{(\nu)} f_{k-i}, \tag{1} $$

where coefficients $a_i^{(\nu)}$ are defined as follows

$$ a_i^{(\nu)} = \begin{cases} 1 & \text{for} \quad i = 0 \\ (-1)^i \frac{\nu(\nu-1)\ldots(\nu-i+1)}{i!} & \text{for} \quad i = 1,2,\ldots \end{cases}, \tag{2} $$

and $\nu \in \mathbb{R}_+$ is an order. Applying to both sides the one-sided $\mathcal{Z}$-Transform one immediately gets

$$ \mathcal{Z}\left\{ {}_{0}^{GL}\Delta_k^{(\nu)} f(k) \right\} = \mathcal{Z}\left\{ \sum_{i=0}^{k} a_i^{(\nu)} f_{k-i} \right\} = (1 - z^{-1})^{\nu}. \tag{3} $$

A fractional-order linear time-invariant differential equation is

$$ \sum_{i=0}^{p} \bar{A}_i \, {}_{0}^{GL}\Delta_k^{(\nu_i)} y(k) = \sum_{i=0}^{q} \bar{B}_i \, {}_{0}^{GL}\Delta_k^{(\mu_i)} u(k), \tag{4} $$

where:

$$ \bar{A}_p = 1, \quad \bar{A}_i, \bar{B}_i \in \mathbb{R} $$
$$ 0 = \nu_0 > \nu_1 < \cdots < \nu_p $$
$$ 0 = \mu_0 > \mu_1 < \cdots < \mu_q $$
$$ \mu_q < \nu_p $$

An application of the one-sided Z-Transform to both sides of equation (4) yields

$$ \sum_{i=0}^{p} \bar{A}_i (1 - z^{-1})^{\nu_i} Y(z) = \sum_{i=0}^{q} \bar{B}_i (1 - z^{-1})^{\mu_i} U(z), \tag{5} $$

with $\mathcal{Z}\{y(k)\} = Y(z)$, $\mathcal{Z}\{u(k)\} = U(z)$. From equation (5) one gets discrete transfer function [2,6,8]

$$ G(z) = \frac{Y(z)}{U(z)} = \frac{\sum_{i=0}^{q} \bar{B}_i (1 - z^{-1})^{\mu_i}}{\sum_{i=0}^{p} \bar{A}_i (1 - z^{-1})^{\nu_i}}. \tag{6} $$

Now on orders $\mu_i, \nu_j \in \mathbb{R}_+$ one imposes a condition that they are the rational numbers. Hence the orders can be expressed as fractions

$$ \nu_i = \frac{e_i}{d_i} \quad \text{for} \quad i = 1,2,\cdots,p, \tag{7} $$
$$ \mu_i = \frac{g_i}{f_i} \quad \text{for} \quad i = 1,2,\cdots,q, $$

where $e_i, d_i, g_i, f_i \in \mathbb{Z}_+$. Next one assumes that $d_m \in \mathbb{Z}_+$ is the least common denominator of fractions (7). Then

$$ \nu_i = \frac{n_i}{d_m} \quad \text{for} \quad i = 1,2,\cdots,p, \tag{8} $$

$$ \mu_i = \frac{m_i}{d_m} \quad \text{for} \quad i = 1,2,\cdots,q. \tag{9} $$

Denoting

$$ \nu = \frac{1}{d_m} \tag{10} $$

such that

$$ 0 < \nu = \frac{1}{d_m} < 1 \tag{11} $$

one express orders

$$ \nu_i = \nu n_i \quad \text{for} \quad i = 1,2,\cdots,p \tag{12} $$

$$ \mu_i = \nu m_i \quad \text{for} \quad i = 1,2,\cdots,q \tag{13} $$

By inequalities in formula (4)

$$ 0 = n_0 < n_1 < \cdots < n_p \tag{14} $$

$$ 0 = m_0 < m_1 < \cdots < m_q \tag{15} $$

$$ m_q < n_p \tag{16} $$

In the light of equations (12) and (13) formula (5) takes the form

$$\sum_{i=0}^{p} \bar{A}_i (1-z^{-1})^{\nu n_i} Y(z) = \\ = \sum_{i=0}^{q} \bar{B}_i (1-z^{-1})^{\nu m_i} U(z) \quad (17)$$

3. Modelling of the Flow System

Following the presented theoretical assumptions the following models of the system were assumed.

3.1. Classical first-order model

A classical first-order difference equation is

$$\frac{{}_{0}^{GL}\Delta_k^{(1)} y(kh)}{h} + a_0 y(kh) = b_0 u(kh) \quad (18)$$

$${}_{0}^{GL}\Delta_k^{(1)} y(kh) + h a_0 y(kh) = h b_0 u(kh) \quad (19)$$

$${}_{0}^{GL}\Delta_k^{(1)} y(kh) + A_0 y(kh) = B_0 u(kh) \quad (20)$$

with a classical first-order model discrete transfer function:

$$G_1(z) = \frac{B_0}{(1-z^{-1})^1 + A_0} = \frac{B_0}{(1-z^{-1}) + A_0} = \frac{B_0}{-z^{-1} + A_0 + 1} = \\ = \frac{B_0 z}{(A_0+1)z - 1} = \frac{\frac{B_0}{A_0+1} z}{z - \frac{1}{A_0+1}} \quad (21)$$

Coefficients a_0, b_0 or $a_0 = b_0$ have to be identified when changing the level of $u(kh)$. h – denotes simulation step.

Fractional-order model

$$\frac{{}_{0}^{GL}\Delta_k^{(\nu)} y(kh)}{h^{\nu}} + a_0 y(kh) = b_0 u(kh) \quad (22)$$

$${}_{0}^{GL}\Delta_k^{(\nu)} y(kh) + h^{\nu} a_0 y(kh) = h^{\nu} b_0 u(kh) \quad (23)$$

$${}_{0}^{GL}\Delta_k^{(\nu)} y(kh) + A_0 y(kh) = B_0 u(kh) \text{ with} \\ A_0 = h^{\nu} a_0, B_0 = h^{\nu} b_0 \quad (24)$$

Coefficients and fractional order a_0, b_0, ν or only a_0, ν when $a_0 = b_0$ have to be identified and one can change the level of $u(kh)$.

A fractional-order model discrete transfer function is

$$G_{\nu}(z) = \frac{B_0}{(1-z^{-1})^{\nu} + A_0} \quad (25)$$

The fractional-model solution is

$$y(kh) = \\ -\frac{1}{1+A_0} \begin{bmatrix} a_1^{(\nu)} & a_2^{(\nu)} & \cdots & a_{k-1}^{(\nu)} \end{bmatrix} \begin{bmatrix} y(kh-h) \\ y(kh-2h) \\ \vdots \\ y(0h) \end{bmatrix} + \\ \frac{B_0}{1+A_0} u(kh) \quad (26)$$

where

$$a_i^{(\nu)} = \begin{cases} 1 & \text{for} \quad i = 0 \\ a_{i-1}^{(\nu)} \left(1 - \frac{\nu+1}{i}\right) & \text{for} \quad i = 1,2,\cdots \end{cases} \quad (27)$$

Integer first-order model solution. One should only put $\nu = 1$ and use the above equations

A fractional-order oscillation element is

$$G_{2\mu}(z) = \frac{D_0}{(1-z^{-1})^{2\mu} + C_1 (1-z^{-1})^{\mu} + C_0} \quad (28)$$

for $0 < \mu \leq 1$

The linear model and non-linear model (FO-inertia & oscillation) are shown in Figure 3.

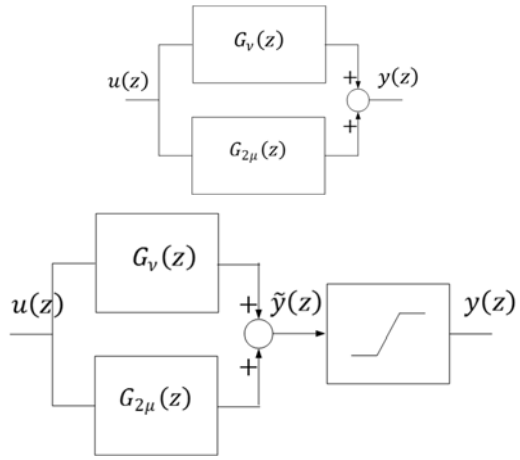

Fig. 3. The linear model and non-linear model (FO-inertia & oscillation)

Elements to evaluation: A_0, B_0, ν, C_0, D_0, μ , S_l - saturation level, s_l – range of linearity.

4. Flow Model Identification

The above theoretical solution was implemented in MatLab to determine the parameters of the fractional derivative model, which fits the best to the measured flow phenomena. Figure 4 shows results of liquid fraction calculations based on ECT measurements of an air/propylene glycol two-phase flow. The horizontal axis presents measurement frame number. The average acquisition speed was 11 FPS. During experiments the supply parameters of flow components were set to obtain flow, which was recognised as regularly repeating long bubbles of air in the liquid. An example of such a case is shown in Figure 5.

To identify model parameters, part of the flow pattern was selected, presented in Figure 6. For this set of measurement data, calculations performed in MatLab showed that the differential equation with fractional order of 0,82 – shown with small rectangles on Figure 7 RMS matches best to the originally measured data.

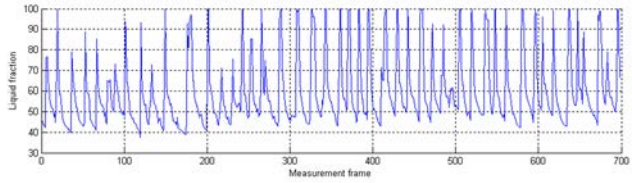

Fig. 4. Liquid fraction calculation from ECT measurements

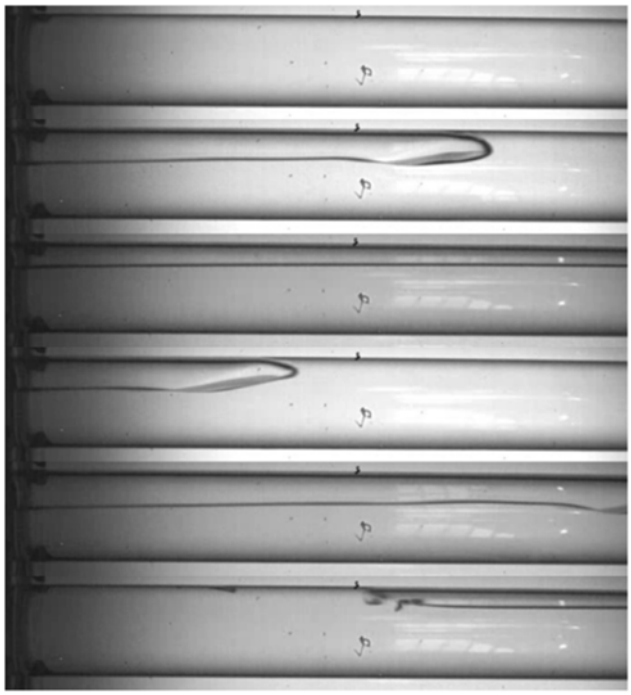

Fig. 5. Sequence of images of the measured flow

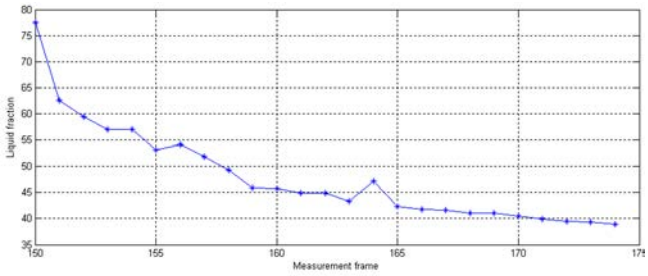

Fig. 6. Part of selected diagram from Figure 4

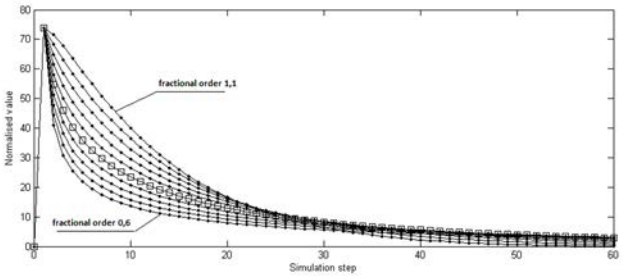

Fig. 7. Matlab simulation of the model for different fractional order values

5. Conclusions

More complex models based on fractional calculus allowed accurate system identification and allowed developing efficient control and data processing. The above presented case shows that application of fractional calculus allowed accurate system identification and preparing efficient control. The above presented example is part of research on flow identification and control, which covers among others flow regime identification using AI tools based on different measurement data acquired by different ECT systems and imaging cameras. The results confirmed the applicability of fractional calculus in two-phase flow modelling.

References

[1] Babout L., Sankowski D.: Denidia project: A Marie Curie action to increase excellence in hardware and software development related to tomography application, Zeszyty Naukowe Politechniki Łódzkiej, Seria: Elektryka, 121/2010, 45–53.
[2] Jacquot R.G.: Modern Digital Control Systems, Electrical Engineering and Electronics, Marcel Dekker, Inc. New York, 1994.
[3] Kapusta P., Banasiak R., Sankowski D.: Efficient computation of linearized inverse problem for 3D electrical capacitance tomography using GPU and CUDA technology, XVII International Conference on Information Technology Systems: Theory, Design, Implementations, Applications, 3-4 November, 2010, Lodz, Poland.
[4] Kapusta P., Majchrowicz M., Banasiak R.: Applying parallel and distributed computing for image reconstruction in 3D Electrical Capacitance Tomography. Zeszyty naukowe AGH AUTOMATYKA tom 14(3)/2010.
[5] Miller K., Ross B.: An introduction to Fractional Calculus and Fractional Differential Equations. Wiley, New York, 1993.
[6] Ogata K.: Discrete-Time Control Systems. Prentice – Hall International, Inc., Englewood Cliffs, 1997.
[7] Ostalczyk P.: Some remarks on a fractional backward difference evaluation, Proc. 3rd IFAC Workshop on Fractional Differentiation and its Applications Numerical_Methods_3_4, 2008.
[8] Ostalczyk P.: The non-integer difference of the discrete-time function and its application to the control system synthesis. International Journal of System Science, 31(12)/2000, 1551–1561.
[9] Sankowski D.: Computer Vision in Robotics and Industrial Applications, Series in Computer Vision, ed. D. Sankowski, J. Nowakowski, World Scientific 3/2014, Chapter 3, 49–70, Chapter 8, 159–172.
[10] Sankowski D., Mosorov V., Grudzien K.: Mass Flow Measurement based on a Virtual Channel Concept, Proc. 5th ISDA'05, 2005, Wroclaw, Poland, 274–279.
[11] Smith T.R., Schlegel J.P., Hibiki T., Ishii M.: Two-phase flow structure in large diameter pipes, International Journal of Heat and Fluid Flow, 33/2012, 156–167.
[12] Zhang T.J., Wen J.T., Julius A., Peles Y., Jensen M.K.: Stability analysis and maldistribution control of two-phase flow in parallel evaporating channels. International Journal of Heat and Mass Transfer, 54/2011, 5298–5305.

Ph.D. Jacek Nowakowski
e-mail: jacnow@kis.p.lodz.pl

Jacek Nowakowski works as an Assistant Professor at the Institute of Applied Computer Science at Lodz University of Technology in Poland. He graduated Mechanical Engineering Faculty and currently his research area focuses on the modelling and control of multiphase flows with the application of fractional calculus. Measurements are based on multimodal tomography developed during his stay in University of Bergen.

Prof. Piotr Ostalczyk
e-mail: piotr.ostalczyk@p.lodz.pl

Received the M.S. degree in electrical engineering from Electrical Engineering Faculty of Lodz University of Technology in Łódź in 1976. There, in 1981 he received the Ph.D. degree. In 1991 he received M.Sc. degree and a professor title in 2008. Since 1994 his main field of interest has been the application of the fractional calculus in the discrete-time control and dynamic systems identification using fractional-order difference equations.

Prof. Dominik Sankowski
e-mail: dsan@iis.p.lodz.pl

Prof. Sankowski is the head of Institute of Applied Computer Science. Hi has formed scientific teams in the following fields: signal processing, image processing and analysis, process tomography, software engineering, artificial intelligence and automatic identification and control of industrial objects in real-time systems. Recent publications have been concerned with issues related to the information society and the computerization of public administration.

otrzymano/received: 20.09.2016 *przyjęto do druku/accepted: 15.02.2017*

DOI: 10.5604/01.3001.0010.4581

MULTI PHASE FLOW MEASUREMENTS WITH THE APPLICATION OF ECT/ERT DECART MULTIMODALITY TOMOGRAPH

Jacek Nowakowski, Robert Banasiak, Radosław Wajman, Dominik Sankowski
Lodz University of Technology, Institute of Applied Computer Science

Abstract. *The multi-phase flow measurements are very important tasks in many areas of industrial processes applications. One of them is undersea exploration of oil in the petroleum industry. The submitted paper presents application of DECART tomograph designed and built in Lodz University of Technology - together with combined measurements of signals acquired from gamma ray measurement system. Use of all measuring modalities allowed for performing measurements of a flow composed of sea water, oil and gas. The paper presents theoretical principles applied to design multimodality tomograph and results of experiments performed in the University of Bergen. Measurement confirmed that multi-modality approach allows giving fast and reliable on-line results of measurements of composition of multi-phase flow. Applied algorithms allowed to speed up on-line measurements and presenting results in a form required in industrial applications. The derived conclusions can be used as guidelines for preparation of industrial applicable construction of tomograph.*

Keywords: tomography, electrical capacitance tomography, gamma rays

POMIARY PRZEPŁYWÓW WIELOFAZOWYCH Z WYKORZYSTANIEM TOMOGRAFU MULTIMODALNEGO DECART

Streszczenie*. Pomiary przepływów wielofazowych są szeroko wykorzystywane w wielu procesach przemysłowych. Jednym z nich jest przemysł petrochemiczny, w szczególności dziedzina eksploatacji podwodnych złóż ropy naftowej. W artykule zostało przedstawione zastosowanie tomografu DECART - zaprojektowanego i zbudowanego w Instytucie Informatyki Stosowanej Politechniki Łódzkiej. Pomiary z tomografu zostały powiązane z sygnałami uzyskanymi z systemu pomiaru promieniowania gamma. Wykorzystanie danych uzyskanych z różnych rodzajów czujników umożliwiło pomiar przepływu mieszaniny składającej się z wody morskiej, ropy naftowej i gazu. W pracy przedstawiono podstawy teoretyczne, które stanowiły punkt wyjścia do wykorzystania tomografu multimodalnego jak i wyniki eksperymentów przeprowadzonych na Uniwersytecie w Bergen. Pomiary potwierdziły, że podejście multimodalne umożliwia szybki i niezawodny pomiar udziału faz w przepływie wielofazowym. Zastosowane algorytmy pozwalają na przyspieszenie pomiarów on-line i przedstawienie wyników w formie wymaganej w zastosowaniach przemysłowych. Wnioski z badań mogą być wykorzystane jako wskazówki dla konstrukcji tomografu do praktycznych zastosowań przemysłowych.*

Słowa kluczowe: tomografia, elektryczna tomografia pojemnościowa, promieniowanie gamma

Introduction

The multi-phase flow measurements are very important tasks in many areas of industrial processes applications. One of them is undersea exploration of oil in the petroleum industry.

Atkinson I., Theuveny B., et. al. [1] present review of current and possible future technologies in multiphase flow measurements. There were around 1300 such installations in 2004. Currently there are in use mixed flow measurement systems based on separation and independent measurements of component flow. An example of construction of separator is presented on Fig. 1.

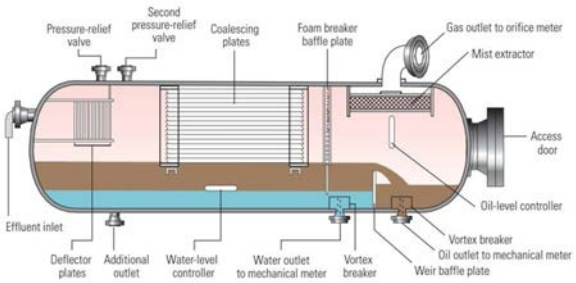

Fig. 1. Schematic design of water/oil/gas separator [1]

After separation of the components, fluid flow is measured by mechanical meters, gas flow is measured by an orifice meter. Cost of single separator installation comes to about 500 000 US$. Therefore there is a great demand for installation of low cost multiphase meters to avoid use of costly separators. Another type of three phase meter uses Venturi equipped with absolute and differential pressure sensor and dual energy gamma ray detectors. This device measures total mass flow and fractions of gas, oil and water. Different aspects of application of gamma radiation in process tomography is presented by Holstad [5, 6], Tjugum et. al [9, 10].

One of the aims of the research performed within DENIDIA MC ToK project in cooperation of the Institute of Applied Computer Science of the Lodz University of Technology and Department of Physics and Technology of the University of Bergen was to design and test three phase flow meter based on principle of combining three modalities: electrical capacitance tomography (ECT) , resistance tomography (ERT) and gamma ray radiation toography (GRT). Compact three phase flow meters have existed for more than 30 years but they are only working for well-mixed flows in vertical pipes. There is a demand for multiphase flow meters down holes, in the oil production industry, where the pipes are inclined or horizontally positioned.

1. Description of the system

The system is built on 90 mm diameter PVC pipe and consist of 8 stainless steel pin shaped resistance electrodes and 8 copper capacitance electrodes with dimensions 100x25 mm placed outside the pipe. The system uses ECT measurements from copper electrodes when the mixture is oil or gas continuous and not conducting and ERT mode when the mixture is water continuous and conductive. ECT/ERT sensor is connected to the 16-channel electronic measurement unit, DENIDIA ECT designed and manufactured in the Lodz University of Technology. In addition to this, a vertical and a horizontal directed narrow gamma beam from two pin sources (AMC.P1, QSA Global) are placed in the radial mid plane of the EIT system. These two beams are detected by two CTZ - sensors (eValuator 1000) including all necessary electronics for giving out a TTS shaped signal equal to number of counts. The presented measurement system was submitted to European Patent Office and a patent was granted by EPO in 2015.

A sketch of the multimodality sensor is given in Figure 2. Sensor is built as 50 cm pipe segment with flanges for ease of replacement within the flow rig. The radioactive sources are inserted into protective lead holders. The construction is closed in 1,5mm thick steel housing.

2. Calibration of the measurement system

Prior to performing measurements in an installation the system has to be calibrated. Calibration of EIT system is performed in few steps.

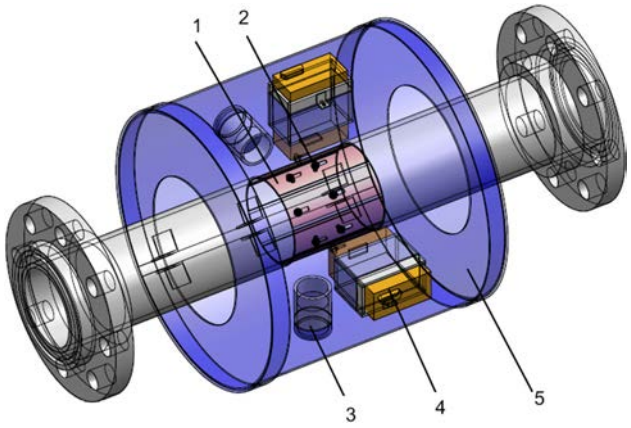

Fig. 2. Schematic view of the sensor: 1-ECT copper electrodes, 2- ERT pin electrodes, 3-gamma source holder, 4-eValuator 1000 gamma ray detector, 5-steel gamma ray protective housing

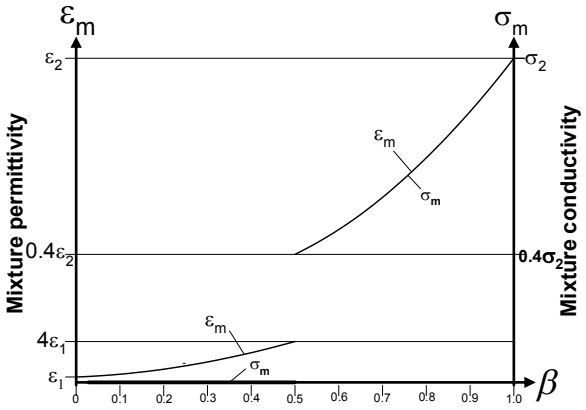

Fig. 3. Mixture permittivity and conductivity versus the volume fraction of component 2 of a homogeneous mixture of component 1 and 2. Only component 2 is conductive [3]

As it can be seen from the chart, the water content in oil can only be determined accurately, when the distribution of the water is exactly known. In practice this means that usually only homogeneous mixtures of oil and water can reliably be determined. The continuous component in a process oil/water mixture changes from oil to water at around 20 to 40% water concentration. The transition point in a mixture of crude oil and water will occur somewhere between 60% and 80% water fraction, depending on the type of crude, temperature and content of emulsion breaker etc. In North Sea the conductivity of the water component in the crude oil will approximately be 5 S/m and the relative permittivity approximately 70. The water content of North Sea crude can therefore not be measured with capacitance sensors if the mixture is water continuous ($\beta > \beta_C$). It limits application of capacitance measurements, therefore other modalities – resistance and gamma radiation were also introduced.

2.1. The ECT-system

The ECT- system must be calibrated at empty pipe and the pipe filled with oil, and the calibration data stored in the flow computer. It can also be calibrated at distilled water to control the validity of the calibration equations.

1) Pipe filled with gas:

$$C_i^{gas} = K_i^{gas} \varepsilon_0 \varepsilon_{gas} \tag{1}$$

2) Pipe filled with oil:

$$C_i^{oil} = K_i^{oil} \varepsilon_0 \varepsilon_{oil} \tag{2}$$

3) Pipe filled with distilled water:

$$C_i^{w_d} = K_i^{w_d} \varepsilon_0 \varepsilon_{w_d} \tag{3}$$

where i = 1-2,1-3,…1-N, 2-3, 2-4…..2-N…… N=total numbers of electrodes, $\varepsilon_0 \varepsilon_{gas}$, $\varepsilon_0 \varepsilon_{gas}$, ε_{w_d} are dielectric constant and relative permittivity of gas, oil and distilled water respectively.

$$K_i^{gas} = \frac{C_i^{gas}}{\varepsilon_0 \varepsilon_{gas}} \tag{4}$$

Thus all the K_i^{oil}, $K_i^{w_d}$, K_i^{gas} can be derived from equations corresponding to water and gas.

2.2. The ERT-system

The ERT-system can only be calibrated at salt water. Since this tomograph is mainly intended for use in the North Sea, sea water or water at same conductivity (5 S/m) should be used.

1) Pipe filled with saline water:

$$R_i^{w_s} = K_i^{w_s} \frac{1}{\sigma_{w_s}} \tag{5}$$

where values for i are the same for all electrode pairs, as for ECT system. Thus

$$K_i^{w} = R_i^{w} \sigma_{w_s} \tag{6}$$

2.3. The GRT-system

The used system consists of two perpendicular narrow beams. It is therefore not a full tomography system but never the less of necessity it helps in a three-component flow specially designed for horizontal pipes. Calibration procedure of the GRT-system is performed in a similar way, sensor is filled with all flow components: gas, oil and water.

1) Pipe filled with gas:

$$I_{gas} = I_0 e^{-\mu_{gas} D - 2\mu_d d} \tag{7}$$

2) Pipe filled with oil:

$$I_{oil} = I_0 e^{-\mu_{oil} D - 2\mu_d d} \tag{8}$$

3) Pipe filled with water:

$$I_w = I_0 e^{-\mu_w D - 2\mu_d d} \tag{9}$$

Where I_{gas}, I_{oil}, I_w are number of counts elapsed for sensor filled with gas, oil and water respectively, I_0 is the initial count elapsed with empty gamma sensor.

Using ECT it is often difficult to determine the border between gas and oil. It is usually easier to determine the interphase between water and oil where the difference in electrical permittivities are large (71/2.3). This inter-phase border can be applied to increase the accuracy of determining the border between oil and gas using the GRT. If the sensor is filled with a mixture of the components: gas, oil and process water, the linear absorption coefficient along the gamma ray beam in an oil/gas/water- mixture can be presented in the following form:

$$\mu_{mix} = \mu_{gas}\alpha_{gas} + \mu_{oil}\alpha_{oil} + \mu_w\alpha_w \tag{10}$$

$$\alpha_{gas} + \alpha_{oil} + \alpha_w = 1,\ \alpha_{oil} = 1 - \alpha_{gas} - \alpha_w \tag{11}$$

This gives:

$$\mu_{mix} = \alpha_{gas}(\mu_{gas} - \mu_{oil}) + \alpha_w(\mu_w - \mu_{oil}) + \mu_{oil} \tag{12}$$

where α_{gas}, α_{oil} and α_w are the fraction of the components in the gamma beam and μ_{mix}, μ_{mix}, μ_{mix} are linear absorption coefficients of gas, oil and water respectively.

Elapsed number of counts for the multi-phase mixture can be described by the following formula.

$$I_{mix} = I_0 e^{-\mu_{mix} D - 2\mu_d d} =$$
$$= I_0 e^{-\alpha_{gas}(\mu_{gas}-\mu_{oil})D - \alpha_w(\mu_w-\mu_{oil})D - \mu_{oil}D - 2\mu_d d} \quad (13)$$
$$\frac{I_{mix}}{I_{gas}} = e^{-\alpha_{gas}(\mu_{gas}-\mu_{oil})D - \alpha_w(\mu_w-\mu_{oil})D - (\mu_{oil}-\mu_g)D}$$

Since α_w is known from the EIT image we can find α_{gas} from gamma measurements. After some calculations the fractions of different phases can be derived from the following formulae:

$$\alpha_{gas} = \frac{\ln\frac{I_{mix}}{I_{oil}} - \alpha_w \ln\frac{I_w}{I_{oil}}}{\ln\frac{I_{gas}}{I_{oil}}} \quad (14)$$

$$\alpha_{oil} = \frac{\ln\frac{I_{mix}}{I_w} - \alpha_{gas} \ln\frac{I_{gas}}{I_w}}{\ln\frac{I_{oil}}{I_w}} \quad (15)$$

Examples of GRT sensor calibration are shown in the following table.

Table 1. Gamma sensor calibration.

System description	Average Counts	Scatter
Empty sensor housing (5)	6336	Not measured
Empty sensor housing (5) with 1 Cu layer	6016	20,18
Empty complete sensor (full air)	4909	2,93
Complete sensor (full oil)	1584	19,52
Complete sensor (full water)	956	12,84

3. Experimental results

The experiments on multi-modality sensor were performed in University of Bergen using flow rig with capacity of 35,6 l. For experiments North Sea water and diesel petrol was used. Experimental setup of the installation is presented in Figure 3. After calibrating of the system (ECT, ERT, GRT) the flow measurements were performed for series of two phase and three phase flow compositions.

The following graphs present measurements performed for liquid mixture containing 50% of sea water and 50% of Diesel oil. In a steady state the flow is stratified, so lower part of the sensor is filled with water. The graphs show flow measurements captured while start of the pump and volume fraction oscillations leading to water/oil emulsion. The graphs of ECT and ERT show relative values of capacitances and resistances. The negative values of capacitances are caused by salt water and noise component of the signal. GRT graph shows oscillations of counts acquired by vertical and horizontal gamma sensor. Horizontal axis corresponds to gamma counting periods.

Within the DENIDIA Project the program called TomoKIS Studio was developed. This program works as an user interface for multimodal tomograph and allows to register, save to file, process off-line and visualize measurement data obtained from both capacitance and resistance tomographic sensor. The left hand side of the program screen contains configuration panel, where the user can set up measurement environment, including 2D or 3D mode selection of data acquisition and post processing. For proper reconstruction user has to set up sensor configuration selecting number of electrode planes and electrodes in plane. In the case of used sensor its configuration was set to one plane and 8 electrodes.

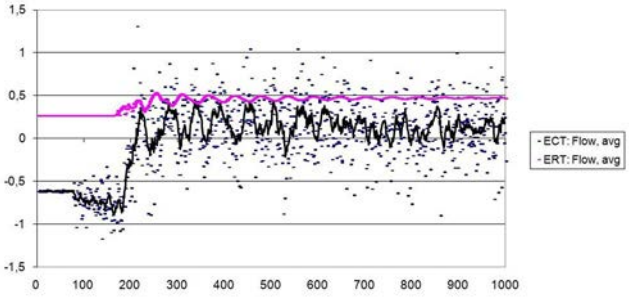

Fig. 4. Measurements of relative values of capacitances and resistances while pump start in a flow rig. Rig filling: 50% sea water, 50% Diesel oil. Horizontal axis: measurement frames

For proper sensitivity matrix calculation the appropriate mesh model of the sensor has to be generated. The special tool – Mesh Generator can be easily accessed from Tools menu. This program allows defining and generating mesh modelling the sensor. The user defines geometrical parameters of the sensor and mesh by submitting sensor dimensions and mesh density parameters.

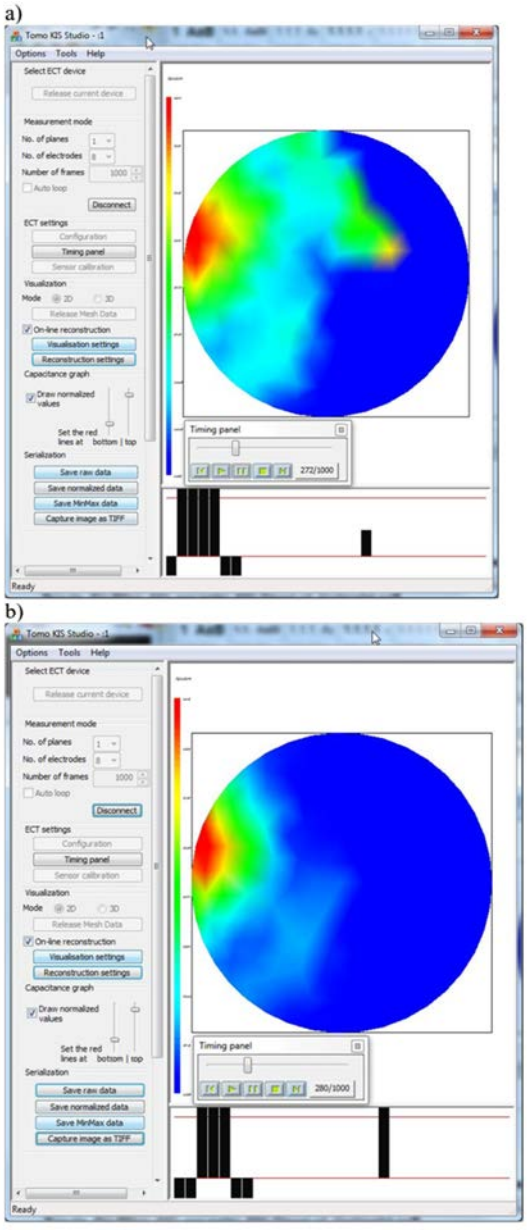

Fig. 5. Image reconstructed from ECT sensor a), and ERT sensor b)

The TomoKIS Studio software is constantly under development. The current version allows processing data acquired from different tomography devices owned by the Institute of Applied Computer Science. Various types and modes of measurement can be selected from the appropriate pull down menu. System allows also for storing on disk measurement data both from ECR and ERT system (up to 1000 frames). Figure 5 presents reconstruction of the flow in the rig containing 50% of sea water and 25% of diesel oil. On reconstructed image left part of a picture corresponds to the sensor bottom.

To calculate all three phase fractions in the flow, new software for gamma ray measurements and processing was developed. The program allows acquiring, store to file and process off line data obtained from gamma sensors. System works with NI6259 multifunction card using counters' inputs connected to eV1000 gamma radiation sensors.

Program displays continuously counts elapsed by vertical (V), horizontal (H) counters and calculated fractions of three flow components: G – gas, O – oil, SW – sea water. Counting time is set to 100ms, flow fractions are calculated every 1s using averaged values of last 10 elapsed counts. The graph on Figure 6 shows flow behaviour while starting pump in the rig filled with 50% of sea water and 25% of diesel oil.

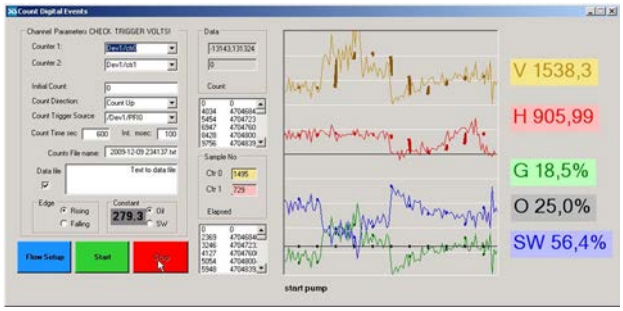

Fig. 6. Flow composition measurements for mixture 50% of sea water and 25% of diesel oil

The experiments on multi-modality sensor were performed in University of Bergen using flow rig with capacity of 35,6 l. For experiments North Sea water and diesel petrol was used. After calibrating of the system (ECT, ERT, gamma) the flow measurements were performed for series of two phase and three phase flow compositions covering wide range of fractions of flow components. According to the technical aspects of rig filling/emptying diesel and sea water fractions were changing with the steps of 25%. The shown graphs present measurements performed for liquid mixture containing 50% of sea water and 25% of diesel oil. In a steady state the flow is stratified, so lower part of the sensor is filled with water. The graphs show flow composition oscillations caused by pomp start. The calculated average flow composition are displayed every 1s, the count oscillations, which are normal for eV1000 signal show, that calculated real water fraction is around 6% higher.

4. Conclusions

The experiments with newly designed multi modality sensor performed on a multi phase flow rig in Bergen showed, that combined mode tomograph (ECT/ERT) with added gamma sensors (horizontal and vertical strongly helps to determine flow composition of a mixed flow. Different experiments showed, that accuracy of measurement of water or oil cut varies from 3% to 12%. The construction of the sensor enables robust measurements. Some efforts have to be made according to the electronic ECT/ERT measurement unit to protect the system against noise, mainly originating from pump power inverter.

References

[1] Atkinson I., Theuveny B., et. al.: A New Horizon in Multiphase Flow Measurements Oilfield Review Winter 2004/2005, 52–63.
[2] Falcone G., Hewitt G.F., Alimonti C.: Multiphase flow metering, Elsevier, 2009.
[3] Hammer E.A.: Three-Component Flow Measurement in Oil/Gas/Water Mixtures using Capacitance Transducers, Ph.D. thesis, University of Manchester, 1983, CMI-No. 831251-2.
[4] Hammer E.A., Johansen G.A., Dyakowski T., Roberts E.P.L., Cullivan J.C., Williams R.A., Hassan Y.A., Claiborn C.S.: Advanced experimental techniques, In: CROWE C.T. (ed.), Multiphase Flow Handbook, CRC/Taylor and Francis, Boca Raton, 2005, 14.1–14.37.
[5] Holstad M.B.: Gamma-Ray Scatter Methods Applied to Industrial Measurement Systems PhD Thesis, University of Bergen, 2004.
[6] Holstad M.B., Johansen G.A., Jackson P., Eidsens K.S.: Scattered gamma radiation Utilized for Level Measurements in Gravitational Separators. Sensors, 2003, 00598.
[7] Johansen G.A., Jackson P.: Salinity independent measurement of gas volume fraction in oil/gas/water pipe flow. Applied Radiation and Isotopes, 53/2000, 595–601.
[8] Mofunlewi S., Ajienka J., Appah D.: Determination of Multiphase Flow Meter Reliability and Development of Correction Charts for the Prediction of Oilfield Fluid Flow Rates. Leonardo Journal of Sciences, 12/2008, 165–174.
[9] Tjugum S.A., Johansen G.A., Holstad M.B.: The use of gamma radiation in fluid flow measurements. Radiation Physics and Chemistry 61/2001, 797–798.
[10] Tjugum S.A., Johansen G.A., Holstad M.B.: A multiple voxel model for scattered gamma radiation in pipe flow. Measurement Science and Technology 14/2003, 1777–1782.
[11] EP10461526.5 A method and a device for measuring component fractions in a multi-phase flow. European Patent Application.

Ph.D. Jacek Nowakowski
e-mail: jacnow@kis.p.lodz.pl

Jacek Nowakowski works as an Assistant Professor at the Institute of Applied Computer Science at Lodz University of Technology in Poland. He graduated Mechanical Engineering Faculty and currently his research area focuses on the modelling and control of multiphase flows with the application of fractional calculus. Measurements are based on multimodal tomography developed during his stay in University of Bergen.

Ph.D. Eng. Robert Banasiak
e-mail: robert.banasiak@p.lodz.pl

Dr Robert Banasiak is an Assistant Professor at the Institute of Applied Computer Science at Lodz University of Technology in Poland. His work deals with the industrial applications of electrical process tomography, in particular the computational problems of image reconstruction and numerical modelling of capacitance tomography systems.

Ph.D. Eng. Radosław Wajman,
e-mail: rwajman@iis.p.lodz.pl

Dr Radoslaw Wajman is an Assistant Professor at the Institute of Applied Computer Science at Lodz University of Technology in Poland. His research area focuses on the application of three-dimensional capacitance tomography systems for non-invasive monitoring, diagnosis and industrial automatic control system for pneumatic transport of bulk materials and two-phase gas–liquid flows.

Prof. Dominik Sankowski
e-mail: dsan@iis.p.lodz.pl

Prof. Sankowski is the head of Institute of Applied Computer Science. Hi has formed scientific teams in the following fields: signal processing, image processing and analysis, process tomography, software engineering, artificial intelligence and automatic identification and control of industrial objects in real-time systems. Recent publications have been concerned with issues related to the information society and the computerization of public administration.

otrzymano/received: 20.09.2016 *przyjęto do druku/accepted: 15.02.2017*

DOI: 10.5604/01.3001.0010.4582

PARAMETRIC METHODS FOR ECT INVERSE PROBLEM SOLUTION IN SOLID FLOW MONITORING

Andrzej Romanowski, Krzysztof Grudzień, Hela Garbaa, Lidia Jackowska-Strumiłło
Lodz University of Technology, Institute of Applied Computer Science

Abstract. *The article presents the parametrisation-based methods of monitoring of the process of gravitational silo discharging with aid of capacitance tomography techniques. Proposed methods cover probabilistic Bayes' modelling, including spatial and temporal analysis and Markov chain Monte Carlo methods as well as process parametrisation with artificial neural networks. In contrast to classical image reconstruction-based methods, parametric modelling allows to omit this stage as well as abandon the associated reconstruction errors. Parametric modelling enables the direct analysis of significant parameters of investigated process that in turn results in easier incorporation into the control feedback loop. Presented examples are given for the gravitational flow of bulk solids in silos.*

Keywords: electrical capacitance tomography, tomography image processing, gravitational flow, granular material

METODY PARAMETRYCZNE W ROZWIĄZYWANIU PROBLEMU ODWROTNEGO DLA MONITOROWANIA PRZEPŁYWÓW MATERIAŁÓW SYPKICH

Streszczenie. *Niniejszy artykuł przedstawia parametryczne metody rozwiązywania problemu odwrotnego w tomografii pojemnościowej na przykładzie monitorowania procesu przepływu materiałów sypkich przy użyciu tomografii pojemnościowej. Wybrane metody obejmują modelowanie probabilistyczne Bayesa, w tym przestrzenne i czasowe oraz metody Monte Carlo łańcuchów Markowa, a także parametryzację procesu z użyciem sztucznych sieci neuronowych. W odróżnieniu od klasycznych metod opartych na algorytmach rekonstrukcji obrazu parametryzacja pozwala na pominięcie tego etapu, a co za tym idzie brak dodatkowych błędów związanych z rekonstrukcją. Parametryzacja pozwala na bezpośrednią analizę istotnych parametrów badanego procesu, przez co łatwiejsze jest użycie tych wyników w pętli sprzężenia zwrotnego sterowania. Przykłady rozpatrywane w tekście są opisane dla procesu grawitacyjnego opróżniania materiałów sypkich przechowywanych w silosach.*

Słowa kluczowe: elektryczna tomografia pojemnościowa, przetwarzanie obrazów tomograficznych, przepływ grawitacyjny, materiał sypki

Introduction

Understanding the path of retrieving the information from the tomography measurement systems is a key point of the discussion. It should be emphasized that there are different points of view on this topic. The most common is the image reconstruction based one (referred here also as the „pixel" based). It represents the group of techniques of data treatment associated with image reconstruction, processing and post-processing including numerical, statistical, etc. methodologies [1, 2, 8, 15, 18, 23, 24]. The image reconstruction itself seems to be an obvious choice when concerning process tomography, especially since 'tomography' means nothing else but drawing a picture of an inside of the investigated object [18, 22, 24, 32] (from Greek tomos and graph). However, in some cases the pixel-based philosophy is applied regardless the actual conditions; even when it is useless concerning the particular requirements of the investigation e.g. specific sort of information needed, nature of the phenomenon, etc. This supports the opposite point of view when discussing the information retrieval from the process being under investigation. According to that different philosophy the reconstruction-based data analysis methods are usually not suitable to the purpose of gaining sufficient information about the process, especially in control systems.

Pixel-based tomography has been applied in medicine, where interpretation of tomograms is traditionally accomplished with human inspection. In contrast, majority of industrial applications require quick response in terms of understanding. The process dynamics forces high data acquisition rates and, for example as for ECT and pneumatic conveying, analysis on the level of hundreds of tomograms per second is needed in order to control the process. In medical applications, the detailed imaging is almost always required, while for industrial purposes the more or less quantitative information may be sufficient in order to save process from catastrophe. The flashing red light alarming about the process failure can be enough for engineers. In such constraints of required fast response the image reconstruction solving the ill-posed inverse problem in electrical tomography needs substantial regularization. Such regularisation techniques helping to cope with inverse problem introduce unquantifiable errors [13, 21, 32], but obtained reconstruction still conveys some information. Moreover, as we stated above, the resulting tomograms do not have to be 100% reliable as long as they satisfy their job.

In parallel to progress in image reconstruction and analysis methods an agreement on the common target: a joint model base image concept has arisen. The aim is to parameterise the image. It relies on adding knowledge about the examined phenomenon to the stage of solving inverse problem. The example of such parameterisation is presented by Isaksen and Nordtvedt [12], for oil/gas distribution in the pipeline. Parametric modelling was also applied to hydrocyclon performance investigation by West et al. [28]. The similar approach was used by McCormick and Wade [14], where tomograms were created with use of basis functions that suit the geometry of the problem. The parameters and their determination were the weights for these functions. The selection of basis functions that best represent the expected image variations is deeply investigated by Vaukhonen [27]. The key advantage of this approach, besides improving mathematical properties of the inverse problem, is the possible application in the control system, as the vector of characteristic industrial process parameters is obtained.

This paper presents overview and validation of application of the process parameterisation methodology, for ECT tomography systems and for application to granular material flow, based on two different approaches, based on Bayesian theorem and artificial neural network techniques [6, 9, 10, 19]. Different new concept of contextual input to the process of retrieval of fruitful information from the measurement system was proposed by [20]. One of the possibilities is to add some extra context awareness of the system operational conditions the other is to pre-model the system with some extra constraints such as the blockage-based fingerprinting the flow rig in order to gain contextual knowledge of the pre-malfunction and emergency states to incorporate this knowledge in normal operational conditions as proposed by authors.

1. Electrical Capacitance Tomography – classical inverse problem solution

The main idea of ECT technique is producing an image of the cross-section area within a process vessel on the basis of measurements taken on its outer boundaries in this case on the boundary of the pipe as was shown in [5, 18, 22, 24]. This is accomplished by measuring capacitance and displaying associated

permittivity distribution of a mixture of dielectric materials inside a closed pipe or a vessel. The obtained reconstructed image or image sequence can be further processed and analysed in order to acquire important information about the industrial process. The extraction of industrial process characteristic parameters based on reconstructed images is a classical approach, however sometimes it results in consumption of additional time of computation and further errors in results.

2. Inverse and forward problem in ECT system

In order to understand advantages of apply parametric modelling of process in inverse problem solutions is worth of attention to understand inverse and forward problem in process tomography systems.

In case of ECT, if the permittivity distribution $\boldsymbol{\varepsilon}$ is known, the boundary capacitance can be calculated by solving Eq.1. This is the so-called forward problem, which is non-linear, yet well-posed, and allows calculation of capacitances by the finite element method (FEM) or Boundary Elements Methods (BEM), [21].

However, the inverse problem is associated with finding the distribution of certain physical property of the material given the measurements made from the outside the body. Electrical tomography is associated with the so-called soft-field effect. In a soft-field case the electric field lines associated with the measurement are dependent on the electrical properties of the materials in the measurement space. Moreover, inverse problem in case of soft-filed tomography is ill posed and ill conditioned [13, 21, 32]. This kind of inverse problem has the property that the solution is neither unique nor stable. To deliver a practical and stable solution it is necessary to use some prior information or regularization techniques. The common practice is using the simplest non-iterative reconstruction algorithms such as LBP or Tikhonov regularization, when the time consumed on image production is the critical parameter for efficient process control and monitoring. In order to find more detailed reconstruction, when needed, the iterative methods are applied, such as Gauss-Newton; although iterative algorithms are more time consuming.

In paper we show two different approaches, which cope with these difficulties. These methods based on the Bayesian approach coupled with Markov chain Monte Carlo (MCMC) sampling and applied Neural Network ANN. Firstly, it enables delivery of a practical stable solution to the inverse problem with the aid of considerable prior information. Secondly, it allows the direct estimation of the distribution of chosen, key parameters defining the specifics of the given industrial process.

3. Gravitational flow parameterization

In paper the parameterisation of examined process will be demonstrated on example of gravitational silo discharging process. In order to determine such parametrical model it is necessary to understand the process, especially the possible material distribution and their changes inside silo over the time.

3.1. Gravitational flow of solid

Presented geometrical model for gravitational flow of bulk solids in silos monitored with ECT is based on the knowledge of the flow properties. The model divides the cross-section into the three spatial regions (Fig. 1). This model was derived based on numerous experiments and theoretical considerations for the solids flows in containers [2, 3, 4, 16, 17, 23, 25].

Movement of the bulk in the central part of the cross section is characterised by a lower packing density in contrast to the other cross-sectional region (Fig. 1a). This region is called the funnel of the flow may vary in size and shape over the time of silo unloading. The shape of the central part depends on the shape of the container outlet and the shape of the container itself (presented results are given for cylindrical silo). Another specific property of this process is the little movement of the material in the zones located close to the container's wall that actually result in a slight increase of bulk packing density in this region. In case of funnel flow the most important is to analyse the centre of the cross section. Therefore the proposed model under consideration in this paper consists of two regions as shown on Fig 1b, [7, 10, 19]:

a) funnel zone in the centre;
b) the rest of the container cross-section (the so-called stagnant zone)

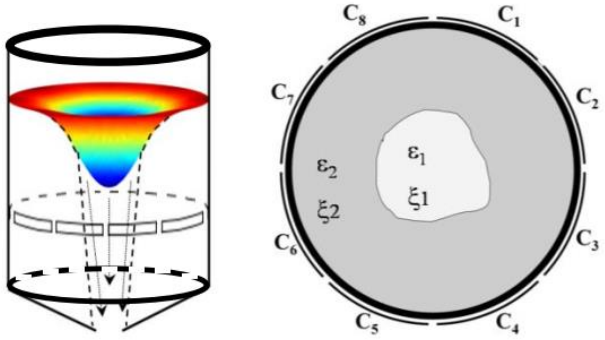

Fig. 1. Geometrical model of silo (a) (left hand-side) simplified sketch of the container unloading with a belt of ECT electrodes depicted in a ring (b) (right hand-side) cross-sectional view of the container with a funnel indicated in the centre surrounded by the rest of the bulk. ECT electrodes belt is depicted on the outer boundary. Silo flow modelled with the set of estimated parameters $\eta=\{\xi 1, \varepsilon 1, \xi 2, \varepsilon 2\}$

Each region is estimated with two parameters, namely: the size ξ and bulk concentration related to ε. Hence, any state of the funnel flow can be described with four 4 parameters $\gamma g=\{\xi_1, \xi_2, \varepsilon_1, \varepsilon_2\}$. Note the parameters related to the funnel are actually related to the cross-section of the funnel at a certain level of the location of the ECT electrodes belt. Geometrical modelling, i.e. parametrisation in terms of geometrical representation, allow direct estimation of process monitoring parameters, and therefore optimise use of data.

4. Bayesian approach and MCMC methods for inverse problem solution

Solving an inverse problem is looking for a relationship of the measurement (result - C) with the source data (cause - ε). This is looking for the cause, which gives the measurement. Usually there are some theoretically based expectations associated with behaviour or properties of the investigated process, and the proposed tool to incorporate this additional knowledge into solution is the Bayesian framework. Since the cause and the result can be shown as events in terms of probability – it let us use the Bayes' theorem to solve the inverse problem in tomography as was shown in [7, 10, 29, 30]. Bayes theorem in application to ECT can be presented as follows (Eq. 1):

$$p(\varepsilon|C) \propto p(C|\varepsilon) * \pi(\varepsilon) \tag{1}$$

The formula (Eq. 1) above describes the unknown – the inverse probability, e.g. the state of the investigated object on the basis of the conducted measurement result. The term $\pi(\boldsymbol{\varepsilon})$ is called the prior probability, whereas the posterior probability term corresponds to inverse probability. As the $p(\boldsymbol{C}|\boldsymbol{\varepsilon})$ term was described above to be associated with theoretical knowledge (forward probability) it can be shown as a function of cause set $\boldsymbol{\varepsilon}$ for a fixed result $\boldsymbol{C}$. In this case we call it the likelihood function. The likelihood density function, the conditional distribution of the capacitance for a given permittivity distribution, has the following form (Eq. 2):

$$\mathrm{p}(\mathrm{C}|\varepsilon) = \frac{1}{(2\pi\tau^2)^{n/2}} \exp\left\{-\frac{1}{2\tau^2}\|\mathrm{C} - \mathrm{C}(\varepsilon)^*\|^2\right\} \tag{2}$$

Whereas prior knowledge can be presented in form (Eq. 3):

$$\pi(\eta^t|\eta^{t-1}) \propto \exp\{-\alpha\|\eta^t - \eta^{t-1}\|_p^p\} \tag{3}$$

where η^{t} is the set of estimated parameters at time t, parameter α stands for level of likelihood of these estimated parameters in successive time points. The prior can involve either temporal or spatial dependencies as well as convey both, spatial-temporal information. The posterior distribution can be obtained by combining the prior and likelihood.

The Markov chain Monte Carlo method is a common approach to probability density function exploration, and a Metropolis–Hastings algorithm is also an often choice. It was used to produce approximate samples from the posterior distribution by simulating a Markov chain with the posterior distribution as its equilibrium distribution as reported in [29]. Algorithm procedure is as follows: choose an arbitrary starting point – parameter value (permittivity distribution in low-level modelling or set of parameters in high – level modelling) and iterate. Changes are proposed to the parameter values at each iteration. These changes are either accepted or rejected according to a probability depending on the posterior distribution and the parameter values. Proposed values for permittivity or set of parameters were drawn from independent Gaussian distributions centred on the current parameter values. The acceptance of the proposal is dependent on the following probability formula Eq. 4:

$$\alpha(\mathrm{X},\Theta) = \min\left\{1, \frac{\mathrm{p}(\mathrm{X}|\mathrm{C})\mathrm{q}((\mathrm{X}|\Theta)}{\mathrm{p}(\Theta|\mathrm{C})\mathrm{q}(\Theta|\mathrm{X})}\right\} \quad (4)$$

where χ is the proposed value coming from proposal distribution $q(\chi|\Theta)$ and Θ is the set of parameter values at the previous iteration.

4.1. Incorporating prior knowledge

The exemplary process, for which the direct parameters estimation is useful, is the gravitational flow of bulk in silos as described in section 3 above. The prior knowledge involves relationship between successive parameters of measurement data (for consecutive time points), which are reasonably similar to each other, as the process is taking place relatively slowly (with respect to the measurement acquisition rate). To evaluate the likelihood, the model parameters have to be transformed into the permittivity distribution. In the above example, the permittivity distribution must be obtained from location and size parameters. In this case the area of cross–section (pixels in tomographic images) belonging to funnel was described indirectly with the aid of ellipse. Circle in the (x, y) coordinates with the centre in point (x_0, y_0) and with radius r>0 is equivalent to set of all points (x, y) satisfying the Eq. 5:

$$(\mathrm{x}-\mathrm{x}_0)^2 + (\mathrm{x}-\mathrm{y}_0)^2 = \mathrm{r}^2 \quad (5)$$

The ellipse represents the boundary between the funnel and the stagnant zone in the horizontal cross section plane of the hopper. The proposed algorithm allows transforming set of parameters into permittivity distribution in sensor space. This permittivity distribution is used in forward problem solution unit to have vector of calculated capacitance for known material distribution [7, 10].

4.2. Silo flow parameters estimation based on MCMC methods

The parameters estimation algorithm starts from the first iteration (ii=1), where the image reconstruction obtained with classical method is used as a first input for parameters calculation. Based on this reconstructed image first set of parameters is determined. The basic schema of estimation is as follows: a proposed set of parameters $\eta^{t_k} = \{\xi_1^{t_k}, \varepsilon_1^{t_k}, \xi_2^{t_k}, \varepsilon_2^{t_k}\}$ for the first frame k=1 is taken, the parameter distribution is generated, compared with capacitance measurement on the basis of solving the forward problem, accepted or rejected, then the average over all the accepted simulations is calculated. Next, this average of parameters is fitted into the proposal for the successive frames at consecutive time points (illustrated on Fig. 2, [10]). Therefore, the temporal dependence on the previous time point is established and Markov chain is formed. The simplified graphical representation of algorithm procedure is shown on Fig. 5, [10]. The consecutive time points on the figures presented in this discussion are described with letters t with subscripts t_k, where k means the number of frame for considered measurement sequence, ii is the number of iteration in algorithm.

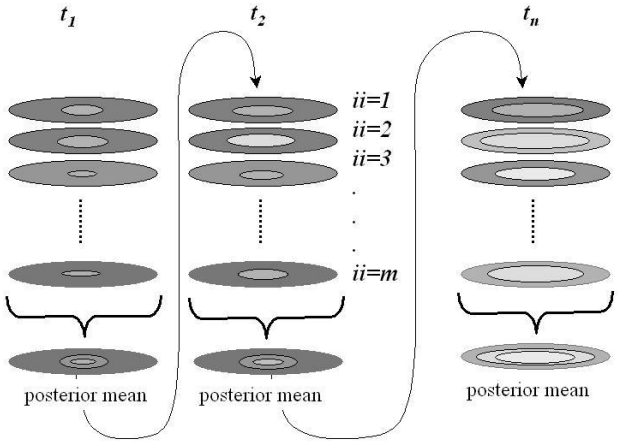

Fig.2. Algorithm diagram for silo modelling with indicated averaging after each iteration sequence for single frame estimation and fitting the posterior mean as the proposal to the next time point (ii – successive iteration index) as starting point

A plot of the estimated parameters for the silo flow shows funnel size ξ1 (related to progress of hopper unloading) and the funnel permittivity ε1 (related to packing density of bulk) with respect to time is shown on Fig. 3. Fig. 3a depicts the plot of the estimated area occupied by the funnel as percentage of the entire cross-section whereas Fig. 3b plots the permittivity of the funnel.

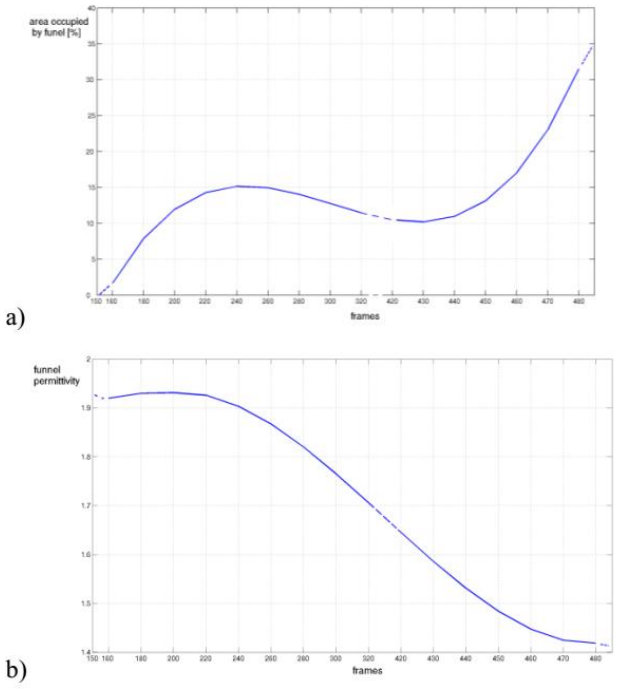

Fig. 3. Plot of estimated funnel parameters versus time, a) area occupied by funnel ξ1, b) funnel permittivity ε1

5. Artificial neural network methods of parameters estimation

The application of ANN to solve inverse problem for monitoring granular flow based on ECT data allows, similar as MCMC techniques, to obtain set of characteristic parameters of process. The capacitance data is fed to the artificial neural network

at the input layer and the silo flow parameters (funnel area and permittivity of the funnel) are obtained at the output layer.

ANN-based inverse model is built on the basis of relations between the network input and output vectors. The knowledge about the inverse mapping is stored within the network structure and network connection weights. An unknown mapping of the input vector to the output vector is approximated in an iterative procedure known as neural network training.

The objective of the learning algorithm is to adjust network weights on the basis of a given set of input-output pairs for a given cost function to be minimized. Back propagation algorithm, a supervised learning network algorithm, uses the gradient of the performance function to determine how to adjust the weights to minimize performance. In back propagation, the error data is propagated from the output layer backwards through the network. The resulting computations allow updating the incoming weights at each layer. Present approach propagates the network learning phase error until a set value of the training error vector is reached. The activation function f (·) may be a simple linear or a non-linear function. Widely used activation functions are the following: threshold function, sigmoidal function, hyperbolic tangent function and radial basis function. We employed the sigmoidal function in both hidden and output layers.

ANNs are known as universal approximators [11], which were successfully used for similar shape inverse problems solving [6, 26]. Therefore application of ANN is proposed to direct estimation of flow parameters on the basis of the measured capacitances. As shown in [26] ANN method, combined with principal component analysis, allowed real time solution of inverse problem in electrical impedance tomography.

Figure 4 shows examples of ANN applied to estimate size of funnel area. Comparison between results gathered from parametrical modelling and ANN solution (Fig. 4 left hand-side) and classical image reconstruction (Fig. 4 right hand-side) highlight the essence of deployed parametric modelling to inverse problem solving for solid flow monitoring, [6].

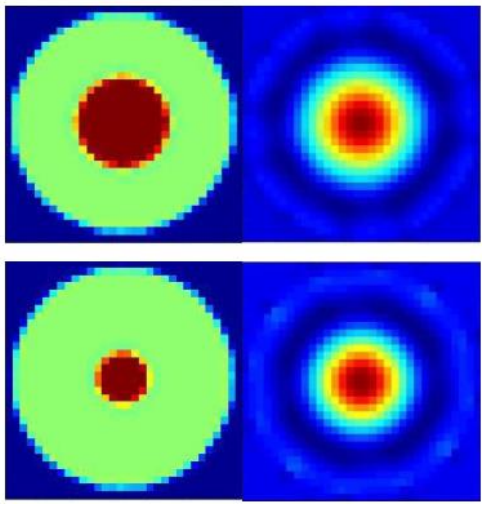

Fig. 4. Reconstructed images from MLP and Landweber algorithm

A Multi-Layer Perceptron (MLP) ANN type with one hidden layer was trained using back propagation algorithm to perform the estimation of two funnel parameters (ξ_1, ε_1) from ECT measurement data. A sequence of ECT reconstructed images for funnel flow was prepared. Comparison of the characteristic funnel parameters estimated in traditional way with the use of the Landweber method and image-processing methods with the ones estimated by the use of ANN is shown in Fig. 5.

The obtained area and permittivity of the funnel simulated by ANN are almost the same or very close to the parameters estimated in traditional way, what confirms the ability of the ANN to simulate the silo discharge process and track the changes of characteristic parameters of the flow over the time.

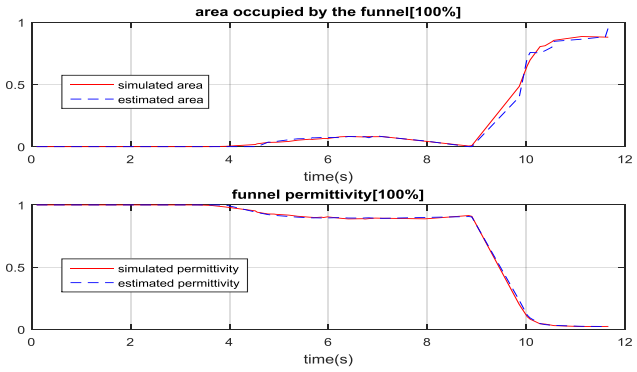

Fig. 5. ANN simulated results vs. estimated data for gravitational flow of bulk in silos. Upper diagram shows funnel area while bottom diagram presents funnel permittivity

The most important issue for ANN application is to determine the proper network structure. Such discussion was presented in [6], where different number of neurons in the hidden layer were tested. The most appropriate structure is selected relying on different chosen criteria. The trained MLP has the advantages to have simple structure one hidden layer and to directly solve the ECT inverse problem and estimate the funnel parameters (ξ_1, ε_1).

6. Discussion

Two main aspects to be considered in context of silo flow are understanding of the bulk flow behaviour and real-time monitoring of a process state. In this paper we demonstrate methods allow monitoring state of process based on tracking of characteristic parameters' changes during the flow. As demonstrated, the application of methods for silo flow behaviour monitoring with aid of process tomography and parameters estimation are feasible and fruitful. The main advantage is to omit the stage of image reconstruction on the way to analyse the measured flow behaviour. Though this advantage could be of key importance particularly in case of deployment parametrisation into the control and automation systems in the industrial settings, when the on-the-fly decision process takes place. The presented approach of direct estimation of flow parameters is beneficial especially from engineering point of view, since tracking of parameters values may allow to control process, i.e. quickly react when parameters are outside of the safe range of normal process operation. On the other hand, first step before decide what parameters should be tracked on the way to eventually incorporating this knowledge into the control feedback loop is to conduct experiments and analyse tomography images, since such analysis would allow to develop methods on how to estimate parameters based on measurement data.

ECT systems are suitable to apply in control systems, however the computational algorithms for parametrisation methods are still to be developed further. Iterative nature of MCMC methods shall be suited to on-line monitoring by both increase of computational resources (in terms of processing power and dedicated industrial FPGA hardware) and parallelisation through dedicated algorithms structures. In case on ANN methodology, time calculation is relatively short, but the actual ANN-based estimation has to be preceded with initial system learning.

The other direction for development is further regularization of the inverse problem through incorporation of more contextual data processing as proposed in [20].

7. Conclusions

Parametrisation and direct parameters estimation instead of classical image reconstruction analysis is a well advocated choice in a range of applications, especially since the inverse problem in ECT is loaded with mathematical difficulties related to nonlinearity of electric field properties. We showed here instances of two families of methods for parametrisation of gravitational

flow of bulk solids monitored with use of ECT. The first approach is Bayesian inference coupled with MCMC methods and the second possibility shown here is the employment of ANN. Both methods give sufficient accuracy allowing to produce results for both spatial and temporal modelling of process behaviour. The future work is however to develop algorithms in order to use their output parameters as input values in the industrial process control feedback loop.

References

[1] Banasiak R., Wajman R., Jaworski T., Fiderek P., Fidos H., Nowakowski J., Sankowski D.: Study on two-phase flow regime visualization and identification using 3D electrical capacitance tomography and fuzzy-logic classification. International Journal of Multiphase Flow, 58/2014, 1–14.

[2] Buick J.M., Chavez-Sagarnaga J., Zhing Z., Ooi J.Y., Pankaj D.M., Cambell D.M., Greated C.A.: Investigation of silo-honking: slip-stick excitation and wall vibration. Journal of Engineering Mechanics ASCE, 131(3)/2005, 299–307.

[3] Chaniecki Z., Dyakowski T., Niedostatkiewicz M., Sankowski D.: Application of electrical capacitance tomography for bulk solids flow analysis in silos. Particle and Particle Systems Characterization, 23(3-4)/2006, 306–312.

[4] Dhoriyani M.L., Jonnalagadda K.K., Kandikatla R.K., Rao K.K.: Silo music: sound emission during the flow of granular materials through tubes. Powder Technology, 167/2006, 55–71.

[5] Dyakowski T., Edwards R.B., Xie C.G., Williams RA.: Application of capacitance tomography to gas-solid flows. Chemical Engineering Science, 52/1997, 2099–2110.

[6] Garbaa H., Jaksowska-Strumiłło L., Grudzień K., Romanowski A.: Neural network approach to ECT Inverse problem solving for estimation of gravitational solids flow, Proceedings of the Federated Conference, Computer Science and Information Systems, 2014, 19–26.

[7] Grudzień K., Romanowski A., and Williams RA.: Application of a Bayesian Approach to the Tomographic Analysis of Hopper Flow. Particle & Particle Systems Characterization, 22/2006, 246–253.

[8] Grudzień K., Chaniecki Z., Romanowski A., Niedostatkiewicz M., Sankowski D.: Image Analysis Methods for Shear Zone Measurements during Silo Discharging Process. Chinese Journal of Chemical Engineering, 22/2012, 337–345.

[9] Grudzień K., Romanowski A., Aykroyd RG., Williams RA.: Advanced statistical computing for capacitance tomography as a monitoring and control tool. Intelligent Systems Design and Applications, 2005, 49–54.

[10] Grudzień K., Romanowski A., Aykroyd R.G., Williams R.A., Mosorov V.: Parametric Modelling Algorithms in Electrical Capacitance Tomography for Multiphase Flow Monitoring, Perspective Technologies and Methods in MEMS Design. Proceedings of the 2nd International Conference on, 2006, 100–106.

[11] Haykin S.: Neural Networks: a comprehensive foundation – 2nd ed. Prentice Hall, 1999.

[12] Isaksen Ø., Nordtvedt J.E.: A new reconstruction algorithm for use with capacitance-based tomography. Modeling, Identification and Control, 15/1994, 9–21.

[13] Lionheart W.R.B.: Review: Developments in EIT reconstruction algorithms: pitfalls, challenges and recent development. Physiol. Meas., 25/2004, 125–142.

[14] McCormick Sf., Wade J.G.: Multigrid solution of a linearized, regularized least-squares problem in electrical impedance tomography. Inverse Problems, 9/1993, 697.

[15] Mosorov V.: Flow Pattern Tracing for Mass Flow Rate Measurement in Pneumatic Conveying Using Twin Plane Electrical Capacitance Tomography. Particle & Particle Systems Characterization, 25(3)/2008, 259–265.

[16] Muite B.K., Quinn F.S., Sundaresan S., Rao K.K.: Silo music and silo quake: granular flow-induced vibration. Powder Technology, 145/2004, 190–202.

[17] Niedostatkiewicz M., Tejchman J.: Experimental and theoretical studies on resonance dynamic effects during silo flow. Powder Handling and Processing, 15(1)/2003, 36–42.

[18] Pląskowski A., Beck M.S., Thorn R., Dyakowski T.: Imaging industrial flows, applications of electrical process tomography. Institute of Physics Publishing, Bristol, 1995, 214.

[19] Romanowski A., Grudzień K., Williams R.A.: Analysis and Interpretation of Hopper Flow Behaviour Using Electrical Capacitance Tomography. Particle & Particle Systems Characterization, 23/2006, 297–305.

[20] Romanowski A., Grudzień K., Chaniecki Z., Woźniak P.: Contextual processing of ECT measurement information towards detection of process emergency states. Thirteenth International Conference on Hybdrid Intelligent Systems (HIS 2013), 2013, 292–298.

[21] Rymarczyk T., Filipowicz S.F., Sikora J.: Comparing methods of image reconstruction in electrical impedance tomography. Computer Applications In Electrical Engineering, 9/2011, 23–33.

[22] Sankowski D., Sikora J.: Electrical Capacitance Tomography: Theoretical Basis and Applications, edited by Dominik Sankowski and Jan Sikora, Wydawnictwa Książkowe Instytutu Elektrotechniki, 2010.

[23] Schulze D.: Powders and Bulk Solids, Springer, 2008, 516.

[24] Scott D.M., McCann H.: Process Imaging for automatic control, Taylor and Francis Group, 2005.

[25] Seville J.P.K., Tuzun U., Clift R.: Processing of Particulate Solids, Blackie Academic, London, 1997.

[26] Stasiak M., Sikora J., Filipowicz S.F., Nita K.: Principal component analysis and artificial neural network approach to electrical impedance tomography problems approximated by multi-region boundary element method. Engineering Analyses with Boundary Elements, 31/2007, 713–720.

[27] Vauhkonen M., Vadasz D., Karjalainen P.A., Somersalo E., Kaipio J.P.: Tikhonov regularization and prior information in electrical impedance tomography. Medical Imaging, IEEE Transactions on, 17/1998, 285–293.

[28] West R.M, Jia X, Williams R.A.: Parametric modeling in industrial process tomography. Chemical Engineering Journal, 77/2000, 31–36.

[29] West R.M., Meng S., Aykroyd R.G., Williams R.A.: Spatial-temporal modeling for electrical impedance imaging of a mixing process. Rev. Sci. Instrum. 76/2005, 073703.

[30] Winkler G.: Image Analysis, Random Fields and Markov Chain Monte Carlo: A Mathematical Introduction (2nd Ed.). Berlin, Heidelberg: Springer-Verlag., 2003.

[31] Yang W.Q., Liu S.: Role of tomography in gas/solids flow measurement. Flow Meas. and Instrum., 11/2000, 237–244.

[32] Yang W.Q., Peng L.: Image reconstruction algorithms for electrical capacitance tomography. Meas. Sci. Technol. 14/2003, R1–R13.

Ph.D. Eng. Andrzej Romanowski
e-mail: androm@kis.p.lodz.pl

Doctor of Technical Sciences, Computer Science specialized in tomography measurement data processing and inverse problems, Lodz University of Technology 2008.
Recent interests cover applications of tomography methods to industry and crowdsourcing as well as research on human factors in ubiquitous computing and human computer interaction. President of ACM and PIPS Łódź Chapters.

Ph.D. Eng. Krzysztof Grudzień
e-mail: kgrudzi@kis.p.lodz.pl

Assistant Professor of Applied Computer Science at Lodz University of Technology. Member of Polish Information Processing Society and ACM Lodz Chapter. He obtained PhD in 2007 in the field of Computer Science, Process Tomography specialty.
His research interests include applications of non-invasive imaging techniques and identification of dynamic industrial processes parameters, development of algorithms for image processing and analysis with particular reference to the analysis of sequences of 2D tomography images gathered from the ECT and X-rays tomography systems.

M.Sc. Hela Garbaa
e-mail:hgarbaa@kis.p.lodz.pl

Hela GARBAA was born in Sfax, Tunisia, in 1987. She graduated in Electrical Engineering in 2010 and obtained her Master Degree in Automatic Control and Industrial Computing from the National School of Engineers (ENIS), University of Sfax, Tunisia. She is currently a PhD student in the Institute of Applied Computer Science, Lodz University of Technology, Poland.

Prof. Lidia Jackowska-Strumiłło
e-mail: lidia_js@kis.p.lodz.pl

Professor at Lodz University of Technology (TUL), Poland and Vice-Director for didactics in the Institute of Applied Computer Science at TUL. She received the M.Sc., the Ph.D. and the DSc. degrees in electrical engineering from TUL in 1986, 1994 and 2010, respectively. In 1990/91 she has been staying in the Industrial Control Unit at the University of Strathclyde in Scotland where she worked on her Ph.D. project. From 1986 to 1998 she worked in the Institute of Textile Machines and Devices TUL.
Her research interests include computer engineering, modelling of industrial objects and processes, artificial intelligence, computer measurement systems, identification methods, text processing, image processing and analysis.

otrzymano/received: 20.09.2016 *przyjęto do druku/accepted: 15.02.2017*

DOI: 10.5604/01.3001.0010.4583

TOPOLOGICAL ALGORITHMS TO SOLVE INVERSE PROBLEM IN ELECTRICAL TOMOGRAPHY

Tomasz Rymarczyk
Netrix S.A., Research and Development Center, Związkowa Str. 26, 20-148 Lublin

Abstract. *In this paper, there were investigated topological algorithms to solve the inverse problem in electrical tomography. The level set method, material derivative, shape derivative and topological derivative are based on shape and topology optimization approach to electrical impedance tomography problems with piecewise constant conductivities. The cost of the numerical algorithm is enough good, because the shape is captured on a fixed grid. The proposed solution is initialized by using topological sensitivity analysis. Shape derivative and material derivative (or topological derivative) have been incorporated with level set methods to investigate shape optimization problems.*

Keywords: topological methods, inverse problem, finite element method, electrical impedance tomography

ALGORYTMY TOPOLOGICZNE DO ROZWIĄZYWANIA ZAGADNIENIA ODWROTNEGO W TOMOGRAFII ELEKTRYCZNEJ

Streszczenie*. W artykule przedstawiono algorytmy topologiczne do rozwiązania problemu odwrotnego w tomografii elektrycznej. Metoda zbiorów poziomicowych, pochodna materialna, pochodna kształtu i pochodna topologiczna zostały oparte na topologii optymalizacji kształtu do rozwiązania odwrotnego w elektrycznej tomografii impedancyjnej. Koszt algorytmu numerycznego jest wystarczająco dobry, ponieważ kształt jest osadzony na stałej siatce. Proponowany algorytm inicjowano za pomocą topologicznej analizy wrażliwościowej. Pochodna kształtu, pochodna materialna (lub pochodna topologiczna) zostały połączone z metodą zbiorów poziomicowych do badania problemów optymalizacji kształtu.*

Słowa kluczowe: metody topologiczne, zagadnienie odwrotne, metoda elementów skończonych, tomografia impedancyjna

Introduction

In this paper there was investigated the application of the topological algorithm for the topology optimization based on shape derivative, material derivative or topological derivative. Numerical methods of the shape and the topology optimization were based on the level set representation and there were made possible topology changes during the optimization process [1, 3, 14, 15, 16]. Level set methods have been applied very successfully in many areas of the scientific modelling, for example in propagating fronts and interfaces [3, 4, 6–8, 18]. Therefore, they are used to study shape optimization problems. Instead of using the physically driven velocity, the level set method typically moves the surfaces by the gradient flow of an energy functional. These approaches based on shape sensitivity include the boundary design of elastic. There are two features that make these methods suitable for the topology optimization. The structure is represented by an implicit function such that its zero level set defines the boundary of the object. This function is often discretized on a regular grid that conveniently coincides with the finite or boundary element mesh used for structural analysis. The next valid feature is the simple update of the implicit function using the Hamilton-Jacobi equation, where the velocity function is determined by the shape sensitivity of the structure. These properties enable natural topology changes. The discussed technique can be applied to the solution of inverse problems in electrical impedance tomography [5, 9–13, 17].

1. Numerical Methods

1.1. Level Set Method

Level set methods have been applied very successfully in many areas of the scientific modelling, for example in propagating fronts and interfaces (Fig. 1). Therefore, they are used to study shape optimization problems. Instead of using the physically driven velocity, the level set method typically moves the surfaces by the gradient flow of an energy functional. These approaches based on shape sensitivity include the boundary design of elastic. There are two features that make these methods suitable for the topology optimization. The structure is represented by an implicit function such that its zero level set defines the boundary of the object.

Figure 2 presents six algorithms of the level set methods: the level set method, the parametric level set method, the Mumford-Shah model, the variational level set methods, the Mumford-Shah variational level set methods, the Levenberg–Marquardt level set method.

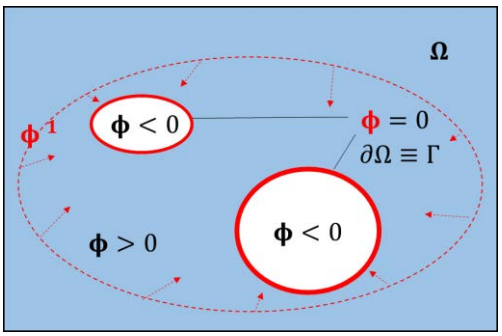

Fig. 1. The idea of the level set function

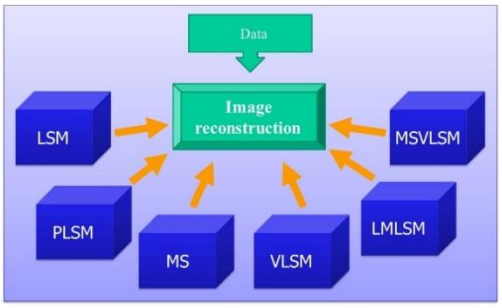

Fig. 2. The reconstruction methods

The representation of the level set method was shown in Figure 1. The level set function ϕ has the following properties:

$$\begin{gathered}\phi(\vec{r},t)=0 \text{ for } (x,y)\epsilon\partial\Omega(t)\equiv\Gamma(t)\\ \phi(\vec{r},t)>0\ for\ (x,y)\epsilon\Omega(t)\\ \phi(\vec{r},t)<0\ for\ (x,y)\notin\Omega(t)\end{gathered} \tag{1}$$

The motion is seen as the convection of values (levels) from the function ϕ with the velocity field $\vec{v}$ Such process is described by the Hamilton-Jacobi equation:

$$\frac{\partial\phi}{\partial t}+\vec{v}\cdot\nabla\phi=0 \tag{2}$$

Here $\vec{v}$ is the desired velocity on the interface, and is arbitrary elsewhere. Actually, only the normal component of $\vec{v}$ is needed $v_n\equiv\vec{v}\cdot\vec{n}\equiv\vec{v}\cdot\nabla\phi/|\nabla\phi|$, so (2) becomes:

$$\frac{\partial\phi}{\partial t}+v_n\cdot|\nabla\phi|=0 \tag{3}$$

There can update the level set function ϕ by solving discretized version of the Hamilton-Jacobi equation:

$$\frac{\phi^{k+1}-\phi^k}{\Delta t} + v_n^k \cdot \left|\nabla\phi^k\right| = 0 \quad (4)$$

Transforming above equation:

$$\phi^{k+1} = \phi^k - v_n^k \cdot \left|\nabla\phi^k\right|\Delta t \quad (5)$$

The gradient of the level set function in the k-th time step $\left(\left|\nabla\phi^k\right|\right)$ has been calculated by the essentially non-oscillatory (ENO) polynomial interpolation scheme. The stability of received solution is achieved by Courant-Friedreichs-Lewy condition (CFL condition):

$$\Delta t < \frac{min(\Delta x,\Delta y)}{max(|\vec{v}|)} \quad (6)$$

Inequality (6) is satisfied by choosing the CFL number α:

$$\Delta t \frac{max(|\vec{v}|)}{min(\Delta x,\Delta y)} = \alpha \quad (7)$$

where $0 < \alpha < 1$. The optimum value equals 0.9:

The calculated velocity must be extended off the interface to the whole domain. This process is called the extension of velocity and is based on the solution of the additional partial differential equation:

$$\frac{\partial v_n}{\partial t} + S(\phi)\frac{\nabla\phi}{|\nabla\phi|}\cdot\nabla v_n = 0 \quad (8)$$

where $S(\phi)$ is defined as following:

$$S(\phi) = \frac{\phi}{\sqrt{\phi^2+\varepsilon^2}} \quad (9)$$

In (9) $|\varepsilon| \ll 1$. Additionally, the velocity is extended to neighborhood of the interface, by defining velocity along normal direction.

Reinitialization is necessary when flat or steep regions complicate the determination of the zero contour. The level set function ϕ is signed distance function if at given time for every point (x,y):

$$|\nabla\phi| = 1 \quad (10)$$

Reinitialization is based on replacing ϕ by another function that has the same zero level set, but satisfies condition.

In the level set representation, the interface, which is the set of points (x,y) satisfying $\phi(x,t) = 0$ is not explicitly given. There is only information $\phi(x_i, t_i)$ at each grid point.

When flat or steep regions complicate the determination of the contour, reinitialization is necessary. The reinitialization procedure is based by replacing ϕ by another function that has the same zero level set but behaves better. This is based on following partial differential equation:

$$\frac{\partial}{\partial t}\phi + S(\phi)(|\nabla\phi| - 1) = 0 \quad (11)$$

where $S(\phi)$ is defined as:

$$S(\phi) = \begin{cases} -1 & \text{for} \quad \phi < 1 \\ 0 & \text{for} \quad \phi = 1 \\ 1 & \text{for} \quad \phi > 1 \end{cases} \quad (12)$$

1.2. Material derivative and shape derivative

The topological method is based on so-called conical differentiability of solutions to variational inequalities with respect to the coefficients of the governing differential operator. It is required that the metric projection in the energy space. Such property is sufficient to obtain the directional differentiability of solutions to the variational inequality with respect to the boundary variations with respect to the changes in the topology by the creation of a small object. A useful concept for calculating derivatives for cost functional is the so-called material and shape derivative of states u. In the application of inverse problems, these states typically are the solutions of partial differential equations which model the probing fields and which depend one way or another on the shape.

Let λ be the adjoint function satisfying:

$$-\Delta\lambda = u - u_m \quad (13)$$

The material derivative concept is applied to the formulation of an inverse obstacle problem. This is the derivative with respect to the geometry for a moving interface. The material derivative $\dot{u}(\vec{r})$ is given by:

$$\dot{u}(\vec{r}) \equiv \lim_{t\to 0}\frac{u_t(\vec{r}+t\vec{v}(\vec{r}))-u(\vec{r})}{t} \quad (14)$$

where $(x,y)\epsilon\Omega_t$.

The shape derivative concept is extended by material derivatives. This method is based on the fact that the definition of shape derivatives is presented to differentiate boundary and domain integrals with respect to a deformation of the contour. The shape derivative is defined as below:

$$u'(\vec{r}) \equiv \lim_{t\to 0}\frac{u_t(\vec{r})-u(\vec{r})}{t} = \dot{u}(\vec{r}) - \vec{v}(\vec{r})\cdot\nabla u(\vec{r}) \quad (15)$$

The steepest descent direction $\vec{v}$ is given by:

$$\vec{v} = -(\nabla u\cdot\nabla\lambda)\vec{n} \quad (16)$$

The normal velocity is evaluated by using weighted least squares interpolation to get:

$$v_n^k = \nabla u^k\cdot\nabla\lambda^k + \varepsilon\kappa^k \quad (17)$$

In next step the level set function is updated:

$$\phi^{k+1} = \phi^k - (\nabla u^k\cdot\nabla\lambda^k + \varepsilon\kappa^k)\left|\nabla\phi^k\right|\Delta t \quad (18)$$

where Δt is obtained from CFL condition (11).

1.3. Topological derivative

Topological derivative (TD) is defined as the first term of the asymptotic expansion of a given shape functional (with expect to a small parameter that measures the size of singular domain perturbation). Topological derivative evaluates for a given shape functional defined in a geometrical domain and dependent on a classical solution to elliptic boundary value problem (Fig. 3).

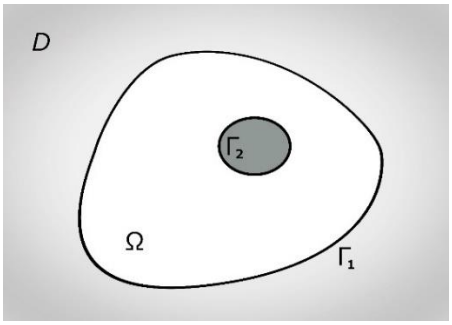

Fig. 3. The idea of topological derivative

Topological derivative represents the change of the shape (functional) when the domain is perturbed by holes, inclusions, defects or cracks. Shape derivative is defined as a minimization of a given shape functional (Fig. 4).

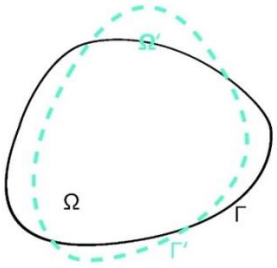

Fig. 4. The idea of shape derivative

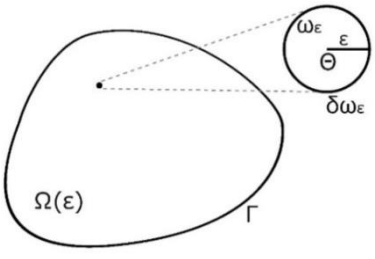

Fig. 5. Topological derivative – the small hole

Perforation of the domain by creating small holes inside Ω was presented in Figure 5. Figure 6 shows the domain with searched objects.

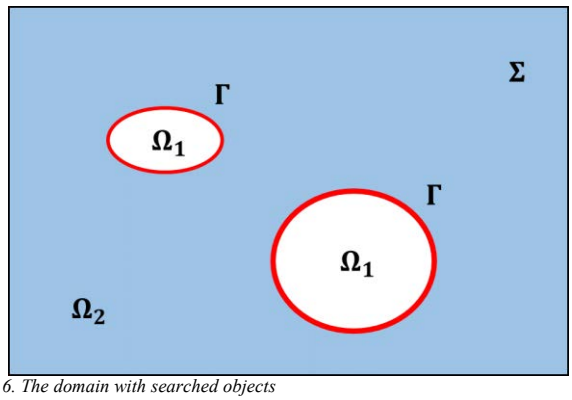

Fig. 6. The domain with searched objects

Topological derivative using the level set function to solve the inverse problem in electrical impedance tomography. Velocity in Hamilton-Jacobi equation is defined following:

$$v_n = -[(\gamma - \gamma_i)(\nabla p_i \cdot \nabla u) + \beta|\gamma - \gamma_i|\mathcal{H}] \text{ on } \Gamma_i \quad (19)$$

Laplace'a equaton is described as:

$$-\Delta u = 0 \text{ in } \Omega^*, q\partial_n u = f \text{ on } \Sigma, q\partial_n u = q_i \partial_n u_i \text{ on } \Gamma_i,$$
$$-\Delta u_i = 0 \text{ in } \Omega_i, u_i = u \text{ on } \Gamma_i \quad (20)$$

The adjoint equation is following:

$$-\Delta p = 0 \text{ in } \Omega^*, q\partial_n p = 2(u - u_m) \text{ on } \Sigma,$$
$$q\partial_n p = q_i \partial_n p_i \text{ on } \Gamma_i, -\Delta p_i = 0 \text{ in } \Omega_i, p_i = p \text{ on } \Gamma_i \quad (21)$$

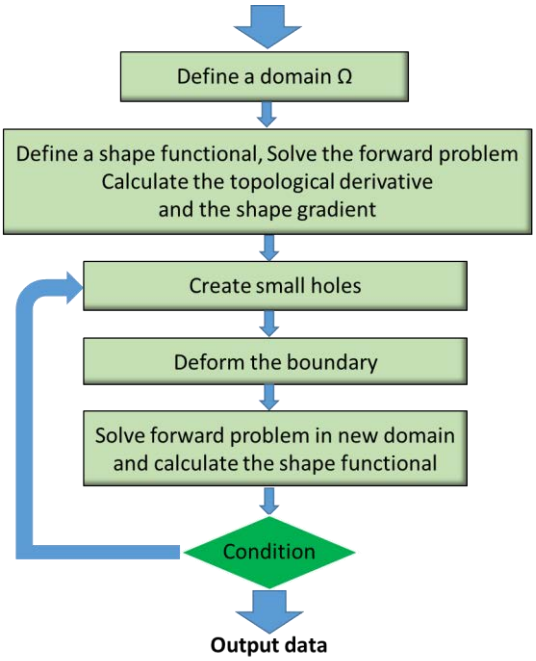

Fig. 7. The iterative algorithm – the inverse problem

For some $\varepsilon > 0$, the topological derivative $\mathcal{T}_\varepsilon$ is defined as

$$\mathcal{T}_\varepsilon = \left(\varepsilon \left| S_\varepsilon^{N-1} \right|\right)^{-1} \sum_{k=1}^{4} \mathcal{T}_{k,\varepsilon} \quad (22)$$

The algorithm is initialized by $\Omega_2 := \Omega$ and

$$\Omega_1 := \left\{x \in \Omega \mid \mathcal{T}_\varepsilon(x) < \xi \min_{y \in \Omega} \mathcal{T}_\varepsilon(y)\right\} \quad (23)$$

where $0 < \xi < 1$ is a given threshold.

The proposed algorithm (Fig. 7):

- define a domain Ω for the shape optimization,
- define a shape functional,
- solve the forward problem,
- calculate the topological derivative and the shape gradient,
- create small holes,
- deform the boundary,
- solve forward problem in new domain and calculate the shape functional,
- minimization $\mathcal{T}(\Omega; u)$ (go to the step create small holes or finish the process).

2. Electrical Impedance Tomography

There were proposed algorithms based on level set function to solve the inverse problem in electrical impedance tomography. The conductivity values in different regions are determined by the finite element method. Numerical iterative algorithm is a combination of the level set methods for following the evolving step edges and the finite element method for computing the velocity. The objective function is defined as the difference between the potential due to the applied current and the measured potential.

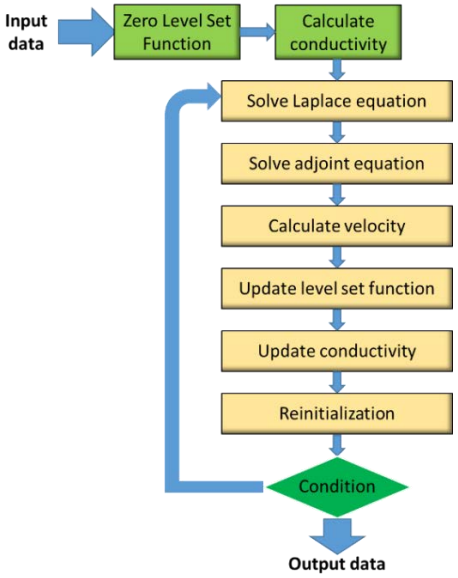

Fig. 8. The iterative algorithm – EIT

For the minimization problem, the level set method and the topological gradient method has been proposed. Both methods are gradient-type algorithms, and the coupled approach can be cast into the framework of alternate directions descent algorithms. The level set method relies on shape derivative, while the topological gradient method is based on the topological derivative or material derivative.

The proposed algorithm is iterative method, structured as follows (Fig.8):

- from the level set function at initial time, find necessary interface information;
- use the Finite/Boundary Element Method to solve the Laplace's equation and next compute the difference of the obtained solution with the observed data;
- solve the Poisson's equation (adjoint equation);
- find velocity in the normal direction;
- update the level set function;
- reinitialize the level set function.

3. Results

In examples reported below, several numerical models are presented. Additionally, there was present different geometries of the conductivity distributions. The conductivity of searched objects is known. The representation of the boundary shape and its evolution during an iterative reconstruction process is achieved by the level set method and the gradient method coupled together. In forward problem, which is given by Laplace's equation, the finite element method has been used. Additionally, different zero level set functions have been selected.

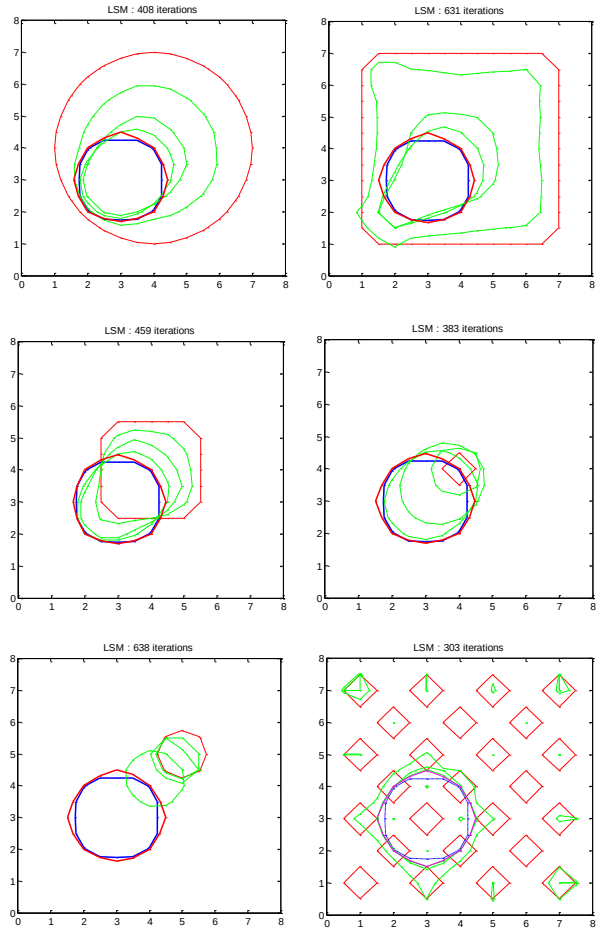

Fig. 9. The image reconstruction with the different zero level set function (red line – zero level set, bold red line – reconstructed object, blue line – original object, green line – steps of reconstruction)

Figure 9 presents the image reconstruction with the different zero level set function (red line – zero level set, bold red line – reconstructed object, blue line – original object, green line – steps of reconstruction). Figure 10 shows the two images: (a) the original objects and the zero contour from the level set function and (b) the process of the image reconstruction.

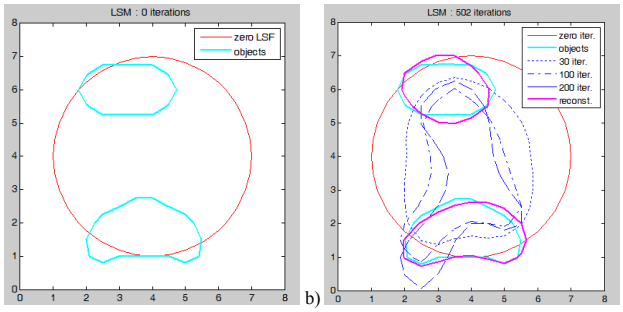

a) b)

Fig. 10. Images reconstruction: a) the original objects and the zero contour from the level set function; b) the process of the image reconstruction

4. Conclusion

The algorithms based on material and shape derivative, topological derivative and the level set method have been proposed in this work. There are iterative algorithms where the shape boundary evolves smoothly and new small objects are detected. An efficient algorithm for solving the forward and inverse problems would also improve a lot of the numerical performances of the proposed methods. In model problem from EIT is required to identify unknown conductivities from near-boundary measurements of the potential. The number of iterations determine the position and shape of zero level set functions. In these algorithms, it can control the process of the image reconstruction. The level set function techniques have been shown to be successful to identify the unknown boundary shapes. The accuracy of the image reconstruction is better than gradient methods. The purpose of the presented method is obtaining the better image reconstruction than gradient methods and accelerates the iterative process by using different shapes of the zero level set functions. Applying the line measurement model is very effective to solve the inverse problem in the copper-mine ceiling and flood embankment. The right selection of the zero level set function gives the better results, reduces the time of the reconstruction process and improves the better quality of the image reconstruction.

References

[1] Allaire G., Gournay F. De, Jouve F., Toader A. M.: Structural optimization using topological and shape sensitivity via a level set method, Control and Cybernetics, vol. 34, 2005, 59–80.
[2] Chan T. and Vese L.: Active contours without edges, IEEE Transactions on Image Processing, vol. 10, 2001, 266–277.
[3] Hintermüller M., Laurain A., Novotny A.A.: Second-order topological expansion for electrical impedance tomography, Advances in Computational Mathematics, 36(2), 2012, 235–265.
[4] Ito K., Kunish K., Li Z.: The Level-Set Function Approach to an Inverse Interface Problem. Inverse Problems, Vol. 17, No. 5, 2001, 1225–1242.
[5] Kapusta P., Majchrowicz M., Sankowski D., Jackowska-Strumiłło L., Banasiak R.: Distributed multi-node, multi-GPU, heterogeneous system for 3D image reconstruction in Electrical Capacitance Tomography – network performance and application analysis. Przegląd Elektrotechniczny, Vol. 89, No. 2b, 2013, 339–342.
[6] Osher S., Sethian J.A.: Fronts Propagating with Curvature Dependent Speed: Algorithms Based on Hamilton-Jacobi Formulations, Journal of Computational Physics, 79, 1988, 12–49.
[7] Osher S., Fedkiw R.: Level Set Methods and Dynamic Implicit Surfaces. Springer, New York 2003
[8] Osher S., Santosa F.: Level set methods for optimization problems involving geometry and constraints. Frequencies of a two-density inhomogeneous drum. Journal of Computational Physics, 171, 2001, 272–288.
[9] Rymarczyk T.: Using electrical impedance tomography to monitoring flood banks, International Journal of Applied Electromagnetics and Mechanics 45, 2014, 489–494.
[10] Rymarczyk T.: Characterization of the shape of unknown objects by inverse numerical methods, Przegląd Elektrotechniczny, R. 88, nr 7b/2012, 138–140.
[11] Rymarczyk T., Sikora J.: Different Approaches to Level Set Method and Its Applications, chapter in Algorithms, Networking and Sensing for Data Processing Mobile Computing and Applications, edited by A. Romanowski, D. Sankowski and J. Sikora, Lodz University of Technology Monograph, Lodz 2016.
[12] Rymarczyk T, Adamkiewicz P., Duda K., Szumowski J., Sikora J.: New Electrical Tomographic Method to Determine Dampness in Historical Buildings, Achieve of Electrical Engineering, v.65, 2/2016, 273–283.
[13] Smolik W.: Forward Problem Solver for Image Reconstruction by Nonlinear Optimization in Electrical Capacitance Tomography, Flow Measurement and Instrumentation, Vol. 21, Issue 1, 2010, 70–77.
[14] Sokolowski J., Zochowski A.: On the topological derivative in shape optimization, SIAM Journal on Control and Optimization, vol. 37, 1999, 1251–1272.
[15] Szulc K.: Topological derivative-theory and applications. Informatyka, Automatyka, Pomiary w Gospodarce i Ochronie Środowiska, 1, 2015, 7–13 [DOI: 10.5604/20830157.1148040].
[16] Tai C., Chung E., Chan T.: Electrical impedance tomography using level set representation and total variational regularization. Journal of Computational Physics, vol. 205, no. 1, 2005, 357–372.
[17] Wajman R., Banasiak R.: Tunnel-based method of sensitivity matrix calculation for 3D-ECT imaging, Sensor Review, Vol. 34 Iss: 3, 273–283, 2014.
[18] Zhao H.-K., Osher S., Fedkiw R.: Fast Surface Reconstruction using the Level Set Method. 1st IEEE Workshop on Variational and Level Set Methods, in conjunction with the 8th International Conference on Computer Vision (ICCV), Vancouver, Canada, 2001, 194–202.

Ph.D. Eng. Tomasz Rymarczyk
e-mail: tomasz.rymarczyk@netrix.com.pl

Director in Research and Development Center Netrix S.A. His research area focuses on the application of non-invasive imaging techniques, electrical tomography, image reconstruction, numerical modelling, image processing and analysis, process tomography, software engineering, knowledge engineering, artificial intelligence and computer measurement systems.

otrzymano/received: 20.09.2016 *przyjęto do druku/accepted: 15.02.2017*

DOI: 10.5604/01.3001.0010.4584

MONITORING DAMAGE AND DAMPNESS IN FLOOD EMBANKMENT BY ELECTRICAL IMPEDANCE TOMOGRAPHY

Tomasz Rymarczyk, Przemysław Adamkiewicz
Netrix S.A., Research and Development Center, Związkowa Str. 26, 20-148 Lublin

Abstract. *The article presents a model of the measuring system for image reconstruction. Electrical impedance tomography was used to determine the moisture of the test flood blank on a specially built model. The Gauss-Newton methods have been applied very successfully in many areas of the scientific modelling. The basic information about the built model system is given. The finite element method was used to solve the forward problem. The level set method and the Gauss-Newton method were applied to solve the inverse problem.*

Keywords: inverse problem, finite element method, electrical impedance tomography, flood embankment

TOMOGRAFIA IMPEDANCYJNA DO WYZNACZANIA WILGOTNOŚCI W MODELU WAŁU

Streszczenie. *W artykule zaprezentowano model systemu, układ pomiarowy oraz metody rekonstrukcji obrazów. Elektryczna tomografia impedancyjna została użyta do określenia wilgotności w specjalnie przygotowanym testowym modelu wału przeciwpowodziowego. Zastosowane metody gradientowe i topologiczne są bardzo skuteczne w wielu obszarach modelowania. Zostały przedstawione podstawowe informacje o koncepcji systemu. Do rozwiązania zagadnienia odwrotnego zostały wykorzystane metody zbiorów poziomicowych i Gausa-Newtona.*

Słowa kluczowe: zagadnienie odwrotne, metoda elementów skończonych, tomografia impedancyjna, wał przeciwpowodziowy

Introduction

This paper presents the new method examining the flood embankment dampness by electrical impedance tomography (EIT) [1-3]. Numerical methods were based on gradient techniques [8, 9, 12]. Discussed algorithms can be applied to the solution of inverse problems to determine a dampness in electrical impedance tomography. The finite element method coupled with Gauss-Newton or (and) the level set function has been used [4, 6]. The model of the flood embankment creates nonhomogeneous testing environment where object properties conductivity varied smoothly with one more coordinates. Surface potential measurements are performed at different angles of projection whereby the information needed to determine an approximate distribution of conductivity inside the object is obtained. This idea has been used successfully in the context of the inverse problem in the flood embankment [5, 7, 10, 11, 13-15].

1. Flood embankment model

The flood embankment dampness was examined by electrical impedance tomography system. The examples of embankment's damage were presented in Figure 1 such as: piping, erosion outer slope, micro instability, drifting ice, slip circle inner slop, slip circle outer slop, wave overtopping, overflow and liquefaction.

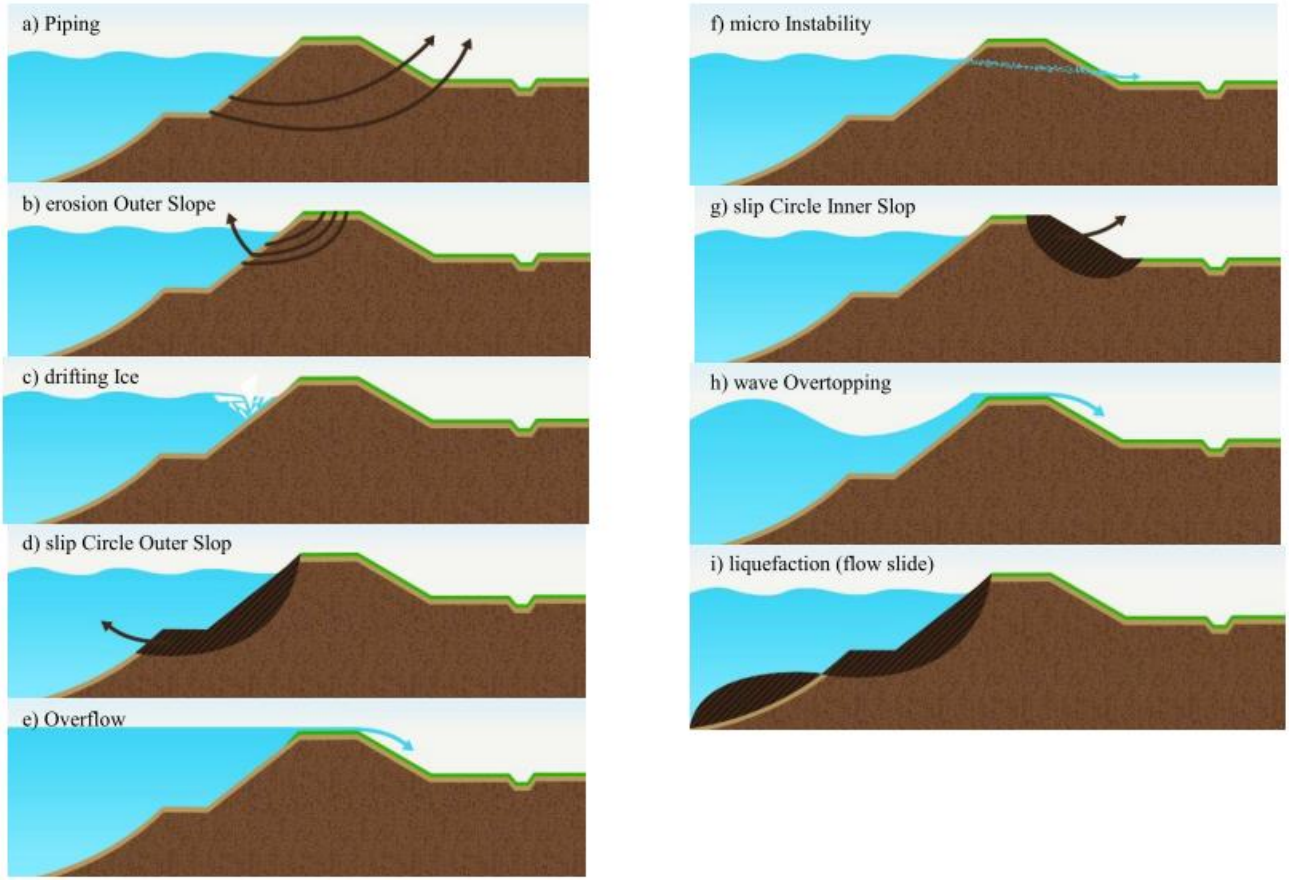

Fig. 1. The model of the flood embankment

The architecture of the flood embankment system is shown in Figure 2.

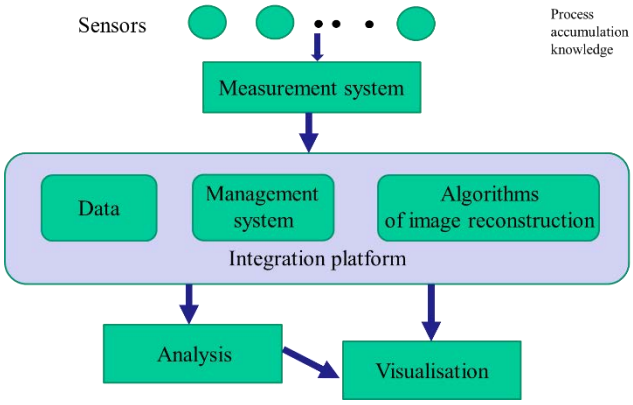

Fig. 2. The architecture of the flood embankment system

There is well known that for EIT scanning system with 16 electrodes on 2 dimension, we can get 13 independent electrode-to-electrode measurements and 8 independent potential distributions and 104 linearly independent values. The distribution of potentials on the edge of saturated sand and the top of the bank is linear, it may be because the electrode was placed near the edge. Surface potential measurements are performed at different angles of projection whereby the information needed to determine an approximate distribution of conductivity inside the object is obtained.

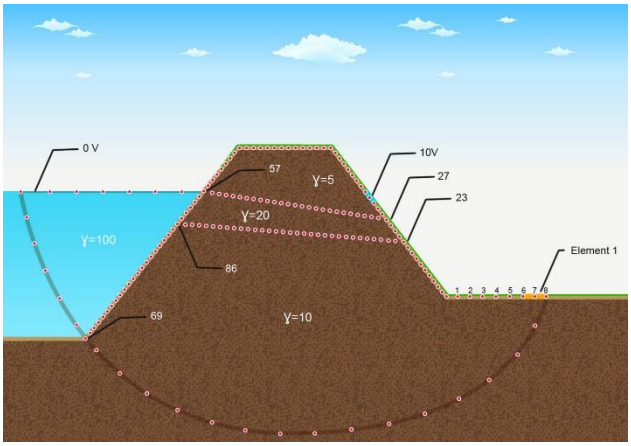

Fig. 3. The distribution of elements on the edge of the flood embankment

The example of embankment's model was shown in Figure 3. This object was divided into 57elements, 111 nodes. Each element consists of three nodes. The red element symbolizes the electrode 10V. In black marked 0V ground potential. For the area of γ4 is water. The measurement voltage is from node 1 to 57 - 28 items (27 electrodes from node 2 at the second node to node until the number 56, in addition to node 32 where it was applied 10V). Green color indicated the first item.

The distribution of potentials on the edge of the flood embankment results can easily check the state of saturation in the layer of sand γ_2. The greater permeability of the sand is lower potential at the edge of the flood embankment. The lower permeability area γ_3 is lower potentials. As you can see from the chart the impact of water conductivity in a very small influence on the distribution of potentials in most places (at the edge of the flood embankment and on the border between the saturated sand and the top layer of dry sand and the boundary between the saturated sand and a lower layer of the bank). Only the results differ on the border of the bank - the water. The distribution of potentials on the border of saturated sand and the top of the bank is linear, it may be because the electrode was placed near the 10V and the other side of the border of three centers is 0V.

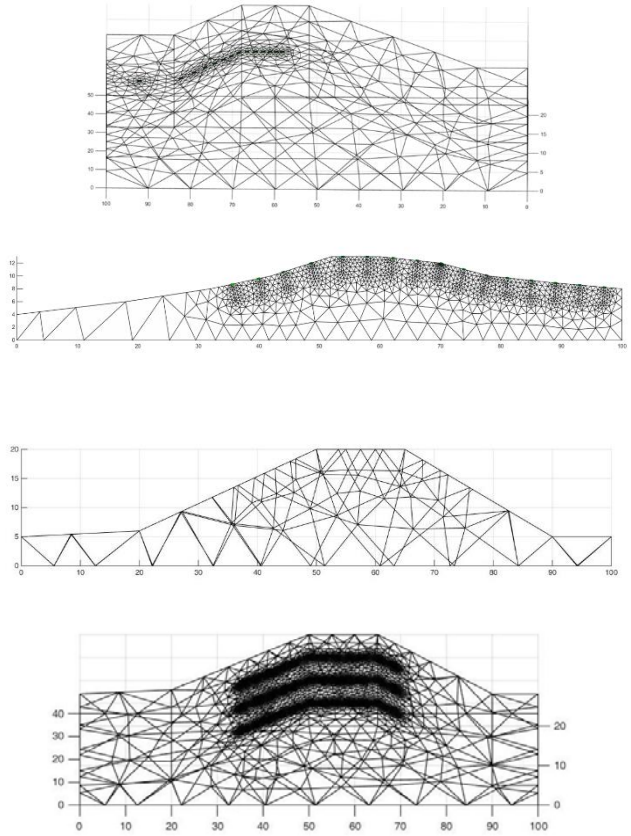

Fig. 4. Numerical models of the flood embankments

Figure 4 presents the numerical models of the flood embankments. EIT measurement models of the flood embankment are shown in Figure 5 and 6. The laboratory prototype model with devices is presented in Figure 7.

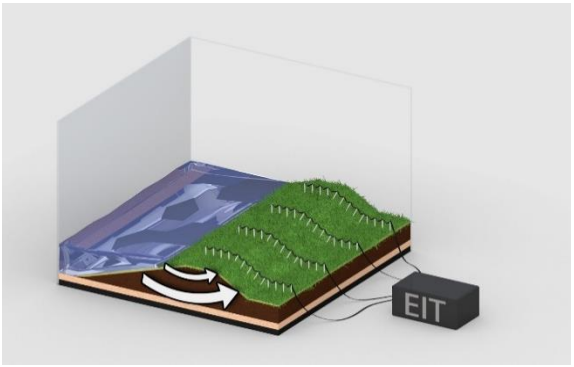

Fig. 5. The EIT measurement model I of the flood embankment

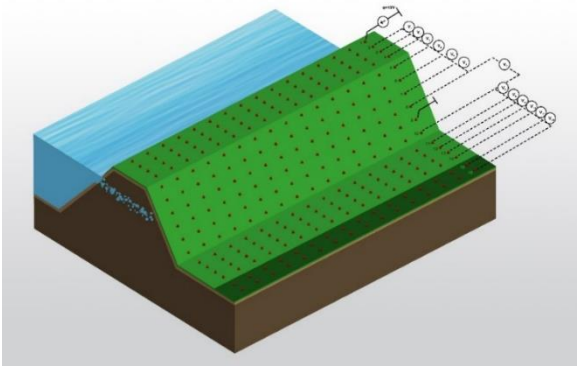

Fig. 6. EIT measurement model II of the flood embankment

Fig. 7. The laboratory prototype of the measurement system

2. Image reconstruction

Electrical impedance tomography is known that the inverse problem is nonlinear and highly ill-posed. The forward problem solution in EIT consists in determining potential distribution inside the region Ω under given boundary conditions and full information about region under consideration. That is in solving Laplace's equation:

$$\mathrm{div}(\boldsymbol{\gamma}\,\mathrm{grad}\,\mathbf{u}) = 0 \tag{1}$$

where **u** - voltage, **γ** - conductivity.

The objective function is formed following:

$$\mathrm{F} = 0.5\sum_{i=1}^{n}(\boldsymbol{U}-\boldsymbol{U}_m)^T(\boldsymbol{U}-\boldsymbol{U}_m) \tag{2}$$

where n is a projection angle, $\mathbf{U}_m$ – the measured voltage, **U** – the calculated voltage by solving the equation (1).

A Gauss-Newton method is deployed to the regularized tangential movement problem. The electrodes move tangentially to the domain at each iteration and so do not in general lie on the boundary of the domain after each iteration. These are thus projected back onto the fixed domain by computing the nearest boundary simplex of the finite element mesh. The Gauss-Newton algorithm is following form:

$$\boldsymbol{\gamma}^{k+1} = \boldsymbol{\gamma}^k + \alpha\left(\mathbf{J}_t^k\mathbf{J}^k + \lambda\mathbf{W}\right)^{-1}\cdot \cdot\left(\mathbf{J}_t^k\mathbf{W}\left(\mathbf{u}_m - \mathbf{h}(\boldsymbol{\gamma}^k)\right) - \lambda\mathbf{W}\boldsymbol{\gamma}^k\right) \tag{3}$$

where **γ** denotes the vector of the unknown conductivity, α is the step size, λ is a regularization parameter, $\mathbf{J}^k$is the Jacobian matrix, **W** is a regularization matrix and $\mathbf{h}(\boldsymbol{\gamma}^k)$ is the observation model derived from a finite elements model.

The forward problem solution in EIT consists in determining potential distribution inside the region under given boundary conditions and full information about region under consideration, that is in solving Laplace's equation. In this paper there was proposed combination the Gauss-Newton method, the level set method and the finite element method to solve the inverse problem. The representation of the boundary shape and its evolution during an iterative reconstruction process is achieved by the level set method. The image reconstruction in the different geometrical model of the micro instability was presented. The conductivity of searched objects is known. Figures 8, 9 show the simulation of one and two objects. The image reconstruction obtained by the Gauss Newton Level Set Method with simulation data was shown in Figure 10. Picture 11 shows the image reconstruction obtained by the Gauss Newton method with real data: the model (a), data taken after 15 minutes (b), after 30 minutes (c). Figure 12 presents the image reconstruction of the 3D model of the flood embankment.

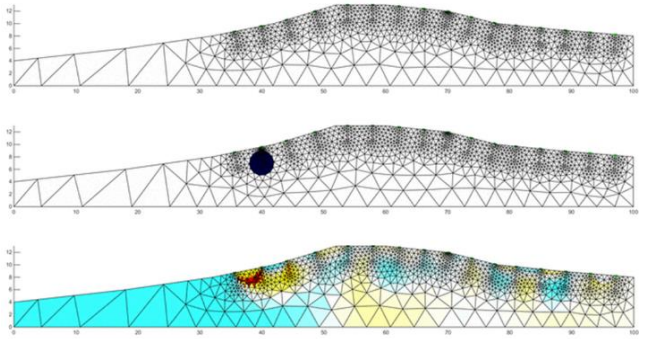

Fig. 8. The model of the one objects and image reconstruction

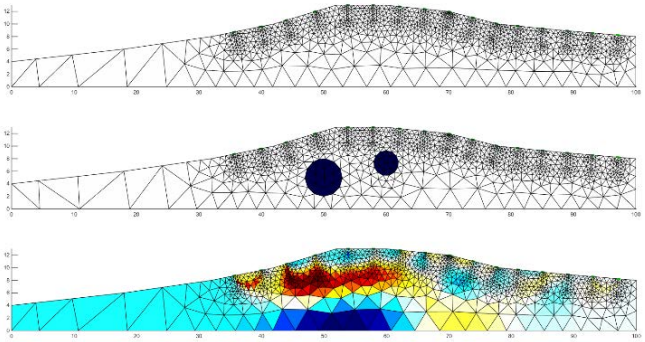

Fig. 9. The model of the two objects and image reconstruction

a)

b)

c)

d)

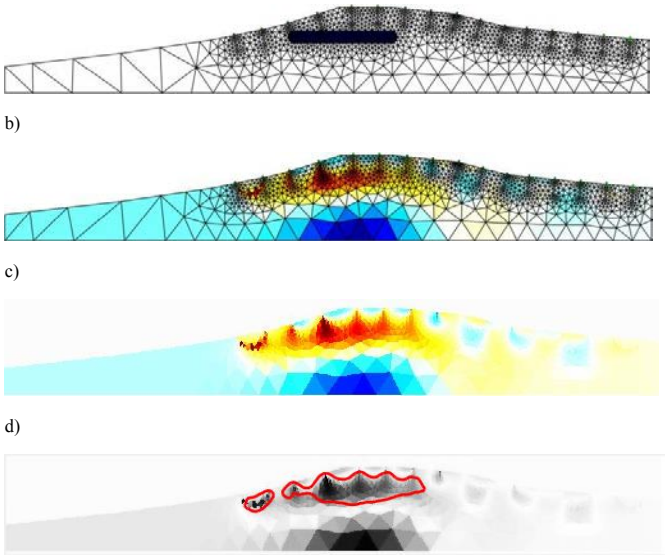

Fig. 10. The image reconstruction obtained by the Gauss Newton Level Set Method with simulation data: a) the model, b) the reconstructed image, c) the image without mesh, d) the level set method component after 15 iterations

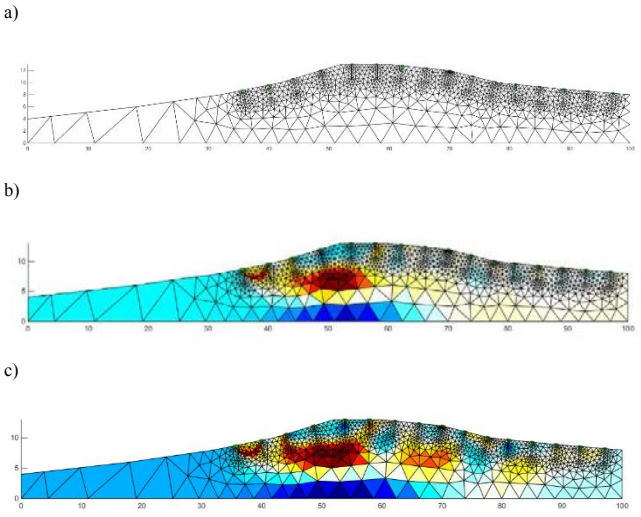

Fig. 11. The image reconstruction obtained by the Gauss Newton method with real data: a) the model, b) data taken after 15 minutes, c) after 30 minutes

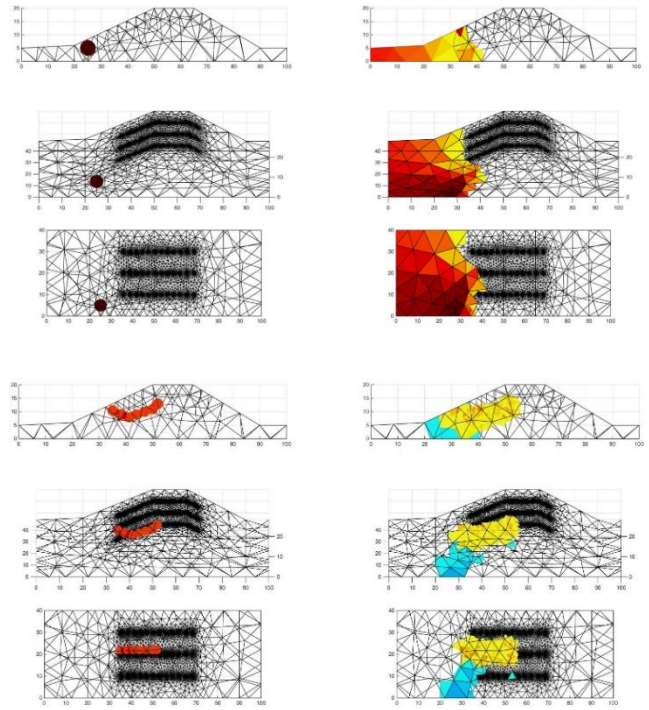

Fig. 12. The image reconstruction 3D model of the flood embankment

3. Conclusion

New nondestructive methods of the monitoring flood embankment model were tested. There were used iterative algorithms where repeatedly the shape boundary evolves smoothly and the searched object is detected. The combination of the proposed algorithms and the line measurement is effective in the simulation and the laboratory experiment. The finite element method was used to solve forward problem. The presented techniques are successful to identify the unknown properties of the object. Image reconstruction for identifying the unknown shape of an interface in a problem motivated by electrical impedance tomography can be done by proposed method. The Gauss-Newton and level set function techniques are useful in this system. The application depends on a specially built model. The proposed method was verified by simulations and its main components were verified experimentally in the laboratory. The presented method determines the moisture of the test model. Applying the line measurement model is enough effective to solve the inverse problem in the moisture flood embankment.

Acknowledgments

Projekt współfinansowany przez Unię Europejską z Europejskiego Funduszu Regionalnego. Działanie 1.4 – wsparcie projektów celowych. Umowa nr UDA-POIG.01.04.00-06-007/10-00. Nazwa Beneficjenta – Netrix S.A. dawniej Net-Art Paweł Rymarczyk. Tytuł projektu „Implementacja nowatorskich metod tomografii impedancyjnej do badania stanu wałów przeciwpowodziowych" (2011–2015).

References

[1] Adler A., Lionheart W.R.B.: Uses and abuses of EIDORS: an extensible software base for EIT, Physiological Measurement, Vol. 27, 2006.
[2] Gunna D.A., Chambersa J.E., Uhlemanna S., Wilkinsona P.B., Meldruma P.I., Dijkstraa T.A.: Moisture monitoring in clay embankments using electrical resistivity tomography, Construction and Building Materials, 2014.
[3] Holder D.S.: Electrical Impedance Tomography: Methods, History and Applications, Series in Medical Physics and Biomedical Engineering, London, 2005.
[4] Lechleiter A., Rieder A.: Newton regularizations for impedance tomography: convergence by local injectivity. Inverse Problems, 24(6), 2008.
[5] Mosorov V.: A method of transit time measurement using twin plane electrical tomography, Measurement Science and Technology, v17, 4, 2006, 753–760.
[6] Osher S., Fedkiw R.: Level Set Methods and Dynamic Implicit Surfaces. Springer, New York 2003.
[7] Rymarczyk T.: Using electrical impedance tomography to monitoring flood banks, International Journal of Applied Electromagnetics and Mechanics 45, 2014, 489–494.
[8] Rymarczyk T.: Characterization of the shape of unknown objects by inverse numerical methods, Przegląd Elektrotechniczny, nr 5/2012/7b, 138–140.
[9] Rymarczyk T., Filipowicz S.F., Sikora J., Polakowski K.: A piecewise-constant minimal partition problem in the image reconstruction, Przegląd Elektrotechniczny, R. 85, nr 12/2009, 141–143.
[10] Rymarczyk T, Adamkiewicz P., Duda K., Szumowski J., Sikora J.: New Electrical Tomographic Method to Determine Dampness in Historical Buildings, Achieve of Electrical Engineering, v.65, 2/2016, 273–283.
[11] Sikora J.: Numeryczne metody rozwiązywania zagadnień brzegowych: Podstawy metody elementów skończonych i metody elementów brzegowych, Wydawnictwa Politechniki Lubelskiej, 2008, 2012, 2016.
[12] Smolik W., Radomski D, Performance evaluation of the iterative image reconstruction algorithm with sensitivity matrix updating based on real measurements for electrical capacitance tomography, Meas. Sci. Technol. Vol. 20, No. 11, 2009, 115502.
[13] Tai C., Chung E., Chan T.: Electrical impedance tomography using level set representation and total variational regularization. Journal of Computational Physics, vol. 205, no. 1, 2005, 357–372.
[14] Wajman R., Fiderek P., Fidos H., Jaworski T., Nowakowski J., Sankowski D., Banasiak R.: Metrological evaluation of a 3D electrical capacitance tomography measurement system for two-phase flow fraction determination; Meas. Sci. Technol. 2013, Vol. 24, No. 065302.
[15] Wang M.: Industrial Tomography: Systems and Applications, Elsevier, 2015

Ph.D. Eng. Tomasz Rymarczyk
e-mail: tomasz.rymarczyk@netrix.com.pl

Director in Research and Development Center Netrix S.A. His research area focuses on the application of non-invasive imaging techniques, electrical tomography, image reconstruction, numerical modelling, image processing and analysis, process tomography, software engineering, knowledge engineering, artificial intelligence and computer measurement systems.

Ph.D. Przemysław Adamkiewicz
e-mail: p.adamkiewicz@netrix.com.pl

Doctor of Physics, graduate of Maria Curia-Sklodowska University in Lublin. Head of R&D Department at Netrix SA.
His research area focuses on electrical tomography, image reconstruction, numerical modelling, image analysis and computer measurement systems.

otrzymano/received: 20.09.2016 *przyjęto do druku/accepted: 15.02.2017*

DOI: 10.5604/01.3001.0010.4585

LEVEL SETS AND COMPUTATIONAL INTELLIGENCE ALGORITHMS TO MEDICAL IMAGE ANALYSIS IN E-MEDICUS SYSTEM

Tomasz Rymarczyk
Netrix S.A., Research and Development Center, Związkowa Str. 26, 20-148 Lublin

Abstract. *In this work, there were implemented methods to analyze and segmentation medical images by using topological, statistical algorithms and artificial intelligence techniques. The solution shows the architecture of the system collecting and analyzing data. There was tried to develop an algorithm for level set method (LSM) applied to piecewise constant image segmentation. These algorithms are needed to identify arbitrary number of phases for the segmentation problem. The image segmentation refers to the process of partitioning a digital image into multiple regions. There is typically used to locate objects and boundaries in images. There was also shown an algorithm for analyzing medical images using a neural network MLP.*

Keywords: segmentation, image analysis, level set method

ZBIORY POZIOMICOWE I ALGORYTMY INTELIGENCJI OBLICZENIOWEJ DO ANALIZY OBRAZÓW MEDYCZNYCH W SYSTEMIE E-MEDICUS

Streszczenie*. W artykule zostały zaimplementowane metody do analizy i segmentacji obrazów medycznych przy użyciu algorytmów topologicznych, statystycznych i technik sztucznej inteligencji. Rozwiązanie przedstawia architekturę systemu do gromadzenia i analizy danych. Opracowano algorytmy oparte na metodzie zbiorów poziomicowych (MZP) jako odcinkowo stałą segmentację obrazu. Algorytmy te są potrzebne do identyfikacji dowolnej liczby faz dla problemu segmentacji, która odnosi się do procesu dzielenia cyfrowego obrazu w różnych regionach. Metoda używana jest zwykle do lokalizacji obiektów i brzegów w obrazach. W pracy przedstawiono również algorytm do analizy obrazów medycznych z wykorzystaniem sieci neuronowej MLP.*

Słowa kluczowe: segmentacja, analiza obrazów, metoda zbiorów poziomicowych

Introduction

This paper presents the architecture of the system collecting data and analyzing medical images. The picture understanding is the process of actually interpreting those regions/objects to figure out what's actually happening in the image. This may include figuring out what the objects are, their spatial relationship to each other. It may also include ultimately making some decision for further action. Medical images are pictures which make it possible to visualize the inner part of the body of an organism. There are used in the clinical diagnostic. Such images can make it possible to analyze a specific function performed in a specific area. Level set methods are the numerical techniques which can follow the evolution of interfaces. These interfaces can develop sharp corners, break apart, and merge together.

In medical clinical research and practice, imaging has become an essential part to diagnose and to study anatomy and function of the human body. The proposed algorithms have been used to real pictures with promising results in the medical images segmentation. The level set methods have natural flexibility to create various shapes. The segmentation gives good results, because the region borders accurately locating the object edges. An increasing numbers of iteration the quantitative results are better but it is not the principle [4, 18].

The application can use the following data sources:

- Electrical Impedance Tomography,
- DICOM,
- Images,
- Databases.

In medical clinical research and practice, imaging has become an essential part to diagnose and to study anatomy and function of the human body. The architecture of such the medical system was projected in the Figure 1.

The e-Medicus system consists:

- artificial intelligence algorithms,
- segmentation algorithms
- the framework,
- agents,
- topological algorithms,
- databases,
- visualization systems,
- the user interface.

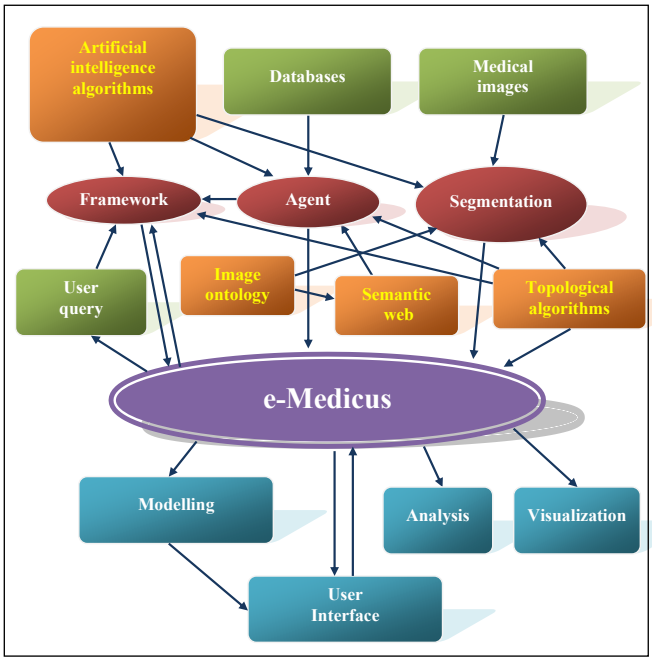

Fig. 1. The architecture of the e-Medicus system

1. Electrical Impedance Tomography

In medical research there was noted that among the healthy tissue and the diseased there are differences in electrical properties. Electrical impedance tomography can be used in some fields of medical diagnostics, such as gastroscopy and lung ventilation. Completed research allow to analyze changes resistance in the chest during the two physiological processes. In the first case, the observed resistance changes in the breathing cycle. The amount of air in the lungs, which is a poor conductor of electric current changes during breathing, at the same time so the resistance of the body. The second physiological process can be observed resistance changes caused by heart work. Blood is a good conductor of electricity and thus can easily visualize changes in blood volume in the selected plane chest.

Figure 2 shows the image reconstruction on the basis of numerical simulation of the measurement data using the level set method.

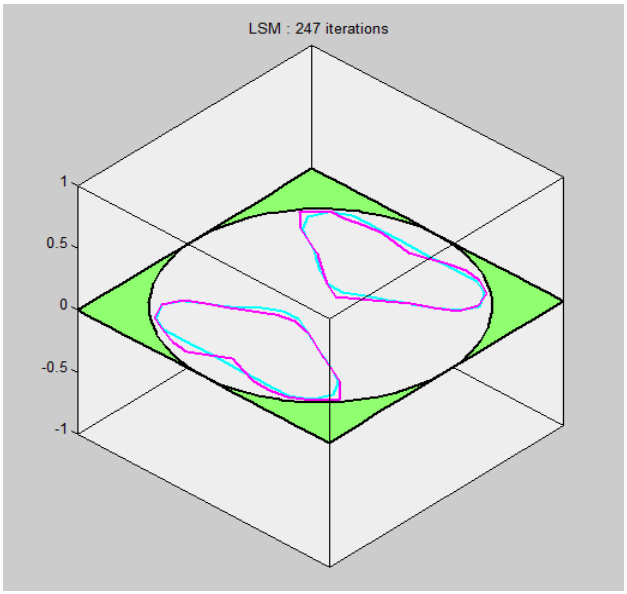

Fig. 2. Image reconstruction in the lung using the level set method - after 247 iteration (pink line – reconstructed image, aquamarine color- original objects)

2. Diagnosis and Segmentation

The image segmentation refers to the process of partitioning a digital image into multiple regions. There is typically used to locate objects and boundaries in images. The level set method is a powerful tool for representing moving or stationary interfaces. There was used the idea of the variational formulation for geometric active contours. There was used to the problem minimization in image processing to compute piecewise-smooth optimal approximations of the given image. The proposed algorithm has been applied to real pictures with promising results in the image segmentation. The level set method tracks the motion of an interface by embedding the interface as the zero level set of the signed distance function. The motion of the interface is matched with the zero level set, and the resulting initial value partial differential equation for the evolution of the level set function. The idea is merely to define a smooth function $\phi(x,t)$, that represents the interface as the set where $\phi(x,t)=0$. The motion is analyzed by the convection the ϕ values (levels) with the velocity field.

For more than two phases was introduced the multiple level sets idea by Vese and Chan. The algorithm set formulation and algorithm for the general Mumford-Shah minimization problem in image processing, to compute piecewise-smooth optimal approximations of a given image [9-11, 22].

The problem can be easily generalized to the case where the domain contains more than two materials.

$$F(s,C)=\omega L(C)+\eta\int_{\Omega}(s_o-s)^2d\Omega+\int_{\Omega\setminus C}|\nabla s|^2d\Omega \quad (1)$$

The process for minimization of the functional is the following:

$$\frac{\partial\phi}{\partial t}=\delta_{\varepsilon}(\phi)\left[\omega\nabla\cdot\left(\frac{\nabla\phi}{|\nabla\phi|}\right)-\eta_1(s_o-c_1)^2+\eta_2(s_o-c_2)^2\right] \quad (2)$$

where coefficients c_1 and c_2 are mean values of points in the picture.

The formulation of the variational level set method consists of an internal energy term that penalizes the deviation of the level set function and an external energy term that drives the motion of the zero level set toward the desired image features. When flat or steep regions complicate the determination of the contour, the reinitialization is necessary. This reinitialization procedure is based by replacing by another function that has the same zero level set. Variational formulation for geometric active contours that forces the level set function to be close to a signed distance function, and therefore completely eliminates the need of the costly reinitialization procedure [12-17, 19].

The resulting evolution of the level set function is the gradient flow that minimizes the overall energy functional:

$$P(\phi)=\int_{\Omega}\frac{1}{2}(|\nabla\phi|-1)^2dxdy \quad (3)$$

An external energy for a function $\phi(x, y)$ is defined as below:

$$E(\phi)=\mu P(\phi)+E_m(\phi) \quad (4)$$

where

$P(\phi)$ – internal energy, $E_m(\phi)$ – external energy.

Denoting by $\frac{\partial E}{\partial\phi}$ the Gateaux derivative of the functional **E** receiving the following evolution equation:

$$\frac{\partial\phi}{\partial t}=-\frac{\partial E}{\partial\phi} \quad (5)$$

In the image segmentation active contours are dynamic curves that moves towards the object boundaries. Denoting letter I as an image, and g be the edge indicator function defined by:

$$g=\frac{1}{1+|\nabla G_{\sigma}*I|^2} \quad (6)$$

where G_{σ} is the Gaussian kernel with standard deviation σ.

The process for minimization of the functional E is the following:

$$\frac{\partial\phi}{\partial t}=\mu\left[\Delta\phi-div\left(\frac{\nabla\phi}{|\nabla\phi|}\right)\right]+\lambda\delta(\phi)div\left(g\frac{\nabla\phi}{|\nabla\phi|}\right)+\omega g\delta(\phi) \quad (7)$$

The formulation of the variational level set method with Mumford-Shah model is following:

$$F(\phi,C_1,C_2)=\int_{\Omega}\frac{1}{2}(|\nabla\phi|-1)^2dxdy+\omega\int_{\Omega}|\nabla H(\phi)|\,d\Omega+$$
$$+\lambda_1\int_{\Omega}(u_o-c_1)^2H(\phi)\,d\Omega+\lambda_2\int_{\Omega}(u_o-c_2)^2\big(1-H(\phi)\big)\,d\Omega \quad (8)$$

3. Thorax analysis

Medical image segmentation is an essential technique. Among the many available methods it is impossible to identify the ultimate method in medical applications. In the level set method there is provided the algorithm with parameters. So it isn't fully automatic. The user has to type in a number of parameters and every time the parameters are changed, the output of the algorithm changes, meaning that we have to spend a lot of time to tell the algorithm what exactly it is that we want to find on the picture, and after several tries, it will do, what we want it to do, but this solution is not perfect (Fig 3). The downside is that it does not perform well with medical images.

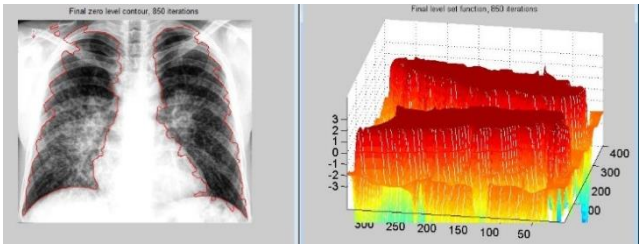

Fig. 3. The image reconstruction by the variational level set method

Souleymane Balla-Arabé, Xinbo Gao and Bin Wang introduce a fast and robust level set method for image segmentation using fuzzy clustering and lattice Boltzmann method [2]. Using: Fuzzy c-means, image segmentation, intensity inhomogeneity, lattice Boltzmann method, level set equation, partial differential equation. Considering the current pixel to be inside or outside of the active contour. Using modified fuzzy C-means objective function which also takes into consideration the shading image due to the intensity inhomogenity. In this method, using a modified FCM objective function, was formed a new fuzzy external force. The image reconstruction of chest by the fast and robust level set method is presented in Figure 4.

Fig. 4. The image reconstruction by the fast and robust level set method

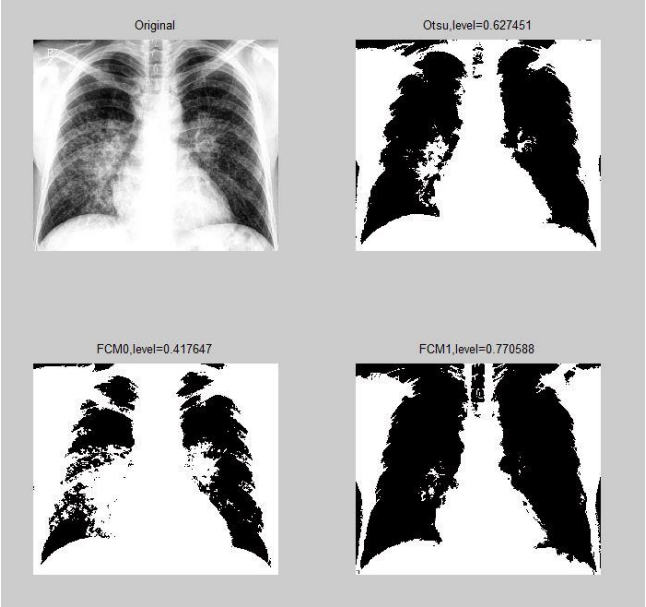

Fig. 5. FCMThresholding - sarcoidosis

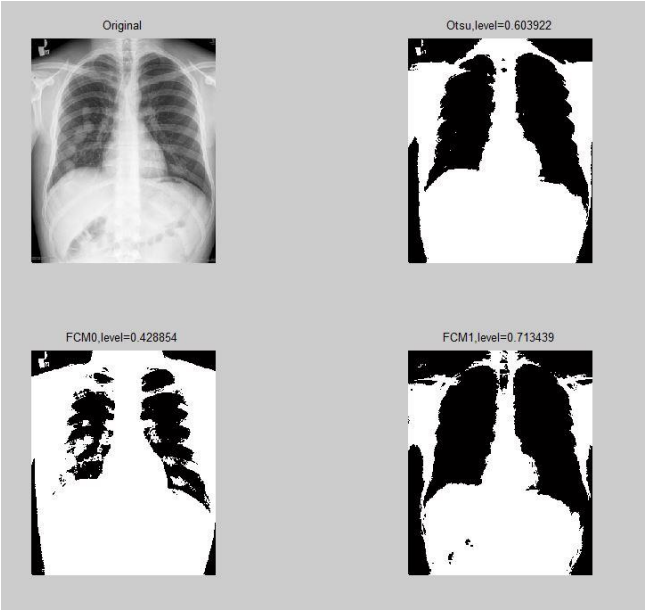

Fig. 6. FCMThresholding - metastasis

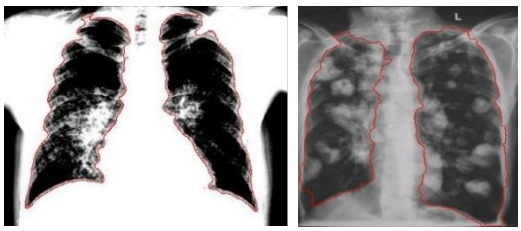

Fig. 7. Sarcoidosis on the left image, metastasis on the right one, the contour function is a result of the level set function

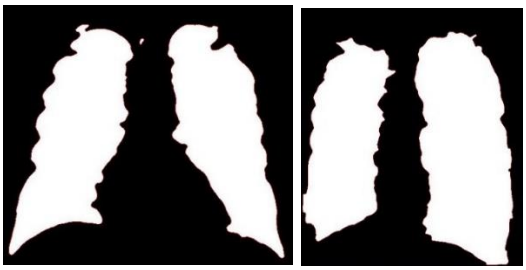

Fig. 8. The divides an image into two areas – black and white, where white area is the area that we are interested in for further analysis

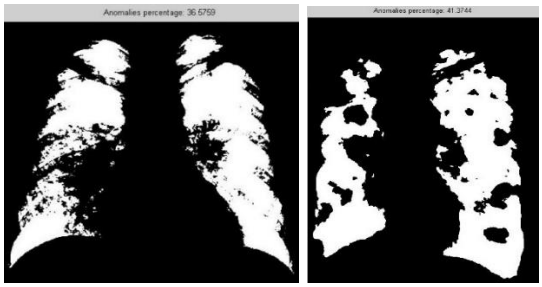

Fig. 9. Final results, we get an estimated percentage of anomalies present on the area of interest; results are visible on the top of every image, where image on the left shows sarcoidosis results, and image on the right shows metastasis

The fuzzy c-means thresholding is the simplest method of segmentation available, and yet it performs perfectly. Images obtained by running this algorithm are created in well under a minute, and the results are easy to see with a naked eye, even to a person who has never seen a medical image before. It is very easy to notice the difference between a healthy lung x-ray and one that has any changes in it. The main advantage of this method is that it barely required any computing power, thus the resolution of an input image becomes irrelevant. There have chosen two chest x-rays, one with sarcoidosis and one with metastasis (Fig. 5-9).

4. Pigmented skin lesions

Skin surface microscopy rules were formed in 1920 by Saphier, but just from 90' this method is widely used by dermatologists as most popular, easy and noninvasive techniques for in-vivo observation of the pigmented skin lesions. Using the simple epiluminescence microscope (dermatoscope) it gives the possibility to evaluate pigmented structures within epidermis, the dermoepidermal junction and the superficial dermis. The standard evaluation procedure is based on 2 basic steps developed by Braun-Falco. The first step should be identification of the lesion as melanocytic or non-melanocytic [1, 3, 6, 7, 20–23]. In case of the identification of the melanocytic lesion next step should be classification as benign, malignant or "suspicious" (Fig. 10).

Currently the most commonly used method for screening and the fast evaluation of the melanocytic lesions is ABCD rule, which according to Nachbar showed 92% specificity, 91% sensitivity and 80% of diagnostic accuracy in evaluation of malignant melanoma. It bases on evaluation of lesion in 4 aspects: A – Asymmetry, B – Borders, C – Colours, and D – Differential structures (tab. 1).

Figures 11 presents the image segmentation by using the level set algorithm (the pigmented skin lesions).

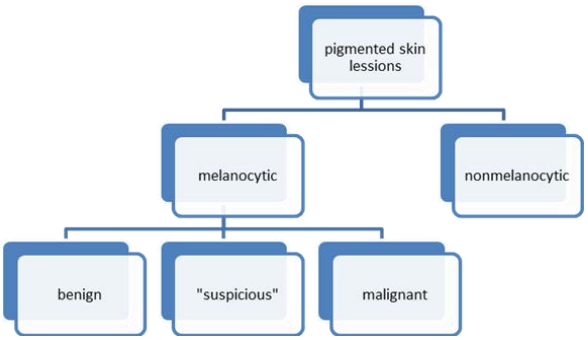

Fig. 10. The two-step procedure for the classification of pigmented skin lesions

Table 1. ABCD rule parameters description

Parameter		Description	Values	TDS weight factor
A	Assymetry	Complete symmetry, asymmetry in 1 or 2 axis	0-2	1,3
B	Borders	8 segments, 1 point for abrupt cut-off of pigment	0-8	0,1
C	Colours	1 point for each color: white, red, light brown, dark brown, black, blue-gray	1-6	0,5
D	Differential structures	1 point for every structure: pigment network, structureless areas, dots, globules, streaks	1-5	0,5

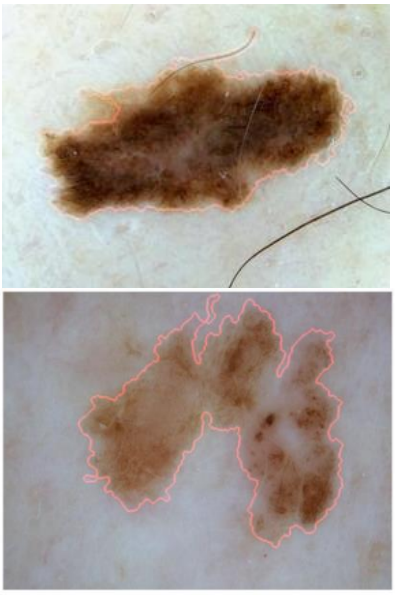

Fig. 11. The medical image analysis by Level Set Method with the Mumford-Shah model (looking for areas with specific characteristics)

5. Dental images

Segmentation presented in this chapter is an attempt of such a classification pixel in the image to the appropriate groups to receive separate areas as a result and thus to locate the disease states of soft tissue around the teeth. Object recognition using statistical methods can be divided into two categories: unsupervised classification methods and the methods of supervised classification. In the first case, belonging data to the classes is determined by the largest similarity of the classified pixels. In the second case, there is known training set that already contains information about belonging data to classes. The work proposes k-mean algorithm, k-nearest neighbour algorithm and Bayesian algorithm. The Euclidean metric was used to measure the distance between points in the first two algorithms.

Although, this algorithm as an example of supervised classification has a learning set, it does not have a classical learning stage, but only a recognition stage, which relies on calculating the distance between classified point and all the points in training set. Then, the smallest distance is selected e.g. there are selected k points which lie closed to the classified point. Finally, this point is included to the group, to which most of its neighbours were included (Fig. 12 and 13).

Fig. 12. The original image

Fig. 13. The segmentation result on 4 clusters using k-nearest neighbour with euclidean distance

The Bayesian algorithm based on Bayesian's Theorem is another method used to classify objects. Also in this case, the number of classes M is known in advance and is usually fixed by specialist from the area, on which the classification refers to. In turn, the allocating of objects x to classes takes place in an unambiguous manner. Because they can be described with plenty of features, before the applying the algorithm it must be first selected only those that are significant in terms of the classification [5, 8].

This algorithm, for $j = 1, \dots, M$, is determined by the formula:

$$P(J = j \mid X = x) = \frac{P(X=x \mid J=j)P(J=j)}{P(X=x)} \tag{9}$$

where $P(J = j)$ is the probability distribution of classes, $P(X = x \mid J = j)$ is the probability distribution features in these classes and $P(X = x)$ is the probability distribution all features. The decision function has the form:

$$\Leftrightarrow P(J = i \mid X = x) = \max_{j=1,2,\dots,M} \frac{1}{N\sqrt{2\pi}} \sum_{i=1}^{N_j} h_j exp\left\{-\frac{(x=x_{j,i})^2}{2}\right\} \tag{10}$$

for $i = 1,2,..,M$.

Another algorithms are neural networks MLP (Multi Layer Perceptron) to detect changes periapical on digital dental images. There were used a collection of 160 images. In order to recognize changes on periapical dental digital image there was created neural network MLP with eight inputs and one output. Number of inputs describes the number of descriptors, while the number of outputs is determined by obtaining one of two responses: find or not find a change of the apical. The network has one hidden layer. As a result of learning there was achieved 98% effectiveness. The object was described by eight coefficients: surface area, ratio Feret, sphericity factor, compactness, the beads and shredding. In addition, two other factors: the coefficient of compactness and circularity convex there were used to describe the isolated areas, based upon the convex shells of these areas. The convex hull algorithm there was recovered by Graham. Designated descriptors were subjected to a process of normalization.

Figure 14 shows the medical image analysis – Neural Networks: (a) original picture, (b) searched object, (c) segmentation – Bayes algorithm.

6. Conclusion

In medical clinical research and practice, imaging has become an essential part to diagnose and to study anatomy and function of the human body. The proposed algorithms have been used to real pictures with promising results in the medical images segmentation. The level set methods. statistical algorithms, and the artificial intelligence algorithms have natural flexibility to create various shapes. The segmentation gives good results, because the region borders accurately locating the object edges. In the level set methods an increasing numbers of iteration the quantitative results are better but it is not the principle. There was also shown an algorithm for analysing medical images using a neural network MLP, which detects changes in apical. For the verification the method there were used dental images. There was achieved high efficiency of the learning network. In this work there were developed and implemented effective algorithms to segmentation, machine learning, analysis and compare medical images.

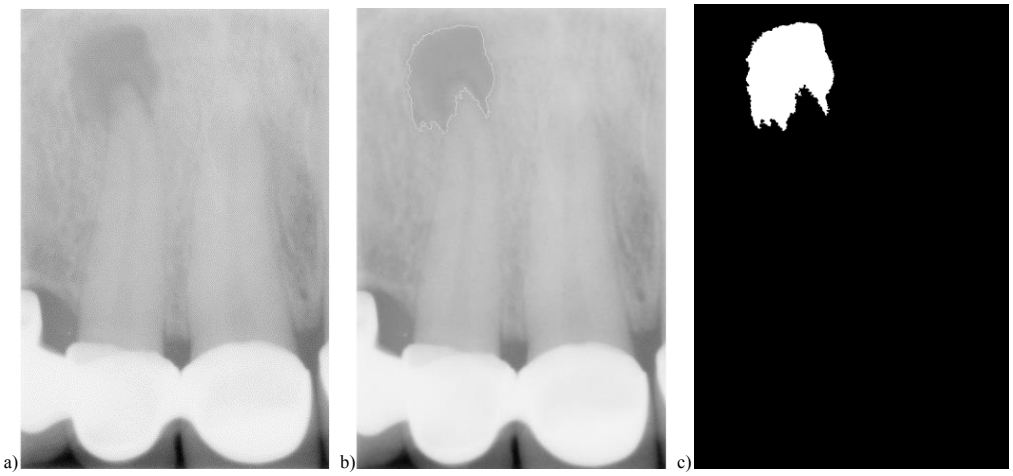

Fig. 14. The medical image analysis – Neural Networks: (a) original picture, (b) searched object, (c) segmentation – Bayes algorithm

References

[1] Argenziano G., Soyer P.H., De Giorgi V., Piccolo D.: Interactive atlas of dermatoscopy, EDRA 2000.
[2] Balla-Arabe S., Gao X.: A Fast and Robust Level Set Method for Image Segmentation Using Fuzzy Clustering and Lattice Boltzmann Method, IEEE Trans Cybern. 43(3), 2013.
[3] Braun R. P., Rabinovitz H. S.: Dermoscopy of pigmented skin lesions, J Am Acad Dermatol, 52, 2005, 109-121.
[4] Gdula A., Rymarczyk T.: Application Computational Algorithms for Analysis of Dental Image, WD 2015.
[5] Jajuga K.: Statystyczna teoria rozpoznawania obrazów, PWN, Warszawa 1990.
[6] Johr R.H.: Dermoscopy: Alternative melanocytic algorithms-the ABCD rule of dermatoscopy, Menzies scoring method, and 7-point checklist. Clin. DermC.atol. 2002.
[7] Kamińska J., Winciorek G.: Dermatologia cyfrowa, Cornetis 2008.
[8] Kurzyński M.: Rozpoznawanie obiektów. Metody statystyczne, Oficyna Wydawnicza Politechniki Wrocławskiej, Wrocław 1997.
[9] Li C., Kao C., Gore J.C., Ding Z.: Minimization of Region-Scalable Fitting Energy for Image Segmentation, IEEE Trans. Image Processing, vol. 17 (10), 2008, 1940-1949.
[10] Mumford D., Shah J.: Optimal approximation by piecewise smooth functions and associated variational problems. Comm. Pure Appl. Math., 42, 1989, 577–685.
[11] Osher S., Fedkiw R.: Level Set Methods and Dynamic Implicit Surfaces, Springer, New York 2003.
[12] Osher S., Sethian J.A.: Fronts Propagating with Curvature Dependent Speed: Algorithms Based on Hamilton-Jacobi Formulations. Journal of Computational Physics, 79, 1988, 12–49.
[13] Ossowski S.: Sieci neuronowe do przetwarzania informacji, Politechnika Warszawska, Warszawa 2006.
[14] Osowski S., Markiewicz T., Kruk M., Kozłowski W.: Metody sztucznej inteligencji do wspomagania diagnostyki patologii tkanek, WAT, Warszawa 2011.
[15] Rymarczyk T.: Characterization of the shape of unknown objects by inverse numerical methods, Electrical Review, 7b/2012, 138–140.
[16] Rymarczyk T., Osior K.: E-Medicus System for Analysis and Images Segmentation, IIPhWD 2013.
[17] Rymarczyk T., Filipowicz S.F., Sikora J., Polakowski K.: A piecewise-constant minimal partition problem in the image reconstruction, Przegląd Elektrotechniczny, 12/2009, 141–143.
[18] Sadowski T, Rymarczyk T.: Method for Segmentation Medical Images of Thorax and Detecting Anomalies, WD2014, 2014.
[19] Sethian J.A.: Level Set Methods and Fast Marching Methods, Cambridge University Press, 1999.
[20] Stąpor K.: Metody klasyfikacji obiektów w wizji komputerowej. Wydawnictwo Naukowe PWN, Warszawa 2011.
[21] Stolz W., Braun-Falco O.: Color atlas of dermatoscopy, Blackwell Science, 1994.
[22] Vese L. Chan T.: A new multiphase level set framework for image segmentation via the Mumford and Shah model, CAM Report 01-25, UCLA Math. Dept., 2001.
[23] Xiong G., Zhou X., Ji L., Bradley P., Perrimon N., Wong S.: Automated Segmentation of Drosophila RNAi Fluorescence Cellular Images using Deformable Models, IEEE Transactions on Circuits and Systems, Vol. 53, No. 11, 2006, 2415–2424.

Ph.D. Eng. Tomasz Rymarczyk
e-mail: tomasz.rymarczyk@netrix.com.pl

Director in Research and Development Center Netrix S.A. His research area focuses on the application of non-invasive imaging techniques, electrical tomography, image reconstruction, numerical modelling, image processing and analysis, process tomography, software engineering, knowledge engineering, artificial intelligence and computer measurement systems.

otrzymano/received: 20.09.2016 *przyjęto do druku/accepted: 15.02.2017*

DOI: 10.5604/01.3001.0010.4586

NONDESTRUCTIVE METHOD TO DETERMINE MOISTURE AREA IN HISTORICAL BUILDING

Tomasz Rymarczyk, Przemysław Adamkiewicz
Netrix S.A., Research and Development Center, Związkowa Str. 26, 20-148 Lublin

Abstract. *This paper presents a nondestructive method of brick wall dampness testing in real building structures. The proposed algorithm was used to determine the moisture of test brick walls on the specially models. The finite element method has been used to solve the forward problem. The algorithm is initialized by using one step methods and topological sensitivity analysis. There was constructed the forward model and solved the inverse for visualization of moisture inside objects.*

Keywords: Inverse Problem, Finite Element Method, Electrical Impedance Tomography, Wall Dampness

IMPLEMENTACJA ALGORYTMÓW NUMERYCZNYCH DO WYZNACZANIA ZAWILGOCONYCH OBSZARÓW W BUDYNKACH HISTORYCZNYCH

Streszczenie*. W artykule przedstawiono nieinwazyjną metodę badania wilgotności w konstrukcjach budowlanych. Rozwiązanie zostało wykorzystane do określenia wilgotności w zamodelowanych murach. Metoda elementów skończonych została wykorzystana do rozwiązania zagadnienia prostego. Proponowany algorytm jest inicjowany za pomocą metod jednokrokowych i topologiczną analizę wrażliwościową. Został skonstruowany model prosty zadania i rozwiązane zagadnienie odwrotne do wizualizacji wilgotności wewnątrz obiektów.*

Słowa kluczowe: zagadnienie odwrotne, metoda elementów skończonych, tomografia impedancyjna, zawilgocenie murów

Introduction

This paper presents the new method examining the brick wall dampness by the electrical tomography [2, 4–9, 12, 13]. There were implemented the new algorithms to identify unknown conductivities. The discussed technique can be applied to the solution of inverse problems in electrical impedance tomography. The purpose of the presented method is obtaining the better image reconstruction than gradient methods. One of the major causes of pathologies in historic buildings all over the world is the presence of moisture, particularly rising damp. The traditional techniques used to deal with this kind of problem show, to be ineffective, justifying the need to find a new approach [3, 10]. Moisture transfer in walls of an old buildings, which are in direct contact with the soil, leads to a migration.

The forward problem solution consists in determining potential distribution inside the region Ω under given boundary conditions and full information about region under consideration, that is in solving Laplace's equation:

$$\operatorname{div}(\boldsymbol{\gamma} \operatorname{grad} \mathbf{u}) = 0 \tag{1}$$

where $\boldsymbol{\gamma}$ denotes conductivity, symbol $\mathbf{u}$ represents electrical potential.

The objective function is formed following:

$$\mathrm{F} = 0.5 \sum_{i=1}^{n} (\boldsymbol{U} - \boldsymbol{U}_m)^T (\boldsymbol{U} - \boldsymbol{U}_m) \tag{2}$$

where n is a projection angle (the number of measurement sequences: 13 measurements × 8 angle projections = 104 independent measurements), $\mathbf{U}_m$ – the measured voltage, $\mathbf{U}$ – the calculated voltage by solving the equation (1).

The object is a brick wall with damp rising from the ground (Fig. 1 and 2). The test results obtained by the nondestructive impedance tomography method are compared with the results obtained by numerical simulations. There were prepared two prototype measuring systems. First of them contains 16 electrodes for measuring damp brick wall on one side (Fig. 1). Second one is a full EIT system with 32 electrodes for test on both sides of wall (Fig. 2).

1. Models and Results

Geometrical models and image reconstruction were obtained by using the Gauss-Newton method (Fig. 3 and 4). Figure 5 shows exemplary numerical reconstruction of moisture in the damp wall with different values of the noise. Figure 6 shows the image reconstruction obtained by the Gauss Newton one step method with real data: (a) the original measurement object, (b) the reconstructed object with 16 electrodes on one side of the wall, (c) the reconstructed object with 16 electrodes on both sides of the wall. The reason these measurements was the inappropriate selection of the supply voltage frequency (50 kHz). The most accurate results can be obtained for frequency around 1kHz as it shown in Figure 7 (the highest voltage potential on the surface electrodes).

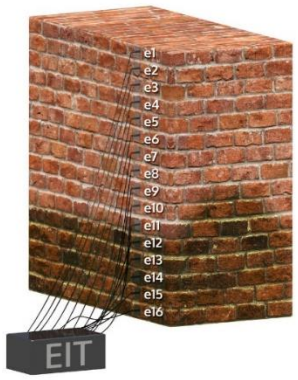

Fig. 1. Measurement EIT systems with 16 electrodes on the damp brick wall

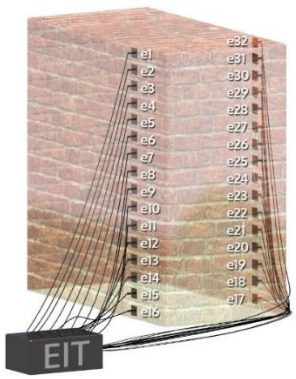

Fig. 2. Measurement EIT systems with 32 electrodes on the damp brick wall

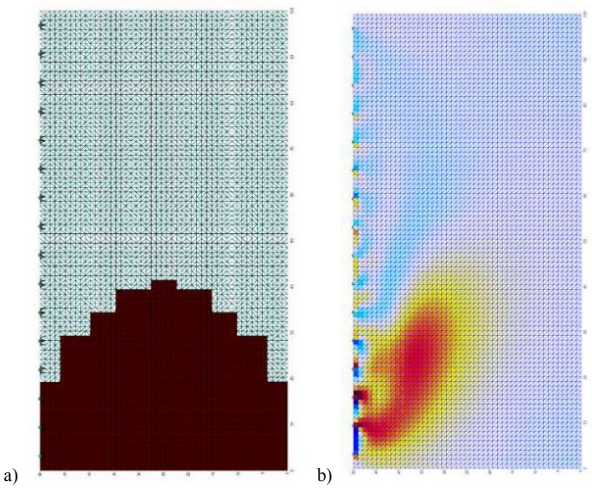

Fig. 3. Geometrical model and image reconstruction of the investigated dumped wall with (a) 16 and (b) 32 electrodes

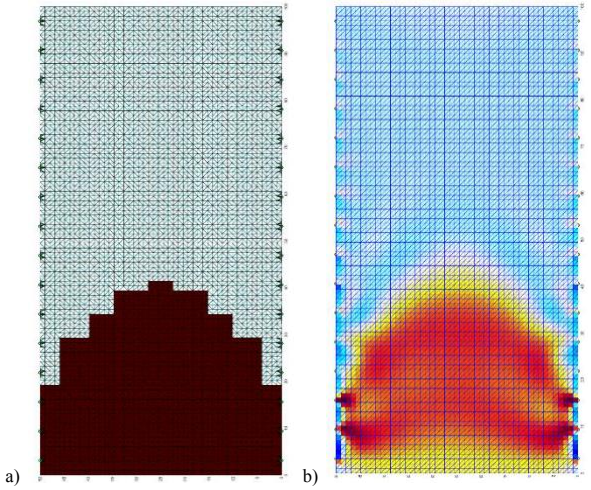

Fig. 4. Geometrical model and image reconstruction of the investigated dumped wall with (a) 16 and (b) 32 electrodes

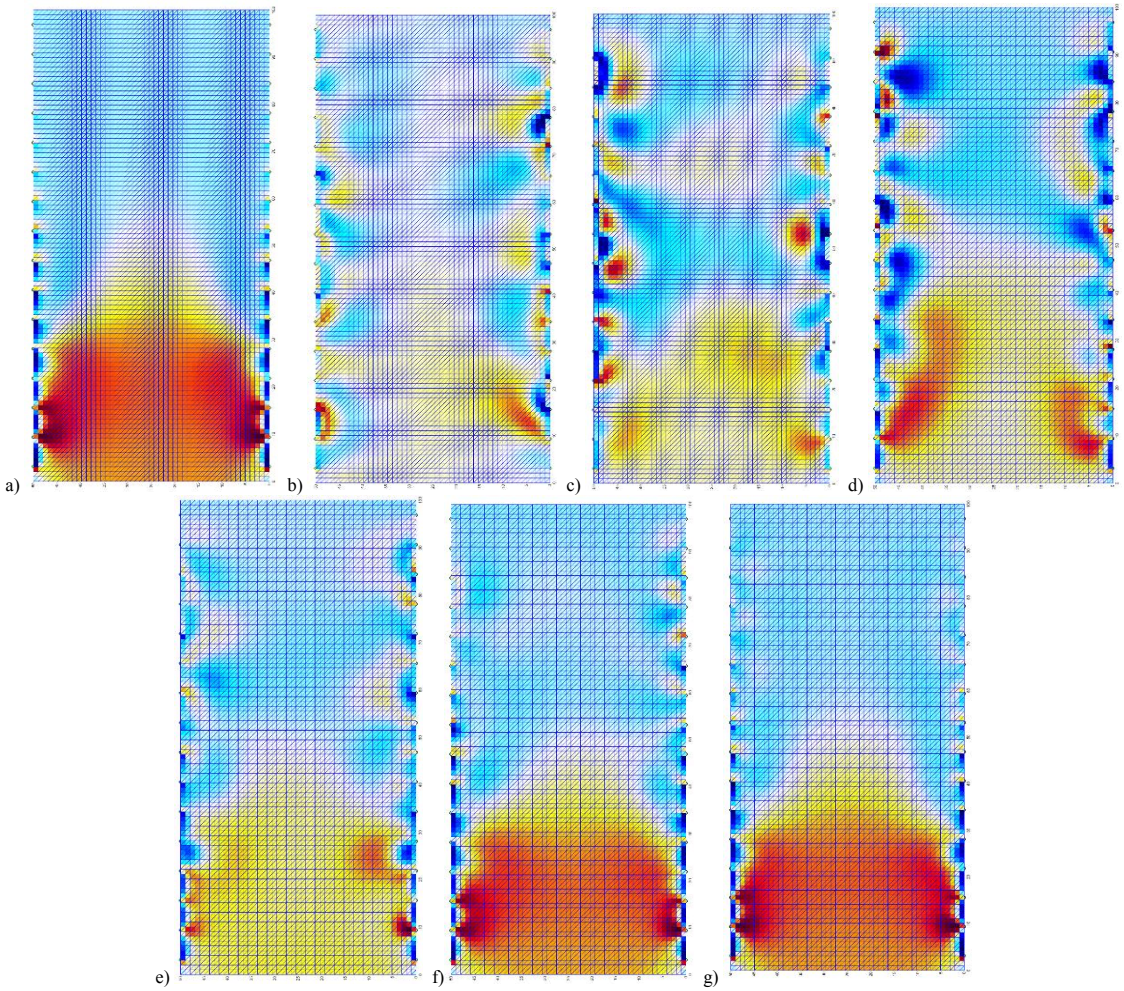

Fig. 5. Numerical reconstruction of moisture in the damp wall with different values of the noise: a) without noise, b) 6 dB, c) 9 dB, d) 12 dB, e) 20 dB, f) 24 dB, g) 30 dB

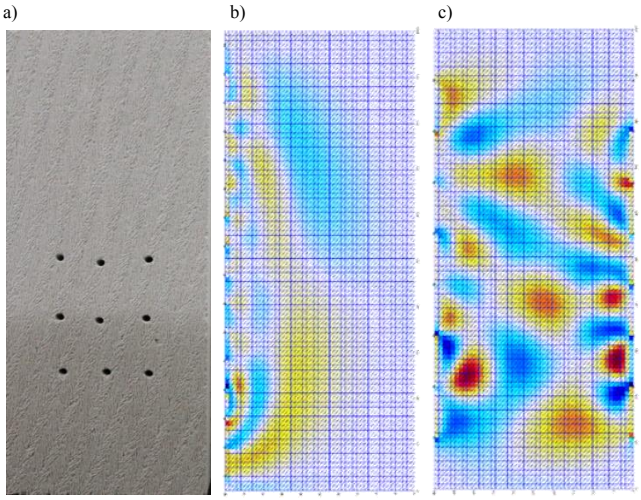

Fig. 6. The image reconstruction obtained by the Gauss Newton one step method: (a) the original measurement object, (b) the reconstructed object with 16 electrodes on one side of the wall, (c) the reconstructed object with 16 electrodes on both sides of the wall

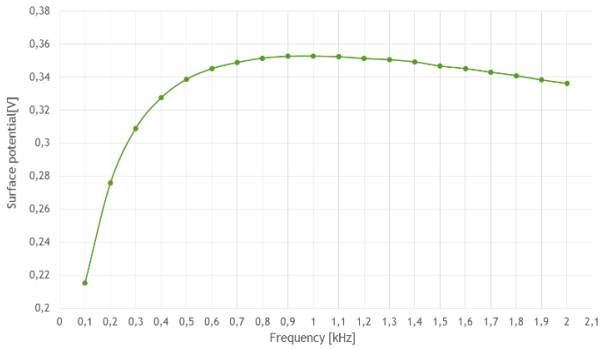

Fig. 7. Voltage level on surface electrodes in dependence of supply voltage frequency

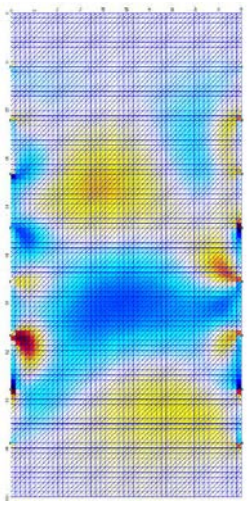

Fig. 8. The image reconstruction obtained by the Gauss Newton one step method - the reconstructed object with 16 electrodes on both sides of the wall (frequency 1kHz)

After finding the most suitable power supply voltage frequency (1 kHz) we repeated measurements with electrodes on both sides of the airbrick. The results were beater then lower frequency, but still unsatisfactory and differ from simulation. Figure 8 shows the image reconstruction obtained by the Gauss-Newton one step method.

Figure 9 shows two exemplary models with square electrodes place on both sides and different number of elements. Distribution of equipotential lines for the first couple of measurement was shown in Figure 10. The model of the wall with the inserted one object and image reconstruction was presented in Figure 11.

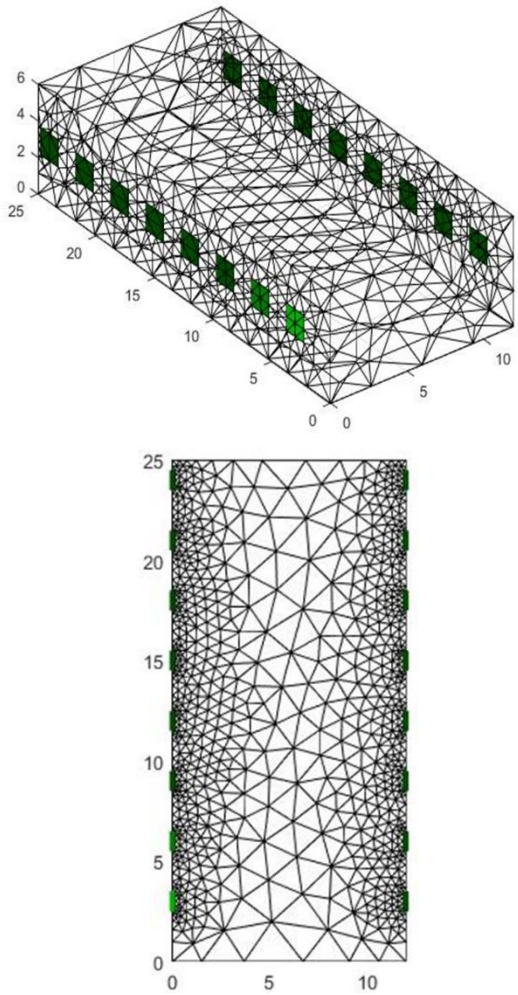

Fig. 9. Geometrical models of the investigated dumped wall with square electrodes

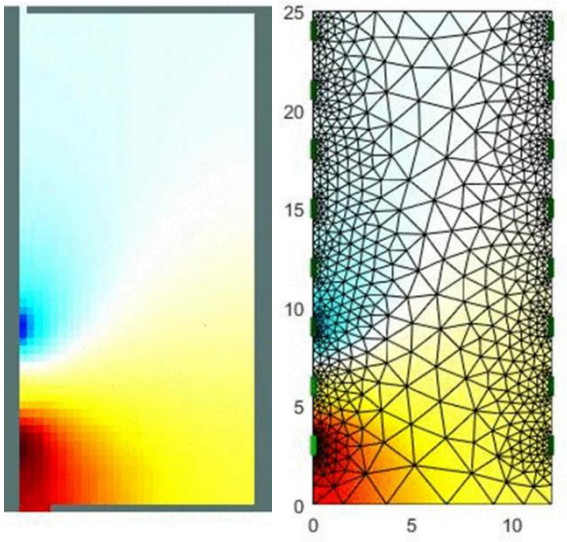

Fig. 10. Distribution of equipotential lines for the first couple of measurement

The next step to improve quality of the reconstruction there was generated more complex model with larger number of elements and electrodes on both sides of damps wall [1, 11]. Figure 12 shows two exemplary models with 26 electrodes place on both sides and different number of elements.

New models with larger number of electrodes provided us to beater reconstruction results. Contribution of moisture in damp wall both brick and air brick seems to be more complex in compared to the results obtained from than the simulations. Figure 13 shows image reconstruction obtained by the Gauss-Newton one step method from the original measurement object with 26 electrodes. It is clear that more measurements should be taken and

new algorithms should be prepared for determine moisture areas in damps walls.

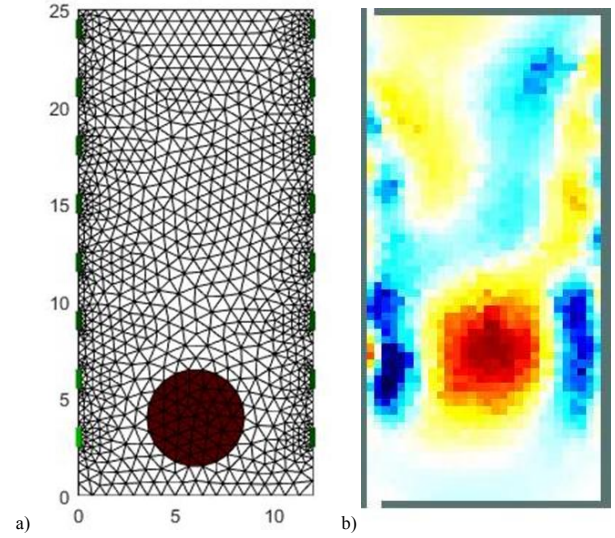

Fig. 11. The model of the wall with the inserted one object: a) model, b) reconstruction

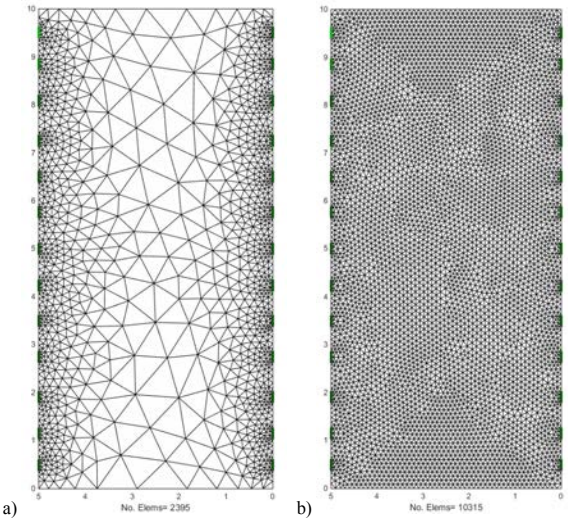

Fig. 12. Geometrical models of the investigated dumped wall with 23 electrodes and: (a) 2395 and (b) 10315 elements

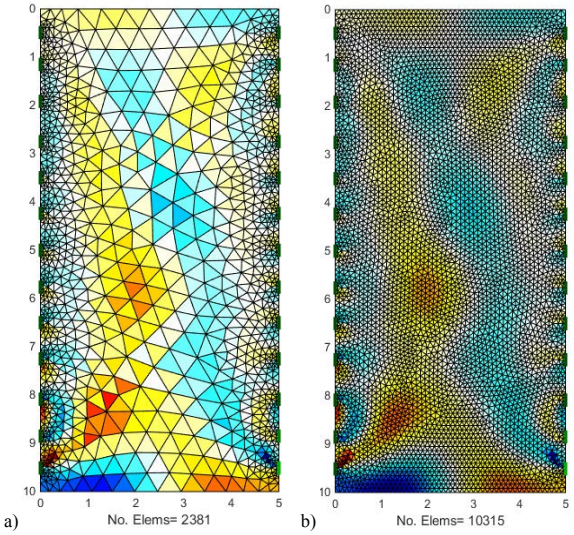

Fig. 13. The image reconstruction obtained in EIDORS by the Gauss Newton one step method from the original measurement object with 26 electrodes: (a) 2395 and (b) 10315 elements

2. Conclusion

The nondestructive method of the brick wall dampness was tested by electrical impedance tomography. The proposed algorithm was used to determine the moisture of the test wall on a specially built model. Numerical methods were based on the gradient techniques. An efficient algorithm for solving the forward and inverse problems would also improve a lot of the numerical performances of the proposed methods. The presented algorithms have been applied successfully in the reconstruction of measured data of the model wall. These approaches based on sensitivity approach include the area design of the elastic interface. There are used the one step methods and iterative algorithms base on Gauss-Newton model where the examined objects there were detected.

References

[1] Adler A., Lionheart W.R.B.: Uses and abuses of EIDORS: an extensible software base for EIT, Physiological Measurement, 2006, Vol. 27
[2] Holder D.S.: Electrical Impedance Tomography: Methods, History and Applications Series in Medical Physics and Biomedical Engineering, London, 2005
[3] Hoła J., Matkowski Z., Schabowic K., Sikora J., Nita K., Wójtowicz S.: Identification of Moisture Content in Brick Walls by means of Impedance Tomography, COMPEL, Vol. 31, Issue 6, 2012, pp. 1774-1792
[4] Ito I, Kunish K., Li Z.: The Level-Set Function Approach to an Inverse Interface Problem", Inverse Problems, vol. 17, no. 5, 2001, pp. 1225-1242
[5] Mosorov V.: A method of transit time measurement using twin plane electrical tomography, Measurement Science and Technology, v17, 4/2006, 753-760.
[6] Rymarczyk T., Tchórzewski P., Sikora J.: Topological Approach to Image Reconstruction in Electrical Impedance Tomography, ADVCOMP 2014, ISBN: 978-1-61208-354-4, Rome, Italy, 2014, pp. 42-45
[7] Rymarczyk T.: Using electrical impedance tomography to monitoring flood banks, International Journal of Applied Electromagnetics and Mechanics 45, 2014, pp. 489–494
[8] Rymarczyk T.: Characterization of the shape of unknown objects by inverse numerical methods, Przegląd Elektrotechniczny, R. 88 NR 7b/2012, pp. 138-140, 2012
[9] Rymarczyk T., Sikora J., Waleska B.: Coupled Boundary Element Method and Level Set Function for Solving Inverse Problem in EIT, 7th World Congress on Industrial Process Tomography, WCIPT7, 2-5 September 2013, Krakow, Poland
[10] Rymarczyk T, Adamkiewicz P., Duda K., Szumowski J., Sikora J.: New Electrical Tomographic Method to Determine Dampness in Historical Buildings, v.65, 2/2016, Achieve of Electrical Engineering, 2016, pp 273-283
[11] Schöberl J.: NETGEN An advancing front 2D/3D-mesh generator based on abstract rules, Computing and Visualization in Science, Volume 1, 1997
[12] Smolik W., Radomski D, Performance evaluation of the iterative image reconstruction algorithm with sensitivity matrix updating based on real measurements for electrical capacitance tomography, Meas. Sci. Technol. Vol. 20, No. 11., 2009, 115502.
[13] Wajman R., Fiderek P., Fidos H., Jaworski T., Nowakowski J., Sankowski D., Banasiak R.: Metrological evaluation of a 3D electrical capacitance tomography measurement system for two-phase flow fraction determination; Meas. Sci. Technol. 2013, Vol. 24 No. 065302

Ph.D. Eng. Tomasz Rymarczyk
e-mail: tomasz.rymarczyk@netrix.com.pl

Director in Research and Development Center Netrix S.A. His research area focuses on the application of non-invasive imaging techniques, electrical tomography, image reconstruction, numerical modelling, image processing and analysis, process tomography, software engineering, knowledge engineering, artificial intelligence and computer measurement systems.

Ph.D. Przemysław Adamkiewicz
e-mail: p.adamkiewicz@netrix.com.pl

Doctor of Physics, graduate of Maria Curia-Sklodowska University in Lublin. Head of R&D Department at Netrix SA.
His research area focuses on electrical tomography, image reconstruction, numerical modelling, image analysis and computer measurement systems.

otrzymano/received: 20.09.2016 *przyjęto do druku/accepted: 15.02.2017*

DOI: 10.5604/01.3001.0010.4587

HYBRID TECHNIQUES TO SOLVE OPTIMIZATION PROBLEMS IN EIT

Tomasz Rymarczyk, Paweł Tchórzewski
Netrix S.A., Research and Development Center, Związkowa Str. 26, 20-148 Lublin

Abstract. *This paper presents the hybrid algorithm for identification the unknown shape of an interface to solve the inverse problem in electrical impedance tomography. The conductivity values in different regions are determined by the finite element method. The numerical algorithm is a combination of the level set method, Gauss-Newton method and the finite element method. The representation of the shape of the boundary and its evolution during an iterative reconstruction process is achieved by the level set function. The cost of the numerical algorithm is enough effective. These algorithms are a relatively new procedure to overcome this problem.*

Keywords: Inverse Problem, Level Set Method, Electrical Impedance Tomography

TECHNIKI HYBRYDOWE DO ROZWIĄZYWANIA ZAGADNIEŃ OPTYMALIZACYJNYCH W ETI

Streszczenie*. W artykule przedstawiono hybrydowy algorytm do identyfikacji nieznanego kształtu interfejsu, w celu rozwiązania zagadnienia odwrotnego w elektrycznej tomografii impedancyjnej. Wartości przewodności w różnych regionach określono za pomocą metody elementów skończonych. Algorytm numeryczny jest kombinacją metody zbiorów poziomicowych oraz metody Gaussa-Newtona i metody elementów skończonych. Odwzorowanie kształtu granicy i jej ewolucję w trakcie iteracyjnego procesu rekonstrukcji osiągnięto poprzez użycie metody zbiorów poziomicowych. Koszt algorytmu numerycznego jest dosyć efektywny. Algorytmy te są relatywnie nowymi rozwiązaniami dla tego typu problemu.*

Słowa kluczowe: zagadnienie odwrotne, metoda zbiorów poziomicowych, tomografia impedancyjna

Introduction

The article focuses on the inverse problem of identifying an unknown object. There were implemented the new algorithms to identify unknown conductivities. Numerical methods were based on the level set method (LSM) and the Gauss-Newton method. Level set methods have been applied very successfully in many areas of the scientific modelling [1, 3-6, 12, 17]. The level set function and the gradient techniques are based on shape and topology optimization in electrical impedance tomography (EIT) [8-11, 16]. The finite element method has been used to solve the forward problem. The cost of the numerical algorithm is enough effective. The proposed solution algorithm is initialized by using topological sensitivity analysis [13]. The Gauss-Newton method has been incorporated with the level set method to investigate shape optimization problems. The coupled algorithm is a relatively new procedure to overcome this problem. There was implemented the new hybrid algorithm to identify unknown values by electrical tomography [2, 3, 14, 15]. The purpose of the presented method is obtaining the better image reconstruction than gradient methods.

1. Optimization

Electrical impedance tomography is known that the inverse problem is nonlinear and highly ill-posed. Level set methods are often discretized on a regular grid that conveniently coincides with the finite element mesh (used for structural analysis). Typical problem in EIT requires the identification of the unknown internal area from near-boundary measurements of the electrical potential. It is assumed that the value of the conductivity is known in sub-regions whose boundaries are unknown. Figure 1 presents the algorithm based on the level set method.

The level set method is the numerical technique which can follow the evolution of interfaces. These interfaces can develop sharp corners, break apart and merge together. The level set function ϕ has the following properties:

$$\begin{gathered}\boldsymbol{\phi}(\mathbf{x},\mathbf{y},t)=0 \text{ for } (\mathrm{x},\mathrm{y})\in\partial\Omega(t)\equiv\Gamma(t),\\ \boldsymbol{\phi}(\mathbf{x},\mathbf{y},t)>0\ for\ (\mathrm{x},\mathrm{y})\in\Omega(t),\\ \boldsymbol{\phi}(\mathbf{x},\mathbf{y},t)<0\ for\ (\mathrm{x},\mathrm{y})\notin\Omega(t)\end{gathered} \tag{1}$$

where t is time.

The level set function ϕ is updated by solving discretized version of the Hamilton-Jacobi equation:

$$\boldsymbol{\phi}^{\mathrm{k+1}}=\boldsymbol{\phi}^{\mathrm{k}}-\mathbf{v}_{\mathrm{n}}^{\mathrm{k}}\left|\boldsymbol{\nabla}\boldsymbol{\phi}^{\mathrm{k}}\right|\Delta\mathrm{t} \tag{2}$$

where **v** is velocity.

Reinitialization is necessary when flat or steep regions complicate the determination of the zero contour.

This process is described by following partial differential equation [6]:

$$\frac{\partial\boldsymbol{\phi}}{\partial t}+S(\boldsymbol{\phi})(|\nabla\boldsymbol{\phi}|-1)=0 \tag{3}$$

where $S(\boldsymbol{\phi})=\frac{\boldsymbol{\phi}}{\sqrt{\boldsymbol{\phi}^2+\varepsilon^2}}, |\varepsilon|\ll 1$

Differential equation (3) is solved until a steady state is achieved.

A Gauss-Newton method is deployed to the regularized tangential movement problem. The electrodes move tangentially to the domain at each iteration and so do not in general lie on the boundary of the domain after each iteration. These are thus projected back onto the fixed domain by computing the nearest boundary simplex of the finite element mesh.

The Gauss-Newton algorithm is following form [3]:

$$\begin{aligned}\boldsymbol{\gamma}^{k+1}&=\boldsymbol{\gamma}^{k}+\alpha\left(\mathbf{J}_t^k\mathbf{J}^{\boldsymbol{k}}+\lambda\mathbf{W}\right)^{-1}\cdot\\ &\cdot\left(\mathbf{J}_t^k\mathbf{W}\left(\mathbf{u}_{\boldsymbol{m}}-\mathbf{h}(\boldsymbol{\gamma}^k)\right)-\lambda\mathbf{W}\boldsymbol{\gamma}^k\right)\end{aligned} \tag{4}$$

where $\boldsymbol{\gamma}$ denotes the vector of the unknown conductivity, α is the step size, λ is a regularization parameter, $\mathbf{J}^{\mathrm{k}}$is the Jacobian matrix, **W** is a regularization matrix and $\mathbf{h}(\boldsymbol{\gamma}^k)$ is the observation model derived from a finite elements model.

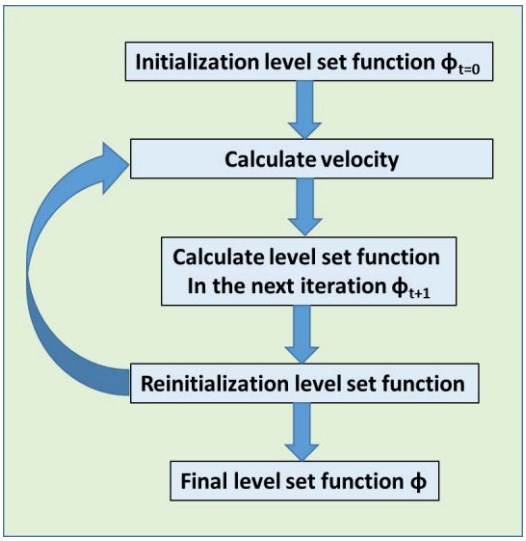

Fig. 1. The level set method- algorithm

The evolution of the level set function presents in Figure 2. Level sets are shown in Figure 3. The reinitialization of the level set function is presented in Figure 4. The numerical algorithm requires to solve the forward problem and the adjoint equation, these solutions present Figure 5 and 6.

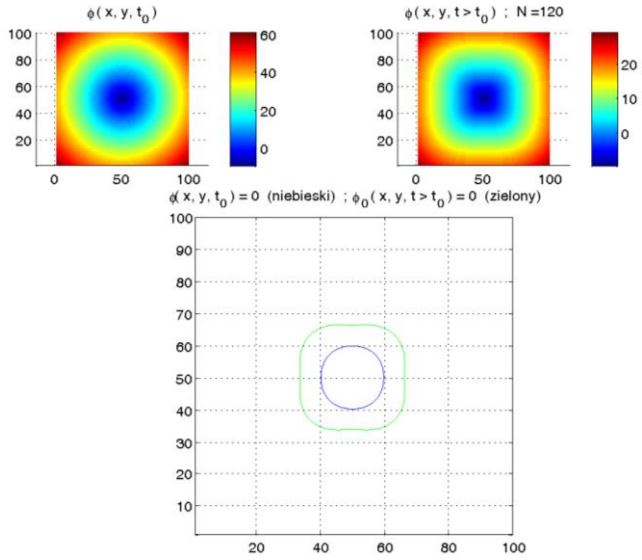

Fig. 2. The level set function – evolution

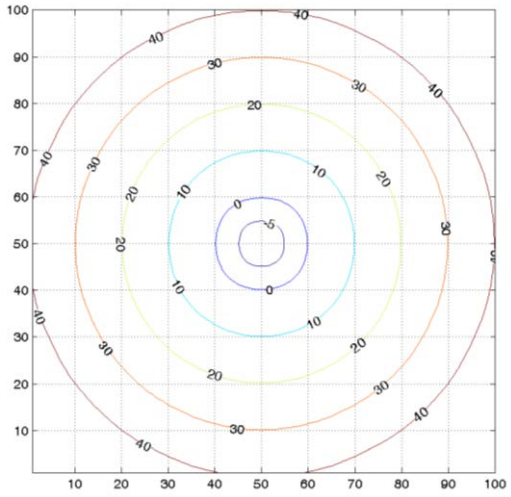

Fig. 3. Level sets

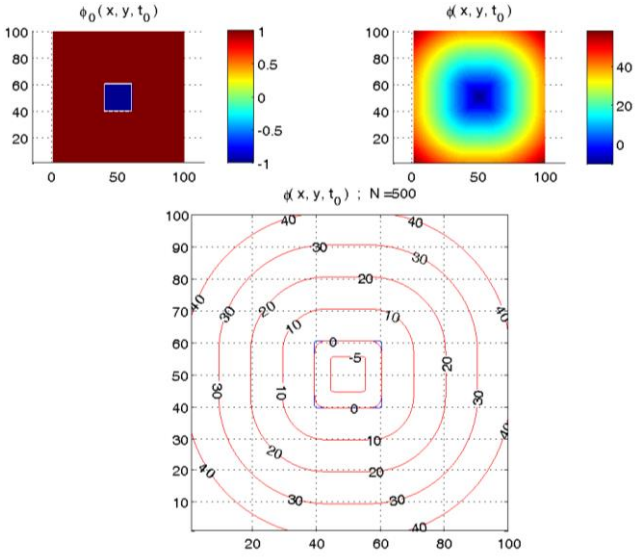

Fig. 4. Level set function -- reinitialization

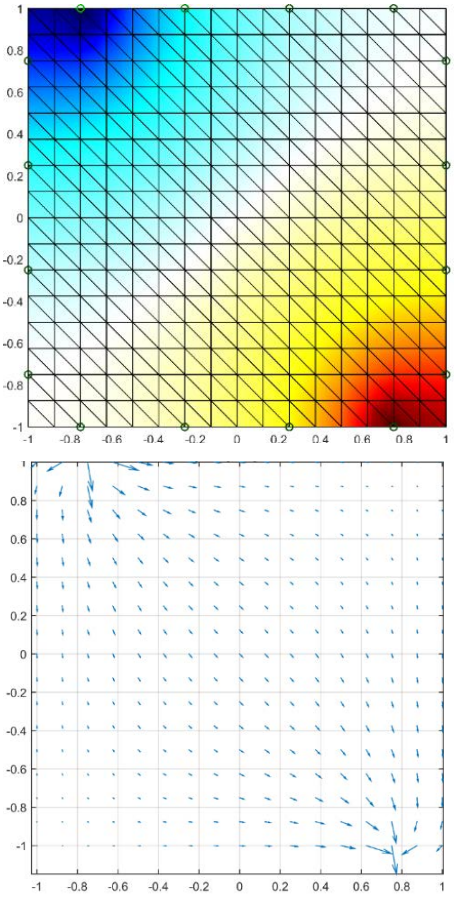

Fig.5. The forward problem

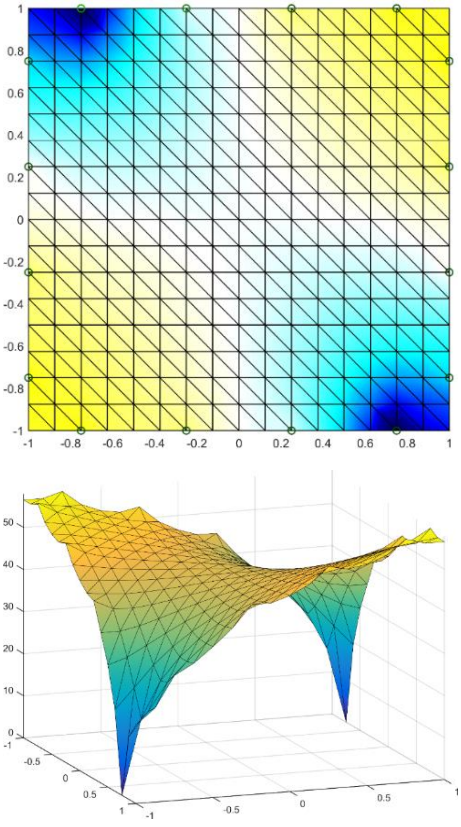

Fig. 6. The adjoint problem

2. Image reconstruction

In examples reported below, several numerical models with different discretization elements are presented. Additionally, there was shown different geometries of the conductivity distributions. The conductivity of searched objects is known. The representation of the boundary shape and its evolution during an iterative reconstruction process is achieved by the level set method and the Gauss-Newton method coupled together. In forward problem, which is given by Laplace's equation, we have used the finite element method. Figure 7 presents the model with the one object in the corner: (a) the initial model, (b) the reconstructed by Gauss-Newton method. Figure 8 shows the model with 1 object in the center: (a) the initial model, (b) the reconstructed by Gauss-Newton method, (c) zero level set, (d) the reconstructed by the level set method. Figure 9 presents the objective function for the model in Figure 8. Figure 10 shows the geometrical model with 5 objects.

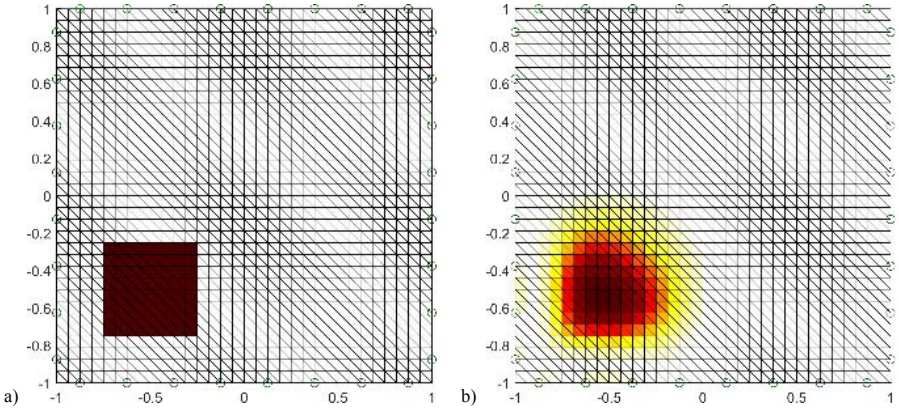

Fig. 7. The model with the one object: a) the initial model, b) the reconstructed by Gauss-Newton method

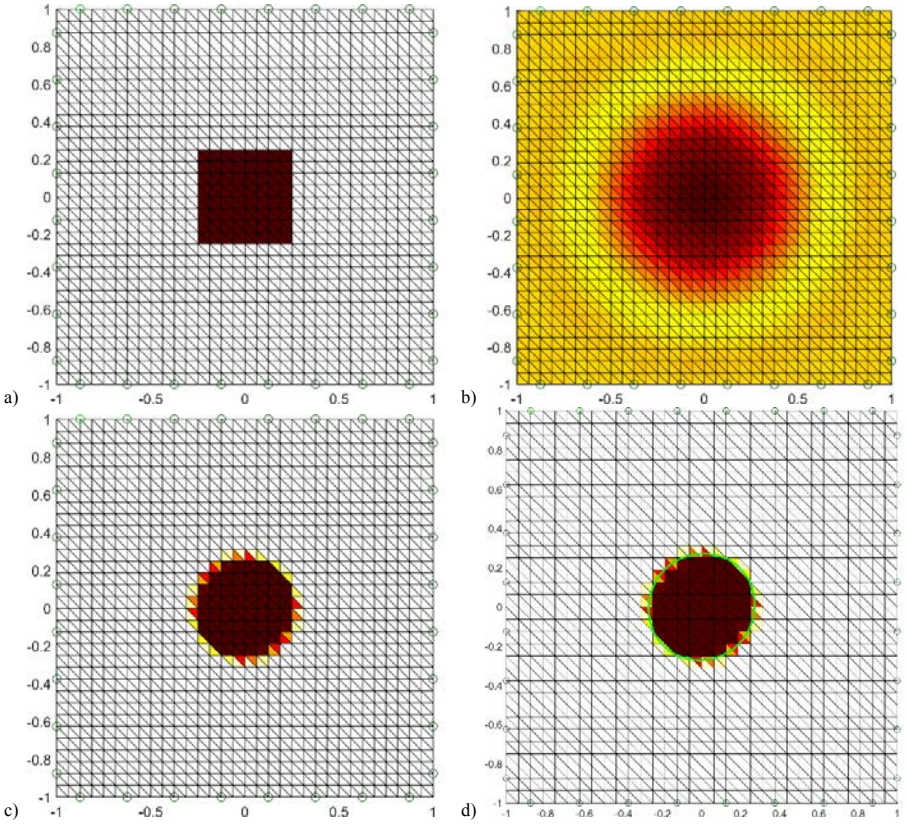

Fig. 8. The model with 1 object: a) the initial model, b) the reconstructed by Gauss-Newton method, c) zero level set, d) the reconstructed by the level set method

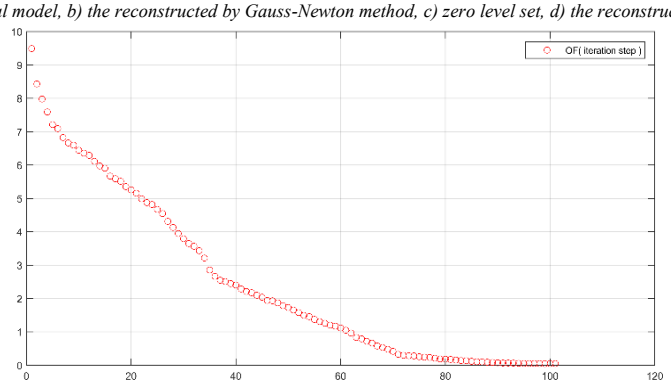

Fig. 9. The objective function for the model in Figure 8

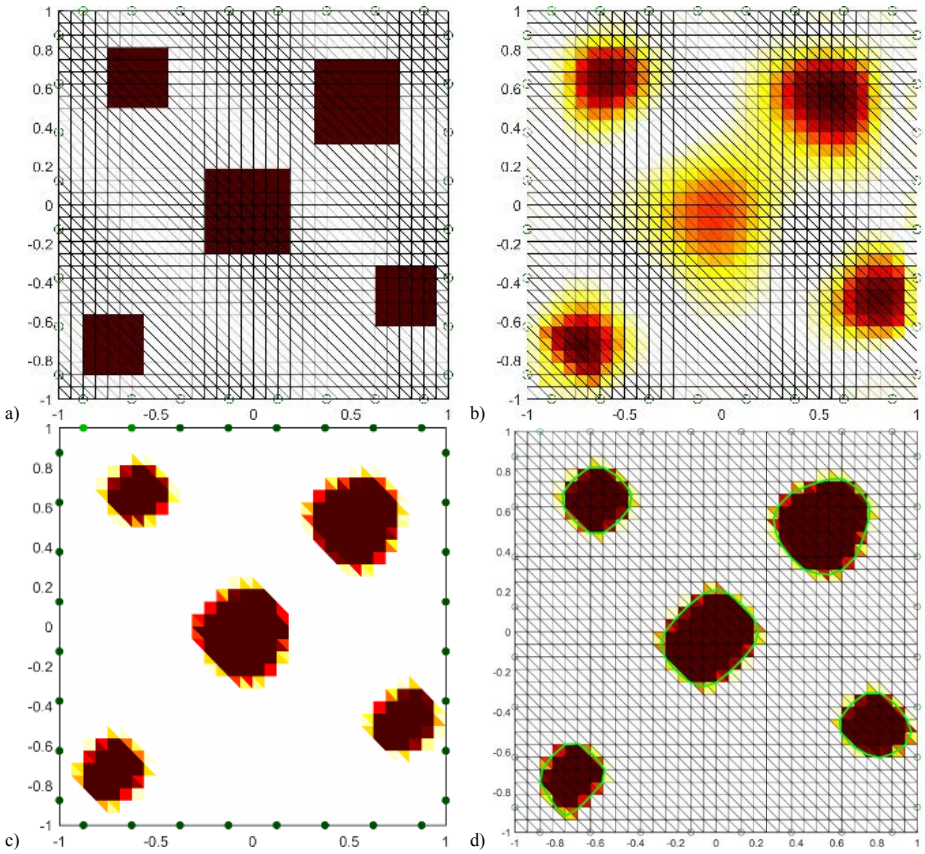

Fig. 10. The model with 5 objects: a) the initial model, b) the reconstructed by Gauss-Newton method, c) zero level sets, d) the reconstructed by the level set method

3. Conclusion

In this paper there was presented the method of approximation of material coefficient. The applications of the level set function, the Gauss-Newton method and the finite element method for the electrical impedance tomography were shown here. They are iterative algorithms, where multiple boundary shape changes smoothly and the searched object is detected. The level set idea is the good tool to the topological changes of the interface. The method of Gauss-Newton gives the best quality of the reconstruction of multiple objects and the hybrid algorithm is faster than the level set model.

References

[1] Chan T. and Vese L.: Active contours without edges, IEEE Transactions on Image Processing, vol. 10, 2001, 266–277.
[2] Ito K., Kunish K., Li Z.: The Level-Set Function Approach to an Inverse Interface Problem. Inverse Problems, 2001, Vol. 17, No. 5, 1225–1242.
[3] Lechleiter A., Rieder A.: Newton regularizations for impedance tomography: convergence by local injectivity. Inverse Problems, 24(6), 2008.
[4] Li C., Xu C., Gui C., Fox M. D.: Level set evolution without re-initialization. A new variational formulation, In IEEE Conference on Computer Vision and Pattern Recognition (CVPR), 2005, volume 1, 430–436.
[5] Osher S., Sethian J.A.: Fronts Propagating with Curvature Dependent Speed: Algorithms Based on Hamilton-Jacobi Formulations, Journal of Computational Physics, 1988, 79, 12–49.
[6] Osher S., Fedkiw R.: Level Set Methods and Dynamic Implicit Surfaces. Springer, New York 2003.
[7] Osher S., Santosa F.: Level set methods for optimization problems involving geometry and constraints. Frequencies of a two-density inhomogeneous drum. Journal of Computational Physics, 2001, 171, 272–288.
[8] Rymarczyk T.: New Methods to Determine Moisture Areas by Electrical Impedance Tomography, International Journal of Applied Electromagnetics and Mechanics 08/2016, 1–9.
[9] Rymarczyk T., Filipowicz S.F.: The Shape Reconstruction of Unknown Objects for Inverse Problems, Electrical Review, NR 5/2012/3a.
[10] Rymarczyk T.: Characterization of the shape of unknown objects by inverse numerical methods, Przegląd Elektrotechniczny, R. 88 NR 7b/2012, 138–140, 2012.
[11] Rymarczyk T, Adamkiewicz P., Duda K., Szumowski J., Sikora J.: New Electrical Tomographic Method to Determine Dampness in Historical Buildings, v.65, 2/2016, Achieve of Electrical Engineering, 2016, 273–283.
[12] Sethian J.A.: Level Set Methods and Fast Marching Methods. Cambridge University Press, 1999.
[13] Sokolowski J., Zochowski A.: On the topological derivative in shape optimization, SIAM Journal on Control and Optimization, vol. 37, 1999, 1251–1272.
[14] Smolik W, Forward Problem Solver for Image Reconstruction by Nonlinear Optimization in Electrical Capacitance Tomography, Flow Measurement and Instrumentation, Vol. 21, Issue 1, March 2010, 70–77.
[15] Wajman R., Fiderek P., Fidos H., Jaworski T., Nowakowski J., Sankowski D., Banasiak R.: Metrological evaluation of a 3D electrical capacitance tomography measurement system for two-phase flow fraction determination; Meas. Sci. Technol. 2013, Vol. 24 No. 065302.
[16] Tai C., Chung E., Chan T.: Electrical impedance tomography using level set representation and total variational regularization. Journal of Computational Physics, 2005, vol. 205, no. 1, 357–372.
[17] Zhao H.-K., Osher S., Fedkiw R.: Fast Surface Reconstruction using the Level Set Method. 1st IEEE Workshop on Variational and Level Set Methods, in conjunction with the 8th International Conference on Computer Vision (ICCV), Vancouver, Canada, 2001, 194–202.

Ph.D. Eng. Tomasz Rymarczyk
e-mail: tomasz.rymarczyk@netrix.com.pl

Director in Research and Development Center Netrix S.A. His research area focuses on the application of non-invasive imaging techniques, electrical tomography, image reconstruction, numerical modelling, image processing and analysis, process tomography, software engineering, knowledge engineering, artificial intelligence and computer measurement systems.

M.A. Paweł Tchórzewski
e-mail: pawel.tchorzewski@netrix.com.pl

Researcher in R&D Department - Netrix S.A.
A graduate of the Maria Curie-Sklodowska University Lublin on the physics (specializing in theoretical physics). Currently, the work carries out tasks profile research and development in the field of numerical methods for solving partial differential equations, electrical tomography in image reconstruction, forward and inverse problem. He is a Ph.D. student of the Institute of Electrical Engineering in Warsaw.

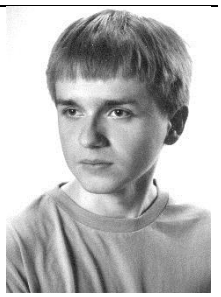

otrzymano/received: 20.09.2016 *przyjęto do druku/accepted: 15.02.2017*

DOI: 10.5604/01.3001.0010.4588

USING ELECTRICAL IMPEDANCE TOMOGRAPHY IN LINEAR ARRAYS OF MEASUREMENT

Tomasz Rymarczyk
Netrix S.A., Research and Development Center, Związkowa Str. 26, 20-148 Lublin

Abstract. *The article presents an application to the topology optimization in electrical impedance tomography using the level set method. The level set function is based on shape and topology optimization for areas with partly continuous conductivities. The finite element method has been used to solve the forward problem. The proposed algorithm is initialized using topological sensitivity analysis. Shape derivative and material derivative have been incorporated with the level set method to investigate shape optimization problems. The coupled algorithm is a relatively new procedure to overcome this problem. Using the line measurement model is very useful to solve the inverse problem in the copper-mine ceiling and the flood embankment.*

Keywords: inverse problem, level set method, electrical impedance tomography

ZASTOSOWANIE ELEKTRYCZNEJ TOMOGRAFII IMPEDANCYJNEJ W UKŁADACH POMIARU LINIOWEGO

Streszczenie. *W artykule przedstawiono aplikację do optymalizacji topologicznej w elektrycznej tomografii impedancyjnej przy użyciu metody zbiorów poziomicowych. Funkcja poziomicowa oparta jest optymalizacji topologii i kształtu dla obszarów z częściowo ciągłymi konduktywnościami. Metoda elementów skończonych została wykorzystana do rozwiązania tego problemu. Proponowany algorytm jest inicjalizowany przy użyciu topologicznej analizy wrażliwościowej. Pochodna kształtu i pochodna topologiczna zostały zaimplementowane z metodą zbiorów poziomicowych do rozwiązania problemu optymalizacji. Sprzężony algorytm jest stosunkowo nową procedurą do rozwiązania tego zadania. Zastosowanie modelu pomiaru tablicowego jest bardzo użyteczne w celu rozwiązania problemu odwrotnego m.in. w chodniku kopalni miedzi i wałach przeciwpowodziowych*.

Słowa kluczowe: zagadnienie odwrotne, metoda zbiorów poziomicowych, tomografia impedancyjna

Introduction

Numerical methods of the shape and the topology optimization were based on the level set representation and the shape differentiation [1, 2, 13, 14]. Possible changes made during the topology optimization process. Level set methods have been applied very successfully in many areas of the scientific modelling [3-5, 10]. This approach is based on the sensitivity of the shape and includes a form of the edge of interface. There are two features that make these methods are suitable for optimization of the topology. The structure is represented by an implicit function. The zero level set defines the boundary of the object. This function is often discretized on a regular grid with the finite element mesh. The next valid feature is the simple update of the implicit function using the Hamilton-Jacobi equation, where the velocity function is determined by the shape sensitivity of the structure. The discussed technique can be applied to the solution of inverse problems in the electrical tomography [6-9, 11, 12]. There were implemented the new algorithms to identify unknown conductivities. The purpose of the presented method is obtaining the better image reconstruction than gradient methods. Next advantage there is accelerating the iterative process by using different shapes of the zero-level set function.

1. Level Set Method

In the level set method, $\phi(x,t)$ is always a function. Numerical simulations can be carried out with the use of discrete grid points in x and substitute a finite approximation of differential for spatial derivatives. The derivative of the spatial approximation of the differential time it is possible by a suitable finite differential operator. Iterative process starts by defining a zero level set function ϕ (time dependent). The function $\phi(x,t)$ is assigned to the area, where the test object is belonged (x - point of space, t - time). Initialization the level set function ϕ starts at t = 0, and the solution can be approximated by the function value in small increments of time (Fig. 1).

The function $\phi(x,t) = 0$ (where x is a point in the area R^n) is defined as follows:

$$\phi(x,t) = \pm \mathrm{d} \tag{1}$$

where: d – the distance between point x, and the edge of the closed surface Ω(t=0), sign +/- represents the location of the point x, respectively inside or outside the area.

The state in which the zero-level set always to this area are:

$$\phi(x(t),t) = 0 \tag{2}$$

Calculating the derivative of this function by the time:

$$\phi' + v|\nabla\phi| = 0 \tag{3}$$

where: v – is a function of the velocity vector Γ.

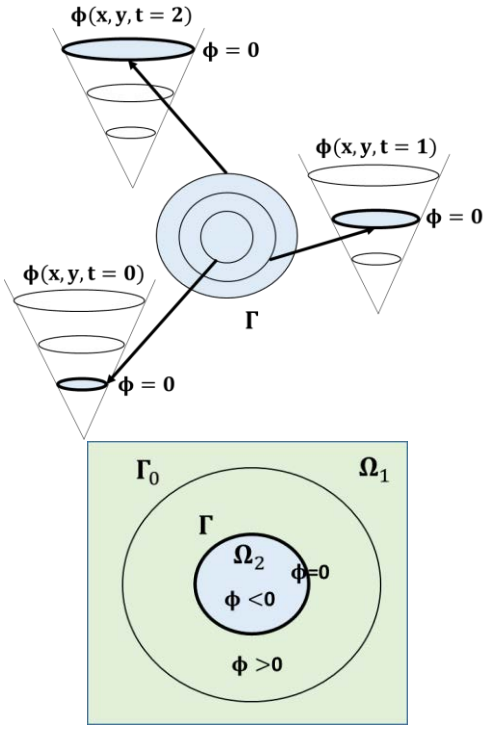

Fig. 1. The idea of the level set function

Properties of the edge of tested area are depend on the level set function ϕ, where at each point of the edge normal vector to this point is given by:

$$\vec{n} = \frac{\nabla\phi}{|\nabla\phi|} \tag{4}$$

The curvature in two dimensions on a plane is described by the equation:

$$\kappa = \nabla \cdot \frac{\nabla\phi}{|\nabla\phi|} = \frac{\phi_{zx}\phi_y^2 - 2\phi_y\phi_z\phi_{xy} + \phi_{xy}\phi_x^2}{\left(\phi_x^2+\phi_y^2\right)^{3/2}} \tag{5}$$

If the surface is growing in three dimensions, the curvature can be described as a mean value of curvature κ_M, or as a Gaussian curvature κ_G. Under the terms of the level set function, these two values are given appropriate expression:

$$\kappa_M = \nabla \cdot \frac{\nabla\phi}{|\nabla\phi|} = \frac{\left\{\begin{matrix}(\phi_{yy}+\phi_{zz})\phi_x^2+(\phi_{xx}+\phi_{zz})\phi_y^2+(\phi_{xx}+\phi_{yy})\phi_z^2+\\ -2\phi_x\phi_x\phi_{xy}-2\phi_x\phi_z\phi_{xz}-2\phi_y\phi_z\phi_{yz}\end{matrix}\right\}}{(\phi_x^2+\phi_y^2+\phi_z^2)^{3/2}} \quad (6)$$

$$\kappa_G = \nabla \cdot \frac{\nabla\phi}{|\nabla\phi|} = \frac{\left\{\begin{matrix}\phi_z^2(\phi_{yy}\phi_{zz}-\phi_{yz}^2)+\phi_y^2(\phi_{xx}\phi_{zz}-\phi_{xz}^2)+\\ \phi_z^2(\phi_{xx}\phi_{yy}-\phi_{xy}^2)+\\ -2\left[\begin{matrix}\phi_x\phi_y(\phi_{xz}\phi_{yz}-\phi_{xy}\phi_{zz})+\\ \phi_y\phi_z(\phi_{xy}\phi_{xz}-\phi_{yz}\phi_{xx})+\\ \phi_x\phi_z(\phi_{xy}\phi_{yz}-\phi_{xz}\phi_{yy})\end{matrix}\right]\end{matrix}\right\}}{(\phi_x^2+\phi_y^2+\phi_z^2)^{3/2}} \quad (7)$$

The curvature of each level set is determined by calculating the divergence of the vector (4):

$$\kappa = \nabla \cdot \vec{n} = \nabla \frac{\nabla\phi}{|\nabla\phi|} \quad (8)$$

When function creates sharp edges, or a sudden collapse, the approximating function cannot be estimated by partial derivative. In such cases, the methods for smoothing sharp edges are used. Level set methods are derived from the mathematical theory of " viscosity solution ". The smoothing function is done by adding to the equation " viscous term" ε. Figure 2 shows the effect of the regularization coefficient on the process function.

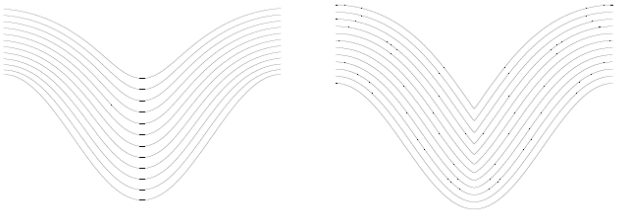

Fig. 2. The impact factor ε limiting viscosity on the process function

Extraction of the border viscosity is to examine the behavior of potential solutions during their search. The equation of motion in such case is described in the following:

$$\Psi_t = v(1+\Psi_x^2)^{\frac{1}{2}} \quad (9)$$

where Ψ_t is the value of the propagation function of time t, therefore $\Psi(x,0) = f(x)$.

For such a waveform function, an initial shape for the calculation is defined as "V" (Fig. 3).

$$\Psi(x,0) = f(x) = \begin{cases}\frac{1}{2}-x & x \le \frac{1}{2}\\ x-\frac{1}{2} & x > \frac{1}{2}\end{cases} \quad (10)$$

Approximation of the above tasks is based on the central calculating of the difference equation:

$$\Psi_t = \frac{\Psi_i^{n+1}-\Psi_i^n}{\Delta t} = \left[1+\left[\frac{\Psi_{i+1}^n-\Psi_{i-1}^n}{2\Delta x}\right]^2\right]^{\frac{1}{2}} \quad (11)$$

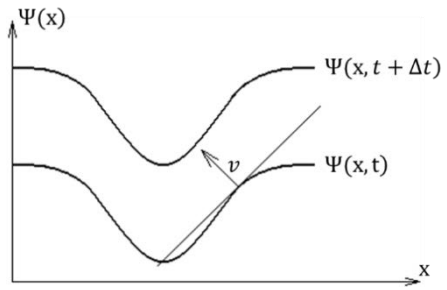

Fig. 3. Variables for the plot propagation

For all $x \neq 1/2$ there is a solution to one value Ψ_i. However, accurate determination of the value $x = 1/2$ (in which the edge shape is not defined) is not possible. Taking the difference reveals unexpected occurrence of oscillations around the point x = 1/2, depending on the time step (Fig. 4).

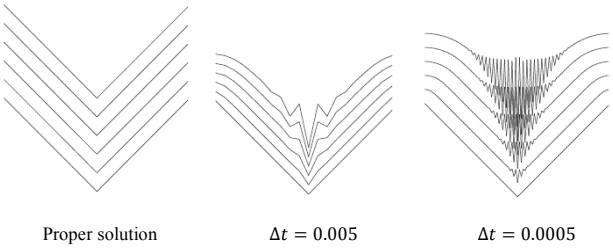

Fig. 4. Approximation of the central difference method according to the Δt

Focusing on the gradient component: $(1+\Psi_x^2)$ - it can be approximated as follows:

$$\Psi_x^2 \approx [\max(D_i^{+x}\Psi,0)^2 + \min(D_i^{-x}\Psi,0)^2] \quad (12)$$

where

$$D_i^{-x}\Psi = \frac{\Psi_i - \Psi_{i-1}}{h}$$

$$D_i^{+x}\Psi = \frac{\Psi_{i+1} - \Psi_i}{h}$$

Ψ_i – value of the function Ψ at the point with step *h*.

The assumptions can be applied to the level set function where the formula for the initial level set method in three-dimensional space becomes:

$$\phi_{ij}^{n+1} = \phi_{ij}^n - \Delta t\left[(\max(v_{ij},0))\nabla^+ + (\min(v_{ij},0))\nabla^-\right] \quad (13)$$

where:

$$\nabla^+ = \Big[(\max(D_{ij}^{-x}\phi_{ij}^n,0))^2 + (\min(D_{ij}^{+x}\phi_{ij}^n,0))^2 + (\max(D_{ij}^{-y}\phi_{ij}^n,0))^2 + (\min(D_{ij}^{+y}\phi_{ij}^n,0))^2\Big]$$

$$\nabla^- = \Big[(\max(D_{ij}^{+x}\phi_{ij}^n,0))^2 + (\min(D_{ij}^{-x}\phi_{ij}^n,0))^2 + (\max(D_{ij}^{+y}\phi_{ij}^n,0))^2 + (\min(D_{ij}^{-y}\phi_{ij}^n,0))^2\Big]$$

This is the equation of partial derivatives and it means that the velocity v is defined for all sets of contour lines, not just for a set of zero corresponds to the interface. The consequence of this is the need to upgrade the level set function at each grid point, using the velocity v.

2. Electrical Impedance Tomography

The electrical impedance tomography (EIT) is a non-destructive imaging technique which has various applications. Its purpose is to reconstruct the conductivity of hidden objects inside a medium with the help of boundary field measurements. Efficient algorithms for solving forward and inverse problem have to be developed in order to use this approach for practical tasks. Moreover, it is necessity to improve performance of selected numerical methods. Typical problem in EIT requires the identification of the unknown internal area from near-boundary measurements of the electrical potential. It is assumed that the value of the conductivity is known in subregions whose boundaries are unknown. The forward problem in EIT is described by Laplace's equation:

$$\nabla \cdot (\gamma \nabla u) = 0 \quad (14)$$

where γ denotes conductivity. Symbol u represents electrical potential. Function u is taken under Dirichlet condition in boundary points adjacent to electrodes and Neumann condition on remaining part of the boundary. Problem can be reduced to determination of the minimum value of the functional:

$$I[u] = \frac{1}{2}\int_\Omega \gamma |\nabla u|^2 dxdy \quad (15)$$

For the minimization problem iterative coupling of the level set method and the finite element method has been proposed.

3. Numerical results

In examples, two numerical models with different discretization elements are presented. Additionally, it is shown different geometries of the boundary shape. The conductivity of searched objects is known. The representation of the boundary shape and its evolution during an iterative reconstruction process is achieved by the level set method. In forward problem, which is given by Laplace's equation, there was used the finite element method.

Figures 5 and 6 display: square measurement system with the inserted object, the image reconstruction with the original objects, the zero level set function, the process reconstruction and the image reconstruction. Figures 7 and 8 show similar object with the one side of measurements.

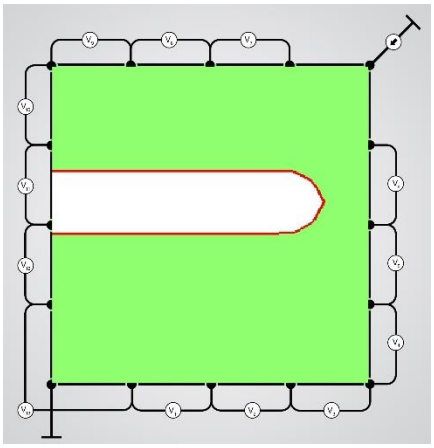

Fig. 5. The square measurement system with the inserted object

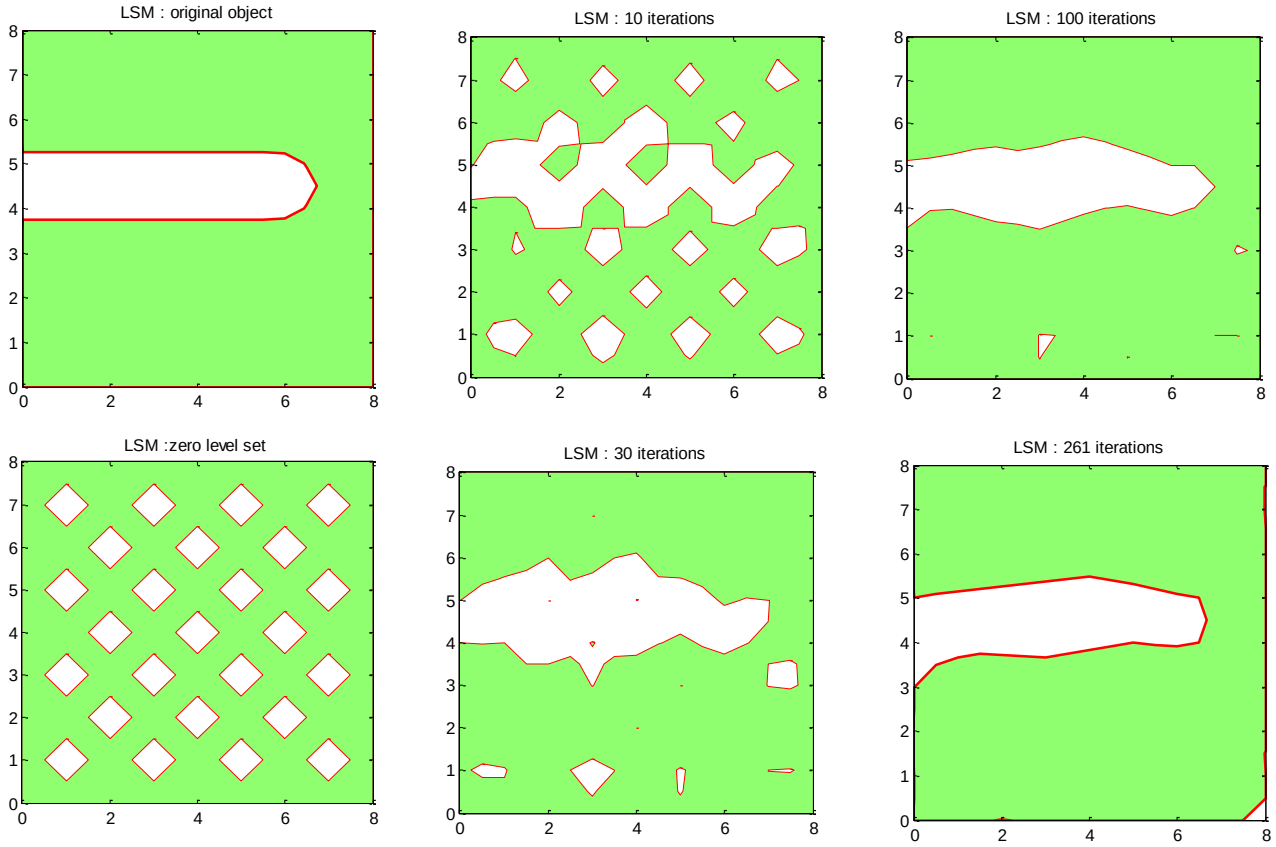

Fig. 6. The image reconstruction - the original object, the zero level set function, the process reconstruction and the image reconstruction

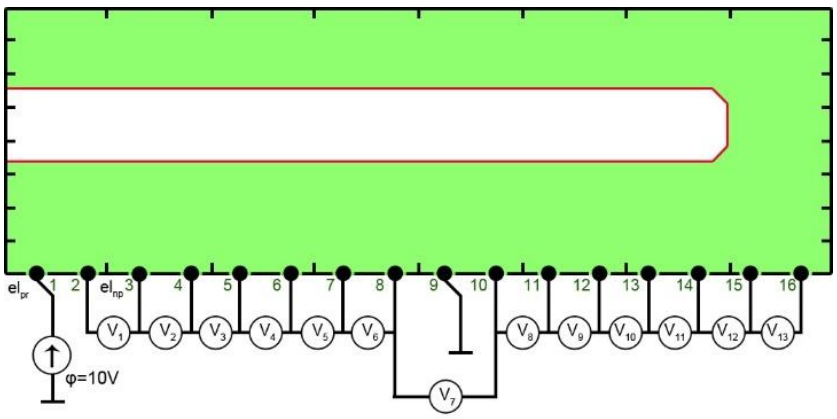

Fig. 7. The rectangular measurement system with the "line" object

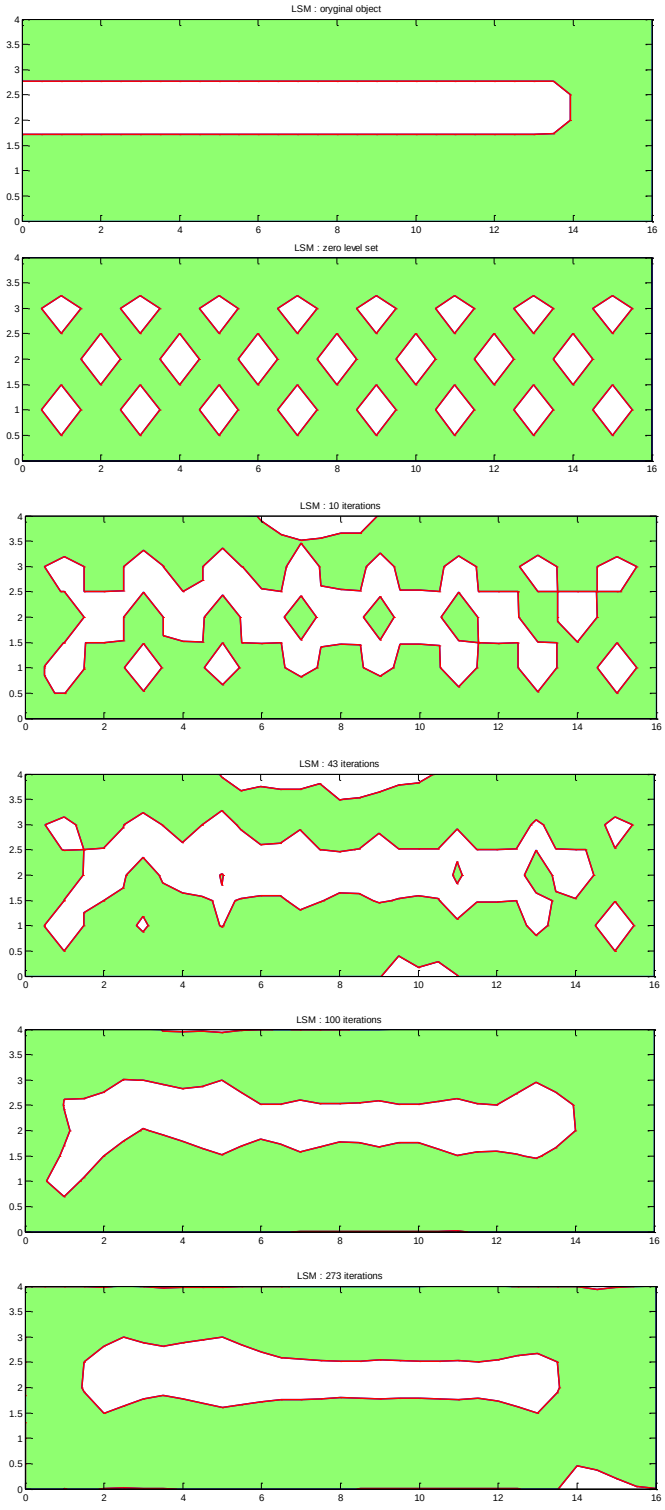

Fig. 8. The image reconstruction with the one side of measurements - the original objects, the zero level set function, the process reconstruction and the image reconstruction

4. Conclusion

The algorithm based on the level set method have been proposed in this work. It is iterative algorithm where repeatedly the shape boundary evolves smoothly and the object is detected. An efficient algorithm for solving the forward and inverse problems would also improve a lot of the numerical performances of the proposed method. In model problem from EIT is required to identify unknown conductivities from near-boundary measurements of the potential. The number of iterations determine the position and shape of zero level set functions. In this algorithm, there can control the process of the image reconstruction. The level set function techniques have been shown to be successful to identify the unknown boundary shapes. The accuracy of the image reconstruction is better than gradient methods. Applying the line measurement model is very effective to solve the inverse problem in the copper-mine ceiling and flood embankment. The right selection of the zero level set function gives the better results, reduces the time of reconstruction process and improves the quality of the image reconstruction.

References

[1] Ito K., Kunish K., Li Z.: The Level-Set Function Approach to an Inverse Interface Problem. Inverse Problems, Vol. 17, No. 5, 2001, 1225–1242.
[2] Li C., Xu C., Gui C., Fox M. D.: Level set evolution without re-initialization. A new variational formulation, In IEEE Conference on Computer Vision and Pattern Recognition (CVPR), volume 1, 2005, 430–436.
[3] Osher S., Sethian J.A.: Fronts Propagating with Curvature Dependent Speed: Algorithms Based on Hamilton-Jacobi Formulations, Journal of Computational Physics, 79, 1988, 12–49.
[4] Osher S., Fedkiw R.: Level Set Methods and Dynamic Implicit Surfaces. Springer, New York 2003.
[5] Osher S., Santosa F.: Level set methods for optimization problems involving geometry and constraints. Frequencies of a two-density inhomogeneous drum. Journal of Computational Physics, 171, 2001, 272–288.
[6] Rymarczyk T.: Using electrical impedance tomography to monitoring flood banks, International Journal of Applied Electromagnetics and Mechanics 45, 2014, 489–494.
[7] Rymarczyk T.: Characterization of the shape of unknown objects by inverse numerical methods, Przegląd Elektrotechniczny, R. 88 NR, 7b/2012, 2012, 138–140.
[8] Rymarczyk T., Sikora J., Waleska B.: Coupled Boundary Element Method and Level Set Function for Solving Inverse Problem in EIT, 7th World Congress on Industrial Process Tomography, WCIPT7, Krakow 2013.
[9] Rymarczyk T, Adamkiewicz P., Duda K., Szumowski J., Sikora J.: New Electrical Tomographic Method to Determine Dampness in Historical Buildings, Achieve of Electrical Engineering, v.65, 2, 2016, 273–283.
[10] Sethian J.A.: Level Set Methods and Fast Marching Methods. Cambridge University Press, 1999.
[11] Smolik W, Forward Problem Solver for Image Reconstruction by Nonlinear Optimization in Electrical Capacitance Tomography, Flow Measurement and Instrumentation, Vol. 21, Issue 1, 2010, 70–77.
[12] Wajman R., Fiderek P., Fidos H., Jaworski T., Nowakowski J., Sankowski D., Banasiak R.: Metrological evaluation of a 3D electrical capacitance tomography measurement system for two-phase flow fraction determination; Meas. Sci. Technol., Vol. 24, 2013, No. 065302.
[13] Tai C., Chung E., Chan T.: Electrical impedance tomography using level set representation and total variational regularization. Journal of Computational Physics, vol. 205, no. 1, 2005, 357–372.
[14] Zhao H.-K., Osher S., Fedkiw R.: Fast Surface Reconstruction using the Level Set Method. 1st IEEE Workshop on Variational and Level Set Methods, in conjunction with the 8th International Conference on Computer Vision (ICCV), Vancouver, Canada, 2001, 194–202.

Ph.D. Eng. Tomasz Rymarczyk
e-mail: tomasz.rymarczyk@netrix.com.pl

Director in Research and Development Center Netrix S.A. His research area focuses on the application of non-invasive imaging techniques, electrical tomography, image reconstruction, numerical modelling, image processing and analysis, process tomography, software engineering, knowledge engineering, artificial intelligence and computer measurement systems.

otrzymano/received: 20.09.2016 *przyjęto do druku/accepted: 15.02.2017*

DOI: 10.5604/01.3001.0010.4589

COUPLING BOUNDARY ELEMENT METHOD WITH LEVEL SET METHOD TO SOLVE INVERSE PROBLEM

Tomasz Rymarczyk[1], Paweł Tchórzewski[1], Jan Sikora[2,3]
[1]Netrix S.A., Research and Development Center, Związkowa Str. 26, 20-148 Lublin, [2]Lublin University of Technology, Institute of Electronics and Information Technology, [3]Electrotechnical Institute

Abstract. *The boundary element method and the level set method can be used in order to solve the inverse problem for electric field. In this approach the adjoint equation arises in each iteration step. Results of the numerical calculations show that the boundary element method can be applied successfully to obtain approximate solution of the adjoint equation. The proposed solution algorithm is initialized by using topological sensitivity analysis. Shape derivatives and material derivatives have been incorporated with the level set method to investigate shape optimization problems. The shape derivative measures the sensitivity of boundary perturbations. The coupled algorithm is a relatively new procedure to overcome this problem. Experimental results have demonstrated the efficiency of the proposed approach to achieve the solution of the inverse problem.*

Keywords: inverse problem, boundary element method, level set method

POŁĄCZENIE METODY ELEMENTÓW BRZEGOWYCH I ZBIORÓW POZIOMICOWYCH W ROZWIĄZYWANIU ZAGADNIENIA ODWROTNEGO

Streszczenie*. Metoda elementów brzegowych i metoda zbiorów poziomicowych mogą być wykorzystane to rozwiązania zagadnienia odwrotnego pola elektrycznego. W takim podejściu równanie sprzężone jest rozwiązywane w każdym kroku iteracyjnym. Wyniki obliczeń numerycznych pokazują, że metoda elementów brzegowych może być zastosowana z powodzeniem do uzyskania przybliżonego rozwiązania równania sprzężonego. Proponowany algorytm jest inicjalizowany za pomocą topologicznej analizy wrażliwościowej. Pochodna kształtu i pochodna materialna zostały połączone z metodą zbiorów poziomicowych w celu zbadania problemów optymalizacji kształtu. Pochodna kształtu mierzy wrażliwość perturbacji brzegowych. Zespolony algorytm jest stosunkowo nową procedurą do rozwiązania tego problemu. Wyniki doświadczenia pokazały skuteczność proponowanego podejścia w rozwiązywaniu zagadnienia odwrotnego.*

Słowa kluczowe: zagadnienie odwrotne, metoda elementów skończonych, tomografia impedancyjna

Introduction

The electrical impedance is non-destructive imaging technique [14, 15], which has various applications. For example, it can be used in medical imaging. In our approach the algorithm of the inverse problem bases on the boundary element method (BEM) [4, 13], the gradient technique and the level set method [1, 2, 5–7, 12, 16, 17]. In the gradient technique so-called adjoint equation has to be solved [3, 8–11]. The solution has to be obtained in each iteration step. Numerical techniques give us opportunity to find approximate solutions of differential equations which cannot be solved by means of analytical ones. Among various numerical tools like the finite element method, the finite difference method or BEM we concentrated our attention on the last one. BEM can be effectively employed on condition that partial differential equation can be transformed to integral form. Additionally, the Green's function has to be calculated. In our numerical calculations for simplicity zero order approximation has been chosen. The function which describes electrical conductivity distribution in our system possesses two different nonzero values. Finally, we have successfully solved the inverse problem in two-dimensional system with 16 electrodes. Therefore, the proposed numerical model has been verified.

1. Boundary Element Method

The field studies might be split on two main branches. In that case are defined: the topology of the structure (interface boundary – outside and/or inside), boundary conditions, material coefficients (e.g. conductivity), the internal source or sources etc. The second case concerns with the inverse problem solution. In this case the unknown parameters are searched when the field distribution is known. Unknown shape of the interface could play the role of the unknown parameters and the inverse problem could be called for example Electrical Impedance Tomography (EIT). Normally we only known the field distribution on the most external boundary of the object.

The partial differential equation in its integral form was defined in order to compute the field distribution for the inhomogeneous regions presented in Figure 1:

$$c(\vec{r_i})\Phi_1(\vec{r_i}) + \int_{\Gamma_1+\Gamma_2+\Gamma_3} \Phi_1(\vec{r})\frac{\partial G_1(\vec{r},\vec{r_i})}{\partial n}d\Gamma = \int_{\Gamma_1+\Gamma_2+\Gamma_3} G_1(\vec{r},\vec{r_i})\frac{\partial \Phi_1(\vec{r})}{\partial n}d\Gamma$$

$$c(\vec{r_i})\Phi_2(\vec{r_i}) + \int_{\Gamma_2} \Phi_2(\vec{r})\frac{\partial G_2(\vec{r},\vec{r_i})}{\partial n}d\Gamma = \int_{\Gamma_2} G_2(\vec{r},\vec{r_i})\frac{\partial \Phi_2(\vec{r})}{\partial n}d\Gamma$$

$$c(\vec{r_i})\Phi_3(\vec{r_i}) + \int_{\Gamma_3} \Phi_3(\vec{r})\frac{\partial G_3(\vec{r},\vec{r_i})}{\partial n}d\Gamma = \int_{\Gamma_3} G_3(\vec{r},\vec{r_i})\frac{\partial \Phi_3(\vec{r})}{\partial n}d\Gamma \quad (1)$$

where the value of c coefficient is defined by the location of the point indicated by the position vector $\vec{r_i}$:

$$c(\vec{r_i}) = \begin{cases} 1, & \vec{r_i} \in \Omega \\ \frac{1}{2}, & \vec{r_i} \in \partial\Omega \\ 0, & \vec{r_i} \notin \Omega \end{cases} \quad (2)$$

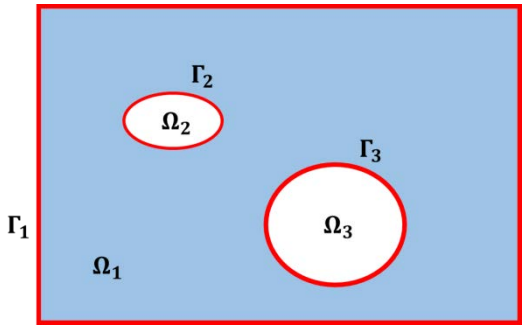

Fig. 1. The example of the structure: region Ω_1 limited by border Γ_1 with two internal objects: Ω_2 limited by border Γ_2 and Ω_3 limited by border Γ_3

The objective is to find interface (inside boundary) using voltage measurements on the periphery of the region. The boundary Γ_1 is known, but the starting shape of interface in request has been chosen randomly (at the beginning of the iteration process). For so called "current electrodes" (nodes of the boundary elements) the Dirichlet boundary conditions are imposed (emulate the voltage source), for the rest (the "voltage electrodes") the homogeneous Neumann boundary condition $\frac{\partial \Phi}{\partial n} = 0$ are imposed.

The state function (electric potential) and its normal derivative on the particular boundary $\Gamma_1, \Gamma_2, \Gamma_3$ of each substructures $\Omega_1, \Omega_2, \Omega_3$ are denoted as:

$$\begin{gathered}\boldsymbol{\Phi}_1(\Gamma_1) = \boldsymbol{\Phi}_1^1,\ \boldsymbol{\Phi}_1(\Gamma_2) = \boldsymbol{\Phi}_2^1, \boldsymbol{\Phi}_1(\Gamma_3) = \boldsymbol{\Phi}_3^1,\\ \boldsymbol{\Phi}_2(\Gamma_2) = \boldsymbol{\Phi}_2^2, \boldsymbol{\Phi}_3(\Gamma_3) = \boldsymbol{\Phi}_3^3,\\ \frac{\partial \boldsymbol{\Phi}_1(\Gamma_1)}{\partial n} = \left(\frac{\partial \boldsymbol{\Phi}}{\partial n}\right)_1^1, \frac{\partial \boldsymbol{\Phi}_1(\Gamma_2)}{\partial n} = \left(\frac{\partial \boldsymbol{\Phi}}{\partial n}\right)_2^1,\\ \frac{\partial \boldsymbol{\Phi}_1(\Gamma_3)}{\partial n} = \left(\frac{\partial \boldsymbol{\Phi}}{\partial n}\right)_3^1, \frac{\partial \boldsymbol{\Phi}_2(\Gamma_2)}{\partial n} = \left(\frac{\partial \boldsymbol{\Phi}}{\partial n}\right)_2^2,\\ \frac{\partial \boldsymbol{\Phi}_3(\Gamma_3)}{\partial n} = \left(\frac{\partial \boldsymbol{\Phi}}{\partial n}\right)_3^3 \end{gathered} \tag{3}$$

Substitute:

$$A_{ij}^* = \int_{\Gamma_j} \frac{\partial G(\vec{r_i}, \vec{r})}{\partial n} d\Gamma \tag{4}$$

where $A_{ij} = \begin{cases} A_{ij}^*, & i \neq j \\ A_{ij}^* + c(\vec{r_i}), & i = j \end{cases}$

and

$$B_{ij} = \int_{\Gamma_j} G(\vec{r_i}, \vec{r})\, d\Gamma \tag{5}$$

we will rewrite eq. (1) in a matrix form. The same manner was used to mark the matrices $\boldsymbol{A}$ and $\boldsymbol{B}$ as the state function and its normal derivative (see equation (3)):

$$\begin{gathered}\mathbf{A}^1(\Gamma_1) = \mathbf{A}_1^1, \mathbf{A}^1(\Gamma_2) = \mathbf{A}_2^1, \mathbf{A}^1(\Gamma_3) = \mathbf{A}_3^1,\\ \mathbf{A}^2(\Gamma_2) = \mathbf{A}_2^2, \mathbf{A}^3(\Gamma_3) = \mathbf{A}_3^3,\\ \mathbf{B}^1(\Gamma_1) = \mathbf{B}_1^1, \mathbf{B}^1(\Gamma_2) = \mathbf{B}_2^1,\\ \mathbf{B}^1(\Gamma_3) = \mathbf{B}_3^1, \mathbf{B}^2(\Gamma_2) = \mathbf{B}_2^2,\\ \mathbf{B}^3(\Gamma_3) = \mathbf{B}_3^3 \end{gathered} \tag{6}$$

The voltage on the internal boundary (interface) Γ_2 or Γ_3 fulfill the continuous conditions:

$$\begin{gathered}\boldsymbol{\Phi}_1(\Gamma_2) = \boldsymbol{\Phi}_2(\Gamma_2)\\ \boldsymbol{\Phi}_1(\Gamma_3) = \boldsymbol{\Phi}_3(\Gamma_3)\end{gathered} \tag{7}$$

If the conductivity Ω_1 is equal γ_1, Ω_2 is equal γ_2 and conductivity of Ω_3 is γ_3 (as it was previously noted: the conductivity in objects are constant) then:

$$\begin{gathered}\gamma_1 \frac{\boldsymbol{\Phi}_1(\Gamma_2)}{\partial n} = -\gamma_2 \frac{\boldsymbol{\Phi}_2(\Gamma_2)}{\partial n}\\ \gamma_1 \frac{\boldsymbol{\Phi}_1(\Gamma_3)}{\partial n} = -\gamma_3 \frac{\boldsymbol{\Phi}_3(\Gamma_3)}{\partial n}\end{gathered} \tag{8}$$

where: minus means the opposite direction of the normal unit vector to the border of $\Omega_1 - \Omega_2$ and $\Omega_1 - \Omega_3$.

Rewrite equations for inhomogeneous regions in the matrix form we have got:

$$\begin{bmatrix} \mathbf{A}_2^1 & -\mathbf{B}_2^1 & \mathbf{A}_3^1 & -\mathbf{B}_3^1 \\ \mathbf{A}_2^2 & -\left(-\frac{\gamma_1}{\gamma_2}\right)\mathbf{B}_2^2 & \mathbf{0} & \mathbf{0} \\ \mathbf{0} & \mathbf{0} & \mathbf{A}_3^3 & -\left(-\frac{\gamma_1}{\gamma_3}\right)\mathbf{B}_3^3 \end{bmatrix} \begin{bmatrix} \boldsymbol{\Phi}_2^1 \\ \left(\frac{\partial \boldsymbol{\Phi}}{\partial n}\right)_2^1 \\ \boldsymbol{\Phi}_3^1 \\ \left(\frac{\partial \boldsymbol{\Phi}}{\partial n}\right)_3^1 \end{bmatrix} = \begin{bmatrix} -\mathbf{A}_1^1 \boldsymbol{\Phi}_1^1 + \mathbf{B}_1^1 \left(\frac{\partial \boldsymbol{\Phi}}{\partial n}\right)_1^1 \\ \mathbf{0} \\ \mathbf{0} \end{bmatrix} \tag{9}$$

where the following values $\boldsymbol{\Phi}_2^1$, $\left(\frac{\partial \boldsymbol{\Phi}}{\partial n}\right)_2^1$, $\boldsymbol{\Phi}_3^1$, $\left(\frac{\partial \boldsymbol{\Phi}}{\partial n}\right)_3^1$ are unknown. It is needed to solve the equation (1) for all projection angles.

2. Inverse Problem

To solve the inverse problem with the aid of the level set method there was needed the adjoint equation. Let us consider the following partial differential equation in two-dimensional Cartesian coordinate system:

$$\nabla \cdot [\sigma(\vec{r}) \nabla \lambda(\vec{r})] = b(\vec{r}) \tag{10}$$

where $\vec{r} \epsilon \Omega$. We assumed that $\sigma(\vec{r})$ denotes electrical conductivity distribution. The source term $b(\vec{r})$ is defined only on the boundary of the domain Ω. It depends on differences between voltages obtained from measurements and numerical simulations. The source term has to be calculated on each iteration step. The formula for $b(\vec{r})$ is given in [13]. Additionally, we assumed that the adjoint function λ or its normal derivative β is known for all boundary points. The differential problem defined in described manner may be regarded as the boundary value problem for the adjoint equation (10).

Starting point for our research is typical for BEM integral equation [13], where the boundary curve is divided into N elements:

$$\begin{gathered}c(\vec{r_i})\lambda(\vec{r_i}) + \sum_{j=1}^N \int_{\Gamma_j} \lambda(\vec{r})\, h(\vec{r}, \vec{r_i}) d\gamma_j + \int_\Omega b(\vec{r}) g(\vec{r}, \vec{r_i}) d\omega =\\ = \sum_{j=1}^N \int_{\Gamma_j} \beta(\vec{r_i})\, g(\vec{r}, \vec{r_i}) d\gamma_j \end{gathered} \tag{11}$$

Equation (11) is valid if the electrical conductivity is constant in the whole domain. In the case of constant boundary elements only three values of the function c are possible. If a given point belongs to boundary of the domain Ω, then the value equals 0.5. The value of function c equals 1, when a given point lies inside of Ω and equals 0 in other cases. The Green's function g may be obtained by solving the fundamental equation and is given by:

$$g(\vec{r}, \vec{r_i}) = \frac{1}{2\pi} ln\left(\frac{A}{|\vec{r} - \vec{r_i}|}\right) \tag{12}$$

In above formula A is a positive constant. Function h represents the derivative of the Green's function in normal direction appointed by unit vector $\vec{n}(\vec{r})$. After calculations we get:

$$h(\vec{r}, \vec{r_i}) = -\frac{1}{2\pi} \frac{\vec{n}(\vec{r}) \cdot (\vec{r} - \vec{r_i})}{|\vec{r} - \vec{r_i}|^2} \tag{13}$$

The vector formula for j-th constant boundary element is given by:

$$\vec{r}_j(\xi) = \vec{r}_{(m)j} + 0{,}5\left(\vec{r}_{(l)j} - \vec{r}_{(f)j}\right)\xi \tag{14}$$

where $\xi \epsilon \langle -1, 1 \rangle$. Position vectors $\vec{r}_{(f)j}$, $\vec{r}_{(l)j}$ and $\vec{r}_{(m)j}$ represent the first vertex, the last vertex and the middle point (node) of j-th boundary element, respectively. We use constant boundary elements, therefore:

$$\begin{gathered}c(\vec{r_i})\lambda(\vec{r_i}) + \sum_{j=1}^N \lambda(\vec{r}) \int_{\Gamma_j} h(\vec{r}, \vec{r_i}) d\gamma_j + \int_\Omega b(\vec{r}) g(\vec{r}, \vec{r_i}) d\omega =\\ = \sum_{j=1}^N \beta(\vec{r_i}) \int_{\Gamma_j} g(\vec{r}, \vec{r_i}) d\gamma_j \end{gathered} \tag{15}$$

Formulas (12), (13), and (15) can be utilised to solve the adjoint equation (10) because the domain Ω can be decomposed into two subdomains where electrical conductivity is constant for each one.

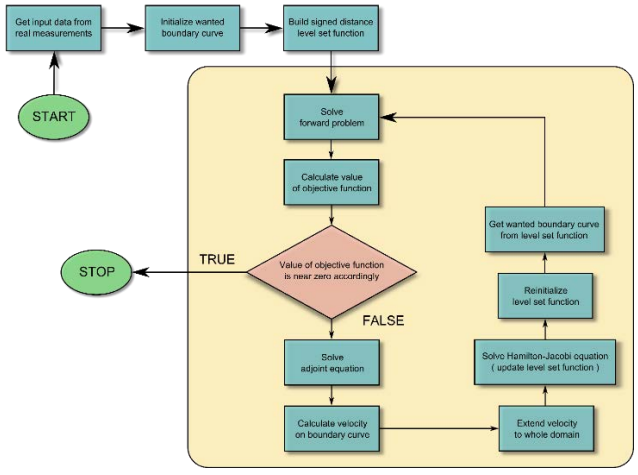

Fig. 2. The scheme of the algorithm to minimize the objective function

The following algorithm is used to find out the shape and the position of the unknown internal obstacles (Fig. 2):

a) make discretization of the outer boundary $\boldsymbol{\Gamma_1}$ (for example on 32 elements),
b) collect measurements from the electrodes for all projection angles,
c) conduct simulation for randomly placed objects inside,
d) use the Laplace equation and compute electric potential distribution with the aid of BEM,
e) determine difference between the "measured" $\boldsymbol{u_0}$ and computed potential $\boldsymbol{\Phi}$ and use them for the adjoint equation,
f) update the Hamilton-Jacobi equation,
g) check if it's necessary to reinitialize set level function,
h) get zero level contour of updated φ function and select discretization points,
i) calculate the objective function according to the equation

$$F_c = \frac{1}{2}\sum_{j=1}^{p} F_j = \frac{1}{2}\sum_{j=1}^{p}\left\{\left(\boldsymbol{\Phi}^1_{1\,j} - \boldsymbol{u}_{0\,j}\right)^T \left(\boldsymbol{\Phi}^1_{1\,j} - \boldsymbol{u}_{0\,j}\right)\right\} \quad (16)$$

where: $\boldsymbol{\Phi}$ – is computed electric potential distribution; $\boldsymbol{u}_0$ – is measured values for real object, if the objective function is lower than assumed threshold, then "stop", else go to the point (d).

3. Results

Figure 3 shows the solution of the inverse problem. All points in both figures represent vertices of boundary elements. Our algorithm needed about 50 iterations to minimalize the objective function (see Fig. 4). Obtained result is appropriate. Proposed numerical model has been successfully verified. We can make use of BEM in algorithm which solves the inverse problem in EIT.

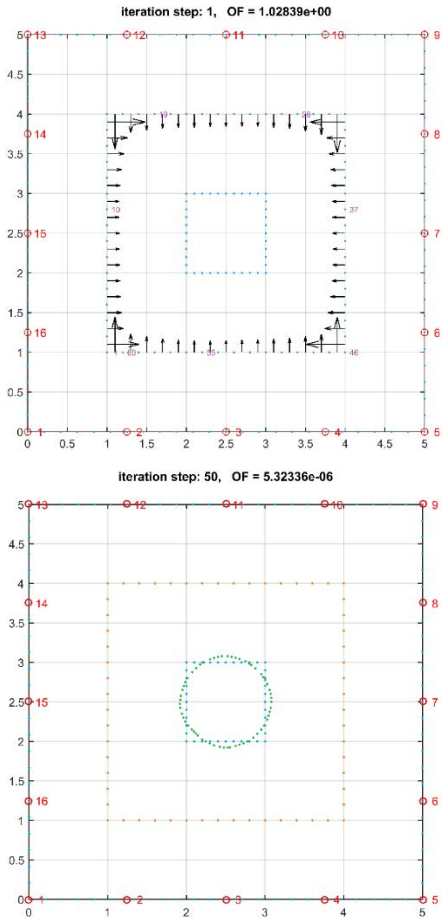

Fig. 3. The solution of the inverse problem (green points). internal square indicated by blue points represents proper position of the interface, orange points represent initial position of the interface, symbol OF denotes the value of the objective function

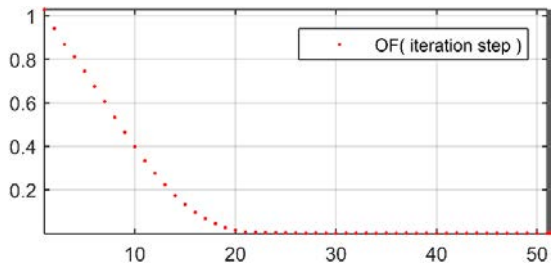

Fig. 4. The objective function versus the number of iteration step

Figure 5 presents the image reconstruction with the one object. Figure 6a shows two obstacles marked by the blue dashed line. Such a test example will be considered as an EIT problem. The phantom object with unknown topology inside was reconstructed. In such case the level set function with four zero level objects will be applied as most appropriate one. For each simulated object the velocity would be calculated under assumption that the conductivities of all objects are known. Unknown structures are marked by the blue line; simulated objects are marked by the red line. For last 300 iterations step the unknown structure was found. The result is presented in Figure 6d. The objective function distribution versus the number of iteration steps is shown in Figure 7.

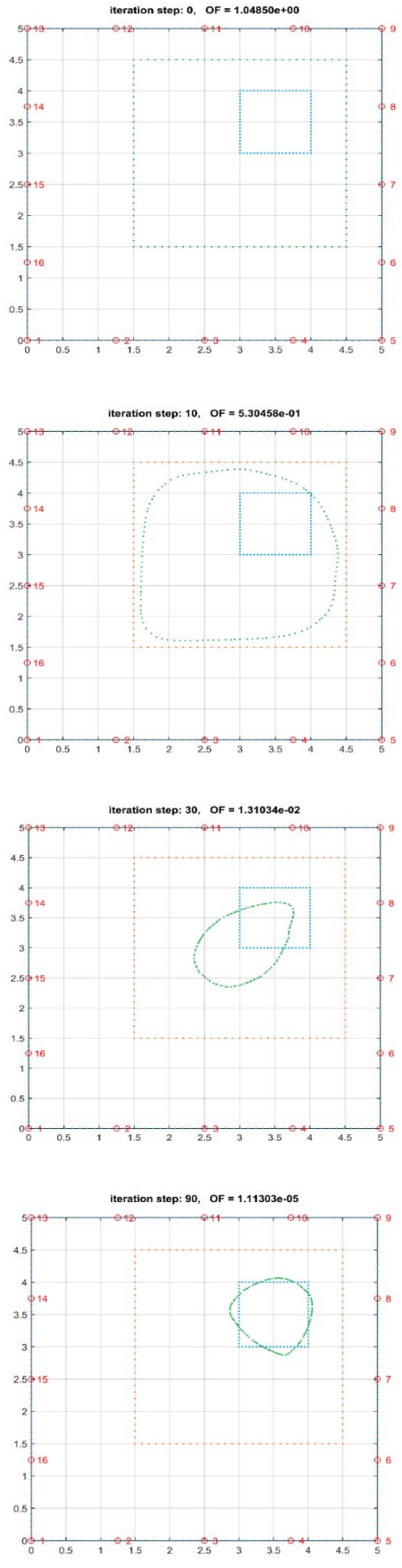

Fig. 5. The image reconstruction of the one object (BEM-LSM)

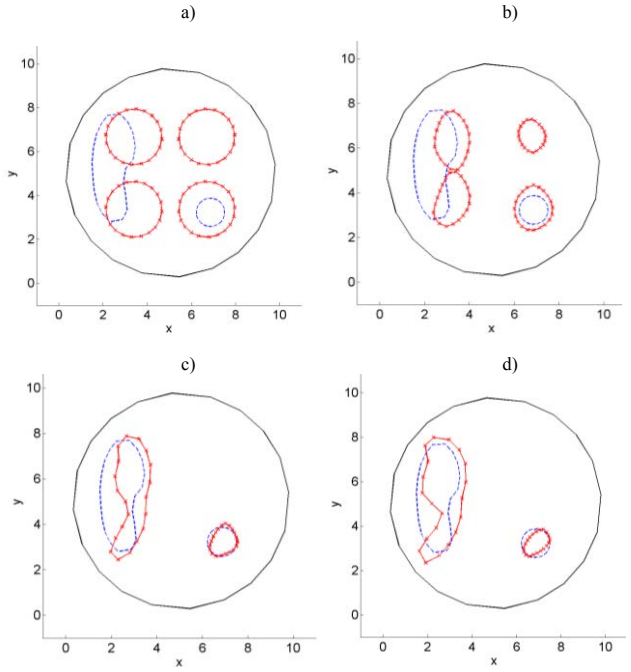

Fig. 6. The black line marks the outside border of the structure with the internal unknown objects (marked by the blue dashed line). The red line marks zero level contours, a) starting point, b) after 98 iterations, one step before merging two objects, c) after 225 iterations with the lowest value of the cost function equal to=0.96; d) after 300 iteration steps when the objective functions again increased

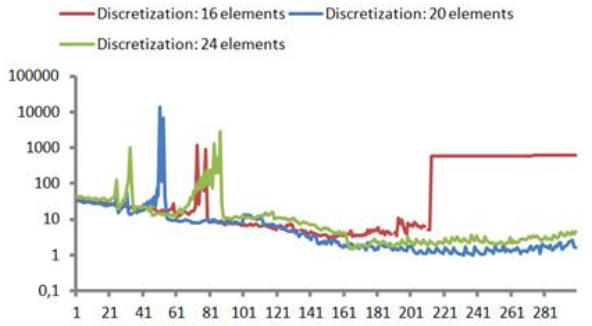

Fig. 7. The objective function distribution versus the number of iteration steps

4. Conclusion

The inverse problem was solved using the combination of the level set function with the boundary element. The level set method and BEM show a way how to compute the interface by updating the Hamilton-Jacobi equation. This is particularly easy when the BEM is applied because the normal derivatives of the state function and adjoint function are the primary values directly achieved after the simulation process. In many cases occurs that the reinitialization is necessary to fix the correct shape of the level set function and also the signed distance function. Experimental results confirmed that presented method is efficient and the only one which is able to change the topology during the iteration process.

References

[1] Allaire G., Gournay F. De, Jouve F., Toader A. M.: Structural optimization using topological and shape sensitivity via a level set method, Control and Cybernetics, vol. 34, 2005, 59–80.
[2] Chen W., Cheng J., Lin W.: A level set method to reconstruct the discontinuity of the conductivity in EIT, Science in China Series A: Mathematics, vol. 52, 2009.
[3] Ito K., Kunish K., Li Z.: The Level-Set Function Approach to an Inverse Interface Problem, Inverse Problems, vol. 17, no. 5, 2001, 1225–1242.
[4] Jabłoński P.: Metoda elementów brzegowych w analizie pola elektromagnetycznego, Wydawnictwo Politechniki Częstochowskiej, 2003.
[5] Osher S., Sethian J. A.: Fronts Propagating with Curvature Dependent Speed: Algorithms Based on Hamilton-Jacobi Formulations, Journal of Computational Physics, vol. 79, 1988, 12–49.
[6] Osher S., Santosa F.: Level set methods for optimization problems involving geometry and constraints. Frequencies of a two-density inhomogeneous drum, Journal of Computational Physics, vol. 171, 2001, 272–288.
[7] Osher S., Fedkiw R.: Level Set Methods and Dynamic Implicit Surfaces, Springer New York, 2003.
[8] Rymarczyk T.: Using electrical impedance tomography to monitoring flood banks, International Journal of Applied Electromagnetics and Mechanics 45, 2014, 489–494.
[9] Rymarczyk T.: Characterization of the shape of unknown objects by inverse numerical methods, Przegląd Elektrotechniczny, R. 88, 7b, 2012, 138-140.
[10] Rymarczyk T., Sikora J., Waleska B.: Coupled Boundary Element Method and Level Set Function for Solving Inverse Problem in EIT, 7th World Congress on Industrial Process Tomography, WCIPT7, Krakow 2013.
[11] Rymarczyk:T., Adamkiewicz P., Duda K., Szumowski J., Sikora J.: New Electrical Tomographic Method to Determine Dampness in Historical Buildings, Achieve of Electrical Engineering, v.65, 2/2016, 273–283
[12] Sethian J.A.: Level Set Methods and Fast Marching Methods, Cambridge Univeristy Press, 1999.
[13] Sikora J.: Boundary Element Method for Impedance and Optical Tomography, Warsaw University of Technology Publisher, 2007.
[14] Smolik W, Forward Problem Solver for Image Reconstruction by Nonlinear Optimization in Electrical Capacitance Tomography, Flow Measurement and Instrumentation, Vol. 21, Issue 1, 2010, 70–77.
[15] Wajman R., Fiderek P., Fidos H., Jaworski T., Nowakowski J., Sankowski D., Banasiak R.: Metrological evaluation of a 3D electrical capacitance tomography measurement system for two-phase flow fraction determination; Meas. Sci. Technol. Vol. 24, 2013, No. 065302.
[16] Tai C., Chung E., Chan T.: Electrical impedance tomography using level set representation and total variational regularization, Journal of Computational Physics, vol. 205, no. 1, 2005, 357–372.
[17] Vese L., Chan T.: A new multiphase level set framework for image segmentation via the Mumford and Shah model. CAM Report 01-25, UCLA Math. Dept., 2001.

Ph.D. Eng. Tomasz Rymarczyk
e-mail: tomasz.rymarczyk@netrix.com.pl

Director in Research and Development Center Netrix S.A. His research area focuses on the application of non-invasive imaging techniques, electrical tomography, image reconstruction, numerical modelling, image processing and analysis, process tomography, software engineering, knowledge engineering, artificial intelligence and computer measurement systems.

M.A. Paweł Tchórzewski
e-mail: pawel.tchorzewski@netrix.com.pl

Researcher in R&D Department – Netrix S.A.
A graduate of the Maria Curie-Sklodowska University Lublin on the physics (specializing in theoretical physics). Currently, the work carries out tasks profile research and development in the field of numerical methods for solving partial differential equations, electrical tomography in image reconstruction, forward and inverse problem. He is a Ph.D. student of the Institute of Electrical Engineering in Warsaw.

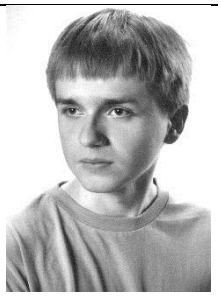

Prof. Jan Sikora
e-mail: sik59@wp.pl

Prof. Jan Sikora (PhD. DSc. Eng.) graduated from Warsaw University of Technology Faculty of Electrical Engineering. During 40 years of professional work he has proceeded all grades, including the position of full professor at his alma mater. Since 1998 he has worked for the Institute of Electrical Engineering in Warsaw. In 2008 he has joined Electrical Engineering and Computer Science Faculty In Lublin University of Technology. During 2001-2004 he has worked as a Senior Research Fellow at University College London in the prof. S. Arridge's Group of Optical Tomography. His research interests are focused on numerical methods for electromagnetic field.

otrzymano/received: 20.09.2017 *przyjęto do druku/accepted: 15.02.2017*

DOI: 10.5604/01.3001.0010.4590

DETECTION OF AIR GAPS IN COPPER-MINE CEILING BY ELECTRICAL IMPEDANCE TOMOGRAPHY

Tomasz Rymarczyk[1], Paweł Tchórzewski[1], Jan Sikora[2,3]
[1]Netrix S.A., Research and Development Center, ul. Związkowa 26, 20-148 Lublin, [2]Lublin University of Technology, Institute of Electronics and Information Technology, [3]Electrotechnical Institute

Abstract *In this paper, we investigate the inverse problem for the electric field so-called copper mine problem. In general, this task assumes detection of all air gaps. Gaps are localised above ceiling in a copper mine. Such task can be considered as application of the electrical impedance tomography. In order to solve forward problem there was used the boundary element method or the finite element method. The inverse problem is based on the level set method. There was considered extension of boundary element method (BEM). For simplicity zero order approximation has been chosen. The BEM has been connected with the infinite boundary elements. Hence, open domain problems with infinite boundary curves can be analysed. For such domain, we have solved the Dirichlet problem for two-dimensional Laplace's equation. The proposed numerical model has been verified.*

Keywords: inverse problem, boundary element method, electrical impedance tomography

WYKRYWANIE SZCZELIN POWIETRZNYCH W CHODNIKU KOPALNI MIEDZI ZA POMOCĄ ELEKTRYCZNEJ TOMOGRAFII IMPEDANCYJNEJ

Streszczenie *W tym artykule przyjrzymy się problemowi odwrotnemu dla pola elektrycznego na tak zwanym problemie kopalni miedzi. Głównym zadaniem w tym zagadnieniu jest wykrycie szczelin powietrznych, które są zlokalizowane w stropie kopalni. Takie zadanie można rozwiązać za pomocą elektrycznej tomografii impedancyjnej. W celu rozwiązania zagadnienia prostego można użyć metody elementów brzegowych (MEB) lub metody elementów skończonych. Zagadnienie odwrotne zostało oparte na metodzie zbiorów poziomicowych. Dla uproszczenia zostały zastosowane elementy zerowego rzędu. Metoda elementów brzegowych została rozszerzona o elementy nieskończone. Stąd problemy otwarte domeny z nieskończonymi brzegami mogą być analizowane. Dla takiej domeny, musimy rozwiązać zagadnienie Dirichleta dla równania dwuwymiarowy Laplace'a. Zaproponowany model numeryczny został zweryfikowany.*

Słowa kluczowe: zagadnienie odwrotne, metoda elementów brzegowych, tomografia impedancyjna

Introduction

In this paper, we propose algorithm based on the combination of the boundary element method (or the finite element method) and the level set method to solve the inverse problem arising from electrical impedance tomography (EIT) [11–14]. The representation of the boundary shape and its evolution during an iterative reconstruction process is achieved by the level set method [2, 5–8, 15]. In our numerical algorithm we have used the gradient technique in order to calculate the velocity. This idea has been applied successfully in the context of inverse problem [3, 12, 16].

We focus our attention on so-called copper mine problem. Generally, this problem involves the detection of all air gaps are located above the roof of the copper mine (see Fig. 1). This task is very important for safety reasons. It could be done EIT.

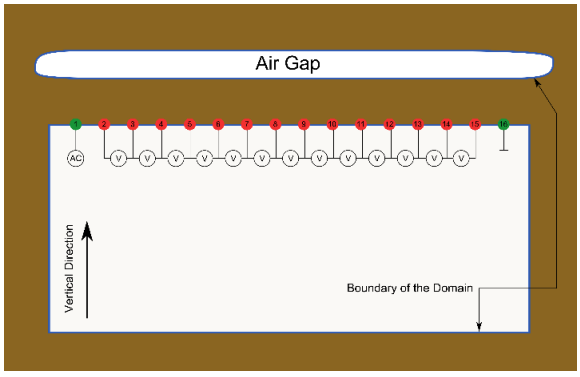

Fig. 1. Cross section of a copper mine, green and red circles denotes current and voltage electrodes, respectively, the boundary of air gap have to be localised as the final solution of the inverse problem

The electrical impedance tomography is very important field of research nowadays. It possesses many applications, for example this technique may be used in medical imaging, geophysics and other scientific areas. However, EIT is not easy to use due to necessity of solving the inverse problem during calculations. In three dimensional cases this requires a lot of computational effort. Using the level set method and the finite element method coupled together is proper way to solve the inverse problem. In particular all gaps in copper-mine ceiling can be localized.

1. Boundary element method

Physical phenomena are described usually by sets of differential equations. Numerical techniques give us opportunity to find approximate solutions of differential equations which cannot be solved by means of analytical ones. Among various numerical tools let us concentrate our attention on the boundary element method. BEM can be effectively employed on condition that partial differential equation can be transformed to integral form. Additionally, the Green's function has to be calculated. The explicit form of this one is desired. Often BEM can be easy coupled with other numerical methods or even analytical ones [1, 4]. Application of infinite boundary elements (IBEs) in BEM is rather less common because of difficulties with accurate numerical calculations of integrals with infinite limits of integration. In this paper we propose the generalisation of classical BEM with constant element interpolation for field function and its normal derivative by coupling with IBEs. For simplicity we consider Laplace's equation in two spatial dimensions.

Exterior domain with open boundary curve cannot be completely discretised by standard boundary elements with finite length. Hence, in the numerical model the IBEs should be introduced. So far several kinds of such boundary elements have been researched [9, 10, 17]. In case of IBEs one have to select interpolation functions which carry out appropriate conditions. In this paper we propose utilisation of the interpolation functions with exponential decay. This approach assumes that along IBEs the solution of differential equation and its normal derivative tend exponentially to zero. Speed of decay is described by one positive parameter.

It is clear that in realistic technical problems domains are usually finite. However, some engineering phenomena can be considered as unbounded domain problems and they are effectively solved using infinite elements.

Section 3 is the heart of this work and contains explanation of the theoretical model. The third section is devoted to numerical results and conclusions.

Let us consider the Laplace's equation in two-dimensional Cartesian coordinate system:

$$\frac{\partial^2 u(x,y)}{\partial x^2} + \frac{\partial^2 u(x,y)}{\partial y^2} = 0 \tag{1}$$

where $(x,y)\epsilon\Omega$. We assume that Ω is homogeneous open set in general. Additionally electrical potential (u) or its normal derivative (q) is known for all boundary points. The differential problem defined in described manner may be regarded as forward problem for the electric field. Starting point for our research is typical for BEM integral equation, where the boundary curve is divided into N elements:

$$c(\vec{r_i})u(\vec{r_i}) + \sum_{j=1}^{N}\int_{\Gamma_j} u(\vec{r})\,q^*(\vec{r},\vec{r_i})d\gamma_j = \\ = \sum_{j=1}^{N}\int_{\Gamma_j} q(\vec{r_i})\,u^*(\vec{r},\vec{r_i})d\gamma_j \quad (2)$$

Only three values of function c are possible for constant boundary elements. If a given point belongs to boundary of domain Ω, then the value equals 0.5. The value of function c equals 1, when a given point lies inside of Ω and equals 0 in other cases. The Green's function u* may be obtained by solving the fundamental equation and is given by the following formula:

$$u^*(\vec{r},\vec{r_i}) = \frac{1}{2\pi}\ln\left(\frac{A}{|\vec{r}-\vec{r_j}|}\right) \quad (3)$$

where A is a positive constant. Function q* represents derivative of the Green's function in normal direction appointed by unit vector $\vec{n}(\vec{r})$. After elementary calculations we get:

$$q^*(\vec{r},\vec{r_i}) = -\frac{1}{2\pi}\frac{\vec{n}(\vec{r})\cdot(\vec{r}-\vec{r_j})}{|\vec{r}-\vec{r_j}|^2} \quad (4)$$

The vector formula for j-th constant boundary element is given by:

$$q^*(\vec{r},\vec{r_i}) = -\frac{1}{2\pi}\frac{\vec{n}(\vec{r})\cdot(\vec{r}-\vec{r_j})}{|\vec{r}-\vec{r_j}|^2} \quad (5)$$

In order to extend our theoretical formalism into cases of open domain problems with infinite boundary curves, we have to introduce some modifications. Those modifications are attributable to infinite elements, which must be added to the set containing all finite boundary elements. If both quantities u and q are constant along given IBE, then some integrals appearing in BEM will be divergent. This difficulty disappears if we assume that quantities u and q tend asymptotically to zero.

The key step in our generalisation is proper choice of interpolation of u and q along IBE. If the boundary element is finite and we have three values for each quantity (three nodes), then the interpolation can be defined in the following way:

$$u(\xi) = \sum_{\alpha=f,m,l} \mathrm{N}_\alpha(\xi)u_\alpha \\ q(\xi) = \sum_{\alpha=f,m,l} \mathrm{N}_\alpha(\xi)q_\alpha \quad (6)$$

where, $\xi\epsilon\langle-1,1\rangle$, $\mathrm{N}_\alpha(\xi)$ are so-called interpolation functions:

$$\mathrm{N}_f(\xi) = 0.5\xi(\xi-1) \\ \mathrm{N}_m(\xi) = 1-\xi^2 \\ \mathrm{N}_l(\xi) = 0.5\xi(\xi+1) \quad (7)$$

One should notice that the function $\mathrm{N}_\alpha(\xi)$ takes value 1 for his "own" node and it takes value 0 for all other nodes. First of all, in order to expand the theory on IBEs we should multiply equations (7) by appropriate exponential factors. Every factor not have to modify the value of the interpolation function for her "own" node and it have to tends to zero for asymptotical values of the parameter ξ. For subsequent considerations let us assume $\xi\epsilon\langle-1,+\infty\rangle$. This conditions are satisfy when:

$$\mathrm{M}_f(\xi) = 0.5\xi(\xi-1)e^{-\frac{(1+\xi)}{\xi_e}} \\ \mathrm{M}_m(\xi) = (1-\xi^2)e^{-\frac{\xi}{\xi_e}} \\ \mathrm{M}_l(\xi) = 0.5\xi(\xi+1)e^{\frac{(1-\xi)}{\xi_e}} \quad (8)$$

Positive and dimensionless parameter ξ_e is responsible for speed of decay of electrical potential and its normal derivative along IBEs. Since for constant elements we have $u_f = u_l = u_m$ and $q_f = q_l = q_m$, so after changing $\mathrm{N}_\alpha(\xi)$ to $\mathrm{M}_\alpha(\xi)$ formulas (6) becomes:

$$u(\xi) = u_m S_\infty(\xi) \\ q(\xi) = q_m S_\infty(\xi) \quad (9)$$

where:

$$S_\infty(\xi) = \sum_{\alpha=f,m,l} \mathrm{M}_\alpha(\xi) \quad (10)$$

is the sum of the interpolation functions providing exponential decay. Generally, the sum (10) can be expressed as follows:

$$S_\infty(s_0\xi) = \left[2(s_0\xi)^2\sinh^2\left(\frac{1}{2\xi_e}\right) + s_0\xi\sinh\left(\frac{1}{\xi_e}\right) + 1\right]e^{-\frac{s_0\xi}{\xi_e}} \quad (11)$$

In above expression we assume that $s_0 = +1$ when the set of admissible values for parameter representing the IBE takes form $\Gamma_\xi = \langle-1,+\infty\rangle$, and $s_0 = -1$ when $\Gamma_\xi = \langle-\infty,+1\rangle$. Let us notice from formula (11) that in case of discussed elements the sum of interpolation functions is not equal one. The graph of the function $S_\infty(\xi)$ for several selected parameters ξ_e is shown in Figure 2. This figure shows unequivocal oscillations for small values of ξ_e. Therefore, during numerical calculations the condition $\xi_e \geq 2$ should be satisfied. One can notice that the amplitude of unphysical oscillations decreases when ξ_e is larger and larger.

On this stage of consideration it is possible to write down the new version of integral equation (2). Collecting previous modifications and making discretization we obtain:

$$c(\vec{r_i})u(\vec{r_i}) + \sum_{j=2}^{N-1} u_j\int_{\xi=-1}^{\xi=+1} q^*\left(\vec{r_j}(\xi),\vec{r_i}\right)d\gamma_j \\ +u_1\int_{\xi\to-\infty}^{\xi=+1} S_\infty(-\xi)q^*(\vec{r_1}(\xi),\vec{r_i})d\gamma_1 + \\ u_N\int_{\xi=-1}^{\xi\to+\infty} S_\infty(\xi)q^*(\vec{r_N}(\xi),\vec{r_i})d\gamma_N \\ = \sum_{j=2}^{N-1} q_j\int_{\xi=-1}^{\xi=+1} u^*\left(\vec{r_j}(\xi),\vec{r_i}\right)d\gamma_j + \\ q_1\int_{\xi\to-\infty}^{\xi=+1} S_\infty(-\xi)u^*(\vec{r_1}(\xi),\vec{r_i})d\gamma_1 + \\ q_N\int_{\xi=-1}^{\xi\to+\infty} S_\infty(\xi)u^*(\vec{r_N}(\xi),\vec{r_i})d\gamma_N \quad (12)$$

It is natural that the first and the last element of the boundary are infinite. The other N – 2 boundary elements have finite length. Equation (12) represents model in which area Ω is described by one open curve only. However, generalisation of the formula (12) is easy and may be done by adding appropriate terms.

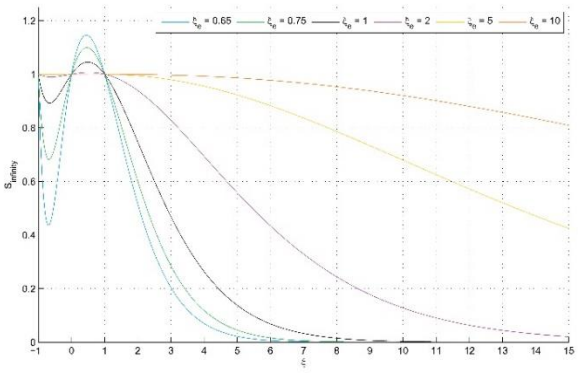

Fig. 2. The sum of the interpolation functions for IBEs defined by equation (11) (where s0 = +1) versus the curve parameter ξ for selected coefficients ξe

2. Electrical Impedance Tomography

Efficient algorithms for solving forward and inverse problem in electrical impedance tomography have to be developed in order to use this approach for practical tasks. Moreover, it is necessity to improve performance of selected numerical methods. Typical problem in EIT requires identification of unknown internal area from near-boundary measurements of the electrical potential. It is assumed that the value of the conductivity is known in subdomains whose boundaries are unknown. Geometrical structure of the problem researched in this paper is shown in Figure 7. Boundary element method is well known and effective numerical technique used to solve partial differential equations. Infinite boundary elements give us possibility to solve equations with boundaries described by open curves. Proposed model consists of several numerical methods. The optimisation algorithm, which minimalizes the objective function is shown in Figure 3.

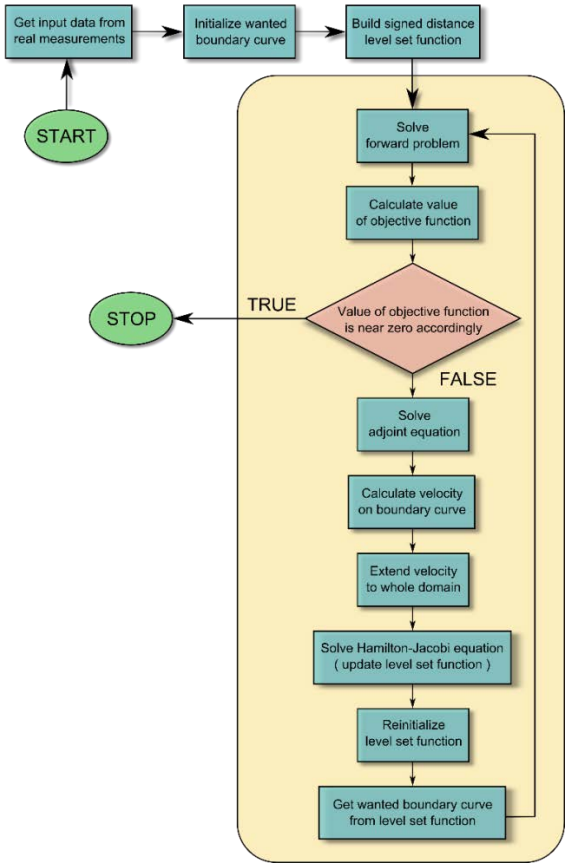

Fig. 3. Block diagram of the optimisation algorithm

3. Numerical results

The definite integrals present in equation (12) have been calculated by means of Gauss-Legendre quadrature, Gauss-Laguerre quadrature and Gauss quadrature with logarithmic weight function. Some diagonal integrals have been calculated analytically. The appropriate method has been chosen according to existence of singularity and type of domain of integration (finiteness or infiniteness). In numerical experiments we set $A = 10^{15}m$ *and* $\xi_e = 50$. Let us introduce open domain, where unit of length is the meter. The sketch of geometrical structure is given in Figure 4. One can notice that our geometry contains four IBEs. Whole boundary of the domain Ω is divided into forty elements (N = 40). Exact boundary conditions are expressed as:

$$u(x,y) = \begin{cases} -5V & for \quad x = 0 \\ +5V & for \quad x = m \end{cases} \tag{13}$$

In case of Laplace's equation (1), Dirichlet problem (13) has analytical solution. Normal derivative q is trivial to obtain and it takes following form on the boundary of the domain Ω:

$$q(x,y) = \begin{cases} -10Vm^{-1} & for \quad x = 0 \\ +10Vm^{-1} & for \quad x = m \end{cases} \tag{14}$$

However, one should remember that electrical potential tends exponentially to zero along IBEs. Therefore, parameter ξ_e should be large enough in order to create good approximation of conditions (13). Fig. 5a shows electrical potential for all nodes.

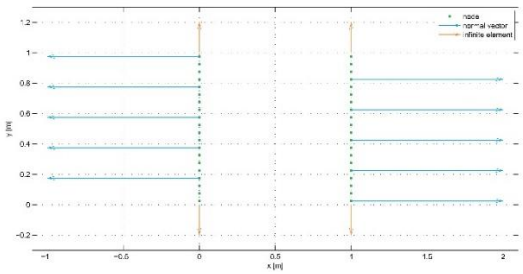

Fig. 4. The boundary problem: unit normal vectors are always outward pointing, positions of infinite elements are indicated

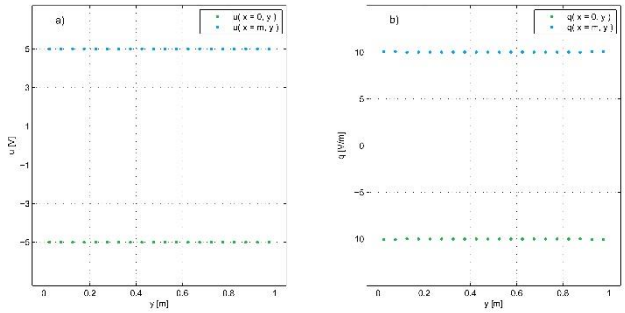

Fig. 5. The left graph a) presents the boundary conditions imposed on Laplace's equation, whereas the right graph b) shows the numerical solution

The solution of considered problem is given in Fig. 5b. From Fig. 6 we can see that percent errors are less than 0.7%. Good agreement of the numerical result with exact solution (14) is demonstrated. As we expected, reflectional symmetry exists in Fig. 6. Additionally, percent errors are the same for each straight line (x = 0; x = m). The numerical results show that our theoretical formalism gives appropriate approach to forward problem described by open boundary curves.

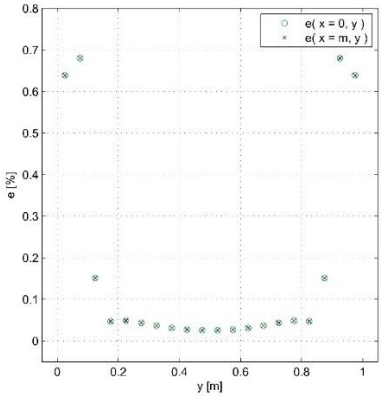

Fig. 6. The percent error obtained for the numerical solution of the Dirichlet problem

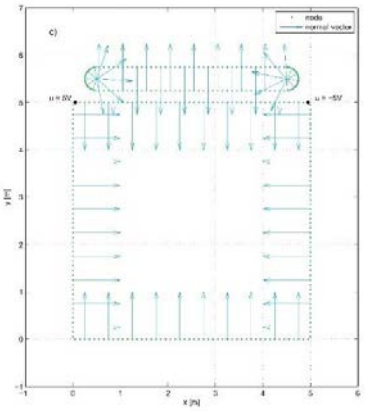

Fig. 7. Boundary problem: normal vectors and nodes on boundary elements are indicated

The definition of the boundary problem is shown in Figure 7. Normal vectors and nodes on boundary elements are indicated here. Figure 8 presents the image reconstruction of the copper-mine ceiling using BEM. The picture shows different object and the reconstructed image. The original object is noted by the blue line and the final figure is red. Figure 9 presents the image reconstruction in EIT obtained through the finite element method. The final contour represents the zero value of the level set function. The process of reconstruction is good, because the region borders are located nearly the object edges.

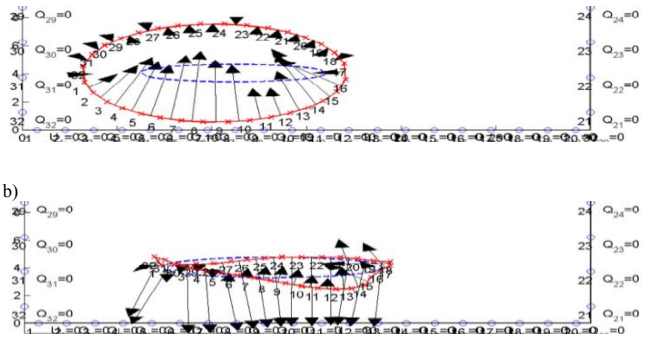

Fig. 8. Reconstruction by BEM and the level set method for the square area of the ceiling: a) the zero level set function and the searched object. b) the final reconstruction

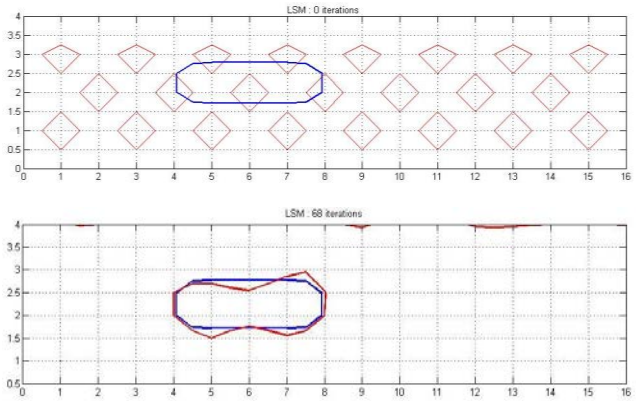

Fig. 9. Reconstruction by the finite element method and the level set method for the square area of the ceiling: a) the zero level set function and the searched object, b) the final reconstruction

4. Conclusion

In this paper, there was presented the method to solve the inverse problem for the electric field so-called copper mine problem. The level set idea is the good tool to the topological changes of the interface and gives the good quality reconstruction of unknown areas with one or many objects. All gaps in copper-mine ceiling were properly localized. This problem was motivated by electrical impedance tomography. Gaps were localised above ceiling in a copper mine. The applications were depended on a specially built model. There were used the boundary element method or the finite element method with the level set method to solve this problem. The level set function techniques were shown to be useful in this system. The boundary (finite) element method with the level set method gave the successfully results to identify the unknown properties of the object.

References

[1] Brebbia C.A., Dominguez J.: Boundary Elements – An Introductory Course, WIT Press, UK, 1992
[2] Burger M.: Levenberg-Marquardt: Level set methods for inverse obstacle problems, Inverse Problem 20, 2004, 259–282.
[3] Ito K., Kunish K., Li Z.: The Level-Set Function Approach to an Inverse Interface Problem, 2001, Vol. 17, 11.
[4] Kythe P.K.: An introduction to Boundary Element Methods, CRC Press, USA, 1995.
[5] Li C., Xu C., Gui C., Fox M. D.: Level set evolution without re-initialization: A new variational formulation, IEEE Conference on Computer Vision and Pattern Recognition (CVPR), volume 1, 2005, 430–436.
[6] Osher S., Fedkiw R.: Level Set Methods and Dynamic Implicit Surfaces. Springer, New York 2003.
[7] Osher, S., Fedkiw, R.: Level Set Methods: An Overview and Some Recent Results. J. Comput. Phys. 169, 2001, 463–502.
[8] Osher S., Sethian J.A.: Fronts Propagating with Curvature Dependent Speed: Algorithms Based on Hamilton-Jacobi Formulations, Journal of Computational Physics 79, 1988.
[9] Pańczyk M.: Elementy nieskończone w metodzie elementów brzegowych, PhD thesis, Lublin University of Technology, 2009.
[10] Pańczyk M., Sikora J.: Geometry and physical quantity transformations in 2D boundary element method with infinite elements, Proceedings of Electrotechnical Institute 3, 2007, 233.
[11] Rymarczyk T.: Using electrical impedance tomography to monitoring flood banks, International Journal of Applied Electromagnetics and Mechanics 45, 2014, 489–494.
[12] Rymarczyk T.: Characterization of the shape of unknown objects by inverse numerical methods, Przegląd Elektrotechniczny, R. 88 NR 7b/2012, 138–140.
[13] Rymarczyk T., Sikora J., Waleska B.: Coupled Boundary Element Method and Level Set Function for Solving Inverse Problem in EIT, 7th World Congress on Industrial Process Tomography, WCIPT7, 2-5 September 2013, Krakow, Poland
[14] Rymarczyk T., Adamkiewicz P., Duda K., Szumowski J., Sikora J.: New Electrical Tomographic Method to Determine Dampness in Historical Buildings, Achieve of Electrical Engineering 65, 2/2016, 273–283.
[15] Sethian J.A.: Level Set Methods and Fast Marching Methods. Cambridge University Press, 1999.
[16] Tai C., Chung E., Chan T.: Electrical impedance tomography using level set representation and total variational regularization. Journal of Computational Physics, vol. 205, no. 1, 2005, 357–372.
[17] Xia K., Zhang Z.: Three-dimensional finite/infinite elements analysis of fluid flow in porous media, Applied Mathematical Modelling, 30, 6, 2005.

Ph.D. Eng. Tomasz Rymarczyk
e-mail: tomasz.rymarczyk@netrix.com.pl

Director in Research and Development Center Netrix S.A. His research area focuses on the application of non-invasive imaging techniques, electrical tomography, image reconstruction, numerical modelling, image processing and analysis, process tomography, software engineering, knowledge engineering, artificial intelligence and computer measurement systems.

M.A. Paweł Tchórzewski
e-mail: pawel.tchorzewski@netrix.com.pl

Researcher in R&D Department – Netrix S.A.
A graduate of the Maria Curie-Sklodowska University Lublin on the physics (specializing in theoretical physics). Currently, the work carries out tasks profile research and development in the field of numerical methods for solving partial differential equations, electrical tomography in image reconstruction, forward and inverse problem. He is a Ph.D. student of the Institute of Electrical Engineering in Warsaw.

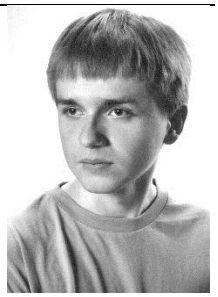

Prof. Jan Sikora
e-mail: sik59@wp.pl

Prof. Jan Sikora (Ph.D. D.Sc. Eng.) graduated from Warsaw University of Technology Faculty of Electrical Engineering. During 40 years of professional work he has proceeded all grades, including the position of full professor at his alma mater. Since 1998 he has worked for the Institute of Electrical Engineering in Warsaw. In 2008 he has joined Electrical Engineering and Computer Science Faculty In Lublin University of Technology. During 2001-2004 he has worked as a Senior Research Fellow at University College London in the prof. S. Arridge's Group of Optical Tomography. His research interests are focused on numerical methods for electromagnetic field.

otrzymano/received: 20.09.2016 *przyjęto do druku/accepted: 15.02.2017*

DOI: 10.5604/01.3001.0010.4591

MEASURING DATA ACQUISITION HARDWARE FOR ELECTRICAL IMPEDANCE TOMOGRAPHY

Tomasz Rymarczyk[1], Karol Duda[1], Paweł Rymarczyk[1], Daniel Olchowy[1], Jan Sikora[2,3]
[1]Netrix S.A., Research and Development Center, ul. Związkowa 26, 20-148 Lublin, [2]Lublin University of Technology, Institute of Electronics and Information Technology, [3]Electrotechnical Institute

Abstract. *This article presents the design of the device with active electrodes to examine the flood embankment. There was discussed the method of determining the conductivity. The presented solution was based on electrical impedance tomography. There was described the concept of active electrodes and measuring equipment for data acquisition. Electrical impedance tomography, which is based on measuring potential difference, can be used to calculate conductivity. The problem depends on the fact that every material has unique conductance.*

Keywords: Electrical Impedance Tomography, Active Electrodes, Flood Embankment

SYSTEM AKWIZYCJI DANYCH W ELEKTRYCZNEJ TOMOGRAFII IMPEDANCYJNEJ

Streszczenie. *W tym artykule przedstawiono konstrukcję urządzenia z aktywnymi elektrodami do badania stanu wału przeciwpowodziowego. Omówiono metodę wyznaczania konduktywności. Prezentowane rozwiązanie zostało oparte na elektrycznej tomografii impedancyjnej. Opisano koncepcję aktywnych elektrod i sprzętu pomiarowego do akwizycji danych. Elektryczna tomografia impedancyjna, która jest oparta na pomiarze różnicy potencjałów może być użyta do pomiaru konduktywności. Sposób, w jaki może być zdefiniowany polega na tym, że każdy materiał ma unikalną przewodność.*

Słowa kluczowe: elektryczna tomografia impedancyjna, aktywne elektrody, wał przeciwpowodziowy

1. System with Active Electrodes

Electrical impedance tomography (EIT) is known that the inverse problem is nonlinear and highly ill-posed [1,8-10]. The problem is the low level of measured values which should be measured quite accurately and in a very short time. EIT involves placing electrodes on the examined object. The two electrodes are connected to AC power and the voltage drop is measured on others [3, 7]. Then, power supply is connected to the next two electrodes, and measuring steps are repeated until each electrode is connected to power supply. Figures 1 and 2 present electrodes and model measurements of the flood embankments.

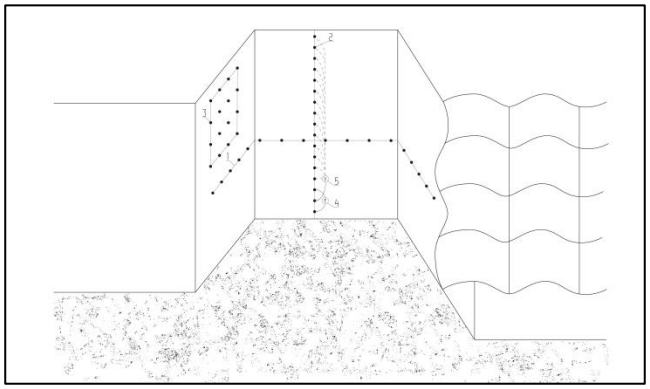

Fig. 1. The profile of the flood embankments

Figure 2 shows a plan view of an electrode with a straight front, with cross-section. Active electrode is designed to be placed in the ground, and its aim is to introduce current and measuring potential differences. The electrode consists of two parts: an active electrode and a quick rotating, which enables the galvanic connection of the active electrode portion of the electric wire. The active part of the electrode is made of rod 1, the tapered tip 2 and 3 lesions according to the drawing, which allow you to quickly pivot connection with the second part of the electrode. The electrode is located in the insulation 4. The second element electrodes - quick swivel consists of six parts: the cylindrical cap comprising a connector 7, the housing 8 of the spring 9, the tab 11, the locking ring spring 10, and connecting pins 12.

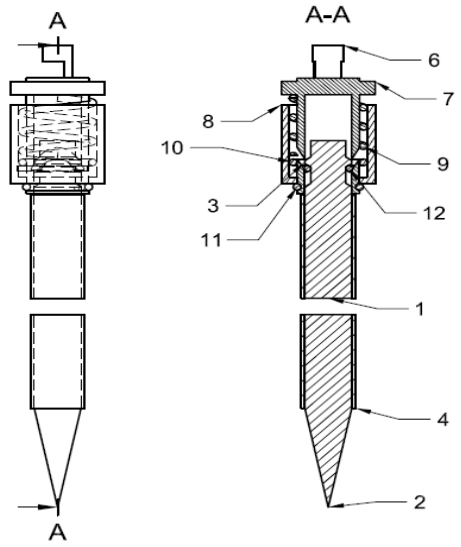

Fig. 2. The construction of active electrodes

2. EIT measurement device

The measurement in electrical impedance tomography involves placing electrodes on the examined object. This solution allows to obtain a conductivity distribution within the test object, and this consequently allows a distinction between materials of different conductivity. In carrying out further measurements over time and comparing them with previous we can observe the changes occurring in the study area [4]. Figure 3 presents the electrode arrangement for one projection angle [2, 5, 6].

The resolution of the image depends on the number of electrodes used and the accuracy of measured signals. To enhance the resolution, the number of electrodes should be increased. Then the number of necessary measurements will increase, which will result in greater demand for memory [11–14]. Figure 4 shows an exemplary result of the reconstruction of measurements on the circular container with 16 electrodes. The container was filled with water, in which was an empty glass bottle. Its position is marked with light green color.

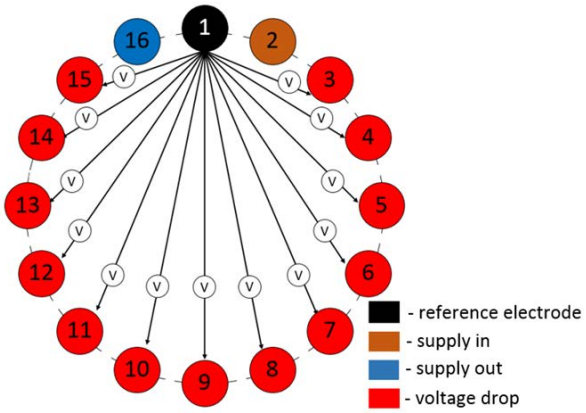

Fig. 3. Electrode arrangement for one projection angle

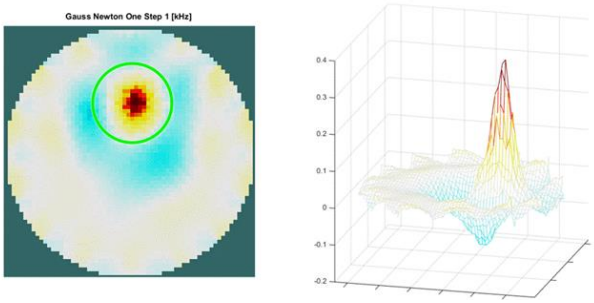

Fig. 4. An exemplary result of the reconstruction of measurements on the circular container with 16 electrodes

After achieving good with results, there was created a prototype of our device (Fig. 5). Its aim is to verify the repeatability of test results by eliminating laboratory equipment, and to validate the use of simple and cheap electronics the structure of the EIT.

The asset of such a device is to put the generator and the multiplexer on a small single circuit board, which allows mobility and enhances work comfort. Another advantage of this device is that the power supply voltage is 12V, and the maximum current is 60 mA, this reduces the energy requirements for carrying out image reconstruction of the test area.

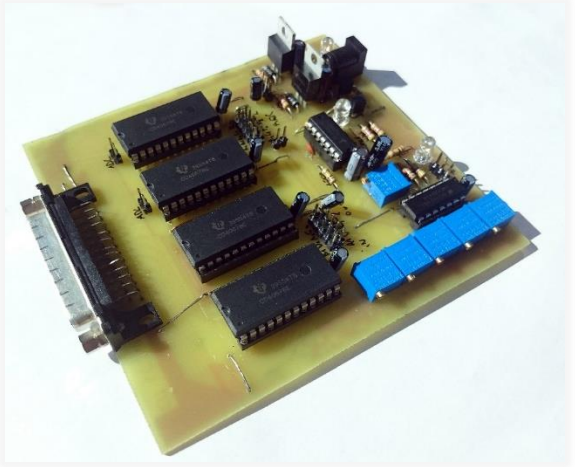

Fig. 5. The prototype of measuring device

The prototype device is controlled from a program written in LabView. The device allows for measurement of voltage drops for all angles of projection and save them to a file. The measuring device includes a program written in LabView environment, microcontroller evaluation board STM32 F4 Discovery, board with the generator and multiplexers. The general scheme of cooperation between all the components of the measurement system is shown in Figure 6.

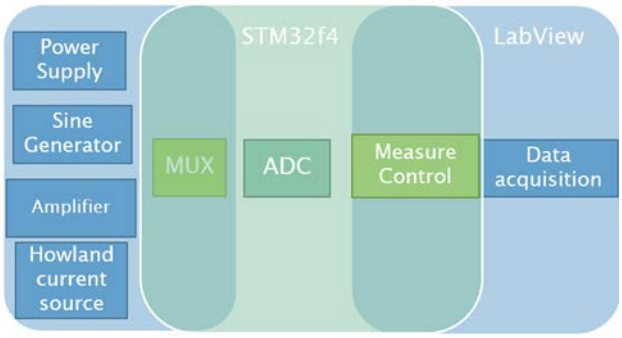

Fig. 6. Scheme of the block diagram operation of the measuring device

Modules measuring system - components

A. Measuring module Smart EIT in SMD – block (Fig. 7):
- 12V DC power supply,
- power supply LED,
- voltage regulator lm7805 and lm 7905,
- diodes,
- filtering capacitors.

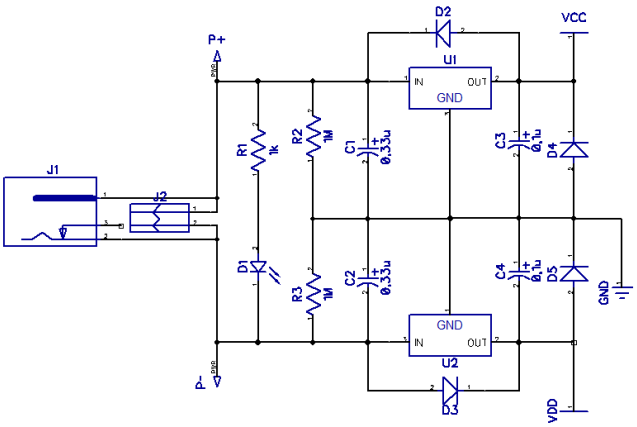

Fig. 7. Measuring module Smart EIT in SMD – power block

B. Measuring module Smart EIT in SMD – generator (Fig. 8):
- power control,
- two frequencies of 1 kHz and 50 kHz.

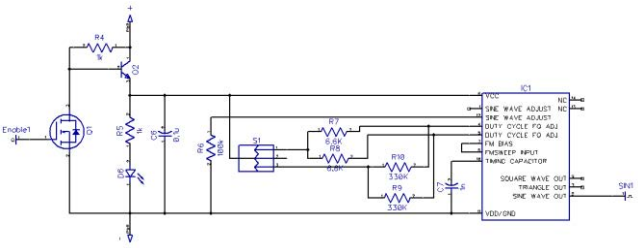

Fig. 8. Measuring module Smart EIT in SMD – generator

C. Measuring module Smart EIT (Fig. 9):
- DC signal filters,
- adjust the level of the control voltage,
- voltage follower,
- a Howland current pump.

D. Measuring module Smart EIT in SMD – multiplexer (Fig. 10):
- output to the electrode,
- 16-channel multiplexers,
- output connectors for ADC.

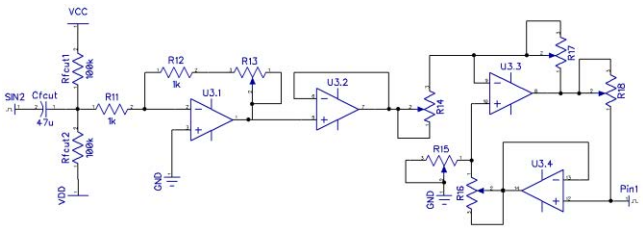

Fig. 9. Measuring module Smart EIT

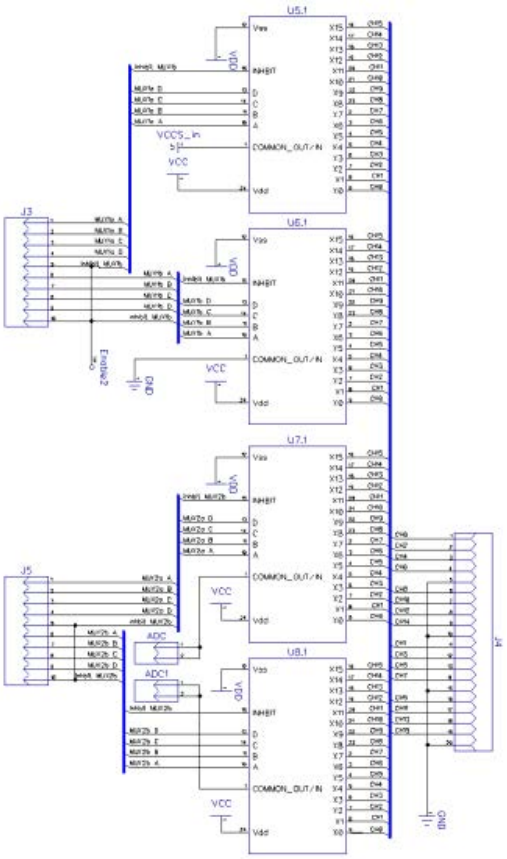

Fig. 10. Measuring module Smart EIT in SMD – multiplexer

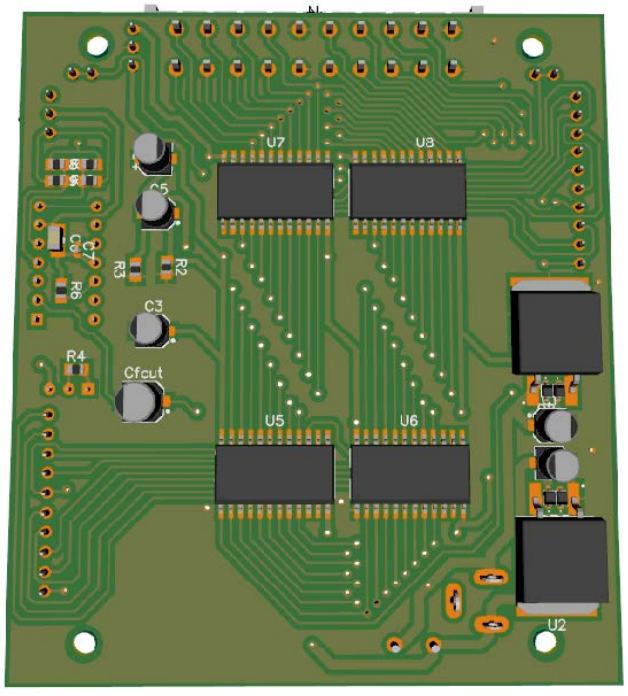

Fig. 11. Measuring module Smart EIT in SMD – plate

Figure 11 presents the measuring module Smart EIT in SMD.

E. Active electrode (Fig. 12):

- measurement of potential differences on the individual electrodes,
- chip LTC 2495,
- I2C communication,
- manual addressing - 27 addresses,
- 12V power supply,
- stabilizing voltage,
- signaling work LEDs
- RJ-45 connector.

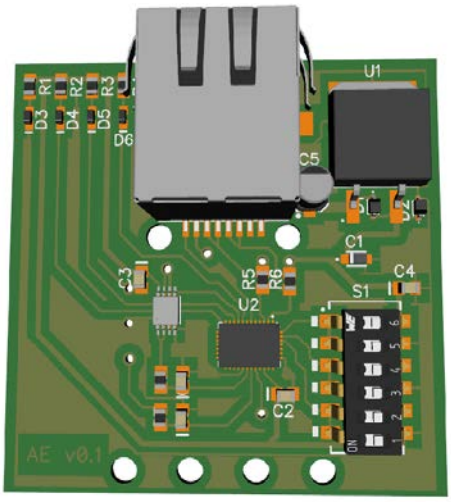

Fig. 12. Active electrode

F. Active electrode – power (Fig. 13):

- lm7905 voltage stabilizer,
- diodes,
- filter capacitors,
- power supply LED.

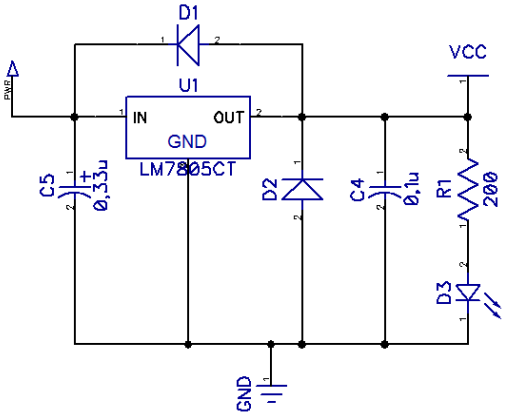

Fig. 13. Active electrode – power

3. Results

Achieved test results of the geometrical model were satisfactory. The flood embankment model was applied with water on the upstream side. Water line was near to the last 16 electrodes. The water started to percolate into the soil of the embankment model. Measurements of the potential were performed after 30 minutes. Measurements of the potential were performed at different angles of projection whereby the information needed to determine an approximate distribution of conductivity inside the object is obtained. The measurement system (flood embankment model, device and active electrodes) was presented in Figure 14. Figure 15 shows the image reconstruction with real data taken 15 minutes after flooding.

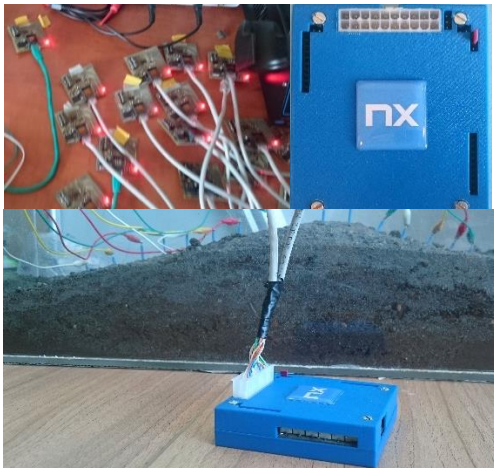

Fig. 14. The measurement system (flood embankment model, device and active electrodes)

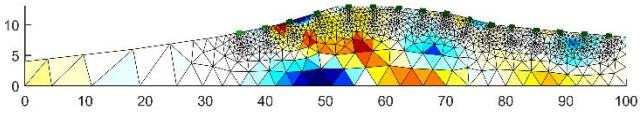

Fig. 15. The image reconstruction with real data obtained by the Gauss Newton method

4. Conclusion

In this paper, there was presented the construction of the device with active electrodes to examine the flood embankment. The prepared solution was based on electrical impedance tomography. The device parameters are correctly assumed According to our analysis and design, it is possible to build a small system EIT system to monitor flood embankments. A new nondestructive device was tested on the laboratory model. The flood embankment model was applied with water on the upstream side. The test results for prototype device were promising.

Acknowledgments

Projekt współfinansowany przez Unię Europejską z Europejskiego Funduszu Regionalnego. Działanie 1.4 – wsparcie projektów celowych. Umowa nr UDA-POIG.01.04.00-06-007/10-00. Nazwa Beneficjenta - Netrix S.A. dawniej Net-Art Paweł Rymarczyk. Tytuł projektu „Implementacja nowatorskich metod tomografii impedancyjnej do badania stanu wałów przeciwpowodziowych" (2011–2015).

References

[1] Adler A., Lionheart W.R.B.: Uses and abuses of EIDORS: an extensible software base for EIT, Physiological Measurement, Vol. 27, 2006.
[2] Gunna D.A., Chambersa J.E., Uhlemanna S., Wilkinsona P.B., Meldruma P.I., Dijkstraa T.A.: Moisture monitoring in clay embankments using electrical resistivity tomography, Construction and Building Materials, 2014.
[3] Hoła J., Matkowski Z., Schabowic K., Sikora J., Nita K., Wójtowicz S.: Identification of Moisture Content in Brick Walls by means of Impedance Tomography, COMPEL, Vol. 31, Issue 6, 2012, 1774–1792.
[4] Holder D.S.: Electrical Impedance Tomography: Methods, History and Applications Series in Medical Physics and Biomedical Engineering, London 2005.
[5] Jones G., Sentenac P., Zielinski M.: Desiccation cracking detection using 2-D and 3-D Electrical Resistivity Tomography: Validation on a flood embankment, Journal of Applied Geophysics, Vol. 106, 2014.
[6] Leondes C.T.: Medical imaging system techniques and applications, Gordon and Breach Science Publishers, Amsterdam 1997.
[7] Rymarczyk T. "Using electrical impedance tomography to monitoring flood banks", International Journal of Applied Electromagnetics and Mechanics 45, 2014, 489–494.
[8] Rymarczyk T., Filipowicz S.F., Sikora J., Polakowski K.: A piecewise-constant minimal partition problem in the image reconstruction, Przegląd Elektrotechniczny, R. 85 NR 12/2009, 141–143.
[9] Rymarczyk T., Adamkiewicz P., Duda K., Szumowski J., Sikora J.: New Electrical Tomographic Method to Determine Dampness in Historical Buildings, Achieve of Electrical Engineering, v.65, 2/2016, 273–283.
[10] Sankowski D., Sikora J.: Electrical capacitance tomography: Theoretical basis and applications, Wydawnictwo IEL, Warszawa 2010.
[11] Sikora J., Wójtowicz S.: Industrial and Biological Tomography: Theoretical Basis and Applications, Wydawnictwo IEL, Warszawa 2010.
[12] Smolik W., Radomski D, Performance evaluation of the iterative image reconstruction algorithm with sensitivity matrix updating based on real measurements for electrical capacitance tomography, Meas. Sci. Technol. Vol. 20, No. 11, 2009, 115502.
[13] Wajman R., Fiderek P., Fidos H., Jaworski T., Nowakowski J., Sankowski D., Banasiak R.: Metrological evaluation of a 3D electrical capacitance tomography measurement system for two-phase flow fraction determination; Meas. Sci. Technol., Vol. 24, 2013, No. 065302.
[14] Wang M.: Industrial Tomography: Systems and Applications, Elsevier 2015.

Ph.D. Eng. Tomasz Rymarczyk
e-mail: tomasz.rymarczyk@netrix.com.pl

Director in Research and Development Center Netrix S.A. His research area focuses on the application of non-invasive imaging techniques, electrical tomography, image reconstruction, numerical modelling, image processing and analysis, process tomography, software engineering, knowledge engineering, artificial intelligence and computer measurement systems.

M.Sc. Karol Krzysztof Duda
e-mail: karol.duda@netrix.com.pl

He graduated from the Technical University of Lublin, Mechatronics. Currently he engaged in the construction of EIT systems in Netrix SA. He is a Ph.D. student of the Institute of Electrical Engineering in Warsaw.

M.A. Paweł Rymarczyk
e-mail: pawel.rymarczyk@netrix.com.pl

He graduated at the School of Computer Science and Management in Rzeszów. Since 2012, He is a Ph.D. student of the Institute of Electrical Engineering in Warsaw. Research interests focus mainly on applications of computer science.

M.Sc. Daniel Olchowy
e-mail: daniel.olchowy@netrix.com.pl

He graduated from the Faculty of Electrical Engineering, Automatics, Computer Science and Electronics of AGH in Krakow and postgraduate studies in management accounting and controlling. The research focuses on the processing of data in impedance tomography and business intelligence systems.

Prof. Jan Sikora
e-mail: sik59@wp.pl

Prof. Jan Sikora (Ph.D. D.Sc. Eng.) graduated from Warsaw University of Technology Faculty of Electrical Engineering. During 40 years of professional work he has proceeded all grades, including the position of full professor at his alma mater. Since 1998 he has worked for the Institute of Electrical Engineering in Warsaw. In 2008 he has joined Electrical Engineering and Computer Science Faculty In Lublin University of Technology. During 2001-2004 he has worked as a Senior Research Fellow at University College London in the prof. S. Arridge's Group of Optical Tomography. His research interests are focused on numerical methods for electromagnetic field.

otrzymano/received: 20.09.2016 *przyjęto do druku/accepted: 15.02.2017*

DOI: 10.5604/01.3001.0010.4592

CONCEPT OF DETECTION SYSTEM TO LOCALIZE INSIDE CLOSED AREA BY RADIO TOMOGRAPHIC IMAGING

Tomasz Rymarczyk[1], Przemysław Adamkiewicz[1], Jakub Szumowski[1], Konrad Niderla[1], Łukasz Gołąbek[1], Jan Sikora[2,3]

[1]Netrix S.A. Dział R&D, ul. Wojciechowska 31, 20-704 Lublin, [2]Lublin University of Technology, Institute of Electronics and Information Technology, [3]Electrotechnical Institute

Abstract. *System for navigation and localization inside buildings will determine man's location in confined spaces with level of accuracy never yet achieved. System's operation will be mainly based on Bluetooth signals in accordance with the Beacon standard. A worldwide innovation will be the use of Radio Tomographic Imaging (RTI). This technology will enable tracking of moving objects by image reconstruction based on changes of electromagnetic field signal strength (RSS).*

Keywords: beacons, bluetooth, location inside buildings, radio tomographic imaging

KONCEPCJA SYSTEMU DETEKCJI DO LOKALIZACJI WEWNĄTRZ OBSZARÓW ZAMKNIĘTYCH Z WYKORZYSTANIEM TOMOGRAFII RADIOWEJ

Streszczenie*. System do nawigacji wewnątrz budynków będzie umożliwiał określenie pozycji człowieka w zamkniętych pomieszczeniach z dużą precyzją. Działanie systemu będzie opierało się na sygnałach Bluetooth zgodnie ze standardem Beacon.. Innowacyjnym rozwiązaniem będzie zastosowanie tomografii radiowej (ang. Radio Tomographic Imaging (RTI)). Wykorzystanie tej technologii umożliwi śledzenie poruszających się obiektów poprzez rekonstrukcję obrazu na podstawie zmian siły sygnału (RSS) pola elektromagnetycznego.*

Słowa kluczowe: beacons, bluetooth, lokalizacja wewnątrz budynków, tomografia radiowa

Introduction

Systems based on tomography and analysis involving the solution of the inverse problem for inaccessible areas are developed over many years [3-9]. In this work it has been presented the idea of creating a hybrid smart navigation and location inside buildings. Real Time Locating Systems is one of the most dynamically developing branches of ICT. They allow the spatial location of the object or person in real time. RLTS systems can be divided into systems operating in open spaces and working inside the buildings. First class system primarily uses technology (Global Positioning System) in combination of cellular systems and its best-known application is the location of persons/vehicles and fleet management. By using reliable and accurate GPS location technology development of systems of this type does not cause trouble. Unlike location systems for open spaces Indoor Positioning Systems cannot use GPS to determine the position inside buildings. For this reason, this issue is the importance of more complex both technically (there is a need to build a dedicated infrastructure) and scientific (the need to use complex algorithms which take into account the phenomenon of propagation inside buildings - multipath) [1, 2, 10].

1. System idea

The present system will make it possible to determine the position of man in confined spaces with unprecedented accuracy. This type of solution will be unique in the world. The system will be based largely on signals Bluetooth 4.0 LowEnergy according to the standard Beacon. At the same time intelligent hybrid system will be determined the position, using multiple sources of WiFi signal and data supplied by the sensors found in smartphones (gyroscope, accelerometer, magnetometer). An innovative solution in the world will also use Radio tomographic imaging (RTI) [11,12]. The use of this technology will enable the tracking of moving objects through image reconstruction on the basis of changes in signal strength (RSS) of the electromagnetic field between the transmitter and receiver (frequency WiFi 2.4 GHz). For this purpose, they will be designed and manufactured copyright dedicated devices "Beacon" using communication protocols WiFi and Bluetooth 4.0 LowEnergy. These devices are also equipped with copyright antenna transceiver directional characteristics.

2. Beacon

Becons are small wireless devices that use wireless communication (mainly Bluetooth BLE) to communicate with phone or tablet. Despite the fact that the device beacons were launched in 2013 and now has a number of entities created their own transmitters, still they are based on the same template uses to communicate only Bluetooth Smart (also known as BLE - Bluetooth 4.0 Low Energy). This is a method very accurate and quite unreliable. Particular attention should be paid to the innovative design of transceivers and the use of tomography using radio waves with a frequency of 2.4 GHz. The proposed innovation is the hybrid technique location different from the previously used using both signals BLE and WiFi.

Currently, in order to determine the approximate location of the mobile device is measured index values of radio signal strength (RSSI) between the two devices covering the range of operation of the passage of the same. Thanks to the hybrid model combining different interfaces and information from multiple sources. The system will be able to give much more accurate position of the localized object. The use of hybrid location will ensure stability of access to information, the stability of tracking the object and reading the dynamics of movement unprecedented in systems of this type. The client application will not focus exclusively on collecting and displaying properly correlated with the transmitter of information, but also take an active part in creating useful statistics for businesses and analyses. In case of any problems with radio communication application using the built-in accelerometer and gyroscope the mobile device will be able to lead the navigation until to restore and stabilize the connection.

3. Radio Tomography Imaging

Radio tomography bases its action on the measurement of the strength of the radio signal between the transmitter and the receiver. In the case where between the transmitter and the receiver an object is measured, signal strength value is changed, the due to reflection, absorption or scattering of electromagnetic waves (Fig. 1 and 2).

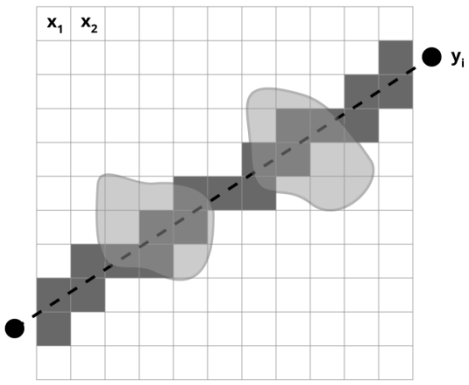

Fig. 1. Schematic diagram the course of a single wave between the transmitter and receiver

If K is the total number of transmitters (receivers) is the total number of independent pairs of "electrodes" expressed by the formula:

$$M = \frac{K^2 - K}{2}. \quad (1)$$

The averaged signal strength of the bidirectional link is referred to R-dependent:

- P_t – power transmitter,
- S_s – losses due to static objects,
- S_m – losses due to moving objects,
- F – signal interference narrowband,
- L_d – loss due to different distances between the transmitters,
- L_a – losses due to antenna mismatch,
- N – noise.

Mathematically, the received signal power (in dB) is described as:

$$R = P_t - L_d - L_a - S_s - S_m + F - N. \quad (2)$$

The model of the objects for the radio tomographic imaging, user and device location show Figure 3-8.

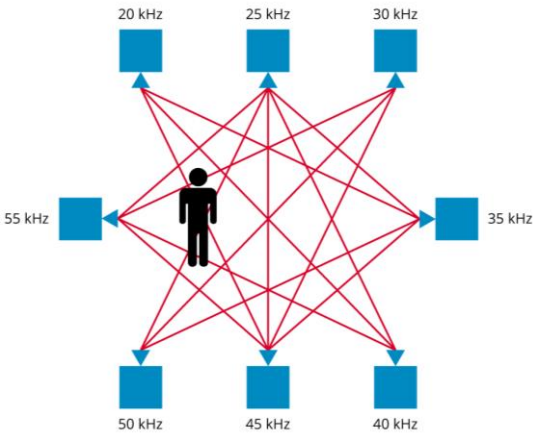

Fig. 2. The idea of radio tomographic imaging

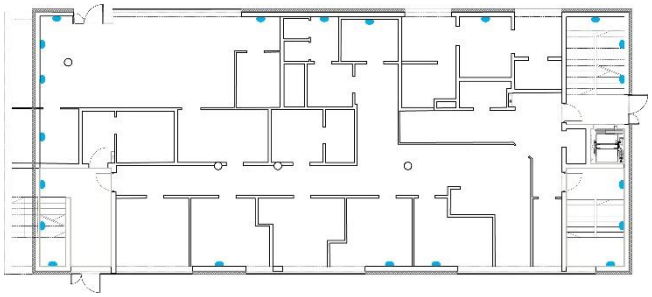

Fig. 3. Model of the object

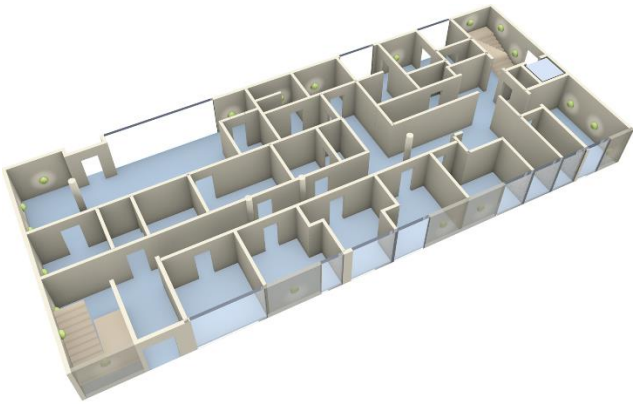

Fig. 4. Model of the object 3D

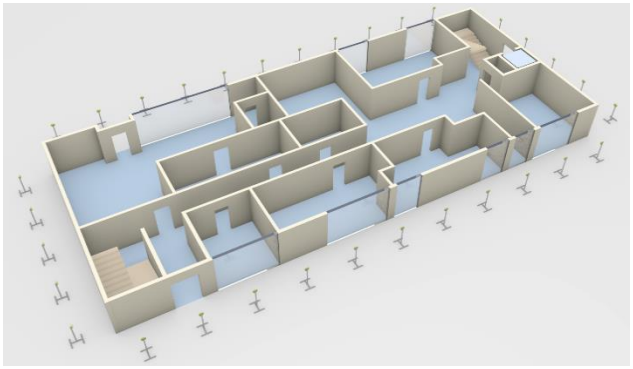

Fig. 5. Model of the object with sensor on the outside

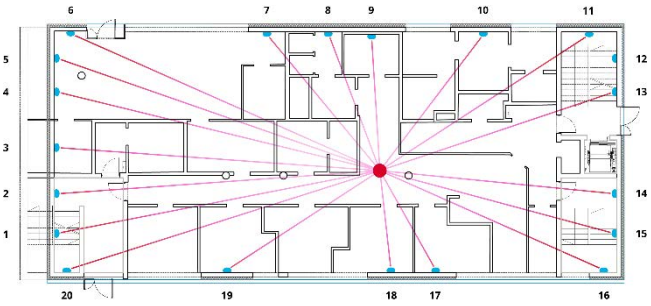

Fig. 6. Device location

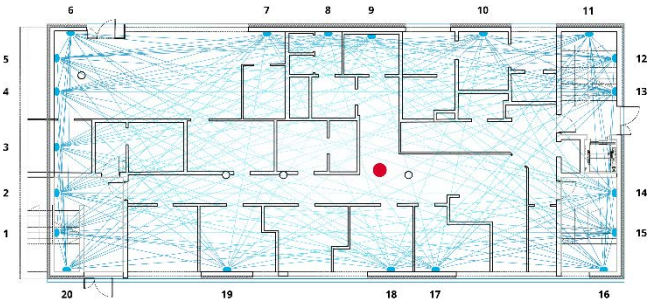

Fig. 7. User location

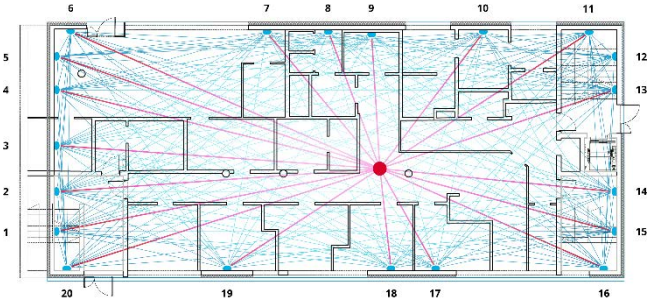

Fig. 8. User and device location

4. Devices

The project of device for radio location and communicating the phone presents in Figures 9 and 10.

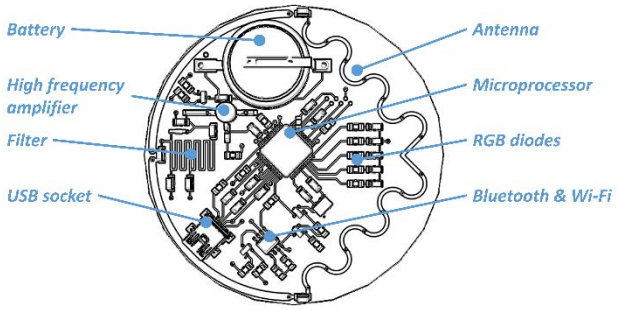

Fig. 9. A device for radio location

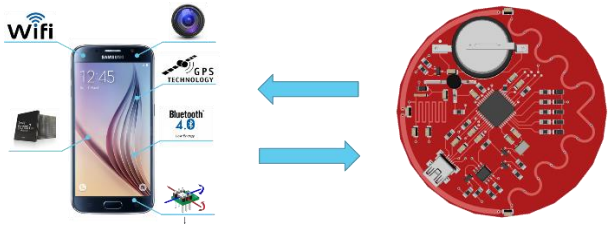

Fig. 10. Communicating the phone with the device

5. Ultra Wideband

Ultra wideband (UWB) is one of the techniques of radio-based fast sending short pulses. The duration of a single pulse of the order of tens of picoseconds, so the emission spectrum is very broad. UWB technology is developing wireless communication, which is characterized by high data rates (up to 2 Gb / s). UWB operates at a low power level, which eliminates interference from other radio systems and allows you to build devices with low power consumption. The system operates in the GHz range 3,1-10,6 (Mutli-Band OFDM).

Once an electrode is suitable (TX) signal, and then records the signals reflected from objects. If within the area there are people that signals are reflected and weakened. In this case, all of the independent electrodes to operate simultaneously.

Energy dependence of frequency for UWB and Narrowband is presented in Figure 11. Figure 12 shows schematic drawing of diffraction of radio waves UWB measurement sequence.

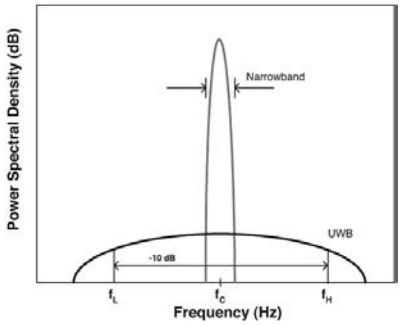

Fig. 11. Energy dependence of frequency for UWB and Narrowband

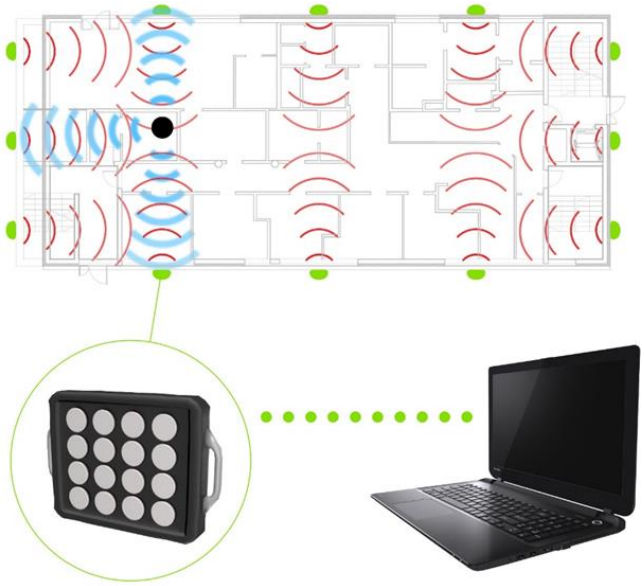

Fig. 12. Schematic drawing of diffraction of radio waves UWB measurement sequence

6. Image reconstruction in RTI

Using radio tomography for to the presented technology allows tracking of moving objects through image reconstruction on the basis of changes in signal strength (RSS) of the electromagnetic field between the transmitter and receiver (frequency WiFi 2.4 GHz). Through reconstruction of the image and the segmentation you will be able to very precisely determine the location of the human (Fig. 13).

The image reconstruction of the distribution of field lines and numbering of mesh elements are shown in Figure 14 and 15.

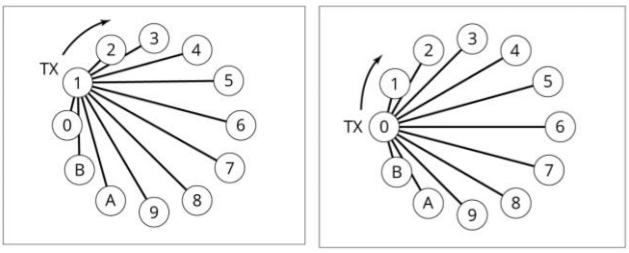

Fig. 13. The idea of location (signal) in the radio tomography

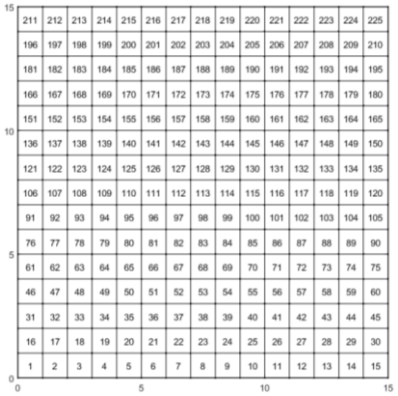

Fig. 14. Numbering of mesh elements

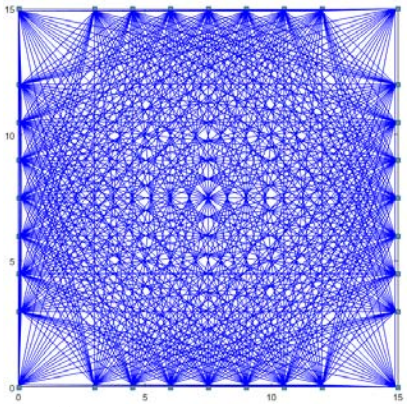

Fig. 15. Distribution of field lines

7. Conclusion

The concept of navigation system inside the buildings is based on radio tomography possible to determine the user's location using public facilities such as a smartphone, tablet and dedicated modules "Beacon". In contrast to currently used technologies proposed solution will enable you to determine the position with high precision (accuracy of 0.5 – 1.0 meters). The new technology will be based on its effect on communication protocols, such as WiFi and Bluetooth 4.0 LowEnergy. At the same time it will use sensors available in portable devices (gyroscope, accelerometer, magnetic field sensor) as well as the camera, so the system will be reliable in all conditions. Hybrid location inside the building, will be able to determine the position of the human even when density housing.

References

[1] Cisco IBSG Report, „Internet rzeczy – jak kolejna rewolucja Internetu wszystko zmienia", 2011.
[2] Narkiewicz J.: GPS. Globalny System Pozycyjny. Budowa. Działanie. Zastosowanie, Warszawa 2003.
[3] Rymarczyk T.: New Methods to Determine Moisture Areas by Electrical Impedance Tomography, International Journal of Applied Electromagnetics and Mechanics 08/2016, 1–9 [DOI:10.3233/JAE-16207].
[4] Rymarczyk T., Filipowicz S.F.: The Shape Reconstruction of Unknown Objects for Inverse Problems, Electrical Review, NR 5/2012/3a.
[5] Rymarczyk T.: Characterization of the shape of unknown objects by inverse numerical methods, Przegląd Elektrotechniczny, R. 88 NR 7b/2012, 138–140.
[6] Rymarczyk T., Filipowicz S.F., Sikora J., Polakowski K.: A piecewise-constant minimal partition problem in the image reconstruction, Przegląd Elektrotechniczny, R. 85 NR 12/2009, 141–143.
[7] Sankowski D., Sikora J.: Electrical capacitance tomography: Theoretical basis and applications, Wydawnictwo Książkowe Instytutu Elektrotechniki, Warszawa 2010.
[8] Sikora J., Wójtowicz S.: Industrial and Biological Tomography: Theoretical Basis and Applications, Wydawnictwo IEL, Warszawa 2010.
[9] Wang M.: Industrial Tomography: Systems and Applications, Elsevier 2015.
[10] Wan Mohd Yaakob Wan Bejuri, Mohd Murtadha Mohamad, Maimunah Sapri, Mohd Adly Rosly: Ubiquitous WLAN/Camera Positioning using Inverse Intensity Chromaticity Space-based Feature Detection and Matching: A Preliminary Result. International Conference on Man-Machine Systems 2012 (ICOMMS 2012), Penang, MALAYSIA.
[11] Wilson J., Patwari N.: Radio Tomographic Imaging with Wireless Networks, IEEE Transactions on Mobile Computing, vol.9, no. 5, 2010, 621–632.
[12] Wilson J, Patwari N.: Radio Tomographic Imaging with Wireless Networks, IEEE Transactions on Mobile Computing, 2009.

Ph.D. Eng. Tomasz Rymarczyk
e-mail: tomasz.rymarczyk@netrix.com.pl

Director in Research and Development Center Netrix S.A. His research area focuses on the application of non-invasive imaging techniques, electrical tomography, image reconstruction, numerical modelling, image processing and analysis, process tomography, software engineering, knowledge engineering, artificial intelligence and computer measurement systems.

Ph.D. Przemysław Adamkiewicz
e-mail: p.adamkiewicz@netrix.com.pl

Doctor of Physics, graduate of Maria Curia-Sklodowska University in Lublin. Head of R&D Department at Netrix SA.
His research area focuses on electrical tomography, image reconstruction, numerical modelling, image analysis and computer measurement systems.

Eng. Jakub Szumowski
e-mail: jakub.szumowski@netrix.com.pl

Electronic Engineer-Constructor. His research area focuses on electrical capacitance tomography - hardware solutions. Currently he works in R&D Department in Netrix SA A graduate of Lublin University of Technology majoring in electrical engineering.

Eng. Konrad Niderla
e-mail: konrad.niderla@netrix.com.pl

Konrad Niderla leads the company's Netrix SA software and-research department.
In his work deals with the development of new methods of control and measurement issues in automation and tomography.

M.A. Łukasz Gołąbek
e-mail: lukasz.golabek@netrix.com.pll

He is a PhD student of the Institute of Electrical Engineering in Warsaw. Research interests focus on the applications of computational intelligence in commercial systems.

Prof. Jan Sikora
e-mail: sik59@wp.pl

Prof. Jan Sikora (Ph.D. D.Sc. Eng.) graduated from Warsaw University of Technology Faculty of Electrical Engineering. During 40 years of professional work he has proceeded all grades, including the position of full professor at his alma mater. Since 1998 he has worked for the Institute of Electrical Engineering in Warsaw. In 2008 he has joined Electrical Engineering and Computer Science Faculty In Lublin University of Technology. During 2001-2004 he has worked as a Senior Research Fellow at University College London in the prof. S. Arridge's Group of Optical Tomography. His research interests are focused on numerical methods for electromagnetic field.

otrzymano/received: 20.09.2016 *przyjęto do druku/accepted: 15.02.2017*

DOI: 10.5604/01.3001.0010.4594

IDEA OF PARAMETRIC AND SEMANTIC OPEN PLATFORM SMART DEVICES SENSOR

Tomasz Rymarczyk[1], Grzegorz Kłosowski[2], Przemysław Adamkiewicz[1], Karol Duda[1], Jakub Szumowski[1], Paweł Tchórzewski[1]

[1]Netrix S.A. Dział R&D, ul. Wojciechowska 31, 20-704 Lublin, [2]Politechnika Lubelska, Katedra Organizacji Przedsiębiorstwa

Abstract. *The parametric and semantic model of open platform of intelligent devices and sensor technologies based on tomography in cyber-physical self-monitoring system contains: new techniques of conducting measurements and construction of novel intelligent measurement devices, system's structure along with communication interface, unique algorithms for data optimization and analysis, algorithms for image reconstruction and technological processes monitoring, cyber-physical system's prototype.*

Keywords: process tomography, artificial intelligence, sensors

KONCEPCJA PARAMETRYCZNO-SEMANTYCZNEJ OTWARTEJ PLATFORMY INTELIGENTNYCH URZĄDZEŃ SENSOROWYCH

Streszczenie*. Parametryczno-semantyczny model otwartej platformy inteligentnych urządzeń sensorowych został oparty na technologiach tomograficznych. W samo-monitorującym się systemie cyber-fizycznym zastosowano nowe techniki pomiarowe i konstrukcje inteligentnych urządzeń pomiarowych. Proponowane rozwiązanie prototypu systemu cyber-fizycznego składa się z interfejsu komunikacyjnego, unikalnych algorytmów do optymalizacji i analizy danych oraz systemu monitoringu procesów logistyczno-technologicznych.*

Słowa kluczowe: tomografia procesowa, sztuczna inteligencja, sensory

Introduction

In this work there was presented the idea of creating a platform for intelligent enterprise architecture open freely configurable and cooperation with external systems.
The system consists of the following components:

- New measurement techniques and design innovative smart metering devices.
- System structure and communication interface.
- New unique algorithms for optimization and data analysis.
- Algorithms for image reconstruction and monitoring processes, logistics and technology.
- The prototype cyber-physical platform.

The platform will be enable to manage the intelligent structure of the companies in terms of processes, products, simulation and virtual products. This will enable the optimization and auto-optimization of design processes, logistics and production. There will allow to track product cycle and provide for collaboration with external applications. The system will operate autonomously, monitoring, controlling, performing measurements and gathering the results. The collected data can be easily visualized. In addition, they will be used to create a unique knowledge base and will support the expert system [1, 3, 5, 13]. Systems based on tomography and solving the inverse problem for inaccessible areas are developed over many years [2, 4, 6–12, 14–21].

1. Platform

The proposed solution consists of the following components (Fig. 1):

I. The device monitoring and measuring

The measuring device will be responsible for data acquisition of sensors, pre-processing and transmission to the system server-web. Additionally, the system allows remote calibration of the sensors as well as monitoring and conditioning equipment manufacturing (Fig. 4-7 and Fig. 8-9).

II. The web-server with the client mobile

The measurement data will be stored on the server. A user from anywhere in the world will be able to manage the data collected through the portal and external systems. The collected data can be plainly visualized (Fig. 2).

III. Portal (Communication Platform)

Portal will allow the user to manage data stored on the server and will have elements such as orders, production orders, deliveries, invoices, statements, complaints virtual product (Fig. 3).

IV. External systems (communication platform)

This element will include interfaces for data exchange with the systems of customers and suppliers. Information on the state of cooperation will be available to suppliers from anywhere in the world thanks to cooperation with any external computer system.

V. Internal systems (communication platform)

Data exchange interface enables the cooperation of internal enterprise system, in which are recorded the economic processes of the server-platform web-based. For processes in which the information will be exchanged, among others: service purchases and sales, in accounting or personnel management.

VI. Expert System (module algorithmic analysis)

Expert system will be possible to optimize processes within the technology based on the knowledge base and data from sensors measuring.

VII. Automation and individualization of production (kernel)

The system based on the measurement data will assist the manufacturing process at each of its steps (automation and optimization).

VIII. Virtual product (Communication Platform)

Virtual product will be innovative and unique element of the system. The user will be able to individually design (select items) of the finished product. This element will enable the visualization of 2D and 3D product.

IX. Big data (kernel)

Base encyclopedic knowledge (experts), based on data from the measurement sensors and data provided by the users themselves (virtual product) will create a unique structure used in intelligent management.

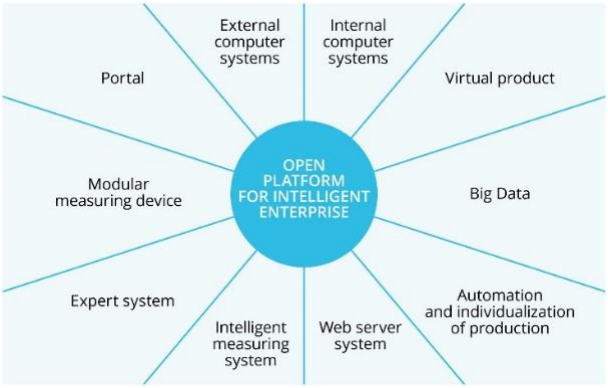

Fig. 1. The Idea of the system

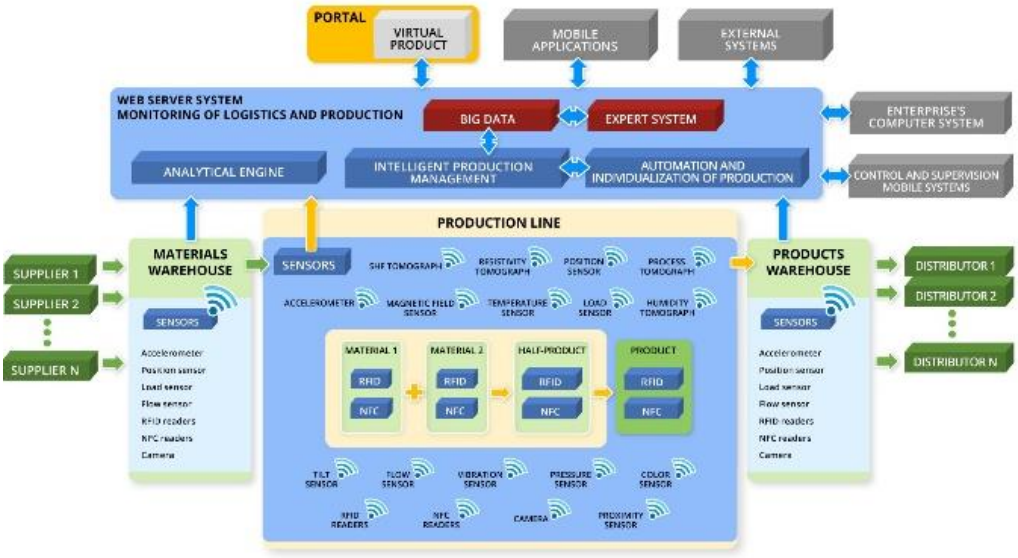

Fig. 2. System's functional model

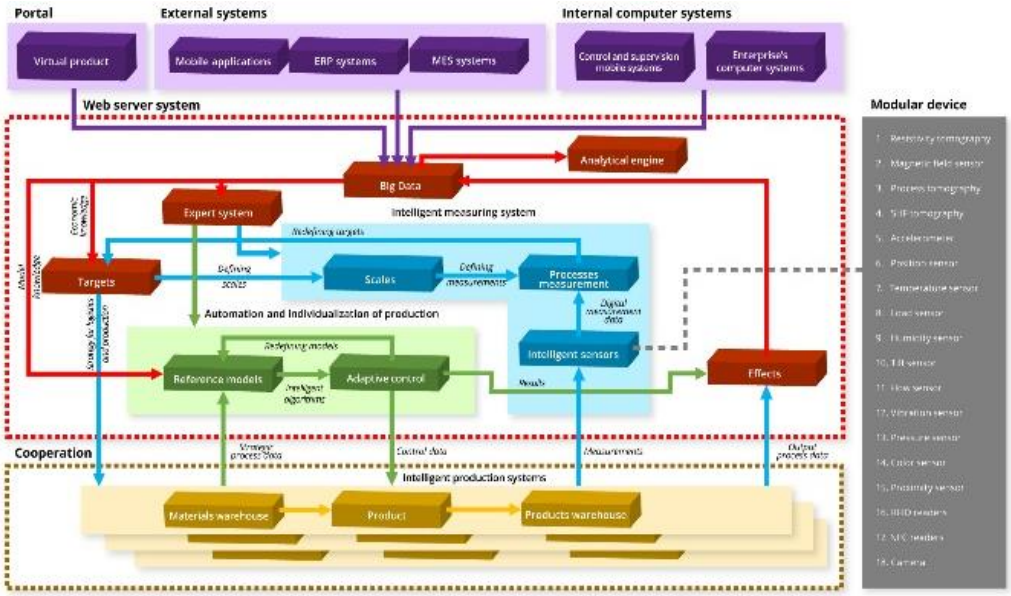

Fig. 3. System's process model

2. Devices

The platform will be communicated to measuring data acquisition and controlling devices and systems, such as: the smart ECT device (Fig. 4), the flow control system (Fig. 5), production lines, EIT device (Fig. 6), the hybrid ET device (Fig. 7), intelligent sensor devices (Fig. 8 and 9) and the multi-module device (Fig. 10).

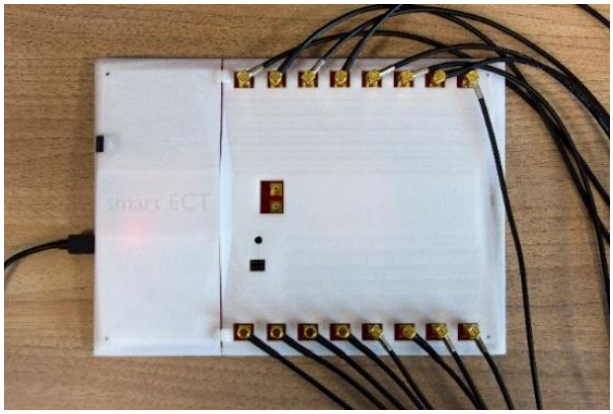

Fig. 4. Smart ECT device

Fig. 5. The main module of the system flow, where microprocessors control measurements

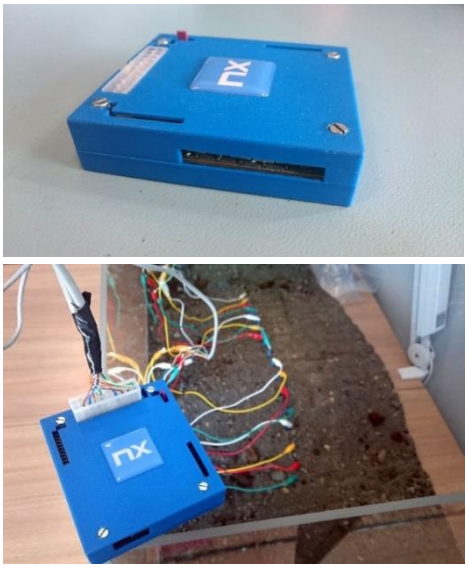

Fig. 6. EIT device

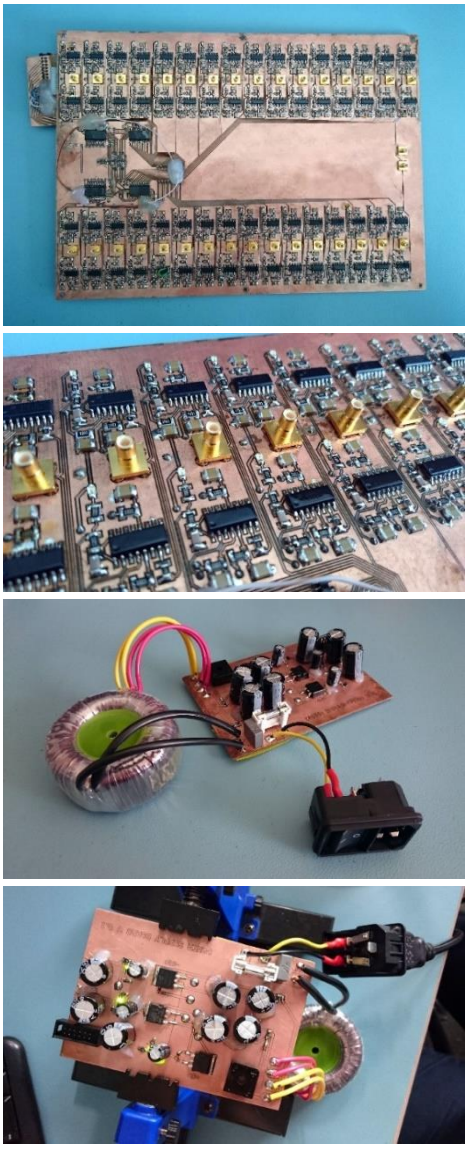

Fig. 7. The project of hybrid electrical tomography device (multiplexer and power supply)

3. Prototype sensor device

A prototype of a multi-module device is based on a multi-module measuring device (Fig. 10). Intelligent components measuring devices are the following: electrical tomography, sensor magnetic field tomography process tomography SHF, acceleration sensor, position sensor, temperature sensor, pressure sensor, humidity sensor, tilt sensor, flow sensor, vibration sensor, pressure sensor, color sensor, proximity sensors, RFID and NFC sensors.

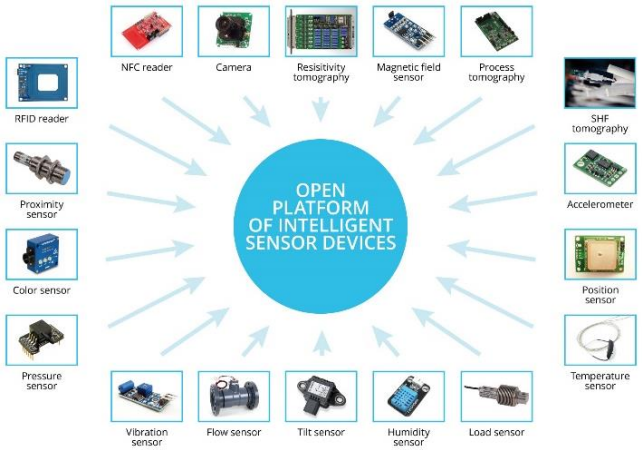

Fig. 8. The open platform of intelligent sensor devices

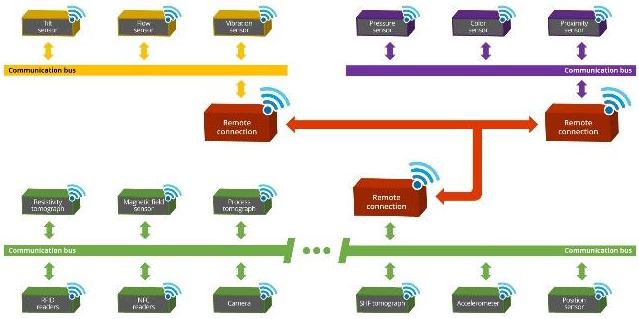

Fig. 9. System architecture of sensors devices

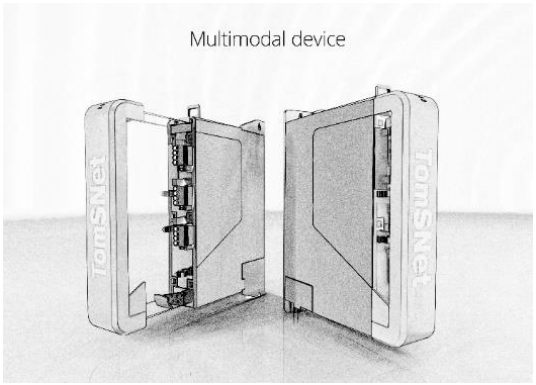

Fig. 10. Multi-module device

4. Results

The reconstructed data can be presented in graphical form using a graphical presentation of the data. The following figures show the reconstructed models and measurement data.

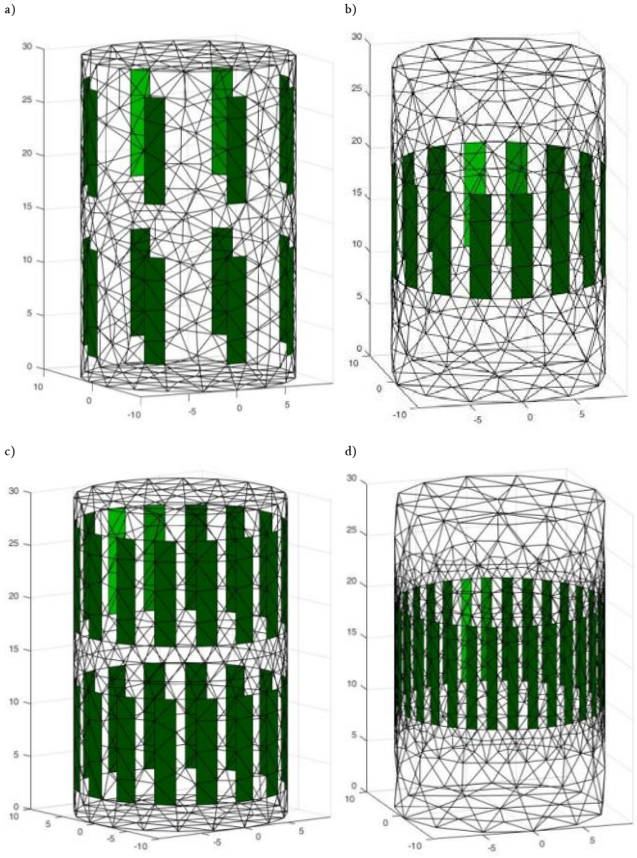

Fig. 11. Models of probes: a) 2×8 electrodes, b) 16 electrodes, c) 2×16 electrodes, d) 32 electrodes

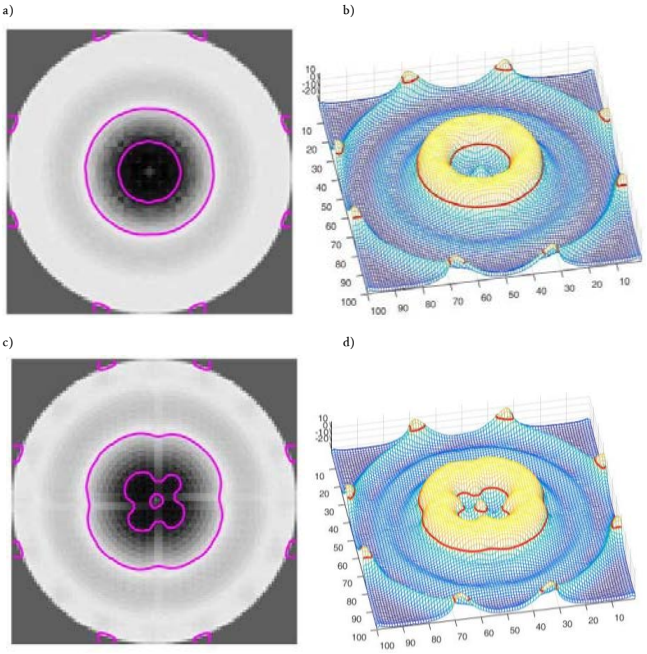

Fig. 12. Segmentation by the level set method

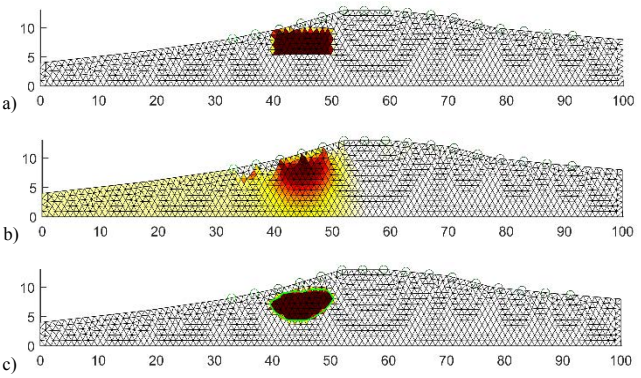

Fig. 13. The geometrical model I of the investigated flood embankment with 16 electrodes: a) the initial model, b) the reconstructed by Gauss-Newton method, c) the reconstructed by the level set method

Figure 11 show models of the different number probes: (a) 2×8 electrodes, (b) 16 electrodes, (c) 2×16 electrodes, (d) 32 electrodes. The segmentation flow by the level set method is presented in Figure 12. Figure 13 shows the geometrical model I of the investigated flood embankment with 16 electrodes, where (a) the initial model, (b) the reconstructed by Gauss-Newton method, (c) the reconstructed by the level set method. The objective function for this problem presents Figure 14.

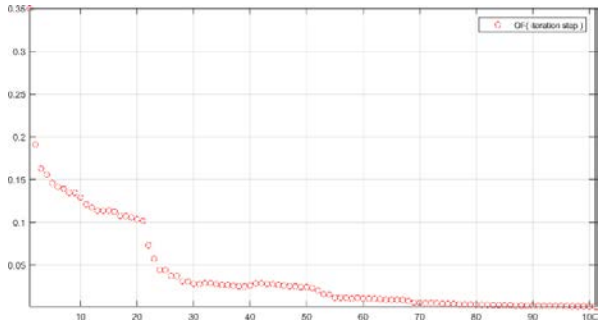

Fig. 14. The objective function for the model in Figure 13

5. Conclusion

The solution model of open platform of intelligent devices and sensor is based on technology tomographic and sensor networks. This system includes new measurement techniques and designs innovative smart measuring devices. The application structure covers a communication interface, unique algorithms for optimization and data analysis algorithms for image reconstruction and process monitoring.

References

[1] Beck M.S.: Process Tomography: Principles, Techniques and Applications, Elsevier Science 1995.
[2] Chen C., Wozniak P., Romanowski A., Obaid M., Jaworski T., Kucharski J., Grudzien K., Zhao S., Fjeld M.: Using Crowdsourcing for Scientific Analysis of Industrial Tomographic Images, ACM Transactions on Intelligent Systems and Technology (TIST),Vol. 7, 4, Article 52, 2016, [DOI: 10.1145/2897370].
[3] Filipowicz S.F., Rymarczyk T.: Tomografia impedancyjna, pomiary, konstrukcje i metody tworzenia obrazu, BEL Studio, Warszawa 2003.
[4] Kapusta P., Majchrowicz M., Sankowski D., Jackowska-Strumiłło L., Banasiak R.: Distributed multi-node, multi-GPU, heterogeneous system for 3D image reconstruction in Electrical Capacitance Tomography – network performance and application analysis. Przegląd Elektrotechniczny, Vol. 89, No. 2b, 2013, 339–342.
[5] Mosorov V.: A method of transit time measurement using twin plane electrical tomography, Measurement Science and Technology, v17, 4, 2006, 753–760.
[6] Musharavati F.: Process Planning Optimization in Reconfigurable Manufacturing Systems, Universal-Publishers 2010.
[7] Panczyk M., Sikora J.: A New imaging Algorithm for Electric Capacitance Tomography, Prace Instytutu Elektrotechniki, LXIII, Issue 274, 2016.
[8] Rymarczyk T.: New Methods to Determine Moisture Areas by Electrical Impedance Tomography, International Journal of Applied Electromagnetics and Mechanics 08/2016, 1-9, [DOI:10.3233/JAE-16207].
[9] Rymarczyk T., Filipowicz S.F.: The Shape Reconstruction of Unknown Objects for Inverse Problems, Electrical Review, NR 5, 3a, 2012.

[10] Rymarczyk T.: Characterization of the shape of unknown objects by inverse numerical methods, Przegląd Elektrotechniczny, R. 88 NR 7b/2012, 138–140.
[11] Rymarczyk T., Filipowicz S.F., Sikora J., Polakowski K.: A piecewise-constant minimal partition problem in the image reconstruction, Przegląd Elektrotechniczny, R. 85 NR 12/2009, 141–143.
[12] Sankowski D., Sikora J.: Electrical capacitance tomography: Theoretical basis and applications, Wydawnictwo Książkowe Instytutu Elektrotechniki, Warszawa 2010.
[13] Saravanan R.: Manufacturing Optimization through Intelligent Techniques, CRC Press 2006.
[14] Sikora J., Wójtowicz S.: Industrial and Biological Tomography: Theoretical Basis and Applications, Wydawnictwo IEL, Warszawa 2010.
[15] Sikora J.: Numeryczne metody rozwiązywania zagadnień brzegowych: Podstawy metody elementów skończonych i metody elementów brzegowych, Wydawnictwa Politechniki Lubelskiej, 2008, 2012, 2016.
[16] Smolik W., Radomski D.: Performance evaluation of the iterative image reconstruction algorithm with sensitivity matrix updating based on real measurements for electrical capacitance tomography, Meas. Sci. Technol. Vol. 20, No. 11, 2009, 115502.
[17] Smolik W.T., Szabatin R.: Non-invasive imaging of dynamic processes in ir-Lift chemical reactor using elextrical capacitance tomograph, 4th International Workshop on Process Tomography (IWPT-4), Chengdu, China, September 21-22, 2011.
[18] Smolik W., Kryszyn J., Radzik B., Stosio M., Wróblewski P., Wanta D., Dańko Ł., Olszewski T., Szabatin R.: Single Shot High Voltage Circuit for Electrical Capacitance Tomography, Meas. Sci. Technol., 2017.
[19] Smolik W, Forward Problem Solver for Image Reconstruction by Nonlinear Optimization in Electrical Capacitance Tomography, Flow Measurement and Instrumentation, Vol. 21, Issue 1, 2010, 70–77.
[20] Wajman R., Fiderek P., Fidos H., Jaworski T., Nowakowski J., Sankowski D., Banasiak R.: Metrological evaluation of a 3D electrical capacitance tomography measurement system for two-phase flow fraction determination; Meas. Sci. Technol., Vol. 24, 2013, No. 065302.
[21] Wang M.: Industrial Tomography: Systems and Applications, Elsevier 2015.

Ph.D. Eng. Tomasz Rymarczyk
e-mail: tomasz.rymarczyk@netrix.com.pl

Director in Research and Development Center Netrix S.A. His research area focuses on the application of non-invasive imaging techniques, electrical tomography, image reconstruction, numerical modelling, image processing and analysis, process tomography, software engineering, knowledge engineering, artificial intelligence and computer measurement systems.

Ph.D. Eng. Grzegorz Kłosowski
e-mail: g.klosowski@pollub.pl

Assistant Professor in the Department of Enterprise Organization in the Faculty of Management University of Lublin. Research interests include the author's artificial intelligence, simulation and modelling of production and business processes. The manager and participant in several implementation projects. Chairman of the board of the target company Lublin University of Technology, POLLUB-Invest Sp. o.o., whose mission is to commercialize indirect.

Ph.D. Przemysław Adamkiewicz
e-mail: p.adamkiewicz@netrix.com.pl

Doctor of Physics, graduate of Maria Curia-Sklodowska University in Lublin. Head of R&D Department at Netrix SA.
His research area focuses on electrical tomography, image reconstruction, numerical modelling, image analysis and computer measurement systems.

M.Sc. Eng. Karol Duda
e-mail: karol.duda@netrix.com.pl

He graduated from the Technical University of Lublin, Mechatronics. Currently he engaged in the construction of EIT systems in Netrix SA. He is a Ph.D. student of the Institute of Electrical Engineering in Warsaw.

Eng. Jakub Szumowski
e-mail: jakub.szumowski@netrix.com.pl

Electronic Engineer-Constructor. His research area focuses on electrical capacitance tomography - hardware solutions. Currently he works in R&D Department in Netrix SA A graduate of Lublin University of Technology majoring in electrical engineering.

M.A. Paweł Tchórzewski
e-mail: pawel.tchorzewski@netrix.com.pl

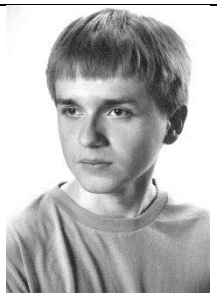

Researcher in R&D Department - Netrix S.A.
A graduate of the Maria Curie-Sklodowska University Lublin on the physics (specializing in theoretical physics). Currently, the work carries out tasks profile research and development in the field of numerical methods for solving partial differential equations, electrical tomography in image reconstruction, forward and inverse problem. He is a Ph.D. student of the Institute of Electrical Engineering in Warsaw.

otrzymano/received: 20.09.2016 *przyjęto do druku/accepted: 15.02.2017*

DOI: 10.5604/01.3001.0010.4595

IDEA OF ELECTRICAL TOMOGRAPHY SYSTEM FOR MONITORING LUNG VENTILATION

Tomasz Rymarczyk, Przemysław Adamkiewicz, Paweł Tchórzewski
Netrix S.A., Research and Development Center, Związkowa Str. 26, 20-148 Lublin, Poland

Abstract. *In many applications of electrical tomography, such as monitoring the lungs of unconscious intensive care patients, data acquisition on the entire boundary of the body is impractical. The boundary area available for electrical tomography measurements is restricted. Physiological processes that produce changes in the electrical conductivity of the body can be monitored by hybrid algorithms. This paper presents the architecture of the system based on electrical tomography.*

Keywords: inverse problem, finite element method, electrical impedance tomography

IDEA SYSTEMU TOMOGRAFII ELEKTRYCZNEJ DO MONITOROWANIU WENTYLACJI PŁUC

Streszczenie*. W wielu zastosowaniach tomografii elektrycznej, takich jak monitorowanie płuc pacjentów podlegających intensywnej opiece medycznej, zbieranie danych na całej powierzchni ciała jest niepraktyczne. Dostępne obszary dla pomiarów tomografii elektrycznej są ograniczane. Procesy fizjologiczne, które wywołują zmiany w przewodnictwie elektrycznym w organizmie mogą być monitorowane za pomocą algorytmów hybrydowych. W artykule przedstawiono architekturę systemu opartego na tomografii elektrycznej.*

Słowa kluczowe: zagadnienie odwrotne, metoda elementów skończonych, tomografia impedancyjna

Introduction

This paper presents the architecture of the system collecting data and analyzing medical data by electrical impedance tomography (EIT) [10–13, 16, 17] and electrical capacitance tomography (ECT) [14, 18]. To develop new technology and equipment for an in vivo human body screening and examination is the aim of this concept. The system will operate using the advanced analog-digital device for high-speed recording and high-sensitivity measurement. It will be able to distinguish very small changes of electrical parameters. In current medical research, it is noted that electrical properties of tissues differ depending whether they are healthy or altered. In this solution, it will be possible to externally examine such properties of various parts of the human body. The solution will allow to image dynamic processes taking place inside internal organs by simultaneous reconstruction of electrical permittivity and conductivity. The system will allow to monitor lung ventilation, lung blood flow, cardiac output and lung pathological changes of ill patients. Images obtained will be of moderate resolution, yet anatomical structures will be possible to identify with reasonable confidence. This new equipment will provide more accurate, reliable and early disease diagnosis, which will lead to improvement of clinical decisions and their outcomes. Proposed system will be able is to assist during medical procedures in which no potentially detrimental analysis methods such as X-ray, high power magnetic field or contrasts should be used. Therefore, those procedures will become much safer for patients.

Respiratory diseases are very common nowadays. Their development in both, acute and chronic cases is determined with multiple factors (e.g. environmental pollution, stress). Early diagnostics or constant non-ambulatory monitoring is, unfortunately, not possible. System will consist of dedicated mobile device for registering heartbeat electrical potentials as well as lungs ventilation. It will support process of diagnostics and monitoring of patients' condition in cases of:

- Acute respiratory distress syndrome.
- Chronic obstructive pulmonary disease.
- Bronchoconstriction.
- Pneumonia.
- Pulmonary hypertension.
- Obstructive sleep apnea.
- Pneumothorax.
- Cardiac hemodynamics.
- Aortic insufficiency.
- Hypertension.
- Ischemic heart disease.

Numerical algorithms were based on the level set methods and Gauss-Newton method [5, 7–9, 15].

1. Electrical Tomography

Electrical tomography is an extremely ill-posed inverse problem and high resolution imaging would require unpractically accurate current injection, voltage measurement, low noise levels, and large number of electrodes attached to the boundary of the object. In electrical impedance tomography, electrical currents are injected into an object using a set of electrodes attached on the boundary of the object and the resulting electrode potentials are measured. The conductivity of the object is reconstructed as a spatially distributed parameter based on the known currents and measured potentials. Electrical tomography is an imaging technology in which the electrical conductivity of a body is estimated as a spatially distributed parameter based on measurements of electrical currents and. In absolute imaging, the conductivity distribution is estimated using a single set of potential measurements, where the conductivity is modeled. Applications of EIT include monitoring of heart and lungs. Several medical solutions have been proposed including lung function monitoring of intensive care patients. In medicine, the injected currents are small and harmless to the patient. Almost real-time imaging with tens of frames per second can be achieved with devices small enough to reside by the bedside. This makes electrical impedance tomography attractive especially for constant monitoring. The accuracy of the positioning of the electrodes on the boundary is also a concern as well as that in two-dimensional imaging the injected currents are not confined to travel on the plane determined by the electrodes [1–6].

The electromagnetic field induced by applying a current density to the surface of the body is governed by Maxwell's equations. At low frequencies and small field strengths the electromagnetic properties of living tissue allow these to be simplified to the conductivity equation:

$$\nabla \cdot \big(\gamma(x,y)\nabla u(x,y)\big) = 0, \qquad (x,y) \in \Omega \tag{1}$$

where, Ω denotes a bounded region in the plane, γ denotes the conductivity of the body, and u the electric potential.

2. System idea

A prototype of multimodal tomographic system for medical applications will be created by building a hardware prototype and preparing dedicated software which will analyze medical images using the topological methods and artificial intelligence algorithms and their hybridization. It will result in much better quality of the image reconstruction than in current solutions.

Figure 1 presents the idea of the electrical tomography measurement system. There was designed Lungs Electrical Tomography System (Fig. 4), 3D model of pulmonary (Fig. 2), the EIT measurement belt (Fig. 3) and active electrodes (Fig. 5). The idea of hardware and software system id presented in Fig. 6-8.

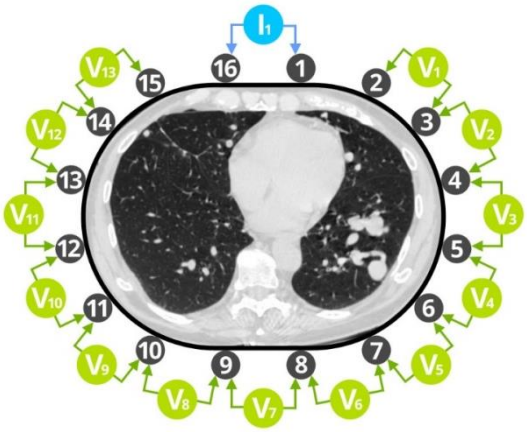

Fig. 1. The idea of the measurement system

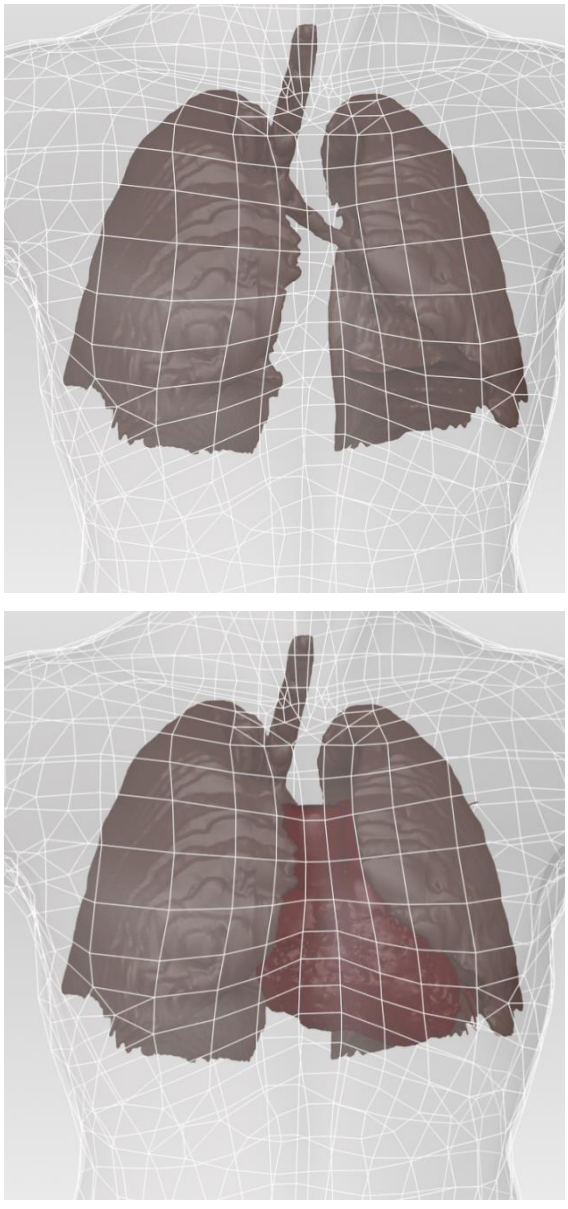

Fig. 2. The model of pulmonary

Fig. 3. The EIT measurement belt

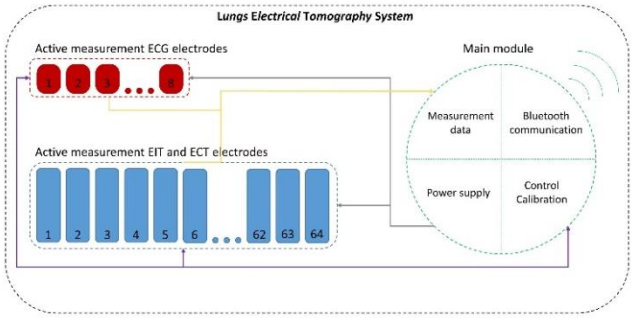

Fig. 4. Lungs Electrical Tomography System

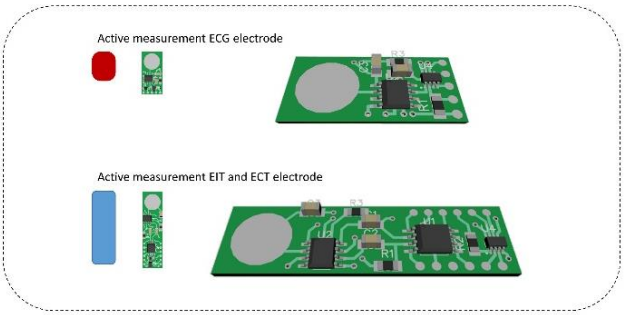

Fig. 5. Active electrodes

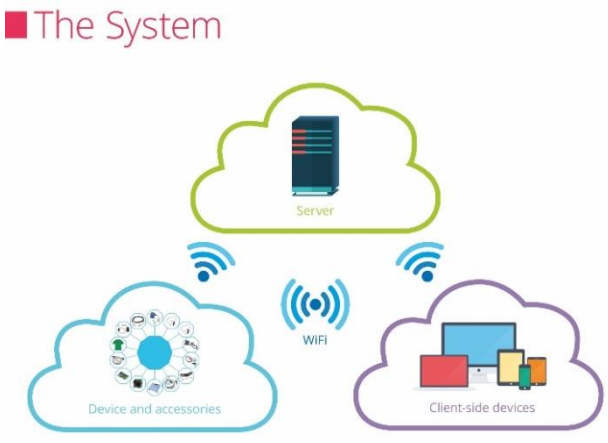

Fig. 6. The idea of system

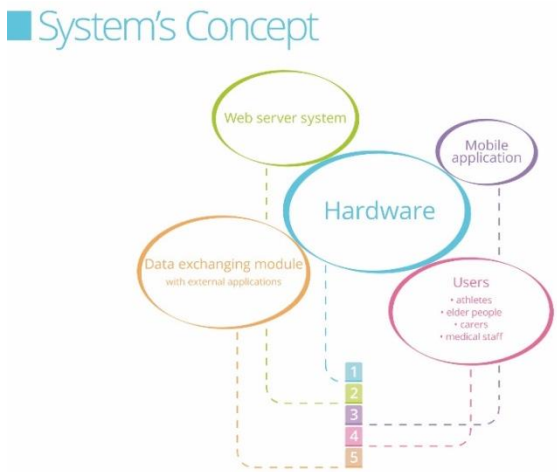

Fig. 7. The concept of solution

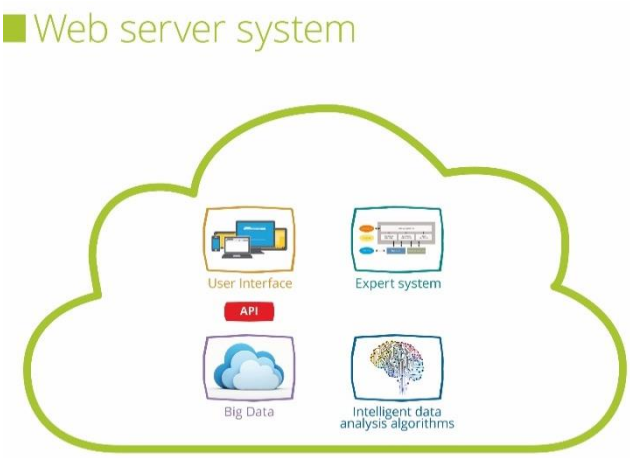

Fig. 8. Web server system

3. Results

Examples show lung imaging without a change of the thorax shape. This test case was done to produce a reference case of lung imaging comparing the image reconstruction between the Gauss-Newton method and the level set method.

In clinical situations, the thorax shape varies due to breathing and changes of the patient position during the measurements. For this reason, we simulate a more realistic case in lung shapes.

Figure 9 and 12 present the geometrical model lungs I and II with 16 electrodes, where (a) the initial model, (b) the reconstructed by Gauss-Newton method, (c) zero level set function, (d) differences between the initial object and the final solution, (e) the reconstructed by the level set method. Figure 10 and 11 present the objective function for the tested models.

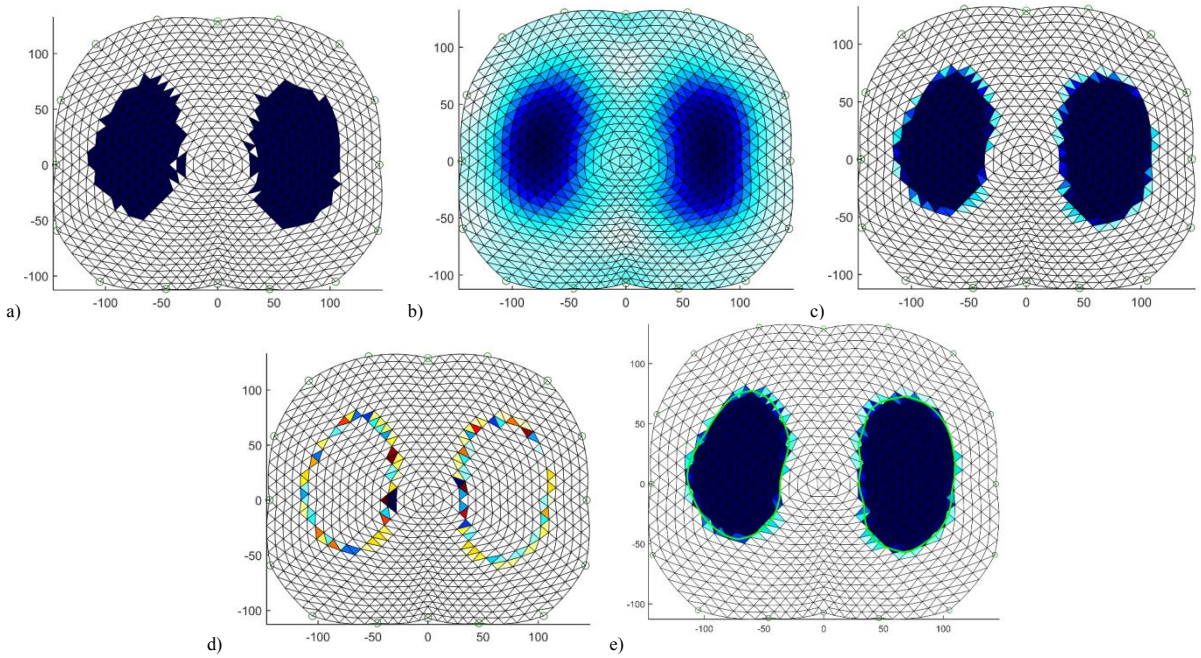

Fig. 9. The geometrical model lungs I with 16 electrodes: a) the initial model, b) the reconstructed by Gauss-Newton method, c) zero level set function, d) differences between the initial object and the final solution, e) the reconstructed by the level set method

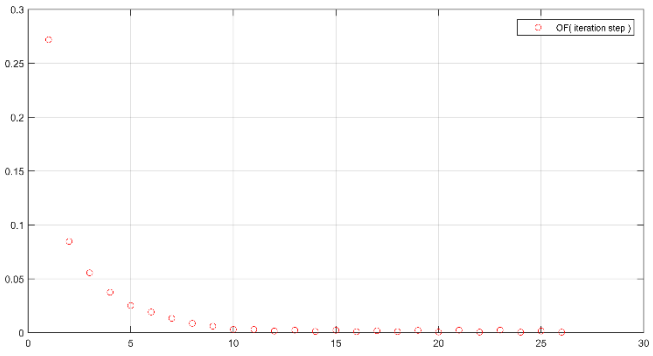

Fig. 10. The objective function for the model in Figure 9

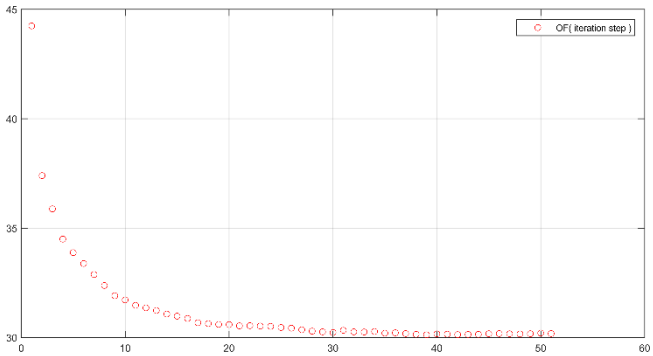

Fig. 11. The objective function for the model in Figure 11

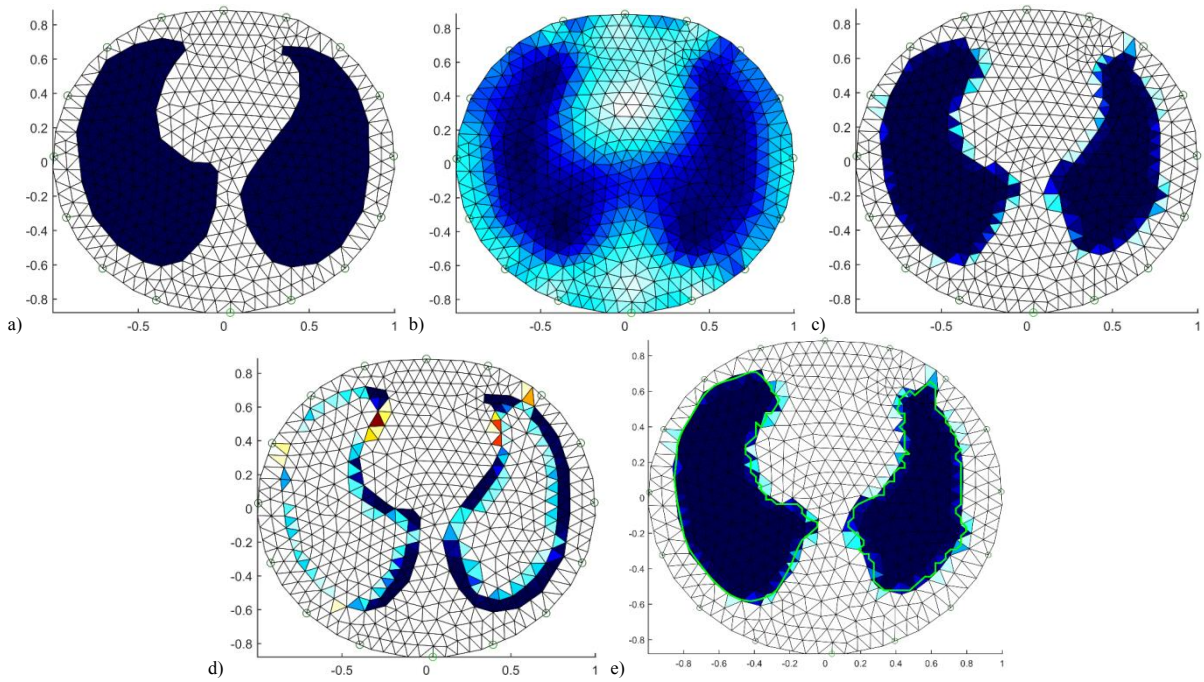

Fig. 12. The geometrical model lungs II with 16 electrodes: a) the initial model, b) the reconstructed by Gauss-Newton method, c) zero level set function, d) differences between the initial object and the final solution, e) the reconstructed by the level set method

4. Conclusion

In this paper, there was proposed an approach to EIT image reconstruction in cases where the Gauss-Newton and level set methods were implemented. In the proposed approach, the conductivity after the change is represented as a linear object. There was presented the architecture of the system based on electrical tomography.

References

[1] Adler A., Lionheart W.R.B.: Uses and abuses of EIDORS: an extensible software base for EIT, Physiological Measurement, Vol. 27, 2006.
[2] Alberto-P. Calder´on, On an inverse boundary value problem, (Rio de Janeiro, 1980), Soc. Brasil. Mat., Rio de Janeiro, 1980, 65–73
[3] Hamilton S.J., Siltanen S.: Nonlinear Inversion from Partial EIT Data: Computational Experiments, Contemporary Mathematics, Vol. 615, 2014, 105–129.
[4] Holder D.S.: Electrical Impedance Tomography: Methods, History and Applications Series in Medical Physics and Biomedical Engineering, London, 2005
[5] Lechleiter A., Rieder A.: Newton regularizations for impedance tomography: convergence by local injectivity. Inverse Problems, 24(6), 2008
[6] Mueller J.L., Siltanen S.: Linear and Nonlinear Inverse Problems with Practical Applications. SIAM 2012.
[7] Osher S., Sethian J.A.: Fronts Propagating with Curvature Dependent Speed: Algorithms Based on Hamilton-Jacobi Formulations, Journal of Computational Physics, 79, 1988, 12–49.
[8] Osher S., Fedkiw R.: Level Set Methods and Dynamic Implicit Surfaces. Springer, New York 2003.
[9] Osher S., Santosa F.: Level set methods for optimization problems involving geometry and constraints. Frequencies of a two-density inhomogeneous drum. Journal of Computational Physics, 171, 2001, 272–288.
[10] Rymarczyk T.: New Methods to Determine Moisture Areas by Electrical Impedance Tomography, International Journal of Applied Electromagnetics and Mechanics 08/2016, 1–9 [DOI:10.3233/JAE-16207].
[11] Rymarczyk T., Filipowicz S.F.: The Shape Reconstruction of Unknown Objects for Inverse Problems, Electrical Review, NR 5/2012/3a.
[12] Rymarczyk T.: Characterization of the shape of unknown objects by inverse numerical methods, Przegląd Elektrotechniczny, R. 88 NR 7b/2012, 138–140.
[13] Rymarczyk T, Adamkiewicz P., Duda K., Szumowski J., Sikora J.: New Electrical Tomographic Method to Determine Dampness in Historical Buildings, Achieve of Electrical Engineering, v.65, 2/2016, 273–283.
[14] Sankowski D., Sikora J.: Electrical capacitance tomography: Theoretical basis and applications, Wydawnictwo IEL, Warszawa 2010.
[15] Sethian J.A., Level Set Methods and Fast Marching Methods, Cambridge University Press, 1999.
[16] Sikora J., Wójtowicz S.: Industrial and Biological Tomography: Theoretical Basis and Applications, Wydawnictwo IEL, Warszawa 2010.
[17] Tai C., Chung E., Chan T.: Electrical impedance tomography using level set representation and total variational regularization. Journal of Computational Physics, vol. 205, no. 1, 2005, 357–372.
[18] Wang M.: Industrial Tomography: Systems and Applications, Elsevier, 2015.

Ph.D. Eng. Tomasz Rymarczyk
e-mail: tomasz.rymarczyk@netrix.com.pl

Director in Research and Development Center Netrix S.A. His research area focuses on the application of non-invasive imaging techniques, electrical tomography, image reconstruction, numerical modelling, image processing and analysis, process tomography, software engineering, knowledge engineering, artificial intelligence and computer measurement systems.

Ph.D. Przemysław Adamkiewicz
e-mail: p.adamkiewicz@netrix.com.pl

Doctor of Physics, graduate of Maria Curia-Sklodowska University in Lublin. Head of R&D Department at Netrix SA.
His research area focuses on electrical tomography, image reconstruction, numerical modelling, image analysis and computer measurement systems.

M.A. Paweł Tchórzewski
e-mail: pawel.tchorzewski@netrix.com.pl

Researcher in R&D Department - Netrix S.A.
A graduate of the Maria Curie-Sklodowska University Lublin on the physics (specializing in theoretical physics). Currently, the work carries out tasks profile research and development in the field of numerical methods for solving partial differential equations, electrical tomography in image reconstruction, forward and inverse problem. He is a Ph.D. student of the Institute of Electrical Engineering in Warsaw.

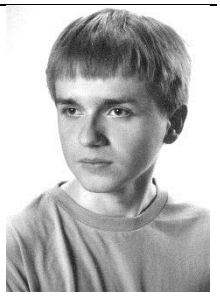

otrzymano/received: 20.09.2016 *przyjęto do druku/accepted: 15.02.2017*

DOI: 10.5604/01.3001.0010.4596

METHODS OF SMALL CAPACITANCE MEASUREMENT IN ELECTRICAL CAPACITANCE TOMOGRAPHY

Waldemar Smolik, Jacek Kryszyn, Tomasz Olszewski, Roman Szabatin
Warsaw University of Technology, Faculty of Electronics and Information Technology, The Institute of Radioelectronics and Multimedia Technology, Nuclear and Medical Electronics Division

Abstract. *The paper presents the main methods of small capacitance measurement used in electrical capacitance tomography: the AC method with a sine wave excitation and the charge-discharge method with square wave excitation. Construction of synchronous detector for both circuits was discussed. A modified "charge-discharge" method was presented.*

Keywords: capacitance measurement, AC method, charge-discharge method, electrical tomography

METODY POMIARU MAŁYCH POJEMNOŚCI W ELEKTRYCZNEJ TOMOGRAFII POJEMNOŚCIOWEJ

Streszczenie*. W artykule przedstawiono główne metody pomiaru małych pojemności stosowane w elektrycznej tomografii pojemnościowej: metodę częstotliwościową z pobudzeniem za pomocą fali sinusoidalnej oraz metodę „ładuj-rozładuj" z pobudzeniem za pomocą fali prostokątnej. Przedstawiono budowę detektora synchronicznego dla obu układów. Zaprezentowano również modyfikację metody „ładuj-rozładuj".*

Słowa kluczowe: pomiar pojemności elektrycznej, metoda częstotliwościowa, metoda „ładuj-rozładuj", tomografia elektryczna

Introduction

The electrical capacitance tomography allows to obtain a three-dimensional distribution or two-dimensional cross-section of the distribution of electric permittivity in the examined volume surrounded by the electrodes of capacitance sensor [4, 9]. An image of permittivity distribution is reconstructed by numerically solving the non-linear inverse problem, where the measurement data are the values of mutual capacitance of electrodes surrounding the examined volume [8].

Because of the problems associated with measurement of very small capacitance, the number of electrodes and hence the number of measurements is limited, thus the inverse problem is undetermined. A small number of measurements decides on the poor spatial resolution of this imaging technique [10].

Increasing the spatial sampling by increasing the number of electrodes is not possible due to the very small values of the mutual capacitance of electrodes of a tomographic sensor, of the order of femtofarads [14]. Reducing the area of electrodes while increasing the number of electrodes can't be compensated by increasing the height of electrodes due to the loss of resolution in an axis perpendicular to the plane of tomographic cross section. A change in the permittivity in a small volume results in a very small change in capacitance of the order of few femtofarads for the adjacent (neighboring) electrodes and a fraction of femtofarad for opposite electrodes (Fig. 1, Fig. 2). Wide measurement range, from picofarads for the neighboring electrodes to fractions of femtofarads for the opposite electrodes (Fig. 3), is a vital problem in the design of the measuring system.

Capacitance measurement circuits for electrical capacitance tomography should: have good linearity, be shielded to remove the effect of external electric field, be insensitive to the parasitic capacitance to ground and generate little noise. There are different methods of capacitance measurements, depending on the value of the measured capacitance, precision and speed. The methods can be divided into the following groups: DC circuits (charging capacitor using a constant voltage or current), RC, IC or LC oscillators in which the capacitance is converted to frequency, synchronous demodulators or synchronous dual-port bridges [1]. DC method (capacitor charging with direct current) can be realized by means of few elements, but at the expense of temperature drift and sensitivity to noise. Resonance circuits can cover a wider range of capacitance values than DC circuits but are sensitive to a parasitic capacitance and noise. The most suitable circuits for capacitance tomography are the dual-port synchronous demodulators, because of their high accuracy and immunity to parasitic capacitance.

The capacitance of coaxial cables that are used to connect the electrodes of tomographic sensor to the transmitting and receiving circuit, is a load of the order of 60 pF/m. The parasitic capacitance of analog CMOS transistors used to switch the electrodes is about 8 pF. The external screen of the probe, protecting against external electric field (signal interference), is an additional load, which capacitance value can reach several tens of picofarads. Due to the large total value of parasitic capacitance of about 150 pF, which is several orders greater than the measured capacitance, which value is in the range from about 1 pF for adjacent electrodes to about 1 fF for opposite electrodes, immunity of the measuring system to the parasitic capacitance is very important [14].

Among several proposed in the literature methods of capacitance measurement, two methods can be distinguished in capacitance tomography: frequency or AC method with sinusoidal excitation and charge-discharge method with square wave excitation. These two methods are used in most modern systems for capacitance tomography.

1. AC method

In the frequency or alternating current method (AC method) a sine wave is used as the excitation signal [15]. The sinusoidal excitation is applied to the capacitance connected in series.

The first stage of the receiver is an alternating signal amplifier (AC amplifier). Application of an amplifier with programmable gain ensures the maintenance of the amplitude of the output signal at the high level for a wide range of capacitance values. The signal from the amplifier is demodulated in the next stage of measurement channel using the rectifier [13] or phase-sensitive detector [4, 5], and smoothed using a low pass filter. Phase synchronization allows accurate measurement of signal amplitude, even when the signal is disturbed by broadband Gaussian noise or uncorrelated interference.

A block diagram of the AC measurement circuit is shown in Fig. 4. A generator of sinusoidal wave:

$$u_G(t) = U_{GEN} \sin(wt) \tag{1}$$

is a source of alternating current flowing through the capacitance C_X connected in series to the generator. The first stage of the receiving circuit is an operational amplifier with feedback loop in the form of parallel connection of the capacitance C_F and the

resistance R_F, which converts the alternating current into a voltage signal given by the formula:

$$U_{AC} = U_{GEN} \frac{jwR_F C_X}{1 + jwR_F C_F}, \quad (2)$$

where w is an angular frequency of sinusoidal excitation. If the time constant $t = R_F C_F$ is large and the excitation frequency f is high (for example $R_F = 1$ MΩ, $C_F = 6{,}8$ pF, $f = 1{,}5$ MHz), the equation (2) simplifies to the form:

$$U_{AC} = U_{GEN} \frac{C_X}{C_F}. \quad (3)$$

The amplitude of the sinusoidal signal is proportional to the measured capacitance.

Demodulation of the sinusoidal signal from the AC amplifier takes place in the second stage of the measuring system consisting of a phase locked loop and low pass filter. Sinusoidal signal:

$$u_{AC}(t) = A \sin(wt + a), \quad (4)$$

where a is the delay introduced by the measured impedance and the amplitude is given by the formula:

$$A = U_{GEN} C_X / C_F, \quad (5)$$

is multiplied by the reference signal:

$$u_R(t) = B \sin(w_R t + b), \quad (6)$$

what gives at output (after using the formula for the product of sines):

$$u_D(t) = \frac{AB}{2}\left[\cos\left((w - w_R)t + a - b\right) - \cos\left((w + w_R)t + a + b\right)\right] \quad (7)$$

If the transmitter and receiver are synchronized ($w_R = w$), in the signal at the multiplier output:

$$u_D(t) = \frac{AB}{2}\left[\cos(a - b) - \cos\left(2wt + (a + b)\right)\right] \quad (8)$$

the DC component will be present. Additionally, if the signals are in phase, that is $a = b$, the voltage at the multiplier output takes the form:

$$u_D(t) = \frac{U_{GEN} C_X B}{2C_F}\left[1 - \cos(2wt + 2a)\right] \quad (9)$$

A low-pass filter which is the last part of the receiving channel allows to obtain a constant signal with value directly proportional to the measured capacitance.

Application of synchronous detector, which is functionally equivalent to a band-pass filter, significantly improves performance of the measurement circuit because of the extremely narrow band filtration.

AC method is immune to parasitic capacitances. Parasitic capacitance C_{S1} is just a load of the sine wave generator and does not affect the measurement. From the driving electrode, parasitic capacitance is supplied from a source with very low internal resistance, so it has no effect on the potential at measured capacitance. The parasitic capacitance C_{S2} does not affect the measurement because it is maintained at virtual ground by the operational amplifier. The voltage accumulated on the parasitic capacitance is very small and its effect on the measurement is very small.

In some applications of electrical capacitance tomography, when the medium is a mixture of dielectric and conductive materials, it is important to measure not only the permittivity but also the conductivity of the medium. Capacitance measurement by synchronous demodulation can be modified to obtain the value of the impedance in the form of a module and phase. For this purpose, the quadrature modulation is applied using two orthogonal signals:

$$u_{R1}(t) = B \sin(w_R t + b), \quad u_{R2}(t) = B \cos(w_R t + b). \quad (10)$$

If we assume that the transmitter and receiver are synchronized, so the reference frequency is equal to the excitation frequency $w_R = w$, the multiplication of the output signal from the measured impedance with the reference signals gives respectively:

$$\begin{aligned} u_{D1}(t) &= \frac{AB}{2}\left[\cos(a - b) - \cos\left(2wt + (a + b)\right)\right] \\ u_{D2}(t) &= \frac{AB}{2}\left[\sin(a - b) + \sin\left(2wt + (a + b)\right)\right] \end{aligned} \quad (11)$$

If the reference signal is in phase with the excitation, so $b = 0$, after the application of low pass filters in each channel, the real part and the imaginary part of the signal will be obtained:

$$u_{D1}(t) = \frac{AB}{2}\cos(a), \quad u_{D2}(t) = \frac{AB}{2}\sin(a), \quad (12)$$

where a stands for the delay introduced by the measured impedance. Impedance modulus and phase shift can be determined using the formulas:

$$\frac{AB}{2} = \sqrt{U_{D1}^2 + U_{D2}^2}, \quad (13)$$

$$a = \arctan\frac{U_{D2}}{U_{D1}}, \quad (14)$$

Quadrature method allows to get information about the measured impedance of the medium (amplitude and phase), but requires an application of a double channel demodulator.

The disadvantage of the AC method is relatively low speed of measurements, resulting from the low-pass filter cutoff frequency. In one of the reported solutions [15] the low-pass filter cutoff frequency is equal to 5 kHz, when the reference frequency is equal to 500 kHz, which gives measurement time of single capacitance equal to about 200 μs. In the case of 120 measurements for a sensor with 16 electrodes and single-channel measurement, the time of measurement of data for one picture is about 24 ms. This gives speed of image registration of about 41 frames per second.

In the case of multi-channel measurement with one driving electrode and a number of measurement electrodes the time of measurement of data for one image is 3.2 ms. This gives the frame rate equal to about 312 frames per second.

2. Charge-discharge method

In the charge-discharge method [5, 9], a transmitter circuit connected to the driving electrode generates a square wave. The circuit connected to the receiving electrode integrates the current pulses during repeated cycles of charging and discharging of the capacitor. Charging and discharging phases are accomplished through synchronous switching of stimulating and receiving circuits. At the receiver the two integrators are provided, one of which sums up the charging current pulses and the second sums up capacitor discharging current pulses. After summing of multiple pulses by both integrators, a fixed voltage level is settled at their outputs, with approximately equal absolute value but opposite sign. Differential processing of signals from both integrators using instrumentation amplifier doubles the value of the measurement signal.

Excitation consist of passing unipolar or bipolar square wave on the driving electrode. Measuring electrodes are virtually grounded, which allows simultaneous measurement of $n - 1$ capacitances, where n is the number of electrodes in the sensor.

Charge-discharge capacitance measurement circuit in differential configuration is shown in Fig. 5. One terminal of measured capacitor C_X is connected to a source of a square wave. The transmitter consists of two analog switches which synchronously switch between two voltage levels U_{T1} and U_{T2}. The other terminal of the capacitor C_X is connected to the pair of integrators selected by the switches controlled synchronously with the transmitter switches. Both integrators are current-voltage converters constructed using an operational amplifier.

Application of operational amplifier in the construction of integrators causes that the output terminal of measured capacitance is maintained at a potential very close to zero. The driving signal in the form of a square wave and the synchronous switching of integrators causes that the capacitance C_X is periodically charged and discharged. Let's assume, that the levels of a symmetrical square wave are respectively equal to: $U_{T1} = -U_T/2$ and $U_{T2} = U_T/2$. The amount of the charge transferred during a voltage jump from level to level is given respectively by the formula:

$$\Delta Q_1 = U_T C_X, \quad \Delta Q_2 = -U_T C_X. \tag{15}$$

The cyclic charging and discharging of the capacitor C_X at a frequency f causes the flow of current in both integrators with an average value respectively equal to:

$$I_1 = fU_T C_X, \quad I_2 = -fU_T C_X. \tag{16}$$

In a real system the typical values of voltage U_T are in the range from 10 to 15 V. The typical values of frequency f are in the range from 1 to 3 MHz. The measured capacitance C_X is in the range from 20 fF to 5 pF for most tomographic probes. Let's assume that the voltage amplitude of excitation waveform U_T is equal to 12V, the driving frequency f is equal to 1.5 MHz and the value of measured capacitance C_X is in the range from 0.01 pF to 2 pF. The charge Q_X determined from equation (15) is in the range from 0.12 pC to 24 pC. So small value of the charge is comparable to or even less than the value of charge injection for most semiconductor analog switches, ranging from 1 pC to 30 pC. Average value of current I_X given by the formula (16) equals from 0.18 μA to 36 μA. Exciting square wave U_A is distorted mainly by the resistance of the source and parasitic capacitances. Raising and falling of the signal last tens of nanoseconds, thus the charge Q_X is transferred in time period of about 20…50 ns with the mean value of the current equal from 3.4 μA to 0.69 mA.

Two integrators convert the current to voltage by a scaling factor determined by the value R_{FB} of resistance in the integrator feedback loop. The capacitor C_{FB} in feedback loop is charged by successive current pulses, but in the meantime it discharges through the resistor R_{FB}. The output value stabilizes when the currents that charge and discharge feedback capacitance C_{FB} compensate each other (Fig. 6). The voltage at the integrators output tends asymptotically to a value of, respectively:

$$U_1 = -fU_T C_X R_{FB}, \quad U_2 = fU_T C_X R_{FB}. \tag{17}$$

Voltage addition is performed in a last element of the receiving channel using an instrumentation amplifier with differential input and programmable gain K. The instrumentation amplifier gives at the output almost constant voltage of average value:

$$U_{OUT} = 2KfU_T C_X R_{FB} \tag{18}$$

directly proportional to the measured capacitance. In the case of measurement of a small capacitance it is necessary to increase the gain, which can be achieved by increasing the excitation voltage U_T, increasing the frequency f or increasing the gain of the integrator by changing R_{FB} or increasing the gain K of differential stage.

Gain adjusting by increasing the resistance in the feedback loop of the integrator causes a simultaneous increase of the time constant of voltage settling what has an impact on the measurement time. The approximately constant voltage U_1 and U_2 have a low variable component in the form of ripple (Fig. 6) resulting from the process of charging and discharging of capacitance C_{FB} [11]. Single pulse changes the output voltage by value equal to:

$$\Delta U_1 = -U_T C_X/C_{FB}, \quad \Delta U_2 = -U_T C_X/C_{FB} \tag{19}$$

respectively for the integrator summing the charging current pulses and the integrator summing the discharging current pulses. Voltage pulses ΔU_1 and ΔU_2 arises in different moments, thus the ripple signal is transmitted by a differential amplifier with gain K. The ratio of the ripple amplitude to the average value of the signal depends on the time constants of the integrators, but does not exceed a maximum value:

$$\frac{\Delta U_{OUT}}{U_{OUT}} = \frac{1}{2fR_{FB}C_{FB}}. \tag{20}$$

This ratio depends on the components in the feedback loop R_{FB} and C_{FB}, and in the real conditions is from about 1/100 to about 1/1000. This means that the charge-discharge circuit produces a signal with a significant ripple component, with a signal-to-ripple ratio typically in the range 40 ÷ 60 dB.

To minimize the impact of ripple, a large time constant $t = R_{FB}C_{FB}$ should be selected. When the measured capacitance value C_X becomes smaller, the resistance R_{FB} in the feedback loop must be increased in order to achieve a measurable signal at the output. The value C_{FB} should be chosen as a compromise between the magnitude of the amplitude of the ripple signal and the measurement time.

A large capacitance value C_{FB} increases the time constant $t = R_{FB}C_{FB}$ and minimizes the ripple signal, but it requires an increased number of charging and discharging pulses. A large number of current pulses increases the measurement time and is not acceptable in high-speed data acquisition. To achieve optimum results the elements R_{FB} and C_{FB} in the feedback loop should be programmatically switched, according to the range of a measured capacitance.

In addition, to obtain a correct average value of voltage, it is necessary to filter the signal before sampling of the signal by the analog-to-digital converter. Band-stop filter for ripple frequency can be used. Another method might be to increase the sampling rate of A/D converter and digital filtering by averaging.

Charge-discharge method is insensitive to parasitic capacitances. The main problem of the circuit is a charge injected by the analog switches used for signal modulation [3, 6]. The example of circuit implementation is described in [2].

To achieve steady state on the integrator outputs some minimal number of pulses is required. This number depends on the value of the measured capacitance and may be approximately constant when switching elements in the feedback loop of the integrators. For the driving frequency equal to 1 MHz and 40 pulses, time of one capacitance measurement equals 40 μs plus conversion time, which for high-speed converters is less than 1 μs. In the case of 120 capacitance values for a sensor with 16 electrodes and single-channel measurement, the measurement time of the data for one image is about 4.8 ms. This means the speed of image acquisition of about 208 frames per second. In the case of multi-channel measurement with one driving electrode and many measurement electrodes, the measurement time of the data for one image is 0.64 ms, which gives about 1562 frames per second.

3. Switch-less charge-discharge circuit

The basic problem that occurs in the charge-discharge circuit is the effect of charge injection of the analog switches. Due to the discrepancy of this parameter between the switches applied in the circuit the charge injected to both integrators does not cancels at differential stage of the measuring amplifier. The zero level is shifted. One possible solution could be to replace the analog switches by diodes in a current rectifying configuration.

Replacement of the switch by the diode in classic charge-discharge circuit will not bring the expected results due to the position of the switch at the input of the system. A much better solution turns out to be the application of the active rectifier circuit with the diode in the feedback loop of the integrator. To sum charging and discharging pulses one operational amplifier can be used with the diode splitter configuration (Fig. 7).

Switch-less charge-discharge circuit was presented in [7, 12]. The circuit works on the same principle as in the classical charge-discharge method. The measured capacitor is sequentially charged and discharged and the charging and discharging current pulses are integrated respectively in two parts of feedback loop of the integrator.

The circuit consists of a square wave generator connected to the driving electrode and the demodulator connected to the measuring electrode. The electrodes of the tomographic sensor are connected to the transmitter and receiver via the analog switches or multiplexer. A square wave with a frequency of 1 MHz and amplitude of 10 V is given on the driving electrode. The receiver, connected to the sensing electrode, consists of a preamplifier and an integrator in a configuration of an active rectifier.

In the circuit there is only one integrator which has two feedback loops separated by a diode splitter. The integrator has two outputs and sums both charge and discharge current pulses. Rising and falling edge of the square wave causes exponential voltage spikes on the capacitors in the feedback loop. After a number of current pulses the voltage in the feedback loops is settled. The voltage values (with the opposite sign) from both outputs are summed in differential stage of instrumentation amplifier and then processed to digital form using 16-bit analog-to-digital converter.

The circuit differs from the classical charge-discharge circuit in using only one integrator in the demodulator. Demodulator with the diode splitter does not require the control, which makes it almost pure analog circuit (except for switching the gain). The elimination of analog switches simplifies the design. The circuit is immune to parasitic capacitances, similarly to the charge-discharge circuit. In the modified circuit the charge injection from analogue switches in not an issue.

The operating frequency of the classic circuit is limited by the speed of analog switches to a few megahertz. Unfortunately, the operating frequency of the modified system, despite the use of high-speed Schottky diodes, is also limited to a few megahertz. Operating frequency is limited by the speed of voltage rise at the output of operational amplifier, which has to switch between voltages on two capacitors in two feedback loops.

4. Summary

The paper presents two basic methods of measuring small capacitance used in electrical capacitance tomography: a frequency method with excitation using a sine wave and the charge-discharge method with excitation using a square wave. The modification of the charge-discharge method was also presented. The construction of the synchronous detector in these circuits was described.

In the charge-discharge method the synchronous detector is placed at the beginning of receiver channel. The charge injected by the analog switches is large comparing to the charge transferred through the measured capacitance. In effect this introduces the shift of the zero level.

Switch-less charge-discharge circuit is characterized by parameters, measurement uncertainty and speed, similar to the classic charge-discharge. The advantage of this circuit is a much simpler structure.

Several models of electrical capacitance tomograph were elaborated at our Division. The charge-discharge circuit was used in ET3 tomograph. The switch-less circuit was used in IREna tomograph. In the recent construction of our team – EVT4 tomograph – a single-shot high voltage (SSHV) circuit, which is another modification of charge-discharge circuit, was applied.

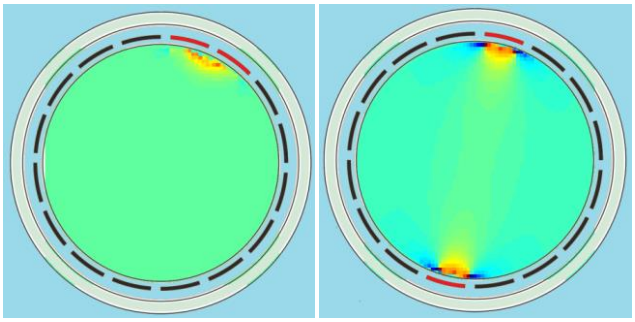

Fig. 1. 2D map of sensitivity of capacitance measurement on small change of permittivity in a small region of examined space. Sensitivity map in the cross section of cylindrical sensor with 16 electrodes for capacitance measurement for: pair of adjacent electrodes (left), pair of opposite electrodes (right)

Fig. 2. Measurements of mutual capacitance of electrodes of cylindrical, tomographic sensor with 12 electrodes in one ring. The characteristic U-shaped plot is obtained when one driving electrode is fixed and the others are sensing electrodes. Three U-shaped parts of the plot for three different driving electrodes is shown. The maximum value corresponds to a pair of adjacent electrodes, the lowest corresponds to pair of opposite electrodes

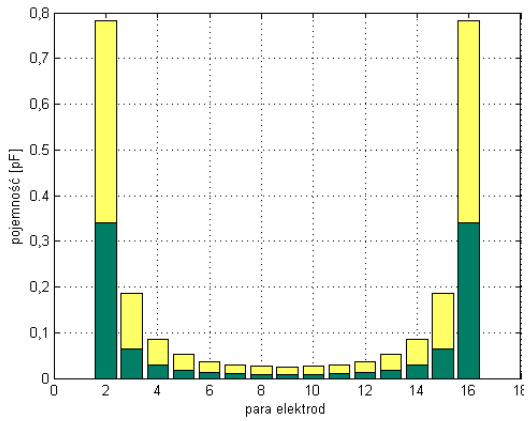

Fig. 3. Mutual capacitance of electrodes of cylindrical sensor (one ring, 16 electrodes) for pairs from 1-2 to 1-16. Values for the sensor filled with a material with a relative permittivity $\varepsilon_r = 3$ (yellow) and filled with air – $\varepsilon_r = 1$ (green)

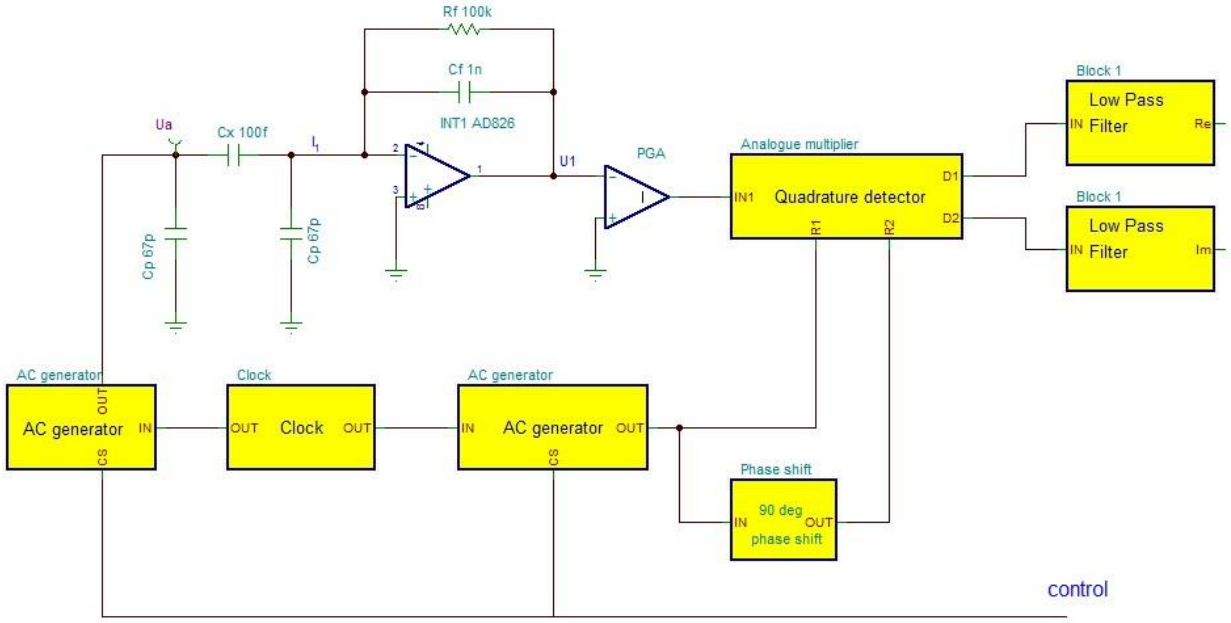

Fig. 4. Block diagram of the AC circuit with the quadrature demodulator for simultaneous measurement of capacitance and conductivity

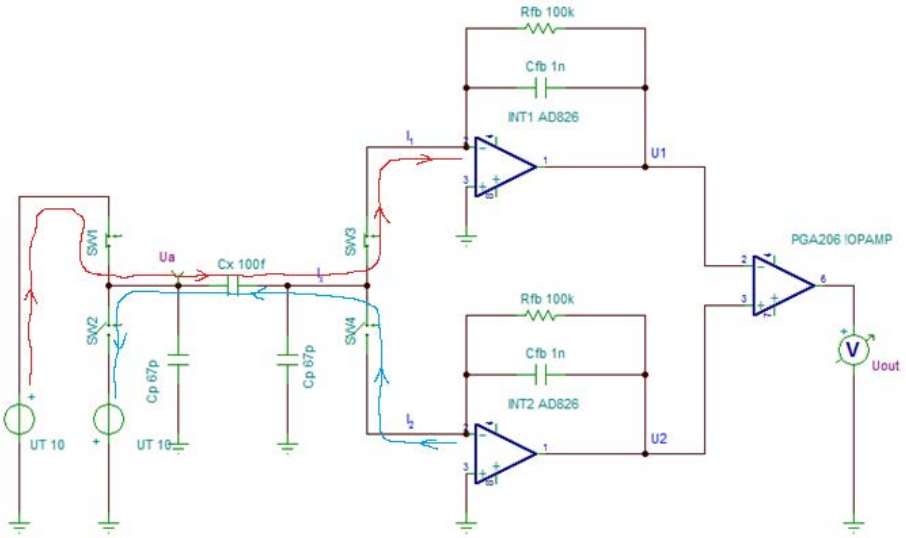

Fig. 5. Schematic diagram of the charge-discharge circuit. The path of current flow in charging and discharging phase is shown

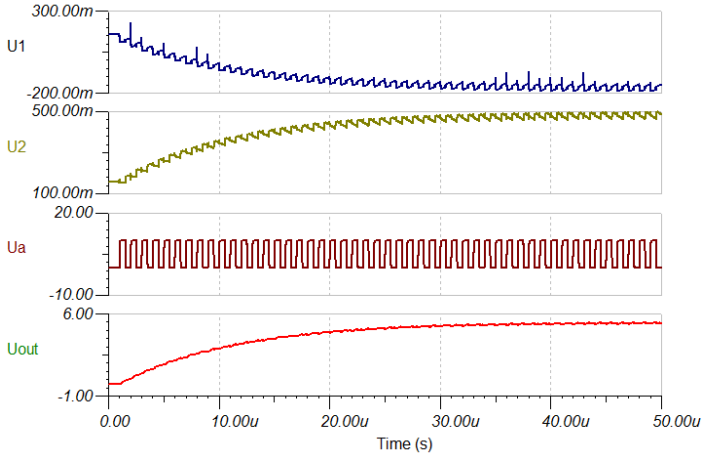

Fig. 6. Numerically simulated voltage waveforms in the charge-discharge circuit (stimulating voltage amplitude: U_A =10 V; U_1, U_2 – voltage at integrators output; U_{OUT} – voltage at output of instrumentation amplifier; measured capacitance C_X = 100 fF; elements in feedback loop: R_{FB} = 100 kΩ; C_{FB} = 470 pF; excitation frequency: f = 1 MHz)

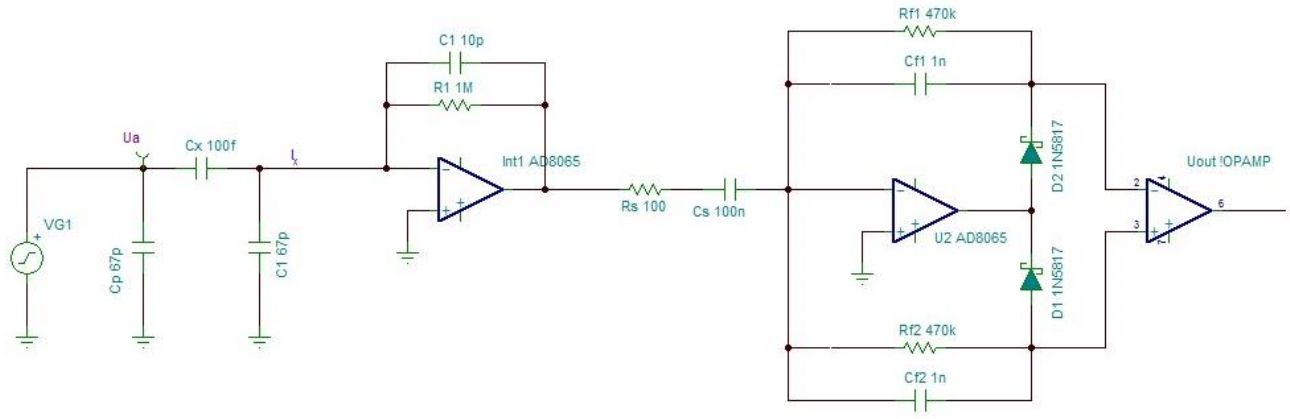

Fig. 7. Switch-less charge-discharge circuit with active rectifier and diode splitter

Bibliography

[1] Baxter L.K.; Capacitive Sensors: Design and Applications. IEEE Press Series on Electronics Technology, 1996.

[2] Brzeski P., Mirkowski J., Olszewski T., Pląskowski A., Smolik W., Szabatin R.: Multichannel capacitance tomograph for dynamic process imaging. Opto-Electronics Review, 2003, 175–180.

[3] Hu H., Katsouros M., Yang W.Q., Huang S.M.: Further analysis of charge/discharge capacitance measurement circuit used with tomography sensors. Sensors & Transducers Journal, 80(6)/2007, 1246–1256.

[4] Huang S.M., Plaskowski A.B., Xie C.G. & Beck M.S.: Capacitance-based tomographic flow imaging system. Electron. Lett., 24/1988, 418–419.

[5] Huang M., Stott A.L., Green R.G., Beck M.S.: Electronic transducers for industrial measurement of low value capacitances. J. Phys. E: Sci. Instrum., 21/1988, 242–250.

[6] Huang S.M., Xie C.G., Thorn R., Snowden D., Beck M.S.: Design of sensor electronics for electrical capacitance tomography. IEE Proceedings-G, 139(1)/1992, 83–88.

[7] Kryszyn J., Smolik W., Radzik B., Olszewski T., Szabatin R.: Switchless Charge-Discharge Circuit for Electrical Capacitance Tomography. Meas. Sci. Technol. 25/2014, 115009 (9).

[8] Lionheart W. R.: EIT reconstruction algorithms: pitfalls, challenges and recent developments. Physiol. Meas., 25/2004, 125–142.

[9] Plaskowski A., Beck M., Thorn R., Dyakowski T.: Imaging industrial flows. Applications of electrical process tomography, IOP Publishing Ltd, 1995.

[10] Reinecke N., Mewes D.: Recent developments and industrial research applications of capacitance tomography. Meas. Sci. Technol., 7/1996, 325–337.

[11] Smolik W., Mirkowski J., Olszewski T., Radomski D., Brzeski P., Szabatin R.: Measurement circuit based on programmable integrators and amplifiers for electrical capacitance tomography, Kwartalnik Elektroniki i Telekomunikacji, 51/2005, 127–137.

[12] Smolik W.T., Olszewski T., Radzik B., Szabatin R.: Switch-Less Charge-Discharge Circuit for Electrical Capacitance Volume Tomograph ET4. 6th International Symposium on Process Tomography. Cape Town, RPA, 2012.

[13] Yang W.Q., Stott A.L., Beck M.S., Xie C.G.: Development of capacitance tomographic imaging systems for oil pipeline measurements. Rev. Sci. Instrum., 66/1995, 4326–4332.

[14] Yang W.Q.: Hardware design of electrical capacitance tomography systems. Meas. Sci. Technol., 7/1996, 225–232.

[15] Yang W.Q., York T.A.: New AC – based capacitance tomography system. IEE Proc-Sci. Measurement Technology, 146(1)/1999, 47–53.

Prof. Waldemar Tomasz Smolik
e-mail: W.Smolik@ire.pw.edu.pl

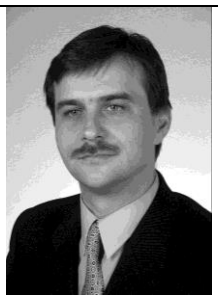

Waldemar T. Smolik received the M.Sc., the Ph.D. and D.Sc. degree in electronics engineering from Warsaw University of Technology, Warsaw, Poland in 1991, 1997 and 2014, respectively. Since 2014, he is an Associate Professor at the Institute of Radioelectronics and Multimedia Technology, Electronics and Information Technology Faculty, Warsaw University of Technology. He is the head of the Laboratory of Electronics Application in Nuclear Medicine at the Division of Nuclear and Medical Electronics. His main research interests are computer engineering, computed tomography and medical imaging. He has published over 70 scientific papers.

M.Sc. Eng. Jacek Kryszyn
e-mail: J.Kryszyn@ire.pw.edu.pl

Received the M.Sc. degree in electronics and computer engineering from Warsaw University of Technology, Warsaw, Poland in 2012. Ph.D. student and the Assistant with the Nuclear and Medical Electronics Division, Institute of Radioelectronics and, Electronics and Information Technology Faculty, Warsaw University of Technology. His field of interest covers Electrical Capacitance Tomography, especially simulations of the electric field and reconstruction of images.

M.Sc. Eng. Tomasz Olszewski
e-mail: T.Olszewski@ire.pw.edu.pl

Tomasz Olszewski received his M.Sc. in electronics from Warsaw University of Technology, Warsaw, Poland in 1982. He has been employed at the University since 1989, currently as a Senior Lecturer. His main interests cover analogue and digital electronics in impedance tomography. He is the main designer of ET and ET3 capacitance tomographs, developed at the Nuclear and Medical Electronics Division.

Ph.D. Eng. Roman Szabatin
e-mail: R.Szabatin@ire.pw.edu.pl

Roman Szabatin received the M.Sc. degree in electronics apparatus and the Ph.D. degree from Warsaw University of Technology, in 1972 and 1983, respectively. Since 1973, he has been with the Nuclear and Medical Electronics Division, Institute of Radioelectronics, Electronics and Information Technology Faculty, Warsaw University of Technology, as an Associate, Senior Associate, and Senior Scientist. His main research interests include nuclear and medical instrumentation and medical imaging (gamma cameras, SPECT and PET). He has published over 50 scientific papers.

otrzymano/received: 20.09.2016 *przyjęto do druku/accepted: 15.02.2017*

DOI: 10.5604/01.3001.0010.4597

DEVELOPMENT OF ELECTRICAL CAPACITANCE TOMOGRAPH DESIGN IN THE NUCLEAR AND MEDICAL ELECTRONICS DIVISION

Jacek Kryszyn, Waldemar Smolik, Tomasz Olszewski, Roman Szabatin
Warsaw University of Technology, Faculty of Electronics and Information Technology, The Institute of Radioelectronics and Multimedia Technology, Nuclear and Medical Electronics Division

Abstract. *Electrical Capacitance Tomography is a technique which allows to visualize a spatial distribution of electric permittivity in an examined volume. ECT allows to achieve hundreds of frames per second which is suitable for the industrial application, e.g. monitoring of multiphase flows or material mixing. Construction of such ECT system which enables precise data acquisition with sufficient speed is a challenge. In the Division of Nuclear and Medical Electronics ECT systems which have found applications in many research facilities in Poland and all over the world have been constructed for over 15 years. In this article a multichannel ET3 tomograph and its successor,EVT4, are presented. EVT4 will allow to obtain more than 10 thousand frames per second. This will allow to make progress in studies of dynamic processes and 3D visualization.*

Słowa kluczowe: electrical capacitance tomography

ROZWÓJ KONSTRUKCJI ELEKTRYCZNEGO TOMOGRAFU POJEMNOŚCIOWEGO W ZAKŁADZIE ELEKTRONIKI JĄDROWEJ I MEDYCZNEJ

Streszczenie. *Elektryczna tomografia pojemnościowa pozwala na obrazowanie przestrzennego rozkładu przenikalności elektrycznej w badanej objętości. Technika ta pozwala na uzyskanie setek obrazów na sekundę, dzięki czemu istnieje możliwość wykorzystania jej w przemyśle, na przykład do monitorowania procesów dynamicznych, takich jak przepływy wielofazowe lub mieszanie materiałów. Skonstruowanie systemu tomograficznego pozwalającego na bardzo szybką akwizycję obrazów o dobrej jakości jest jednak dużym wyzwaniem. W Zakładzie Elektroniki Jądrowej i Medycznej Politechniki Warszawskiej od lat powstają konstrukcje tomografów pojemnościowych, które znajdowały zastosowanie w placówkach naukowych w Polsce i na świecie. W tym artykule prezentowany jest wielokanałowy tomograf ET3 oraz jego następca, EVT4, który pozwoli na uzyskiwanie 10 tysięcy obrazów na sekundę. Pozwoli to na dokładniejsze badanie procesów dynamicznych oraz wizualizację trójwymiarową.*

Keywords: elektryczna tomografia pojemnościowa

Introduction

Electrical Capacitance Tomography (ECT) is used to visualize spatial distribution of electrical permittivity in an examined objects [2]. An image with a cross-section or 3D distribution is reconstructed from capacitance measurements between electrodes placed on a tomographic sensor in which examined objects are put. ECT is a very fast technique which allows to apply it in dynamic process imaging, mainly two-phase flows monitoring [3, 6]. In comparison to other tomographic modalities ECT is relatively cheap. Main drawbacks of ECT are low spatial resolution and low sensitivity. It is assumed, that spatial resolution is equal to around 10% of the diameter of a tomographic sensor. Quality of the image reconstruction is presented in Fig. 1 which shows image reconstruction of the cross-section of the phantom consisting of 7 rods with relative permittivity $\varepsilon_r = 3$.

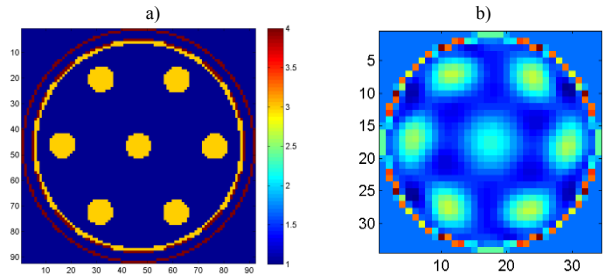

Fig. 1. a) Cross-section of the phantom consisting of seven rods with permittivity ε = 3; b) image reconstrucion with Kaczmarz algorithm from numerically simulated projections

One of main challenges in ECT is a measurement of very small capacitance values. In a typical tomographic sensor which has over a dozen electrodes mutual capacitances vary from tens of femtofarads for opposite electrodes to single picofarads for adjacent electrodes [7]. It is not possible to increase values of mutual capacitances which could be achieved by increasing surface area of electrodes because this would result in a lower number of electrodes and lower sampling rate and thus lower spatial resolution which is already low. Because of this very precise and sensitive measurement methods have to be used in ECT which allow to measure a wide range of small capacitances in a short time.

In Nuclear and Medical Electronics Division of Warsaw University and Technology research works on ECT started around 2000. Under the leadership of doc. dr. eng. Roman Szabatin several models of capacitance tomograph were constructed. The first model ET1 was a 16-channel tomograph working with probes with 8, 12 and 16 electrodes. As part of further work, a prototype of a new model of tomograph ECM was built. Number of channels was increased to 32. Around 2005 the 32-channel ET3 was created. This device was a unique device on a world scale. This article describes the design and construction of ET3 and his successor – EVT4.

1. ET3 tomograph

ET3 Tomograph (shown in Fig. 2) can work with 8, 12, 16 and 32-electrode sensors as well as with three-dimensional probes containing several layers of the electrodes (up to 4 layers of 8 electrodes) [1]. The system consists of:

- motherboard with connectors for measurement cards and control card. The motherboard also includes eight programmable Altera chips for digital signal control;
- 16 signal cards, each of which has two measurement channels. Channels carry out "charge-discharge" measurement method in which alternating capacitance charging and discharging cycles are performed and integration of electric charging and discharging current is held. In the multi-channel device the measurement is possible in which one of the electrodes is a transmitting electrode and the others are the measurement electrodes;
- control card with a programmable FPGA chip which is responsible for measurement process control and communication.

Electrodes of the sensor are connected to the coaxial connectors located on the motherboard. Printed circuit boards are installed in 19-inch Euro rack with own power supply. To communicate with a PC two independent serial ports are used: RS-232 and RS-422. Control of the measurement process and image reconstruction are done by software installed on a PC computer.

ET3 tomograph allows to change amplifications on the signal cards by switching RC elements in feedback loops of AD8620

amplifiers with analogue multiplexers. In addition, amplifications can be set with two PGA206 programmable amplifiers connected in series. It is possible to change the amplification factor programmatically in the range of 1 to 100 in the integrators, and from 1 to 64 in the amplifiers. It is possible to program amplifications for each measurement channel for each pair of electrodes separately. As a result, it is possible to measure the electrical capacitance in a wide range with similar sensitivity for each measurement channel. This can significantly improve the signal to noise ratio. At the time this was a unique solution that has never been used in Electrical Capacitance Tomography before.

The analogue signal which is a result of the "charge-discharge" method is digitized by the analogue-to-digital converter AD676.

Measuring algorithm performed by the control board is as follows:

a) set amplifications in the measurement channels;
b) send the tag of the new data frame when it is a beginning of a frame;
c) start transmission of a signal on a transmitting electrode and start measurements on the measurement electrodes. Signal detection is performed synchronously with the transmission of the active signal;
d) activate analogue-to-digital conversion for a fixed number of periods. The signals from the measurement circuits are sequentially converted by an analogue-to-digital converter. After each conversion result is sent to the output communication interface as a 16-bit word;
e) stop the transmitting signal and turn off measurement switches;
f) after the last period of the transmitting signal proceed to step a) of the next sequence.

After switching on ET3 tomograph immediately realizes measurement cycle which is periodically repeated. The resulting measurement is sent in a frame consisting of 16-bit words after conversion to digital form. The frame contains a marker which denotes start of the frame, a word describing the state of the tomograph and data, the number of which depends on the current tomograph state. The default mode of the tomograph and measuring circuits amplifications settings are stored in configuration memory and can be reprogrammed while the tomograph is turned on with commands sent from the PC.

ET3 tomograph performs one of two measurement modes: with repetitions, i.e. when each electrode is transmitting while all other electrodes are measurement electrodes which leads to repetition of the measurement for the electrode pair, and a mode without repetition, when the capacitance value of a reciprocal pair of electrodes is measured only once. The software used to operate the tomograph using a PC allows to collect data in real time and performs simultaneous visualization. For image reconstruction (32x32 pixels) LBP algorithm is used. Although electronic components with low tolerance values were used for the construction of the tomograph, the channels may have different characteristics. In addition tomographic sensor electrodes may be made with a limited accuracy. Therefore, prior to measurement it is necessary to perform the calibration consisting of the measurement of the smallest and the largest capacitance value. Assuming linear channel characteristics data are normalized using the maximum and minimum values obtained during calibration. Normalization compensates the characteristics of measuring circuits and the measured values are in range from 0 to1.

ET3 tomograph is characterized by exact measurements (measurement uncertainty of less than 0.025%) and small differences between the channels (less than 1% without calibration). The system allows to acquire approximately 300 pictures per second, but the frame rate may be limited by the bandwidth of the serial RS-232 interface.

ET3 tomograph has been applied in many institutions, including the Institute of Applied Computer Science at Lodz University of Technology, TUNRA Bulk Solids Handling Research Associates at University of Newcastle in Australia and the Faculty of Electrical Engineering at Warsaw University of Technology.

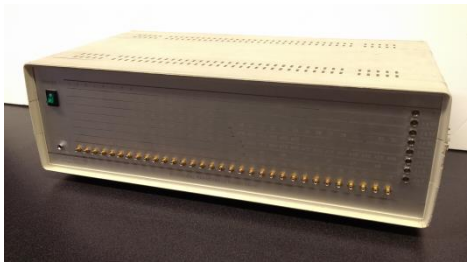

Fig. 2. ET3 tomograph

2. EVT4 tomograph

EVT4 tomograph (Fig. 3) which is currently constructed in the Nuclear and Medical Electronics Division is the successor of ET3 tomograph [4, 5]. The construction is characterized by the following features:

- 32-channel system with the possibility of extending to more channels by combining two or more tomographs;
- parallel measurement of the 31 electrical capacitances in a 32-electrode setup (one electrode is a transmitting electrode and the other are measuring electrodes);
- fully modular - the ability to replace any module without the need of hardware changes in other parts of the tomograph (only replacement of read-out modules embedded software is necessary);
- synchronization between modules implemented through the mechanism of the clock recovery from serial transmission circuits;
- ability to implement different capacitance measurement methods in replaceable analogue cards;
- uniform standard for future creators of capacitance measurement methods;
- flexibility - the ability to cooperate with tomographic sensors with various configurations of electrodes;
- control and diagnostics remotely from a PC via Ethernet;
- system based on the latest available chips on the commercial market of programmable technologies;
- acquisition of 10000 images per second in 32-electrode configuration with measurements repetition for each electrode pair.

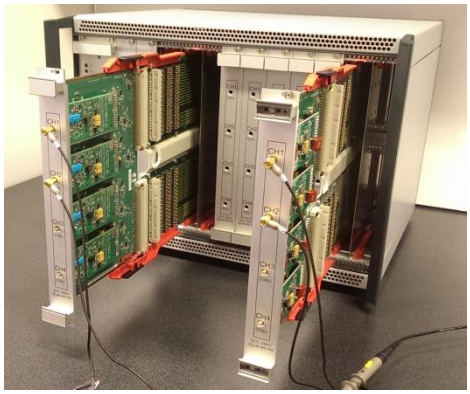

Fig. 3. EVT4 tomograph

EVT4 tomograph consists of the following components:

- control board which contains an ARM Cortex-A8 processor and Spartan-6 FPGA which communicate with each other over the 16-bit General Purpose Memory Controller (GPMC). The control board is responsible for communication with the PC via Ethernet, control of the measurement process and receiving measurement data;
- eight read-out boards controlled by the Spartan-6 FPGAs. Read-out boards receive messages from the control board and transmit data from analogue boards to the control board;
- eight analogue boards that carry out the measurement method and send the data to read-out boards. Analogue cards use high-

speed analogue-to-digital converter AD7626, which reaches 10 million samples per second.

The system works with tomographic sensors having up to 32 electrodes, a PC equipped with an Ethernet and software for data acquisition and image reconstruction.

2.1. Control board

The control board is responsible for communication between a computer and the tomograph, control of measurements, reading the measurement data from the read-out cards, data buffering and data transfer to a computer. Moreover, it provides synchronization between read-out cards. The main elements of the motherboard are:

- 32-bit ARM Cortex-8 Texas Instruments AM3874 RISC processor;
- Xilinx Spartan-6 XC6SLX75T FPGA, coupled to the processor via the GPMC. The GPMC interface is a set of multiple 16-bit registers that the processor sees as addressable memory. GTP transceivers which perform serial communication with speed up to 3.2 Gbps are built-in to FPGA and are ensuring the transmission of data between the control board and read-out boards. An additional advantage of the GTP interface is the ability to recover the clock on the read-out boards which provides synchronization of all of the digital cards of the EVT4 tomograph;
- DDR SDRAM, Flash memory and SD;
- Gigabit Ethernet for communication with the computer. The physical layer is implemented by the transceiver circuit Micrel KSZ9021RL;
- USB-RS232 converter, which is a secondary interface to communicate with the computer. FT232 UART/USB converter was used;
- expansion card with SATA connectors which is connected to the control board via two DIN-41612 connectors.

It is possible to connect up to 8 read-out boards to the motherboard through SATA interface utilizing expansion card. In the EVT4 tomograph physical SATA layer was used due to the high speed data transmission and immunity to electromagnetic interference. Solutions such as multi-layer PCB in which signal layers are separated from powering layers with many layers of ground and a ferrite filters on the power supply lines were used to minimize the distortion and noise.

2.2. Read-out boards

Read-out boards are responsible for controlling the measurement circuits and the analogue-to-digital converters located on the analogue cards (each measurement card contains four measurement channels). Read-out boards are also responsible for the initial data processing and transmission to the motherboard after receiving data from the transmitters.The most important element of each read-out card is Xilinx Spartan-6 XC6SLX75T FPGA containing GTP transceivers used to communicate with the control board. The physical layer of the serial transmission is performed using connectors and SATA cables. Read-out boards are connected to the corresponding analogue boards via 96-pin DIN 41612 connector. Communication with the analogue-to-digital converters AD7626 which are located on analogue measurement boards (each channel of an analogue board contains one transmitter) is implemented in the physical layer using Low-Voltage Differential Signalling (LVDS) standard.

It is possible to additionally mount the DDR SDRAM memory (512 MB) on the cards in case when there is no space for processing measured data in the built-in memory of the FPGA.

Clock signal of the read-out boards is the clock signal coming from the motherboard which is recovered from transmission through the GTP. This solution allows to synchronize all the cards, and thus the measurement cycle in the transmitting and measurement channels.

2.3. Analogue measurement boards

In the EVT4 tomograph it will be possible to mount up to eight measurement cards, wherein each card has four measuring channels, which gives up to 32 channels. The design does not require the use of a particular method of capacitance measurement, which makes the system possible to operate with different sets of measurement cards constructed according to the tomograph project. The limitation is that the size of the PCB has to be in the Eurocard standard, analogue-to-digital converter (AD7626) has to be used as well as GPIO pins which are used to control the measurement card by read-out boards.

Analogue measurement board measures the capacitance and produces a data stream that is transmitted to the read-out board. Every analogue board is connected to the corresponding read-out board with two DIN41612 connectors. By separating the analogue channels from the digital interface it is possible to use different methods for capacitance measurement. It is only needed to exchange measurement board and install a new measurement algorithm in the FPGAs of the read-out boards. At the moment analogue cards with the following measurement methods were created:

- "charge-discharge";
- "single-shot high voltage".

Measuring method "single-shot high voltage" refers to the charging capacitance with a pulse which amplitude is in range of 200 V to 400 V. Fig. 4 shows a block diagram of this method. The measured capacitance is proportional to the U_{diff} voltage.

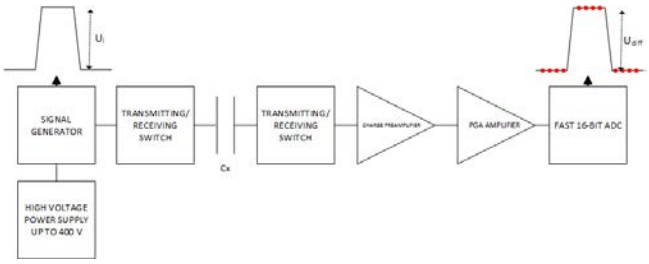

Fig. 4. Block diagram of the analogue board which realizes "single shot high voltage" method

2.4. Embedded software

Embedded software of the EVT4 tomograph is distributed between the control boards and read-out boards. Linux system runs on the control board's ARM processor. Data transmission between the tomograph and the PC is performed by a program written in C language and running on Linux. This program collects data from and transmits data to the Spartan-6 FPGA on the motherboard with a Linux character device driver. FPGA chip on the control board is programmed with a design written in VHDL. Embedded software of Spartan-6 FPGAs of the read-out boards consists of circuits described in VHDL and PicoBlaze software microcontrollers which execute a measurement sequence and are responsible for data transmission.

Each analogue card has four analogue measurement channels where analogue signals are sampled by the AD7626 analogue-to-digital converter which can produce 10 million 16-bit samples per second. Each transmitter therefore transmits 150 Mb of data per second, and therefore each analogue board produces and sends 600 Mb of data per second. Data from the analogue boards are sent to the read-out boards through LVDS which enables the transfer of approximately 655 Mbit/s. The measurement process and data receiving process from analogue boards are controlled by software running on PicoBlaze processors installed on the read-out boards FPGAs. PicoBlaze soft processor is an 8-bit RISC microcontroller running with 100 MHz clock. A special feature of this processor is the fact that each instruction is performed in two ticks of the clock. Accordingly the PicoBlaze enables data transfer at 380 Mb/s. First soft processor receives the commands from the host computers. Second soft processor performs measurement

control. Third PicoBlaze microcontroller is responsible for transferring data to/from the control board through the GTP interface. In the prototype version of the tomograph GTP units are configured to obtain the speed of 1.25 Gbit/s. The data from the read-out boards go to the control board where they are sent as 16-bit words from the FPGA to the ARM processor using the GPMC. In FPGA GPMC protocol support is provided by the Moore finite-state machine described in VHDL. Currently GPMC controller is configured for single readings from the FPGA FIFO queue in which data from the read-out boards reside. Each word should be read by GPMC within 200 ns. This time ensures proper data reception. However, the GPMC introduces additional overhead time associated with the internal arbitration of method for data reading. This additional time is 70 ns for each reading. ARM processor reads data from the GPMC using a driver written in C language. Measuring sequence in the read-out boards has been written so that the CPU of the control board can read data without interruption. This allows it to reach speeds of about 54 Mbit/s. Individual readings by the GPMC are bottleneck of the data transfer in the EVT4 tomograph. With the current measurement method ("single-shot high voltage") where each measurement consists of about 128 samples per channel it is possible to achieve about 44 frames per second in 32-electrode configuration when measurements are made without repetition. In the production version of the device all measurement samples will not be sent. The FPGAs of the read-out boards will calculate measured U_{diff} value and instead all samples only the result will be sent. This will make it possible to obtain more than 2500 frames per second. The further acceleration of data transmission is possible through the use of the DMA transfer in the GPMC. This will speed up the data transmission about the order of magnitude. The target speed of the GPMC is estimated to be about 640 Mb/s. This will allow to obtain over 10000 images per second for the tomographic sensor with 32 electrodes and with repetition of each measurement, i.e. when in each pair of electrodes once one is a transmitting electrode and next the second is a transmitting electrode. Fig. 5 is a diagram of data transmission in the prototype device.

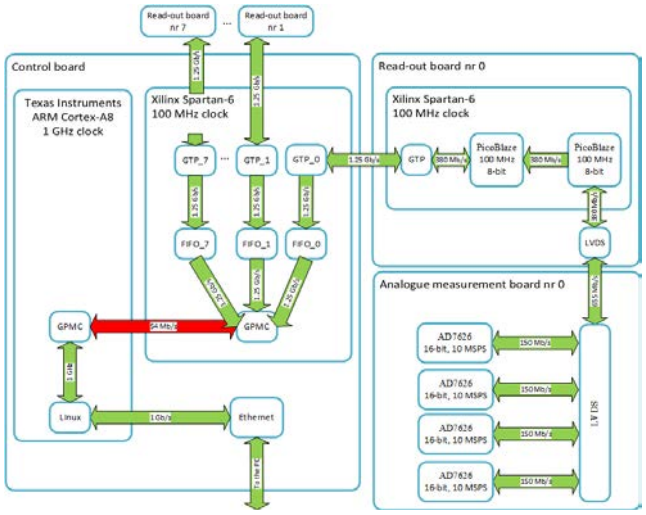

Fig. 5. Diagram of data transmission in EVT4 tomograph

Preliminary tests of the EVT4 tomograph showed that it will be possible to measure capacitance values lower than 10 fF. Further work will include the development of the data acquisition and image reconstruction software for PC.

Bibliography

[1] Brzeski P., Mirkowski J., Olszewski T., Pląskowski A., Smolik W., Szabatin R.: Multichannel capacitance tomograph for dynamic process imaging. Opto-Electronics Review, 11(3), 2003, 175–180.

[2] Huang S.M., Plaskowski A., Xie C.G., Beck M.S.: Capacitance-based tomographic flow imaging system. Electron. Lett., 24, 7/1988, 418–419.

[3] Jaworski A.J., Dyakowski T.: Application of electrical capacitance tomography for measurement of gas-solid flow characteristics in a pneumatic conveying system. Meas. Sci. Technol., 12/2001, 1109–1119.

[4] Kryszyn J., Smolik W., Olszewski T., Szabatin R.: Elektryczny tomograf pojemnościowy EVT4. Elektronika – konstrukcje, technologie, zastosowania, 7/2015, 12–15.

[5] Kryszyn J., Smolik W., Szabatin R., Olszewski T.: Preliminary Measurements with FPGA-based Electrical Capacitance. 7th International Symposium on Process Tomography, Dresden, Germany, 2015.

[6] Plaskowski A., Beck M., Thorn R., Dyakowski T.: Imaging industrial flows. Applications of electrical process tomography, IOP Publishing Ltd., 1995.

[7] Yang W.Q.: Hardware design of electrical capacitance tomography systems. Meas. Sci. Technol., 7/1996, 225–232.

Ph.D. Eng. Waldemar Tomasz Smolik
e-mail: W.Smolik@ire.pw.edu.pl

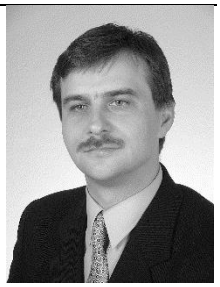

Waldemar T. Smolik received the M.Sc., the Ph.D. and D.Sc. degree in electronics engineering from Warsaw University of Technology, Warsaw, Poland in 1991, 1997 and 2014, respectively. Since 2014, he is an Associate Professor at the Institute of Radioelectronics and Multimedia Technology, Electronics and Information Technology Faculty, Warsaw University of Technology. He is the head of the Laboratory of Electronics Application in Nuclear Medicine at the Division of Nuclear and Medical Electronics. His main research interests are computer engineering, computed tomography and medical imaging. He has published over 70 scientific papers.

M.Sc. Eng. Jacek Kryszyn
e-mail: J.Kryszyn@ire.pw.edu.pl

Received the M. Sc. degree in electronics and computer engineering from Warsaw University of Technology, Warsaw, Poland in 2012. PhD student and the Assistant with the Nuclear and Medical Electronics Division, Institute of Radioelectronics and, Electronics and Information Technology Faculty, Warsaw University of Technology. His field of interest covers Electrical Capacitance Tomography, especially simulations of the electric field and reconstruction of images.

M.Sc. Eng. Tomasz Olszewski
e-mail: T.Olszewski@ire.pw.edu.pl

Tomasz Olszewski received his M.Sc. in electronics from Warsaw University of Technology, Warsaw, Poland in 1982. He has been employed at the University since 1989, currently as a Senior Lecturer. His main interests cover analogue and digital electronics in impedance tomography. He is the main designer of ET and ET3 capacitance tomographs, developed at the Nuclear and Medical Electronics Division.

Ph.D. Roman Szabatin
e-mail: R.Szabatin@ire.pw.edu.pl

Roman Szabatin received the M.Sc. degree in electronics apparatus and the Ph.D. degree from Warsaw University of Technology, in 1972 and 1983, respectively. Since 1973, he has been with the Nuclear and Medical Electronics Division, Institute of Radioelectronics, Electronics and Information Technology Faculty, Warsaw University of Technology, as an Associate, Senior Associate, and Senior Scientist. His main research interests include nuclear and medical instrumentation and medical imaging (gamma cameras, SPECT and PET). He has published over 50 scientific papers.

otrzymano/received: 20.09.2016 *przyjęto do druku/accepted: 15.02.2017*

DOI: 10.5604/01.3001.0010.4598

LINEAR OVER RANGES ITERATIVE ALGORITHMS FOR IMAGE RECONSTRUCTION IN ELECTRICAL CAPACITANCE TOMOGRAPHY

Waldemar T. Smolik, Jacek Kryszyn
Warsaw University of Technology, Faculty of Electronics and Information Technology, The Institute of Radioelectronics and Multimedia Technology, Nuclear and Medical Electronics Division

Abstract. *The paper concerns the non-linear algorithms for image reconstruction in electrical capacitance tomography for which Jacobi matrix computation time is very long. The paper presents the idea of an iterative linearization in nonlinear problems, which leads to a reduction in the number of steps calculating Jacobi matrix. The linear Landweber algorithm with sensitivity matrix updating and non-linear Levenberg-Marquardt algorithm with Jacobi matrix updating in selected steps only were presented.*

Keywords: non-linear problem, iterative linearization, electrical tomography, image reconstruction from projections

PRZEDZIAŁAMI LINIOWE ITERACYJNE ALGORYTMY REKONSTRUKCJI OBRAZÓW W ELEKTRYCZNEJ TOMOGRAFII POJEMNOŚCIOWEJ

Streszczenie*. Artykuł dotyczy nieliniowych algorytmów rekonstrukcji obrazów w elektrycznej tomografii pojemnościowej, dla których czas wyznaczenia macierzy Jacobiego jest bardzo długi. W pracy przedstawiono ideę iteracyjnej linearyzacji w problemach nieliniowych, która prowadzi do zmniejszenia liczby kroków wyznaczających macierz Jacobiego. Przedstawiono liniowy algorytm Landwebera z uaktualnianiem macierzy wrażliwości oraz algorytm Levenberga-Marquardta z wyznaczaniem macierzy Jacobiego tylko w wybranych krokach.*

Słowa kluczowe: problem nieliniowy, iteracyjna linearyzacja, tomografia elektryczna, rekonstrukcja obrazów z projekcji

Introduction

Electrical capacitance tomography is an imaging technique which allows to visualize spatial (three-dimensional or cross-sectional) and temporal distribution of electric permittivity inside tomographic sensor. The image is reconstructed from measurements of mutual capacitance of sensor electrodes surrounding examined space. This method was first time proposed by Maurice Beck and Andrzej Plaskowski from University of Manchester for monitoring of industrial processes [6, 14].

Image reconstruction in electrical capacitance tomography is a non-linear problem [10]. The measured capacitances are non-linear function of the spatial distribution of permittivity. The inverse problem consists of determining the distribution of electric permittivity inside the probe using the measured capacitance. Lack of knowledge of analytical form of non-linear inverse transform forces calculation of permittivity distribution by solving an optimization problem, for example by minimizing the mean square norm.

The Newton-Raphson method could be applied for least-square minimization. Because this method requires the calculation of Hessian matrix which is time consuming, the Gauss-Newton method is preferable in which the approximation of Hessian matrix is used. The application of Gauss-Newton algorithm in the electrical capacitance tomography is presented in [5]. The weakness of the Gauss-Newton method is bad behavior when Jacobi matrix is ill-conditioned, what is the case of electrical tomography. Even small measurement errors cause a significant change of step direction of iterative algorithm searching a functional minimum. For regularized non-linear least-square optimization the Levenberg-Marquardt method can be used. However, the selection of the value of the regularization parameter used in Lavenberg-Marquard method is not a simple task. The value could be selected experimentally or set manually. Some automatic methods of regularization parameter value were proposed like generalized cross validation (GCV) or L-curve.

The application of the Lavenberg-Marquard algorithm in electrical tomography is described in [1]. The application of GCV method for automatic selection of the value of regularization parameter in the Levenberg-Marquardt algorithm did not bring satisfactory results [1]. In contrast to the GCV, L curve method gave good results of image reconstruction [3].

Practical application of non-linear optimization algorithm is limited by the calculation time, because these algorithms need to determine the Jacobian matrix (solve a forward problem) in each step. The forward problem consists of determining the electric field distribution in tomographic probe by numerical solution of the generalized Poisson equation, which is a complex computational problem. For this reason, linearization and iterative algorithms for solving the linear problem are preferred in electrical capacitance tomography.

An interesting idea presented in this paper is to use an iterative linearization in non-linear problem. The iterative linearization reduces the number of steps of the algorithm in which the Jacobian matrix is determined. Transformation of linear and non-linear algorithm in a linear over ranges algorithm was presented in the papers [15, 16]. The linear Landweber algorithm with sensitivity matrix updating and Levenberg-Marquardt algorithm with the calculation of Jacobi matrix only in selected steps were discussed.

1. Landweber algorithm with sensitivity matrix updating

In the linear approach, the image reconstruction in capacitance tomography can be defined as the minimization of a quadratic residue of the standard linear equation with respect to the vector ε, which can be written as:

$$\hat{\varepsilon} = \arg\min_{\varepsilon} \frac{1}{2} \left\| \mathbf{S}\varepsilon - \mathbf{c} \right\|_2^2 \tag{1}$$

where the vector ε describes the spatial distribution of electric permittivity inside the sensor, $\mathbf{S}$ is the sensitivity matrix describing the impact of changes in the distribution of permittivity on the value of the mutual capacitance of electrodes in the tomographic sensor, and $\mathbf{c}$ is the vector of measured capacitances.

The Landweber iterative algorithm, which searches a minimum of quadratic norm functional is given by the formula:

$$\varepsilon^{(i+1)} = \varepsilon^{(i)} - a^{(i)} \mathbf{S}^T \left(\mathbf{S}\varepsilon^{(i)} - \mathbf{c} \right) \tag{2}$$

The Landweber algorithm is steepest descent gradient type method with very small value of step length a which guarantees the convergence of the algorithm [8].

Because the linear model of the tomographic system (sensitivity matrix) depends on the distribution of permittivity in the tomographic sensor, the approximation of the sensitivity matrix is used in the algorithm. Most often, because there is no a priori information about the examined object, the sensitivity matrix calculated for a uniform distribution of the permittivity is used in the linear model. For the same reason, uniform distribution of permittivity is taken as the first stage of an iterative algorithm.

So, taken the form of sensitivity matrix, which is a good option for the first steps of the algorithm, it is becoming worse approximation model of the system with the next steps. Suppose that in subsequent iterations of the algorithm, getting better estimate of the electrical permittivity distribution is found. This information can be used to determine a better approximation model of linear system at given step. If after a certain number of steps, the permittivity distribution changes significantly, a new approximation of the sensitivity matrix can be determined.

In the simplest version, the sensitivity matrix can be updated after a given number of iterations. In this way, ranges linear algorithm can be obtained, which solves the non-linear problem over linear ranges [13, 17] . The step of the algorithm can be written using the following equation:

$$\varepsilon^{(i+1)} = \varepsilon^{(i)} - a^{(i)}\mathbf{S}^{(g(i))T}\left(\mathbf{S}^{(g(i))}\varepsilon^{(i)} - \mathbf{c}\right), \tag{3}$$

where $\mathbf{S}^{(g(i))} = \mathbf{S}\left(\varepsilon^{(g(i))}\right)$ and the function $g(i)$ describes the moments of sensitivity matrix updating.

In the first approach it can be assumed that through a number of steps the algorithm is moving in a small range, in which the function does not change rapidly and can be approximated by linear relationship. If the sensitivity matrix has to be updated every certain number of iterations, the function has the form of a stepped function given by the formula:

$$g(i) = \mathrm{ceil}\left(i - i \bmod \mathrm{D}i\right) \tag{4}$$

where ceil is a rounding up to the nearest integer, mod is the remainder of the division. In the case of observing changes in the estimated vector, the function defining moment of renovation sensitivity matrix may have the form:

$$g(i) = \begin{cases} 0 & \text{dla} \quad i = 0, \\ g(i-1) & \text{dla} \quad \left\|\varepsilon^{(i)} - \varepsilon^{(g(i-1))}\right\| < d, \\ i & \text{dla} \quad \left\|\varepsilon^{(i)} - \varepsilon^{(g(i-1))}\right\| \geq d, \end{cases} \tag{5}$$

where d is a certain small value. The value of the parameter that determine when to upgrade the sensitivity matrix, such as the number of iterations or threshold by which must change estimate the distribution permittivity is not obvious. This issue was the subject of research. Some papers [9, 17] show that the modified Landweber algorithm with sensitivity matrix updating achieves far better results than the linear version. Even the use of two, three modifications of the sensitivity matrix, with the total number of steps equal to several hundreds, brings a great improvement in the quality of the reconstructed image. The additional modifications of the above-described ranges linear iterative algorithm are possible [12]. The first modification is adaptive control of step length parameter $a^{(i)}$. The standard approach is a relaxation strategy, involving reduction of step length during the calculation, which allows the algorithm to reach a stabilized solution.

The proposed modification consists of checking whether the value of the residue decreases in the next step. If in the next step the condition of decreasing the value of the residuum is not reached, the algorithm returns to the previous estimate of the solution, and the value of the parameter $a^{(i)}$ is decreased. This strategy allows to take greater step length at the beginning of calculations to accelerate the search and prevents divergence of the algorithm in the case of too long step. Another modification of the Landweber algorithm is to use the normalized sensitivity matrix [12]. The method of normalization of the sensitivity matrix was taken from a linear back projection (LBP) algorithm [7]. The matrix is normalized in columns, so that the sum of the coefficients in the columns is equal to unity. The matrix normalized in columns is given by the formula:

$$\bar{\mathbf{S}} = \mathbf{S}\,\mathrm{diag}\left(\mathbf{S}^T\mathbf{u}\right)^{-1} \tag{6}$$

where $\mathbf{u} = [1, 1, \ldots, 1]^T$ is column unit vector, and diag is an operator that creates diagonal matrix from a vector. If the measurements are normalized according to the following formula:

$$\bar{\mathbf{c}} = \mathrm{diag}\left(\mathbf{c}_{\max} - \mathbf{c}_{\min}\right)^{-1}\left(\mathbf{c} - \mathbf{c}_{\min}\right) \tag{7}$$

where $\mathbf{c}$, $\mathbf{c}_{\max}$, $\mathbf{c}_{\min}$ are vectors of capacitance measurements for the object, for the uniform distribution of electric permittivity with the minimum $e_{\min}$ and maximum $e_{\max}$ value of the measurement range respectively, the reconstructed permittivity values are normalized and bounded in the range $\langle 0;1\rangle$.

The iterative algorithm with the application of normalized sensitivity matrix which searches for a minimum of a quadratic norm is given by the formula:

$$\bar{\varepsilon}^{(i+1)} = \bar{\varepsilon}^{(i)} - a^{(i)}\bar{\mathbf{S}}^T\left(\bar{\mathbf{S}}\bar{\varepsilon}^{(i)} - \bar{\mathbf{c}}\right) \tag{8}$$

If the initial solution is the uniform permittivity distribution with the value $\bar{\varepsilon}^{(0)} = 0$, the first step of the algorithm is given by the equation

$$\bar{\varepsilon}^{(1)} = \bar{\varepsilon}^{(0)} - a^{(0)}\bar{\mathbf{S}}^T\bar{\mathbf{S}}\bar{\varepsilon}^{(0)} + a^{(0)}\bar{\mathbf{S}}^T\bar{\mathbf{c}}. \tag{9}$$

The first step of this algorithm is equivalent to a linear back projection algorithm LBP when step length $a^{(0)} = 1$.

The application of normalized sensitivity matrix compensates for the lack of sensitivity in the center of the field of view of the tomographic sensor. In our forward problem solver the sensitivity matrix is calculated inaccurately at the edges of the field of view because of the used Cartesian grid. It turned out that sensitivity matrix normalization minimized the impact of the errors of the sensitivity matrix coefficients for the edges of the field of view.

This approach is preferred in the case of image reconstruction with the sensitivity matrix calculated using a regular Cartesian discretization grid because it is less sensitive to the errors of calculation of the sensitivity coefficients on the edges of the sensor.

2. Levenberg-Marquardt algorithm with the calculation of Jacobi matrix only in selected steps

The problem of image reconstruction in electric capacitance tomography described by a nonlinear equation:

$$\mathbf{C} = h(\varepsilon) \tag{10}$$

can be defined as a search for roots of the function:

$$f(\varepsilon) = h(\varepsilon) - \mathbf{C} \tag{11}$$

In the electric capacitance tomography, it can be assumed that the problem is underdetermined and there are many solutions. The task is to find such N dimensional vector $\varepsilon = [e_1, e_2, \ldots, e_N]^T$, for which the condition:

$$f(\varepsilon) = 0 \tag{12}$$

is satisfied. If the function f is continuous and differentiable in the vicinity of the point e, it can be expanded in a Taylor series:

$$f(\varepsilon + \mathrm{D}\varepsilon) = f(\varepsilon) + \mathbf{J}(\varepsilon)\mathrm{D}\varepsilon + O(\varepsilon). \tag{13}$$

where $\mathbf{J}(\varepsilon)$ is a partial derivative matrix and $O(\varepsilon)$ represents the components of the higher order. Neglecting higher order components, the following relationship is obtained:

$$\mathrm{D}\varepsilon = -\mathbf{J}^{-1}(\varepsilon)f(\varepsilon) \tag{14}$$

where $\mathrm{D}e$ is the increase defined by the tangent to the function at a point ε or in other words the distance from this point to the intersection of the tangent with the abscissa. From the above equation and using linear approximation of function h, the following iterative formula can be obtained:

$$\varepsilon^{(i+1)} = \varepsilon^{(i)} - \left(\mathbf{J}^{(i)}\right)^{-1} \left[\mathbf{J}^{(i)}\varepsilon^{(i)} - \mathbf{C}\right] \quad (15)$$

where $\mathbf{J}^{(i)} = \mathbf{J}\left(\varepsilon^{(i)}\right)$.

The matrix $\mathbf{J}^{-1}$ does not exist in most cases in electric capacitance tomography because the problem is undetermined. Instead of the direct inverse the left pseudoinverse can be used what leads to the formula known as the Gauss-Newton method:

$$\varepsilon^{(i+1)} = \varepsilon^{(i)} - \mathbf{J}^{(i)T}\left(\mathbf{J}^{(i)}\mathbf{J}^{(i)T}\right)^{-1}\left[\mathbf{J}^{(i)}\varepsilon^{(i)} - \mathbf{C}\right] \quad (16)$$

If we introduce regularization parameter $m^2\mathbf{I}$, where m is a positive number, and $\mathbf{I}$ is the identity matrix, we get regularized Gauss-Newton algorithm called Levenberg-Marquardt (LM) algorithm [11]. Additionally, if we take into account the step length $a^{(i)}$, we obtain the following iterative formula:

$$\varepsilon^{(i+1)} = \varepsilon^{(i)} - a^{(i)}\mathbf{J}^{(i)T}\left(\mathbf{J}^{(i)}\mathbf{J}^{(i)T} + m^2\mathbf{I}\right)^{-1}\left[\mathbf{J}^{(i)}\varepsilon^{(i)} - \mathbf{C}\right] \quad (17)$$

where $\mathbf{J}^{(i)} = \mathbf{J}\left(\varepsilon^{(i)}\right)$. If the function is highly non-linear, Jacobi matrix (sensitivity matrix) should be calculated in each step of the algorithm. However, if a function within a certain range is approximately linear, Jacobi matrix does not change much. If we assume that the function domain could be divided into several ranges where the function is approximately linear, it is possible to modify the algorithm, so that the Jacobi matrix will be constant in each range and it will change only when moving to an adjacent range [18]. Then the algorithm takes the form:

$$\varepsilon^{(i+1)} = \varepsilon^{(i)} - a^{(i)}\mathbf{J}^{(g(i))T}\left[\mathbf{J}^{(g(i))}\mathbf{J}^{(g(i))T} + m^2\mathbf{I}\right]^{-1}\left[\mathbf{J}^{(g(i))}\varepsilon^{(i)} - \mathbf{C}\right] \quad (18)$$

where $g(i)$ is the function describing moments of updating of sensitivity matrix. The problem is to determine linear ranges in this method. There are different approaches, including simple, assuming that the linear approximation is valid for a certain number of steps, during which the Jacobi matrix is not updated.
In this approach, the function has the form of a step function given by the formula (4), as in the modified algorithm Landweber with sensitivity matrix updating. A more sophisticated method for determining the moment of Jacobi matrix calculation can consist in observation of changes of the estimated vector ε. If the change of the estimated vector from the last modification of Jacobi matrix exceeds a certain preset threshold, the Jacobi matrix should be recalculated. In this method, the function describing the update moments of the sensitivity matrix may be in the form given by (5).

3. Results of image reconstruction

The described above linear over ranges algorithms were verified experimentally using numerical simulated data and real measurements. Here, exemplary results of the experiments will be shown only for modified Levenberg-Marquardt algorithm. The sensitivity matrix updating scheme used in both algorithms is similar. The Levenberg-Marquardt algorithm switches between the Gauss-Newton algorithm (when the regularization parameter is very small) and steepest descent algorithm (where the regularization parameter is large).

Measurements were performed using ET3 tomograph build at our Division [2]. The multichannel device worked with different gains for pairs of adjacent (low amplification) and opposite electrodes (high amplification). The cylindrical sensor with one ring of 16 electrodes was used. The diameter of the cylinder was equal to 160 mm. The height of the electrodes was equal to the cylinder diameter (the dimension in the direction of the axis of the cylinder). The physical object used in the experiments consisted of 6 Perspex rods with relative permittivity value equal about 2.9. The diameter of the rods was equal 20 mm. The length of rods was much greater than electrode height. The shape of the test object was selected arbitrary to allow two-dimensional modeling of the electric field distribution in a tomographic sensor. The object placed in the sensor is shown in Fig. 1. The collected data for the object were normalized using the measurements for empty and fully filled with Perspex sensor.

Two-dimensional simulations of measurements were performed using Matlab toolbox „ECTsim" developed by our group. The numerical modeling of the sensor and the object, electric field calculation and sensitivity matrix calculation is performed using regular Cartesian grid. The size of discretization matrix of sensor model used in that simulation was 52×52 elements. The shape of the object does not change in the Z-axis so that the two-dimensional approximation of the electric field distribution is close to the three-dimensional distribution. The numerical representation of the object used in the real measurements is shown in Fig. 2. The capacitance measurements were simulated for the object. To simulate a measurement process in electrical capacitance tomography so called forward problem has to be solved. The potential distribution in the sensor with boundary conditions imposed by voltage applications on the electrodes has to be calculated. Knowing the voltage distribution the mutual capacitance formed by two electrodes selected from the set of electrodes surrounding the object can be calculated using the Gauss's law. An alternative method of capacitance calculation is application of discrete linear approximation

$$\mathbf{c} = \mathbf{S}\boldsymbol{\varepsilon}. \quad (19)$$

This method was used in ECTsim toolbox. The potential distribution was calculated for all application electrodes for the specified sensor geometry and the permittivity distribution inside the sensor. The mutual impedance principle is used for sensitivity matrix calculation. The sensitivity distributions for all electrode pairs are calculated. The calculated two-dimensional sensitivity maps constitute the rows of the sensitivity matrix. Because the measured value of capacitance formed by two electrodes is the same independently of the fact which electrode is an application or measuring electrode, there are $M = L(L-1)/2$ measurements for L electrodes. For $L = 16$ electrodes, there are $M = 120$ measurements.

The Gaussian noise was added to the generated data. The measurement error (standard deviation) corresponds to around 0.1 % of the measurement range limited by the maximum value measured for the sensor full filled with the material of high permittivity.

The modified LM algorithm was implemented using the equation (18). The regularization parameter was calculated automatically by the L-curve method [4]. The value of the regularization parameter is a compromise between the value of residual error and the norm of the regularized solution. The norm of a regularized solution versus the norm of the residual norm for different value of regularization parameter is plotted in log-log scale. The value of the regularization parameter is selected as a point that corresponds to the corner of L-curve. The curves for reconstruction from simulated data and real measurement are shown in Fig. 3 and Fig. 4 respectively. The value of the regularization parameter is calculated after every update of the sensitivity matrix. The step length $a^{(i)}$ was constant for all iterations. The value was set arbitrarily and equal 0.15 for reconstruction from simulated data and 0.1 for reconstruction from real measurements.

The sensitivity matrix (Jacobian) was calculated only a few times in the iterative process. In the shown example the sensitivity matrix was updated every 100 steps. The moments of sensitivity matrix recalculation are visible on the plot of reconstruction error. The algorithm was stopped arbitrarily after 650 steps when the algorithm reached a steady state. The reconstructed distribution of permittivity for simulated and real data are shown in Fig. 5 and Fig. 6.

To evaluate the reconstruction quality quantitatively a square norm was used. The norm was calculated in image space, capacitance measurements space and sensitivity matrix space. In image space, the norm is a discrepancy between the reconstructed

and true permittivity distribution. In case of real measurement data, the numerical representation of the object is used as true permittivity. In capacitance space, the capacitance residual error is the normalized discrepancy between the measured capacitances and the values calculated for the given estimate of permittivity. In sensitivity matrix space the error is the norm between the sensitivity matrix computed for a true permittivity distribution and the sensitivity matrix computed for given estimate of a permittivity distribution. In case of real data the sensitivity matrix for a true permittivity distribution is calculated using the numerical model of a physical object. The presented in this paper nonlinear iterative algorithm updates the sensitivity matrix. The norm in sensitivity space shows how the approximated model fits to the true model. The square norm is normalized using the formula:

$$err = \left\| \mathbf{x}^i - \mathbf{x}_t \right\|^2 \Big/ \left\| \mathbf{x}^0 - \mathbf{x}_t \right\|^2 \tag{20}$$

For example in image space $\mathbf{x}_t$ denotes the true permittivity distribution. $\mathbf{x}^0$ is the start solution and $\mathbf{x}^i$ is the permittivity estimate at i-th step of iterative algorithm.

The plots of reconstruction error for simulated and real data are shown in Fig. 7 and Fig. 8. The points of discontinuity in sensitivity matrix error corresponds to the moments of sensitivity matrix recalculation. The sensitivity 2D map calculated for uniform distribution and obtained after 6 updates are shown in Fig. 9 and Fig. 10 respectively.

Fig. 1. The test object (six Perspex (PMMA) rods) placed in the cylindrical sensor

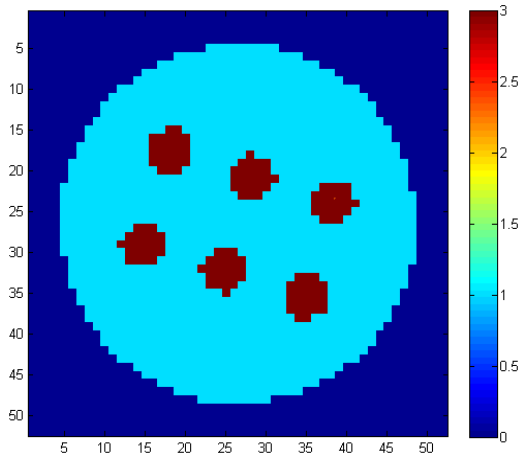

Fig. 2. Numerical representation of permittivity distribution in the axial cross section of the sensor with the test object. Relative permittivity of PMMA rods: $\varepsilon_{PMMA} = 3$, permittivity of air in sensor: $\varepsilon_{air} = 1$

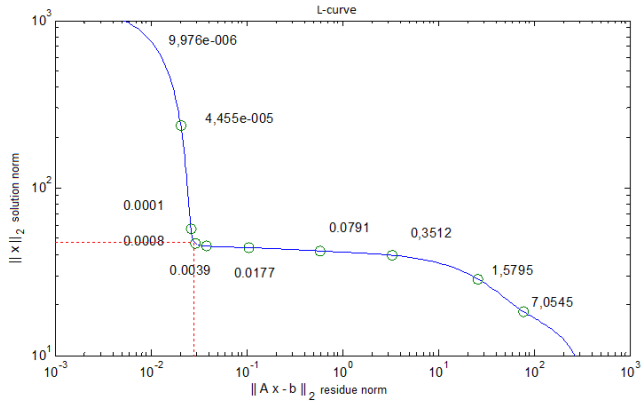

Fig. 3. L-curve for reconstruction from simulated data. Plot of regularized solution norm in function of residuum norm for different value of regularization parameter (value of regularization parameter given for selected points)

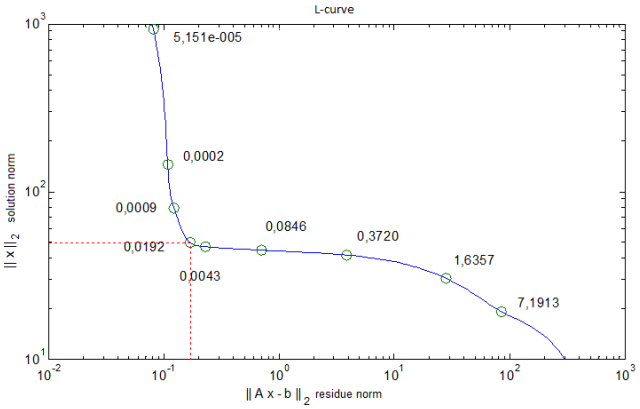

Fig. 4. L-curve for reconstruction from real measurements. Plot of regularized solution norm in function of residuum norm for different value of regularization parameter (value of regularization parameter given for selected points)

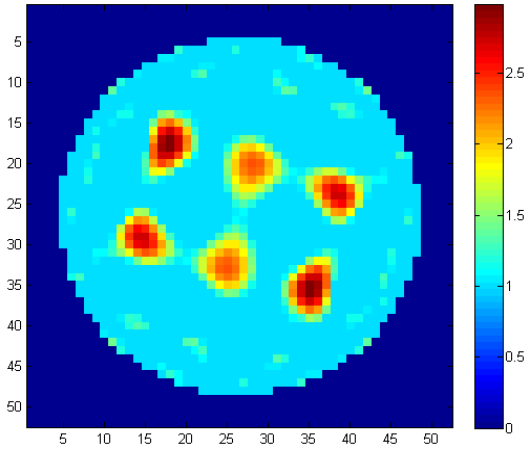

Fig. 5. Permittivity distribution in axial cross-section of sensor reconstructed using modified LM algorithm from simulated data

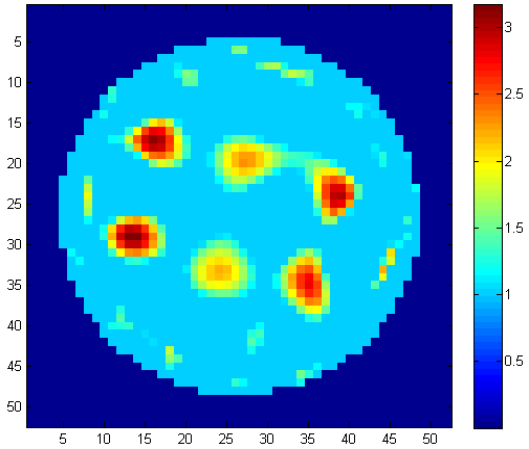

Fig. 6. Permittivity distribution in axial cross-section of sensor reconstructed using modified LM algorithm from real measurements

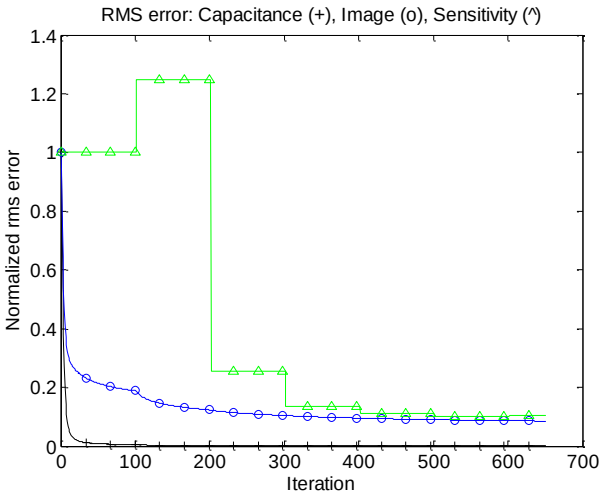

Fig. 7. Reconstruction error in function of number of iterations. Capacitance measurement error (+), image error (O), sensitivity matrix error (Δ).Reconstruction for simulated data

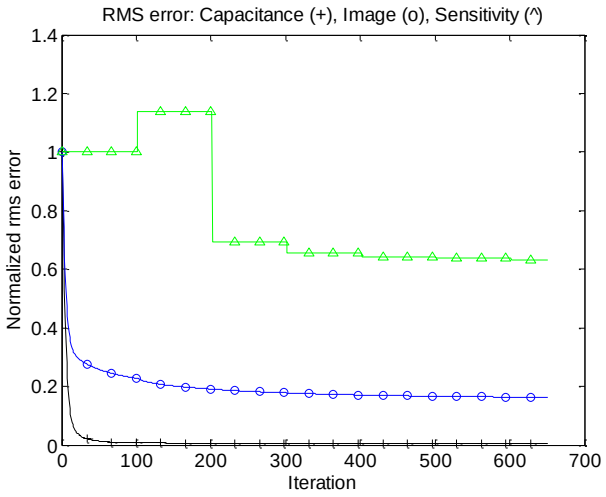

Fig. 8. Reconstruction error in function of number of iterations. Capacitance measurement error (+), image error (O), sensitivity matrix error (Δ).Reconstruction for real measurements

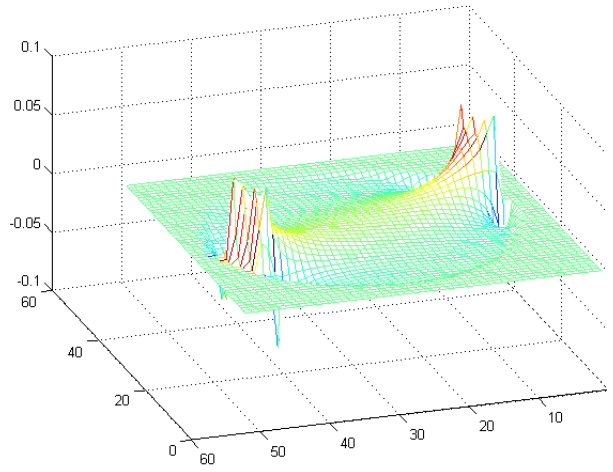

Fig. 9. Two dimensional sensitivity map for opposite electrodes calculated for uniform permittivity distribution in a sensor

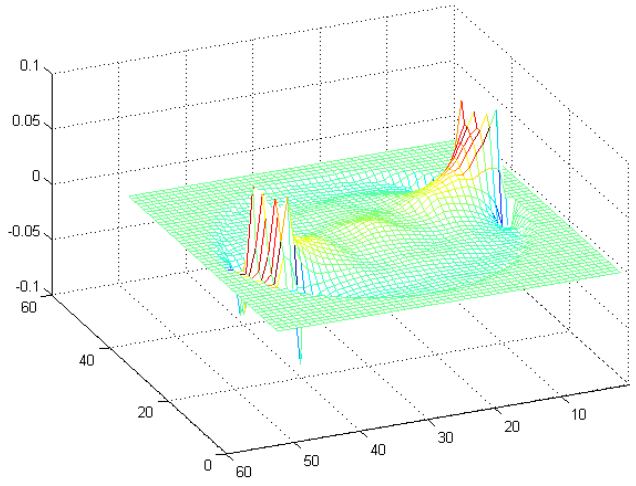

Fig. 10. Two dimensional sensitivity map for opposite electrodes obtained after six recalculation of sensitivity matrix

4. Conclusions

The linear over ranges algorithms were introduced in this paper. The results of image reconstruction using modified Levenberg-Marquardt algorithm were presented. The linear over ranges LM algorithm was convergent. The reconstruction quality norms decrease in function of iteration number with one exception. The discrepancy norm for a sensitivity matrix increases after first update of sensitivity matrix but decreases after next updates. This behavior was observed for both cases: reconstruction from simulated data and reconstruction from real measurements.

Only a few updates of the sensitivity matrix were enough to obtain acceptable image quality. The limited number of updates of Jacobi matrix up to six for dozens of iterations of the modified LM algorithm did not degrade image quality, and significantly reduces the number of calculations. Moreover, in the experiments the simplest method of selection of the moments when the sensitivity matrix was recalculated was used.

The carried out experiments had shown that the linear over ranges algorithm are very effective in terms of picture quality relative to the number of calculations. The application of the custom finite element method previously elaborated for sensitivity matrix calculation [19] accelerates the computations but the forward problem computations are still very time consuming comparing to the computation of the inverse transform.

Bibliography

[1] Brandstatter B., Holler G., Watzenig, D.: Reconstruction of inhomogeneities in fluids by means of capacitance tomography. COMPEL—Int. J. Comput. Math. Electr. Electron. Eng., 22/2003, 508–19.
[2] Brzeski P., Mirkowski J., Olszewski T., Pląskowski A., Smolik W., Szabatin R.: Multichannel capacitance tomograph for dynamic process imaging. Opto-Electronics Review, 11(3)/2003, 175–180.
[3] Gomez S., Ono M., Gamio C., Fraguela A.: Reconstruction of capacitance tomography images of simulated two-phase flow regimes. Appl. Num. Math., 2003, 197–208.
[4] Hansen P.C., O'leary D.P.: The use of the L-curve in the regularization of discrete ill-posed problems. SIAM J. Sci. Comput., 14/1993, 1487–1503.
[5] Holler G., Watzenig D., Brandstatter B.: A fast Gauss–Newton based ECT algorithm with automatic adjustment of the regularization parameter. Proc. 3rd World Congress on Industrial Process Tomography, Banff, Alberta, Canada, 2003, 415–420.
[6] Huang S.M., Plaskowski A.B., Xie C.G., Beck M.S.: Capacitance-based tomographic flow imaging system. Electron. Lett., 24/1988, 418–419.
[7] Huang S.M., Plaskowski A., Xie C.G., Beck M.S.: Tomographic imaging of two-component flow using capacitance sensors. J.Phys. E:Sci. Instrum., 22/1989, 173–177.
[8] Landweber L.: An Iterative Formula for Fredholm Integral Equations of the First Kind. Amer. J. Math., 73/1951, 615–624.
[9] Li Y., Yang W.Q.: Image reconstruction by nonlinear Landweber iteration for complicated distributions. Meas. Sci. Technol., 19/2008, 1–8.
[10] Lionheart W. R.: EIT reconstruction algorithms: pitfalls, challenges and recent developments. Physiol. Meas., 25/2004, 125–142.
[11] Lionheart W., Polydordes N., Borsic A.: The reconstruction problem. In: Holder D.S. (ed.) Electrical Impedance Tomography: Methods, History and Applications. Institute of Physics, 2004.

[12] Mirkowski J., Smolik W., Olszewski T., Radomski D., Szabatin R., Brzeski P.: Parameters Optimization For Model Based Image Reconstruction In Electrical Capacitance Tomography. Proc. 4th World Congress on Industrial Process Tomography, Aizu, Japan, 2005, 703–707.
[13] Mirkowski J., Smolik W.T., Yang M., Olszewski T., Szabatin R., Radomski D.S., Yang W.Q.: A New Forward-Problem Solver Based on a Capacitor-Mesh Model for Electrical Capacitance Tomography. IEEE Trans. Instrumentation and Measurement, Vol. 57, No 5, 2008, 973–980.
[14] Plaskowski, A., Beck, M., Thorn, R. & Dyakowski, T.: Imaging industrial flows. Applications of electrical process tomography, IOP Publishing Ltd., 1995.
[15] Smolik W.: Reconstruction of complex objects in electrical capacitance tomography. IEEE International Workshop on Imaging Systems and Techniques (IST 2009), Shenzhen, China, 2009, 432–437.
[16] Smolik W.T., Radomski D.: Performance evaluation of the iterative image reconstruction algorithm with sensitivity matrix updating based on real measurements for electrical capacitance tomography. Meas. Sci. Technol., 20/2009, 115502 (12pp).
[17] Smolik W., Mirkowski J., Olszewski T., Szabatin R.: Verification of image reconstruction algorithm with sensitivity matrix updating for real data in electrical capacitance tomography. Proc. 4th International Symposium on Process Tomography in Poland, Warsaw, Poland, 2006.
[18] Smolik W.T., Accelerated Levenberg-Marquardt Method With an Optimal Step Length in Electrical Capacitance Tomography, Proc. of IEEE International Conference on Imaging Systems and Techniques (IST 2010), Thessaloniki, Greece, 2010, 204–209.
[19] Smolik W.: Forward Problem Solver for Image Reconstruction by Nonlinear Optimization in Electrical Capacitance Tomography. Flow Measurement and Instrumentation, 21/2010, 70–77.

Prof. Eng. Waldemar Tomasz Smolik
e-mail: W.Smolik@ire.pw.edu.pl

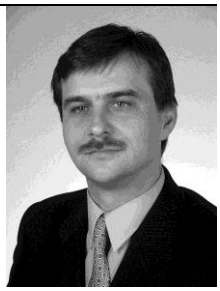

Waldemar T. Smolik received the M.Sc., the Ph.D. and D.Sc. degree in electronics engineering from Warsaw University of Technology, Warsaw, Poland in 1991, 1997 and 2014, respectively. Since 2014, he is an Associate Professor at the Institute of Radioelectronics and Multimedia Technology, Electronics and Information Technology Faculty, Warsaw University of Technology. He is the head of the Laboratory of Electronics Application in Nuclear Medicine at the Division of Nuclear and Medical Electronics. His main research interests are computer engineering, computed tomography and medical imaging. He has published over 70 scientific papers.

M.Sc. Eng. Jacek Kryszyn
e-mail: J.Kryszyn@ire.pw.edu.pl

Received the M. Sc. degree in electronics and computer engineering from Warsaw University of Technology, Warsaw, Poland in 2012. PhD student and the Assistant with the Nuclear and Medical Electronics Division, Institute of Radioelectronics and, Electronics and Information Technology Faculty, Warsaw University of Technology. His field of interest covers Electrical Capacitance Tomography, especially simulations of the electric field and reconstruction of images.

otrzymano/received: 20.09.2016 *przyjęto do druku/accepted: 15.02.2017*

DOI: 10.5604/01.3001.0010.4599

NEEDLE DETECTOR OF X-RAY AND GAMMA RADIATION

Grzegorz Domański, Roman Szabatin, Piotr Brzeski, Bogumił Konarzewski
Warsaw University of Technology, The Institute of Radioelectronics and Multimedia Technology

Abstract. *The article presents the developed structure of the novel needle proportional gas detector (NPC – Needle Proportional Counter) used for the detection of X-rays and gamma rays. The advantage of the detector is its simple mechanical construction and the possibility of detection of incident radiation in a direction parallel to the needle. The measured energy spectrum of the isotope Fe-55 by means of the developed detector is presented.*

Keywords: gas detector with electron multiplication, x-ray detector, gamma radiation

DETEKTOR IGŁOWY PROMIENIOWANIA X I GAMMA

Streszczenie. *Artykuł przedstawia opracowaną konstrukcję nowego typu gazowego detektora igłowego, służącego do detekcji promieniowania X i gamma. Zaletą detektora jest jego prosta konstrukcja mechaniczna i możliwość detekcji promieniowania w kierunku równoległym do igły. Zmierzono widmo energetyczne izotopu Fe-55 opracowanym detektorem.*

Słowa kluczowe: Detektor z gazowym powielaniem elektronów, detektor promieniowania X, promieniowanie gamma

Introduction

Gas detectors history dates back to the first half of the twentieth century, when in 1908 H. Geiger and E. Rutherford developed a proportional counter [7]. The further development led to a Geiger-Müller counter by H. Geiger and W. Müller in 1928. [3]. In the second half of the twentieth century G. Charpak developed the Multiwire Proportional Chamber [2] (in 1968). In 1988, A. Oed proposed Micro-Strip Gas Chamber [6], and in 1997, F. Sauli introduced Gas Electron Multiplier [8]. The general concept of gas detector is shown in the Figure 1. Gas detectors of ionizing radiation are used among other things in medicine, astronomy [1], and high energy physics experiments [4, 5].

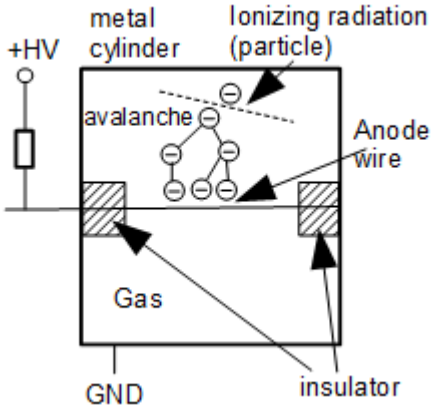

Fig. 1. General concept of a gas detector

The construction of the detector is shown schematically in the Figure 1. Ionizing radiation, passing through the matter, it loses its energy, among other things on its ionization. X-ray and gamma ray is electromagnetic radiation that can ionizing matter indirectly. First quantum of electromagnetic radiation can interact with an atom in photoelectric, Compton or creation of pairs effect [5]. As a result of this interaction arises, one or more charged particles that moving in a material medium, ionize them. The gas detectors have an active volume of the filling gas in which ionization occurs. Metal electrodes produce electric field and separate electrical charges that drift toward the electrodes. Radiation produced by the original electric charge can be amplified if close to one of the electrodes - the anode - there is a sufficiently strong electric field [8]. One type of gas detectors are proportional counters, which have anode metal wire of a small diameter. Formed during a single gamma quantum detection electric charge in the detector is proportional to the quantum energy. One of the problems is low detection efficiency of X-rays or gamma rays in gas detectors. This article presents a new type of gas detector, wherein a metal needle plays role of an anode, while the radiation is incident in a direction parallel to the needle. The anode is supported on one side only, which simplifies the construction of such a detector.

1. Methods

The concept of the needle detector is as follows: a metal acupuncture needle having a diameter of less than 0.2 mm is soldered to the PCB. The needle is connected to a high positive potential, while the detector is placed in a metal housing, which is at zero potential. Electrostatic field in gas detectors is described by Laplace equation

$$\nabla^2 \Phi = 0\,, \tag{1}$$

where Φ – electric potential. Electric field E is given by

$$E = -\nabla \Phi \tag{2}$$

In cylindrical coordinates with axial symmetry the Laplace equation takes the form

$$\frac{1}{r}\frac{\partial}{\partial r}\left(r\frac{\partial \Phi}{\partial r}\right) = 0\,, \tag{3}$$

where r – radial distance from the axis of symmetry. For a detector with an anode made of a wire having a radius R_A, placed in the axis of symmetry of the cylinder of radius R_C, the potential is given by the following formula electric field strength is given by the formula

$$\Phi(r) = \frac{U}{\ln(R_C / R_A)}\ln\left(\frac{r}{R_A}\right), \tag{4}$$

where U - the voltage between the anode and the cathode, r - the distance from the axis of symmetry of the anode.

The electric field strength is given by the formula

$$E = \frac{U}{r\ln(R_C / R_A)}\,, \tag{5}$$

Near the anode $r = R_A$ and field strength is equal to

$$E = \frac{U}{R_A \ln(R_C / R_A)}\,. \tag{6}$$

The capacitance per unit length of tube is given by

$$C = \frac{2\pi\varepsilon_0}{\ln(R_C / R_A)}\,, \tag{7}$$

where ε_0 – vacuum permittivity.

In spherical coordinates with spherical symmetry the Laplace equation takes the form

$$\frac{1}{r^2}\frac{\partial}{\partial r}\left(r^2\frac{\partial \Phi}{\partial r}\right) = 0\,, \tag{8}$$

If we approximate the shape of the tip of the needle by the sphere of radius R_S and the cathode by the sphere of radius R_X then the potential is given by

$$\Phi = U\left(\frac{1}{1-\frac{R_S}{R_X}}-\frac{1}{\frac{1}{R_S}-\frac{1}{R_X}}\right) \tag{9}$$

The electric field is given by

$$E = \frac{U}{\left(\frac{1}{R_S}-\frac{1}{R_X}\right)r^2} \tag{10}$$

Near the rounded end of the needle electric field strength is

$$E = \frac{U}{R_S\left(1-\frac{R_S}{R_X}\right)} \tag{11}$$

and may be much larger than the intensity at the surface of the anode wire as the conditions $R_S < R_A$, $R_S << R_X$ are usually fulfilled, and additionally in formula (5) the factor $ln(R_C / R_A)$ reduces at least several times the value of the field strength.

The interior of the detector is filled with noble gas (helium, neon, argon, xenon). Ionizing particle, flowing into the detector produces original electric charge - electrons and positive ions. Electrons are attracted to the positively charged needle. Ionization and avalanche multiplication of electric charge occurs in strong electric field. The needle serves as the anode and the outer casing serves as the cathode.

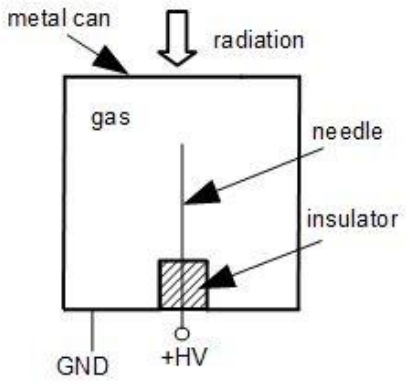

Fig. 2. Scheme of the needle detector

The construction of the detector is shown schematically in Figure 2. The geometry of the needle tip is shown in the Figure 3.

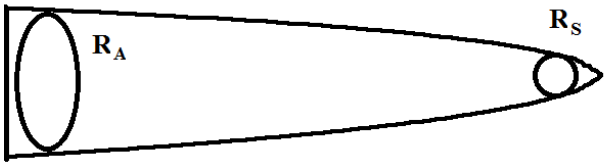

Fig. 3. The geometry of the needle tip

The actual shape of the needle cylinder deviates from the rounded end. Calculation of field distribution requires the use of one of the numerical methods, for example Finite Differences, Finite Element Method or Boundary Element Method. The photo of the developed device is shown in the Figure 4. One can see the metal housing and the anode in the middle of it. The anode is made of a steel acupuncture needle coated with a layer of gold having a diameter of 0.16 mm.

Fig. 4. Photo of the developed device

In order to verify the correctness of the concept of building a new type of gamma and x-ray detector based on acupuncture needle the simulation of the electric field distribution has been carried out by means of the program COMSOL. An electric potential distribution in a plane perpendicular to the needle is shown in the Figure 5.

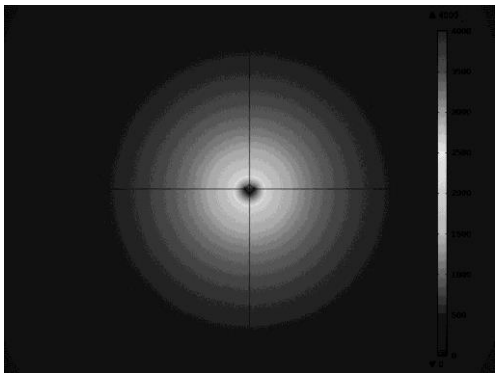

Fig. 5. An electric potential distribution in a plane perpendicular to the needle

An axial symmetry in potential distribution is visible. An electric potential distribution in a plane parallel to the needle is shown in the Figure 6. The strongest electric field is near the tip of the needle.

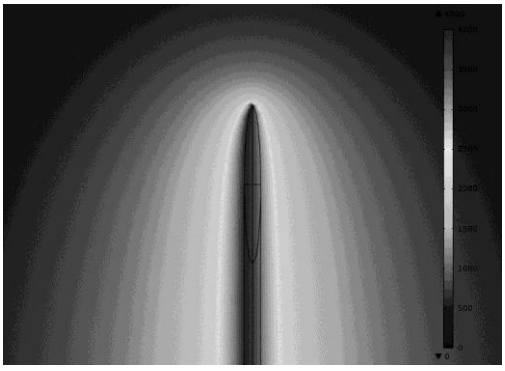

Fig. 6. An electric potential distribution in a plane parallel to the needle

An electric potential distribution in a plane perpendicular to sixteen needles is shown in the Figure 7.

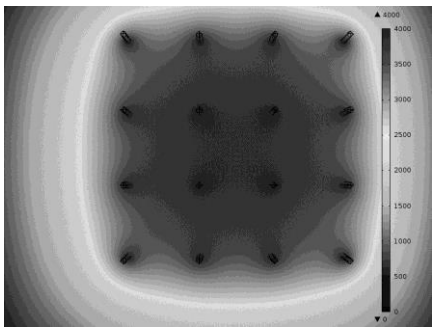

Fig. 7. An electric potential distribution in a plane perpendicular to sixteen needles

An electric potential distribution in a plane parallel to sixteen needles is shown in the Figure 8.

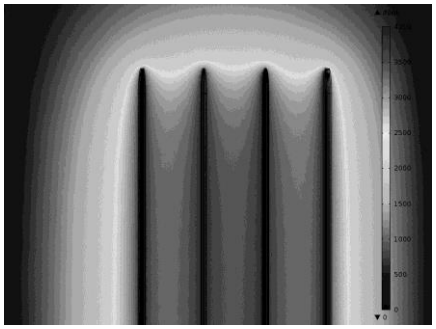

Fig. 8. An electric potential distribution in a plane parallel to sixteen needles

2. Results

Designed needle detector has been connected to a high voltage power supply with a value of 1440 V, generated by the power supply type HRS-41 produced by POLON. As a radioactive source isotope Fe-55 that emits X-rays with an energy of 5.9 keV has been used. Radiation beam has been collimated, so it has hit near the tip of the needle. The interior was filled with a detector gas composition of 90% Ar + 10% CH_4. Schematic of the measuring system is shown in the Figure 9. As a preamplifier the CR-112 chip produced by Cremat has been used. The signal from the preamplifier has been gained by the linear amplifier type 1101 produced by POLON. The gain value has been 320V/V.

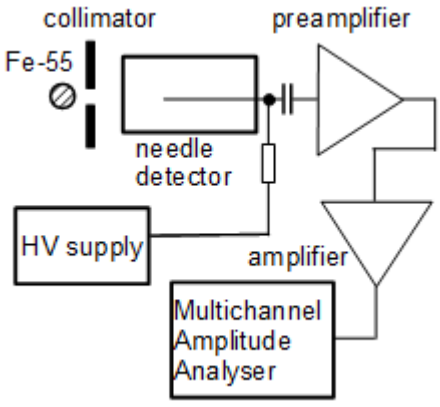

Fig. 9. Diagram of the measuring system of the needle detector

Photo of the proportional counter used as the reference detector is shown in the Figure 10. Pulse amplitude spectrum has been measured by multichannel pulse amplitude analyzer TUKAN 8K produced by IPJ. The spectrum of X-rays coming from the isotope Fe-55 measured by the reference detector is shown in the Figure 11. The multichannel amplitude analyzer has worked in the mode of 1024 channels. The input voltage range has been 0..+10V.

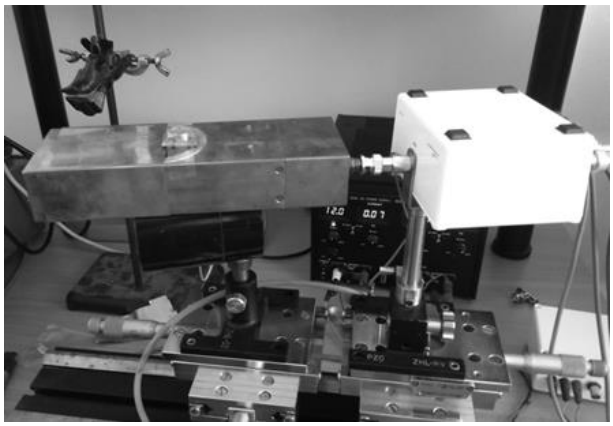

Fig. 10. Photo of the proportional counter used as the reference detector

The spectrum of X-rays coming from the isotope Fe-55 measured by the developed detector is shown in the Figure 12. The clear peak is visible in the spectrum, dating from the photoelectric effect. Energy resolution was approximately 30%.

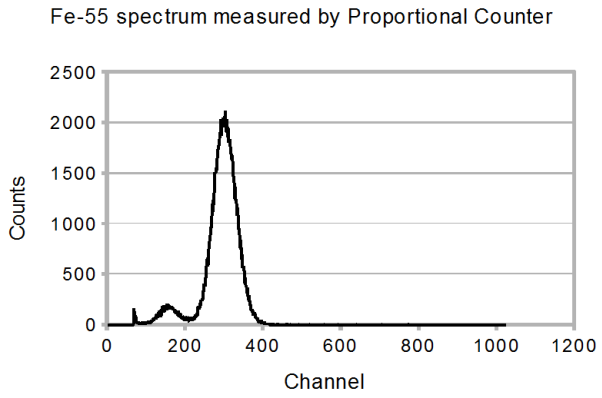

Fig. 11. The spectrum of X-rays coming from the isotope Fe-55 measured by the reference detector – proportional counter

The obtained spectrum is consistent with the reference one.

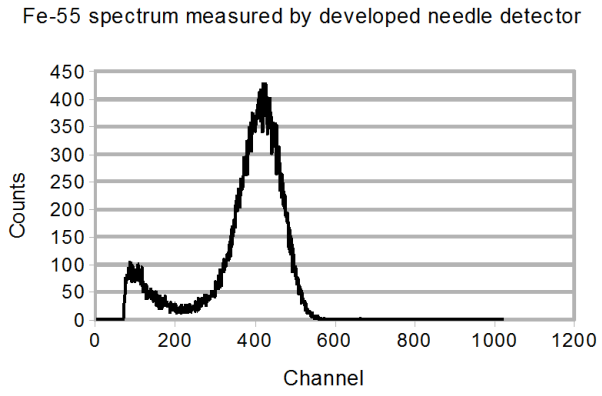

Fig. 12. The spectrum of X-rays coming from the isotope Fe-55 measured by the developed detector

Pulse amplitude spectrum measurements have confirmed the developed device ability to detect x-ray and gamma radiation.

3. Conclusions

The advantage of the detector is its simple mechanical construction. Acupuncture needles produced on a mass scale are relatively cheap and have a very good quality parameters. They are also used not only in medicine [9]. Due to the treatment a lack of support on the one side it is possible to detect incident radiation in a direction parallel to the needle. As a result, the thickness of the gas layer at which an x-ray detection occurs can be large, which increases the efficiency of the detection. It is also possible to construct a positional detector MN-PC (Multi-Needle Proportional Chamber) analogous to the multi-wire proportional chamber (MWPC) [2].

References

[1] Borkhari A.F., Yasserian K.: Influence of the hot filament on the electrical breakdown characteristics in the presence of Ar/N2. Journal of Theoretical and Applied Physics, 7/2013.
[2] Charpak G., Bouclier R., Bressani T., Favier J., Zupančič Č.: The use of multiwire proportional counters to select and localize charged particles. Nuclear Instruments and Methods, 62(3)/1968, 262–268.
[3] Geiger H., Müller W.: Das Elektronenzählrohr, Physikalische Zeitshrift, 29/1928, 839–841.
[4] Ketzer B., Bachmann S., Cape M., Deutel M., Friedrich J., Kapple S., Konorov I., Placci A., Reisinge K., Ropelewski L., Shekhtman L., Sauli F.: GEM detectors for COMPASS. IEEE Transaction on Nuclear Science, 48/2001, 1065–1069.
[5] Knoll Glenn F.: Radiation Detection and Measurement. John Wiley and Sons, New York, 1999.
[6] Oed A.: Position-sensitive detector with microstrip anode for electron multiplication with gases. Nuclear Instruments and Methods, A263/1988, 351–359.
[7] Rutherford E., Geiger H.: An electrical method of counting the number of alpha particles from radioactive substances. Proceedings of the Royal Society A81/1908, 141–161.
[8] Sauli F.: GEM A new concept for electron amplification in gas detectors. Nuclear Instruments and Methods in Physics Research, 386/1997, 531–534.
[9] Yun Z.L., Bin C., Yiming Z.: Fabrication of anti-reflective micro-structure at terahertz frequency by using Chinese acupuncture needles. Optics Letters, 2015, 2917–2920.

Ph.D. Eng. Grzegorz Domański
e-mail: G.Domanski@ire.pw.edu.pl

M.Sc. (’94), Ph.D. (‘01); nuclear and medical electronics; Assistant Professor, Nuclear and Medical Electronics Division, Institute of Radioelectronics and Multimedia Technology, Faculty of Electronics and Information Technology, Warsaw University of Technology. Faculty Coordinator of Radiological Protection (’02-); Tutorial assistance of Biomedical and Nuclear Engineering Students Scientific Group (’13-).

Ph.D. Eng. Roman Szabatin
e-mail: R.Szabatin@ire.pw.edu.pl

Roman Szabatin received the M.Sc. degree in electronics apparatus and the Ph.D. degree from Warsaw University of Technology, in 1972 and 1983, respectively. Since 1973, he has been with the Nuclear and Medical Electronics Division, Institute of Radioelectronics, Electronics and Information Technology Faculty, Warsaw University of Technology, as an Associate, Senior Associate, and Senior Scientist. His main research interests include nuclear and medical instrumentation and medical imaging (gamma cameras, SPECT and PET). He has published over 50 scientific papers.

Ph.D. Eng. Piotr Brzeski
e-mail: P.Brzeski@ire.pw.edu.pl

Piotr Brzeski received the M.Sc. degree in electronics apparatus and the Ph.D. degree from Warsaw University of Technology, in 1970 and 1982, respectively. Member of the Faculty Council (’90-); Head of the Dean’s Financial Committee (’12-); Member of the Faculty Council Committee on Education (’05-); Director’s Representative for Economy and Administration (’12-).

Ph.D. Eng. Bogumil Konarzewski
e-mail: B.Konarzewski@ire.pw.edu.pl

M.Sc. (’91), Ph.D. (‘98); nuclear and medical electronics; Assistant Professor, Nuclear and Medical Electronics Division, Institute of Radioelectronics and Multimedia Technology, Faculty of Electronics and Information Technology, Warsaw University of Technology.

otrzymano/received: 20.09.2016 *przyjęto do druku/accepted: 15.02.2017*

DOI: 10.5604/01.3001.0010.4600

DEVELOPMENT OF MAGNETIC NANOPARTICLES TOMOGRAPHY IN NUCLEAR AND MEDICAL ELECTRONICS DIVISION

Przemysław Wróblewski, Waldemar Smolik
Warsaw University of Technology, Institute of Radioelectronic and Multimedia Technology, Nuclear and Medical Electronics Division

Abstract. *In this article summary of all accomplishments of Nuclear and Medical Electronics Division in the field of Magnetic Nanoparticles Imaging. Magnetic Nanoparticles Imaging is a new tomographic and molecular imaging method that employs superparamagnetic nanoparticles as the tracer. This article includes the most importuned definition regarding this technique, its most interesting features, as well as report about research conducted in the Division in prospect to advance this imaging method in Poland.*

Keywords: nanoparticles, superparamagnetic materials, tomography, molecular imaging

ROZWÓJ TOMOGRAFII NANOCZĄSTECZEK MAGNETYCZNYCH W ZAKŁADZIE ELEKTRONIKI JĄDROWEJ I MEDYCZNEJ

Streszczenie*. Artykuł ten podsumowuje dotychczasowe osiągnięcia Zakładu Elektroniki Jądrowej i Medycznej w dziedzinie obrazowania nanocząsteczek magnetycznych. Obrazowanie nanocząsteczek magnetycznych jest to nowa metoda obrazowania molekularnego i tomograficznego wykorzystująca jako znacznik nanocząsteczki superparamagnetyczne. W treści artykułu zawarto najważniejsze definicje dotyczące tego zagadnienia. Obecny stan rozwoju tej techniki oraz jej najbardziej interesujące właściwości, jak również opis prac badawczych podjętych przez Zespół w celu rozwoju tej metody obrazowania w Polsce.*

Słowa kluczowe: nanocząsteczki, materiały superparamagnetyczne, tomografia, obrazowanie molekularne

Introduction

Magnetic Particle Imaging (MPI) is novel imaging diagnostic technique. This new molecular imaging method was developed by researchers from Philips Research Laboratories: Bernhard Gleich and Jürgen Weizenecker. In 2005 the first results of their works on imaging using magnetic nanoparticles were published in Nature. Since that publication some research institutes commenced investigations on this imaging technique. Currently the leading scientific centers in this field are University of Lubeck (Thorsten M. Buzug) and University of Berkley, California (Patrick W. Goodwill). Division has ambition to became such a pioneer in Poland.

The increased attention regarding this modality is result of unique features characterizing MPI. First of all, initial research results reviled its high sensitivity, comparable in this regard with the best available molecular imaging techniques such as SPECT or PET, combined with high spatial and time resolution, rivaling Magnetic Resonance Imaging. Secondly, MPI is a method simple to implement. However, not as easily scalable. Although the third and most importuned reason is variety of possible applications of MPI. Some of which are quite unique. Magnetic nanoparticles, which are used as a marker in this technique, can fused with bio-molecules to label specific of organic substances or tissues. Which in turn allows study of biological and physiological through observation of time and spatial changes of markers density in the subject. MPI can be applied to function imaging of kidneys or liver, examination of blood flow in the coronary arteries, in diagnostic of pulmonary diseases as well as localization of cancers or implanted stem cells. Potentially, if used along with magnetic hyperthermia, the same nanoparticles or even the same equipment can be applied for both diagnostic and therapy of malignant diseases. MPI scanner can be design as typical tomographic scanner similar in appearance to CT scanner or one-sided scanner of similar uses as mini-gamma camera. At last, this technique can be used to research properties of superparamagnetic nanoparticle itself [1].

Table 1. Comparison of parameters of chosen molecular imaging modalities.

Modality	PET	SPECT	MRI	MPI
Time resolution	1 min	1 min	1 s	<0,1 s
Spatial resolution	3 mm	10 mm	1 mm	<1 mm
Sensitivity	Very high 10^{-11} - 10^{-12} mol/L	High 10^{-9} mol/L	Low (Moderate - hyperpolarization) 10^{-3} mol/L (10^{-6} mol/L)	High 10^{-8} mol/L

1. Theory of Magnetic Particles Imaging

In MPI superparamagnetic nanoparticles are used as a tracer. The core of such particles is usually manufactured from super-paramagnetic iron oxide (SPION) (Fig. 1). It is of radius from 10 to 100 nm and coated with biocompatible polymers.

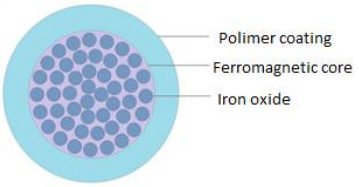

Fig. 1. Cross-section of superparamagnetic iron oxide nanoparticle. Core is made of magnetite or maghemite. Coating consist of biocompatible and biodegradable polymers (for example Dextran) and eventual attached molecules, giving the nanoparticle an affinity for specific substances or tissues

Superparamagnetism is form of magnetism in which ferromagnetic material nanoparticles of sufficiently small size and magnetically isolated from one another can be recognized as separate magnetic domains and randomly flip direction of magnetization vectors under the influence of temperature. In this state nanoparticles behavior can be described by Langevin's theory of paramagnetism and their magnetization curve by equation:

$$M(t) = m_s c_p (\coth(kH_D(t)) - \frac{1}{kH_D(t)}) \quad (1)$$

where c_p – particles concentration, H_D – magnetic field strength, $k = \frac{\mu_0 m_s}{k_B T}$, μ_0 – magnetic permeability of vacuum, k_B – Boltzman's constant, T – temperature, m_s – magnetic momentum of saturation, equal to: $m_s = \frac{1}{6}\pi d_c^3 M_s$, where M_s is saturation magnetization of magnetite and d_c is diameter of nanoparticle. The most imported features of nanoparticles that can be deducted from this equation are nonlinear magnetization curve, high magnetic moment compere to normal paramagnets and fact that in high enough magnetic field nanoparticle undergo saturation.

Thanks to this properties detection of nanoparticles is possible if tracers containing them are placed in changing magnetic field (preferably sinusoidal) and signal from their magnetization is simultaneously acquired by appropriate receiving coil. Unfortunately, in this case one would acquire both signal from

magnetization changes and excitation signal, which is stronger by about six orders of magnitude.

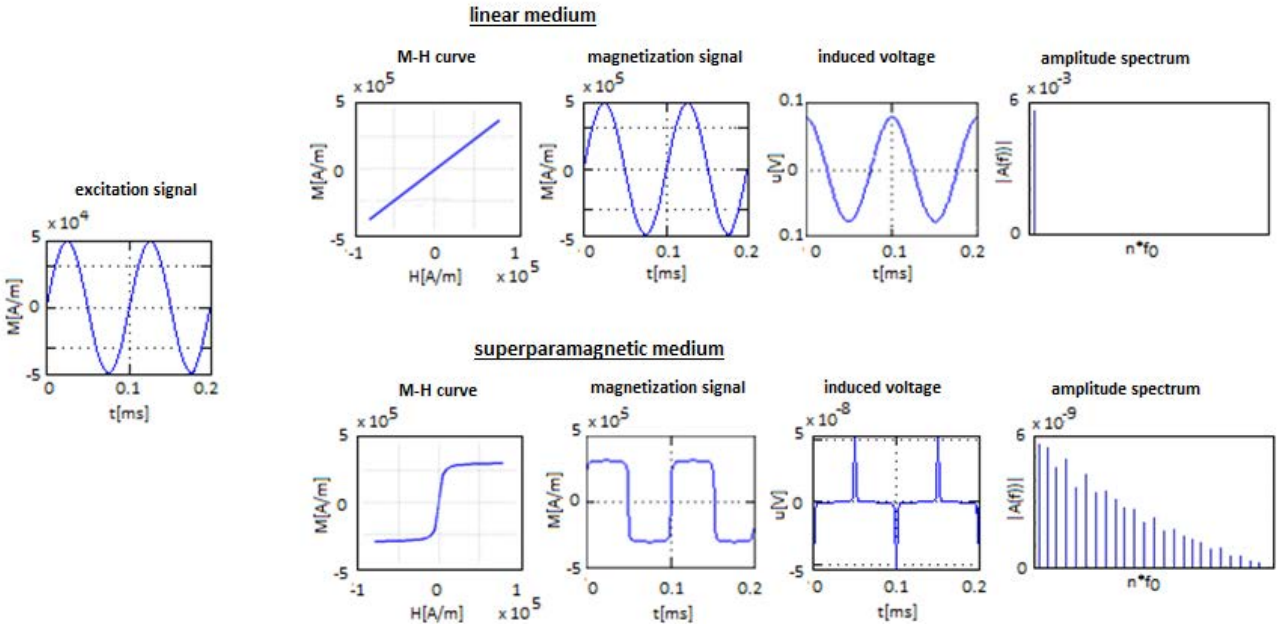

Fig. 2. Magnetization signals, signals induced in receiving coil and their amplitude spectra for medium excited with sinusoidal signal depending on the magnetization curve: linear medium (top) and nonlinear medium - superparamagnetic nanoparticles (bottom)

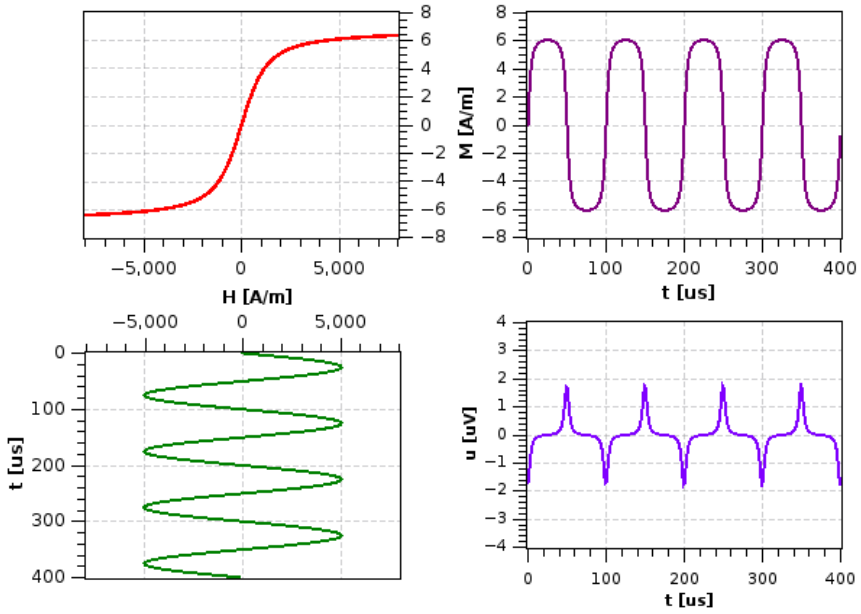

Fig. 3. Dependence of magnetization signal induced in receiving coils on nonlinear magnetization curve (M-H curve). Excitation signal (bottom left), magnetization curve (top left), superparamagnetic nanoparticels magnetization (top right), voltage signal induced in receiving coil (bottom left)

If nanoparticles magnetization curve was liner, separation of this signal would be impossible (Fig. 2). However, as the magnetization curve is nonlinear signal from nanoparticles contains harmonics of excitation frequency (Fig. 3). It is possible than to separate those high frequencies by filtering out excitation frequency (broadband method) or by measurement of each harmonic separately (narrowband method). Through analysis of this harmonics signals for example particles concentration can be estimated.

Localization of the tracer can be achieved by application of gradient magnetic field, which cause nearly all nanoparticles to undergo saturation thus preventing them from contributing in signal generation, except those in small volume near the zero magnetization field strength, called field free point (FFP). In such circumstances magnetization signal induced in receiving coil originates only from particles in FFP [3]. To scan whole imaged volume FFP can be moved. There are two known procedures of scanning using this method of localization – frequency mixing method (excitation frequency much higher than movement of FFP) and driving field method (high frequency movement of FFP used as exciting field) [2]. Time resolution of imaging is highly dependent on applied scanning process.

2. Research conducted in Division

In Nuclear And Medical Electronics Division research on model of tomographic scanner for nanoparticles imaging are being carried out since 2011. In the wake previous studies, conducted under statutory works, one dimensional nanoparticles scanner was created. Presently system for nanoparticles spectroscopy is being developed. Furthermore, numerical calculation MATLAB toolbox is being written that will allow simulation of MPI measurement system, generation of simulated measurement result of such systems and reconstruction of MPI images from both artificial and real data.

2.1. Magnetic Nanoparticles Scanner

MPI scanner developed in Nuclear And Medical Electronics Division allows one dimensional imaging of nanoparticles concentration [4] (Fig. 4 and 5). It is designed for research of small objects. Current acquisition system employs narrowband detection method using lock-in amplifier and mix frequency method for field free point displacement. Particles are excited with signal of 10 kHz frequency and 8 mT of amplitude. Gradient coils generate field of about 1 T/m strength. Field of view of the scanner has about 30 mm diameter. Using this setup first real measurements were conducted [7] (Fig. 7). The phantoms with the chambers for water solution of nanoparticles with 0.5 mol/L concentration (Fig. 6) were used in the experiments. The phantoms were made using 3D printing technology.

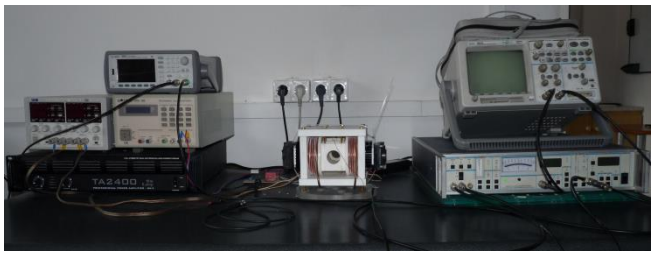

Fig. 4. Measurement setup for one dimensional MPI scanner. On the left side, equipment used for generation of excitation signal and gradient field (function generator, power supply, audio power amplifier). In the middle, MPI scanner gentry containing coils and cooling system. On the right side, equipment used in acquisition setup (lock-in amplifier and oscilloscope)

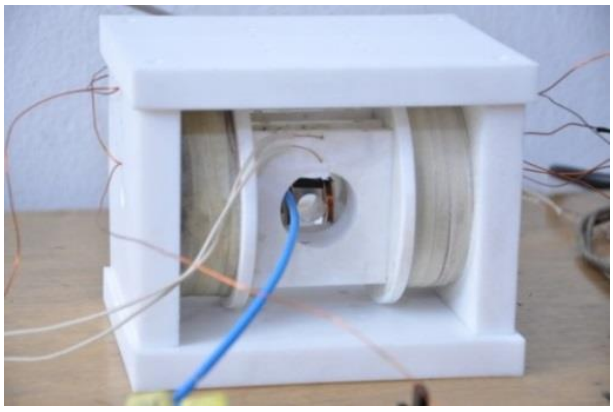

Fig. 5. MPI scanner gentry. View of gradient coils and receiving coil

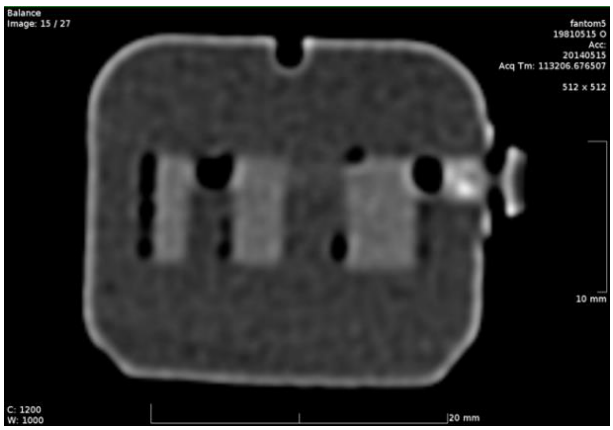

Fig. 6. CT image of phantom with three chambers filled with ferrofluid. Phantom was printed in 3D printing technology and use for MPI scanner research

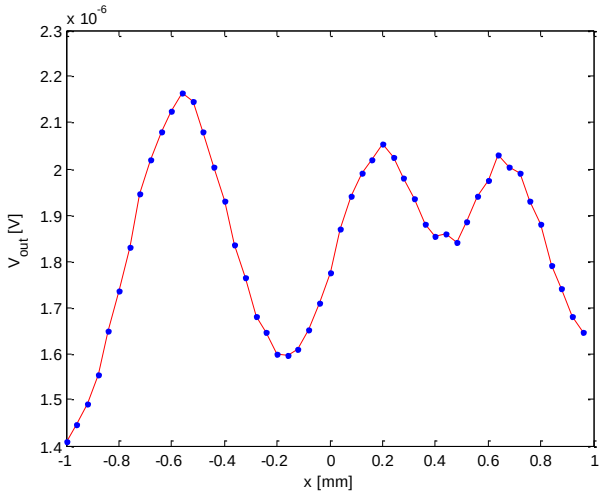

Fig. 7. Measurement along X axis of scanner of magnetic response of 60 nm nanoparticles dispersed in water in three chamber phantom. "Zero" position corresponds to center of the FOV of the scanner. Amplitude of 5rd harmonic measured by lock-in amplifier is proportional to concentration of nanoparticles

2.2. Magnetic Nanoparticles Spectroscopy

Magnetic Particles Spectroscopy (MPS) allows measurement of harmonic spectra of magnetization signal of magnetic nanoparticles. It is used for research of properties of nanoparticles, for example particle diameter or magnetization curve estimation. Magnetic particles spectrometer may can be considered a zero dimensional MPI scanner. To acquire the spectra of magnetization signal harmonics only detection of magnetization signal is necessary. In this case gradient coils are irrelevant. Signal from whole volume is acquired and afterwards amplitude and phase of each harmonic is measured or calculated by Discreet Fourier Transform from signal. Set of amplitudes and phase angles of all harmonics in function of frequency is called magnetic particle spectrum and is unique for specific nanoparticles batch. First trial measurements of amplitude and phase angle spectra of nanoparticles using modified MPI scanner model (Fig. 8) were conducted in Division (Fig. 9 and 10). Development of new magnetic particles spectroscope is planned in the near future.

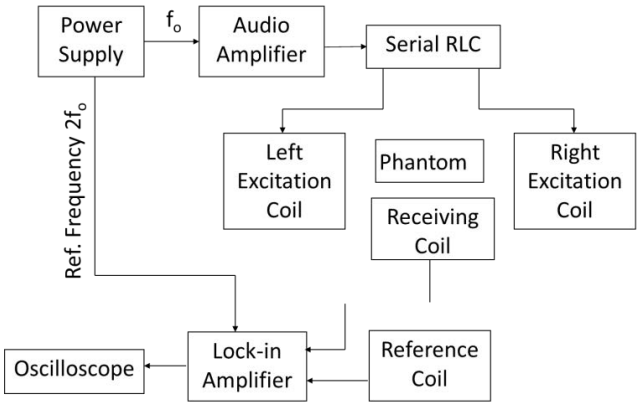

Fig. 8. Scheme of MPS setup, using narrowband detection method. It is in fact MPI scanner setup without driving and gradient coils. In this configuration signal is acquired from whole volume

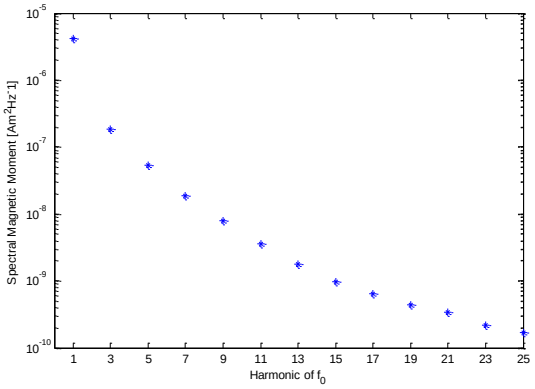

Fig. 9. Magnetic moment spectrum of FeraSpin™ XL nanoparticles at a field strength of 8 mT/μ0

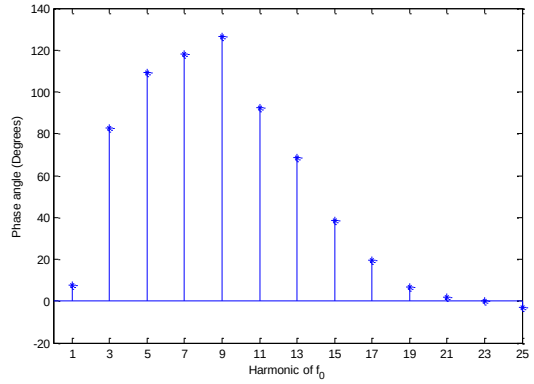

Fig. 10. Phase angle spectrum of FeraSpin™ XL nanoparticles at a field strength of 8 mT/μ0

2.3. Numerical Simulation Toolbox

The last important project connected to MPI developed in Division is work on program for numerical calculations. MPIsim software is written in MATLAB. When completed this toolbox will be ideal scientific help for designing new models of the MPI scanner or coils setups or for verification of results of real measurements. Its first module will allow simulation of magnetic field generated by coils of the scanner [5, 6], including gradient field, driving field and excitation field (Fig. 11 and 12). Second part will be used for simulation of 1D/2D/3D MPI measurements (Fig. 15), which theoretical with allow numerical estimation of system function of analyzed scanner. Last function of the program will be reconstruction of MPI images and particles concentration distribution. Using this toolbox it will also be possible to numerical calculation of magnetic particles spectra (Fig. 13) and estimation of particle magnetization curve, from both simulated and real data (Fig. 14). This feature will allow not only estimation of magnetic parameters of nanoparticles but also may lead to better theory describing superparamagnets behavior.

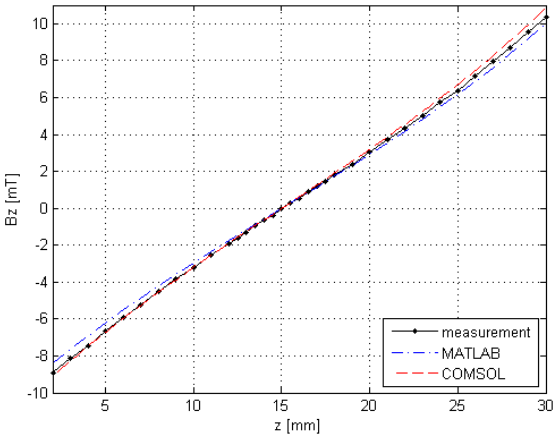

Fig. 11. Comparison of result of simulation and real measurement of Z-component of magnetic induction of field generated by gradient coils of MPI scanner model

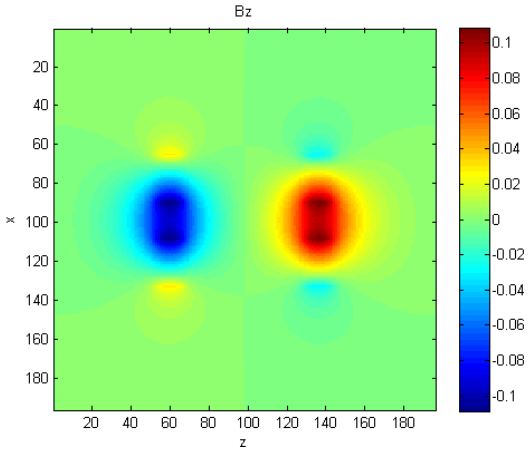

Fig. 12. Distribution of Z-component of magnetic induction of field generated by gradient coils of MPI scanner model. Computed in MPIsim toolbox

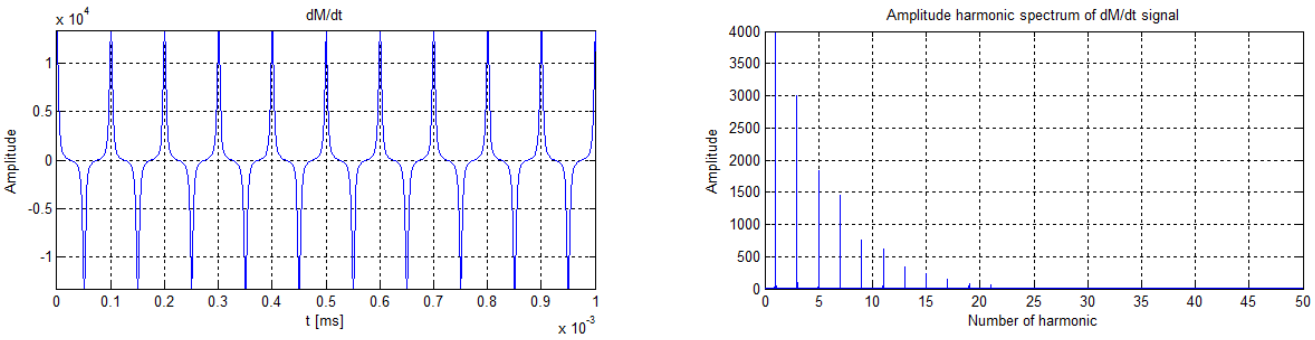

Fig. 13. On the left side, signal induced by changing magnetization of nanoparticles in receiving coil calculated in MPI toolbox. On the right side, amplitude harmonic spectrum of this signal

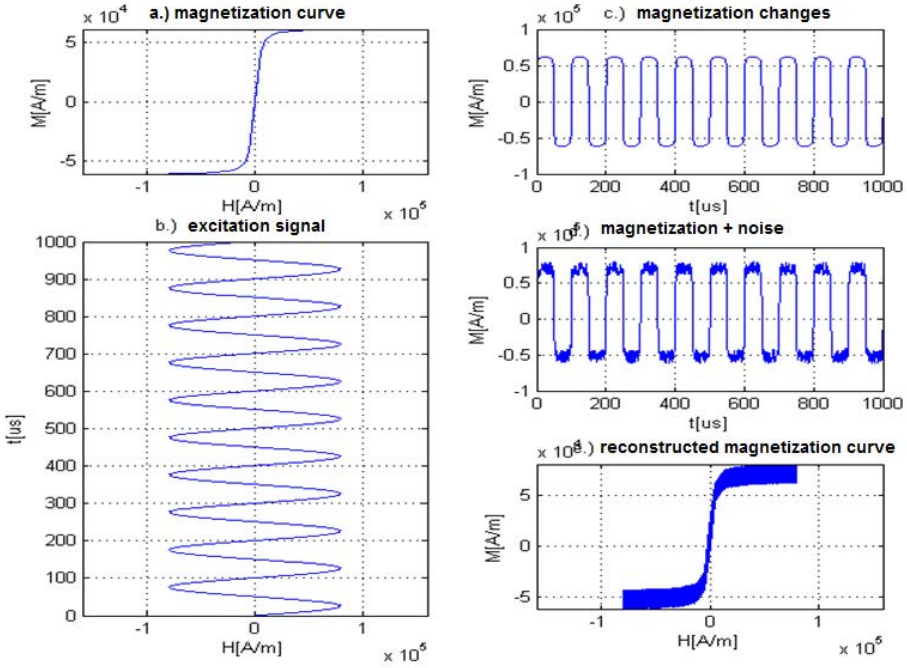

Fig. 14. In left top corner, theoretical Langevin's curve of magnetization. In left bottom corner, excitation signal. On the right side, from top to bottom, clear magnetization signal, magnetization with noise, reconstruction of Langevin's curve from signal with noise. Calculated in MPI toolbox

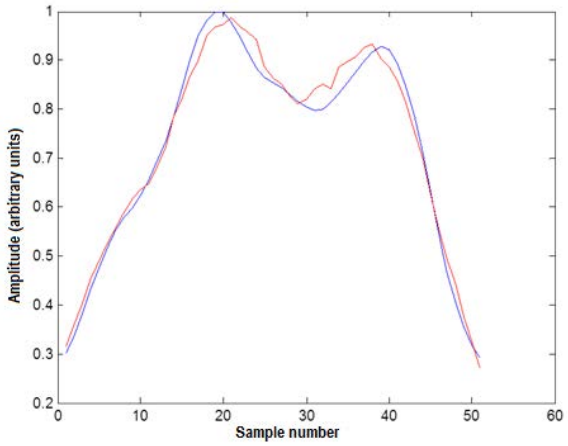

Fig. 15. Comparison of results of real measurement (red) of 3rd harmonic amplitude and result of 1D numerical simulation (blue). Measurement of three chamber phantom filled with nanoparticles of 40 nm diameter dissolved in water

3. Conclusions

Magnetic Particles Imaging is a very promising molecular imaging technique with wide range of potential applications. Its progress will surly contribute to expansion of knowledge in both fields of electronics and medicine. Due to this rezone it became one of the main topics of interest in the Nuclear And Medical Electronics Division. Past results motivate us to continue work in this field. Probable next step will be extension of functionality of current MPI scanner model to 2D or 3D imaging, which in turn will allow further research in this new imaging technique.

Bibliography

[1] Buzug T.M., Biederer S., Knopp T., Sattel T.F., Lüdtke-Buzug K.: Magnetic particle imaging – challenges and promises of a new modality, WC 2009, IFMBE Proceedings 25/IV, 1471–1474.
[2] Goodwill P.W., Scott G.C., Stang P.P., Conolly S.M.: Narrowband magnetic particle imaging, IEEE transactions on medical imaging, vol. 28, no. 8, 2009.
[3] Weizenecker J., Gleich B., Borgert J.: Magnetic particle imaging using a field free line, J. Phys. D: Appl. Phys. 41, 2008.
[4] Wróblewski P., Szyszko J., Smolik W. T.: Development of MPI mini scanner prototype - coils design, Imaging Systems and Techniques (IST), 2013 IEEE International Conference on, Beijing, 2013, 164–168.
[5] Wróblewski P., Szyszko J., Smolik W.T.: Numerical Calculating of Magnetic Field for MPI Scanner, 7th World Congress on Industrial Process Tomography, WCIPT 7, Kraków, 2013, 288–294.
[6] Wróblewski P., Szyszko J., Smolik W.T.: Numerical modeling of magnetic field for magnetic particle imaging, Imaging Systems and Techniques (IST), 2012 IEEE International Conference on, Manchester, 2012, 436–441.
[7] Wróblewski P., Szyszko J., Smolik W.T., Kryszyn J., Olszewski T., Brzeski P., Szabatin R.: Detekcja sygnału w obrazowaniu nanocząstek magnetycznych, XVIII Krajowa Konferencja Biocybernetyka i Inżynieria biomedyczna, Gdańsk, 2013, 49–57.

M.Sc. Eng. Przemysław Wróblewski
e-mail: P.Wróblewski@ire.pw.edu.pl

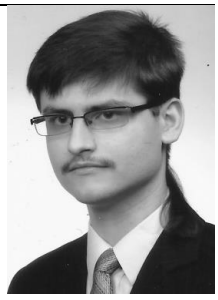

Received the M. Sc. degree in biomedical engineering from Warsaw University of Technology, Warsaw, Poland in 2013. Ph.D. student in the Nuclear and Medical Electronics Division, Institute of Radioelectronics and, Electronics and Information Technology Faculty, Warsaw University of Technology. His field of interest covers Magnetic Particles Imaging and Magnetic Particles Spectroscopy, especially design of scanners and simulations of the magnetic field.

Prof. Waldemar Tomasz Smolik
e-mail: W.Smolik@ire.pw.edu.pl

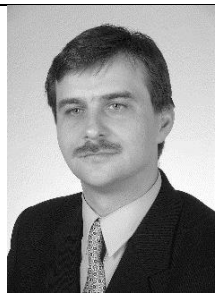

Waldemar T. Smolik received the M.Sc., the Ph.D. and D.Sc. degree in electronics engineering from Warsaw University of Technology, Warsaw, Poland in 1991, 1997 and 2014, respectively. Since 2014, he is an Associate Professor at the Institute of Radioelectronics and Multimedia Technology, Electronics and Information Technology Faculty, Warsaw University of Technology. He is the head of the Laboratory of Electronics Application in Nuclear Medicine at the Division of Nuclear and Medical Electronics. His main research interests are computer engineering, computed tomography and medical imaging. He has published over 70 scientific papers.

otrzymano/received: 20.09.2016 *przyjęto do druku/accepted: 15.02.2017*

DOI: 10.5604/01.3001.0010.4601

GAIN PREDICTION THEORY OF SINGLE FOIL GAS ELECTRON MULTIPLIER DETECTOR

Grzegorz Domański[1], Ryszard Szabatin[1], Jerzy Kalenik[2], Adam Jaworski[1], Przemysław Wróblewski[1], Waldemar Smolik[1], Robert Kurjata[1], Bogusław Konarzewski[1], Michał Dziewiecki[1], Janusz Marzec[1], Krzysztof Zaremba[1], Marcin Ziembicki[1], Andrzej Rychter[1], Jacek Kryszyn[1], Piotr Brzeski[1], Jan Szmidt[2]

[1]Warsaw University of Technology, The Institute of Radioelectronics and Multimedia Technology, [2]Warsaw University of Technology, The Institute of Microelectronics and Optoelectronics

Abstract. *Gain prediction theory of single foil Gas Electron Multiplier detector was developed. Gas electron multiplier (GEM) detector with single foil was developed. Soft X-ray spectra with an energy of 5.9 keV emitted by the isotope Fe-55 were measured. On this basis, the dependence of gain and energy resolution from the detector voltage was determined. The simple theory of gain dependence on various detector parameters was developed. Preliminary results of the study confirmed the potential usefulness of the GEM detector as a substitute for the multiwire proportional chamber.*

Keywords: Gas Electron Multiplier, ionizing radiation detector

TEORIA WZMOCNIENIA JEDNOFOLIOWEGO DETEKTORA Z GAZOWYM POWIELANIEM ELEKTRONÓW

Streszczenie*. Opracowano teorię wzmocnienia jednofoliowego detektora z gazowym powielaniem elektronów. Opracowano detektor z gazowym powielaniem elektronów z pojedynczą folią. Zmierzono widmo miękkiego promieniowania X, o energii 5,9 keV, emitowanego przez izotop Fe-55. Na tej podstawie wyznaczono zależność wzmocnienia i energetycznej zdolności rozdzielczej od napięcia zasilającego detektor. Opracowano prosta teorią zależności wzmocnienia od różnych parametrów detektora. Wstępne rezultaty badań potwierdzają potencjalną przydatność detektora GEM jako substytutu wielodrutowej komory proporcjonalnej.*

Słowa kluczowe: detektor z gazowym powielaniem elektronów, detektor promieniowania

Introduction

Gas Electron Multiplier is a gas detector composed of a thin polymer film with insulating properties, that is coated on both sides with a conductive layer [4]. GEM film is composed from a plurality of small channels arranged regularly on the surface and passing through all the layers. Applying a potential difference of upper and lower conductive layer gives rise to a strong electric field inside the channels, causing the acceleration of the movement of electrons and their multiplication. Typical film thickness is about 50 microns Kapton and the thickness of the copper layer is 5 μm. The holes typically have an outer diameter of 70 μm, while the inner 50 microns. Typical spacing between the holes is 140 μm. External dimensions of the copper box with holes are in range from 100×100 mm to 300×300 mm. GEM detectors can be used as a substitute for position sensitive multiwire proportional chambers in high energy physics experiments [2].

1. Methods

The dependence of the gas gain in function of the electric field is described by the formula [3]

$$\log M = \int_a^b \alpha(s)ds \tag{1}$$

where α - first Townsend coefficient. The limits of integration (*a*, *b*) of the above integral include the area of the electrical field.

The formula (2) is derived assuming a constant electric field in the holes of the GEM film and first Townsend coefficient α dependence on the pressure of gas in the form [1]

$$\frac{\alpha}{p} = A \cdot \exp\left(-B\frac{p}{E}\right) \tag{2}$$

where *A*, *B* are constants depending on gas mixture, *p* - gas pressure in Torr, *E* – electric field.

For constant electric field on the distance *L* we obtain

$$M = exp\left[ApL\exp\left(-Bp/E\right)\right] \tag{3}$$

Assuming that total potential difference is located in a hole between both conductive layers of a GEM foil, the gas gain M is equal

$$M = \exp\left[A \cdot p \cdot L\left(-\frac{BpL}{U}\right)\right] \tag{4}$$

where L - foil thickness, U - supply voltage in Volts.

The formula (4) was derived from (3) assuming constant electric field $E = U/L$. Location of the peak is proportional to the gain of the gas detector, $m = S \times M$, where *S* is the coefficient of proportionality. The theoretical value of the coefficient can be obtained from the formula

$$S = \frac{k_u E q_e 2^n}{C_f U_{range} w} \tag{5}$$

where k_u – gain of the amplifier, *E* – energy of the quantum of radiation, q_e – elementary charge, *n* – number of the A/D converter bits in the multichannel amplitude analyser (MAA), *w* – ionization work, U_{range} - the voltage range of the MAA, C_f - capacitance in the feedback loop in the preamplifier.

The values of the parameters are the following: k_u = 80V/V, *E* = 5900 eV, *w* = 24 eV, *n* = 12, $q_e = 1.6\ 10^{-19}$ C, U_{range} = 10 V, C_f = 1 pF. The computed value of the coefficient is S = 2.58. The following values were assumed in the analysis: *L* = 0.005 cm, *p* = 760 Torr. The variance of the output signal was modeled by the formula

$$\sigma^2(m) = C + H \cdot m^2 \tag{6}$$

The formula (6) was developed assuming that there are two sources of variance in the measured signal: amplifier noise and fluctuation of electric charge in the detector. The amplifier noise is independent from the main peak position (particle energy). The fluctuation of the electric charge in the detector was assumed proportional to measured energy. It assumption neglects fluctuation in gas gain. Energy resolution R was calculated from the formula

$$R = \frac{FWHM}{m} = \frac{2.35 \cdot \sigma(m)}{m} = \frac{2.35 \cdot \sqrt{C + H \cdot m^2}}{m} \tag{7}$$

The built GEM detector uses film manufactured by Techtra using technology Micro-Chemical-Vias, consisting of chemical etching holes. GEM foil was placed in the housing of multiwire proportional chamber, which the anode wires has been removed from. The active area is 100×100 mm, and the window in which the film is placed is wider by about 3 mm on each side. The aim of

pressing the film is to reduce the deflection of its center of gravity from a point on the plane defined by the edges to the minimum. In order to eliminate the interferences induced on fragments of wire without insulation (the entire structure is exposed and unprotected against external influence of the electromagnetic field), special design has been adapted from a male BNC connector, which covers part of the high voltage supply line to the system. Copper rims that were previously close to the anode wires and which were located about 4 cm from the active region of the film GEM have been connected to the ground potential, which does not lead to additional capacity to the system and not cause outflow of charge carriers in undesired directions. After initial assessments of the possibility to add the multiplicative GEM foil to the gas chamber, the polymer plate, that was a replacement for the disc with anode wires in the proportional chamber, was made. The disc has the same external dimensions as mounting plate with the anode wires, but instead of the wires it has a space for the placement of the GEM foil cap. The place was prepared to pass the copper strips, soldered to the terminals GEM foil, which were connected to the high voltage power supply. The image in Figure 1 shows the interior of the gas chamber and the positioning of the film GEM detector (ceramic polymer film with a centrally located, connected by leads to a crafted BNC). The GEM foil is shown in the foreground.

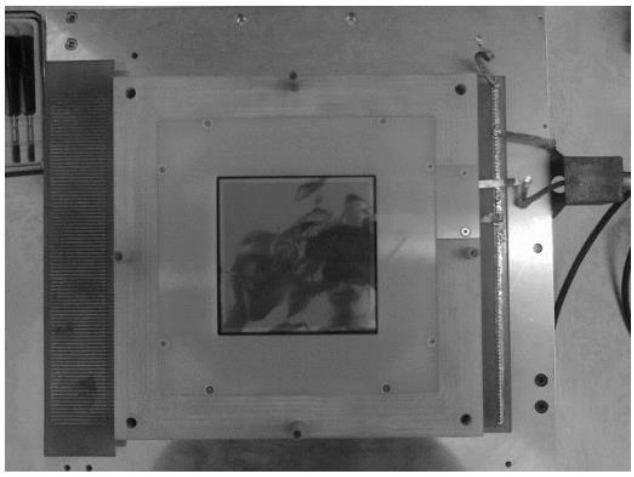

Fig. 1. Photo of the interior of the gas detector

Gas mixture that fills the detectors, was composed from Ar (90%) and CH4 (10%). High voltage generated by the high-voltage power supply type ZWN-41 (manufactured by POLON Warsaw), was given by the resistor R value of 3 MΩ on top of the GEM foil cover and the lower cover was connected to ground (Figure 2).

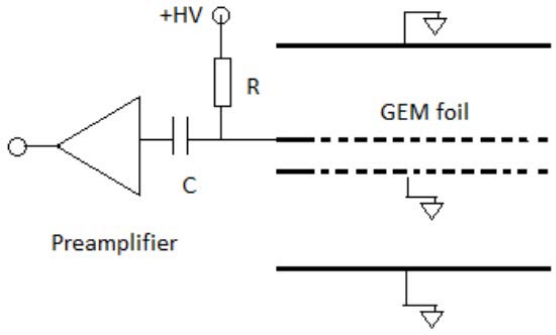

Fig. 2. Power connection diagram of the GEM foil

The signal from the top cover, after cutting the DC component off by the capacitor C with a capacity of 680 pF, is applied to the input of the charge sensitive preamplifier type 1002 (manufactured by POLON Warsaw). The signal from the preamplifier output was fed to the input of the shaping amplifier with adjustable gain type 1101 (POLON Warsaw). Shaped pulses from the output of the amplifier were fed to the input of multichannel amplitude analyser type Tukan-8k-USB.

2. Results

Sample spectrum of Fe-55 isotope measured in the system at 475V high voltage is shown in Figure 3. The main band of the spectrum contains in fact two superimposed bands: the main Kα energy 5.90 keV and lower energy Kβ 6.50 keV.

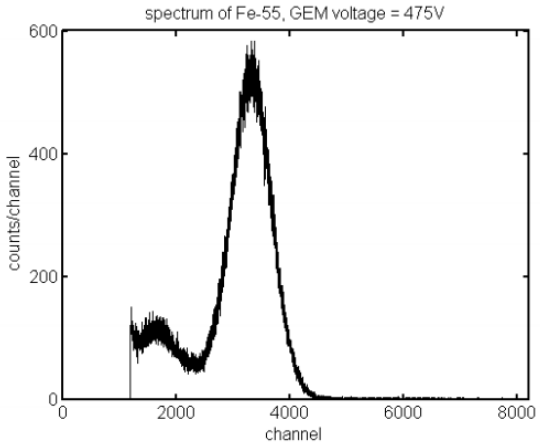

Fig. 3. Sample spectrum measured in the system Fe-55 475V voltage

The measurements were used to determine the spectrum according to strengthen the power supply voltage. To this end, for each spectrum collected at a given voltage, the position of the maximum absorption band was determined by fitting a Gaussian distribution function

$$\sigma^2(m) = C + H \cdot m^2 \tag{8}$$

where *n* - channel number, *m* - peak channel number.

The dependence of the peak position in the function of the power supply voltage is shown in figure 4.

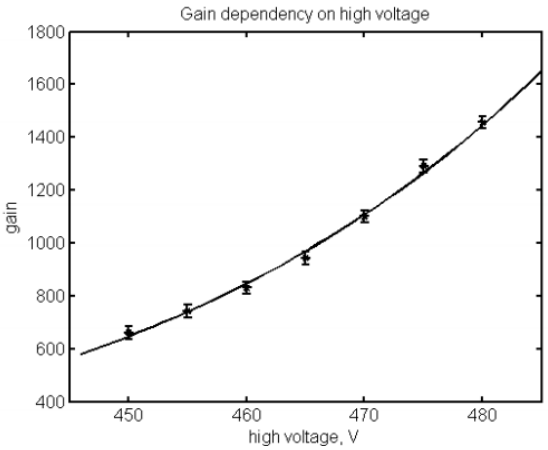

Fig. 4. Gain dependency on high voltage

The theoretical dependence of the gas gain M from the gas pressure, voltage and GEM film thickness was fitted to the measurement data, according to the formula (8). Experimental values of the constants A, B are the following: A = 10.9 ± 0.6 $Torr^{-1}cm^{-1}$, B = 220 ± 6 V $Torr^{-1}cm^{-1}$. Further measurements of FWHM (energy resolution expressed in band width at half height) in the dependence from the supply voltage and the position of the centre of the main peak were carried out. The measurements were carried out in the voltage range of 450 – 480 V. The graph in Figure 5 shows that the resolution improves with the supply voltage growth. The theoretical dependence of the standard deviation from the position of the main peak was fitted to the measurement data. The position of the main peak in turn depends on the voltage.

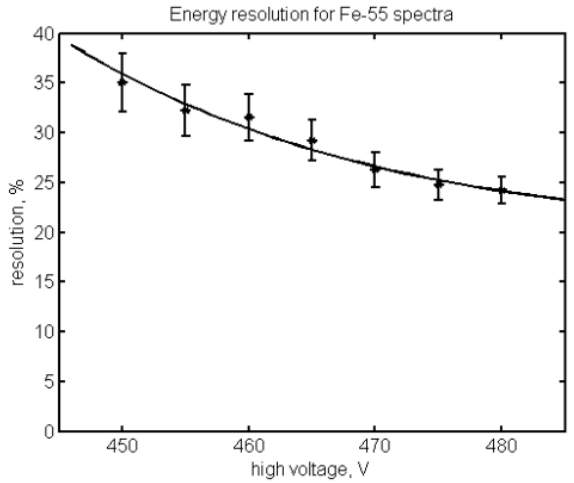

Fig. 5. Energy resolution dependence on the supply voltage

The H, C coefficients were found by least squares. Experimental values are the following H = 0.0073 ± 0.0014, C = $4.46 \times 10^4 \pm 1.01 \times 10^4$. The dependence of the centre of the main peak of the power supply is fully in accordance with expectations. The voltage dependence of FWHM suggests that increasing the supply voltage will result in better energy resolution. However, it was not possible to measure the FWHM for higher voltages due to sparking, so one cannot say where is the optimum operation point. Only voltage 475 V and 480 V allowed to observe escape peak Kα band with energies of 2.68 keV extracting from the noise.

3. Conclusion

Built GEM detector was used to measure the spectra of Fe-55. Measured gas gain and energy resolution are in accordance with expectations. The simple theory of gain dependence on various detector parameters was developed and confirmed by experiments. Preliminary results of the study confirmed the potential usefulness of the GEM detector as a substitute for the multiwire proportional chamber.

References

[1] Borkhari A.F., Yasserian K.: Influence of the hot filament on the electrical breakdown characteristics in the presence of Ar/N2. Journal of Theoretical and Applied Physics, 7/2013, 5.
[2] Ketzer B., Bachmann S., Cape M., Deutel M., Friedrich J., Kapple S., Konorov I., Placci A., Reisinge K., Ropelewski L., Shekhtman L., Sauli F.: GEM detectors for COMPASS. IEEE Transaction on Nuclear Science, 48/2001, 1065–1069.
[3] Knoll Glenn F.: Radiation Detection and Measurement. John Wiley and Sons, New York, 1999.
[4] Sauli, F.: GEM: A new concept for electron amplification in gas detectors. Nuclear Instruments and Methods in Physics Research A, 386/1997, 531–534.

Ph.D. Eng. Roman Szabatin
e-mail: R.Szabatin@ire.pw.edu.pl

Roman Szabatin received the M.Sc. degree in electronics apparatus and the Ph.D. degree from Warsaw University of Technology, in 1972 and 1983, respectively. Since 1973, he has been with the Nuclear and Medical Electronics Division, Institute of Radioelectronics, Electronics and Information Technology Faculty, Warsaw University of Technology, as an Associate, Senior Associate, and Senior Scientist. His main research interests include nuclear and medical instrumentation and medical imaging (gamma cameras, SPECT and PET). He has published over 50 scientific papers.

Ph.D. Eng. Grzegorz Domański
e-mail: G.Domanski@ire.pw.edu.pl

M.Sc. ('94), Ph.D. ('01); nuclear and medical electronics; Assistant Professor, Nuclear and Medical Electronics Division, Institute of Radioelectronics and Multimedia Technology, Faculty of Electronics and Information Technology, Warsaw University of Technology. Faculty Coordinator of Radiological Protection ('02-); Tutorial assistance of Biomedical and Nuclear Engineering Students Scientific Group ('13-).

Ph.D. Eng. Grzegorz Domanski
Ph.D. Eng. Jerzy Kalenik
M.Sc. Eng. Adam Jaworski
M.Sc. Eng. Przem. Wroblewski
Ph.D. Eng. Robert Kurjata
Ph.D. Eng. Bogumil Konarzewski
Ph.D. Eng. Michal Dziewiecki
Prof. Marzec Janusz
Prof. Krzysztof Zaremba
Ph.D. Eng. Marcin Ziembicki
Ph.D. Eng. Andrzzej Rychter
M.Sc. Eng. Jacek Kryszyn
Ph.D. Eng. Piotr Brzeski
Prof. Jan Szmidt
Ph.D. Eng. Waldemar Smolik

otrzymano/received: 20.09.2016 *przyjęto do druku/accepted: 15.02.2017*

DOI: 10.5604/01.3001.0010.4602

INCREASING THE SIGNAL TO NOISE RATIO IN LOW-FIELD MR SCANNER AT DEPARTMENT OF NUCLEAR AND MEDICAL ELECTRONICS

Michał Wieteska, Wojciech Obrębski, Ewa Piątkowska-Janko, Błażej Sawionek, Piotr Bogorodzki
Warsaw University of Technology, Faculty of Electronics and Information Technology, Department of Nuclear and Medical Electronics

Abstract. *This article presents studies carried by laboratory of Biomedical and Nucleonic Computer Systems. Our research concerns improvement of quality of imaging in low-field MRI scanner with field strength of 0.23 T as well as development of techniques of proton-electron dual resonance imaging and hyperpolarization of noble gases. Achieved results may contribute to improvement of multiple techniques of medical diagnostics, in particular functional study of lungs and heart as well as brain perfusion.*

Keywords: magnetic resonance imaging

TECHNIKI WZMOCNIENIA STOSUNKU SYGNAŁ-SZUM W NISKOPOLOWYM SKANERZE MR W ZAKŁADZIE ELEKTRONIKI JĄDROWEJ I MEDYCZNEJ

Streszczenie. *Niniejszy artykuł przedstawia przegląd prac prowadzonych przez zespół pracowni Biomedycznych i Nukleonicznych Systemów Komputerowych. Zaprezentowane badania dotyczą poprawy jakości obrazowania w niskopolowym skanerze rezonansu magnetycznego o indukcji pola głównego 0,23 T oraz rozwoju technik podwójnego rezonansu protonowo-elektronowego i hiperpolaryzacji gazów szlachetnych. Rezultaty naszych prac mogą przyczynić się do poprawy technik diagnostyki medycznej, w szczególności takich jak funkcjonalne badanie płuc i serca jak i perfuzja mózgu.*

Słowa kluczowe: tomografia rezonansu magnetycznego

Introduction

Magnetic resonance imaging (MRI) is a technique which allows the investigation of spatial distribution of isotopes with non-zero magnetic spin. A sample containing such atoms is placed in main magnetic field of the scanner (B_0) and then excited with radio-frequency (RF) pulses. As a result the sample itself becomes a source of the signal, which is received by the acquisition system of the scanner. During the period between excitation and acquisition, the gradient coils of the scanner modify the B_0 in such a way, that the received signal carries information regarding the spatial distribution of the isotope of interest. Hydrogen is the most frequently investigated isotope, since it is a part of water molecules, that can be found in all living organisms. That is the reason why MRI has found use mostly in medical diagnostics.

Quality of MRI images depends on the signal-to-noise ratio (SNR) of received signal. Low SNR causes spatial resolution to drop and the total time of experiment to lenghten (scanning additional number of times and averaging the results helps to reduce the effect of low SNR). Higher value of magnetic resonance signal may be achieved through increase in B_0, which is directly proportional to magnetization of the sample. High-field MRI scanners (7 T) are currently being tested and are to enter the clinical market shortly (so far 3 T scanners are mostly used). The main disadvantage of high-field scanners is their high price and expensive maintenance. Low-field scanners are cheaper, and their use does not generate such costs since they do not require the helium colling system. Open access to the patient is an additional advantage in those system and is possible because B_0 can be oriented vertically.

In Department of Medical and Nuclear Electronics at Warsaw University of Technology we possess two low-field scanners: G-Scan with B_0 of 0.24 T (permanent magnet) and 0.23 T Picker produced by Marconi (electromagnet). Our group conducts studies regarding various techniques for increasing the quality of imaging in those systems. This work includes hardware development, pulse sequences and data processing, and their goal is to increase the SNR through improving the parameters of transmit-receive system and use of contrast agents which increase the polarization [hyperpolarization of noble gases and proton-electron double resonance imaging (PEDRI)].

1. Transmit/receive system

MRI coil is the part of the system responsible for transmitting the RF pulse and receiving the signal. Those activities can be done using two separate coils or just one, if T/R switch is a part of the system. The magnetic field B_1 produced by the coil should be possibly homogeneous so that the distribution of magnetization within the sample is the main factor responsible for signal intensity. Quality value of the coil is another important parameter, as it determines the SNR of the experiment. Losses are mainly due to coil series resistance, current generated by electric field within the examined sample and eddy currents which are result of changing magnetic field within the conducting sample.

In order to maximize the homogeneous area as well as minimize the losses we developed a prototype probe consisting of 12 magnetically coupled rings, each of 292 mm diameter (Fig. 1). The coil is 300 mm long, and within it there is a aluminum shield of 250 mm radius, which prevents the electric field from entering the area of imaging. The probe is inductively coupled to 50 Ω with additional coupling ring.

Fig. 1. Coil prototype with shield and coupling ring placed within the imaging area of Picker 0.23 T scanner

With use of Picker scanner and KEA console attached to it (scientific spectrometer/generator of prototype MR pulse sequences) we acquired 2 images of water phantom (flip angle 60/120°), which were later used to establish the B_1 distribution within the sample (Fig. 2).

Loss factor of the coil was studied based on its quality factor Q. A series of measurements were made, filling the probe with different volumes of demineralized water and saline (Fig. 3).

Measured values of Q are satisfactory and ensure decent SNR in received images. The prototype was constructed basing on a certain template procedure, which in the future will help in constructing a larger amount of similar coils for different volumes and nuclei in a quick and easy manner.

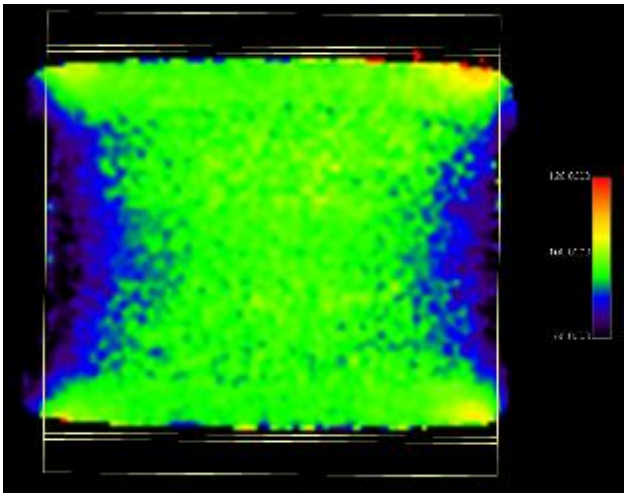

Fig. 2. B_1 field distribution inside of a water phantom. Field values are normalized, the contours of coil and shield have been displayed

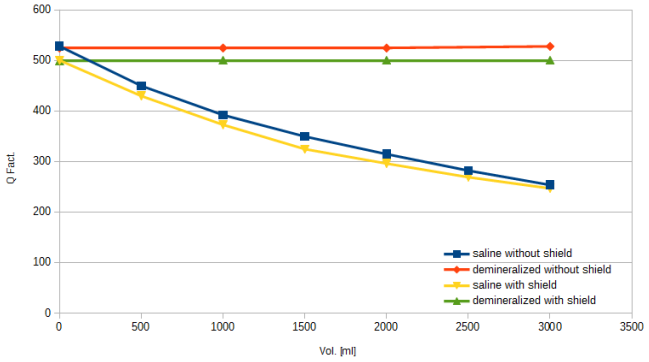

Fig. 3. Quality factor of the coil as a function of volumes of demineralised water and saline placed within it. Measurements both with and without shield present

2. Proton Electron Double Resonance Imaging

PEDRI uses substances containing free radicals (with non-zero electron spin) [4]. Overhauser effect is a physical base for this technique- it causes polarization transfer from one spin population to another, in this case from electrons to protons. This allows to achieve polarization level higher than the one resulting from thermal polarization, and as a result higher SNR. Fig. 4 compares two images, both with and without signal amplification from EPR (electron paramagnetic resonance). Increased value of NMR (nuclear magnetic resonance) signal can be observed with presence of the EPR effect.

We have prepared a set of equipment for conducting PEDRI experiments in our laboratory (Fig. 5). Electrons present in free radicals undergo polarization inside of a microwave resonator under 6.45 GHz microwave pulse. Due to Overhauser effect, those electrons pass their polarization to surrounding protons. The solution flows to the NMR coil, where proton excitation with RF pulse occurs. The signal is then rapidly received. Both NMR coil and EPR resonator are within the main field of the scanner (0.23 T). Measurements have shown that the use of PEDRI technique has increased the level of NMR signal by the factor of 10, in comparison to the signal with just thermal polarization (Fig. 6).

This technique finds practical use in studies of perfusion, where polarized liquid is used as a contrast agent. Higher level of SNR allows to conduct very short and quick scans. This grants the opportunity to conduct functional heart studies or brain perfusion. Preliminary studies have shown relevant connection between local increase in concentration of free radicals and diseases such as tumors, inflammations and neurodegenerative diseases.

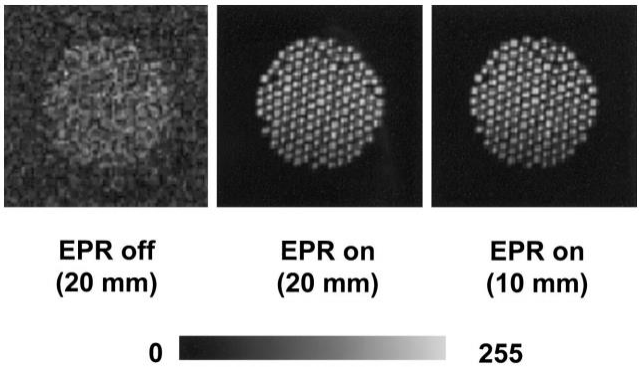

Fig. 4. Images of capillaries of 850 μm inner diameter and wall thickness of 280 μm. Capilarries are filled with 2.5 mM TEMPONE in PBS solution (phosphate-buffered saline). Images were taken with and without the signal amplification coming from Overhauser effect [3]

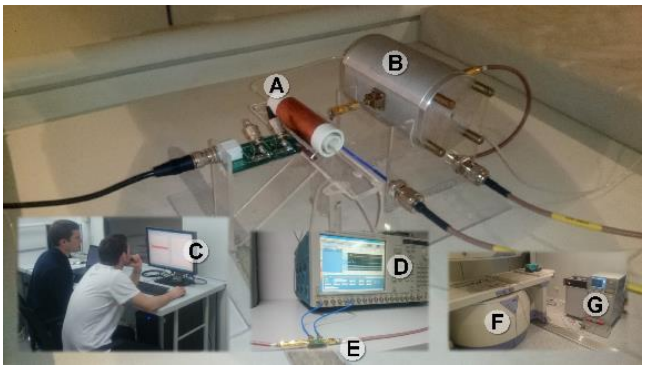

Fig. 5. Laboratory station for PEDRI experiments. NMR coil (A), microwave resonator TE011 (B), spectrometer/concole NMR KEA (C), generator Tektronix AWG5004B generating modulating signal modulating microwave signal of frequency equal Fepr=6.45 GHz (D), quadrature mixer IQ Hittite HMC525LC4 (E), MRI scanner (F) and microwave amplifier with output power of P=40 W (G) [5]

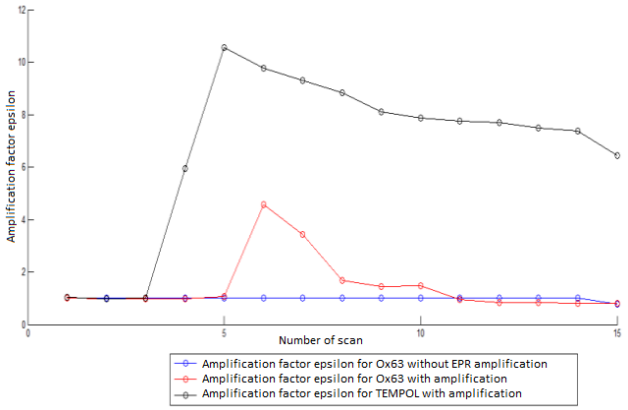

Fig. 6. Plot of amplification factor epsilon for 2 mM OX63 and 3 mM TEMPOL solutions at flow speed of 11ml/min

3. Hyperpolarization of noble gases

Gases are a state of matter much less concentrated than solids and liquids. For this reason imaging them with MRI is not normally possible, as the strength of the signal is directly proportional to concentration of hydrogen atoms. The signal received from gases is 1000 times weaker than that received from liquids and solids. This can be helped with use of hyperpolarization techniques, that allow us to increase the level of polarization even by 5 orders of magnitude. This allows to perform functional imaging of human lungs. Exemplary scans have been shown in Fig. 7.

Hyperpolarization state is achieved through optical pumping. There are two techniques based on this method: MEOP (Metastability Exchange Optical Pumping) and SEOP (Spin Exchange Optical Pumping).

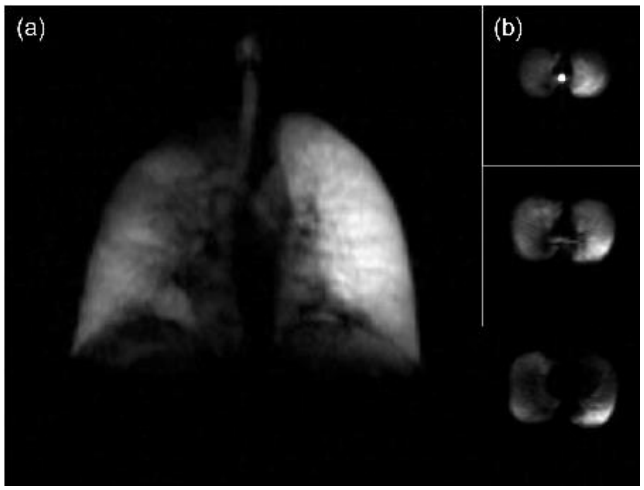

Fig. 7. MRI image of human lungs achieved with use of hyperpolarized ^{3}He [2]

MEOP uses metastable excitation state of ^{3}He isotope [1]. Atom excitation occurs with presence of electrical discharge and laser beam with circular polarization and wavelength of 1083 nm. The whole process lasts several minutes and takes place at very low pressure (10 Torr), which only allows polarization of small volumes of gases. In order to use this method in practice an additional system for stabilizing the pressure would be required.

SEOP hyperpolarization uses alkali metal vapors, which are polarized and then pass their spin to gas particles as they collide with them [7]. This allows the use of both ^{3}He and ^{129}Xe (isotopes are mixed with nitrogen). The excitation occurs with use of laser beam with circular polarization and wavelength of 795 nm. The pressure within polarization chamber equals 10 bars.

In our laboratory we possess vacuum equipment to prepare hyperpolarized samples of ^{3}He and ^{129}Xe gases (Fig. 8). Sample preparation consists of following steps:

- Acquiring high vacuum for purposes of preliminary cleansing of the system.
- Preparation of gas mixture of ^{3}He (or ^{129}Xe) and N_2 under 10 bar pressure and pumping it to a transparent glass container later referred to as 'cell'.
- SEOP polarization of gas within the cell. The cell is placed in 30 mT magnetic field.
- Cooling the gas in order to remove the Rb vapors which condensate on glass walls of the cell.
- Extraction of gas sample with use of dedicated syringe.
- Acquiring high vacuum yet again and cleansing the system.

Aforementioned cell is a crucial part of the system. Before conducting the experiment it has to undergo a cleaning procedure consisting of following steps:

- Rinsing in ultrasonic rinse three times.
- Roasting in 300°C for 3 hours. The cell is at the same time connected to vacuum pump lowering the pressure to 10^{-6} mBar.
- „Plasma scrubbing" (Fig. 9). During this process the cell is filled with 1–2 mBar mixture of ^{3}He/^{129}Xe/N_2 and with use of dedicated device plasmic discharges are generated within it. The process lasts several hours, depending on the level of impurities within the cell and may require 5–15 exchanges of gas mixture.

The preliminary launch of the system confirmed capability of acquiring desired pumping speed and vacuum parameters. The cell cleansing procedure passed the tests positively. System has been verified in terms of capabilities to prepare required gas mixture. The electromagnet generated homogeneous magnetic field which meets the requirements. The system is ready to conduct SEOP hyperpolarization.

Fig. 8. Vacuum system developed on special order in Tele- and Radiotechnical Institute in Warsaw

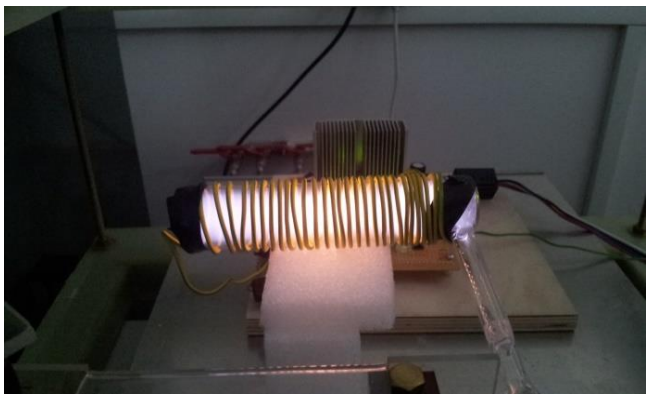

Fig. 9. „Plasma scrubbing", one of the steps in preparing the cell to work in hyperpolarizer system [6]

Bibliography

[1] Colegrove F., Schearer L., Walters G.: Polarization of He3 Gas by Optical Pumping, Phys. Rev., t. 132, nr 6, 1963, 2561–2572.

[2] Collier G., Pałasz T., Wojna A., Głowacz B., Suchanek M., Olejniczak Z., Dohnalik T.: A high-field 3He metastability exchange optical pumping polarizer operating in a 1.5 T medical scanner for lung magnetic resonance imaging, J. Appl. Phys., t. 113, nr 20, 2013, 204905.

[3] Liebgott T., Li H., Deng Y., Zweier J.: Proton Electron Double Resonance Imaging (PEDRI) of the Isolated Beating Rat Heart, Magnetic Resonance in Medicine 50, 2003, 391–399.

[4] Lurie D.: Proton-Electron Double-Resonance Imaging (PEDRI), Biological Magnetic Resonance, Vol. 18, 547–578.

[5] Obrębski W., Piątkowska-Janko E., Sawionek B., Orzeł J., Kossowski B., Werys K., Szczepankowski M., Tor P., Bogorodzki P.: Laboratorium hiperpolaryzowanych środków cieniujących NMR. Tomografia MR hiperpolaryzowanych środków cieniujących, Elektronika – konstrukcje, technologie, zastosowania, nr 7, 2015, 7–11.

[6] Obrębski W., Zawada A., Woźniak R., Miśnik M., Konarski P.: High pressure and vacuum system for magnetic polarisation of gases, http://www.itr.org.pl/10konferencjaptp/. [Accessed: 03.05.2015].

[7] Walker T., Happer W.: Spin-exchange optical pumping of noble-gas nuclei, Rev. Mod. Phys., t. 69, nr 2, 1997, 629–642.

D.Sc. Eng. Piotr Bogorodzki
e-mail: P.Bogorodzki@ire.pw.edu.pl

Associate professor at Faculty of Electronics and Information Technology of Warsaw Institute of Technology. Workfield: biocybernetics and biomedical engineering.

Ph.D. Eng. Ewa Piątkowska-Janko
e-mail: E.Piatkowska@ire.pw.edu.pl

Ph.D. at Faculty of Electronics and Information Technology of Warsaw Institute of Technology since 2001. Researcher at Department of Nuclear and Medical Electronics.

Ph.D. Eng. Błażej Sawionek
e-mail: B.Sawionek@ire.pw.edu.pl

Ph.D. at Faculty of Electronics and Information Technology of Warsaw Institute of Technology since 1999. Researcher at Department of Nuclear and Medical Electronics.

M.Sc. Eng. Wojciech Obrębski
e-mail: W.Obrebski@ire.pw.edu.pl

Defended his master thesis titled 'Pobudzenie adiabatyczne w obrazowaniu techniką rezonansu magnetycznego (MR) ' in 2008 at Warsaw University of Technology. Researcher at Department of Nuclear and Medical Electronics.

M.Sc. Eng. Michał Wieteska
e-mail: M.Wieteska@ire.pw.edu.pl

Defended his master thesis titled 'System for electrical stimulation in pre-clinical fMRI studies' in 2015 at Warsaw University of Technology. Ph.D. student at Department of Nuclear and Medical Electronics.

otrzymano/received: 20.09.2016 *przyjęto do druku/accepted: 15.02.2017*

DOI: 10.5604/01.3001.0010.4603

TOOLBOX FOR 3D MODELLING AND IMAGE RECONSTRUCTION IN ELECTRICAL CAPACITANCE TOMOGRAPHY

Jacek Kryszyn, Waldemar Smolik
Warsaw University of Technology, Faculty of Electronics and Information Technology, The Institute of Radioelectronics and Multimedia Technology, Nuclear and Medical Electronics Division

Abstract. *Electrical Capacitance Tomography is used to visualize a spatial distribution of electric permittivity in a tomographic sensor. ECT is able to create even thousands of frames per second which is suitable for application in the industry, e.g. monitoring of multiphase flows or material mixing. A tool for sensor modelling and image reconstruction is needed in order to develop improved solutions and to better understand phenomena in ECT. A software for 2D and 2D modelling is developed in the Division of Nuclear and Medical Electronics. In this paper a Matlab toolbox called ECTsim for 3D modelling is presented.*

Keywords: electrical capacitance tomography, 3D modelling, image reconstruction

PAKIET DO TRÓJWYMIAROWEGO MODELOWANIA I REKONSTRUKCJI OBRAZÓW W ELEKTRYCZNEJ TOMOGRAFII POJEMNOŚCIOWEJ

Streszczenie. *Elektryczna tomografia pojemnościowa jest używana do obrazowania przestrzennego rozkładu przenikalności elektrycznej w sondzie tomograficznej. Elektryczna tomografia pojemnościowa pozwala uzyskać nawet kilka tysięcy obrazów na sekundę co sprawia, że znajduje zastosowanie w przemyśle, na przykład do monitorowania przepływów wielofazowych lub mieszania materiałów. Dla uzyskania lepszych rezultatów obrazowania i lepszego zrozumienia zjawisk zachodzących w elektrycznej tomografii pojemnościowej potrzebne są narzędzia do modelowania i rekonstrukcji obrazów. W Zakładzie Elektroniki Jądrowej i Medycznej rozwijane jest oprogramowanie do modelowania 2D i 3D. W artykule przedstawiono pakiet ECTsim dla środowiska Matlab do modelowania trójwymiarowego*

Słowa kluczowe: elektryczna tomografia pojemnościowa, modelowanie trójwymiarowe, rekonstrukcja obrazów

Introduction

Electrical Capacitance Tomography (ECT) is a method which is used to visualize a spatial distribution of the dielectric permittivity of objects placed inside a tomographic sensor. The image is reconstructed form measurements of mutual capacitances between electrodes placed around the examined volume [2]. It is possible to achieve even several thousand images per second with ECT. This technique has applications mainly in industrial processes like visualizing multiphase flows, mixing and stirring of materials and monitoring combustion processes [3, 7].

In the Division of Nuclear and Medical Electronics a software and hardware for ECT is being developed. The Matlab toolbox ECTsim 1.1 for 2D modelling was elaborated a decade ago. The custom finite element method implemented in this software accelerates the computations of a sensitivity matrix and enables fast nonlinear image reconstruction. For several years the ECTsim 3.0 toolbox for 3D modeling is being developed. This paper presents features and exemplary results achievable with ECTsim 3.0.

1. Challenges in ECT

1.1. Design and modelling of a 3D sensor

One of important parts of ECT system is a tomographic sensor. Parameters of the probe have an influence on quality of reconstructed images.

Usually tomographic sensors have a cylindrical or cuboidal geometry with one ring of 8 to 32 electrodes. Spatial resolution of reconstructed images depends on number of electrodes. More electrodes give better resolution but result in smaller mutual capacitances due to decreasing area of the electrodes. More precise measurement methods have to be used in order to maintain satisfactory quality of capacitance measurements [8]. Typically, in a 2D sensor which has one ring of electrodes height of the electrodes is equal to the diameter of the sensor. The pair of adjacent electrodes has a capacitance value equal to around 1 pF whereas opposite electrodes can have a capacitance value lower by two orders of magnitude [11]. Such a wide range of measured values complicates measurement process. In order to decrease capacitance value between adjacent electrodes it is possible to insert electric screens between them. Sensors with one ring of electrodes are characterized with poor resolution in z axis due to large height of electrodes. A sensor with more than one ring of electrodes allows to measure capacitances needed to reconstruct three dimensional images. In such case measurements are performed between electrodes in all rings. To further increase resolution in 3D sensors it is possible to apply solution called "wobbling" in CT: shifting rings by half of electrodes' width.

To limit influence of external electrical field a sensor has to be isolated with an electric screen which wraps the sensor around. Additionally, guard electrodes above and below rings of electrodes can be added to minimize influence of objects placed near opened boundaries of the sensor. The guard electrodes can be set to zero potential or can be excited synchronously with application electrodes. Fig. 1 shows lines of electric field in a sensor without and with guard electrodes.

Electrodes in a tomographic sensor can be placed on the outer side of the wall of the sensor, on the inner side of the wall of the sensor or in the wall of the sensor. In case of external electrodes, the construction of such a sensor is simple. Measurement process is not invasive because electrodes do not interact with measured material. Moreover, electrodes do not corrode because of that fact. Downside of such a solution is that the wall of the sensor modifies the field of view of the electrodes and makes measurements less linear. The better solution is to have internal electrodes which is much harder to implement because of required isolation.

To enable 3D measurements, the size of electrodes has to decrease. This means that methods of measuring small capacitances have to improve. It is also important to be able to model tomographic sensors in order to simulate mutual capacitance values between electrodes which can be used to evaluate usefulness of such a sensor.

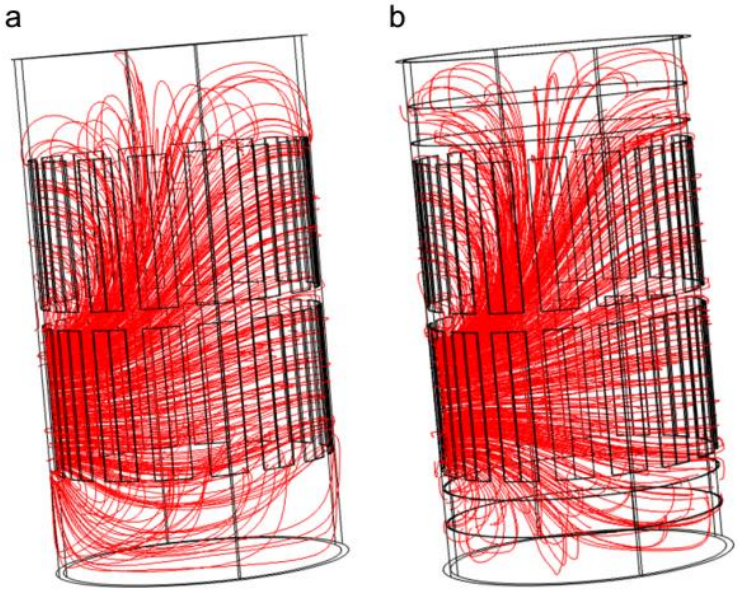

Fig. 1. Tomographic sensor with 4 rings of 8 electrodes each and electric field lines inside the sensor a) without guard electrodes; b) with guard electrodes

1.2. Image reconstruction

One of main challenges in ECT is image reconstruction. A number of independent measurements is lower (sometimes even by an order of magnitude) than a number of pixels in reconstructed image. Additionally, the sensitivity of capacitance measurement on permittivity change in a small volume is very low especially in the center of the sensor. This means that the inverse problem in ECT is ill-posed and numerically ill-conditioned [4]. Three dimensional calculations result in even worse conditioned problem. That is why there is a need for a toolbox which allows efficient image reconstruction with nonlinear, regularized methods [5]. In the nonlinear approach the challenge is that a sensitivity matrix has to be recalculated in every step which can be time consuming in case of 3D image reconstruction.

2. ECTsim 3.0

ECT 3.0 is a software for three-dimensional modelling and image reconstruction in electrical capacitance tomography designed for Matlab environment [1]. It allows to:

- create a model of the cylindrical sensor with one or more rings of electrodes,
- create a model of a phantom,
- simulate a distribution of electric field in the sensor,
- calculate sensitivity matrix for the model,
- calculate values of mutual capacitance between electrodes,
- reconstruct image from simulated or measured data,
- visualize models and calculated data in order to allow qualitative assessment of simulations.

All models are three dimensional and are built with a regular cubic mesh. In order to avoid so called inverse crime, the forward problem is calculated in a high density mesh while the image reconstruction uses a coarse mesh.

ECTsim 3.0 is an object oriented toolbox. It consists of the following classes:

- eSet class – represents sensors and phantoms as a set of primitive shapes;
- *eSphere* – a primitive's shape – a sphere;
- *eCylinder* – a primitive shape – a cylinder;
- *eCuboid* – one of primitive shape – a cuboid;
- eMaterial – a material from which the shape is built characterized by electrical permittivity;
- phantom_generator – a graphical generator of phantoms consisting of PVC rods placed in hexagonal nodes;
- eModel – represents a model of the sensor and the phantom; contains methods for 2D and 3D data visualization;
- *eCube_Mesh* – generate a cubical mesh. Interpolates the data if model elements are thinner than discrete element size. Contains linear and Cartesian coordinates of mesh points;
- *eElectrical_Field* – calculates the distribution of electric field in the model;
- *eFwd_Problem* – represents the forward problem; allows to calculate 3D sensitivity matrix and mutual capacitances;
- *eInv_Problem* – represents the inverse problem. To implement a reconstruction algorithm a class which inherits from *eInv_Problem* has to be created;
- *eInv_Problem_LBP* – a class which inherits from *eInv_Problem* and reconstructs images with the LBP algorithm (one step linear back projection);
- *eInv_Problem_Landweber* – a class which inherits from *eInv_Problem* and reconstructs images with the Landweber algorithm (a simplified gradient method); a user can adjust parameters like number of iterations, length of step, stop condition.

In order to calculate the distribution of electric field a cell method is used which uses integral form of Maxwell equations [6, 9]. Because of this there is no need to calculate second order derivatives (no divergence or rotation).

In case of a cubical mesh every element has 6 neighbours. Coordinates of elements are noted with (i, j, k). In each element the electrical permittivity and the potential are constant. Electrical field in each element is described with an equation:

$$\sum_{l=1}^{6} \varepsilon_l \nabla \varphi_l \cdot \vec{ds} = \sum_{l=1}^{6} \varepsilon_l \nabla \varphi_l \cdot \vec{n}_l h_l = 0 \tag{1}$$

where ε_l is an arithmetic average of permittivity of a given element and its current neighbour, h_l is a size of the grid and φ_l is a potential in the element. If

$$\nabla \varphi_l \cdot \vec{n}_l = \frac{\varphi_{i,j,k} - \varphi_{i+\Delta i, j+\Delta j, k+\Delta k}}{h_l} \tag{2}$$

and $h_l = 1$, then the equation for the potential in the element is

$$\varphi_{i,j,k} = \frac{\sum_{m=-1,1} \varphi_{i+m,j,k}(\varepsilon_{i+m,j,k} + \varepsilon_{i,j,k}) + \sum_{n=-1,1} \varphi_{i,j+n,k}(\varepsilon_{i,j+n,k} + \varepsilon_{i,j,k})}{6\varepsilon_{i,j,k} + \varepsilon_{i+1,j,k} + \varepsilon_{i-1,j,k} + \varepsilon_{i,j+1,k} + \varepsilon_{i,j-1,k} + \varepsilon_{i,j,k+1} + \varepsilon_{i,j,k-1}} + \frac{\sum_{l=-1,1} \varphi_{i,j,k-l}(\varepsilon_{i,j,k-l} + \varepsilon_{i,j,k})}{6\varepsilon_{i,j,k} + \varepsilon_{i+1,j,k} + \varepsilon_{i-1,j,k} + \varepsilon_{i,j+1,k} + \varepsilon_{i,j-1,k} + \varepsilon_{i,j,k+1} + \varepsilon_{i,j,k-1}} \tag{3}$$

In order to calculate the distribution of the electric field a linear system consisting of above equations for all elements has to be prepared but it would be too large (tens of GB) to put it in memory of a computer. In ECTsim 3.0 a modification of Kaczmarz iterative algorithm is used which forms an equation for one element and solves it in each step. In order to accelerate calculations a MEX file with an external procedure in C language was written.

Capacitances are calculated using the linear aproximation:

$$\mathbf{C} = \mathbf{S}\boldsymbol{\varepsilon}$$

where $\mathbf{C}$ is a mutual capacitance vector, $\mathbf{S}$ is a sensitivity matrix and $\boldsymbol{\varepsilon}$ is a permittivity vector. In order to avoid numerical errors coming from cubical mesh the capacitance values are not calculated with Gauss law. Because of usage of cubical mesh, the electrodes of cylindrical sensor have different shapes depending of placement. A special function called *geometric_correction* was made to minimize such errors. The function ensures equality of integral sensitivity of all pairs of electrodes shifted by the same angle.

The forward problem is calculated three times: for the empty sensor, the sensor filled with material with maximum permittivity and the sensor filled with the phantom. To decrease the time needed for the calculations they can be performed simultaneously on machines with more than one core using *parfor* instruction.

In case of the inverse problem solution the uniform distribution of electric permittivity in the field of view of the sensor is used as the starting point of image reconstruction. Images are reconstructed in a low resolution grid whereas forward problem is calculated in high resolution grid so special methods for down sampling of the sensitivity matrix and permittivity distribution are provided in the *eInv_Problem* class. To reconstruct images from measured data a *get_C_from_file* method has to be used which allows to read data from ET3 tomograph in a form of a text file. Methods for evaluation of errors and image quality and errors are provided. For example, it is possible to compare a reconstructed image to a numerical model. The reconstructed images can be visualized in 2D and 3D with one of many methods provided in the *eInv_Problem* class. In the case of application of regularization in the image reconstruction, it is possible to use TSVD or Tikhonov method.

3. Example of use

3.1. Forward problem

A sensor with following parameters was modeled:

- cylindrical sensor,
- inner diameter = 153 mm,
- wall thickness = 3 mm,
- height = 250 mm,
- electric permittivity of the wall = 3 (PVC material),
- 2 rings of 16 electrodes in each ring,
- height of electrodes = 80 mm,
- width of electrodes = 20 mm,
- internal electrodes.

The sensor was modeled in two variants: without guard electrodes and with them (Fig. 2). The former was used only to present the difference in the distribution of electric field between not guarded and guarded sensor. The latter was used for further experiments. The height of guard electrodes was set to 20 mm.

The size of mesh cells was set to 4 mm in x, y and z. The numerical model consisted of 105489 cells.

Models of empty sensor from ECTsim 3.0 were compared with models created in COMSOL (Fig. 2b and Fig. 2d) in order to validate the method of the simulation used in ECTsim 3.0.

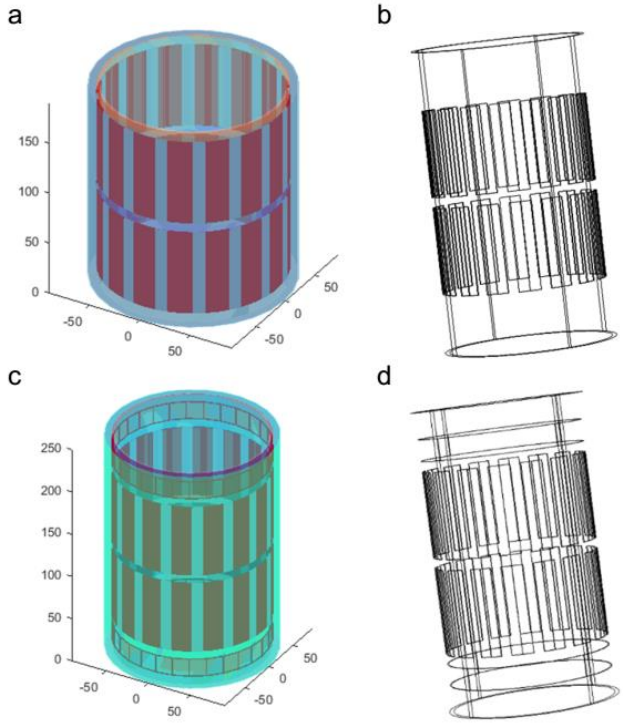

Fig. 2. Model of a sensor a) without guard electrodes; ECTsim 3.0 b) without guard electrodes; COMSOL c) with guard electrodes; ECTsim 3.0 d) COMSOL

Fig. 3 shows simulated distributions of electric field in ECTsim 3.0 and COMSOL for both variants of the sensor. *Slice* function from Matlab was used to show volumetric data in ECTsim 3.0. It is possible to see that lines of electric field in a sensor with guard screens are limited to the electrodes whereas in not guarded sensor they flow out of the sensor in z axis. Further results will only include the model with guard electrodes.

Fig. 4 shows one-dimensional cross section from two different planes (along x axis perpendicularly to the center of the excitation electrode and y axis going through the middle of the field of view) of the distribution of electric field calculated with ECTsim 3.0 and COMSOL. Results from ECTsim 3.0 and COMSOL are very close to each other. The discrepancy is due to the different interpolation used in both numerical solvers.

Figure 5 shows sensitivity maps calculated by ECTsim 3.0. The maps are presented in 2D and 3D.

Fig. 6 and Fig. 7 show mutual capacitance values between electrodes of the sensor which were numerically calculated in ECTsim 3.0 respectively in linear and logarithmic scale. First electrode was the excitation electrode (10 V) and electrodes from 2 to 32 were measurement electrodes. Capacitance values were calculated for the empty sensor (green bars) and the sensor filled with a solid material with permittivity equal to 3 (yellow bars). The highest value is over 2 orders of magnitude bigger than the lowest. This presents one of challenges of ECT which is measuring not only small values of capacitance but also values in a very wide range.

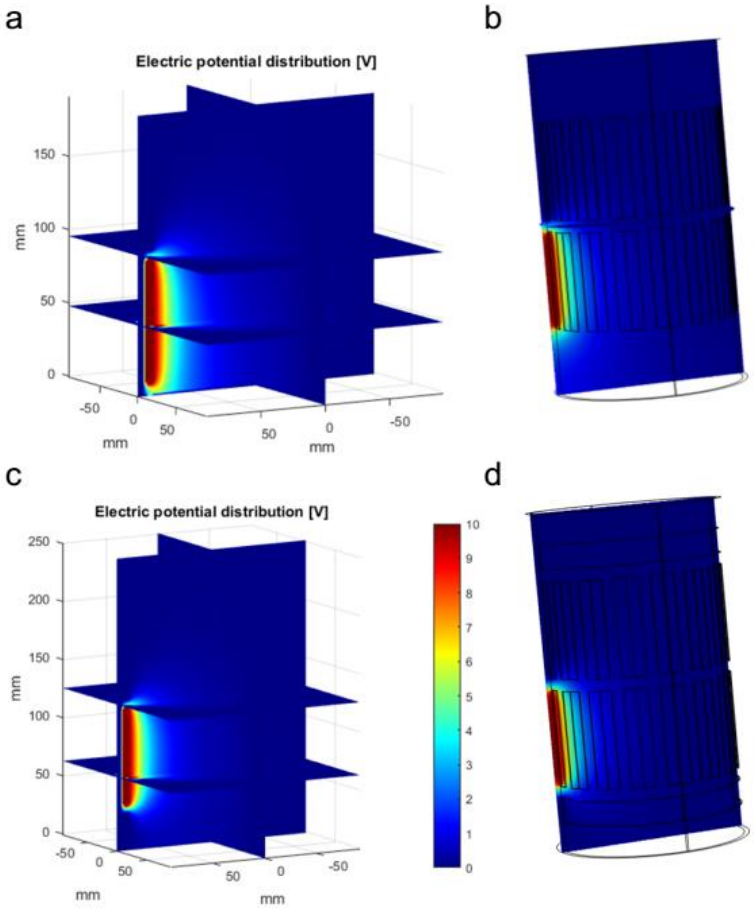

Fig. 3. Distribution of electric potential in a model without guard electrodes a) ECTsim 3.0 b) COMSOL and in a model with guard electrodes c) ECTsim 3.0 d) COMSOL

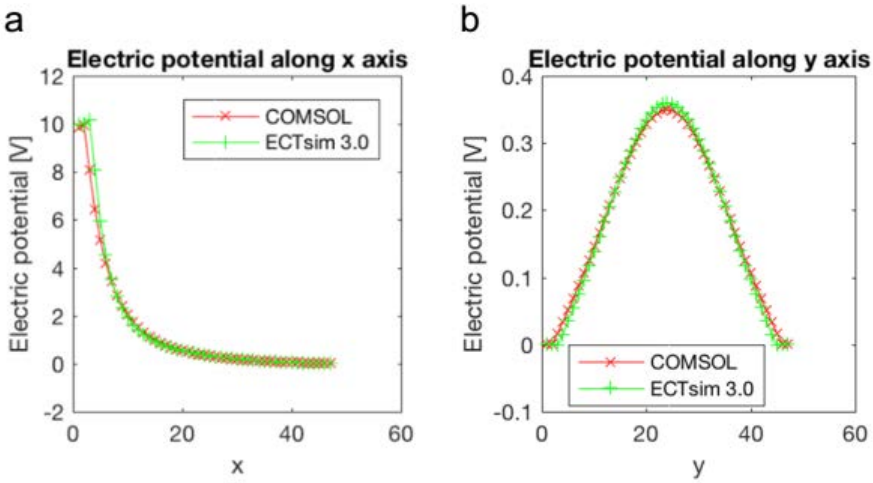

Fig. 4. Comparison of electric field calculated numerically in ECTsim 3.0 and COMSOL. Electric potential along: (a) x axis. Plane is perpendicular to the excitation electrode and goes through the middle of the electrode; (b) y axis. Plane is parallel to the excitation electrode and goes through the middle of the field of view

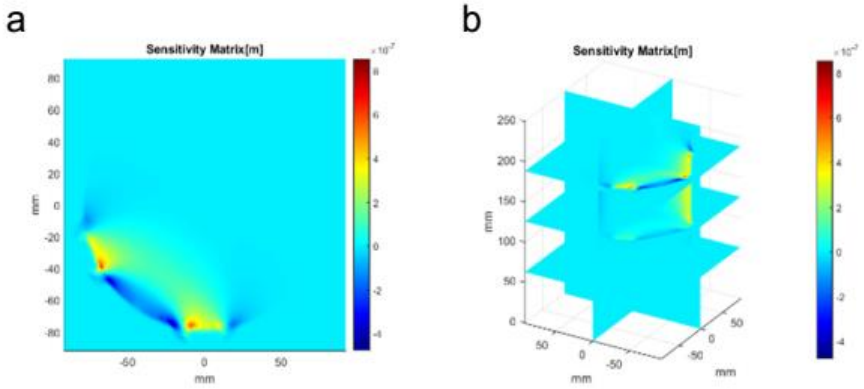

Fig. 5. Sensitivity maps calculated in ECTsim 3.0: a) 2D axial cross section; b) 3D view

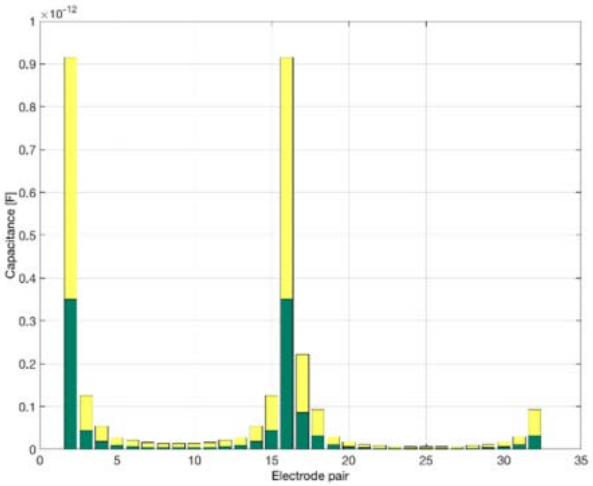

Fig. 6. Numerically calculated interelectrode capacitance. First electrode is the excitation electrode, electrodes 2-32 are measurement electrodes. Green bars represent capacitance values in the sensor filled with a low permittivity material (air). Yellow bar corresponds to capacitance values in a sensor filled with a material with relative dielectric permittivity equal to 3. Linear scale

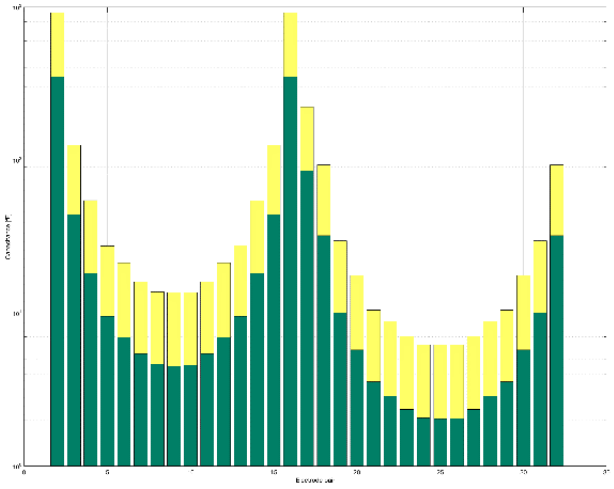

Fig. 7. Numerically calculated interelectrode capacitance. First electrode is the excitation electrode, electrodes 2-32 are measurement electrodes. Green bars represent capacitance values in a sensor filled with low permittivity material (air). Yellow bar corresponds to capacitance values in a sensor filled with a material with relative dielectric permittivity equal to 3. Logarithmic scale

3.2. Inverse problem

To compare simulated with real measurements a sensor with exact same parameters was built (Fig 8a). Electrodes from copper foil were placed inside PVC pipe. To screen the whole sensor, the pipe was wrapped with an insulator and metal screen.

A phantom consisting of four PVC rods with height equal to 40 mm was modeled. Two rods were placed in such a way that their centers were in axis with the center of lower ring of electrodes and another two were placed in a similar way, but aligned to the center of the upper ring of electrodes (Fig. 8b). A phantom corresponding to the one numerically modeled in ECTsim 3.0 was built. PVC elements were wrapped with aluminum foil in order to get a higher signal. ET3 tomograph was used for measurements. ET3 tomograph returns measured values normalized using calibration measurements (sensor filled with air – minimum electric permittivity material and PVC beads – maximum permittivity material).

Parameters of Landweber algorithm were: 500 iterations, alfa parameter equal to 0.005.

All simulations were performed on a laptop with Intel Core i5 2.6 GHz CPU and 8 GB of RAM.

Calculation of the distribution of electric field took 553 seconds (cumulative time of simulations for the empty sensor, the sensor with the phantom and the sensor filled with solid material with electric permittivity equal to 3). Calculation of sensitivity matrices for all cases took 28.5 seconds. Calculation of the capacitances took 10.7 seconds.

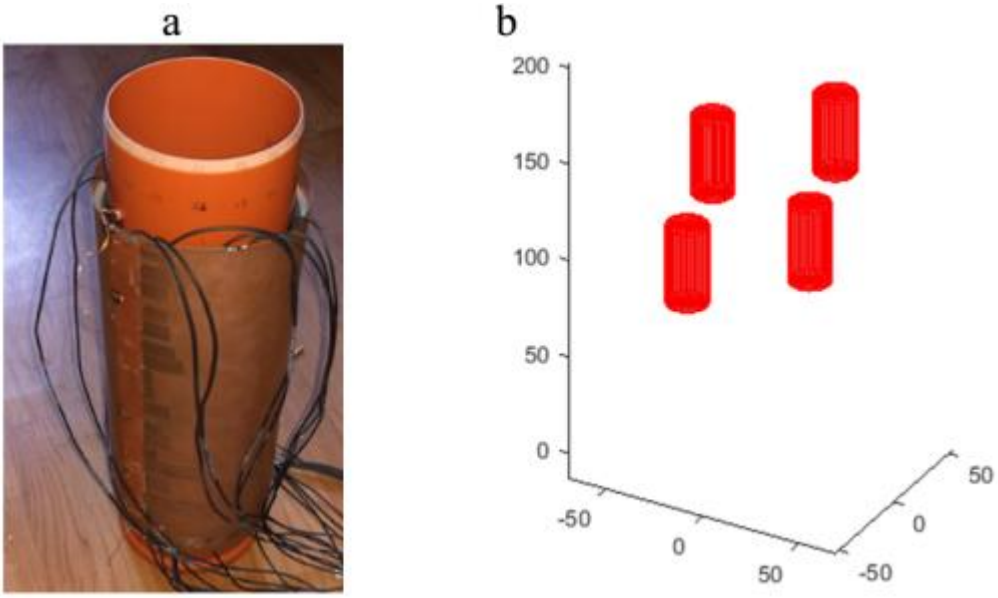

Fig. 8. a) Built sensor; b) Modelled phantom

Fig. 9 and Fig. 10 show capacitance values between electrodes in the built sensor and measured with ET3 tomograph when the first electrode was the excitation electrode and electrodes from 2 to 32 were measurement electrodes respectively in linear and logarithmic scale. Measurements were performed with the empty sensor (green bars) and the sensor filled with PVC beads which dielectric permittivity is equal to 3 (yellow bars).

Figure 11 shows image reconstruction performed with LBP algorithm using simulated capacitances. *Slice* Matlab function was used to show volumetric data. Figure 11 shows xy, xz and xy cross sections of the reconstructed 3D image. LBP algorithms performs badly – it is impossible to distinguish rods which merged into one volume.

Figure 12 shows image reconstruction performed with Landweber algorithm using simulated data. The same views as in Figure 11 were presented. The result shows that to reconstruct 3D images an iterative algorithm has to be used. All four elements are distinguished in the reconstructed image. ECTsim 3.0 allows to visualize 3D data in many ways. Fig. 13 shows 3D maximum intensity projection of the reconstructed volume.

Time of calculation was following:

- LBP algorithm – 0.84 s,
- Landweber algorithm – 35 seconds.

LBP algorithm can be used to calculate an initial solution for iterative algorithm.

Figure 14 shows image reconstruction performed with Landweber algorithm using measured data. The same views as in Figure 11 and Figure 12 were presented. It turned out that electrodes in the designed sensor were too small in order to allow capacitance measurements with ET3 tomograph which has limited sensitivity (about 10 fF). Signal to noise ratio for the smallest capacitances was too low.

Figure 15 shows the normalized capacitance error err_c in next iterations for the Landweber algorithm using the simulated data and the measured data. The error was calculated with formulas:

$$err_C = \left\| \mathbf{C}_r - \mathbf{C}_m \right\|$$

where $\mathbf{C}_r$ – reconstructed capacitance values, $\mathbf{C}_m$ – simulated capacitance values for the sensor with the phantom. After 500 iterations errors were following:

- err_c – 0.001410;
- err_c – 0.261900;

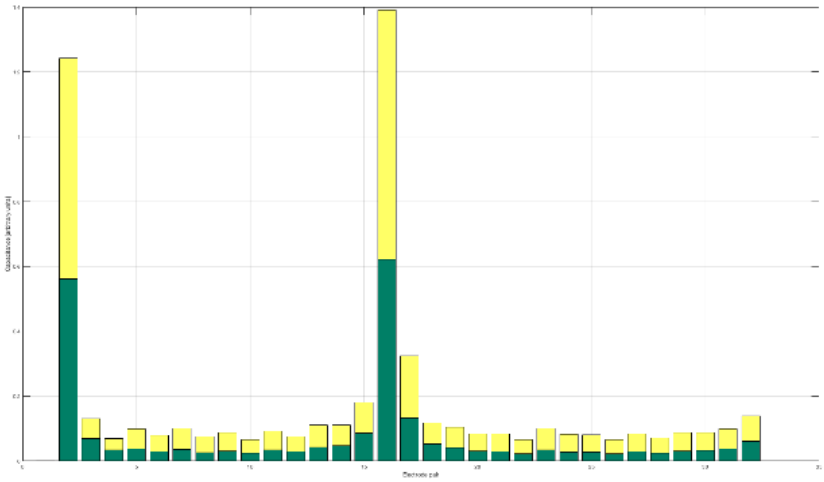

Fig. 9. Measured inter electrode capacitance values. First electrode is the excitation electrode, electrodes 2-32 are measurement electrodes. Green bars represent capacitance values in the sensor filled with a low permittivity material (air). Yellow bars correspond to capacitance values in the sensor filled with a material with relative dielectric permittivity equal to 3. Linear scale

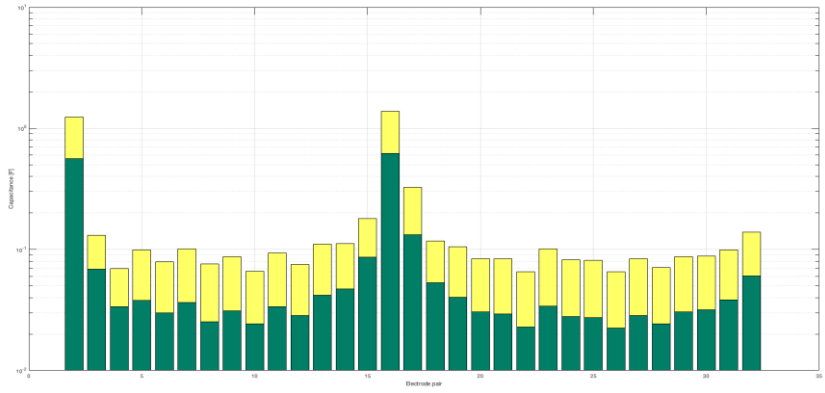

Fig. 10. Measured interelectrode capacitance values. First electrode is the excitation electrode, electrodes 2-32 are measurement electrodes. Green bars represent capacitance values in the sensor filled with a low permittivity material (air). Yellow bars correspond to capacitance values in the sensor filled with a material with relative dielectric permittivity equal to 3. Logarithmic scale

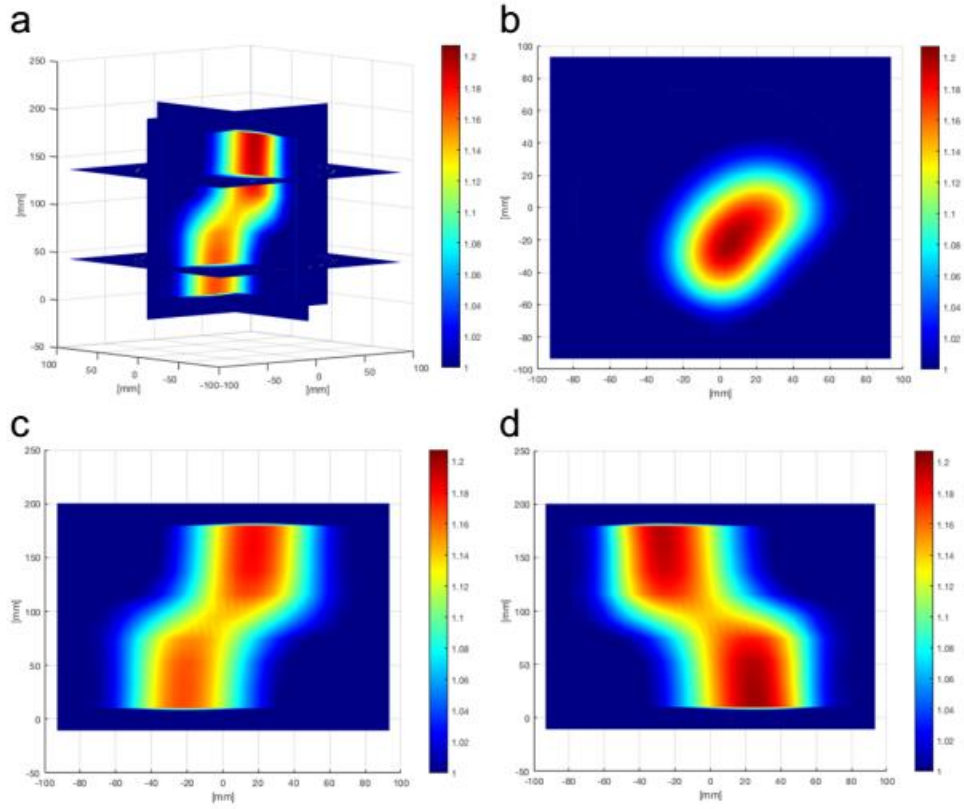

Fig. 11. LBP reconstruction from simulated capacitances: a) four planes from 3D reconstruction image; b) xy slice of the reconstructed volume; c) xz slice of the reconstructed volume; d) yz slice of the reconstructed volume

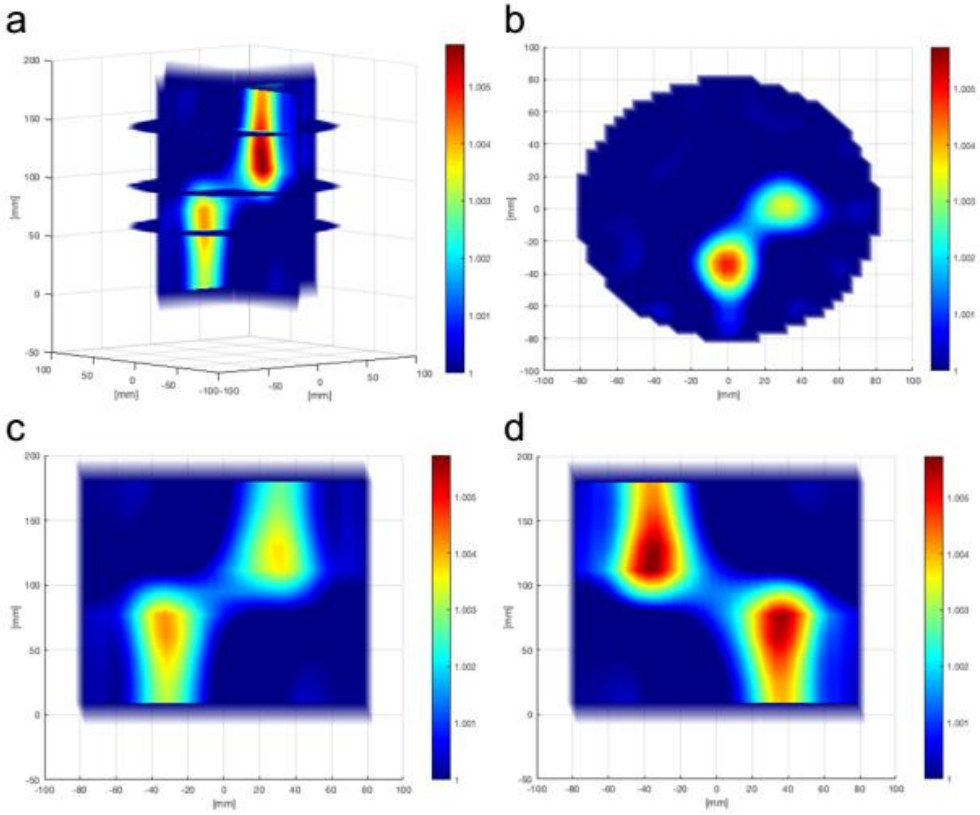

Fig. 12. Landweber reconstruction from simulated capacitances: a) four planes from 3D reconstruction image; b) xy slice of the reconstructed volume; c) xz slice of the reconstructed volume; d) yz slice of the reconstructed volume

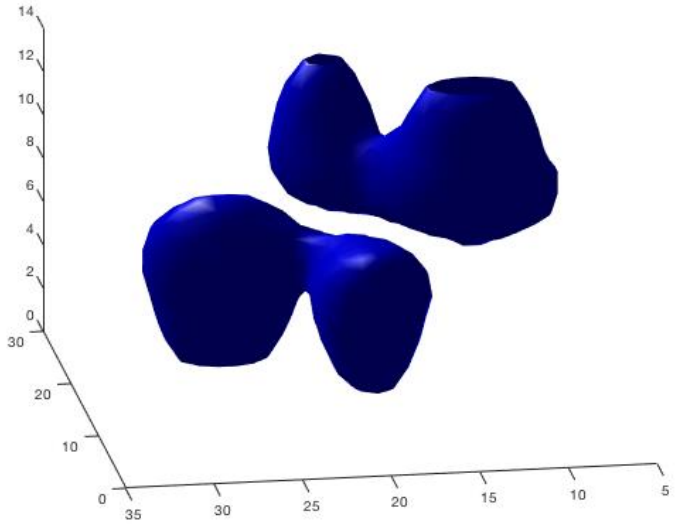

Fig. 13. 3D visualization of the phantom after the reconstruction with the Landweber algorithm

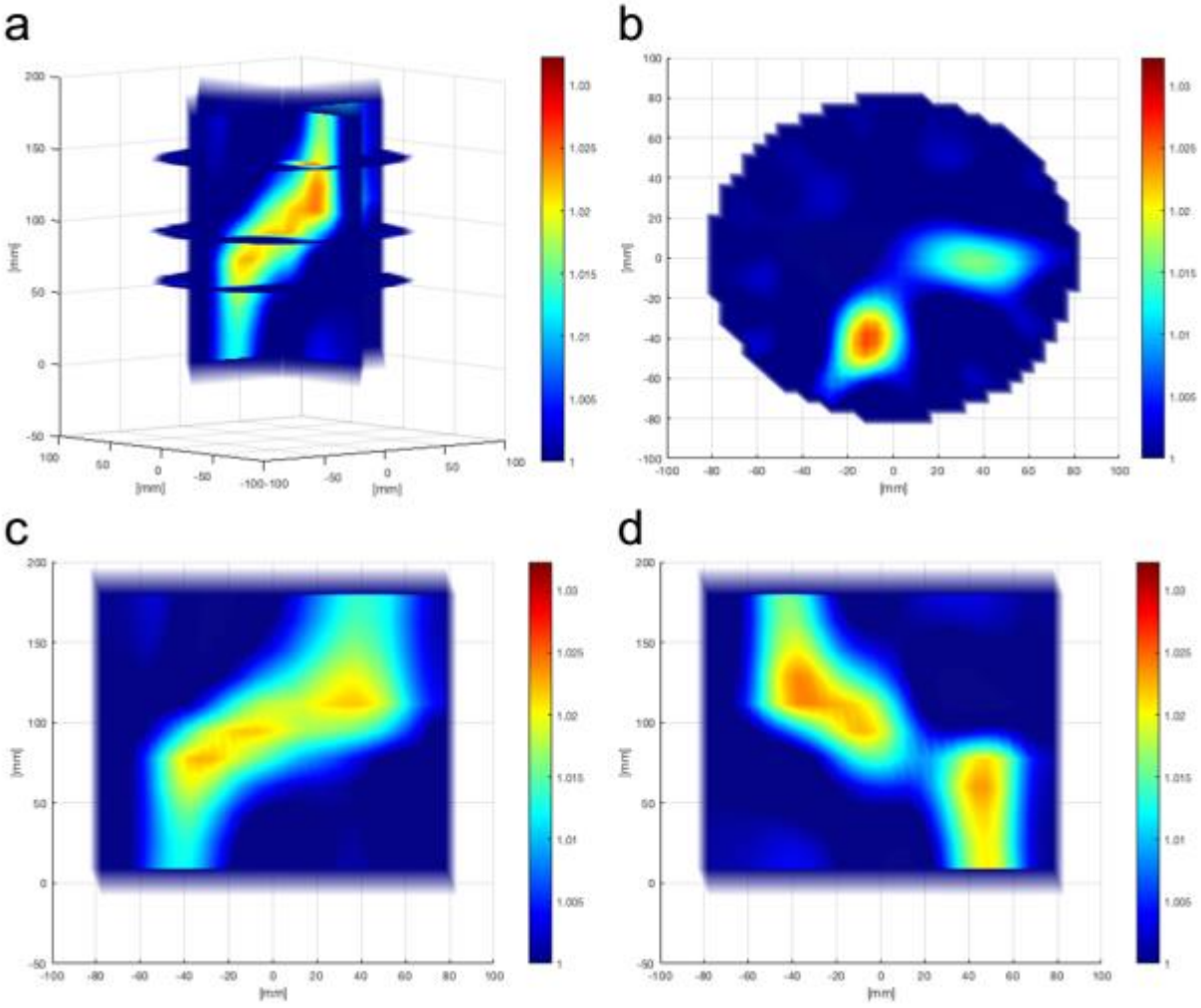

Fig. 14. Landweber reconstruction from measured capacitances: a) four planes from 3D reconstruction image; b) xy slice of the reconstructed volume; c) xz slice of the reconstructed volume; d) yz slice of the reconstructed volume

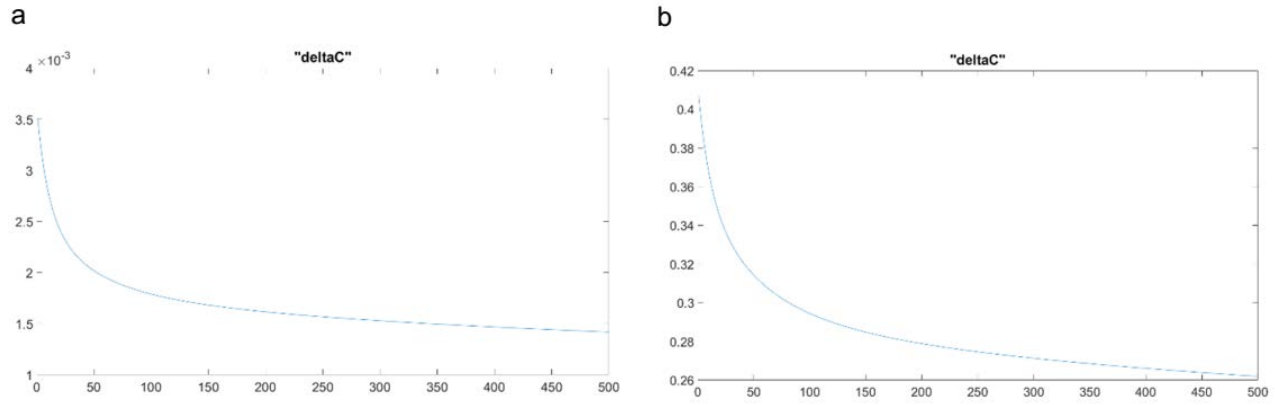

Fig. 15. Normalized capacitance error as a function of number of iterations of the Landweber algorithm: a) simulated data, b) real data

4. Conclusions

ECTsim 3.0 toolbox for modeling and image reconstruction in ECT was presented. It allows to perform 3D simulations of distribution of electric field with a precision comparable to a commercial software like COMSOL. Using ECTsim it is possible to model a sensor before constructing it in order to evaluate its parameters. Creation of a model is easy and straightforward. ECTsim 3.0 allows to calculates forward problem which results in 3D sensitivity matrix for the sensor and simulated measurements for assumed permittivity distribution in examined object. ECTsim 3.0 allows also to reconstruct images from simulated data which allows to test different reconstruction algorithms. It is also possible to reconstruct images using imported data from real tomographic system. This allows to evaluate ECT system usefulness for 3D imaging.

The main drawback of the proposed software is time needed for calculations. Forward problem is solves using an iterative algorithm due to extreme size of matrices which are produced in 3D modelling. One of the solutions of the problem could be a usage of sparse matrices and Krylov algorithms which solve linear systems using matrix-vector multiplications.

Although iterative linear reconstruction algorithm produces good quality images, it is possible to obtain better results with nonlinear algorithms. Sensitivity matrix (Jacobian) changes in every iteration in such algorithms which is computationally expensive in case of 3D image reconstruction. The solution of this problem may be an iterative algorithm which is linear in certain ranges. In [10] authors prove that it is not necessary to change sensitivity matrix in every step. Even few recalculations of sensitivity matrix may significantly improve quality of image reconstruction.

Bibliography

[1] Bielecki K., Smolik W.: Pakiet ectsim do modelowania w elektrycznej tomografii pojemnościowej, VI Sympozjum Naukowe Techniki Przetwarzania Obrazu – TPO'2010, Serock, 2010, 106–114.
[2] Huang S. M., Plaskowski A., Xie C. G., Beck M. S.: Capacitance-based tomographic flow imaging system. Electron. Lett., 24/1988, 418–419.
[3] Jaworski A. J., Dyakowski T.: Application of electrical capacitance tomography for measurement of gas-solid flow characteristics in a pneumatic conveying system. Meas. Sci. Technol., 12/2001, 1109–1119.
[4] Lionheart W. R.: EIT reconstruction algorithms: pitfalls, challenges and recent developments. Physiol. Meas., 25/2004, 125–142.
[5] Lionheart W., Polydordes N., Borsic A.: The reconstruction problem, Electrical Impedance Tomography: Methods, History and Applications, D. S. Holder, Ed., ed: Institute of Physics, 2004, 3–64.
[6] Mirkowski J., Smolik W. T., Yang M., Olszewski T., Szabatin R., Radomski D., Yang W. Q.: A New Forward-Problem Solver Based on a Capacitor-Mesh Model for Electrical Capacitance Tomography. IEEE Trans. Instrumentation and Measurement, 57/2008.
[7] Plaskowski A., Beck M., Thorn R., Dyakowski T.: Imaging industrial flows. Applications of electrical process tomography. IOP Publishing Ltd., 1995.
[8] Reinecke N., Mewes D.: Recent developments and industrial research applications of capacitance tomography, Meas. Sci. Technol., 7/1996., 325–337.
[9] Smolik W.: Forward Problem Solver for Image Reconstruction by Nonlinear Optimization in Electrical Capacitance Tomography, Flow Measurement and Instrumentation, 21/2010, 70–77.
[10] Smolik W., Mirkowski J., Olszewski T., Szabatin R.: Verification of image reconstruction algorithm with sensitivity matrix updating for real data in electrical capacitance tomography. Proc. 4th International Symposium on Process Tomography in Poland, Warsaw, Poland, 2006.
[11] Yang W. Q.: Hardware design of electrical capacitance tomography systems. Meas. Sci. Technol., 7/1996, 225–232.

M.Sc. Jacek Kryszyn
e-mail: j.kryszyn@ire.pw.edu.pl

Received the M. Sc. degree in electronics and computer engineering from Warsaw University of Technology, Warsaw, Poland in 2012. PhD student and the Assistant with the Nuclear and Medical Electronics Division, Institute of Radioelectronics, Electronics and Information Technology Faculty, Warsaw University of Technology. His field of interest covers Electrical Capacitance Tomography, especially simulations of the electric field and reconstruction of images.

Ph.D. Eng. Waldemar T. Smolik
e-mail: w.smolik@ire.pw.edu.pl

Waldemar T. Smolik received the M.Sc., the Ph.D. and D.Sc. degree in electronics engineering from Warsaw University of Technology, Warsaw, Poland in 1991, 1997 and 2014, respectively. Since 2014, he is an Associate Professor at the Institute of Radioelectronics and Multimedia Technology, Electronics and Information Technology Faculty, Warsaw University of Technology. He is the head of the Laboratory of Electronics Application in Nuclear Medicine at the Division of Nuclear and Medical Electronics. His main research interests are computer engineering, computed tomography and medical imaging. He has published over 70 scientific papers.

otrzymano/received: 20.09.2016 *przyjęto do druku/accepted: 15.02.2017*

DOI: 10.5604/01.3001.0010.4604

2D MODELLING OF A SENSOR FOR ELECTRICAL CAPACITANCE TOMOGRAPHY IN ECTSIM TOOLBOX

Jacek Kryszyn, Waldemar Smolik
Warsaw University of Technology, Faculty of Electronics and Information Technology, The Institute of Radioelectronics and Multimedia Technology, Nuclear and Medical Electronics Division

Abstract. *Electrical capacitance tomography is used to visualize a spatial distribution of dielectrical permittivity of materials placed in a tomographic sensor. An image is reconstructed from measurements of mutual capacitances of electrodes placed around the examined volume. This technique is characterized by very high temporal resolution – it is possible to achieve even few thousands of images per second. One of drawbacks of the method is low spatial resolution. Electrical capacitance tomography is mainly used in industry, e.g. for multiphase flow visualization. One of important elements of a tomographic system is a sensor which parameters influence quality of measurements and therefore affects quality of reconstructed images. In the Division of Nuclear and Medical Electronics a Matlab toolbox called ECTsim was developed. It is used for modelling of sensors, simulations of electrical field and image reconstruction. In this article we present the latest improvement which is modelling of a sensor using algebra of sets. Using primitive elements like rectangle and sector of a ring it is possible to perform operations like union, intersection and difference of two elements with a designed language. With such tools it is easy to prepare complex models of tomographic sensors which have different geometries. In this paper we show two models of sensors with different geometry in order to show how ECTsim solves forward problem.*

Keywords: electrical capacitance tomography, 2D modelling, algebra of sets

DWUWYMIAROWE MODELOWANIE SONDY DO ELEKTRYCZNEJ TOMOGRAFII POJEMNOŚCIOWEJ W PAKIECIE ECTSIM

Streszczenie. *Elektryczna tomografia pojemnościowa służy do obrazowania rozkładu przenikalności elektrycznej materiałów w sondzie. Obraz rekonstruowany jest dzięki pomiarom pojemności wzajemnych elektrod umieszczonych wokół badanego obszaru. Ta technika obrazowa charakteryzuje się dużą rozdzielczością czasową – możliwe jest obrazowanie nawet kilku tysięcy przekrojów na minutę. Wadą jest niska przestrzenna zdolność rozdzielcza. Elektryczną tomografię pojemnościową stosuje się w przemyśle, między innymi do obrazowania przepływów wielofazowych. Istotnym elementem systemu tomograficznego jest sonda, której parametry wpływają na jakość pomiaru, a tym samym na jakość rekonstruowanego obrazu. W Zakładzie Elektroniki Jądrowej i Medycznej stworzono pakiet ECTsim uruchamiany w środowisku Matlab, który służy do modelowania sond tomograficznych, symulacji pola elektrycznego oraz rekonstrukcji obrazów. W niniejszym artykule opisano najnowszą modyfikację pakietu polegającą na modelowaniu sondy przy pomocy algebry zbiorów. Wprowadzono podstawowe kształty geometryczne, takie jak prostokąt i wycinek pierścienia, oraz zaproponowano język opisujący operacje sumowania, odejmowania i iloczynu elementów, co pozwala na proste tworzenie złożonych modeli sond tomograficznych o różnych geometriach. W artykule pokazujemy modele dwóch różnych sond tomograficznych i prezentujemy, jak ECTsim rozwiązuje problem prosty.*

Słowa kluczowe: elektryczna tomografia pojemnościowa, modelowanie dwuwymiarowe, algebra zbiorów

Introduction

Electrical capacitance tomography is an imaging technique used to visualize a spatial distribution of electrical permittivity of materials placed in a tomographic sensor. An image is reconstructed from measurements of mutual capacitances of electrodes placed around the examined volume [1]. This technique is characterized by very high temporal resolution – it is possible to achieve even few thousands of images per second. One of drawbacks of the method is low spatial resolution which comes from small number of electrodes used for measurements. It is not possible to place many electrodes because this means decrease in size of electrodes and therefore decrease of measured capacitances which are already low – from tens of femtofarads to single picofarads [6]. Electrical capacitance tomography is mainly used in industry, e.g. for multiphase flow visualization or monitoring of processes which involve combustion [2][4]. One of important elements of a tomographic system is a sensor which parameters (geometric dimensions, number of electrodes) influence quality of measurements and therefore affects quality of reconstructed images. In the Division of Nuclear and Medical Electronics a Matlab toolbox called ECTsim was developed. It is used for modelling of sensors, simulations of electrical field and image reconstruction. In this article we present the latest improvement which is modelling of a sensor using algebra of sets. Using primitive elements like rectangle and circle it is possible to perform operations like union, intersection and difference of two elements with a designed language. With such tools it is easy to prepare complex models of tomographic sensors which have different geometries.

1. ECTsim

ECTsim is a Matlab toolbox which purpose is to aid studies on electrical capacitance tomography. It allows to perform modelling and simulations in two dimensions. A square mesh is used to discretize modelled sensor. A cell method is used to establish equations which describe distribution of electrical field in the modelled sensor [3]. Linear equations system is solved using specialized algorithm of Gaussian elimination for band diagonal matrix. The simulations are performed three times: for the empty sensor, the sensor filled with a phantom and the sensor fully filled with a material with maximum permittivity used in an experiment. Those simulations are performed in order to allow image reconstruction using normalized values of mutual capacitances. Sensitivity matrices for all cases are calculated as well as simulated capacitances. ECTsim allows to reconstruct images from simulated capacitances as well as measurements made with tomographs made in the Division of Nuclear and Medical Electronics. LBP, Landweber and Levenberg-Marquardt algorithms are used.

1.1. Algebra of sets

Until now ECTsim allowed to create only cylindrical sensors. Only several parameters like diameter of the sensor, number of electrodes and their axial width could be set. To extend capabilities of the toolbox and give more flexibility to users a new way of defining sensors was implemented. Two primitive shapes were introduced:

- rectangle (Fig. 1a),
- sector of a ring (Fig. 1b).

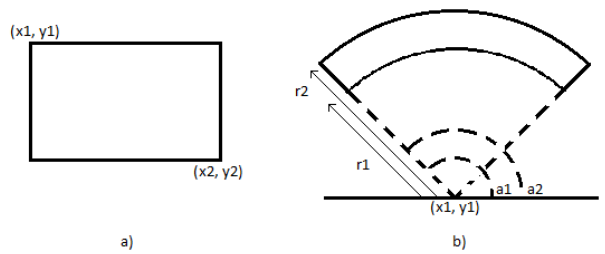

Fig. 1. Primitive shapes: a) rectangle; b) sector of a ring

Rectangle is defined by coordinates of the left upper corner *(x1, y1)* and the right bottom corner *(x2, y2)*. Sector of a ring is defined by inner radius *r1*, outer radius *r2*, angles *a1* and *a2* between left and right edge and a line x = 0 and coordinates of the point from which both radii start *(x1, y1)*. Every shape has constant permittivity value inside. Having those two primitive shapes it is possible to create complex sensors by defining regions consisting of one or more shapes connected by operations known from algebra of sets like union, intersection and difference. Each region has a unique name which can be used to perform further operations on selected regions and is described by an equation which use unique names of other regions or primitive shapes. This way it is possible to define more complex regions which interact with another. Each model has to have required regions:

- boundary – a region in which boundary conditions are set (value of electric potential is known);
- calc_potential – a region in which a distribution of electric field is calculated;
- calc_sensitivity – a region in which a sensitivity matrix is calculated;
- model_points – all points of model.

Following is an excerpt from a script which defines a sensor to show how to define a sensor using developed language:

'boundary', '+electrodes +screen', ...
'calc_potential', '+fov +insulators', ...
'calc_sensitivity', '+fov +insulators', ...
'model_points', '+fov +insulators +boundary'

An exemplary model is shown in Fig 2. A model consists of following elements: a field of view (*FOV*), a sensor wall (*insulator1*), electrodes (16 *electrode* elements), an insulator between electrodes (*insulator2*), an insulator which wraps the whole sensor (*insulator3*) and separates electrodes from a metal screen (*screen*) used to limit an influence of external electric fields on measurements.

Next the designed sensor is discretized with a square mesh. The index of mesh points is built for all regions.

Using designed sensor a forward problem could be solved. Assuming permittivity distribution in a sensor capacitance measurements may be simulated. The calculated sensitivity matrix of the tomographic sensor may be exported to a tomograph software which performs data acquisition and image reconstruction.

2. Results

Two different types of sensors were modelled and simulated in order to show how ECTsim solves a forward problem.

2.1. Cylindrical sensor

A cylindrical sensor was modeled. It consisted of:

- field of view (diameter = 156 mm),
- wall (ε = 2, thickness = 3),
- 16 electrodes (height = 80, angular width = 16 degrees, ε = 10000, thickness = 0.1 mm),
- Insulator between electrodes and the screen (ε = 2, thickness = 5 mm),
- screen (ε = 10000, thickness = 0.1 mm).

A phantom consisting of 6 rods having electric permittivity equal to 3 was modeled.

The model was meshed using square elements having side length equal to 2.54 mm.

Permittivity in the model is shown in Fig 3. For clarity all high permittivity values (electrodes and the screen) were changed from 10000 to 4. Using cell method and the given distribution of electric permittivity it is possible to create a linear system matrix which describes electric potential in the model. The sparsity pattern of this matrix is shown in Fig 4. ECTsim calculates potential only in pixels which are inside the screen in order to decrease number of equations. In case of 2D forward problem matrices are small enough to be calculated using methods like Gauss elimination. This method was used in the described study to calculate potential. ECTsim is also able to use Krylov methods along with sparse matrices which decreases time needed for calculations.

The distribution of electric potential when the first electrode was the excitation electrode and other electrodes were the measurement electrodes is shown on Fig. 5. The sensitivity matrix is calculated using simulated electric fields using reciprocity rule. The sensitivity map for electrodes 1 and 9 is shown on Fig. 6.

Capacitance between electrodes can be numerically calculated using linear model $\mathbf{C} = \mathbf{S}\boldsymbol{\varepsilon}$. Simulated capacitances for the empty sensor, the sensor filled with the phantom and the sensor fully filled with the maximum value of permittivity are shown on Fig. 7. Logarithmic scale was used to better visualize small values. All values were scaled to the minimum value. It is noticeable that the phantom which was used for simulations doesn't change much capacitances between electrodes. The difference between neighbor and opposite electrodes in the modeled sensor is of two orders of magnitude. This shows that the range of capacitances which have to be measured is very wide. Fig. 8. shows the capacitance change between the empty and fully filled sensor.

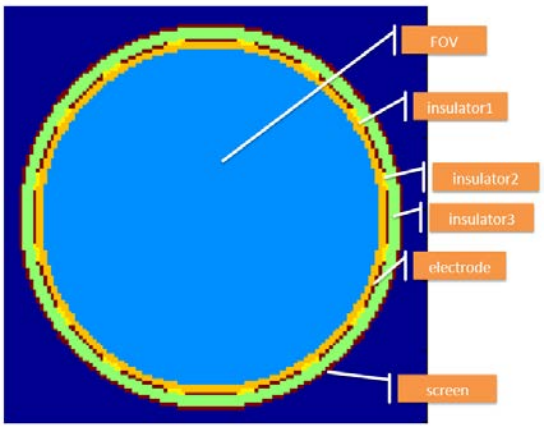

Fig. 2. A model of a cylindrical sensor consisting of a field of view (FOV), a sensor wall (insulator 1), electrodes (16 electrode elements), insulator between electrodes (insulator 2), an insulator which wraps the whole sensor (insulator 3) and a metal screen (screen)

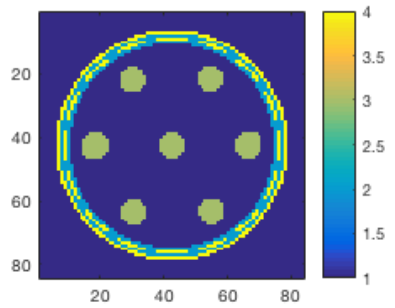

Fig. 3. Permittivity distribution in a model of a cylindrical sensor with 16 external electrodes filled with a phantom consisting of 6 rods made from a material with electric permittivity equal to 3

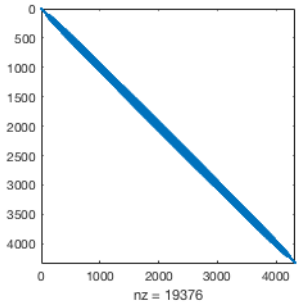

Fig. 4. Sparsity pattern of linear system matrix which describes electric potential in the model. Number of non-zero elements is equal to 19376

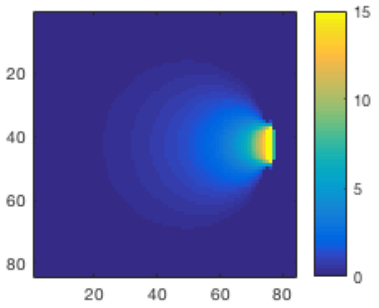

Fig. 5. Distribution of electric potential when the first electrode is the excitation electrode and other electrodes are measurement electrode

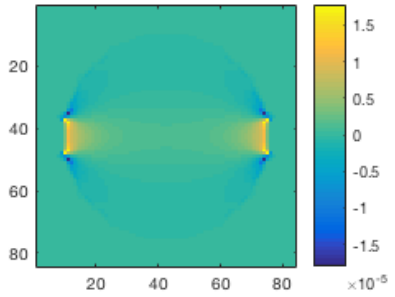

Fig. 6. Sensitivity map calculated from distributions of electric potential when first and ninth electrodes where excitation electrodes

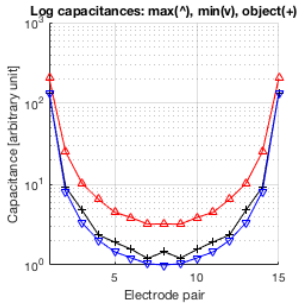

Fig. 7. Simulated capacitance measurements for the empty sensor, the sensor filled with the phantom and the sensor fully filled with the maximum permittivity

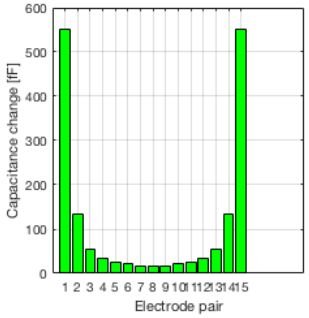

Fig. 8. Differences between simulated capacitances for the empty and fully filled sensor

2.2. Square sensor

A square sensor was modeled. It consisted of:

- field of view (diameter = 160 mm),
- wall (ε = 2, thickness = 4),
- 16 electrodes (height = 160, width = 26 mm, ε = 10000, thickness = 0.1 mm),
- Insulator between electrodes and the screen (ε = 2, thickness = 5 mm),
- screen (ε = 10000, thickness = 0.1 mm).

A phantom consisting of 6 rods having electric permittivity equal to 3 was modeled.

The model was meshed using square elements having side length equal to 2.54 mm.

Permittivity in the model is shown in Fig. 9. As previously, all high permittivity values (electrodes and the screen) were changed from 10000 to 4 for clarity of the figure. The sparsity pattern of this linear equation matrix prepared using the given distribution of permittivity is shown in Fig. 10.

The distribution of electric potential when the first electrode was the excitation electrode and other electrodes were the measurement electrodes is shown on Fig. 11. The sensitivity map for electrodes 1 and 9 is shown on Fig. 12.

Simulated capacitances for the empty sensor, the sensor filled with the phantom and the sensor fully filled with the maximum value of permittivity are shown on Fig. 13. Logarithmic scale was used to better visualize small values. All values were scaled to the minimum value. The difference between neighbor and opposite electrodes in the modeled sensor is of two orders of magnitude, just like in the cylindrical sensor. Fig. 14. shows the capacitance change between the empty and fully filled sensor.

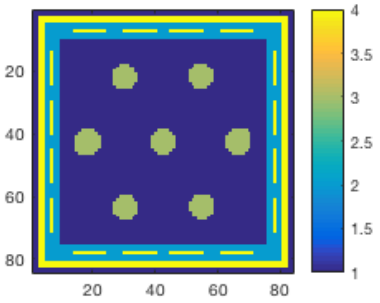

Fig. 9. Permittivity distributuion in a model of a square sensor with 16 external electrodes filled with a phantom consisting of 6 rods made from a material with electric permittivity equal to 3

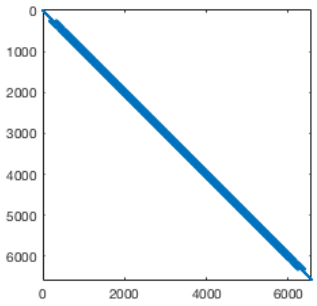

Fig. 10. Sparsity pattern of linear system matrix which describes electric potential in the model. Number of non-zero elements is equal to 28968

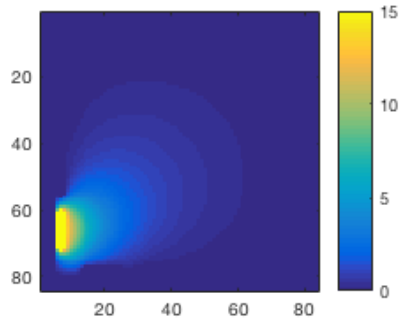

Fig. 11. Distribution of electric potential when the first electrode is the excitation electrode and other electrodes are measurement electrodes.

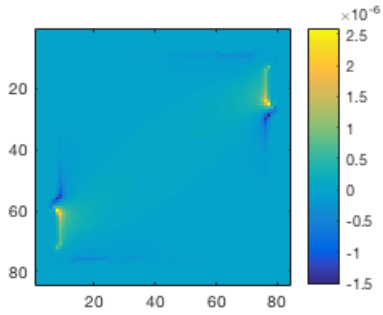

Fig. 12. Sensitivity map calculated from distributions of electric potential when first and ninth electrodes where excitation electrodes

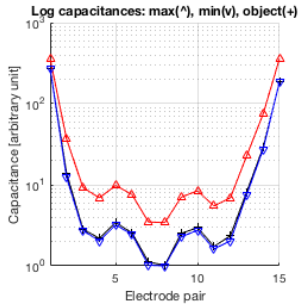

Fig. 13. Simulated capacitance measurements for the empty sensor, the sensor filled with the phantom and the sensor fully filled with the maximum permittivity. Fig 8. Differences between simulated measurements for the empty and fully filled sensor

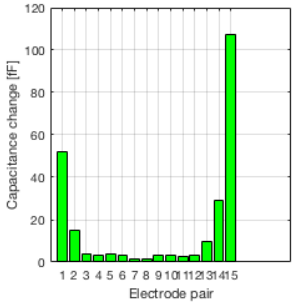

Fig. 14. Differences between simulated capacitances for the empty and fully filled sensor

3. Conclusions

ECTsim is a robust toolbox for two dimensional modeling and simulations in electrical capacitance tomography. It allows to model a sensor and evaluate its parameters before construction of a real equivalent of the model. In order to increase usefulness of the toolbox a new way of sensor definition was implemented. Using an intuitive language which allows to perform algebraic operations on primitive shapes it is possible to design a sensor with expected geometry. This feature extends possible fields in which ECTsim can be applied not only to cylindrical sensors but also cubical or even not regular geometries.

In this paper we showed simulations of models with different geometry: cylindrical and square. Distributions of electric potential for each model were calculated as well as sensitivity matrices. Numerically simulated capacitances were shown. This knowledge can be used to establish if hardware used for measurements would be able to measure such values.

Bibliography

[1] Huang S.M., Plaskowski A., Xie C.G., Beck M.S.: Capacitance-based tomographic flow imaging system. Electron. Lett., 2/1998.
[2] Jaworski A.J., Dyakowski T.: Application of electrical capacitance tomography for measurement of gas-solid flow characteristics in a pneumatic conveying system. Meas. Sci. Technol., 12/2001, 1109–1119.
[3] Mirkowski J., Smolik W.T., Yang M., Olszewski T., Szabatin R., Radomski D., Yang W.Q.: A New Forward-Problem Solver Based on a Capacitor-Mesh Model for Electrical Capacitance Tomography. IEEE Trans. Instrumentation and Measurement, 57/2008.
[4] Plaskowski A., Beck M., Thorn R., Dyakowski T.: Imaging industrial flows. Applications of electrical process tomography, IOP Publishing Ltd., 1995.
[5] Smolik W.: Forward Problem Solver for Image Reconstruction by Nonlinear Optimization in Electrical Capacitance Tomography. Flow Measurement and Instrumentation, 21/2010, 70–77.
[6] Yang W.Q.: Hardware design of electrical capacitance tomography systems. Meas. Sci. Technol., 7/1996, 225–232.

M.Sc. Eng. Jacek Kryszyn
e-mail: j.kryszyn@ire.pw.edu.pl

Received the M. Sc. degree in electronics and computer engineering from Warsaw University of Technology, Warsaw, Poland in 2012. PhD student and the Assistant with the Nuclear and Medical Electronics Division, Institute of Radioelectronics, Electronics and Information Technology Faculty, Warsaw University of Technology. His field of interest covers Electrical Capacitance Tomography, especially simulations of the electric field and reconstruction of images.

Ph.D. Eng. Waldemar T. Smolik
e-mail: w.smolik@ire.pw.edu.pl

Waldemar T. Smolik received the M.Sc., the Ph.D. and D.Sc. degree in electronics engineering from Warsaw University of Technology, Warsaw, Poland, in 1991, 1997 and 2014, respectively. Since 2014, he is an Associate Professor with the Institute of Radioelectronics, Electronics and Information Technology Faculty, Warsaw University of Technology. He is head of Laboratory at the Division of Nuclear and Medical Electronics. His main research interests are computed tomography and medical imaging. He has published over 70 scientific papers.

otrzymano/received: 20.09.2016 *przyjęto do druku/accepted: 15.02.2017*

DOI: 10.5604/01.3001.0010.4605

COIL DESIGN WITH LITZE WIRE FOR MAGNETIC PARTICLE SPECTROMETRY

Przemysław Wróblewski, Waldemar Smolik
Warsaw University of Technology, Institute of Radioelectronics and Multimedia Technology, Department of Nuclear and Medical Electronics

Abstract. *The design of an excitation coil for magnetic particles spectrometer (MPS) was described. It was assumed that the spectrometer should measure the spectra of particles of diameter in the range 10-100 nm. To measure the amplitude and phase angle spectra of magnetic nanoparticles it is required to generate sinusoidal alternating spatially homogeneous magnetic field of magnitude of 20 mT. The work volume of the designed spectrometer was 20×20×20 mm allowing measurement of small samples. The estimation of magnetic properties of magnetic nanoparticles is crucial in Magnetic Particles Imaging. In this paper we described the excitation coil design which minimizes power losses on the coil related to heat emission. The resonance circuit operating on 20 kHz frequency was applied. Optimal litze wire configuration was proposed to negate skin and proximity effects. The numeric simulations for the optimal and commercially available suboptimal litze wire configurations were performed. The comparison of the results was shown and discussed.*

Keywords: magnetic field, nanoparticles, coils, spectroscopy

KONSTRUKCJA CEWKI Z WYKORZYSTANIEM LICA DO SPEKTROMETRII CZĄSTEK MAGNETYCZNYCH

Abstrakt. W artykule tym została opisana konstrukcja cewki pobudzającej do wykorzystania w spektroskopii cząstek magnetycznych. W projekcie złożono, że spektrometr, którego częścią będzie cewka, będzie w stanie mierzyć widma odpowiedzi nanocząsteczek o średnicy od 10 d0 100 nm. Do skutecznego pomiaru widm amplitudowych i fazowych cząstek magnetycznych potrzebne jest pobudzenie ich sinusoidalnie zmiennym w czasie, ale przestrzenie jednorodnym polem magnetycznym o amplitudzie powyżej 20 mT przy częstotliwości 20 kHz. Robocza objętość projektowanego spektrometru została ustalona na 20×20×20 mm, co pozwala na pomiar małych próbek. Estymacja parametrów magnetycznych nanocząsteczek jest niezwykle ważna do prawidłowego odtworzenia obrazu w tomografii nanocząsteczek magnetycznych. Opisana w artykule konstrukcja cewki pobudzającej pozwala na minimalizacje strat mocy na cewce i związanego z tym przegrzewania się układu. Zaproponowana optymalna konfiguracja lica pozwala skutecznie zmniejszyć wpływ efektu naskórkowego i efektu zbliżenia. Zastosowano również układ rezonansowy pracujący przy częstotliwości 20 kHz. Przeprowadzono symulacje numeryczne pola generowanego przez cewki z wykorzystaniem zarówno optymalnych rozwiązań, jak i dostępnych na rynku konfiguracji drutu lica. W artykule zaprezentowano oraz omówiono wyniki części tych symulacji.

Słowa kluczowe: pole magnetyczne, nanocząstki, cewki, spektroskopia

Introduction

Magnetic Particles Spectrometry (MPS) is a measurement technique can be used to directly acquire amplitude and phase spectra of magnetic nanoparticles magnetization signal [1]. Knowledge of amplitude spectrum allows to estimate the distribution of particle size, while phase angle can allow research the impact of various parameters on nanoparticle's Brownian motion. By combining information from both of those sources valuable information about the particle's environment can be gathered. Such information are essential for the Magnetic Particles Imaging (MPI). It is a tomographic technique that allows to visualize the spatial distribution of superparamagnetic nanoparticles in a living body. Quality and value of those measurement is highly dependent on the type and parameters of the nanoparticles used as well as the properties of the environment that they are in.

The motivation for this work was to design a excitation coil able to generate sinusoidal alternating magnetic field of magnitude of at least 20 mT, which is necessary to correctly excite nanoparticles in Magnetic Particles Spectroscopy. Due to signal acquisition method used this field should be highly homogeneous in a volume of at least 50 cm^3. Coil should also be suitable to work in resonance circuit set to excitation frequency, in this case 20 kHz. The main challenges that had to be overcome were skin effect and proximity effect. Ideal solution was to use the litze wire as winding of the coil.

1. Theory

Magnetic Particles Spectrometry (MPS) measures spectra of superparamagnetic nanoparticles, typically iron oxide nanoparticles.

Superparamagnetism is form of magnetism that shares some characteristics with both ferromagnetism and paramagnetism. It occurs in typically ferromagnetic materials in very specific conditions. Nanoparticles of such material have to be separated from each other magnetically and/or spatially to be considered independent magnetic domains. Such circumstances are present for example in iron-oxide particles of diameter between 10 to 100 nm, coated with thick enough layer of polymer. Ideal superparamagnets have nonlinear magnetization curve (Fig. 1), undergo saturation in high external magnetic field after which they magnetize linearly like paramagnets and do not magnetize permanently.

Magnetization M of superparamagnets can be described by Langevin's theory of paramagnetism:

$$M(t) = m_s c_p (\coth(kH_D(t)) - \frac{1}{kH_D(t)}) \quad (1)$$

where c_p – particles concentration, H_D – magnetic field strength, $k=(\mu_0 m_s)/(k_B T)$, μ_0 – magnetic permeability of vacuum, k_B – Boltzman's constant, T – temperature, m_s – magnetic momentum of saturation, equal to: $m_s=1/6\ \pi d_c^3 M_s$, where M_s is saturation magnetization of magnetite and d_c is diameter of nanoparticle.

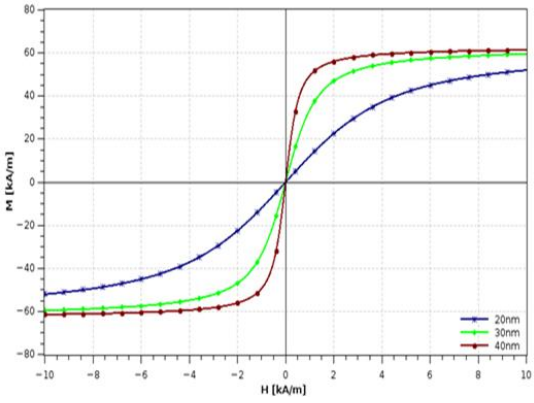

Fig. 1. Magnetization curves of nanoparticles of different diameter calculated using Langevin's equation

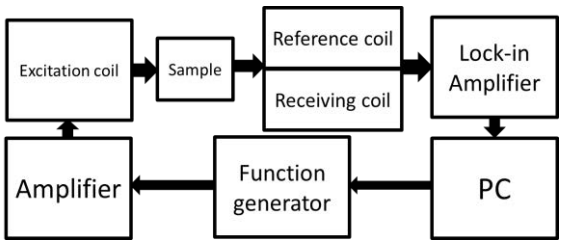

Fig. 2. Possible MPS measurement setup using Lock-in amplifier and pait of reference/receiving coils

In MPS nanoparticles are excited by sinusoidal magnetic signal generated by excitation coil. Magnetization signal from nanoparticles and excitation signal is than pick up by receiving coil. Of course excitation signal is much higher than magnetization signal of nanoparticles. Fortunately, due to nonlinear magnetization curve, signal from particles consists of harmonics of excitation frequency. Those harmonics can be distinguished from excitation signal and measured. One possible setup involves the use of matched pair of reference and receiving coils (Fig. 2). First one picks up only excitation signal, while second one both excitation and magnetization signals. By connecting them in opposite direction or applying those signal to differential input of lock-in amplifier most of excitation signal can be dampened. In MPS both amplitude and phase angle of those harmonics are measured [2]. Spectrum in MPS is defined as amplitude or phase of magnetization signal in function of harmonics of excitation frequency.

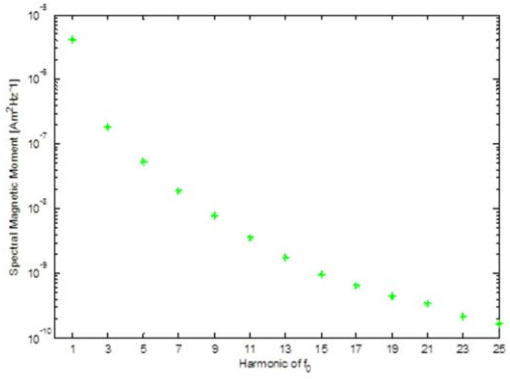

Fig. 3. Example of amplitude spectrum of nanoparticles magnetization signal measured in MPS. In MPS amplitude of each harmonic is typically given as spectral magnetic moment.

To acquire full signal of harmonics nanoparticles have to be excite with magnetic field strong enough to work on nonlinear part of magnetization curve. For most of nanoparticles such field should have magnitude between 20 and 30 mT. To obtain such field appropriately high current supply have to be used and/or coil need to have high number of turn per length of coil. Both of this conditions increase the power dissipated at the coil, which have to be limited not to overheat the coil. Thus restricting the maximal magnitude of magnetic field that can be produces by specific coil.

Frequency of excitation fields used in MPS range from 10 kHz up to 150 kHz. In this frequency range result of skin and proximity effects start to be quite noticeable. Skin effect manifests in the tendency of an AC current to become distributed unevenly within a conductor such that the current density is largest near the surface of the conductor. It is caused by opposing eddy currents induced in the changing magnetic field resulting from the alternating current flowing through the conductor. Due to skin effect the effective resistance of the conductor increases at higher frequencies. In frequency range typical to MPS skin depth (δ) through which current is flowing can be calculated as:

$$\delta = \sqrt{\frac{2\rho}{\omega\mu_0\mu_r}} \tag{2}$$

where ρ is resistivity of the conductor, ω is angular frequency of current, μ_0 is the permeability of free space and μ_r is relative magnetic permeability of the conductor. One of possible solution to overcome this effect is use of so called litz wire [3].

Litz wire is a multi-strand cable in which electrically isolated single wires are braided in specific patterns, often consisting of several levels (bundles of signal wires stranded together). Diameter of single wire is much smaller than skin depth for working frequency, thus there is no skin effect on the wire-level. But use of multiple wires causes another detrimental effect to occur called proximity effect.

Proximity effect is also caused by opposing eddy currents but in this case induced by magnetic fields from currents in separate wires. It also contributes to increase of power losses, but by twisting the wires, with the pitch of twisting much small than the overall length of wire, proximity effect can be highly mitigated.

To prevent skin effect on the bundle-level Litz wire has to be constructed with multiple levels of twisting. Firstly cross section area of a bundle needs to be smaller or equal to cross section area of wire of maximum diameter in which there is no skin effect. In this case the approximate maximum recommended number of single wires to be twisted together in the bundle is:

$$n_{\max} = 4\frac{\delta^2}{d_s^2} \tag{3}$$

where δ is the skin depth for a solid conductor given by (2) and d_s is the diameter of an individual wire. Secondly while twisted bundles need to be transposed between different radial positions over the length Litz wire. Possible approach to make sure that skin effect is avoided between the bundles is to twist no more than five bundles together. A group of five or fewer has no bundle in the center, so radial position of each bundle changes over the length of the cable. Whereas a group of seven has six around the outside and one in the center, which one would not change its radial position. That is why in some cases it is preferred to use multi-level constructions, each time using 5 or less sub-bundles.

2. Material and Methods

In design of our previous excitation coil [4], which was of Helmholtz type, we used single wire of diameter below skin depth (which in case of 10 kHz is about 0.6 mm) to ensure that skin effect was not present. Resonance circuit set to excitation frequency was used so that most of impedance due to reactance could be neglected. This resulted in magnetic field of magnitude of less than 8 mT even when power dissipated on coil was over 400 W and current of 6 A. Unfortunately due high power losses both coil and resonance circuit heated up and resonance frequency fluctuated resulting in impedance of the coil higher than anticipated. Higher impedance may also been caused by proximity effect which was not considered than. Such amplitude was not enough to fully saturate magnetic particles that we used as sample. Furthermore use of reference coil was impeded by both inhomogeneity of generated field and construction of exaction coil.

Contrary to our previous work this excitation coil will be a solenoid. It will be bigger than most MPS excitation coils, with inner diameter of 30 mm and length of 200 mm, because we are planning to use it also as excitation coil for Magnetic Particles Imaging Scanner in the future. Bigger volume of homogenous field should also allow improve use of reference coils, as both receiving and reference coils can be stimulated be same field.

To mitigate both skin and proximity effect in this design we decided to apply litz wire. Litz wire that we considered the best option after theoretical analysis was in configuration of 5×21×0.2 mm (which means 5 bundles of 21 single wires of diameter of 0.2 mm). Such litze wire should work best for frequencies between 10 to 20 kHz. According to our rough theoretical calculations it should be able to generate magnetic field with amplitude of 30 mT, while powers dissipated on it will be of about 120 W. To make sure that our calculations were correct we performed numerical simulations of magnetic field (Fig. 2, 3, 4).

The simulations were conducted in Comsol. We assumed that we will be able to wind at least 3 layers of Litz wire. Filling factor of coil was set to 80%. Current flowing through coil was set so that power losses would be less than 120 W.

Unfortunately not only such ideal configuration was not available on the market but also manufacture and purchase of not mass produced litze wire is quite expensive. Due to this reasons it was decided to buy cheaper but suboptimal wire. This configuration of wire was chosen by applying same theoretical principles as in optimal case but taking into account only configuration that was available on the market. From those litze wire in configuration of 7×90×0.1 mm was selected. The simulation fallowing the same assumptions as one for optimal configuration was performed for coil made of this suboptimal wire (Fig. 5, 6).

Design of bobbin for the coil is shown in the Fig. 1. As coil will be water cooled slots along the surface of bobbin are to ensure the flow of water also under the wires. By encasing the coil in an rubber tube it should be possible to efficiently force the flow of water if necessary.

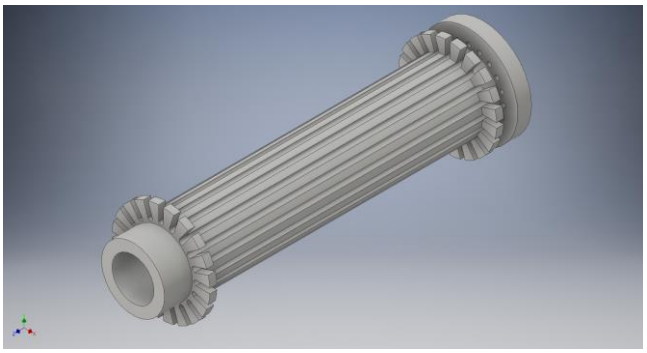

Fig. 4. 3D model of the coil's bobbin

Fig. 5. Manufactured Litz wire excitation coil

Manufactured coil's bobbin is made of PTFE (Teflon) to allow work to up to 200 °C if there is no cooling. Coil consists of about 220 turn of 7×630×0.1 mm Litz wire divided into 4 layers. To work properly coil will be connected to resonance filter set to excitation frequency.

3. Results

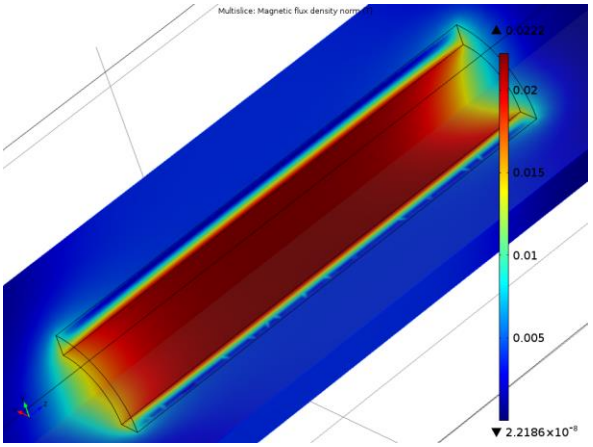

Fig. 6. 3D simulation of magnetic flux density. The value of magnetic flux density for the current value equal to 12 A

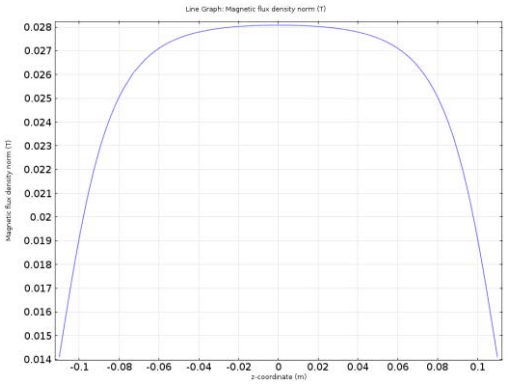

Fig. 7. The magnetic flux density along z axis. Zero corresponds to the center of the coil. Result for Litz wire in 105×0.2 mm configuration

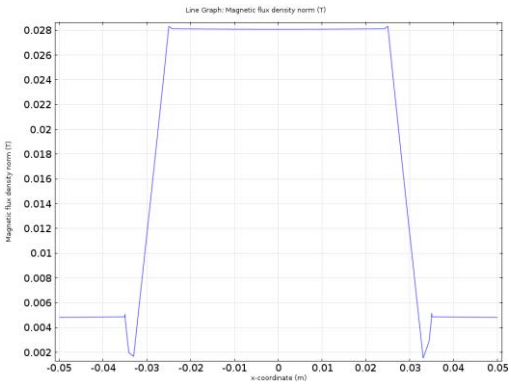

Fig. 8. The magnetic flux density along x axis. Zero corresponds to the center of the coil. Result for Litz wire in 105×0.2 mm configuration

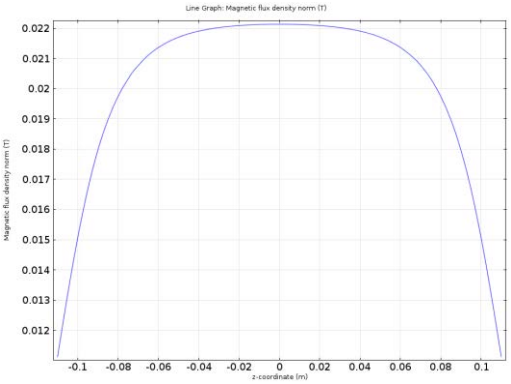

Fig. 9. The magnetic flux density along z axis. Zero corresponds to the center of the coil. Result for Litz wire in 7×90×0.1 mm configuration

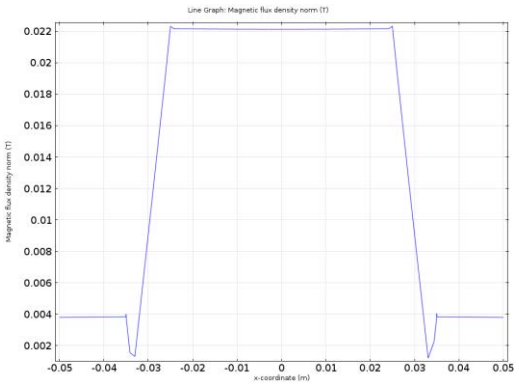

Fig. 10. The magnetic flux density along x axis. Zero corresponds to the center of the coil. Result for Litz wire in 7×90×0.1 mm configuration

4. Conclusion

According to results by use of litz wire in the resonance circuit we will be able to eliminate both skin effect and proximity effect at frequency of excitation, thus lowering the impedance of coil and improving its Q factor. It may seem that coil is too long if compared with actual working volume of spectrometer but high homogeneity of the magnetic excitation field over the length of 8 cm obtained will allow the reference and receiving coils to work efficiently. As one might expect, usage of commercially available litze wire, deviating from optimal configuration, will worsen the performance of the excitation coil but homogenous field of strength above 20 mT could still be acquired. The numerical calculations suggest that required magnetic field magnitude could be obtained with power losses of less than 120 W in the coil of proposed design. Such power losses could be compensated using simple water cooling system. Further measurements of magnetic field generate by coil are needed to confirm it. Finished coil will be used to perform actual MPS measurements.

References

[1] Biederer S., et al.: Magnetization response spectroscopy of superparamagnetic nanoparticles for magnetic particle imaging. Journal of Physics D: Applied Physics 42.20/2009, 205007.
[2] Rauwerdink A.M., Weaver J.B.: Harmonic phase angle as a concentration-independent measure of nanoparticle dynamics. Medical Physics, 37/2010, 2587–2592.
[3] Wróblewski P., Szyszko J., Smolik W.T.: Development of MPI Mini Scanner Prototype - Coils Design. Imaging Systems and Techniques (IST), 2013 IEEE International Conference, Beijing, 164–168.
[4] Sullivan C.R., Zhang R.Y.: Simplified design method for litz wire. IEEE Applied Power Electronics Conference and Exposition-APEC 2014.

M.Sc. Eng. Przemysław Wróblewski
e-mail: P.Wroblewski@ire.pw.edu.pl

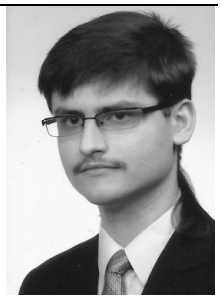

Received the M. Sc. degree in biomedical engineering from Warsaw University of Technology, Warsaw, Poland in 2013. PhD student in the Nuclear and Medical Electronics Division, Institute of Radioelectronics and, Electronics and Information Technology Faculty, Warsaw University of Technology. His field of interest covers Magnetic Particles Imaging and Magnetic Particles Spectroscopy, especially design of scanners and simulations of the magnetic field.

Ph.D. Eng. Waldemar Tomasz Smolik
e-mail: W.Smolik@ire.pw.edu.pl

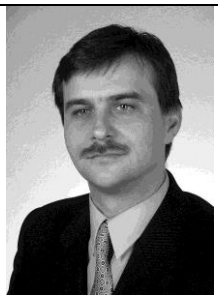

Waldemar T. Smolik received the M.Sc., the Ph.D. and D.Sc. degree in electronics engineering from Warsaw University of Technology, Warsaw, Poland, in 1991, 1997 and 2014, respectively. Since 2014, he is an Associate Professor with the Institute of Radioelectronics, Electronics and Information Technology Faculty, Warsaw University of Technology. He is head of Laboratory at the Division of Nuclear and Medical Electronics. His main research interests are computed tomography and medical imaging.

otrzymano/received: 20.09.2016 *przyjęto do druku/accepted: 15.02.2017*

DOI: 10.5604/01.3001.0010.4606

BOUNDARY ELEMENT METHOD MODYFICATIONS FOR USE IN SOME IMPEDANCE AND OPTICAL TOMOGRAPHY APPLICATIONS

Maciej Pańczyk[1], Jan Sikora[2]
[1]Lublin University of Technology, Institute of Computer Science, [2]Lublin University of Technology, Institute of Electronics and Information Technology

Abstract. *The article presents two elements associated with the practice of application of the boundary element method. The first is associated with BEM ability to analyze an open boundary objects and application of infinite boundary elements in the area of mammography. The second element is associated with the damped wall investigations. Wall humidity and moisture represents heterogeneous environment (Functionally Graded Materials) which has to be treated in a special way.*

Keywords: BEM; infinite elements; optical tomography, functionally graded materials, impedance tomography

MODYFIKACJE METODY ELEMENTÓW BRZEGOWYCH ZASTOSOWANE W WYBRANYCH ASPEKTACH TOMOGRAFII IMPEDANCYJNEJ I OPTYCZNEJ

Streszczenie*. Artykuł prezentuje dwa elementy związane z praktyką stosowania metody elementów brzegowych w zagadnieniach mammografii i środowisk niejednorodnych. Pierwszy związany możliwością analizy obszarów nieograniczonych i zastosowaniem tym celu elementów brzegowych nieskończonych w zagadnieniach mammograficznych. Drugi związany jest z badaniami zawilgoceń murów stanowiących z punktu widzenia obliczeń środowisko niejednorodne.*

Słowa kluczowe: MEB, elementy brzegowe nieskończone, środowiska niejednorodne, tomografia impedancyjna.

Introduction

One of the advantages of the Boundary Element Method is its ability to handle open boundary problems. It is useful either when it is necessary to analyze outer field distribution or when there are some problems describing object surface and related boundary conditions. Another important tomograpic task is to find internal properties spatial distribution within non-homogenous region.

A good example of open boundary and related infinite boundary element is an application for early detection or screening examination of breast cancer using Optical Tomography. Using infinite boundary elements to create an open boundary breast model results in the significant reduction of the mesh size and allows us to avoid problems with unknown boundary conditions. In consequence, hardware requirements are much lower and the results are received faster without accuracy losses. The implementation of two main lines of infinite boundary elements will be discussed on the example of a typical hemispherical breast model.

Boundary Element Method (BEM) is employed in breast cancer investigations to find a forward problem solution and in turn to receive the internal image of breast tissue solving the reverse problem, as it is not possible to place detectors or to precisely define boundary conditions on the surface between breast and chest.

The traditional method used to avoid errors near the breast and chest boundary is to extend the mesh outside the region of interest, deep into the chest and to truncate it at some distance from the investigated breast tissue. Wrong boundary conditions or improper placement of such artificial boundary can introduce an unknown error if the truncation occurs too near. On the other hand, excessive mesh received while setting that boundary too far, increases the number of boundary elements and decreases the computational efficiency. One of the alternative solutions is to use infinite boundary elements and to create an open boundary model. The implementation of these elements can reduce the mesh and help avoid the problem of incorrect boundary conditions assumption.

Moreover, despite constant hardware development the process of finding the inner breast image in computer tomography is still a time-consuming task. The implementation of infinite boundary elements is an attractive option to solve these issues. Results can be found faster due to the significant reduction of the mesh size and without accuracy losses.

There are two main lines of infinite boundary elements development: decay functions infinite elements and mapped infinite elements. The first type uses special decay functions in conjunction with ordinary boundary element interpolation functions [2, 3, 5, 23]. In that case the field variable tends monotonically to its far field value while reaching the element boundary adjacent to the infinite surroundings. Consequently, along finite element length, the variable changes in the way that reflects the physics of the problem up to infinity. The second type transforms the element from finite to infinite domain. The field variable will reach its far value following geometrical coordinates which extend into infinity [5, 12, 25]. Changing the basic interpolation functions interferes in the Boundary Element Method fundamental rules. The application of infinite elements in the open edge of the object usually requires using special quadratic boundary elements. This constitutes another complication for most mesh generators. On the other hand, the process of infinite elements incorporation into BEM is quite logical and results in significant hardware requirements and calculation time reduction. All major aspects of the implementation of both infinite elements types into BEM will be presented on the example of optical mammography.

Second presented subject – application of Functionally Graded Materials into BEM do not allow us to decrease BEM mesh size, like infinite elements mentioned above. Substituting multilayer BEM model related to non-homogenous environment by single layer model with applied FGM keeps full advantage of an important BEM feature, ie. reduction of model size.

Serious problem form many brick masonry historic buildings are their excessive moisture. Too much moisture causes a reduction in the compressive strength of both brick and mortar and to reduce the durability of the walls. Water, usually containing aggressive chemicals (chlorides, sulfates and nitrates), is transmitted to higher altitudes of the wall. High humidity of the walls encourages growth of fungi and mold, which have a negative impact on the human health. Humidity distribution, the type and concentration of salt in the wall are helpful in assessing the causes of damage and should be the basis for selecting the appropriate security methods related to excessive humidity and salinity.

Typical method used to find humidity distribution performed by drilling, sampling and checking samples moisture cannot be applied for continuous monitoring of dehumidification process. Relatively inexpensive method based on Electrical Impedance Tomography (EIT) [4, 6, 7, 9, 15, 18] can be implemented. The wall conductivity is changing with humidity of the wall and its salinity, so object properties – conductivity - varies smoothly with one ore more co-ordinates. Boundary Element Method (BEM) [10, 17] was used to solve the EIT forward problem. BEM implementation requites to use either multiregional model or

Functionally Graded Materials (FGM) to find spatial distribution of wall humidity.

Laboratory walls with 26 electrode impedance tomograph were investigated [7, 9].

Some theoretical aspects of BEM and FGM usage in wall dampness investigations [4], are within the scope of this paper.

1. Infinite boundary elements application for mammography

1.1. Theory of infinite elements

The basic idea of the decay function infinite boundary element construction is that the standard basis interpolation functions Ni are multiplied by so called decay functions Di [2, 3, 5, 23]. Two types of decay functions will be considered: reciprocal and exponential. Reciprocal decay functions for the decay in positive direction of ξ are as follows [5]:

$$D_i(\xi) = \left[(\xi_i - \xi_0)/(\xi - \xi_0)\right]^n \tag{1}$$

where i corresponds to the node number, (ξo ,ηo) is some origin point. This point must be outside the infinite element on the opposite side to the one which extends to infinity, n has to be greater than the highest power of ξ encountered in Ni . If the decay is in the positive ξ direction then ξo < −1. Respectively ηo < −1 for the decay in the positive η direction. This avoids a singularity within the element.

For second order, eight-node quadrilateral elements, basis interpolation functions n=3 was chosen. Decay function infinite basis interpolation function becomes:

$$M_i(\xi,\eta) = N_i(\xi,\eta)\cdot\left[(\xi_i - \xi_0)/(\xi - \xi_0)\right] \tag{2}$$

For the exponential decay function of the form:

$$D_i(\xi) = \exp\left[(\xi_i - \xi)/L\right] \tag{3}$$

where L[m] is the length which determines the severity of the decay, basis infinite interpolation functions are given by:

$$M_i(\xi,\eta) = N_i(\xi,\eta)\cdot\exp\left[(\xi_i - \xi)/L\right] \tag{4}$$

The basis interpolation function Ni for standard eight-node quadrilateral isoparametric boundary elements are given by the following formulas (5):

$$\begin{aligned}
N_0(\xi,\eta) &= -(1-\xi)(1-\eta)(1+\xi+\eta)/4,\\
N_1(\xi,\eta) &= (1-\xi^2)(1-\eta)/2,\\
N_2(\xi,\eta) &= -(1+\xi)(1-\eta)(1-\xi+\eta)/4,\\
N_3(\xi,\eta) &= (1+\xi)(1-\eta^2)/2,\\
N_4(\xi,\eta) &= -(1+\xi)(1+\eta)(1-\xi-\eta)/4,\\
N_5(\xi,\eta) &= (1-\xi^2)(1+\eta)/2,\\
N_6(\xi,\eta) &= -(1-\xi)(1+\eta)(1+\xi-\eta)/4,\\
N_7(\xi,\eta) &= (1-\xi)(1-\eta^2)/2.
\end{aligned} \tag{5}$$

Decay function infinite elements based on 8 nodes, the second type, quadrilateral standard boundary elements are presented in figure 1. It should be noticed that it consists of 8 nodes. The only important thing is to keep the correct relation between decay function and node numbers, which decides in which direction the element, or more exactly the element properties (geometry remains unchanged) extends into infinity.

Mapped infinite boundary elements based on 8 nodes, the second type, quadrilateral standard boundary elements are presented in figure 2. It should be noticed that in this case the element will consist only of five nodes. Nodes 2, 3, 4 tend to infinity and will not take part in the calculations.

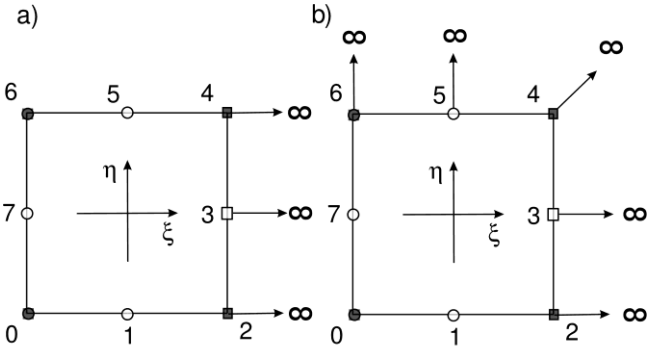

Fig. 1. Transformation of standard 8 node quadrilateral boundary element into decay type infinite element: (a) in one positive ξ direction, (b) in two positive ξ and η directions

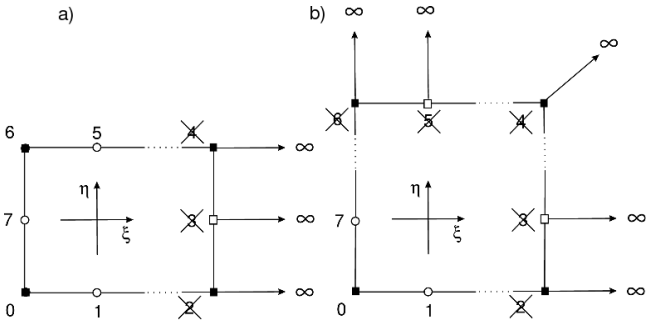

Fig. 2. Transformation of standard 8 node quadrilateral boundary element into mapped infinite element: (a) in one positive ξ direction, (b) in two positive ξ and η directions

Corresponding, so called, serendipity type basis interpolation functions $\hat{M}_i$ for mapped infinite elements are given by formula (6).

$$\begin{aligned}
\hat{M}_0 &= \frac{-1-\xi+\xi\eta+\eta^2}{1-\xi}, \quad \hat{M}_1 = \frac{1+\xi}{1-\xi}\cdot\frac{1}{2}(1-\eta),\\
\hat{M}_5 &= \frac{1+\xi}{1-\xi}\cdot\frac{1}{2}(1+\eta),\\
\hat{M}_6 &= \frac{-1-\xi-\xi\eta+\eta^2}{1-\xi}, \quad \hat{M}_7 = \frac{2}{1-\xi}\cdot(1-\eta^2)
\end{aligned} \tag{6}$$

Despite its name the procedure for deriving these functions is quite logical and clearly described by Bettess [5, in chapter 4]. The infinite basis interpolation functions $\hat{M}_i$ grow without limit as a coordinate approaches infinity, and are applied to the geometry. The ordinary basis interpolation functions Ni are applied to the field variables [5, 12, 23].

It is necessary to use these infinite basis interpolation functions to calculate the Jacobian and regularization transformations. The Jacobian is related to the transformation from two-dimensional intrinsic mesh structures to the global three dimensional coordinate system. In other words, we need to define the way in which we can pass from the x,y,z global Cartesian system to the ξ,η,ζ system defined over the element, where ξ and η are oblique coordinates and ζ is in the direction of the normal. The transformation for a given function Φ is related through the following:

$$\begin{bmatrix} \frac{\partial\Phi}{\partial\xi} \\ \frac{\partial\Phi}{\partial\eta} \\ \frac{\partial\Phi}{\partial\zeta} \end{bmatrix} = \begin{bmatrix} \frac{\partial x}{\partial\xi} & \frac{\partial y}{\partial\xi} & \frac{\partial y}{\partial\xi} \\ \frac{\partial x}{\partial\eta} & \frac{\partial y}{\partial\eta} & \frac{\partial z}{\partial\eta} \\ \frac{\partial x}{\partial\zeta} & \frac{\partial y}{\partial\zeta} & \frac{\partial z}{\partial\zeta} \end{bmatrix} \begin{bmatrix} \frac{\partial\Phi}{\partial x} \\ \frac{\partial\Phi}{\partial y} \\ \frac{\partial\Phi}{\partial z} \end{bmatrix} \tag{7}$$

where the square matrix is the Jacobian matrix (or Jacoby matrix).

A transformation of this type allows us to describe differentials of surface in the Cartesian system in terms of the curvilinear coordinates. A differential of area will be given by:

$$\partial\Gamma = \mathbf{n}\partial\xi\partial\eta = \left|\frac{\partial \mathbf{r}}{\partial\xi}\times\frac{\partial \mathbf{r}}{\partial\eta}\right|\mathbf{1}_{\mathbf{n}}\partial\xi\partial\eta = \\ = \sqrt{n_x^2+n_y^2+n_z^2}\,\mathbf{1}_{\mathbf{n}}\partial\xi\partial\eta, \tag{8}$$

Where

$$n_x = \frac{\partial y}{\partial\xi}\frac{\partial z}{\partial\eta} - \frac{\partial y}{\partial\eta}\frac{\partial z}{\partial\xi}\ ,\ n_y = \frac{\partial x}{\partial\xi}\frac{\partial z}{\partial\eta} - \frac{\partial x}{\partial\eta}\frac{\partial z}{\partial\xi}\ ,\ n_z = \frac{\partial x}{\partial\xi}\frac{\partial y}{\partial\eta} - \frac{\partial x}{\partial\eta}\frac{\partial y}{\partial\xi}$$

and n is a normal vector to the surface element.

The coordinates x, y, z of a point on an element with the intrinsic coordinates ξ and η are given by:

$$x = \sum_{i=0}^{i=7} M_i(\xi,\eta)x_i\ ,\ y = \sum_{i=0}^{i=7} M_i(\xi,\eta)y_i\ , \\ z = \sum_{i=0}^{i=7} M_i(\xi,\eta)z_i, \tag{9}$$

where: M_i is a basis interpolation function at node i, x_i , y_i , z_i represent coordinates of i-th node of the element.

The required components of the unit outward normal (n_x, n_y, n_z) from Equation (8) are given by:

$$\frac{\partial x}{\partial\xi} = \sum_{i=0}^{i=7}\frac{\partial M_i(\xi,\eta)}{\partial\xi}x_i,\ \frac{\partial y}{\partial\xi} = \sum_{i=0}^{i=7}\frac{\partial M_i(\xi,\eta)}{\partial\xi}y_i, \\ \frac{\partial z}{\partial\xi} = \sum_{i=0}^{i=7}\frac{\partial M_i(\xi,\eta)}{\partial\xi}z_i,\ \frac{\partial x}{\partial\eta} = \sum_{i=0}^{i=7}\frac{\partial M_i(\xi,\eta)}{\partial\eta}x_i, \\ \frac{\partial y}{\partial\eta} = \sum_{i=0}^{i=7}\frac{\partial M_i(\xi,\eta)}{\partial\eta}y_i,\ \frac{\partial z}{\partial\eta} = \sum_{i=0}^{i=7}\frac{\partial M_i(\xi,\eta)}{\partial\eta}z_i. \tag{10}$$

The analyzed area as well as the corresponding integral equation will consist of both parts: finite and infinite surrounding of an open edge.

For debugging purposes, in case of ordinary basis interpolation functions one has to check if the sum of all basis interpolation functions is unity and if the sum of all their derivatives is zero. A simple test checks if each function has unit value at its own node and zero at the other nodes. For decay type functions and for nodes remaining in the calculations in case of mapping functions that condition is also fulfilled. There is no exact analogy for the nodes which escape into infinity at mapped infinity elements. Further tests using Zienkiewicz type of mapped infinite elements [25] are devised by Bettess [5].

1.2. Breast models descriptions

Three simple theoretical models of human breast were investigated. For all models one placement of the light source was presented - located near the bottom of the hemisphere model. The first model presented in fig.3 corresponds to the hemisphere with an additional cylindrical part at the bottom.

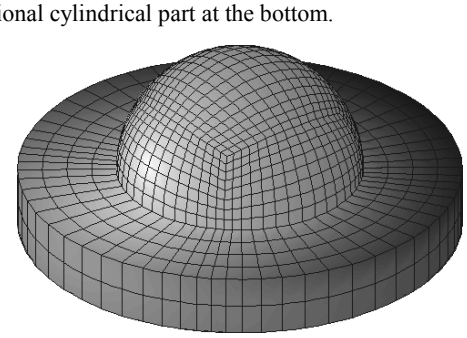

Fig. 3. Hemisphere breast model with an additional cylindrical part of chest at the bottom

The next two open boundary models use infinite boundary elements instead of the additional cylindrical part. The area of interest is limited to the hemisphere. The extra cylindrical part or the infinite elements rings are necessary to be added just to avoid possible errors, which would occur in case of mesh truncation at the bottom of the hemisphere. The standard boundary element model (Fig. 3) was constructed from 1536 second order, eight-node quadrilateral boundary elements and 4610 nodes. Half of the elements cover the hemisphere.

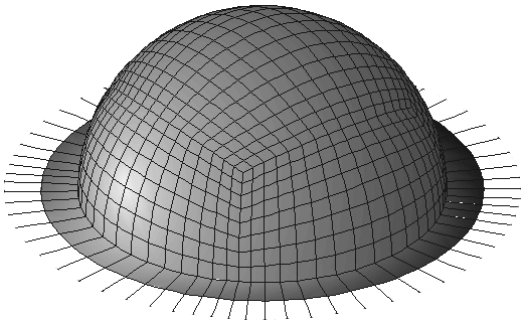

Fig. 4. Open boundary hemisphere breast model with mapped infinite boundary elements at the bottom

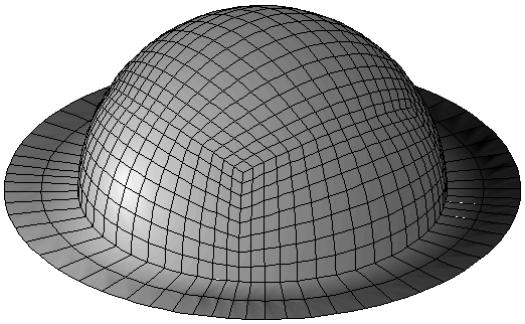

Fig. 5. Open boundary hemisphere breast model with decay function infinite boundary elements at the bottom

The open boundary model consists of 832 standard boundary elements and 64 infinite elements based on eight-node second order quadrilateral boundary elements [12]. The number of nodes was reduced to 2625 nodes in the model with incorporated mapped infinite boundary elements and to 2753 nodes in the decay function infinite element usage.

The governing equation for the problem is the diffusion approximation of the transport equation [1, 16, 21, 24] (Helmholtz (11) - assuming scattering and absorption are homogeneous). There are Robin boundary conditions (12) on surfaces [1, 16, 24]. In Diffusive Optical Tomography the distribution of the absorbing coefficient μ_a and the reduced scattering coefficient μ_S' are investigated.

$$\nabla^2\Phi(\mathbf{r},\omega) - k^2\Phi(\mathbf{r},\omega) = -\frac{q_0(\mathbf{r},\omega)}{D},\quad \forall\mathbf{r}\in\Omega/\Gamma, \tag{11}$$

Where Φ stands for photon density, $k = (\mu_a/D - j\,\omega/cD)^{1/2}$ a complex wave number, $D = [3(\mu_a+\mu_S')]^{-1}[\mathrm{mm}^{-1}]$ a diffusion coefficient, μ_S' is a reduced scattering coefficient, μ_a is an absorbing coefficient, c the speed of light in the medium, q_0 is a source of light (number of photons per volume unit emitted by concentrated light source located in position r with modulation frequency ω).

$$\Phi(\mathbf{r},\omega) + 2\alpha D\frac{\partial\Phi(\mathbf{r},\omega)}{\partial n} = 0,\quad \forall\mathbf{r}\in\Gamma. \tag{12}$$

with different coefficients for breast tissue and for skeletal muscles on the basis [1, 3, 25] imposed. In the analyzed example the following breast tissue properties were taken [1, 2, 16]: $\mu_a = 0.025[\mathrm{mm}^{-1}]$, $\mu_s' = 2[\mathrm{mm}^{-1}]$, $\alpha = 1$, $f = 100\mathrm{MHz}$.

The relevant boundary integral equation for surfaces covered by standard and infinite elements can be written as:

$$C(\mathbf{r})\Phi(\mathbf{r}) + \int_{\Omega} \frac{\partial G(|\mathbf{r}-\mathbf{r}'|,\omega)}{\partial n}\Phi(\mathbf{r}')d\Omega + \\ + \int_{\Omega_\infty} \frac{\partial G(|\mathbf{r}-\mathbf{r}'|,\omega)}{\partial n}\Phi(\mathbf{r}')d\Omega_\infty = \\ = \int_{\Omega} G(|\mathbf{r}-\mathbf{r}'|,\omega)\frac{\partial \Phi(\mathbf{r}')}{\partial n}d\Omega + \\ + \int_{\Omega_\infty} G(|\mathbf{r}-\mathbf{r}'|,\omega)\frac{\partial \Phi(\mathbf{r}')}{\partial n}d\Omega_\infty - \sum_{S=0}^{n_S-1} Q_S G(|\mathbf{r_S}-\mathbf{r}|,\omega) \tag{13}$$

where Q_S is the magnitude of the concentrated source $(q_0 = Q_S\delta(r_S))$ and n_S is the number of these sources, Φ stands for the photon density and G is the fundamental solution for the diffusion equation [1,16,21,24]. In 3D space for the diffusion equation the fundamental solution is [16]:

$$G(|\mathbf{r}-\mathbf{r}'|,\omega) = \frac{1}{4\pi|\mathbf{r}-\mathbf{r}'|}e^{-k|\mathbf{r}-\mathbf{r}'|}. \tag{14}$$

The normal derivative of the Green function in the direction n can be written as:

$$\mathbf{n}\cdot\nabla G = \mathbf{n}\cdot\frac{\mathbf{r}-\mathbf{r}'}{|\mathbf{r}-\mathbf{r}'|}\left(\frac{-1}{4\pi|\mathbf{r}-\mathbf{r}'|^2} - \frac{k}{4\pi|\mathbf{r}-\mathbf{r}'|}\right)e^{-k|\mathbf{r}-\mathbf{r}'|}. \tag{15}$$

1.3. Results and discussion

The values of ∂Φ/∂n were already presented above in figures 3, 4 and 5. It is difficult to compare these color maps, especially as each model and its solution have its own range of values, so the same color on all maps does not correspond to the same value. Taking that into account standard graphs were used to compare the results precisely. The values of ∂Φ/∂n module and the phase of the light at nodes lying on hemisphere circumference cross-section for y=0 are presented in figures 7 and 9 respectively. The values in nodes are presented in relation to angle Ψ (Fig. 6).

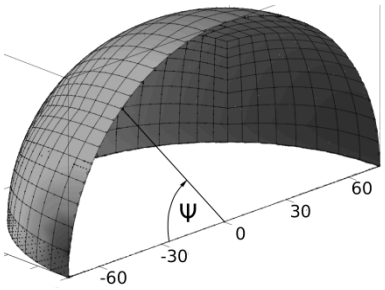

Fig. 6. Hemisphere circumference cross-section, ∂Φ/∂n(ψ) at y=0

To estimate the solution differences, the model with the extended bottom part (Fig. 3) was compared to those with infinite boundary elements implemented (Fig. 4 and 5).

As it was mentioned in the introduction the implementation of infinite boundary elements requires changing one of its fundamental elements – the basic interpolation functions. So, to present and to compare the different types of infinite boundary elements it was necessary to write our own BEM software in C++. The software uses some mathematical libraries from TOAST package [22].

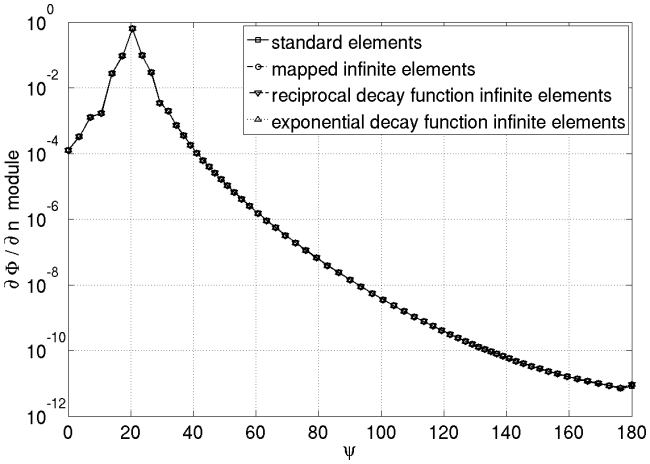

Fig. 7. Results comparison for ∂Φ/∂n(ψ) module

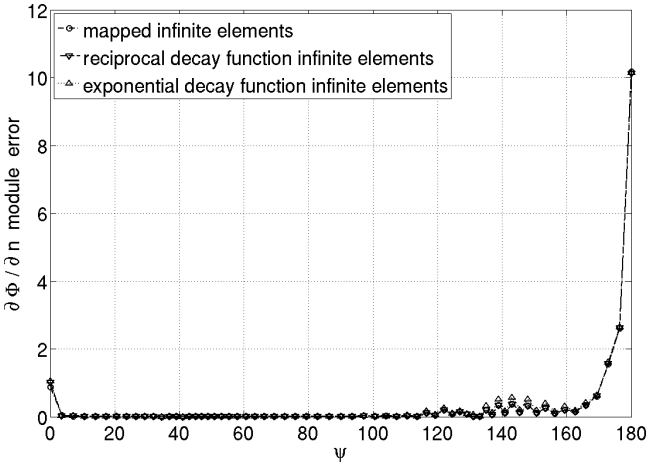

Fig. 8. ∂Φ/∂n(Ψ) module solution differences compared to hemisphere model

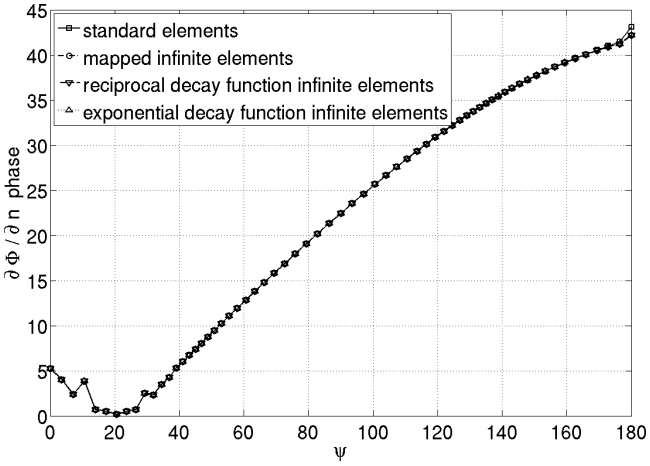

Fig. 9. Results comparison for ∂Φ/∂n(ψ) phase

Generally, all results are almost identical. Differences for module and phase are presented in figures 8 and 10 respectively. Only the part far from the light source shows some fluctuations, less than 1%, in results but it should be noticed that in that region the module is 10 orders of magnitude lower than near the source.

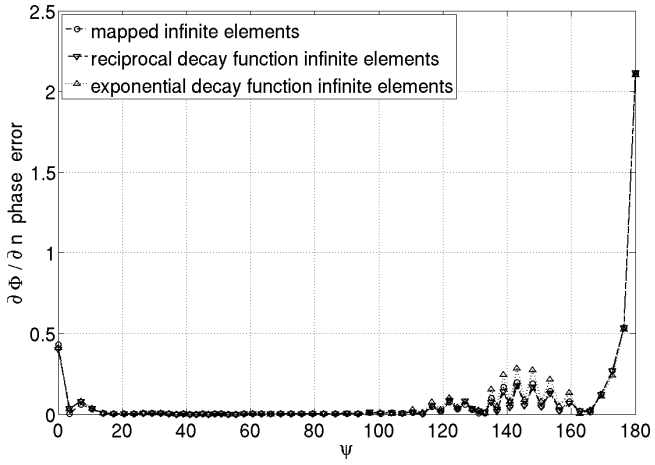

Fig. 10. ∂Φ/∂n(ψ) phase solution differences compared to hemisphere model

2. Functionally Graded Materials applications in BEM

2.1. Laboratory model and problem formulation

Tested wall parameters, measurements and theoretical aspects of EIT will be presented. Real, prepared for the experiment brick wall presented in figure 11 was 1m height, 1m long and 0.51m thick. It was flooded up to half height by water. The measurements were made a day after the water was drained.

Location of electrodes (marked by e1, e2, e3 … e26) and bore-holes for drying-weighing verification (marked 1, 2 and 3) are presented in figure 12.

Projections angles and measurements corresponds to the voltage of 7V with 1kHz frequency applied between pairs of electrodes 1-26, 2-25, 3-24, ... 12-15, 13-14 like presented in figure 13.

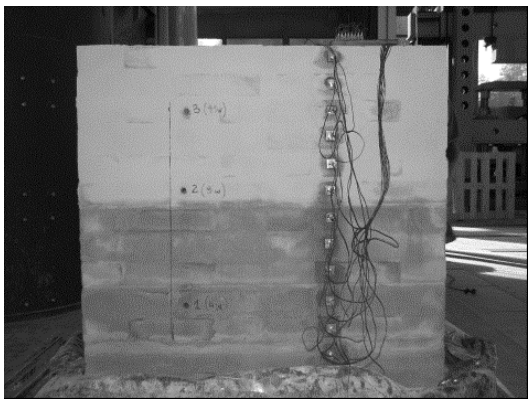

Fig.11. Investigated dumped wall [1]

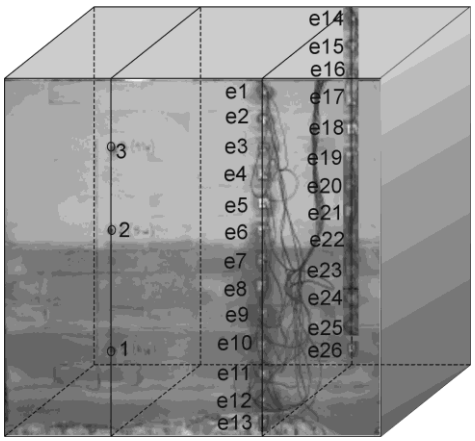

Fig.12. Investigated dumped wall with 26 electrodes for Electrical Impedance Tomography and 3 bore-holes for drying-weighing verification method

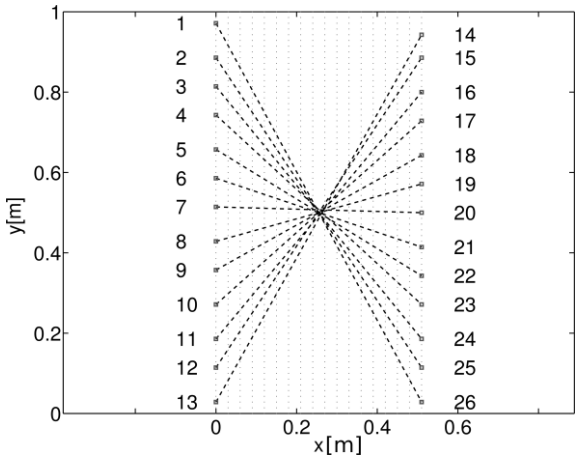

Fig.13. Applied projection angles: 1-26, 2-25, 3-24, ... 12-15, 13-14

Two-dimensional model with 174 (70×17) second order boundary elements of the damped wall was used. Conductivity distribution was interpolated by quadratic function [10]:

$$\gamma(x,y)=\gamma_0\left[a_{00}+a_{10}x+a_{01}y+a_2\left(x^2-y^2\right)\right] \tag{16}$$

where coordinate x corresponds to wall thickness and y to wall height.

Coefficients a00, a10, a01, a11 and a2 where calculated in inverse problem solution in accordance with data measured in Impedance Tomography.

In a simple BEM usage fundamental solutions are known and tabulated. For Functionally Graded Materials it is necessary to find the adequate Green's function [8, 11, 13, 14, 19, 20].

Green's function in two dimensions is derived for graded material represented by damped wall. The corresponding boundary integral equation formulations for this problem is derived, and the two-dimensional case is solved numerically.

2.2. Theoretical considerations

Boundary Integral Equation (BIE) [10,17] corresponding to the problem is:

$$c(\mathbf{r})\Phi(\mathbf{r})+\int_\Gamma \gamma(\mathbf{r}')\frac{\partial G^*(\mathbf{r},\mathbf{r}')}{\partial \mathrm{n}(\mathbf{r}')}\Phi(\mathbf{r}')\mathrm{d}\Gamma(\mathbf{r}')= \\ =\int_\Gamma \gamma(\mathbf{r}')G^*(\mathbf{r},\mathbf{r}')\frac{\partial \boldsymbol{\Phi}(\mathbf{r}')}{\partial \mathrm{n}(\mathbf{r}')}\mathrm{d}\Gamma(\mathbf{r}') \tag{17}$$

Comparing the above equation to the similar BIE for homogenous materials [10,17] two new elements can be found. At first γ(r) in equation (2) represents conductivity spatial distribution and secondly G* stands for so called modified Green function for non-homogenous materials. Curve Γ corresponds to the wall boundaries.

Modified Green function G* is not a Laplace equation fundamental solution. The differential equation for a potential function Φ defined on a surface S bounded by a wall boundary curve Γ, with an outward normal n, can be written as:

$$\nabla\cdot\left[\gamma(\mathbf{r})\nabla\boldsymbol{\Phi}\right]=0. \tag{18}$$

The kernels are based on the Green's function G* defined as:

$$\nabla\cdot\left[\gamma(\mathbf{r})\nabla G^*(\mathbf{r},\mathbf{r}')\right]=-\delta(\mathbf{r},\mathbf{r}') \tag{19}$$

where: r and r' are load and source points respectively.

Following E. Kurgan [11] or A. Sutradhar and G. H. Paulino [13,14,19,20] and assuming that conductivity will fulfil a condition:

$$\nabla^2\left(\sqrt{\gamma(\mathbf{r})}\right)=0 \tag{20}$$

we will receive applicable solution:

$$G^*(\mathbf{r},\mathbf{r}')=\frac{G(\mathbf{r},\mathbf{r}')}{\sqrt{\gamma(\mathbf{r})\gamma(\mathbf{r}')}} \tag{21}$$

where G is a typical Green's function for Laplace equation [10, 17]. Matrices elements A and B [10, 17] can be written as follows:

$$A_{i,j}(\mathbf{r},\mathbf{r}') = \int_{\Gamma} \gamma(\mathbf{r}) \frac{\partial G^*(|\mathbf{r}-\mathbf{r}'|)}{\partial n} d\Gamma \qquad (22)$$

$$B_{i,j}(\mathbf{r},\mathbf{r}') = \int_{\Gamma} \gamma(\mathbf{r}) G^*(|\mathbf{r}-\mathbf{r}'|) d\Gamma$$

3. Remarks and conclusion

3.1. Mammography

All three types of infinite boundary elements: mapped, reciprocal decay functions and exponential decay functions offer almost identical results, similar to these achieved by using the standard model, which contains only finite boundary elements. The role of the infinite elements is to receive the correct solution in the area of interest, so all additional parts like the bottom cylinder in the standard model (Fig. 3) as well as the ring built from infinite elements around the hemisphere (Fig. 4 and 5) are neglected.

The advantages of using infinite elements are to avoid incorrect and unknown boundary conditions such as those on the surface between breast and chest in the breast models, to shorten the calculation time and to keep the accuracy similar to the standard solution (based on mesh extension, in our case mesh outside the hemisphere). All extended models were built from the same number of standard 8-node, second order, quadrilateral boundary elements. Mesh density on the additional surface related to the cylindrical part of the model was lower than on the hemisphere surface. This is a typical practical solution, as the additional part represents the region outside the zone of interests.

Reducing the number of mesh elements almost to 50% is fundamental to the inverse problem solution when the forward problem has to be calculated many times. The implementation of infinite boundary elements into the boundary element method improves the computational efficiency in the breast model almost 4 times and enables us to avoid the problem of setting incorrect boundary conditions.

The forward problem calculations took 4 minutes and 47 seconds in the case of 4160-node model. The model with infinite elements built, in total, from 2625 nodes, with incorporated mapped infinite boundary elements, and the model built from 2753 nodes, with the decay function infinite elements, took respectively 1 minute and 24 seconds and 1 minute and 30 seconds.. The reverse problem solution used to find the inner image of the analyzed objects requires calculating the forward problem many times.

The process of incorporating infinite elements into BEM calculation scheme is quite logical and generally related to the incorporation of new infinite basic approximation function and all further steps for its implications.

The main disadvantage of using infinite boundary elements is that not all mesh generators allow us to create a pure quadrilateral mesh or to distinguish separately both the areas covered by the most popular triangular elements and the infinite part covered by quadrilateral 8-node elements. Moreover, the authors are not familiar with the generator which would create 5-node infinite quadrilateral mapped elements. Therefore, a self-made generator was used to build a mesh containing only quadrilateral elements.

Fortunately, in optical mammography light sensors and sources are located in a special hemispherical or cone shape constant form, so the effort related to the manual creation of the infinite element mesh, which surrounds the area of interest, has to be made only once.

3.2. Damped walls

Measured potential values were compared to these calculated with BEM (used to solve forward problem) and additionally with calculation results taken from FEM.

Inverse problem solution required 7 iterations to find interpolation coefficients related to investigated conductivity function (16).

Potentials - measured and calculated – for selected projection angles: 7 (electrodes 7-20) and 10 (electrodes10-17), as defined in figure (13), are presented in figures 14 and 15. Projection 7-20 presents the best achieved results and projection 10-17 the worst.

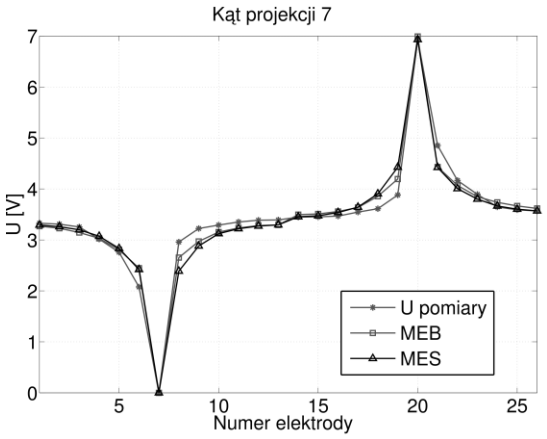

Fig.14. Successive EIT measurements, BEM 2D calculation and FEM 2D calculation results corresponding to the voltage of 7V with 1kHz frequency applied between pairs of electrodes 7-20

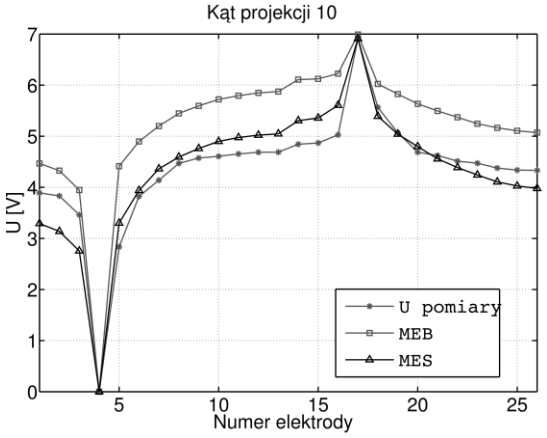

Fig.15. Successive EIT measurements, BEM 2D calculation and FEM 2D calculation results corresponding to the voltage of 7V with 1kHz frequency applied between pairs of electrodes 10-17

Application of Functionally Graded Materials theory into Boundary Element Method used to find spatial distribution of humidity and salinity into damped walls seems to be better idea than using multiregional BEM due to simpler mesh and boundary conditions.

Described method will be used to find thomographic image of dumped wall.

Most of articles discusses objects where FGM changes their properties only in one direction [8, 13, 19, 20].

Damped wall presented above represents the graded material where humidity and salinity varies in at least two directions (corners of the buildings will require 3 dimensional model).

Achieved results are quite promising although are worse than ones received during theoretical calculations based on flat capacitor model with known analytical solution or dumped wall model calculated by BEM and FEM where material properties varied only in one direction.

Possible reason of low accuracy in some projection angles (see Fig. 15) can be caused by the insufficient data associated with too few angle projections. Possessed measurements are more suitable for the model where conductivity distribution varies only in one direction corresponding to the thickness of the wall and not its height.

Next stage will be to calculate theoretical model of the wall where material properties varies in two directions x and y (along wall thickness and height respectively) and compare FEM and BEM results.

We believe that new measurements which will include all possible projections angles allows us to receive results with much better accuracy.

Final model will also include infinite boundary elements to avoid an unknown height of wall humidity and possible related errors. BEM is known to be well suited to handle open boundary models containing infinite elements.

Acknowledgement

Presented BEM-FGM considerations are related with NCBR project “Tomograf hybrydowy do badania zawilgocenia i stanu budynków” (Hybrid CT scanner to examine buildings moisture and condition) number POIR.01.01.01-00-0167/15.

References

[1] Arridge S.R.: Optical tomography in medical imaging. Inverse Problems, 15(2)/1999, 41–93.
[2] Beer G., Watson J.O.: Infinite Boundary Elements. International Journal for Numerical Methods in Engineering, 28/1989, 1233–1247.
[3] Beer G., Watson J.O., Swoboda G.: Three-dimensional analysis of tunnels using infinite boundary elements. Computers and Geotechnics, 3/1987, 37–58.
[4] Berowski P., Filipowicz S.F., Sikora J., Wójtowicz S.: Dehumidification of the wall process monitoring using 3D EIT system, 15th Conference on the Computation of Electromagnetic Fields COMPUMAG 2005, 2, Shenyang, 2005.
[5] Bettess P.: Infinite Elements, Penshaw Press, 1992.
[6] Filipowicz S., Rymarczyk T.: Dobór metod pomiarowych i algorytmów rekonstrukcji obrazu do badania stanu pni drzew. Przegląd Elektrotechniczny, 86(12)/2010, 38–41.
[7] Filipowicz S., Sikora J., Polakowski K., Hoła J., Schabowicz K., Wójtowicz S., Biernat K.: Tworzenie obrazów tomograficznych stanu zawilgocenia murów w przekrojach poprzecznych. Przegląd Elektrotechniczny, 05/2007, 116–121.
[8] Gray L.J., Kaplan T., Richardson J.D., Paulino G.H.: Green's Functions and Bounday Integral Analysis for Exponentially Graded Materials: Heat Conduction. Journal of Applied Mechanics, 70/2003, 543–549.
[9] Hoła J., Matkowski Z., Schabowicz K.: Impedance tomographic method of assessing the dampness of masonry. Z. 1-B/2007 Wydawnictwo Politechniki Krakowskiej http://bc.biblos.pk.edu.pl/bc/resources/CT/CzasopismoTechniczne_1B_2007/HolaJ_TomografiaImpedancyjna.pdf.
[10] Jabłoński P.: Metoda elementów brzegowych w analizie pola elektromagnetycznego. Wydawnictwo Politechniki Częstochowskiej, Częstochowa, 2003.
[11] Kurgan E.: Analiza pola magnetostatycznego w środowisku niejednorodnym metodą elementów brzegowych. Uczelniane wydawnictwa naukowo-dydaktyczne AGH, Kraków, 1999.
[12] Moser W., Duenser Ch., Beer G., et al.: Mapped infinite elements for three-dimensional multiregion boundary element analysis. International Journal for Numerical Methods in Engineering, 61/2004, 317–328.
[13] Paulino G.H., Sutradhar A., Gray L.J.: Boundary element Methods for Functionally Graded Materials. International Association for Boundary Element Methods, IABEM 28-30 May 2002 Austin.
[14] Paulino G.H., Sutradhar A.: The simple boundary element method for multiple cracks in functionally graded media governed by potential theory: a three-dimensional Galerkin approach. International Journal for Numerical Methods in Engineering, 65/2005, 2007–2034.
[15] Rymarczyk T.: Praktyczne implementacje metody zbiorów poziomicowych w tomografii impedancyjnej. Przegląd Elektrotechniczny, 07b/2004, 138–140.
[16] Sikora J.: Boundary Element Method for Impedance and Optical Tomography, Oficyna Wydawnicza Politechniki Warszawskiej, Warsaw 2007.
[17] Sikora J: Numeryczne metody rozwiązywania zagadnień brzegowych. Podstawy metody elementów skończonych i metody elementów brzegowych. Wydawnictwa uczelniane Politechniki Lubelskiej, Lublin 2009.
[18] Stasiak M., Berowski P., Sikora J.: Porównanie algorytmów tomografii impedancyjnej zastosowanych do identyfikacji wnętrza obiektów trójwymiarowych. Przegląd Elektrotechniczny, 12/2006, 13–16.
[19] Sutradhar A., Paulino G.H.: A simple boundary element method for problems of potential in non-homogeneous media. International Journal for Numerical Methods in Engineering, 60/2004, 2203–2230.
[20] Sutradhar A., Paulino G.H., Gray L.J.: On hypersingular surface integrals in the symmetric Galerkin boundary element method: application to heat conduction in exponentially graded materials. International Journal for Numerical Methods in Engineering, 62/2005, 122–157.
[21] Tarvainen T.: Computational Methods for Light Transport in Optical Tomography, PhD Thesis, Department of Physics, University of Kuopio, 2006, http://physics.uku.fi/~vilhunen/phdthesis ttarvainen.pdf .
[22] TOAST software suite for image reconstruction in optical diffusion tomography, developed by Martin Schweiger and Simon Arridge at University College London, 2013, http://web4.cs.ucl.ac.uk/research/vis/toast/
[23] Watson J.O.: Advanced implementation of the boundary element method for two- and three-dimensional elastostatics, Developments in Boundary Element Methods - 1 (Editors P.K. Banerjee and R. Butterfield), Elsevier Applied Science Publishers, 61/1979, 31–63.
[24] Zacharopoulos A., Arridge S.R., Dorn O., Kolehmainen V., Sikora J., et al.: Three-dimensional reconstruction of shape and piecewise constant region values for optical tomography using spherical harmonic parametrization and a boundary element method. Inverse Problems, 22/2006, 1–24.
[25] Zienkiewicz C.O., Emson C., Bettess P., et al.: A novel boundary infinite element. International Journal for Numerical Methods in Engineering, 16/1983, 393–404.

Ph.D. Eng. Maciej Pańczyk
e-mail: m.panczyk@pollub.pl

Maciej Pańczyk, PhD Eng. - graduated from the Faculty of Electrical Engineering, Lublin University of Technology. He worked in the Department of Fundamental Electrical Engineering, Lublin University of Technology, then in Information Technology Department in Bank BDK S.A and since 2004 at the Institute of Computer Science, Lublin University of Technology. His work focuses on the electromagnetic field and programming.

Prof. Jan Sikora
e-mail:sik59@wp.pl

PhD. DSc. Eng. Jan Sikora graduated from Warsaw University of Technology Faculty of Electrical Engineering. During 43 years of professional work he has proceeded all grades, including the position of full professor at his alma mater. Since 1998 he has worked for the Institute of Electrical Engineering in Warsaw. In 2008 he has joined Electrical Engineering and Computer Science Faculty in Lublin University of Technology. During 2001-2004 he has worked as a Senior Research Fellow at University College London in the prof. S.R.. Arridge’s Group of Optical Tomography. His research interests are focused on numerical methods for electromagnetic field.

otrzymano/received: 20.09.2016 *przyjęto do druku/accepted: 15.02.2017*

DOI: 10.5604/01.3001.0010.4607

PRZEGLĄD METOD POMIAROWYCH OPARTYCH NA TOMOGRAFII OPTYCZNEJ W ZASTOSOWANIU DO WYZNACZANIA PARAMETRÓW PRZEPŁYWÓW GAZ-CIECZ

Mariusz Rząsa, Ewelina Podgórni
Politechnika Opolska, Katedra Techniki Cieplnej i Aparatury Przemysłowej

Streszczenie. *W pracy przedstawiono przegląd metod tomografii optycznej, stosowanych do badania przepływu dwufazowego gaz-ciecz. Wykorzystanie tomografii optycznej pozwala wyznaczać parametry ruchu fazy rozproszone (gazowej). W opracowaniu przedstawiono ideę pomiaru oraz opisano własne metody prześwietlania obiektów badanych. Przeprowadzono analizę możliwości zastosowania poszczególnych metod do pomiaru wybranych parametrów przepływu dwufazowego. Opisano metodę prześwietlania równoległą i rozproszoną wiązką światła oraz trójwymiarową metodę analizy obrazu. Prezentowane metody mogą posłużyć do pomiaru pęcherzyków w cieczach przeźroczystych, ale również ruchu kropli cieczy w gazie, ciał stałych w cieczy lub ciał stałych w gazie.*

Słowa kluczowe: tomografia optyczna, analiza obrazu, przepływ dwufazowy

REVIEW OF METHODS OF MEASURING BASED ON OPTICAL TOMOGRAPHY APPLICABLE TO DETERMINING FLOW PARAMETERS OF GAS-LIQUID

Abstract. *Optical tomography is a diagnostic method that allows to obtain a wide range of images. With these images, you can perform the submission of horizontal or spatial test object. This paper presents a number of imaging methods used to study the flow of two-phase gas-liquid. The use of optical tomography allowed to track the movement of air bubbles during their flow through the test column. The presented methods can be used to measure the bubbles in transparent fluids, but also the movement of a drop of liquid in gas, solids in liquids or solids in the gas.*

Keywords: Optical tomography, image processing, two-phase flow

Wstęp

Przepływem dwufazowym nazywa się wspólny ruch dwóch faz, fazy ciągłej i rozproszonej. W szczególności mogą występować przepływy dwufazowe z obiema fazami ciągłymi. Fazą ciągłą oraz rozproszoną może być zarówno ciecz jak i gaz. Przez pojęcie faza rozumie się jednorodną pod względem fizycznym część układu, oddzieloną od pozostałej jego części granicą faz. Przy przechodzeniu przez tę granicę następuje skokowa zmiana stanu termodynamicznego i często zmiana stanu chemicznego. Na ruch i zjawiska zachodzące w mieszaninie dwufazowej mają wpływ oddziaływania zewnętrzne od strony ścian przewodu i elementów urządzeń, a także oddziaływania wewnętrzne (międzyfazowe), wywołujące zmianę pól prędkości, ciśnień i temperatur.

Różnorodność form przepływu sprawia, że pomiar parametrów mieszaniny dwufazowej zalicza się do jednych z najbardziej złożonych problemów metrologii (parametry geometryczne i przepływowe). Dodatkowo pomiary utrudnia stochastyczny charakter zjawisk zachodzących w każdej fazie. Powoduje to, że koncentracja fazy rozproszonej zależy od położenia i czasu. Szybkie zmiany w czasie i przestrzeni: powierzchni międzyfazowej, koncentracji, lokalnych prędkości przemieszczania się faz oraz kierunku ich przemieszczania, w znacznym stopniu utrudnia prowadzenie pomiarów. W pracy przedstawiono przegląd różnych rozwiązań układowych, opartych na tomografii optycznej, mających zastosowanie do wyznaczania wybranych parametrów mieszaniny dwufazowej.

1. Idea optycznej metody pomiarowej

Idea tomografii optycznej oparta jest na zjawiskach optycznych zachodzących na granicy faz. Zasada działania polega na prześwietlaniu badanego przekroju wiązką światła, a następnie pomiarze natężenia światła przechodzącego przez przekrój w wybranym kierunku (rys. 1). Światło emitowane ze źródła przechodząc przez przekrój badany ulega częściowej absorpcji I_a zarówno przez gaz, jak i ciecz. Ponadto po natrafieniu na pęcherzyk gazu strumień światła ulega na granicy faz odbiciu I_R i rozproszeniu, jest to przyczyną znacznego osłabienia natężenia światła docierającego do detektora [6]. Miarą obecności pęcherzyka w polu widzenia detektora jest stosunek natężenia światła I_e padającego na czujnik, do natężenia promieniowania światła emitowanego ze źródła I_0

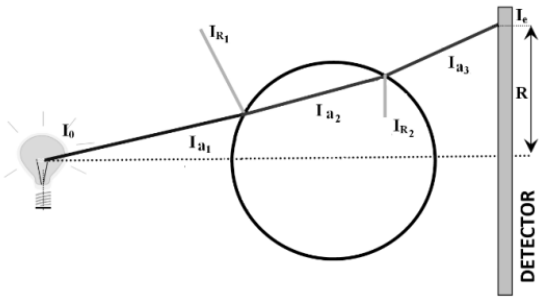

Rys. 1. Idea optycznej metody pomiarowej

Rozkład natężenia światła zależy od geometrii układu, a pęcherzyk gazu można potraktować jak cienką soczewkę, na której następuje załamanie promienia świetlnego z jednoczesnym odbiciem i częściową absorpcją światła. Stosunek natężenia światła wyraża się ogólną zależnością [3]:

$$\frac{I_e}{I_0} = \delta r\, \delta b\, \delta a \tag{1}$$

gdzie: δ_r – współczynnik odbicia światła, δ_b – współczynnik rozproszenia światła, δ_a – współczynnik absorpcji światłą.

Szczegółowy opis zjawiska osłabienia wiązki światła na skutek natrafienia na pęcherzyk znajduje się w pracach [4, 5, 12]. Na błędy związane z detekcją i pomiarem parametrów poruszających się cząstek istotny wpływ ma rodzaj zastosowanego źródła światła. Budowę typowych źródeł światła stosowanych w tomografii optycznej opisano w pracy [8]. Nie bez znaczenia jest również budowa detektora. Bardzo często, w celu zmniejszenia konta aperturowego, stosuje się tulejki kolimacyjne oraz odpowiednie układy kształtowania sygnału elektrycznego pochodzącego z detektora. Szczegóły budowy układu detekcji omówiono w pracy [14].

Za pomocą metod optycznych możliwe jest wyznaczenie podstawowych parametrów fazy rozproszonej, do których zalicza się objętość pęcherzyków lub kropel, prędkość ich ruchu, trajektoria ruchu oraz wielkości pochodne takie jak udział objętościowy lub masowy. W zależności od potrzeb związanych z dokładnością pomiaru poszczególnych wielkości w tomografii optycznej stosuje się prześwietlanie równoległą wiązką światła lub

wiązką rozproszoną. W dalszej części pracy przedstawiono kilka rozwiązań technicznych oraz podano ich wady, zalety i zakres zastosowania.

2. Wyznaczanie objętości poruszających się pęcherzyków gazu z zastosowaniem równoległej wiązki światła

Małe pęcherzyki gazu przyjmują kształty kuliste lub kształty brył obrotowych. Dla tego rodzaju przepływów wystarczające jest prześwietlanie tylko z jednego kierunku. Objętość można wyznaczyć na podstawie przybliżenia kształtu pęcherzyka szeregiem walców (rys.2).

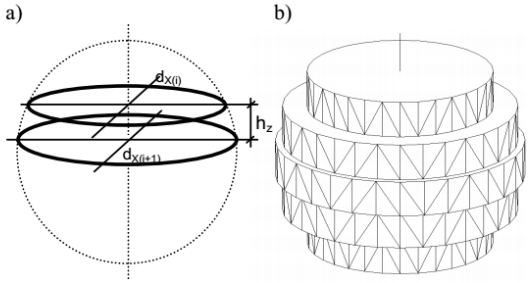

Rys. 2. Przybliżenie kształtu pęcherzyka a) idea b) wyznaczenie objętości [10]

Pomiaru średnicy przekroju badanego dokonuje się poprzez pomiar poziomów natężenia światła, docierającego do poszczególnych czujników znajdujących się w detektorze (rys.3). Na rys. 3 przedstawiono budowę typowego detektora stosowanego w tomografii z równoległą wiązką światła. Detektor składa się z dwóch warstw równolegle ułożonych detektorów światłowodowych (górny-1 i dolny-2), które są od siebie oddalone o odległość *s*. Tego typu rozwiązanie umożliwia pomiar prędkości poruszających się pęcherzyków. Na podstawie prędkości poruszającego się pęcherzyka oblicza się wymiar h_z.

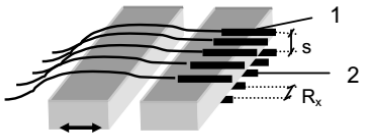

Rys. 3. Budowa detektora

Obliczenie objętości pęcherzyka polega na zsumowaniu objętości walców składających się na pęcherzyk, wzór na objętość przyjmuje następującą postać:

$$V = \sum_{i=1}^{n-1} V_i = \frac{h_z \pi}{4} \sum_{i=1}^{n-1} d_{(i)}{}^2 \tag{2}$$

gdzie: V_i –objętość składowa jednego walca, $d_{(i))}$ – średnice i-tego walca, h_z – wysokość walca, n – liczba walców składających się na pęcherzyk.

3. Rekonstrukcja obrazu z dwóch rzutów

Rozwiązanie z prześwietlaniem obiektu z jednego kierunku, ma stosunkowo ograniczone zastosowanie. W przypadku pęcherzyków których kształt nie jest bryłą obrotową lub gdy w przepływie jest duża koncentracja pęcherzyków, pomiar prędkości i objętości poruszających się pęcherzyków jest możliwy za pomocą tomografu optycznego. Bardzo prostym rozwiązaniem może być rekonstrukcja obrazu na podstawie dwóch rzutów przekroju badanego (rys. 4). Czujnik takiego tomografu składa się z dwóch prostopadle ustawionych źródeł światła, i dwóch detektorów promieniowania światła. Wyniki pomiaru są gromadzone w pamięci komputera, gdzie następnie jest dokonywana rekonstrukcja obrazu, na podstawie której oblicza się podstawowe parametry przepływu gazu.

Rekonstrukcja polega na przybliżeniu kształtu pęcherzyka szeregiem elips. Różnica w stosunku do rozwiązania z prześwietlaniem z jednego kierunku polega na tym, że do wyznaczenia wymiarów pęcherzyka używa się dwóch średnic stanowiących podstawę wyznaczenia elipsy. Rozwiązanie takie może być zastosowane do pęcherzyków o kształtach zarówno obrotowych jak i nieregularnych. Pewną trudność w poprawnej rekonstrukcji kształtu pęcherzyków stanowi to, gdy w jednej płaszczyźnie znajduje się kilka pęcherzyków. Poprawna rekonstrukcja jest możliwa wymaga ona jednak zastosowania algorytmów uwzględniających dodatkową wiedzę na temat procesu. Jeden z takich algorytmów oparty na sieci neuronowej opisano szczegółowo w pracy [14].

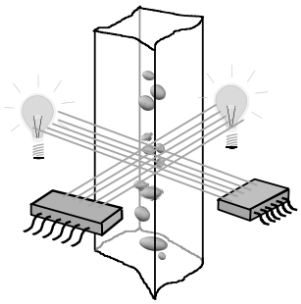

Rys. 4. Tomograf z równoległa wiązką światła

Wyniki działania tego rodzaju algorytmu przedstawiono na rysunku 5. W przypadku niewielkiej grupy pęcherzyków możliwe jest prawidłowe odtworzenie ich przestrzennego położenia. Jednakże metoda ta nie może być stosowana do większej liczby pęcherzyków poruszających się w tej samej płaszczyźnie. Rozwiązanie to w zastosowaniu do pęcherzyków o kształcie nieregularnym prowadzi do powstawania dużych błędów odwzorowania [9] i nie zaleca się stosowania tej metody przy wyznaczaniu objętości pęcherzyków.

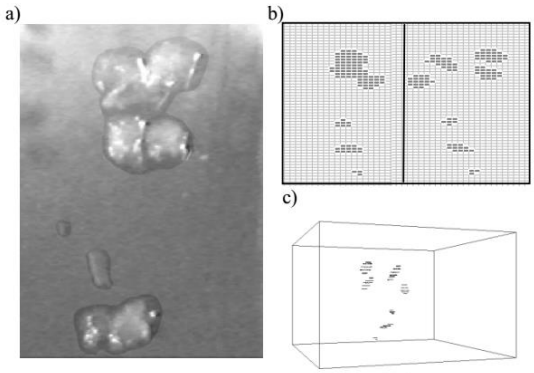

Rys. 5. Obrazy grupy poruszających się pęcherzyków widziany: a) z kamery, b) z detektorów tomografu, c) po rekonstrukcji

4. Tomograf z rozproszoną wiązką światła

Prześwietlanie rozproszoną wiązką światła nie wymaga zastosowania złożonych układów optycznych skupiających światło. Wymaga natomiast stosowania odmiennych algorytmów rekonstrukcji obrazu. Niejednokrotnie stosuje się w tym przypadku algorytmy znane z tomografii rentgenowskiej [2]. Metoda polega na emitowaniu wiązki z jednego punktowego źródła światła, a następnie dokonywaniu detekcji w promieniu pola rozproszenia wiązki (rys. 6). Rozwiązanie przedstawione na rysunku 6a wymaga zastosowania źródeł światła i detektorów o dużym kącie aperturowym, co nie zawsze jest łatwe do wykonania. Ponadto w rozwiązaniu tym, największa strefa nieczułości występuje w środku przekroju badanego. W pewnym stopniu poprawia to asymetryczne ustawienie źródeł i detektorów światła [12]. Zaletą tego rozwiązania jest stosunkowo niewielka ilość par źródło detektor.

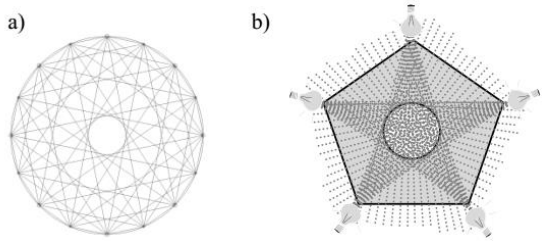

Rys. 6. Idea tomografu optycznego z wiązką rozproszoną: a) z symetrycznie ułożonymi sensorami oraz źródłami światła (naprzemiennie ułożone w ściance) [14] b) ze źródłem umieszczonym na zewnątrz [11]

W rozwiązaniu z rysunku 6a można dostrzec, że w środku obiektu badanego nie ma żadnej drogi promienia świetlnego pomiędzy źródłem, a detektorem. Powoduje to powstawanie martwej strefy w środku obiektu. Metodę umożliwiającą zmniejszenie obszaru nieczułości opisano w pracy [14]. Rozwiązanie z rysunku 6b polega na umieszczeniu źródeł światła w pewnej odległości od obiektu badanego, w taki przypadku możliwe jest zastosowanie źródła światła o stosunkowo małym kącie aparaturowym. W rozwiązaniu z rysunku 6b nie ma niedogodności w postaci obniżonej czułości w środku przekroju badanego, lecz znacząco zwiększa to wymiary tomografu. Z uwagi na konieczność określania prędkości poruszających się pęcherzyków zaleca się przesunięcie płaszczyzn prześwietlania (rys. 7). Umożliwia to wyznaczenie prędkości poruszających się pęcherzyków, stosując metody korelacyjne. Przykładowo dla rozwiązania składającego się z pięciu projekcji można stosować przesunięcie wszystkich wiązek światła o odległość oraz można przesunąć tylko kilka wybranych, a pozostałe są umieszczone w jednej płaszczyźnie.

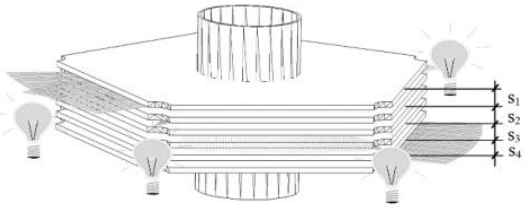

Rys. 7. Przesunięcia wiązek światła w zgodnie z kierunkiem ruchu pęcherzyków [7]

Bazując na metodach rekonstrukcji znanych z tomografii rentgenowskiej bardzo popularny jest algorytm oparty na metodzie macierzowej.

$$W[n,n_p]\cdot F[n]=\Phi[n_p] \tag{3}$$

W równaniu tym F[n] oznacza macierz wartości funkcji obrazu (wartość poszczególnych pikseli), natomiast $\Phi[n_p]$ stanowi wektor dyskretnych wartości pomiarowych. W równaniu tym bardzo istotne jest określenie macierzy wrażliwości W.

W pracy [11] przedstawiono różne metody generowania macierzy wrażliwości. W zastosowaniu do przepływów gaz-ciecz dobre wyniki rekonstrukcji obrazu uzyskuje się przy zastosowaniu metody śledzenia obszaru ograniczonego wiązką światła [14].

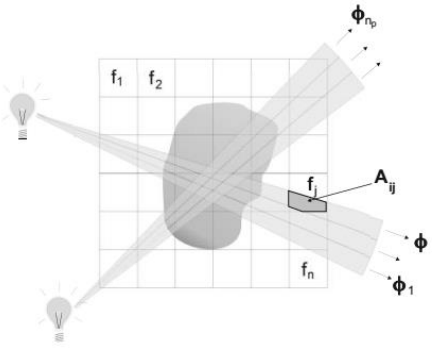

Rys. 8. Idea wyznaczania macierzy wrażliwości metodą śledzenia obszaru ograniczonego wiązką światła [11]

Metoda ta uwzględnia geometrię układu pomiarowego, a wartości elementów macierzy wrażliwości są równe stosunkowi pola powierzchni pokrywanej przez promień wiązki światła do sumy pól wszystkich promieni przechodzących przez dany piksel (rys. 8). A zatem wagi różnych promieni światła, które prześwietlają dany piksel obrazu będą różne. Nie bez znaczenia jest również, położenia wybranego piksela obrazu, gdyż udział powierzchniowy wiązki światła silnie zależy od odległości od źródła światła.

$$w_{i,j}=\begin{cases}\dfrac{A_{ij}}{\sum_{i=1}^{n_p}A_{ij}} & dla \quad k_j\geq 2\\ 0 & dla \quad k_j<2\end{cases} \tag{4}$$

gdzie: k_j – liczba promieni przechodzących przez j-te pole funkcji obrazu, A_{ij} – pole powierzchni, jaką pokrywa wiązka Φ_i w polu obrazu f_j.

W celu poprawy, jakości obrazu i wyraźnego określenia granicy faz niejednokrotnie stosuje się progowanie. Na rysunku 9 przedstawiono przykładową trójwymiarową rekonstrukcję kształtu pęcherzyka gazu. Pomiary wykonano z czasem próbkowania t_p=10 ms, liczba pikseli składająca się na obraz w jednej płaszczyźnie wynosiła 100. Prędkość poruszania się pęcherzyka wynosiła v=0,045 m/s. Pęcherzyk składa się z 54183 elementów. Stosując tego rodzaju metody pomiarowe możliwe jest zarówno wyznaczenie kształtu, jak i obliczenie objętości poruszających się pęcherzyków.

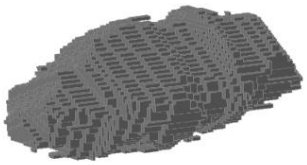

Rys. 9. Przykładowa rekontrukcja 3D pęcherzyka [12]

5. Trójwymiarowa analiza obrazu

Do pełnego opisu ruchu pęcherzyków gazu poza znajomością objętości poruszających się pęcherzyków istotna jest również informacja o trajektorii jego ruchu. Metody polegające na prześwietlaniu przepływu tylko w jednym wybranym przekroju nie umożliwiają wyznaczenia trajektorii ruchu pęcherzyków.

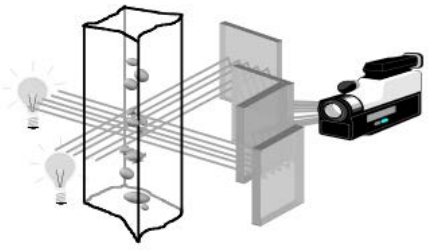

Rys. 10. Budowa skanera do trójwymiarowej analizy obrazu [14]

W odróżnieniu od tomografii optycznej obraz jest rejestrowany dla pewnego wycinka przepływu, a nie jak w tomografie optycznym dla wybranego przekroju poprzecznego. W przypadku cyfrowej rejestracji obrazu możliwa jest nie tylko obserwacja przepływu, lecz po poddaniu obrazu cyfrowej analizie można wyznaczyć pewne parametry charakteryzujące przepływ. Wadą tego rozwiązania jest duży nakład obliczeniowy w przypadku przestrzennego odwzorowania kształtu pęcherzyka.

Na rysunku 10 przedstawiono jedno z rozwiązań układu do trójwymiarowej analizy obrazu. Metoda polega na synchronicznym zarejestrowaniu obrazów przepływu pęcherzyków z dwóch prostopadłych kierunków. Ponieważ rejestracja obrazu z dwóch kierunków za pomocą dwóch kamer wymaga synchronicznego otwierania migawki, zaproponowano

rozwiązanie polegające na rejestracji obrazu za pomocą jednej kamery z odpowiednim układem luster. Zwierciadła ustawiono odpowiednio pod kątem 2×45° i 2×22.5°. Analiza i korelacja obrazowa w ten sposób uzyskanych klatek obrazu umożliwiają określenie zwrotu jak i wartości wektora prędkości poruszającego się pęcherzyka.

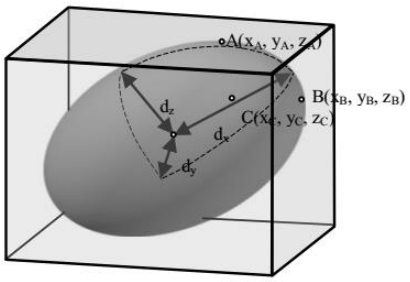

Rys. 11. Przybliżony obraz pęcherzyka za pomocą elipsoidy w przestrzeni 3D [13]

Wektory prędkości miejscowych są wyznaczane na podstawie przemieszczenia się środka masy pęcherzyka. Obraz z kamery jest poddany procesowi binearyzacji [1], a następnie określane są współrzędne środka masy. Z uwagi na analizę ruchu pęcherzyków gazu oraz wzajemne interakcje, bardzo istotna jest informacja na temat prędkości lokalnej poruszających się pęcherzyków, a niejednokrotnie wystarczająca jest przybliżona wartość objętości pęcherzyków. Z tego względu celowe jest przybliżenie kształtu oraz orientacji przestrzennej za pomocą elipsoidy (rys.11). Tego typu figura geometryczna może opisywać usytuowanie pęcherzyka w przestrzeni w oparciu o trzy wartości liczbowe (średnice elipsy dx, dy, dz oraz kątów nachylenia poszczególnych osi elipsy względem układu współrzędnych). Szczegółowy algorytm wyznaczania tych parametrów opisano w pracy [13].

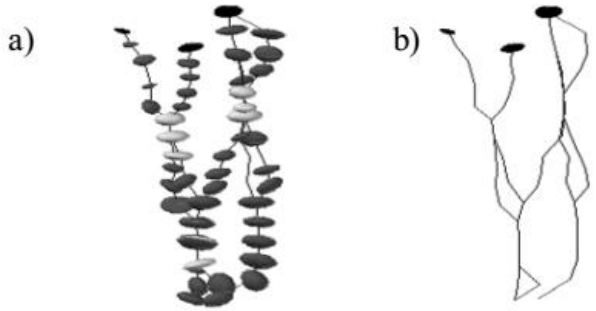

Rys. 12. Przykładowy ruch pęcherzyków gazu: a) przestrzenny obraz ruchu pęcherzyków, b) trajektoria ich ruchu

Przykładowy obraz przedstawiono na rysunku 12. Na podstawie tego rodzaju obrazów możliwa jest nie tylko analiza ruchu pęcherzyków gazu, ale możliwe jest również śledzenie oscylacji jakie wykonuje pęcherzyk podczas ruchu.

6. Podsumowanie

Przedstawione rozwiązanie oparte na tomografii optycznej umożliwia pomiar bardzo małych obiektów o średnicach kilku milimetrów. Możliwe jest rekonstruowanie kształtu poruszających się pęcherzyków oraz obliczenie ich podstawowych parametrów. W przypadku przepływów dwufazowych, gdzie następuje wyraźna granica faz, możliwa jest detekcja obecności gazu w wybranym pikselu przestrzeni pomiarowej, za pomocą zapisu dyskretnego i za pomocą wartości logicznej „0” lub „1”. Zastosowanie dyskretnego przetwarzania sygnałów znacznie upraszcza konstrukcję tomografu i algorytm rekonstrukcji. Zaproponowane rozwiązania umożliwiają wyznaczanie podstawowych parametrów przepływu z zadowalającą dokładnością, wystarczającą do jakościowej oceny zjawisk zachodzących w przepływach dwufazowych.

Literatura

[1] Chałubiec J., Rząsa M.R., Dobrowolski B.: Application of image tomography for determination of gas flow parameters in aeration process. 5th International Symposium on Process Tomography in Poland, 25–26 August Zakopane 2008.
[2] Dehghani H., Srinivasan S., Pogue B.W, Gibson A.: Numerical modeling and image reconstruction in diffuse optical tomography. Philosophical Transactions of The Royal Society A 367/2009, 3073–3093.
[3] Dugdale P., Green R.G., Hartley A.J., Jackson R.G., Landauro J.: Characterisation of Single Bubbles by an Optical Tomographic System. Conference of Workshop on Process Tomography, Karlsruhe 1993.
[4] Dugdale P., Green R.G., Hartley A.J., Jackson R.G., Landauro J.: Optical sensors for process tomography. Computational Mechanics Publications 1993.
[5] Halliday D., Resnick R., Walker J.: Podstawy fizyki, Tom 4, PWN Warszawa 2007.
[6] Kawaguchi T., Akasaka Y., Maeda M.: Size measurements of droplets and bubbles by advanced interferometric laser imaging technique. Measurement Scince and Technology. Institute of Physics Publishing 13/2002, 308–315.
[7] Rząsa M.R.: Metoda wyznaczania kształtu pęcherzyków powietrza poruszających się w przepływie dwufazowym gaz-ciecz z wykorzystaniem tomografu optycznego. Inżynieria i Aparatura Chemiczna, 2/2010, 109–110.
[8] Rząsa M.R., Pląskowski A.: Application of Optical Tomography for Measurements of Small Gas Flows 3rd World Congress on Industrial Process Tomography, Banff, Canada 2003.
[9] Rząsa M.R., Pląskowski A.: Application of optical tomography for measurements of aeration parameters in large water tanks. Measurement Scince and Technology, Institute of Physics Publishing 14(2)/2003, 199–204.
[10] Rząsa M.R., Sawicki J.: Pomiar ilości gazu wydzielającego się z mas formiarskich, Pomiary Automatyka Kontrola 6/2003.
[11] Rząsa M.R.: Selection of parameters of the optical tomograph applied for tests of gas bubble shapes, Chemical and Process Engineering, 35(1)/2014, 19–33.
[12] Rząsa M.R.: The Optical Tomograph for Tests of Dust Concentration Distribution; 2nd International Symposium on Process Tomography in Poland 2002. Wroclaw 11th -12th September 2002.
[13] Rząsa M.R.: Zastosowanie tomografii obrazowej do pomiaru parametrów poruszających się pęcherzyków gazu - algorytm rekonstrukcji. Przegląd Elektrotechniczny 9a/2011, 116–120.
[14] Rząsa R. M.: Ocena możliwości zastosowania tomografii optycznej w badaniu dwufazowych procesów przepływowych, Monografia, Polska Akademia Nauk, Katowice 2011.

Dr hab. inż. Mariusz R. Rząsa
e-mail: m.rzasa@po.opole.pl

Absolwent Wydziału Elektrycznego Politechniki Opolskiej o specjalności Automatyka i metrologia elektryczna. Zatrudniony w Katedrze Techniki Cieplnej i Aparatury Przemysłowej Politechniki Opolskiej. Posiada stopień doktora o specjalności Budowa i Eksploatacja Maszyn. Habilitację uzyskał na Wydziale Inżynierii Mechanicznej i Informatyki, Politechniki Częstochowskiej. Prace naukowe prowadzi z zakresu pomiaru przepływów dwufazowych.

Mgr inż. Ewelina Podgórni
e-mail: e.podgorni@po.opole.pl

Absolwentka Wydziału Mechanicznego Politechniki Opolskiej, o kierunku Inżynieria środowiska - gospodarka wodno-ściekowa. Zatrudniona w Katedrze Techniki Cieplnej i Aparatury Przemysłowej Politechniki Opolskiej. Prace naukowe prowadzi z zakresu sedymentacji zawiesin pokoagulacyjnych.

otrzymano/received: 20.09.2016 *przyjęto do druku/accepted: 15.02.2017*